U. Chandrasekhar
Lung-Jieh Yang
S. Gowthaman   *Editors*

Innovative Design, Analysis and Development Practices in Aerospace and Automotive Engineering (I-DAD 2018)

Volume 1

Springer

Lecture Notes in Mechanical Engineering

Lecture Notes in Mechanical Engineering (LNME) publishes the latest developments in Mechanical Engineering—quickly, informally and with high quality. Original research reported in proceedings and post-proceedings represents the core of LNME. Volumes published in LNME embrace all aspects, subfields and new challenges of mechanical engineering. Topics in the series include:

- Engineering Design
- Machinery and Machine Elements
- Mechanical Structures and Stress Analysis
- Automotive Engineering
- Engine Technology
- Aerospace Technology and Astronautics
- Nanotechnology and Microengineering
- Control, Robotics, Mechatronics
- MEMS
- Theoretical and Applied Mechanics
- Dynamical Systems, Control
- Fluid Mechanics
- Engineering Thermodynamics, Heat and Mass Transfer
- Manufacturing
- Precision Engineering, Instrumentation, Measurement
- Materials Engineering
- Tribology and Surface Technology

To submit a proposal or request further information, please contact: Dr. Leontina Di Cecco Leontina.dicecco@springer.com or Li Shen Li.shen@springer.com.

Please check the Springer Tracts in Mechanical Engineering at http://www.springer.com/series/11693 if you are interested in monographs, textbooks or edited books. To submit a proposal, please contact Leontina.dicecco@springer.com and Li.shen@springer.com.
Indexed by SCOPUS.

More information about this series at http://www.springer.com/series/11236

U. Chandrasekhar · Lung-Jieh Yang
S. Gowthaman
Editors

Innovative Design, Analysis and Development Practices in Aerospace and Automotive Engineering (I-DAD 2018)

Volume 1

🐴 Springer

Editors
U. Chandrasekhar
Vel Tech Rangarajan Dr. Sagunthala R&D
   Institute of Science and Technology
Avadi, Chennai, India

S. Gowthaman
Vel Tech Rangarajan Dr. Sagunthala R&D
   Institute of Science and Technology
Avadi, Chennai, India

Lung-Jieh Yang
Department of Mechanical and
   Electromechanical Engineering
Tamkang University
Tamsui District, New Taipei City, Taiwan

Preface

Designs and developments are the aspirations of tomorrow's technologies for aero and auto industries to be alive in the competitive world, where cost-effective solutions, improvements in a greenhouse environment, longevity/life cycle, eco-friendly materials and manufacturing, certification and government legislation demands are becoming stringent. Whether aerospace or automotive, the pulse and echo are similar in meeting the expected performances in the air or on the road, respectively. Both the industries have come to symbolise the essence of a modern industrial society. Perhaps more than any other single icon, it is associated with a desire for independence and freedom of movement—an expression of economic status. For the next decades, they are marching towards new concept designs, analysis and manufacturing technologies, where more swing is for improved performance through specific and/or multifunctional linguistic design aspect to downsize the system; improve the weight-to-strength ratio, fuel efficiency; make better the operational capability at room and elevated temperatures; reduce wear and tear, NVH aspects while balancing the challenges of beyond Euro IV emission norms, greenhouse effects and recyclable materials. The conference covered the areas such as additive manufacturing, aerodynamics, CAD, CFD, design engineering, environment, finite element method, fuels and energy source, integration of analysis and expected results, life cycle engineering, manufacturing, materials, MDO techniques, modelling of materials, optimisation technologies, propulsion systems, quality, reliability and durability, sensors and health monitoring, simulations, 3D scanning and re-engineering, and 3D printing. The conference aimed at addressing these issues of tomorrow where academia–industry–R&D partnerships and collaborative programs can be shared and implemented. The organisers of the 3rd International Conference on Innovative Design, Analysis and Development Practices in Aerospace and Automotive Engineering (I-DAD 2018) wish to provide

a platform for deliberations on design engineering, numerical methods, analysis/optimisation techniques, life cycle engineering, system engineering, configuration management, advanced materials, novel manufacturing/prototyping, vibration and health monitoring, propulsion system and quality and reliability in the aerospace and automotive fields. The response to the conference was overwhelming on both national and international fronts.

Chennai, India   U. Chandrasekhar
                                                                          Lung-Jieh Yang
                                                                          S. Gowthaman

Contents

About the Editors

Dr. U. Chandrasekhar is Pro Vice Chancellor of Vel Tech Rangarajan Dr. Sagunthala R&D Institute of Science and Technology, Chennai. He was Director of the Engineering Staff College of India (ESCI), an autonomous organ of the Institution of Engineers (India), and prior to that, he was Additional Director at the Gas Turbine Research Establishment, a Ministry of Defence R&D Organization. For the past 26 years, he has been involved in design, analysis, prototyping, rapid manufacturing and testing of aero gas turbine engines. He has set up the first-ever rapid prototyping laboratory in the country. He has received a commendation medal from the scientific advisor to the defence minister in recognition of his research efforts. He received his B.E. in mechanical engineering from NIT, Surathkal; M.Tech. in design stream from IIT Madras; and Ph.D. from VTU. For his academic excellence at IIT Madras, he received an award from the former President of India, Dr. A. P. J. Abdul Kalam. He trained RP and sensor technologies in Germany, UK and Belgium. He is currently leading a critical technology development project on high-temperature thin film sensors in collaboration with NRC, Canada. He serves on the Council of the Institution of Engineers and National Design and Research Forum. He was also chosen to represent India in the Young Leaders Convention of World Federation of Engineering Organisations at Geneva. He has been invited by several national and international professional bodies as the keynote speaker on advanced prototyping and sensor technologies.

Dr. Lung-Jieh Yang received his M.S. from the Tamkang University, Taiwan, in 1991 and Ph.D. from the Institute of Applied Mechanics, National Taiwan University, in 1997. He was Visiting Associate of Electrical Engineering, Caltech, USA, from 2000 to 2001. He is currently Professor in the Department of Mechanical and Electromechanical Engineering and Director of the Instrument and Experiment Center at the Tamkang University. He is also Member of IEEE and AIAA. His current research interests include flapping micro aerial vehicles (MAVs)

and gelatin MEMS technology. His research areas are polymer composites, nano-materials, high-temperature foams, experimental mechanics, sensors for health monitoring and energy harvesting.

Dr. S. Gowthaman is Director of R&D at Vel Tech Rangarajan Dr. Sagunthala R&D Institute of Science and Technology and Associate Professor in the Department of Mechanical Engineering. He received his B.E. in mechanical engineering from Bharathidasan University (Shanmugha College of Engineering) and M.S. and Ph.D. in mechanical engineering from North Carolina A&T State University, USA. His research activities include polymer-based composite materials, experimental mechanics, nano-engineering and advanced materials providing solutions for structural and material needs in various applications. Before joining Vel Tech University in 2013, he worked at Nanyang Technological University (NTU), Singapore, and the Center for Aviation Safety (CAS) at NC A&T State University, USA. He has worked in research projects sponsored by various agencies like NASA (USA), United States Army (USA), ONR (USA), Wright Materials Research (USA), DSTA (Singapore), DST-SERB (India), DRDO-ERIPR (India) and DST-TDT (India). He has collaborated and is collaborating with a number of national and international institutes and research laboratories. He has published more than 30 research papers in international journals and conference proceedings. He is a member of several committees and societies including AIAA Materials Technical Committee, USA, and serves as a reviewer for various journals, including *Composites Part A, Journal of Reinforced Plastics and Composites, AIAA Journal* and *IE Springer Journal*, and is a member of the editorial boards for international conferences like I-DAD and ICAM-3D. He has received several awards from NC A&T State University, USA, and Bharathidasan University for his academic and research achievements, including a NTU (Singapore) Post-Doctorate Fellowship and DST-SERB (India) Early Career Research Project Award.

Performance Analysis of Semi-active Suspension System Based on Suspension Working Space and Dynamic Tire Deflection

Jaydeep Funde, K. P. Wani, N. D. Dhote and S. A. Patil

1 Introduction

Passive suspension does not meet ride comfort and stability over a broad range of road disturbances due to constant damping coefficient. In semi-active suspension system, value of damping coefficient changes which depends on control strategy implemented. So, in semi-active suspension, ride comfort and vehicle stability can be achieved in a wide range of frequency. Design and development of control strategies are according to the application like for city driving, off-road riding, or track racing. There are various control strategies available such as skyhook, groundhook, hybrid, fuzzy, neural network, and H-infinity [1–3].

Patil and Wani [1] designed and analyzed the semi-active suspension system models using skyhook, groundhook, and hybrid control method. The two degree of freedom (2 DOF) quarter car model is used for analysis of vehicle body displacement, vehicle acceleration and suspension working space, and dynamic tire deflection. Simulation of semi-active control models is carried out in MATLAB Simulink which describes performance of passive system, skyhook on-off and continuous control, groundhook control, and hybrid control methods. Time response analysis shows that skyhook on-off control improves ride comfort by

J. Funde (✉) · N. D. Dhote
COEP-ARAI, Pune, India
e-mail: jaydeep.funde111@gmail.com

N. D. Dhote
e-mail: ndd.mech@coep.ac.in

K. P. Wani · S. A. Patil
ARAI Academy, Pune, India
e-mail: wani.pga@araiindia.com

S. A. Patil
e-mail: sapatil.pga@araiindia.com

الزارة للاستشارات

reducing maximum peak-to-peak body displacement. While groundhook control improves vehicle stability by reducing maximum peak-to-peak wheel displacement and dynamic tire deflection. The hybrid control improves ride comfort as well as road stability depending upon the controller gain.

Li Jun et al. [4] investigated passive suspension with and without dynamic absorber, semi-active suspension using fuzzy control, and fuzzy neural network control by computer simulation. It is indicated that the semi-active suspension system employing the FNN control strategy proposed in this paper is more effective in improving the performance of vehicle, and also dynamic absorber reduces the excessive vibration of the wheel mass by a great amount.

Rasal et al. [5] implemented continuous control strategy using fuzzy logic for semi-active suspension and found to provide better overall performance with 22.1% reduction in body displacement and 11.66% reduction in suspension working space. Also, fuzzy logic control retained its stability over whole frequency range.

2 Quarter Car Model

These semi-active control models such as skyhook on-off, groundhook, hybrid and fuzzy control models are designed for a quarter car model. Time response analysis has been carried out in Simulink, and results are compared for better understanding of various semi-active control models for a vehicle.

Figure 1 illustrates the two degree of freedom (2 DOF) system that represents the quarter car suspension model. By applying Newton's second law to the quarter car vehicle model, the equation of motion of sprung mass and unsprung mass are [1].

$$M_b \ddot{x}_b + K_s(x_b - x_w) + f = 0 \tag{1}$$

$$M_w \ddot{x}_w - K_s(x_b - x_w) + K_t(x_w - x_r) - f = 0 \tag{2}$$

Fig. 1 Quarter car suspension model
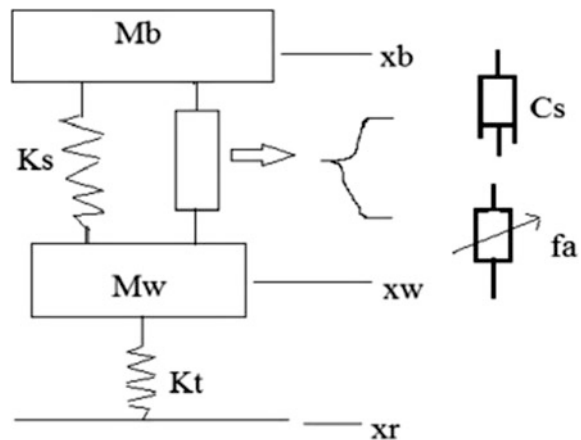
Table 1 Suspension parameters

Parameter	Symbol	Value (Unit)
Sprung mass	M_b	365 (kg)
Unsprung mass	M_w	40 (kg)
Suspension stiffness	K_s	19,960 (N/m)
Tire stiffness	K_t	175,500 (N/m)
Damping coefficient	C_s	1290 (Ns/m)

$$f = \begin{cases} C_s(\dot{x}_b - \dot{x}_w) \\ f_a \end{cases} \tag{3}$$

where

M_b = vehicle body mass (sprung mass)
M_w = tire mass (unsprung mass)
x_b = body displacement
x_w = tire displacement
x_r = excitation due to road disturbance
K_s = suspension spring stiffness
K_t = tire spring constant
f = damping force generated.

Damping force generated (f) by damper depends upon the control strategy implemented out of skyhook, groundhook, hybrid and fuzzy control strategy.

For quarter car system analysis, the following parameters are used in a simulation [1] (Table 1).

2.1 Road Inputs

Two types of road excitation are used for simulation purpose.

2.1.1 Bump Input

For this road input, bump of 70 mm amplitude at three different frequencies of 0.5, 2.5, and 11 Hz is considered for simulation. Bump excitation equation is as follow [1] (Fig. 2)

$$x_r = \begin{cases} a\{1 - \cos(w_r(t))\}, & \text{for } 0 \le t \le d_b/V_c \\ 0, & \text{otherwise} \end{cases} \tag{4}$$
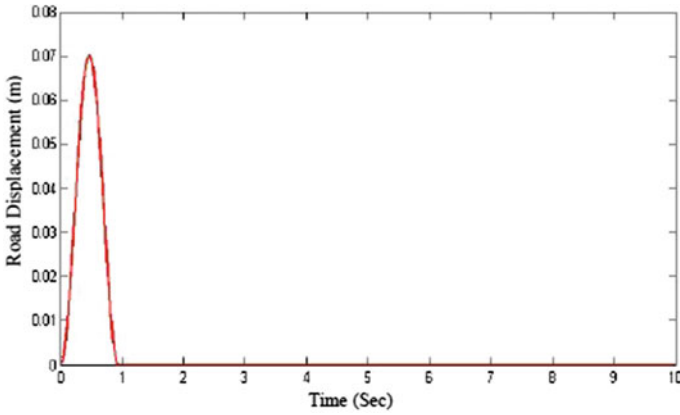
Fig. 2 Bump input

where

a = half of the bump amplitude
w_r = angular velocity
d_b = bump width
V_c = vehicle velocity.

2.1.2 Sine Wave Input

The second road excitation is given as a sine wave for 10 s of 1 mm amplitude. The analysis is carried out for three different frequencies at 0.5, 2.5, and 11 Hz. The ride comfort is critical in frequency range 0–5 Hz, and vehicle stability is critical at 11 Hz therefore the simulation is done for mentioned frequencies.

3 Control Strategies of Semi-active Suspension

3.1 Skyhook Control

In skyhook control strategy, damping value changes between maximum and minimum value only. In this, if the relative velocity of the body with respect to the wheel is in the same direction as that of the body velocity, then a maximum damping is applied otherwise minimum damping for opposite direction [6].

The damping value changes according to following logical rule as [1].

$$C_{sa} = \begin{cases} C_{max}, & \text{If} \quad \dot{x}_b * (\dot{x}_b \dot{-} \dot{x}_w) \geq 0 \\ C_{min}, & \text{else} \quad \dot{x}_b * (\dot{x}_b \dot{-} \dot{x}_w) < 0 \end{cases} \tag{6}$$

3.2 Groundhook Control

Similar to skyhook control, the damping value switches between high and low values in the groundhook control. The groundhook differs with skyhook in damping location as it provides damping to unsprung mass. The logical rule on which it works is as follows [1, 2]

$$C_{sa} = \begin{cases} C_{max}, & \text{If} \quad -\dot{x}_w(\dot{x}_b \dot{-} \dot{x}_w) \geq 0 \\ C_{min}, & \text{else} \quad -\dot{x}_w(\dot{x}_b \dot{-} \dot{x}_w) < 0 \end{cases} \tag{7}$$

This control strategy is mainly used for improvement of vehicle handling.

3.3 Hybrid Control

Hybrid control strategy is a combination of skyhook and groundhook which takes advantage of both. As per the controller gain, damping of body and tire varies. The controller logic is expressed as follows [1]

$$\begin{aligned} \dot{x}_b(\dot{x}_b - \dot{x}_w) \geq 0 \quad & \sigma_{sky} = \dot{x}_b \\ \dot{x}_b(\dot{x}_b - \dot{x}_w) < 0 \quad & \sigma_{sky} = 0 \end{aligned} \tag{8}$$

$$\begin{aligned} -\dot{x}_w(x_b - x_w) \geq 0 \quad & \sigma_{ground} = \dot{x}_w \\ -\dot{x}_b(x_{\dot{b}} - x_{\dot{w}}) < 0 \quad & \sigma_{ground} = 0 \end{aligned} \tag{9}$$

$$f_{sa} = G[\alpha * \sigma_{sky} + (1 - \alpha)\sigma_{gnd}] \tag{10}$$

where

σ_{sky} = skyhook components of the damping force
σ_{gnd} = groundhook components of the damping force
α = relative ratio between the skyhook and groundhook control.
G = damping coefficients of the skyhook and groundhook dampers, which are assumed equivalent as:
$C_{sky} = C_{ground} = G$.

3.4 Fuzzy Logic Control

For development of fuzzy logic controller, "fuzzy logic controller" toolbox with rule viewer is used. The relative displacement and the relative velocity between the body and the wheel are taken as the input to the fuzzy logic controller toolbox. The output is the fuzzy logic damping coefficient. The trapezoidal membership function has been used for the input and the output parameters. Mamdani method is used for the process of fuzzification. The centroid method is used for the process of defuzzification. The membership function for the input parameters is as shown in Figs. 3, 4, 5, and 6.
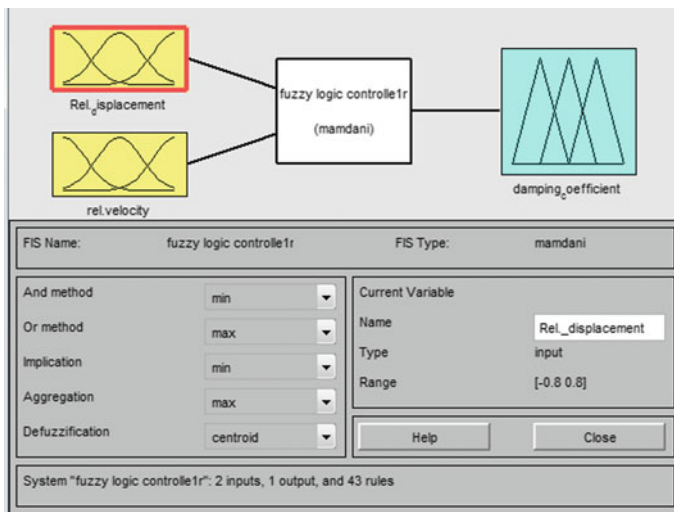
Fig. 3 Input and output variables for Fuzzy-based car suspension model
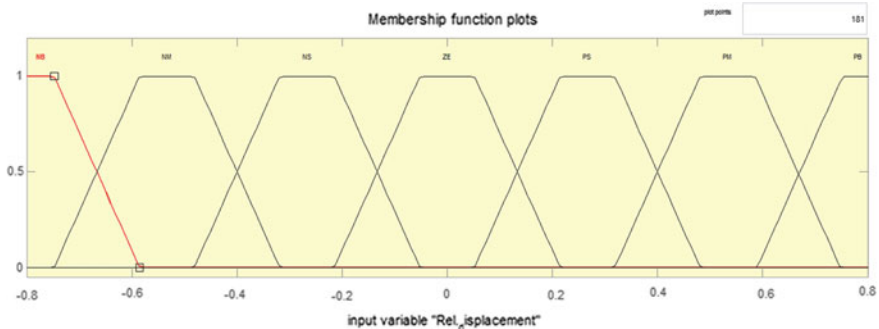
Fig. 4 Membership functions for relative displacement
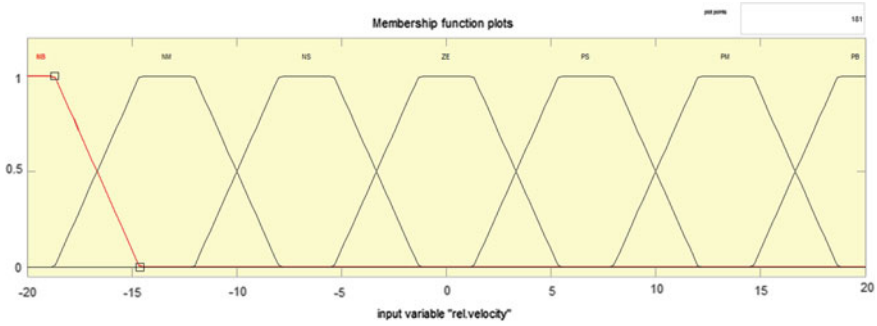
Fig. 5 Membership functions for relative velocity
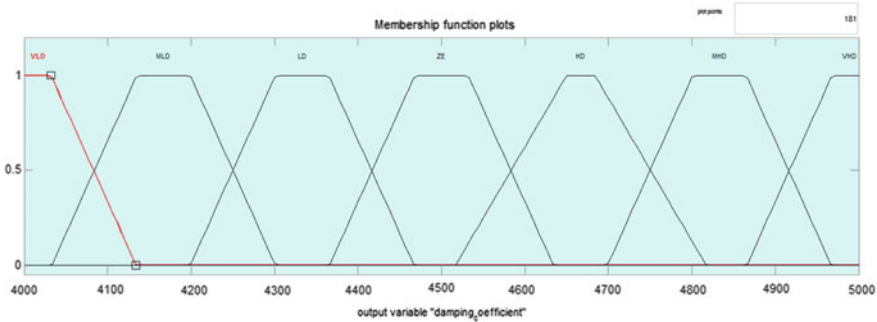
Fig. 6 Membership functions for damping coefficient

"Relative Dis."—negative big (NB), negative medium (NM), negative small (NS), zero (ZE), positive small (PS), positive medium (PM), positive big (PB). The same membership functions were used for "Relative Vel." with a different range.

"Damping"—very low density (VLD), medium low density (MLD), low density (LD), median (ZE), high density (HD), medium high density (MHD), very high density (VHD).

Fuzzy logic works similar to human brain which learns things by itself after some inputs. So total 43 rules are applied as shown in Table 2 by which fuzzy controller develops the relation between input and output.

4 Simulation Results and Discussion

The simulation of four control strategies, namely skyhook, groundhook, hybrid, and fuzzy along with passive suspension has been done for 10 s. The simulation is done for two road profiles at three different frequencies (0.5, 2.5, and 11 Hz). The results

Table 2 Rule set

		Xs–Xus						
		NB	NM	NS	ZE	PS	PM	PB
Xs′–Xus′	NB	VHD	VHD	VHD	VHD	LD	MLD	VLD
	NM	MHD	MHD	MHD	MHD	ZE	LD	LD
	NS	HD	HD	HD	HD	ZE	VLD	VLD
	ZE	*	*	*	ZE	*	*	*
	PS	VLD	MLD	LD	HD	HD	MHD	VHD
	PM	VLD	MLD	ZE	VHD	MHD	MHD	VHD
	PE	MLD	LD	ZE	VHD	VHD	VHD	VHD

of all control strategies are compared with passive suspension based on body displacement, wheel displacement, suspension working space, and dynamic tire deflection responses as shown in Figs. 7, 8, 9, and 10.

The damping force generated by each control strategy is shown in Fig. 11. The nature and damping values will be useful for damper design.

From Tables 3 and 4, skyhook control gives less peak-to-peak body displacement, less settling time, and less suspension working at frequencies 0.5 and 2.5 Hz, so skyhook control strategy gives good ride comfort for lower frequencies which are critical for ride comfort.

Fuzzy logic control strategy gives optimized performance for ride comfort and vehicle stability at all frequencies. Fuzzy logic gives less body displacement, less suspension working space, less settling time and less dynamic tire deflection, majorly for low frequencies.
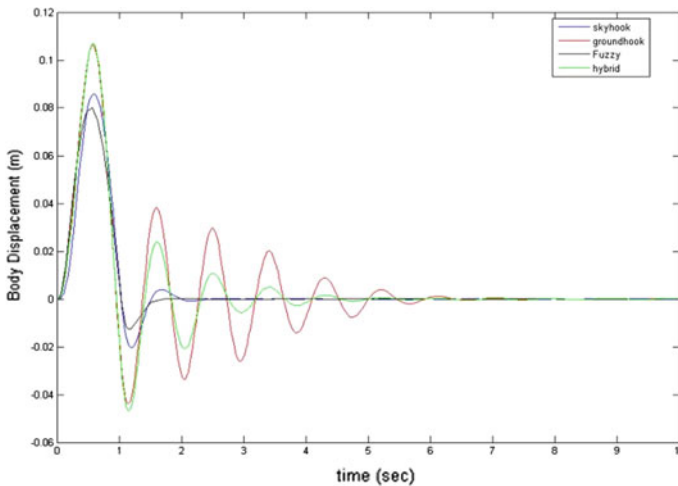
Fig. 7 Body displacement
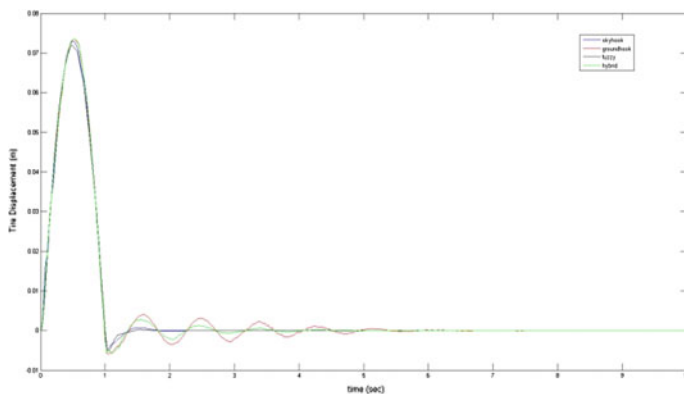
Fig. 8 Tire displacement
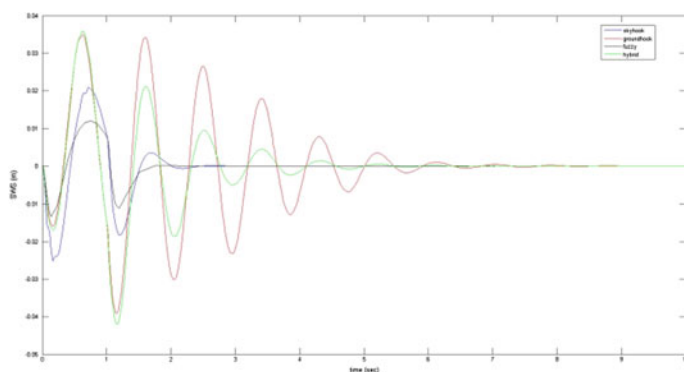
Fig. 9 Suspension working space (SWS)
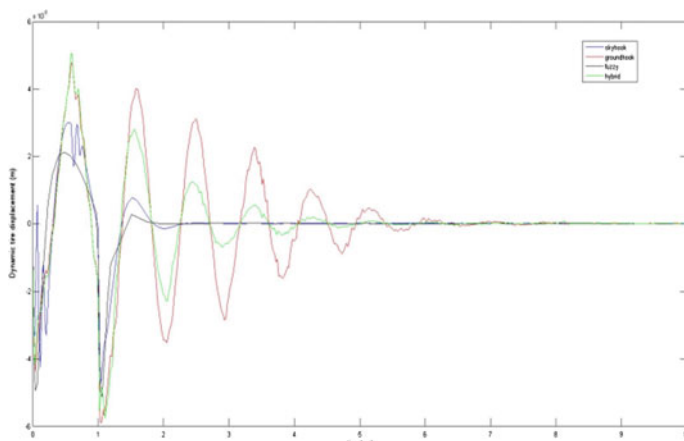
Fig. 10 Dynamic tire deflection
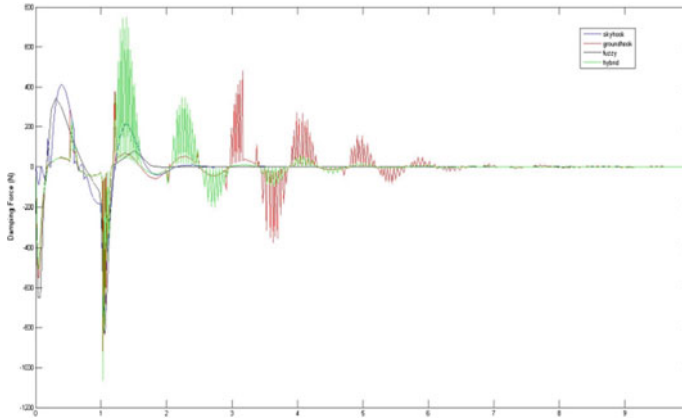
Fig. 11 Damping coefficient

Table 3 Results @0.5 Hz for bump input

	Passive	Skyhook	Groundhook	Hybrid	Fuzzy
Body displacement (m) (peak-to-peak)	0.138	0.105	0.144	0.156	0.092
Tire displacement	0.078	0.075	0.07	0.08	0.074
Suspension working space	0.084	0.045	0.075	0.075	0.0275
Dynamic tire displacement	0.013	0.008	0.011	0.0108	0.0056
Damping force (N)	220 and −450	400 and −700	500 and −800	250 and −1300	380 and −600
Settling time (s)	4.8	2.5	6	6.8	1.8

Table 4 Results @2.5 Hz for bump input

	Passive	Skyhook	Groundhook	Hybrid	Fuzzy
Body displacement (m) (peak-to-peak)	0.075	0.022	0.095	0.087	0.069
Tire displacement	0.075	0.09	0.074	0.072	0.075
Suspension working space	0.114	0.106	0.103	0.1	0.10
Dynamic tire displacement	0.030	0.041	0.043	0.045	0.047
Damping force (N)	1600 and −1700	2900 and −3000	3000 and −2000	3500 and −2500	3000 and −2500
Settling time (s)	4	1.4	3.6	3.4	2

Table 5 Results @11 Hz for bump input

	Passive	Skyhook	Groundhook	Hybrid	Fuzzy
Body displacement (m) (peak-to-peak)	0.02	0.001	0.026	0.02	0.021
Tire displacement	0.106	0.16	0.0585	0.0602	0.066
Suspension working space	0.110	0.163	0.07	0.068	0.072
Dynamic tire displacement	0.126	0.163	0.11	0.11	0.11
Damping force (N)	4500 and −3800	9500 and −7400	6000 and −6000	6100 and −5700	6100 and −5900
Settling time (s)	3.5	1	3.5	2.8	1.2

Table 6 Results @2.5 Hz for Sine wave input

	Passive	Skyhook	Groundhook	Hybrid	Fuzzy
Body displacement (m) (peak-to-peak)	0.048	0.04	0.09	0.104	0.102
Tire displacement	0.132	0.156	0.14	0.14	0.14
Suspension working space	0.162	0.154	0.164	0.113	0.158
Dynamic tire displacement	0.0250	0.038	0.051	0.06	0.055
Damping force (N)	1700 and −1700	3100 and −3100	3800 and −3800	4800 and −4800	3400 and −3200

As suspension working space is reduced, less space is required for suspension mounting so as CG of vehicle reduces which gives good vehicle handling. Fuzzy logic gives the fastest response among all control strategies which are simulated.

From Tables 3, 4, and 5, it is clear that groundhook control strategy works better for vehicle stability at higher frequencies where vehicle stability is critical, but it gives least ride comfort at all frequencies. Hybrid control strategy gives the ride comfort and vehicle stability in between skyhook and groundhook (Table 6).

5　Conclusion

Ride comfort is critical at lower frequencies (up to 5 Hz). Skyhook control strategy improves ride comfort as compared to passive suspension by reducing peak-to-peak body displacement. Skyhook control reduces body displacement by 23.91%, suspension working space by 46%, and settling time by 48%. So for the application

where ride comfort is a design criterion, skyhook control can be used. Vehicle handling mainly depends on road holding of tire, and vehicle stability is critical in the higher frequency range (11 Hz and above).

Groundhook control gives better results for vehicle stability compared to passive system, reducing tire displacement, dynamic tire displacement, and suspension working space by 43.45, 12.7, and 38.18%, respectively. As suspension working space is reduced, less space is required for suspension mounting so as CG of vehicle reduces which gives good vehicle handling.

Hybrid control is combination of skyhook and groundhook, so depending on controller gain, ride comfort and vehicle stability can be varied. For controller gain of 0.9, hybrid control reduces tire displacement, suspension working space, and dynamic tire displacement by 43.4, 38.18, and 12.7%, respectively.

Fuzzy logic control strategy gives optimized performance for ride comfort and vehicle stability at all frequencies. Fuzzy logic gives less body displacement, less suspension working space, less settling time, and less dynamic tire deflection, mostly for low frequencies. It reduces body displacement, tire displacement, dynamic tire deflection, and suspension working space by 8, 37.73, 12.7, and 34.5%. The settling time for fuzzy is least among the all control strategies used for simulation.

Appendix

See Figs. 12, 13, 14, 15, 16, and 17.
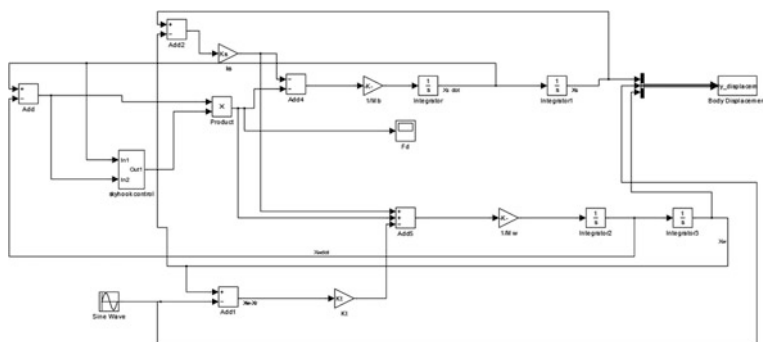
Fig. 12 Skyhook Simulink model
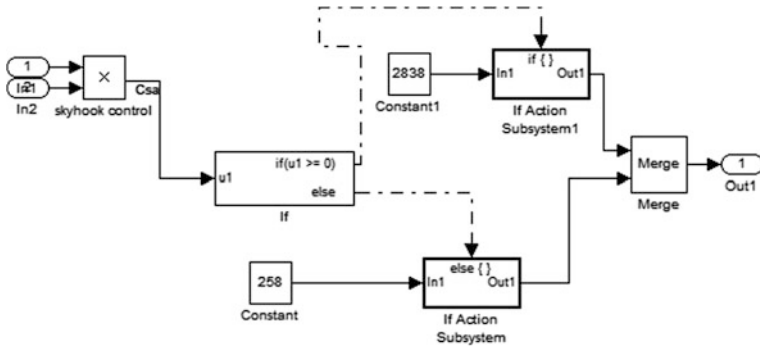
Fig. 13 Subsystem of skyhook controller
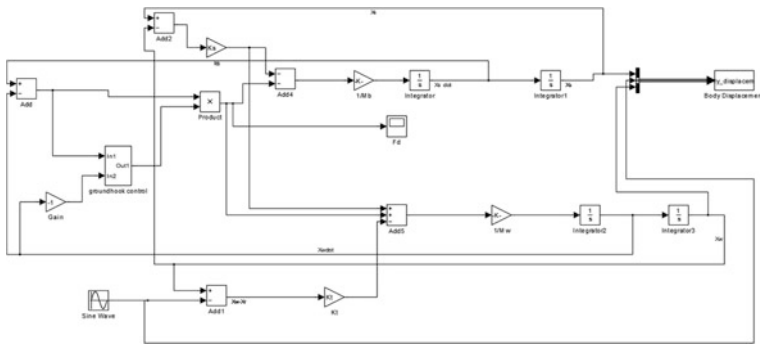
Fig. 14 Groundhook Simulink model
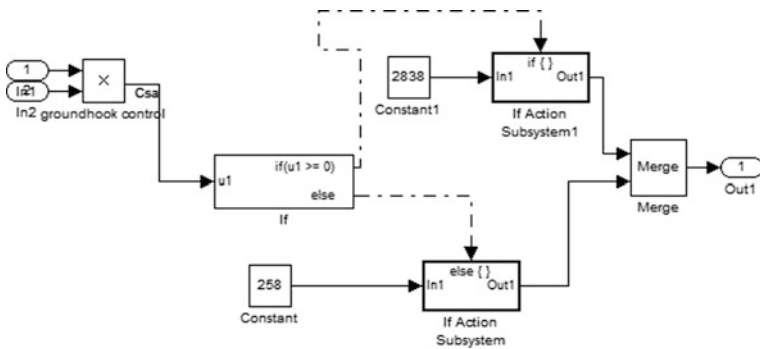
Fig. 15 Subsystem of groundhook controller
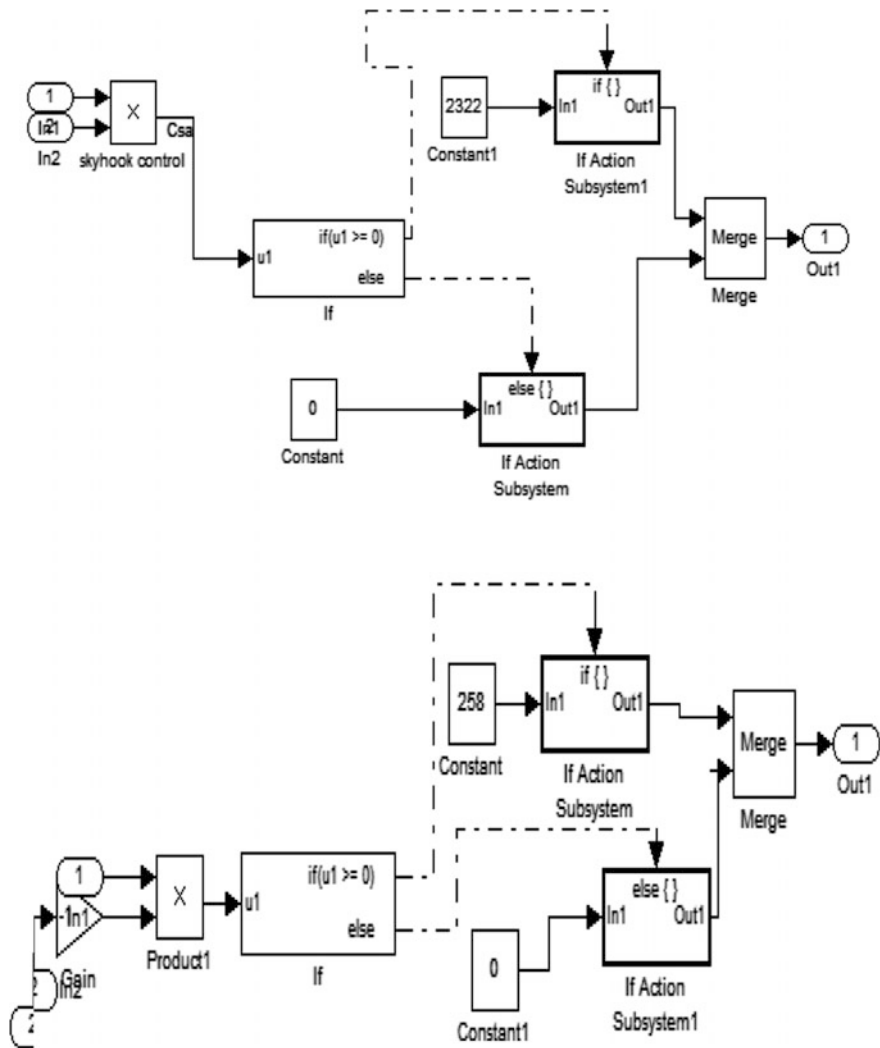
Fig. 16 Subsystem of hybrid controller strategy
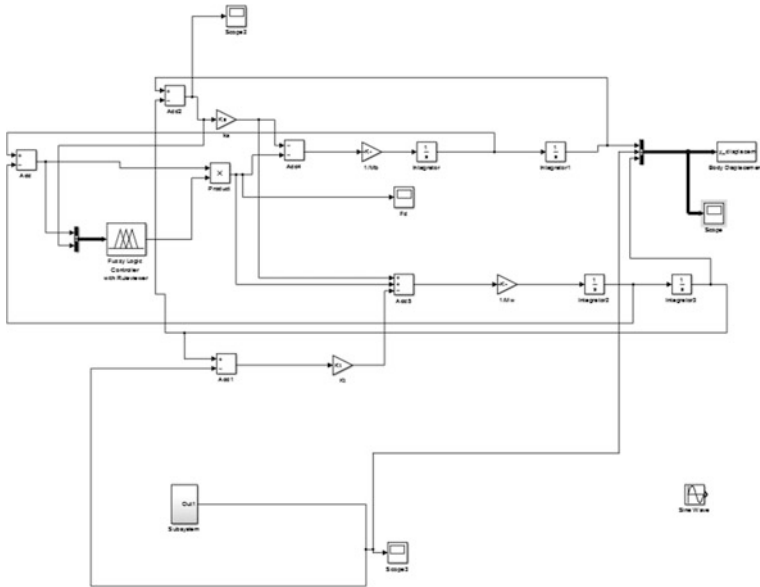
Fig. 17 Simulink model of Fuzzy controller

References

1. Patil, I., Wani, K.: Design and analysis of semi-active suspension using skyhook, ground hook and hybrid control models for a four wheeler. SAE technical paper 2015-26-0084, 2015. https://doi.org/10.4271/2015-26-0084
2. Saravesi, S.M., et al.: Semi-active Suspension Control Design for Vehicles. Elsevier, BH publications
3. Guglielmino, E., et al.: Semi-active Suspension Control. Springer
4. Liu, W., Shi Sr, W.: Kinematics analysis and optimization design of semi-active suspension for a light bus. SAE technical paper 2011-01-0090. https://doi.org/10.4271/2011-01-0090
5. Rasal, S., Wani, K., et al.: Implementation of fuzzy logic control in semiactive suspension for a vehicle using MATLAB SIMULINK. SAE technical paper 2016-28-0035, 2016. https://doi.org/10.4271/2016-28-0035
6. Desikan, A., Kalaichelvi, V.: Design for a Preview Control of Semi-Active Suspension System using Fuzzy-Logic and Image Processing techniques. Birla Institute of technology and Science, Pilani, Dubai
7. Burke W.C.T.: Large force range mechanically adjustable dampers for heavy vehicle applications. M.S. thesis, Dept. Mech. Engg., Virginia Polytechnic Institute and state University, Blacksburg, Virginia, (2010)
8. Rashid, M.M., et al.: Analysis and experimental study of magnetorheological based damper for semiactive suspension system using fuzzy hybrids. IEEE (2011). (William C.T)
9. Dixon, J.C.: The Shock Absorber Handbook, 2nd edn. Wiley-Professional Engineering Publishing (1999)

Study on Wear Behavior of Al-Based Hybrid Metal Matrix Composites Reinforced with Al$_2$O$_3$/SiC Particles

H. P. Raturi, Lalta Prasad, M. Pokhriyal and A. Kumar

1   Introduction

Metal matrix composites (MMCs) and hybrid metal matrix composites (HMMCs) are manufactured using different techniques. These techniques could be classified as liquid-phase (casting) processes, vacuum infiltration, and pressureless infiltration and dispersion methods [1–4]. The sintering powder metallurgy (PM) and compo-casting and semi-solid forming are used in solid-state processes and liquid–solid processes, respectively [5 and 6]. PM techniques are extensively used in the manufacture of particle MMC. Metal matrix composites are obtained by adding hard particles such as Al$_2$O$_3$ and SiC into Al alloys to achieve improved mechanical properties. These composites are used as cutting tools, bearing parts, and medical rigs. Many methods have been developed in the past to add more reinforcement particles into the pure aluminum [7]. Particle-reinforced aluminum composites offer reduced mass, high stiffness and strength and improved wear resistance. The strength of SiC/Al composites with an increase in the volume percentage of ceramic phase, by increasing the strength of the Al matrix and by decreasing the size of the ceramic reinforcement, ductility, nevertheless, diminishes [8]. The wear rate on automobile brake rotor made of A359-20 reinforced with SiC particles was investigated by Daoud and El-khair. They found that the wear rate was decreased

H. P. Raturi
Department of Mechanical Engineering, G.B. Pant Institute of Engineering & Technology, Ghurdauri, Pauri Garhwal 246194, Uttarakhand, India

L. Prasad (✉) · M. Pokhriyal
Department of Mechanical Engineering, National Institute of Technology Uttarkhand, Srinagar (Garhwal) 246174, Uttarakhand, India
e-mail: laltagbpec@gmail.com

A. Kumar
Department of Mechanical Engineering, Feroze Gandhi Institute of Engineering and Technology, Raebareli 229316, Uttar Pradesh, India

with increase in sliding speed for all loading conditions [9]. The wear rate of aluminum alloy (Al-Si10Mg) reinforced with alumina (9%) and graphite (3%) was investigated by Radhika et al. [10]. The influence of applied load, sliding speed, and sliding distance on wear rate was carried out. They found that the sliding distance has the highest influence followed by applied load and sliding speed on the wear rate [10]. The wear rate of the composite material increases with increase in applied load and sliding speed [11]. The wear rate of the composite material (Al-5083) reinforced with B4C particles was reported by Tang et al. [12]. They found that the wear rate was low for composite with higher reinforcement particle [12].

2 Experimental Set-up and Methodology

2.1 Material Selection

The commercial grade aluminum alloy was purchased from M/S Ladhani Metal Corporation Mumbai (India). The reinforcement material used was typically ceramic since it provides a very desirable combination of stiffness, strength, and relatively low density. The composition and properties of Al alloy and reinforcement were obtained from the literature [13].

2.2 Fabrication of HMMCs by Stir Casting Process

Three specimens were fabricated by using different compositions of aluminum alloy matrix reinforced with SiC and Al_2O_3 particles of 400 mesh sizes. Aluminum alloy was reinforced with SiC (1.5, 3, and 4.5 wt%) and Al_2O_3 (1.5, 3, and 4.5 wt%) particles as shown in Table 1. The small ingots of Al6063 were melted in clay graphite crucible using an electric resistance furnace. The magnesium (2 wt%) was added in the liquid metal to achieve a strong bond. The addition of pure magnesium enhanced the fluidity of the molten metal. The SiCp and Al_2O_3p were preheated in muffle furnace at 650 °C for 5 h to make the surface of SiC and Al_2O_3 oxidized for SiC and Al_2O_3. The furnace temperature was raised above the liquidus temperature to melt the alloy completely at 850 °C. The composite slurry was reheated to a fully liquid state, and then automatic mechanical mixing was done for 10 min by stirrer

Table 1 Composition of composites

Composition	Al + SiC + Al_2O_3 (%)	Al + SiC + Al_2O_3 (%)	Al + SiC + Al_2O_3 (%)
Reinforcement (SiC and Al_2O_3) wt%	1.5 + 1.5	3 + 3	4.5 + 4.5

(speed 350 rpm). The molten composite was transferred from the crucible into the mild steel mold (dimension: 160 mm × 50 mm × 50 mm).

2.3 Density and Hardness

The density of fabricated composite material was evaluated by determining the weight fraction of the raw material. The composite material consists of matrix material and filler, and the weight of the composite material is equal to the total sum of weight of the glass fibers, weight of the matrix, and weight of filler. The suffixes *m*, *r,* and ct represent the matrix, filler, and composite material, respectively.

The theoretical density (ρ_{ct}) was determined as per Eq. (1) reported by Agarwal and Broutman [14].

$$\rho_{ct} = \frac{1}{\frac{W_r}{\rho_r} + \frac{W_m}{\rho_m}} \tag{1}$$

ρ indicates the density. The apparent (actual) density (ρ_{ac}) of the different composites using a polymeric matrix can be determined using the liquid displacement method based on the Archimedes' principle. Special care should be taken to avoid the presence of air bubbles. And with the help of theoretical and actual densities of composite material, the volume voids are easily determined. The volume voids were calculated by comparing the theoretical and actual density of composite material, by using Eq. (2).

$$\text{Void content} (\%) = \left[\frac{\rho_{ct} - \rho_{ac}}{\rho_{ct}} \right] \times 100 \tag{2}$$

where ρ_{ct} and ρ_{ac} are theoretical density and actual density of composite laminates, respectively.

The matrix hardness of the composites was measured on metallographic samples using Vickers hardness testing machine (Model: VM50-PC). The samples were tested as per ASTM E92 specifications.

2.4 Sand Abrasion Test Using Taguchi Technique

The samples were prepared as per ASTM G65 standard on three-body sand abrasion wear test machine (supplied by M/s Ducom Instruments, Pune India). The composite specimen was pressed against a rotating wheel with a chlorobutyl rubber tire of specified hardness. The abrasive particles were filled between the rotating rubber wheels and test specimen. The abrasive particle feed rate was 365 g/min.

The tests on samples (size 75 mm × 25 mm × 12 mm) were conducted by varying load time and speed.

2.4.1 Design of Experiment (DOE)

Design-Expert 9 software and L9 array were used in the design of experiments. For the analysis, three parameters and two response factors were used. Thus the whole optimization process is based on design of experiment. The operating conditions or control factors for dry sand abrasion test as per experimental design have been presented in Tables 2 and 3.

Four parameters (composition, load, speed, and time) are used at three levels in accordance with L_9 orthogonal array design. Taguchi factorial experimental approach is used for the analysis. The experimental observations are transformed

Table 2 Control factors sand abrasion test for HMMC

Control factors	Level 1	Level 2	Level 3
A: Composition	Al + SiC (1.5%) + Al$_2$O$_3$ (1.5%)	Al + SiC (3%) + Al$_2$O$_3$ (3%)	Al + SiC (4.5%) + Al$_2$O$_3$ (4.5%)
B: Load (g)	1500	2000	2500
C: Speed (rpm)	100	125	150
D: Time (min)	10	15	20

Table 3 Experimental design for HMMC according to design expert

Run	Factor 1	Factor 2	Factor 3	Factor 4
	A: Composition	B: Revolutions (rpm)	C: Load (g)	D: Time (min)
1	Al + SiC (4.5%) + Al$_2$O$_3$ (4.5%)	150	2000	10
2	Al + SiC (3%) + Al$_2$O$_3$ (3%)	125	2500	10
3	Al + SiC (4.5%) + Al$_2$O$_3$ (4.5%)	100	2500	15
4	Al + SiC (3%) + Al$_2$O$_3$ (3%)	100	2000	20
5	Al + SiC (1.5%) + Al$_2$O$_3$ (1.5%)	150	2500	20
6	Al + SiC (1.5%) + Al$_2$O$_3$ (1.5%)	125	2000	15
7	Al + SiC (3%) + Al$_2$O$_3$ (3%)	150	1500	15
8	Al + SiC (4.5%) + Al$_2$O$_3$ (4.5%)	125	1500	20
9	Al + SiC (1.5%) + Al$_2$O$_3$ (1.5%)	100	1500	10

into a signal-to-noise ratio (*S/N* Ratio) by using Eq. (3). For minimum abrasion wear, the *S/N* ratio should be smaller.

$$S/N \text{ ratio} = -10 \log \frac{1}{n} \left(\sum y^2 \right) \tag{3}$$

where *n* is the number of observations and *y* is the observed data.

3 Results and Discussion

3.1 *Density and Vickers Hardness*

The densities of HMMCs were calculated by using Eq. (1) and same were evaluated by experiments. The void fraction was calculated by using Eq. (3). It was observed that the porosity of the samples with higher filler contents were on higher side. The HMMC with composition of Al + SiC (4.5%) + Al_2O_3 (4.5%) shows the highest porosity (2.09%). The porosity of the HMMCs may be enhenced by various reasons like improper mixing of the filler, evolution of hydrogen, shrinking during solidification and some casting parameters. The Vickers hardness of the HMMC samples was evaluated, and it was observed that the hardness of the composite material increases with the increase in the reinforcement. The maximum hardness (80.1 VH) was observed for composite of Al + SiC (4.5%) + Al_2O_3 (4.5%). This was due to resistance to deformation by adding SiC and Al_2O_3 particles [15].

3.2 *Three-Body Sand Abrasion Wear Test*

Figure 1 shows the effect of the composition and speed on specific wear rate for constant load (1.5 kg) and time (10 min). The specific wear rate (SWR) for the HMMC was evaluated by using the ANNOVA Eq. (4). The specific wear rate decreases with composition and maximum wear rate observed for HMMC (Al + SiC(3%) + Al_2O_3(3%)) at speed of 100 rpm.

$$\begin{aligned} SWR =\ &4.64 + 0.25 \times A[1] + 0.28 \times A[2] + 0.95 \times B[1] - 0.18 \times B[2] \\ &- 0.073 \times C[1] - 0.33 \times C[2] + 0.56 \times D[1] + 0.26 \times D[2] \end{aligned} \tag{4}$$

The effect of composition and load on specific wear rate has been shown in Fig. 2. The speed (100 rpm) and time (10 min) were kept constant during the experiments. The wear rate was minimum for composition of Al + SiC (4.5%) + Al_2O_3 (4.5%) at 2.0 kg load. The main reason for minimum wear rate was proper mixing of the reinforcement, whereas the maximum value of wear rate was

Design-Expert® Software
Factor Coding: Actual
specific wear rate (mm3/Nm ×10-3)

X1 = A: composition
X2 = B: revolutions

Actual Factors
C: load = 1500
D: time = 10
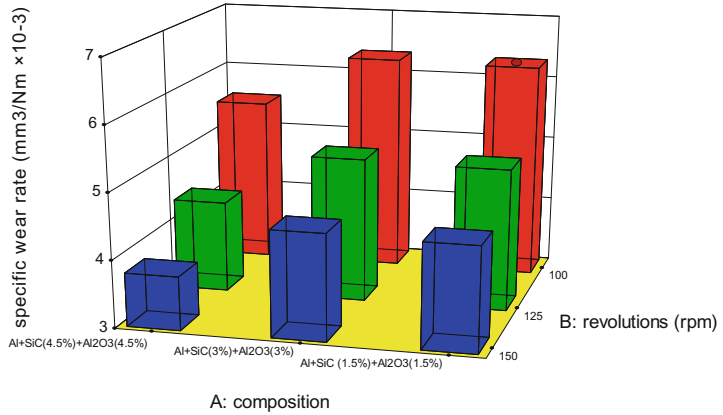
Fig. 1 Effect of compositions and revolutions on specific wear rate

Design-Expert® Software
Factor Coding: Actual
specific wear rate (mm3/Nm ×10-3)

X1 = A: composition
X2 = C: load

Actual Factors
B: revolutions = 100
D: time = 10
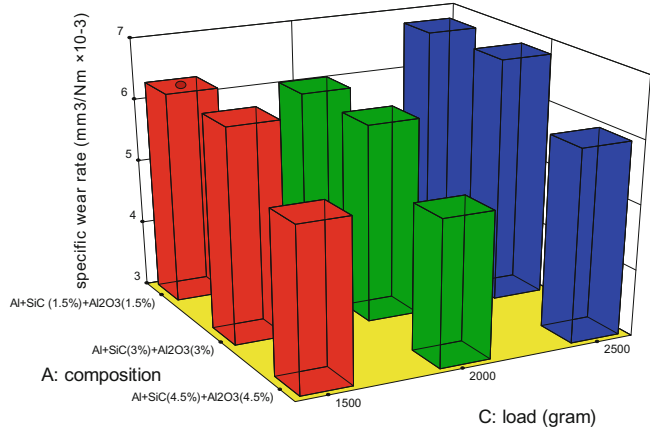
Fig. 2 Effect of composition and load on specific wear rate

observed for composition of Al + SiC (1.5%) + Al$_2$O$_3$ (1.5%) with 2.5 kg load. It was observed that the results for wear rate were similar to the result reported by Unlu [16].

The effect of composition and time on specific wear rate has been shown in Fig. 3. The speed (100 rpm) and load (1.5 kg) were kept constant during the experiments. The wear rate was minimum for composition of Al + SiC

Design-Expert® Software
Factor Coding: Actual
specific wear rate (mm3/Nm ×10-3)
X1 = A: composition
X2 = D: time
Actual Factors
B: revolutions = 100
C: load = 1500
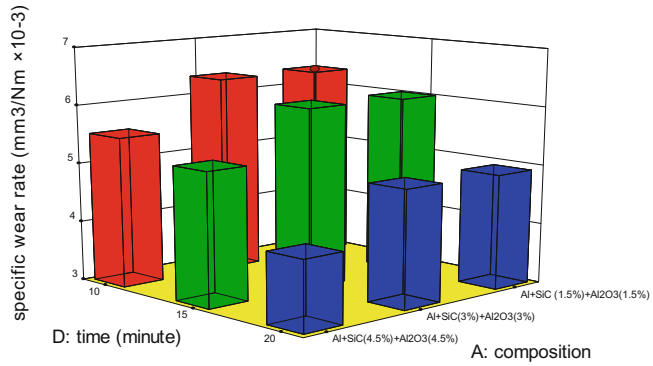
Fig. 3 Effect of composition and time on specific wear rate

$(4.5\%) + Al_2O_3$ (4.5%) at 20 min, whereas the wear rate was maximum for composition of Al + SiC (1.5%) + Al_2O_3 (1.5%) at 10 min.

.

3.3 Effect of Composition and Revolutions on S/N Ratio

The effect of the reinforcement on the material properties was evaluated with help of ANNOVA L_9 array in terms of *S/N* ratio. Equation (5) was used for *S/N* ratio as given below:

$$
\begin{aligned}
\frac{S}{N}\text{ratio} = {} & 45.86 - 0.69 \times A[1] + 0.22 \times A[2] - 0.75 \times B[1] + 0.053 \times B[2] \\
& - 0.25 \times C[1] + 0.55 \times C[2] - 0.20 \times D[1] - 0.43 \times D[2]
\end{aligned} \tag{5}
$$

4 Conclusions

In the present work, experiments were conducted on HMMCs for mechanical properties like abrasive wear rate and hardness. The multi-objective Taguchi optimization technique theory was used in study. The following major points are drawn:

- The HMMCs have better abrasive wear resistance alllloys. Decrease in weight loss within increase in weight percentage of reinforcement indicates higher hardness of composites.

- Higher hardness results in better abrasive wear resistance of the materials. The wear depth decreases with increase in the percentage of SiC in the Al matrix, i.e., wear resistance of the composite increases with increase in SiC content.
- The good interfacial bond was observed between SiC/Al_2O_3 particles and matrix alloy. The wear behavior of particle-reinforced composites mainly depends on the type of interfacial bond between the Al matrix alloy and the reinforcement.
- The major factor that influences the wear behavior of composites is good interfacial bond between the matrix alloy and the reinforcement. A large waer results in the absence of good interfacial bond, fewer than three-body abrasion wear conditions.

References

1. Ibrahim, I.A., Mohamed, F.A., Lavernia, E.J.: Particle reinforced metal matrix composites, a review. Mater. Sci. **26**, 1137–1156 (1991)
2. Cgiou, J.M., Chung, D.D.L.: Characterization of MMC's fabricated by vacuum infiltration of a liquid metal under and inert gas pressure. J. Mater. Sci. **26**, 2583 (1991)
3. Agarwal, B.D., Broutman, L.J.: Analysis and performance of fiber composites USA. Mater. Sci. Eng. A **184**, 1480 (1994)
4. Singh, P.K., Gupta, A., Prasad, L., Kumar, A.: Parametric studies for MRR and TWR using die sinking EDM with electrode of Copper and Brass. Int. J. Advancements Mech. Aeronaut. Eng. **1**(3), 46–50 (2014)
5. Liu, Y.B., Lim, L.S.C., Lu, L., Lai, M.O.: Recent development in the fabrication of metal matrix composites using powder metallurgy techniques. Mater. Sci. **29**, 1999–2007 (1994)
6. Manaba, K., Sumio, S.: Proceedings of second international conference on semi-solid alloys and composites, p. 382 (1992)
7. Gahr, K.H., Schneider, J.: Surface modification of ceramics for improved tribological properties. Ceram. Int. **26**, 363–370 (2000)
8. Bermudez, M.D., Martinez-Nicolas, G., Carrion, F.J.: Dry and lubricated wear resistance of mechanically-alloyed aluminum base sintered composites. Wear **248**, 178–186 (2001)
9. Daoud, A., Abou El-khair, M.T.: Wear and friction behavior of sand cast brake rotor made of A359-20vol% SiC particle composites sliding against automobile friction material. Tribol. Int. **43**, 544–553 (2010)
10. Radhika, N., Subramanian, R., Prasat, S.V.: Tribological behaviour of aluminium/ alumina/ graphite hybrid metal matrix composite using taguchi's techniques. J. Min. Mater. Charact. Eng. **10**(5), 427–443 (2011)
11. Ramachandra, M., Radhakrishna, K., Study of abrasive wear behaviour of Al-SiC (12%) metal matrix composite synthesized using vortex method. In: International Symposium of Research Students on Materials Science and Engineering 20–22 Dec (2004)
12. Tang, F., Wu, X., Ge, S., Ye, J., Zhu, H., Hagiwara, M., Schoenung, J.M.: Dry sliding friction and wear properties of B4C particulate-reinforced Al-5083 matrix composites. Wear **264**, 555–561 (2008)
13. Fard, R.K., Afza, R.A., Teimouri, R.: Experimental investigation, intelligent modelling and multi-characteristics optimization of dry WEDM process of Al–SiC metal matrix composite. J. Manuf. Process. 15483–15494 (2013)
14. Agarwal, B.D., Broutman, L.J.: Analysis and Performance of Fiber Comsites, 2nd edn. Wiley, New York, NY, USA (1990)

15. Alanemea, K.K., Olubambi, P.A.: Corrosion and wear behaviour of rice husk ash-Alumina reinforced Al–Mg–Si alloy matrix hybrid composites. J. Mater. Res. Technol. **2**(2), 188–194 (2013)
16. Unlu, B.S.: Investigation of tribological and mechanical properties Al2O3–SiC reinforced Al composites manufactured by casting or P/M method. Mat. Des. **29**, 2002–2008 (2008)

Development of Simulation Model for Effective Testing and Verification of Servo Vacuum Booster

**A. Selwin Mich Priyadharson, S. Vinson Joshua
and B. Senthil Kumaran**

1 Introduction

In day-to-day life, we are expecting perfection in each and every aspect of everything, and its importance depends on its application or based on customer need. The braking system evolution started from a brake lever, that is, by pressing a simple wooden block against the wheel so as to slow down a wagon by friction. Later on mechanical drum brake and in sequence, internal expanding shoe brake, disk brake, anti-lock brake, vacuum booster brake systems had been developed by many companies.

Among all the above-mentioned braking methods, the servo vacuum booster method is more effective and useful. In between the brake pedal and master cylinder, the vacuum booster is attached, and it reduces the braking force applied by driver. Two chambers are designed in a hollow housing by a movable rubber diaphragm. With the intention of reducing the extent of pedal pressure required for braking, a booster setup is employed to act with the master cylinder to provide higher hydraulic pressure to the brakes. Because of high hydraulic pressure, application of less force is enough on the brake pedal through a brake booster pushrod. In general, in order to increase the force put on pedal, the booster utilizes vacuum from engine. In conventional brake system, the braking is ineffective and hard to give force on the brake pedal when the engine is switched off. Whereas in "active" booster, a solenoid is utilized to open the booster air valve to automatically push the master cylinder frontward to perform dynamic stability control.

Azqueta-Gavaldon et al. [1] designed and tested an automatic braking system for rollators. Ramani et al. [2] proposed the intelligent braking system (IBS) by modifying the anti-lock braking system (ABS) technology. Their simulation idea uses a switching action of IBS and ABS mechanism. Hao et al. [3] designed the

A. Selwin Mich Priyadharson (✉) · S. Vinson Joshua · B. Senthil Kumaran
School of Electrical and Communication, Vel Tech Rangarajan Dr Sagunthala
R&D Institute of Science and Technology, Avadi, Chennai, Tamil Nadu, India
e-mail: selwinmich@gmail.com

controlling system of multifunction durability testing device for durable testing experiments and ABS performance experiments. Vallamkondu Arun et al. improved the safety parameters of brakes for improving the vehicle management system (VMS) and testing of the overall control system of a hybrid vehicle. Massimo et al. [4] mentioned the advantages of LabVIEW platform. Zhou et al. [5] designed LabVIEW-based examination platform and implemented automatic measurement.

In this work, a simulation model which will monitor the performance of the servo vacuum booster is developed. This simulation model is developed by using LabVIEW software. If the tested servo vacuum booster met the measures as per the condition, then it will be segregated as the operative one with no faults and can be further processed. The output graph of the tested part will be obtained in LabVIEW software. This simulation model will help to get the effective servo vacuum booster without any sort of defects and faults with which they can install in their vehicles.

2   LabVIEW Simulation

Laboratory Virtual Instrumentation Engineers Workbench (LabVIEW) is used for giving input values and also used for checking output on LabVIEW screen. In LabVIEW, front panel and rear panel are available, and the front panel of servo performance is shown in Fig. 1. The auto cycle, parameter entry, setting menu, sensor calibration are designed. Those values will be specified in the back panel, and by using loops and clusters in the back panel, output will be displayed when "run" button is enabled in the front panel.

In this front panel, we have auto cycle, parameter entry, setting menu, sensor calibration, help, and exit application. If we press auto cycle, it comes back to
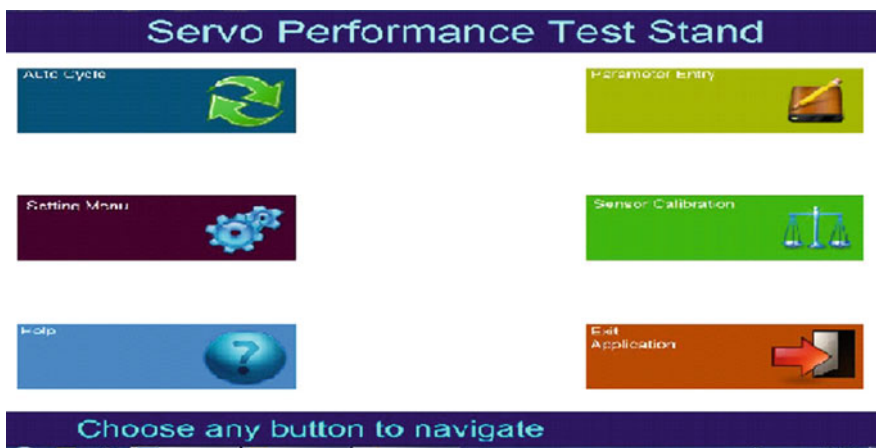
Fig. 1 Servo performance—front panel

original position. The parameters for performance test, calculation parameters and brakes ON vacuum leak test is set by using the parameter entry screen as shown in Fig. 2. The values of the parameters can be set by using setting menu application. Calibrated pressure and torque values are displayed on the sensor calibration screen which will be displayed on the front panel of the LabVIEW screen.

Values can be changed through parameter entry, and it can be saved. Various companies will have different values for their performance; accordingly it can be changed through this parameter entry. In this calibration, we have to set maximum and minimum physical quantities and measured quantities as mentioned in Fig. 3, and its slope will be calculated from these values.

Figure 3 shows the type of sensor to be selected. Pressure or torque can be selected by going to enum option and save it by save option which is present on the screen, and after selection as in Fig. 4 it is necessary to enter the maximum and minimum values of the measured quantity and physical quantity. The final result is displayed in the form of slope from the values of maximum and minimum quantity. In real-time verification of the vacuum booster, the pedaling motion will be given with the help of the servo motor controlled by the programmable logic control (PLC).

Figure 5 represents the 'Timeout' block diagram. In this block diagram, event "case structure" and 'while' loop is used. For event "case structure" 100 seconds time has given. After 100 seconds by using "while" condition it will come back to original position and run continuously. As well as "stop" button for stop purpose and also have numeric data in below of event "case structure". Inside the event "case structure", open and close data files are available in order to open and close the data files.

Fig. 2 Parameter entry—front panel
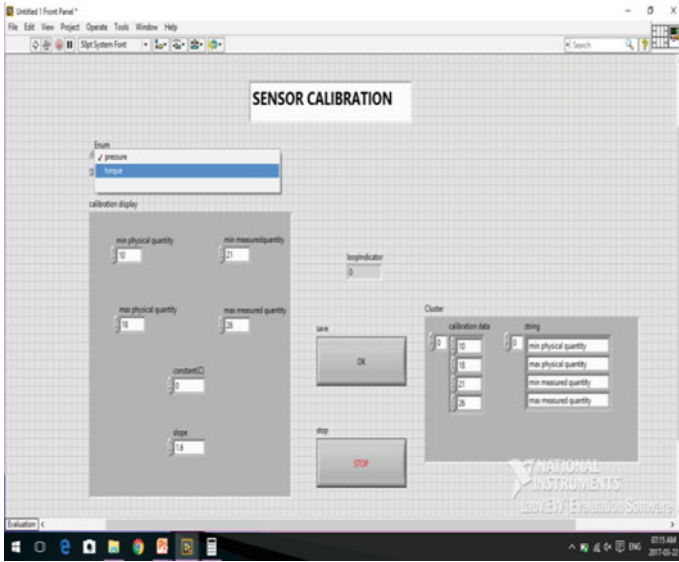
Fig. 3 Sensor calibration (pressure)—front panel
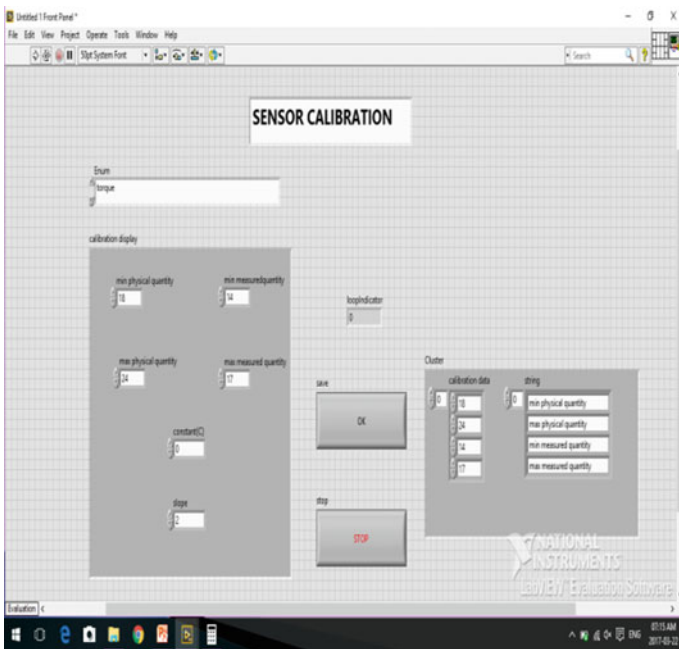
Fig. 4 Sensor calibration (torque)—front panel
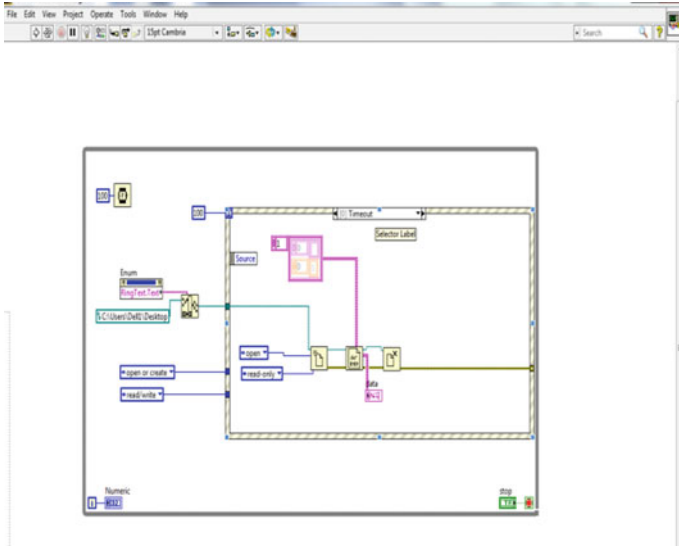
Fig. 5 Timeout—rear panel

3 Result Analysis

The output is obtained in the LabVIEW screen as shown in Fig. 6. Graph method is used to get the plot input versus output.
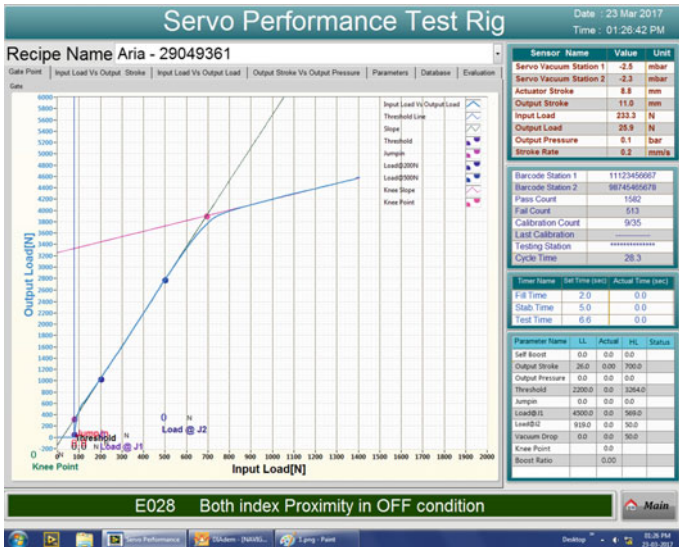
Fig. 6 Servo performance—input versus output

In graph point method, there will be a minimum and maximum level of specified set of limits. After the run check, a line of peak will be obtained. According to that line, the output will be justified. If the obtained line is between the minimum and the maximum values, then the booster is said to be the perfect one, for the usage, or it will get rejected.

4   Conclusion

In this work, a simulation model have been developed for the effective testing and verification of servo vacuum booster on the basis of performance test based on the measures specified by various automotive manufacturers. LabVIEW software is used as a programming tool. This simulation model will support the customer in order to get the effective servo vacuum booster without any sort of defects and faults with which they can install in their vehicles.

References

1. Azqueta-Gavaldon, M., Azqueta-Gavaldon, I., Woiczinski, M.: Automatic braking system and fall detection mechanism for rollators. In: Association for Computing Machinery, ICBBS'17, Singapore (2017)
2. Ramani Ranjan Senapati, P., Sam Jeba Kumar, J., Vimala Juliet, A.: LabVIEW based intelligent braking system for automobile application. I J C T A, Int. Sci. Press **9**(37), 369–376 (2016)
3. Hao, X., Zhang, R., Li, X., Wang, M.: Design of Controlling System in Multi-function Durability Testing Device for Vehicle Vacuum Booster with Brake Master Cylinder, pp. 563–568. Springer, Berlin, Heidelberg (2012)
4. Ceraolo, M., Capozzella, P., Baronti, F.: CAN-Lab VIEW based development platform for fine-tuning hybrid vehicle management systems. In: IEEE Conference Vehicle Power and Propulsion, Chicago, IL, USA (2005)
5. Zhou, K., Wang, X., Zhang, C., Liu, J.: Data acquisition system based on LabVIEW for ABS dynamic simulation test stand. In: Proceedings of the IEEE International Conference on Information and Automation, Harbin, China (2010)

Investigation of Relation Between Ignition Timing and Advance Angle to Improve Engine Performance

Aditya Balkrishna Kale, Jyoti Madhav Phate, Prashant Sarjerao Munfan and Yogesh Suresh Chavan

1 Introduction

"Angle of advance is the angle that is between the ignition spark and the outer dead center." In IC engines, combustion of air and fuel takes place inside the engine cylinder, and the products of combustion expand to produce reciprocating motion of the piston. This reciprocating motion of the piston is in turn converted into rotary motion of the crankshaft through connecting rod and crank. This rotary motion of the crankshaft is in turn used to drive the generators for generating power. Ignition timing is very critical. The charge is to be ignited just before (few degrees before TDC) the end of compression. When the charge is ignited, it will take some time to come to the required rate of burning. The purpose of spark advance mechanism is to assure that under every condition of engine operation, ignition takes place at the most favorable instant in time, i.e., most favorable from a standpoint of engine power, fuel economy, and minimum exhaust dilution. By means of these mechanisms, the advance angle is accurately set so that ignition occurs before TDC point of the piston. The engine speed and the engine load are the control quantities required for the automatic adjustment of the ignition timing. Most of the engines are fitted with mechanisms which are integral with the distributor and automatically regulate the optimum spark advance to account for change of speed and load. The development of automotive electronics, i.e., autotronics has been remarkable in nowadays. Microcontroller is used to control engine operation to maximize fuel economy, monitor the vehicle performance parameter, and diagnosis onboard system malfunction. In these, we replace some mechanical components with electronics components to make automobile engines more efficient [1–4].

A. B. Kale (✉) · J. M. Phate · P. S. Munfan · Y. S. Chavan
Department of Mechanical Engineering, AJMVPS SCSM COE, Nepti,
Ahmednagar, Maharastra, India
e-mail: adityakale26@gmail.com

2   System Description

In these, DC motor is used to in place of the engine. A sensor is used to detect the top dead point of the engine. A timer and a counter in the microcontroller are used to measure the speed of the engine.

2.1   Mechanical Design

The mechanical design for the project consists of a rigid fabricated M.S. Frame, i.e., base foundation. A V belt assembly, bearing and bearing housing, single-phase AC induction motor, a rotating shaft, wheel, position sensors, rigid base for motor assembly.

2.2   Electrical Design

It is based on electromechanical design. The electrical hardware is as follows.

1. Single-phase induction motor
2. Inductive proximity sensors
3. Advance angle measurement hardware
(a) Opto-isolator
(b) Microcontroller
(c) LCD display
(d) Regulated power supply
(e) AC voltmeter
(f) AC current meter.

Inductive proximately sensor detects the metal target and is highly immune to harsh industrial environment such as dust, humidity, dirt, and oil. Namur type switches for installation in hazardous area. Two pulses are arriving at the micro controller's input port with some time difference. The signal pulse from sensor before TDC is given to the port 3, i.e., INT1, and the signal pulse from sensor from the TDC is given to INTO pin of the microcontroller. Pin no. 9 of microcontroller is reset pin. At power on, the ping gets a trigger pulses. The program execution starts. The hardware consists of 10 MF/25 V and 10 K capacitor and resistor combination, respectively. The microcontroller is programmed with assembly language. The programming logic is provided later. At port 0, LCD is interfaced in our case. It is 16×2 alphanumeric type LCD. It has its own microcontroller and memory. LCD is interfaced with microcontroller through the 8-bit data bus and three control lines. The supply, ground, intensity control, and the backlight LED supply are controlled independently. After the microcontroller receives the two inputs at its two

interrupts, it calculates the time delay between these two. This time is converted into angle, and it is shown on LCD display. The entire advance angle meter works on +5 V DC regulated power supply [5].

2.3 PCB Development

PCB means the printed circuit board. It is of glass epoxy material or paper phenolic material. There are rules and regulations for designing the PCB. After the PCB network is ready, the transparency is developed. With the help of transparency, the screen printing is done on PCB from copper side. The printed PCB is allowed for etching in Fecl3. The project being developed using the microcontroller-based technology, the software plays a vital role in our project. Assembly language programming is used. The program requires the assembly cum simulator, emulator. Before developing any software code, the algorithm and the flowchart are to be developed first.

3 Algorithm

1. First of all, when power is ON, the microcontroller is initialized. All the ports of microcontroller are high.
2. LCD is initialized, and message is shown on LCD display.
3. Read input port.
4. Read INTD/INTI
5. If pulse is there, then find out the time difference between the two.
6. If the pulse is no there, show the advance angle = 00.
7. If the pulses arrive at the INTO/INTI pins, the time difference is converted into angle as the entire cycle is of 360 °C.
8. The cycle goes on repeating, and the angle changes if the speed on the position of TDC is changed.

4 Experimental Setup

The trigger wheel rotates as per the motor speed. While rotating, it crosses two different but similar sensors on its path. One of the sensors is located at the top side. Another sensor is located before the top sensor. The location at which the top sensor is located is known as top dead sensor. It is significant in capacitive and inductive type of ignition systems. While starting, there is spark before TDC, so that while reaching at TDC, the fuel and air mixture is totally mixed, and at TDC the spark
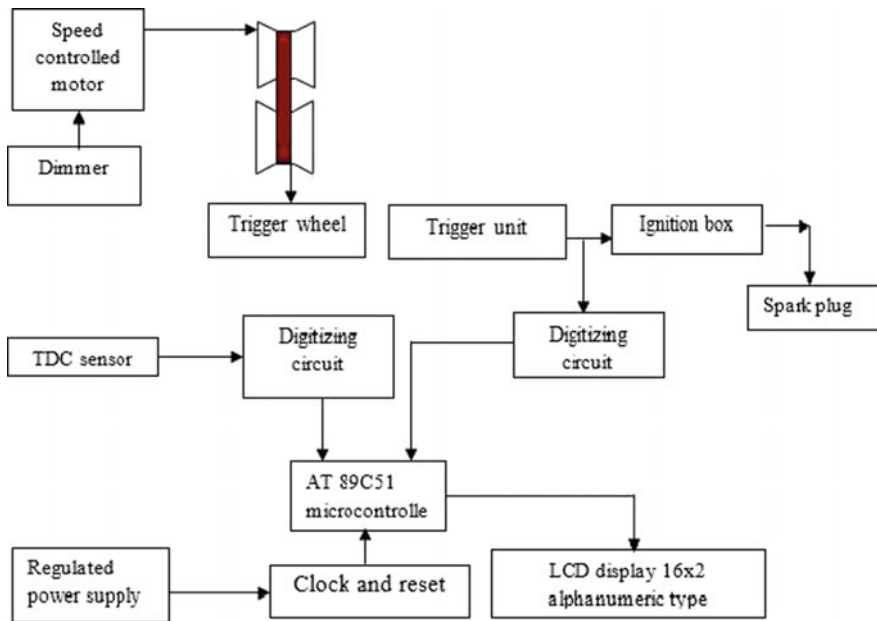
Fig. 1 Block diagram of spark advance angle measurement setup [4]

voltage is observed. The time difference between the TDC and the before the TDC is known as advance time. It is then converted into angle as the entire revolution of the trigger wheel is 360 °C. The angle between TDC sensor and before TDC sensor is known as advance angle. Two inductive pickups are used. The sensors senses the metal object the in its vicinity and accordingly, the pulses are generated at the output (Fig. 1).

5   Algorithm for Spark Timing

1. The algorithm for computer program for ignition procedure is shown as follows.
2. Detect the position of the piston.
3. Count the engine speed (motor speed) of the first revolution.
4. Display the speed.
5. Fetch the time byte of the map from the microcontroller.
6. Fire the spark plug. (The timing of firing is specified by the time byte for the corresponding speed.)

6 System Features

6.1 Microcontroller Features

1. Compatible with MCS-51™ Products
2. 4 K Bytes of In-System reprogrammable flash memory—endurance: 1,000
3. Write/erase cycles
4. Fully static operation: 0 Hz–24 MHz
5. Three-level program memory lock
6. 128×8-bit internal RAM
7. 32 programmable I/O lines
8. Two 16-bit timer/counters
9. Six interrupt sources
10. Programmable serial channel
11. Low-power idle and power-down modes (Fig. 2).

6.2 Electrical Components List

1. Resisters: 1/4th watts, 10 K, 4K7, 100E, etc.
2. Capacitors: 1000 μF/25 V

10 μF/25 V
0.1 μF/25 V
22K pf/25 V

3. Diode: 1N4148, 1N4007
4. Regulator: 7805

Fig. 2 Actual setup of spark advance angle measurement setup [4]
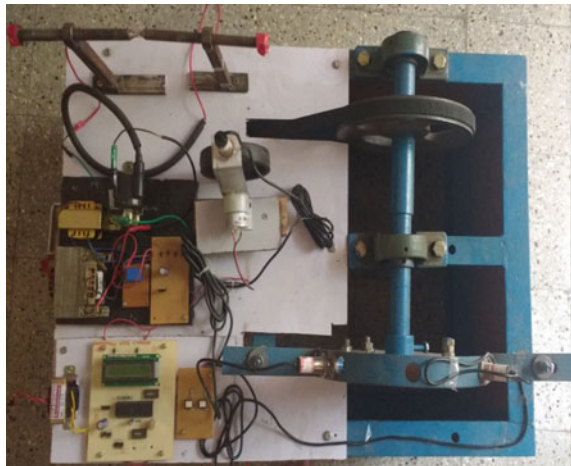
5. IC: AT 89C51 microcontroller
6. Opto-isolator: MC817
7. IC base: 40 pin dip
8. Crystal: 12 MHz
9. LCD Display: 16×2 alphanumeric type
10. Power transformer: 0–12 V, 0.5 A, 230 V AC input
11. 16 pin relimate connectors
12. Inductive proximity sensors: 02
13. PCB development
14. Software development tools
15. Mains cord
16. Miscellaneous.

6.3   Control Panel

1. AC voltmeter analog: 01
2. AC current meter analog: 01
3. AC indicators: 02
4. Toggle S/W: 02
5. Miscellaneous: MS angle frame.

7   Conclusion

For better performance of engine ignition, advance BTDC 10, 14, 18, 22, is suitable for engine speed 500, 1500, 3400, 5000 rpm, respectively for single cylinder four-stroke engine. From the results, it concluded that the ignition angle can be a parameter to control the performance of the engine with relation to engine speed. Also selection of an ignition angle is based on optimum performance. It could be seen that high ignition advance gives maximum pressure in cylinder. Microcontroller-based angle measurement system replaces electronic components in place of mechanical hardware to make automobile engine more effective and inexpensive. In these, DC motor is used in place of automobile engine, and a sensor is used to detect the revolution of motor. Sensor and microcontroller make automobiles monitor and control more effective automobile functions. Programmable nature of microcontroller allows one to easily make adjustment for the different requirement of variety of vehicle operating condition in various climates and conditions. It shows ability to perform automotive system functions electrically with high degree of accuracy and reliability.

References

1. Kale, A.B., Patil, V.R.: Sensitivity and effect of variable ignition timing and engine speed on the performance of a spark ignition engine. IJSRD **3**(10) (2015)
2. Bhot, S., Quayle, R.: Microprocessor Control Ignition Advance Angle, vol. 6. Electrical Engineering Lab., University of Manchester, Greater Manchester M13 9PL., UK (1982)
3. Rode, M.A., Toelle, A.D.: Ignition Advance Timing System. United State Patent, Appl. No. 221,139, Dec 29 1980
4. Kale, A.B., Patil, V.R.: Test rig for measurement of spark advance angle and ignition system using At89c51 microcontroller. IJSRD **3**(10) (2015)
5. Mathialagan, A., Vijayaraghavan, P.: Microprocessor Based Ignition Controller for the Automobile Industry. Madras Institute of Technology, Anna University Chrome pet, Madras-600044, India

Experimental Investigation of Vapour Absorption Refrigeration Cycle for Automobile Cabin Cooling

Sahadev M. Jadhav, M. Arulprakasajothi, U. Chandrasekhar and D. Yuvarajan

1 Introduction

Energy efficiency has been a major topic of discussion on natural resource reservation and cost reduction. The expansion of energy resources is one of the prime motivations for social and technological developments. In the last decades, strong international concern has been raised with regard to the depletion of the natural resources and an increase in pollution levels as a consequence of the higher energy consumption necessary to sustain productive activities. Refrigeration and air-conditioning systems consume considerable amount of energy around the world. In order to reduce this, share some alterations need to be searched for example for cooling application, vapour absorption system is basically driven by low-grade energy such as waste heat, and solar energy is coming in picture for the last few decades. The advantages of this system lie in the possibility of utilizing of waste energy from industrial plants as well as of using solar energy. Aqua ammonia system is employed for applications below 32 °F (0 °C) in which the refrigerating fluid is ammonia and absorbent or carrier is water. The elimination of the necessary shaft work has been the prime reason for the economic success of vapour absorption system. As these systems require only low-grade energy in the form of heat and due to limited energy sources and growing demand, there is a concern in the scientific community to develop energy-efficient system. From general observations and survey from various automobile stations, it has been concluded that introduction of VCC air-conditioning system in cars reduces economy of engine by 10%,

S. M. Jadhav (✉) · M. Arulprakasajothi · D. Yuvarajan
Department of Mechanical Engineering, Vel Tech Rangarajan Dr Sagunthala R&D Institute of Science and Technology, Avadi, Chennai 600 062, Tamil Nadu, India
e-mail: sahadev.jadhav@gmail.com

U. Chandrasekhar
Department of Aeronautical Engineering, Vel Tech Rangarajan Dr Sagunthala R&D Institute of Science and Technology, Avadi, Chennai 600 062, Tamil Nadu, India

i.e. approximately by 1–2 km-Pl. An International Report has suggested that daily petrol consumption in India is about 3,660,000 barrels (581,940,000 L). Also, it has been stated by Government of India that out of total petrol consumption, 27% fuel is consumed by four-wheel vehicles. If it is assumed that 50% of four-wheel vehicles in India are air conditioned, and each AC consumes 10% of shaft power, 7,500,000 L fuel can be saved on daily basis, which can save around Rs. 2000 crores can be saved annually, if the VARC-based system is used in automobiles.

2   Literature Review

Li et al. [1] thermodynamically analysed a novel air-cooled non-adiabatic ejection–absorption refrigeration cycle with R290/oil mixture driven by exhaust heat. An ejector located at the upstream of the non-adiabatic absorber is employed to improve the cycle performance. Variations of COP, circulation ratio and component heat load of the system as a function of generating temperature, pressure ratio, absorption temperature, condensing temperature and evaporating temperature have been investigated in this work. The simulation results show that compared with the conventional absorption refrigeration cycle, this non-adiabatic ejection–absorption refrigeration cycle has higher absorption efficiency, better performance, wider working condition range and lower total heat load and its COP can reach as high as 0.5297. Mansouri et al. [2] reported on the experimental investigations in a non-steady-state mode of a small capacity commercial diffusion–absorption refrigerator (DAR) and the development of a dynamic black-box model for the machine. For these investigations, the refrigerator was equipped with the appropriate metrology.

Temperature time variations of the refrigerated room and of the ambient conditions were measured, monitored and stored using a data acquisition unit connected to a computer. Aly et al. [3] analysed the thermal performance of a diffusion absorption refrigerator (DAR) driven by the waste heat of a diesel engine exhaust gas as an energy source was investigated experimentally. The engine was tested on a bench test dynamometer with the DAR adapted to the exhaust pipe via a heat exchanger. The engine was tested for different torques (15, 30 and 45 N m). The exhaust gas flow to the heat exchanger mounted on the DAR was controlled manually using two control valves. Li et al. [4] analysed the performance of solar cooling absorption system which needs further research, due to its poor coefficient of performance (COP). Therefore, this study investigated the performance of a 23 kW solar-powered single-effect lithium bromide–water (LiBr–H2O) absorption cooling system. Furthermore, the space heating mode was also investigated and the improvement methods were analysed and discussed. Novella et al. [5] dealt with the thermodynamic analysis of an absorption refrigeration cycle used to cool down the temperature of the intake air in an internal combustion engine using as a heat source the exhaust gas of the engine.

The solution of ammonia–water has been selected due to the stability for a wide range of operating temperatures and pressures and the low freezing point. Salmi et al. [6] represented a steady-state thermodynamic model for absorption refrigeration cycles with water–LiBr and ammonia–water working pairs for purpose of application on a ship. The coefficient of performance was studied with different generator and evaporator temperatures in ISO and tropical conditions. Absorption refrigeration systems were examined using exhaust gases, jacket water, and scavenge air as energy sources. Li et al. [7] quantitatively analysed the waste heat from a vehicle engine under different running conditions and calculating the heat load of devices in the absorption compression hybrid refrigeration cycle, the heat transfer area and structure of the main unit are determined. The distributed parameter model of heat transfer between the exhaust gases and working fluids in the generator, as well as the lumped parameter model in the other heat exchangers, is established. Balaji et al. [8] proved that most of the energies are utilized by the industries, due to depletion of fossils fuels and increasing the fuel price to utilize the maximum available energy from the waste heat source. Yang et al. [9] combined power and refrigeration cycle is studied. The proposed cogeneration system consists of an organic Rankine cycle and a refrigeration cycle, connected by an ejector.

The performance of the combined cycle is analysed when the system running in different working fluids, including pure working fluids, R245fa and R600a, and zeotropic mixtures, R245fa/R600a. The mass fraction of the mixtures varies from 10/90 to 70/30, and the results show that the mixtures generate more refrigeration than pure working fluids, and they have better performance under certain conditions. Besides, the effect of some thermodynamic parameters, including evaporator temperature, condenser temperature, boiler temperature and turbine outlet temperature, on the performance of the system is studied.

Alamer [10] analysed the sub-systems of evaporative cooler (EC) combined with desiccant dehumidification and regeneration for automotive air-conditioning purpose. The thermodynamic and psychometric analysis was conducted to design all evaporative cooling system components in terms of desiccant selection, regeneration process, compact heat exchanger and evaporative cooler. Moreover, the effect of the desiccant, heat exchanger and evaporative performances on the mass flow rate and water sprayed required for evaporative cooling system was investigated. Porumb et al. [11] presented a numerical investigation on operating conditions and performances of a solar absorption chiller with LiBr–H_2O. The working cycle of the investigated solar cooling equipment was modelled based on thermodynamic principles by the use of the software platform Engineering Equation Solver and was validated based on similar studies reported in the literature. Further, it was investigated the influence of the operating conditions like solar hot water temperature, cooling water temperature and cold water temperature, on the coefficient of performance of the solar absorption chiller and on the conditions of crystallisation. The numerical model of the solar absorption chiller working cycle proved to be capable to describe the behaviour of the equipment and to evaluate the safe operating conditions from the crystallisation point of view and from degassing point of view.

Wang et al. [12] highlighted solar driven air-conditioning systems can cope with solar collectors working in a wide range of temperatures. Sorption systems, including absorption and adsorption refrigeration systems, are among the best choices for solar cooling. Yildiz et al. [13] did energy, energy and thermo-economic analyses of the Electrolux vapour absorption system. He has shown that the best performances in terms of COP were obtained from a concentration range of the rich solution of 0.2–0.3 ammonia mass fraction and that concentration of the weak solution of 0.1.

3   System Description

As shown in Fig. 1, setup of vapour absorption system has the following components:

(1) Absorber
(2) Generator
(3) Air-cooled condenser
(4) Temperature indicators
(5) Energy meter (Tables 1 and 2).

Fig. 1 VARC

Table 1 Specifications of VAR system

Technical data	Specifications
Total volume (L)	30
Height (mm)	552
Width (mm)	380
Depth (mm)	445
Internal dimensions (*H* * *W* * *D*) (mm)	438 * 295 * 245
Maximum input	230 V (W) 90
Energy consumption annum (kW-h)	266

Table 2 Specifications of IC engine

Model	Maruti 800 (4S-Vertical)	Lubrication system	Pressure feed system
Maximum output	27.6 KW @ 5000 rpm	Cooling system	Water cooling with thermostat
Maximum torque	59 NM @ 2500 rpm	Fuel supply system	MPFI
No. of cylinders	3	Dynamometer	Hydraulic dynamometer
Bore * stroke	66.5 * 72 mm	Calorific value	42,500 kJ/Kg
Compression ratio	9.2:1	Dynamometer radius	200 mm
Cubic capacity	796 cc	Coefficient of discharge for orifice	0.64
Firing order	1-3-2	Orifice diameter	36 mm

4 Results and Discussion

The graph shown Fig. 2 is of most significant since it is cooling curve of air inside cabin. The graph states that the cabin temperature initially rises with time and then starts decreasing. This happens because though generator temperature is increased it requires a particular generator temperature for commencement of refrigeration effect. Since at lower temperatures, no separation of refrigerant and absorbent takes place, and evaporation of refrigerant does not take place. Since high-temperature mixture of refrigerant–absorbent comes in contact with evaporator coils, heat is transferred from mixture to evaporator coil, and thus, heating of air takes place. However once the sufficient generator temperature is achieved, cooling effect is obtained very rapidly. Also apparently, cooling curve states requirement of high generator temperature and time span it proves to be a base of future work.

The graph shown in Fig. 3 confirms that COP initially increases with condenser temperature and then starts decreasing after a particular value. This nature is exactly

Cabin Temperature Vs. Time Elapsed
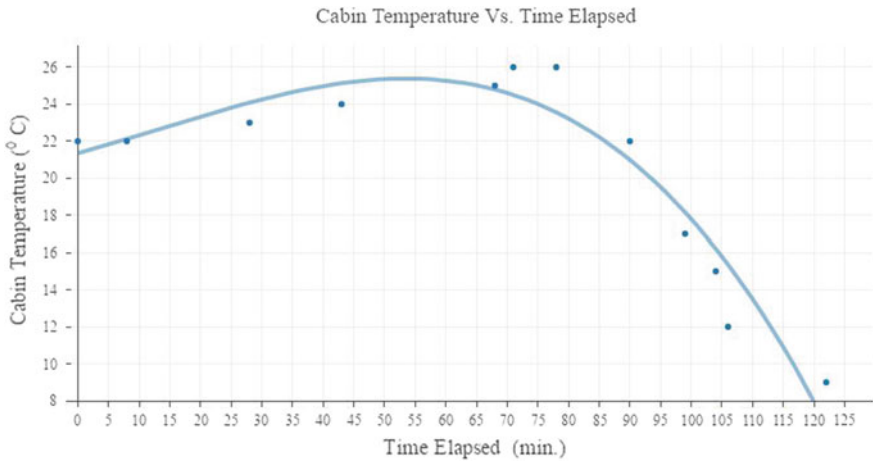
Fig. 2 Cabin temperature versus time elapsed

COP Vs Condenser Temperature
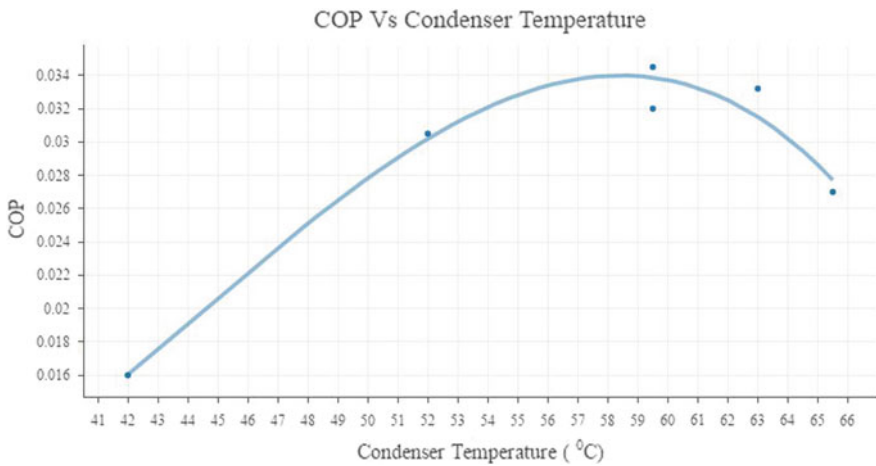
Fig. 3 COP versus average condenser temperature

opposite to that of VCC system. As in VCC system, Carnot COP depends on only
two parameters, i.e. evaporator temperature and condenser temperature, and lesser
condenser temperature results into less heat rejection and good performance.
However, this is not the case with VAR system since COP of VAR system is
function of various temperatures. High-temperature vapours coming out from
condenser result into fast flash evaporation. Again, if temperature is too high it
causes reversible heat transfer from condenser vapours to evaporator, which results
into decreased refrigeration effect. Also, if it is to concern about temperature lim-
itation of refrigerator, cold fluid available for heat exchange is air and its

temperature is almost constant throughout driving intervals. Thus, it becomes very difficult to alter the performance of system by varying condenser-related parameters. However, the use of extended surfaces may definitely improve the condenser performance.

As it can be clearly noticed from Fig. 4 that COP increases with absorber temperature and then starts decreasing, it can be concluded that nature of COP versus condenser temperature and absorber temperature is similar in nature. Absorption is an exothermic reaction; thus, temperature of absorbent increases during the process and hence the temperature of absorber (Fig. 5).
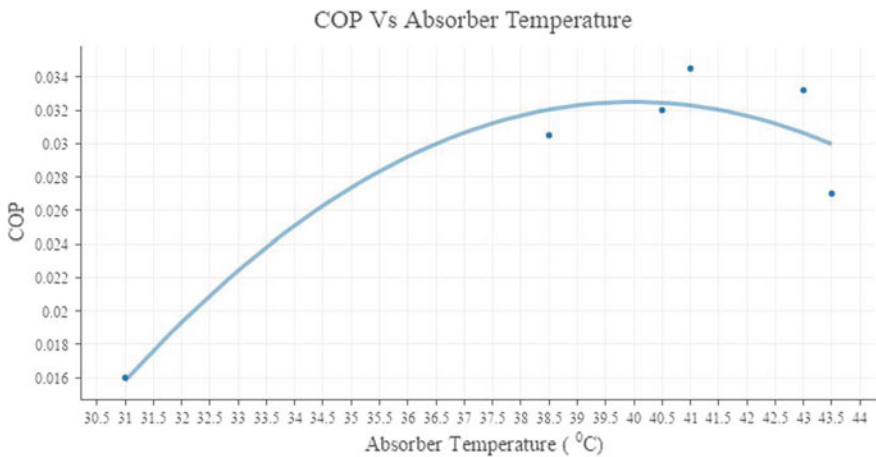
Fig. 4 COP versus average absorber temperature
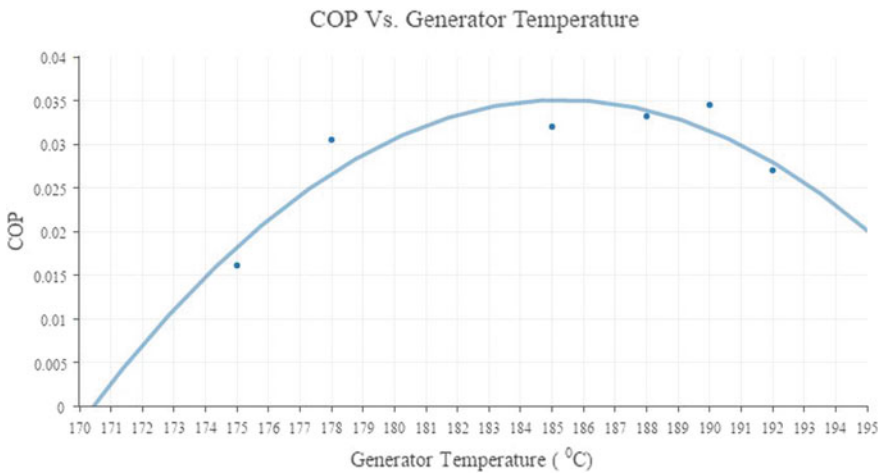
Fig. 5 COP versus generator temperature
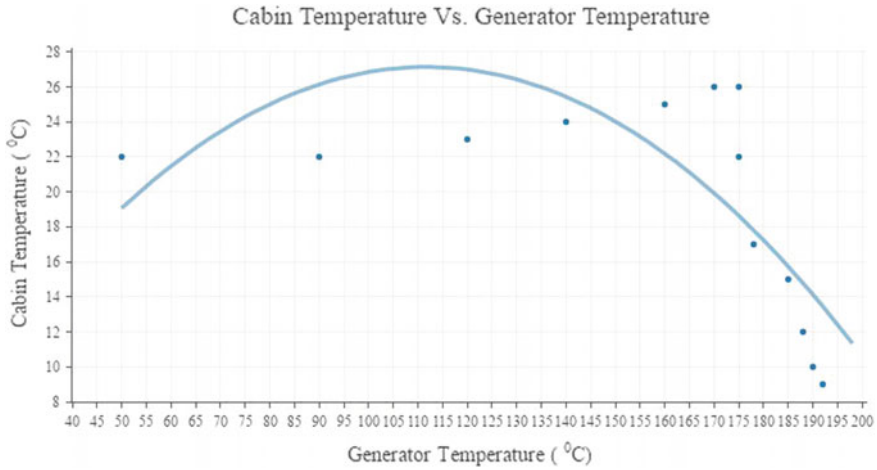
Fig. 6 Cabin temperature versus generator temperature

It should be noted that generator temperature is most important parameter that affects the performance of system and which can be very effective to alter the performance of system. From Fig. 6, it is clearly understood that COP initially increases with generator temperature and then starts decreasing. Very important interpretation is that it requires a particular value of generator temperature to achieve refrigeration effect. At a temperature less than this temperature, there will not be any cooling effect, but the heating of cabin. Thus, achieving a high generator temperature at faster rate is very essential in VAR systems. Also along with getting high generator temperature, it is also quite necessary to maintain the temperature, since any deviation from optimum generator temperature is going to hamper the performance of system.

Very important interpretation made from graph of cabin temperature versus generator temperature is that it requires a particular value of generator temperature to achieve refrigeration effect. At a temperature less than this temperature, there will not be any cooling effect, but the heating of cabin. Thus, achieving a high generator temperature at faster rate is very essential in VAR systems. Also along with getting high generator temperature, it is also quite necessary to maintain the temperature, since any deviation from optimum generator temperature is going to hamper the performance of system. However, the mentioned nature of graph can be proved very effective in different seasons, for heating or cooling the air inside cabin.

In thermodynamics, the first law efficiency of a refrigerator is defined as ratio of refrigeration effect obtained to the net heat input supplied. Thus, it is fraction of input heat energy that is converted into refrigeration effect. Thus, first law does not make any reference to the best possible performance, and thus, first law efficiency is not a realistic measure of performance of system. To overcome this deficiency, we defined second law efficiency of system. It gives measure of actual performance with ideal performance under same operating conditions. It can be noted from
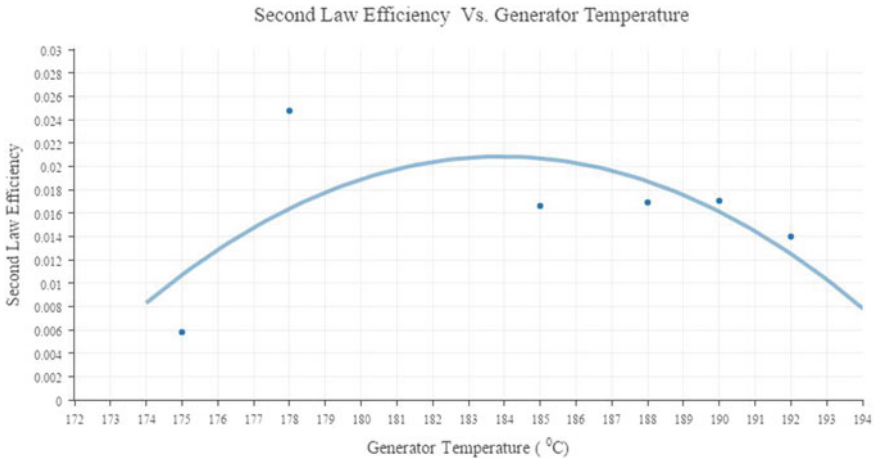
Fig. 7 Second law efficiency versus generator temperature

Fig. 7 that second law efficiency initially increases with generator temperature and then it starts decreasing. Reference of this graph is very necessary while learning thermodynamic performance of system.

5   Conclusions

As it has been discovered that refrigeration effect obtained was much satisfactory, it is proved that proposed concept of cooling of automobile using exhaust gas is of practical concerned. The mentioned concept can be effectively utilized for auto-mobile cooling. As it has been observed that only a part exhaust gas is being utilized for refrigeration purpose, a system can be made where exhaust gets divided into two different flows, and hence, problem of generation of back pressure can be totally eliminated, which is one of the most serious issues associated with control volume systems. The mentioned system can be made more effective or instanta-neous by the concept of hybrid energy source. An electric heater can be implanted as partial source of heat along with exhaust gas, which will come into role only in some specific situations such as cold starting, idle condition, or when the engine is off or is just started. This system will work effectively and economically only when electric input is utilized at optimum level. Also, the experiments conclude that system can work efficiently even when engine rpm is 3500 only. As most of the vehicles can run at much higher speed than this, system is going to work well under conditions when speed is not constant, or average speed is considered. Another very innovative concept which is utilized by reputed chiller manufacturing companies is

of hybrid refrigeration. In this hybrid system, vapour absorption system and vapour compression refrigeration systems are coupled together to form a single system, which yields into better performance. Utilizing this concept into actual can be proved beneficial as some part of engine work is conserved, but the increased cost of the automobile could be the matter of concern. As it is common experience that cabin or truck driver is a warm place, thus an unpleasant seat to take, condition can be improved by cooling the car cabin without expense of any mechanical energy and hence the fuel. Implementation of above system into trucks would not only result into exhaust heat recovery but also in safe driving. Another application of mentioned refrigeration system can be put into providing a small capacity refrigerator in car, which might be helpful in conserving the quality of food products and fluids, during long journeys. It has been highly noticed that proper selection of materials for various components is very necessary for good performance. Innovation can be developed by combining mentioned refrigeration system and catalytic converter. Very important limitation of system is explosive nature of hydrogen gas, which might be proved very harmful if leaked.

References

1. Li, K., Cai, D., Liu, Y., Jiang, J., Sun, W., He, G.: Thermodynamic analysis of a novel exhaust heat-driven non-adiabatic ejection-absorption refrigeration cycle using R290/oil mixture. Energy Convers. Manag. **149**, 244–253 (2017)
2. Mansouri, R., Bourouis, M., Bellagi, A.: Experimental investigations and modelling of a small capacity diffusion absorption refrigerator in dynamic mode. Appl. Therm. Eng. **113**, 653–662 (2017)
3. Aly, W.I.A., Abdo, M., Bedair, G., Hassaneen, A.E.: Thermal performance of a diffusion absorption refrigeration system driven by waste heat from diesel engine exhaust gases. Appl. Therm Eng. **114**, 621–630 (2017)
4. Li, M., Xu, C., Hassanien, R.H.E., Xu, Y., Zhuang, B.: Experimental investigation on the performance of a solar powered lithium bromide–water absorption cooling system. Int. J. Refrig. **71**, 46–59 (2016)
5. Novella, R., Dolz, V., Martín, J., Royo-Pasc, L.: Thermodynamic analysis of an absorption refrigeration system used to cool down the intake air in an internal combustion engine. Appl. Therm. Eng. **111**, 257–270 (2017)
6. Salmi, W., Vanttola, J., Elg, M., Kuosa, M., Lahdelma, R.: Using waste heat of ship as energy source for an absorption refrigeration System. Appl. Therm. Eng. **115**, 501–516 (2017)
7. Li, J., Xu, S.: The performance of absorption compression hybrid refrigeration driven by waste heat and power from coach engine. Appl. Therm. Eng. **61** (2013)
8. Balaji, K., Ramkumar, R.: Study of waste heat recovery from steam turbine exhaust for vapour absorption system in sugar industry. Proc. Eng. **38**, 1352–1356 (2012)
9. Yanga, X., Zhaoa, L.: Thermodynamic analysis of a combined power and ejector refrigeration cycle using zeotropic mixtures. Energy Proc. **75**, 1033–1036 (2015)
10. Alahmer, A.: Thermal analysis of a direct evaporative cooling system enhancement with desiccant dehumidification for vehicular air conditioning. Appl. Therm. Eng. **98**, 1273–1285 (2016)

11. Porumba, R., Porumba, B., Balana, M.: Numerical investigation on solar absorption chillers with LiBr-H2O operating conditions and performances. In: Sustainable Solutions for Energy and Environment, EENVIRO 2016, 26–28 Oct 2016
12. Wang, R.Z., Xu, Z.Y., Pan, Q.W., Du, S., Xia, Z.Z.: Solar driven air conditioning and refrigeration systems corresponding to various heating source temperatures. Appl. Energy **169**, 846–856 (2016)
13. Yildiz, A.: Thermoeconomic analysis of diffusion absorption refrigeration systems. Appl. Therm. Eng. **99**, 23–31 (2016)

Effects of Nano- and Micro-Filler on Water Diffusion and Leakage Current of GRP Composites

Santhy P. Kuruvilla and N. M. Renukappa

1   Introduction

Non-ceramic composite insulators (NCIs) based on glass fiber-reinforced polymer (GRP) rods have been widely used in transmission and distribution applications for several years worldwide. Their advantages over traditional porcelain insulators are numerous; yet, under certain in-service conditions, harsh environmental parameters such as high moisture contents, elevated temperatures, electrical fields, and acidic conditions can cause severe damage to the insulators and in particular to their core material. For instance, brittle fracture of the GRP rods can occur, leading to the failure of the insulators if either water or nitric acid is allowed to penetrate inside the units. The ingress of water into the composite rods can also alter the dielectric properties of the insulators making them less suitable for high-voltage insulation applications [1–3]. It is reported that electrical properties of GRP composites strongly depend on amount of moisture absorbed [4, 5]. Water absorption may also change the structure of epoxy-based composites leading to adverse impact on the mechanical, electrical, and thermal properties [6, 7].

Recent research has shown that an increase in the amount of moisture inside unidirectional (UD) glass polymer composites leads to a higher leakage current [2]. The Standard exist (IEC: 62217 2005-10(E) Section 9.4.2.) for testing NCI composites for their electrical properties by measuring the electrical leakage current after diffusing aqueous salt solution into the composite material. Increase in leakage current (LC) causes generation of heat on surface. This heat damages the insulator

S. P. Kuruvilla
Department of Electronics, JSS Research Foundation, JSSTI Campus,
Mysuru, Karnataka, India

N. M. Renukappa (✉)
Department of Electronics and Communication Engineering,
Sri Jayachamarajendra College of Engineering, Mysuru 570006, Karnataka, India
e-mail: renunijagal@gmail.com

surface and also causes a slightly burned path which gives rise to dry band arcing. This can lead to failure or flashover of insulator [8–10].

The present work focuses on the effect of nano-sized SiO_2 and Al_2O_3, also micro-sized ATH, $MgTiO_3$, and $CaCO_3$ particles and preprocessing techniques on water diffusion and LC of epoxy-based composites and to identify the best composition.

2 Materials and Methods

2.1 Materials

The details of the materials used in the present work are listed in Table 1.

The epoxy resin and surface functionalized Electrically Corrosion Resistant (ECR)-glass continuous fiber (of diameter 18 μm) are used as the primary composites. High-purity grade of uncoated particles of nano-sized SiO_2 and Al_2O_3 as well as micro-sized ATH, $MgTiO_3$, and $CaCO_3$ are used as secondary reinforcements.

2.2 Fabrication of Composites

Epoxy resin and hardener were conditioned in a vacuum chamber for 1 h 15 min at 65 °C prior to mixing in order to lower the viscosity and to remove the trapped air bubbles. Similarly, SiO_2, Al_2O_3, ATH, $MgTiO_3$, and $CaCO_3$ fillers were preheated in a hot air oven for 24 h at 115 °C before being mixed for removal of moisture. High-power dispersion methods such as ultrasonication and high-speed shearing were used as they are the simplest and most convenient methods to improve the dispersion

Table 1 Material details

Materials	Source	Density (g/cm^3)
Diglycidyl ether of Bisphenol A (MY740), Hardener (HY918), Accelerator (DY 062)	Huntsman, USA	1.16
Silica (SiO$_2$)	Sigma Aldrich	2.6
Alumina (Al$_2$O$_3$)		4.0
Magnesium Titanate (MgTiO$_3$)		3.36
Calcium carbonate (CaCO$_3$)		2.93
Aluminatrihydrate (ATH)	Akrochem Corporation	2.42
ECR glass fiber	Owens Corning India Pvt. Ltd	2.00

Table 2 Samples designation

Designation	Description
G	ECR glass fiber epoxy
A	ECR glass fiber epoxy with silica, alumina, and ATH
C	ECR glass fiber epoxy with silica, alumina, and calcium carbonate
M	ECR glass fiber epoxy with silica, alumina, and magnesium titanate

of nano/microparticles in the polymer matrix. The fillers are dispersed in absolute ethanol by gentle stirring. A high shear mixer was used at 1500 rpm for 5 min followed by ultrasonication for 45 min to achieve uniform dispersion of fillers.

Sonication was carried out in an ultrasonic liquid processor using 12-mm-diameter probe at ambient temperature. After breaking up of the agglomerates, silane coupling agent was added and allowed to hydrolyze for 15 min. The mixture was then introduced into the epoxy resin and sonication was continued for 45 min. A high shear mixture at 3500 rpm was used to mix the hardener, release agent, and accelerator with the composite. The mixing was done for 10 min. ECR glass fiber was used as reinforcement to the mixture and samples are prepared by pultrusion technique. Interfacial adhesion between glass fibers and the resin in the composite was improved by modifying glass fibers with silane coupling agent. The composites are designated as in Table 2.

The GRP composite rods were fabricated on a laboratory-scale using a tabletop pultrusion machine which was designed specifically. The machine consists of a resin bath, a pultrusion die with dimensions of 20-mm diameter and a puller. The die is coated with a high-temperature ultra-slippery polytetrafluoro-ethylene (PTFE) tape. The fibers are pulled through pre-form guides to eliminate excess resin before entering a heated die where the composites are cured. The heated die consists of a low-temperature (90 °C) zone for gelation and a high temperature (175 °C) to cure the resin [11, 12]. The pultrusion die is heated by a heater and the temperature is controlled using a thermocouple sensor, which interacts with heater to ensure the temperature is sufficient and to avoid die from overheating which can cause the defect on the pultruded profile. The profiles are pulled through the cutter and are cut to desired lengths. This rod serves as the center core of the composite insulator. Figure 1 depicts the fabricated series of ECR GRP composite rods.

Fig. 1 Finished GRP nano- and micro-composite long rods with different fillers

2.3 Experiments/Measurements

X-Ray Diffraction Analysis
The crystallinity and phase assessment of the GRP composites with fillers are carried out and compared with the sample without fillers using X-ray diffractometer PROTO operating under a current of 20 mA and a voltage of 30 kV in a scattering range (2θ) of 10°–80° under step size of 0.05° for every 2 s.

Morphology and Surface Composition Analysis SEM is used for the morphological study of the nano/microparticle dispersion in the GRP composites. Using a JEOL JSM-IT300 scanning electron microscope (SEM), the specimens were examined, with a backscatter electron detector, operating under a voltage of 25 kV. To closely observe the sample, the SEM was performed at low vacuum mode. The principal elements in the composites were evaluated by energy-dispersive analysis of X-rays (EDAX) using NORAN System 7—Thermo Fisher Scientific.

Dye Penetration Dye penetration test is a non-destructive test which is used to evaluate the quality of the core of composite insulator as per 62217 IEC: 2005(E) Section 9.4.1 [14]. Ten samples were cut from the GRP composite insulator rod, each of 10 ± 0.5 mm thickness, 90° to the axis of the core, using a circular saw blade (diamond-coated) under cool running water. The cut ends were cleaned up and made parallel by smoothening with a 180-grit abrasive cloth. The samples were then placed in a vessel 2–3 mm above the level of the steel balls of diameter 1–2 mm. A dye, 1% methyl alcohol solution of violet methine was poured into the vessel, the level being 2–3 mm higher than the level of the balls. Visual inspection of the dye penetration was done through the upper edge of the samples as shown in Fig. 2, and the penetration of the dye was observed for duration of 15 min.

Leakage Current Measurement of GRP Composite Rods Subjected to Water Diffusion Water diffusion test was carried out according to 62217 IEC: 2005(E) Section 9.4.2 [14]. The insulator was cut into six samples of 30 ± 0.5 mm, 90° to the axis of the core, using a circular saw blade (diamond-coated) under cool running water. The cut ends were cleaned up and made parallel by smoothening with a

Fig. 2 Samples floating on the balls during dye penetration test

180-grit abrasive cloth. The surfaces of the specimens were cleaned with isopropyl alcohol and filter paper. In the water diffusion test, a 30-mm-thick section of the rod shall withstand 12 kV for one minute after being boiled in 0.1% salt water for 100 h. Hence, the samples were boiled in de-ionized water with 0.1% by weight NaCl in a glass container for 100 ± 0.5 h. After boiling, the samples were removed and kept at ambient temperature under normal tap water for 15 min. After drying their surface with filter paper, the samples were placed between two plane brass electrodes and a voltage increasing at the rate of 1 kV per second was applied till it reached a value of 12 kV (rms) and maintained for 1 min, and decreased to zero.

Leakage Current of as Cast GRP Composite Rod The leakage current of 20-mm diameter and 415-mm length GRP composite rods were measured with an applied voltage of 75 kV for 1 min, and if the maximum leakage current is less than 0.05 mA, the sample is acceptable as per the ASTM/IEC.

3 Results and Discussion

3.1 X-Ray Diffraction Analysis

X-Ray Diffraction (XRD) profiles of the samples indicate amorphous nature of composite with a broad peak in 2θ range ($10°$–$35°$) with maxima around $2\theta = 26°$ as seen in Fig. 3a (intensity is plotted in arbitrary units for comparison of patterns). The observed maxima of intensity along with 2θ of each sample are listed in Fig. 3b. The slight variation in these values may be attributed to inclusion of fillers which are crystalline in nature.

Samples	2θ	Intensity (Max)
G	26.39	142
A	26.43	201
C	26.62	292
M	26.19	388
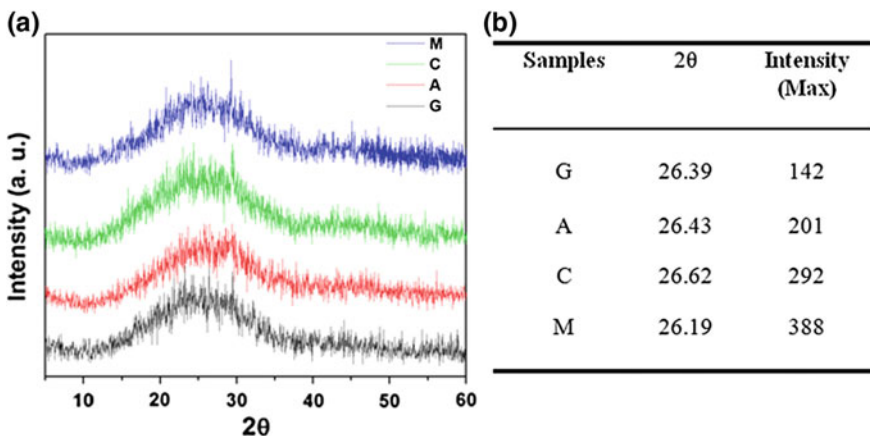
Fig. 3 **a** X-ray diffractogram, **b** Intensity (Max) of samples G, A, C, and M
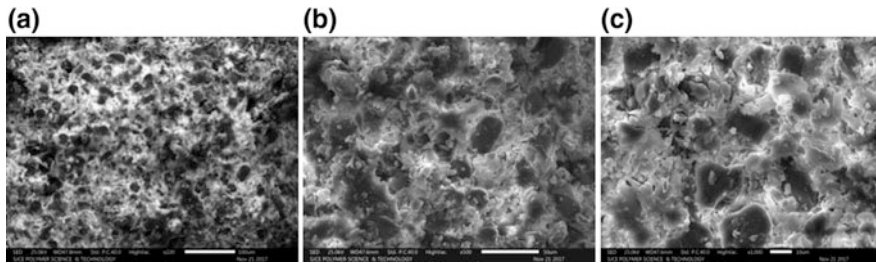
Fig. 4 SEM micrographs of the sample C at different magnification levels **a** 220×, **b** 500×, and **c** 1000×

3.2 Morphology

The typical SEM micrographs at different magnification levels of the GRP composite (sample C) are presented in Fig. 4. A uniform dispersion of the glass fiber and fillers with the presence of fewer voids can be observed in the epoxy resin. The fibers are observed to be cleanly aligned without any fibers pulled out at the point of cut. SEM images of other samples also exhibited similar features. Thus, it can be concluded that the adhesion between the epoxy resin and the fillers is satisfactory. The better bonding between the glass fiber, filler, and the matrix may be due to increased surface area of the nano/micro-fillers and their functionalization [13]. The strong bonding can also be due to the methods employed in the fabrication process.

3.3 Surface Composition Analysis

The chemical composition of ECR glass fibers and nano- and micro-fillers used in the fabrication of the composites was confirmed by EDAX. Figure 5 shows the EDX spectra of the specimen surface. The spectra clearly depict that the samples are composed of Si, O, Al, Ca, C, and Mg elements. The primary elements such as silicon and oxygen are found common in all the composites. The presence of Ca and C is evident in spectrum of sample C and of Mg and Ti is seen in spectrum of sample D, respectively. The presence of the elements is in accordance with the sample designation.

3.4 Dye Penetration

Table 3 shows that the fabricated GRP composite rods were found to be acceptable in accordance with the standards. There was no dye penetration observed in the
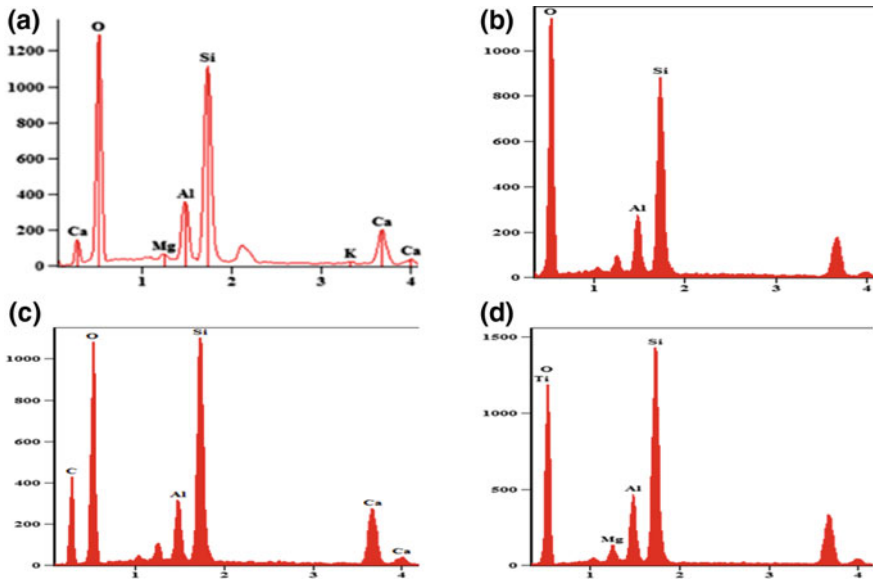
Fig. 5 EDAX spectra of the fillers and fiber **a** G, **b** A, **c** C, and **d** M

Samples	Observation
G	Negligible penetration
A	No penetration
C	No penetration
M	No penetration

Table 3 Dye penetration observed in samples

samples of composite A, C, and M within the specified time. However, negligible penetration of the die was observed at the surface edge of two samples out of ten in sample G.

3.5 Water Diffusion Electrical Test

Water diffusion electrical testing of the samples was carried out to check its resistance to water seepage. The leakage current values observed during water diffusion electrical test are shown in Fig. 6. There was neither a puncture nor any surface flashover during the specified time. The test specimens fulfilled the requirements of the test in accordance with the standards as mentioned previously in Sect. 2.3. The graph clearly indicates that the LC reduced with the inclusion of fillers. In case of magnesium titanate-filled GRP composite (sample M), the LC is reduced by 53% compared to GRP composite without fillers (sample G).

Fig. 6 Variation of LC under water diffusion electrical test
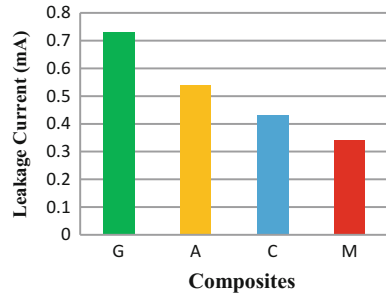
Table 4 Leakage currents of GRP composite rods

Samples	Leakage current (mA)	Observation
G	0.02	Withstood
A	0.02	Withstood
C	0.01	Withstood
M	0.01	Withstood

The reduction in LC values might be due to better interfacial bonding between the filler–filler, fiber–filler with the matrix [13].

3.6 Leakage Current of GRP Composite Rod

As discussed earlier, the fabricated GRP composites found acceptable both in dye penetration and water diffusion test as per the IEC standards. Hence, the samples were further examined for LC at 75 kV. The GRP composite insulator rods have shown a maximum LC of 0.02 mA and found to be acceptable as per the standards and the results are shown in Table 4. The LC of GRP composite rods was found improved with addition of combination of nano- and micro-fillers. They exhibited improved insulating properties which may be due to SiO_2, Al_2O_3, ATH, $MgTiO_3$, and $CaCO_3$ fillers. Off the GRP composite studied, sample M has the optimum LC.

4 Conclusions

We have studied the effect of nano- and microparticles on the dye penetration, water diffusion electrical test, and leakage current of GRP composites.

The following conclusions may be drawn from this work.

(i) The microstructural investigations show that the surface treatment can yield good interfacial adhesion between the nano/microparticles with epoxy and leads to good particle dispersion in the GRP composites.

(ii) The leakage current of the fabricated GRP composite rods (as cast and water diffused) was found to be much less than the IEC-specified levels.

(iii) It appears that the GRP composite with Mg TiO$_3$ filler (sample M) is better insulating material on a comparative basis. However, more work in this direction is necessary.

Further work is envisaged to perform LC tests after outdoor pollution in order to evaluate the significance of this work in practice.

References

1. Armentrout, D., Kumosa, M., Kumosa, L.: Water diffusion into and electrical testing of composite insulator GRP rods. IEEE Trans. Dielectr. Electr. Insul. (July 2004)
2. Kumosa, L., Armentrout, D., Benedikt, B., Kumosa, M.: An investigation of moisture and leakage currents in GRP composite hollow cylinders. IEEE Trans. Dielectr. Electr. Insul. **12** (5) (Oct 2005)
3. Kumosa, M., Qiu, Q.: Failure Analysis of Composite Insulators. Final Report to the Pacific Gas and Electric Company, Department of Engineering, University of Denvar (1996)
4. Kumosa, M., Armentrout, D., Kumosa, L., Han, Y.: Failure Analysis of Composite High Voltage Insulators. EPRI (2002)
5. Gonon, P., Sylvestre, A., Teysseyre, J., Prior, C.: Combined effects of humidity and thermal stress on the dielectric properties of epoxy-silica composites. Mater. Sci. Engg. B **83**, 158–164 (2001)
6. Maxwel, D., Pethric, R.A.: Dielectric studies of water in epoxy resins. Poly. Sci. **28** (1983)
7. Pylarinos, D., Siderakis, K., Pyrgioti, E.: Measuring and analyzing leakage current for Outdoor insulators and specimens. Rev. Adv. Mater. Sci. **29**, 31–53 (2011)
8. Gençoğlu, M.T., Cebeci, M.: The pollution flashover on high voltage insulators. Electr. Power Syst. Res. **78**(11), 1914–1921 (2008)
9. Gencoglu, M.T., Uyar, M.: Prediction of flashover voltage of insulators using least squares support vector machines. Expert Syst. Appl. **36**(7), 10789–10798 (2009)
10. Kumosa, M., Kumosa, L., Armentrout, D.: Failure analyses of Nonceramic insulators. Part 1: Brittle Fracture characteristics. IEEE Electr. Insul. Mag. **21**(3) (2005)
11. Fairuz, A.M., Sapuan, S.M., Zainudin, E.S., Jaafar, C.N.A.: Polymer composite manufacturing using a pultrusion process: a review. Am. J. Appl. Sci/ **11**(10), 1798–1810 (2014)
12. Boyale, A.A., Martin, C.J., Neuner, J.D.: Epoxy Resins. PolyComp.mse (2014)
13. Plesa, I., Notingher, P.V., Schlögl, S., Sumereder, C., Muhr, M.: Properties of polymer composites used in high voltage applications. Polymers **8**(5) (2016)
14. Castellon, J., Ramirez Vazquez, I.R., Fréchette, M., Fabiani, D.: Nanocomposite characterization and diagnostics tools. IEEE Electr. Insul. Mag. **29**(6) (2013)

Effect of Interleaving and Low Velocity Impact on the Dielectric Properties of Composite Laminates

**M. Umashankar, N. M. Renukappa, M. S. Lavanya
and Kunigal Shivakumar**

1 Introduction

The growth rate of carbon fiber reinforced composites (CFRC) in industrial technology triggers the innovative research studies about the different properties of the composites [1]. Carbon fiber polymer composites are dominant among structural composites due to their combination of low density, high strength, and high modulus of elasticity. The anisotropy characteristic of electrical properties in continuous fiber composites has been studied [2]. The electrical characteristic of CFRC depends on the stacking sequence and fabrication techniques. Galedhar et al. [3] explored the electric characteristics of the polymer composite laminates.

Joo and co-workers [4] have reported the use of multilayer films of different thickness which were fabricated by sandwiching (interleaving) a lossy dielectric material of identical thickness between each layer. A thermoplastic particle interleaving layer has been suggested by some researchers [5]. Such composites are reported to exhibit good resistance to damage due to impact loads and fracture toughness. However, the particle interleaved composites have few drawbacks like decreased in-plane stiffness and strength, increased laminate thickness, and lower values of glass transition temperature (T_g). These properties influence the mechanical properties of the composite.

M. Umashankar
JSS Research Foundation, JSSTIC, Mysuru 570006, Karnataka, India

N. M. Renukappa (✉) · M. S. Lavanya
Department of Electronics and Communication Engineering, Sri Jayachamarajendra
College of Engineering, Mysuru 570006, Karnataka, India
e-mail: renunijagal@gmail.com

K. Shivakumar
Department of Mechanical Engineering, Center for Composite Materials Research,
College of Engineering, North Carolina A&T State University,
Greensboro, NC 27411, USA

Polymer nanofiber interleaving technique has been investigated by some authors to overcome the drawbacks of the particle interleaving method by varying the amount of nylon-66 nanofiber [6, 7]. This material, though developed for high mechanical strength, is also reported to be good for electrical applications. Improvement in the dielectric properties has also been achieved by incorporating certain geometric changes in the structure of carbon fibers (CFs) by the use of orientation angles between the alternate layers and by varying the number of layers (plies) [8].

This paper presents the effects of interleaving and low velocity impact on the dielectric properties of non-interleaved and nylon-66 nanofiber interleaved with different concentrations of CF–epoxy composite laminates for electromagnetic interference (EMI) shielding applications.

2 Experimental Method

2.1 Materials

Unidirectional tape prepreg of polyacrylonitrile (PAN)-based CF (AS4) with a fiber volume fraction of 62% embedded in aerospace-grade epoxy resin (3501-6) with resin content of 38% was received from M/s Hexcel Composites. Chemicals like formic acid, chloroform were sourced from M/s Sigma-ALDRICH, USA, and nylon-66 crystals (Zytel 101, Molecular weight = 20,000 g/mol) were received from M/s DuPont, USA. Nylon-66 crystals are dissolved in formic acid and chloroform (75:25) to prepare a 12 wt.% concentrations homogeneous solution. Electrospinning process was used to produce non woven nylon-66 nanofiber mat.

2.2 Fabrication of Laminates

A 32 ply quasi-isotropic stacking sequence was followed to fabricate CF-epoxy non-interleaved composite using four symmetric sets of [-45°/90°/45°/0°] plies. Interleaved composites were prepared by placing one layer of the nanofiber mat in between two consecutive CF-epoxy prepreg layers [6, 7]. Three interleaved CF–epoxy laminates were prepared with 0.23, 0.69, and 1.15% weight per ply. These laminates were cured in an autoclave. The identification of the fabricated laminates is furnished in Table 1. The size of the laminates was 356 × 762 mm.

Table 1 Identification of CF–epoxy composites

Samples	Laminate code
Non-interleaved	IL 0.0
0.23% interleaved	IL 0.5
0.69% interleaved	IL 1.5
1.15% interleaved	IL 2.5

3 Measurements

3.1 Morphology

Microstructures of as-cast and impact-tested laminates were studied by using scanning electron microscope (SEM), Model S-3400N of M/s Hitachi, Japan. The samples were sputter coated with gold prior to SEM analysis.

3.2 Low Velocity Impact Test

The Dynatub drop-weight tower equipment was used to conduct the low velocity impact test as per ASTM D7136 using spherical steel tup mass 5.41 kg with a diameter of 25.4 mm. The test was conducted for impact heights range from 50 to 260 mm. Three specimens were tested for each impact heights. The tower was equipped with a pneumatic rebound brake system to prevent multiple impacts on the composites and instrumentation to measure the velocity just before the impact.

3.3 Dielectric Property

The dielectric properties of as cast and impact-tested composites were measured using ASTM test procedures. Capacitance, dissipation factor (tanδ), and conductance values were measured at 20 Hz–10 MHz by LCR meter, Wayne Kerr Model 6500P. By measuring the thickness of the specimen and area of contact electrode to the specimen, the dielectric constant (ε') and AC conductivity (σ_{ac}) were calculated.

4 Results and Discussion

4.1 SEM Analysis

Changes on surfaces of impacted composites compared to as cast were analyzed using the SEM images and are shown in Fig. 1. The more damage area was
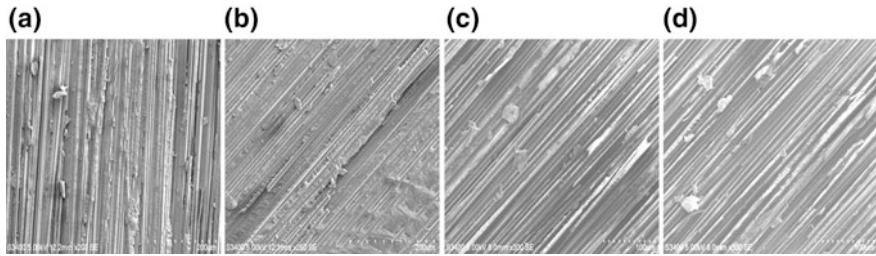
Fig. 1 SEM images of as cast samples: **a** IL 0.0, **c** IL 2.5 and impacted samples: **b** IL 0.0, **d** IL 2.5

Table 2 Low velocity impact damage data of the composites

Sample code	Threshold impact	
	Height (mm)	Force (kN)
IL 0.0	76	4.36
IL 0.5	91	4.70
IL 1.5	144	6.10
IL 2.5	145	6.38

observed in non-interleaved composite (IL 0.0). Less damage was observed in the interleaved composite (IL 2.5), since the carbon fibers are wrapped by the nylon nanofibers. Polymer nanofibers act as a coating to the fiber surface and provide a link between the fiber surface and the matrix to improve the fiber–matrix adhesion. This also improves the physical adhesion between the layers of carbon fibers and the epoxy [9].

4.2 Low Velocity Impact Test

The details of the damage initiated in the composites at the average threshold impact heights with force are shown in Table 2. With increase in the interleaving 0.23, 0.69, and 1.15%, the threshold impact heights and force also increased for interleaved composites.

4.3 Dielectric Constant

(i) Effect of frequency

The plot indicates that variation of ε' occurs in three transitions: (i) remain constant from 20 Hz–10 kHz. In this range, the Maxwell-Wagner polarization [10]

follows the changes in the electric field, and hence, loss is minimum and ε' is maximum, (ii) decreases from 10 kHz–4 MHz, at this band of frequency, polarization effects appears because of the quick changes in the electric field. Also, at a particular frequency, the exchange of electrons fails to follow the applied field condition [11], therefore polarization decreases causing reduction in ε' and (iii) the interfacial polarization can cause an increase in the ε' and hence a slight increase in the ε' is observed after 4 MHz. However, the increment rate is lower compared to that at lower frequencies.

(ii) Effect of interleaving and low velocity impact

From Fig. 2a, ε' decrease as the interleaving concentration increases was observed. This is because of the decrease in the polarizability and also the contact
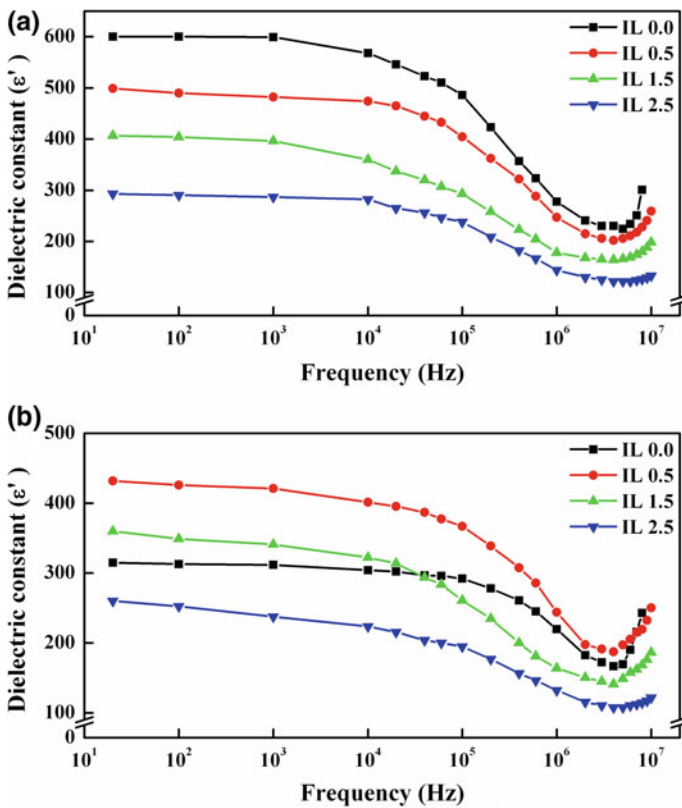
Fig. 2 Variations of ε' with frequency of **a** as cast **b** impacted composites

between the carbon fibers of adjacent layers. The significant reduction of ε' in case of IL 0.0 as compared to all the interleaved composites is observed from Fig. 2b. This is due to fiber breakage and/or change in the conduction path geometry [12]. Interleaving layer acts as a barrier against depth of damage initiation to the other layers in the composites.

4.4 Dissipation Factor

(i) Effect of frequency

The negligible tanδ values were observed (Fig. 3) over the frequency range 20 Hz–100 kHz, thereafter increases marginally. This is due to the local motion of polar groups and relaxation process. The orientation of dipoles synchronizes with the electric field at low frequency range (20 Hz–100 kHz). The relaxation peak
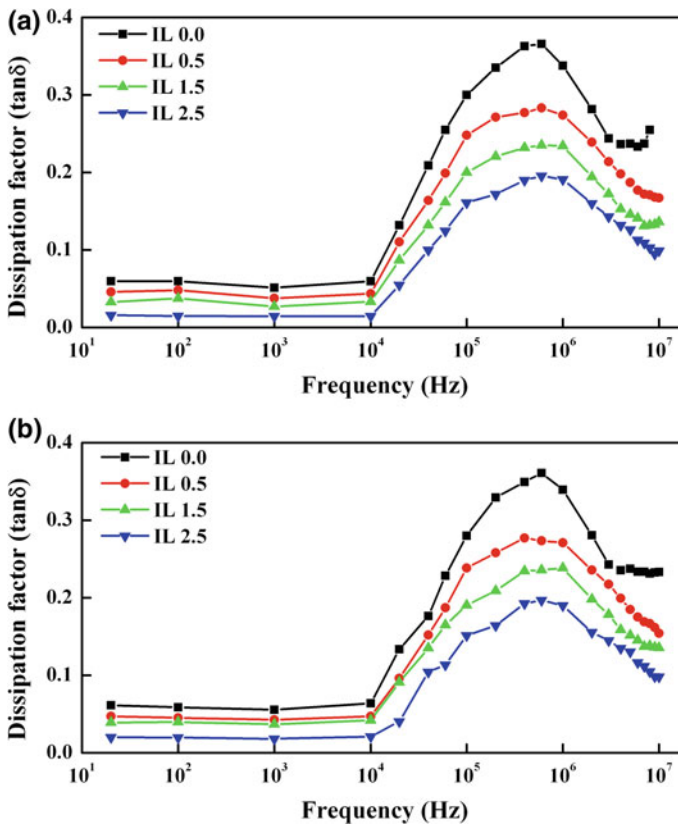
Fig. 3 Variations of tanδ with frequency of **a** as cast **b** impacted composites

occurs at 600 kHz due to charged carrier systems and the motions involved in this process occur at faster rate.

(ii) **Effect of interleaving and low velocity impact**

With increase in the interleaving percentage, tanδ decreased as compared to IL 0.0. This happens due to charges induced which are unable to follow the field which is continuously reversing, therefore reducing electronic oscillations with increase in frequency [13]. As interleaving concentration increases, the height of the tanδ peak lowers, and broadening takes place due to the glass transition process in the epoxy main chains by cooperative micro-Brownian motions within their amorphous regions [14, 15]. All of these characteristics point the feasible applicability of these composites for decoupling capacitor applications [16]. There is no significant variation in tan δ values of impacted composites as compared to the as cast samples.

4.5 AC Conductivity

(i) **Effect of frequency**

From Fig. 4, the σ_{ac} remains constant up to 10 kHz for as cast and 1 MHz for impacted composites, and thereafter increases gradually over measured frequency. The effect is much higher in high frequency compared to low frequency explained from Eq. (1).

$$\sigma_{ac} = \sigma_{dc} + \omega\varepsilon'' \tag{1}$$

The dc conductivity (σ_{dc}) in S/m appears from electronic or ionic conductivity where as the dielectric loss factor (ε'') from interfacial and dipolar polarization. As the frequency increases, σ_{ac} also increases due to polarization which leads to increase in total conductivity.

(ii) **Effect of interleaving and low velocity impact**

The σ_{ac} of the composites is found to be decreasing with increasing interleaving percentages in high frequency ranges. This is because of the insulating interleaved layer offering resistance to the change in electric field of the composites because of the space charge polarization. Impacted composites showed lower conductivities at high frequencies compared to as cast samples due to the disturbed conductive network of the carbon fibers.
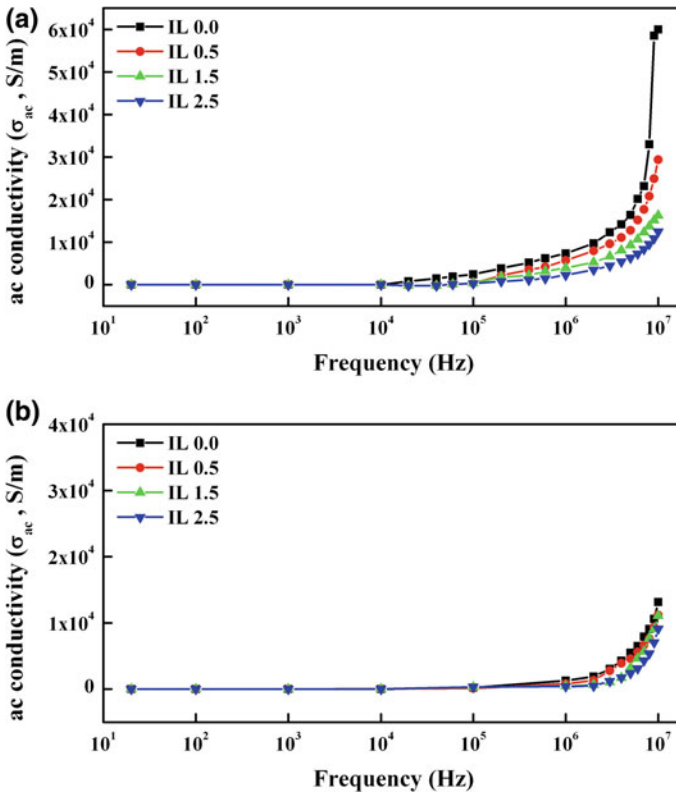
Fig. 4 Variations of σ_{ac} with frequency of **a** as cast **b** impacted composites

5 Conclusion

The conclusions made are as follows:

(i) The ε' decreased by 19, 33, and 52% for IL 0.5, IL 1.5, and IL 2.5 compared to IL 0.0 at 1 kHz for as cast samples.

(ii) The ε' of impacted samples decreased by 47, 12, 14, and 17% for IL 0.0, IL 0.5, IL 1.5, and IL 2.5, respectively, as compared to as cast samples at 1 kHz.

(iii) The tanδ curves have a bell-shaped relaxation peak at 600 kHz for both the as cast and impacted samples which are the characteristics of charged carrier systems.

(iv) Frequency-dependent σ_{ac} was observed in high frequency ranges for both the as cast and impacted samples.

References

1. Ramadin, Y., Jawad, S.A., Musameh, S.M., Ahmad, M., Zihlif, A.M.: Electrical and electromagnetic shielding behavior of laminated epoxy-carbon fiber composite. Polym. Int. **4**, 145–150 (1994)
2. Lee, W.I., Springer, G.S.: Interaction of electromagnetic radiation with organic matrix composites. J. Compos. Mater. **18**, 357–409 (1984)
3. Galehdar, A., Rowe, W.S.T., Ghorbani, K.: The effect of ply orientation on the performance of antennas in or on carbon fiber composites. Progress Electromagn. Res. **116**, 123–136 (2011)
4. Joo, J., Lee, C.Y.: High frequency electromagnetic interference shielding response of mixtures and multilayer films based on conducting polymers. J. Appl. Phys. **88**, 513–518 (2000)
5. Hojo, M., Matsuda, S., Tanaka, M., Ochiai, S., Murakami, A.: Mode I delamination fatigue properties of interlayer-toughened CF/epoxy laminates. Compos. Sci. Technol. **66**, 665–675 (2006)
6. Akangah, P., Shivakumar, K.: Assessment of impact damage resistance and tolerance of polymer nanofiber interleaved composite laminates. J. Chem. Sci. Technol. **2**, 39–52 (2013)
7. Ahmed, H.A., Shivakumar, K.N.: Effect of amount of Nylon-66 nanofiber interleaf on impact performance of AS4/3501-6 carbon epoxy composite laminate. In: 57th AIAA/ASCE/AHS/ ASC Structures, Structural Dynamics and Materials Conference. American Institute of Aeronautics and Astronautics (2016)
8. Kim, H.G., Shin, H.J., Kim, G.C., Park, H.J., Moon, H.J., Kwac, L.K.: Electromagnetic interference shielding characteristics for orientation angle and number of plies of carbon fiber reinforced plastic. Carbon Lett. **15**, 268–276 (2014)
9. Bobadilla Sanchez, E.A., Martínez-Barrera, G., Brostow, W., Datashvili, T.: Effects of polyester fibers and gamma irradiation on mechanical properties of polymer concrete containing $CaCO_3$ and silica sand. Express Polym. Lett. **3**, 615–620 (2009)
10. Panwar, V., Park, J.O., Park, S.H., Kumar, S., Mehra, R.M.: Electrical, dielectric and electromagnetic shielding properties of polypropylene-graphite composites. J. Appl. Polym. Sci. **115**, 1306–1314 (2010)
11. Patil, A.G., Patankar, K.K., Mathe, V.I., Mahajan, R.P., Patil, S.A.: Dielectric behaviour and a.c. conductivity in $Cu_xFe_{3-x}O_4$ ferrite. Bull. Mater. Sci. **23**, 447–452 (2000)
12. Chung, D.D.L.: Carbon materials for structural self-sensing, electromagnetic shielding and thermal interfacing. Carbon **50**, 3342–3353 (2012)
13. Madhuri Nanda, R.N., Chaudhary, P., Tripathy, D.K.: Dielectric relaxation of conductive carbon black reinforced chlorosulfonated polyethylene vulcanizates. Polym. Compos. **31**, 152–162 (2010)
14. Chanmal, C.V., Jog, J.P.: Dielectric relaxations in PVDF/$BaTiO_3$ nanocomposites. Express Polym. Lett. **2**, 294–301 (2008)
15. Kortschot, M.T., Woodhams, T.R.: Computer simulation of the electrical conductivity of polymer composites containing metallic fillers. Polym. Compos. **9**(1), 60–71 (1988)
16. Mahmoodi, M., Arjmand, M., Sundararaj, U.T., Park, S.: The electrical conductivity and electromagnetic interference shielding of injection molded multi-walled carbon nanotube/ polystyrene composites. Carbon **50**, 1455–1464 (2012)

Numerical Modeling and Study of Vaporization of Single Droplet and Mono-dispersed Spray Under Mixed Convection Conditions

Sumer Dirbude, Abhijit Kushari and Vinayak Eswaran

1 Introduction

Modeling of droplet vaporization and dynamics phenomena is a very challenging problem due to complex and simultaneous interactions of various sub-processes. Therefore, the computational costs associated with the multi-scale resolution is likely unacceptable for multi-dimensional simulations of the sprays. Hence, from the computational point of view, a good quantitative model, preferably simple, is best for the modeling of droplet evaporation of liquid fuel.

There are existing models, viz. the classical model, the vortex model, infinite conductivity models, the conduction limit models, and the effective conductivity models [1]. The infinite conductivity, conduction limit, and finite conductivity have been found to provide comparable results of droplet history for single droplet and sprays at low pressure [2–4]. In these models, the forced convection correlations proposed in Refs. [5–9] are generally used. However, it has been noted in Refs. [10–13] that the blowing effect (which is the effect on the evaporation process due to the outwardly moving evaporated vapors from the droplet) is important at high evaporation rates ($B > 3.0$). Sirignano [4] and Golahalli [14] observed that for droplet radius of the order of 1 mm compared to 100 μm there are three orders of magnitude increase in the Gr and the buoyancy effects can occur. Also, near the

S. Dirbude (✉)
Department of Mechanical Engineering, National Institute of Technology Delhi,
Delhi 110040, India
e-mail: sbd@nitdelhi.ac.in; sumery7@gmail.com

A. Kushari
Department of Aerospace Engineering, Indian Institute of Technology Kanpur,
Kanpur 208016, India

V. Eswaran
Department of Mechanical and Aerospace Engineering,
Indian Institute of Technology-Hyderabad, Kandi 502285, India

73

droplet surface, the density of the fuel vapors can be significantly different than that of air. In this situation, there is substantial evidence (for instance, [15] on biofuels viz. rapeseed methyl ester (RME) and sunflower methyl ester (SME), [16] on soybean oil and [17] on vegetable oil droplets) that the evaporation rate may be affected by the natural convection. Therefore, along with the forced convection the free convection or mixed convection become important, especially in the context of evaporation modeling of biofuels. To the knowledge of present authors, mixed convection modeling with blowing effect of conventional and biofuels has not been given considerations in the past.

2 Solution Methodology

In this work, we consider two cases viz. droplet vaporization without droplet dynamics and with droplet dynamics under laminar and ambient conditions. In both the cases, the Sherwood number (Sh^*) and the Nusselt number (Nu^*) are calculated using correlations mentioned in Table 1 for convection. Here, we use an effective Reynolds number [18] which is given as,

$$Re_{\mathrm{eff}} = Re_{\mathrm{d}} + \sqrt{Gr_{\mathrm{d}}} \qquad (1)$$

where the Reynolds number, $Re_{\mathrm{d}} = \frac{u_\infty d_{\mathrm{d}}}{v_\infty}$, the Grashof number, $Gr_{\mathrm{d}} = \frac{g\beta\Delta T d_{\mathrm{d}}^3}{v_\infty^2}$. Here, g is the acceleration due to gravity; u_∞ is the free stream air velocity; d_{d} is the droplet diameter; β is the coefficient of thermal expansion calculated as $1/T_{\mathrm{avg}}$; T_{avg} is the average temperature of the ambient and the droplet; ΔT is the temperature difference between ambient and droplet; v_∞ is the dynamic viscosity of gas phase. It is noted that the models C0–C3 are convection models, whereas C4 and C5 are blowing effect models (see Table 1).

3 Vaporization: Without Droplet Dynamics

3.1 Numerical Methodology

The unsteady differential equation [19] of the droplet temperature and droplet mass for n-decane and n-hexane is solved using the fourth-order Runge–Kutta method. The average properties are evaluated at some reference temperature and composition using the one-third rule [3]. Fuel and air mixture properties (e.g., specific heat, thermal conductivity) are calculated using a mixing rule [20].

Table 1 Gas-phase models used in the present study

Model	Correlations	Refs.
C0	$Nu^* = 2 + 0.6Re_{\mathrm{d}}^{1/2}Pr_{\mathrm{g}}^{1/3}$; $Sh^* = 2 + 0.6Re_{\mathrm{d}}^{1/2}Sc_{\mathrm{g}}^{1/3}$ where $Re_{\mathrm{d}} = \frac{\rho_{\mathrm{g}}\boldsymbol{u}_{\mathrm{rel}}d_{\mathrm{d}}}{\mu_{\mathrm{g}}}$, $Pr_{\mathrm{g}} = \frac{\mu_{\mathrm{g}}C_{\mathrm{g}}}{k_{\mathrm{g}}}$, and $Sc_{\mathrm{g}} = \frac{v_{\mathrm{g}}}{D_{\mathrm{g}}}$. Range: $0 \leq Re_{\mathrm{d}} \leq 200$ $0.6\,\mathrm{mm} \leq d_{\mathrm{d}} \leq 1.1\,\mathrm{mm}$ with ambient at 493 K	[9, 24]
C1	$Nu^* = 2 + 0.552Re_{\mathrm{eff}}^{1/2}Pr_{\mathrm{g}}^{1/3}$; $Sh^* = 2 + 0.552Re_{\mathrm{eff}}^{1/2}Sc_{\mathrm{g}}^{1/3}$ where $Re_{\mathrm{eff}} = Re_{\mathrm{d}} + \sqrt{Gr_{\mathrm{d}}}$, $Re_{\mathrm{d}} = \frac{\rho_{\mathrm{g}}\boldsymbol{u}_{\mathrm{rel}}d_d}{\mu_{\mathrm{g}}}$, $Pr_{\mathrm{g}} = \frac{\mu_{\mathrm{g}}C_{\mathrm{g}}}{k_{\mathrm{g}}}$, and $Sc_{\mathrm{g}} = \frac{v_{\mathrm{g}}}{D_{\mathrm{g}}}$. Range: $0 \leq Re_{\mathrm{eff}} \leq 325$ $0.1\,\mathrm{mm} \leq d_{\mathrm{d}} \leq 1.1\,\mathrm{mm}$ with ambient at room temperature to 613 K	[6, 8, 9]
C2	$Nu^* = 1 + \left(1 + Re_{\mathrm{eff}}Pr_{\mathrm{g}}\right)^{1/3}f(Re_{\mathrm{eff}})$; $Sh^* = 1 + \left(1 + Re_{\mathrm{eff}}Sc_{\mathrm{g}}\right)^{1/3}f(Re_{\mathrm{eff}})$ where $f(Re_{\mathrm{eff}}) = \begin{cases} 1, & 0 < Re_{\mathrm{eff}} < 1 \\ Re_{\mathrm{eff}}^{0.077}, & 1 < Re_{\mathrm{eff}} < 400 \end{cases}$, $Re_{\mathrm{eff}} = Re_{\mathrm{d}} + \sqrt{Gr_{\mathrm{d}}}$, $Re_{\mathrm{d}} = \frac{\rho_{\mathrm{g}}\boldsymbol{u}_{\mathrm{rel}}d_{\mathrm{d}}}{\mu_{\mathrm{g}}}$, $Pr_{\mathrm{g}} = \frac{\mu_{\mathrm{g}}C_{\mathrm{g}}}{k_{\mathrm{g}}}$, and $Sc_{\mathrm{g}} = \frac{v_{\mathrm{g}}}{D_{\mathrm{g}}}$. The region of validity of this correlation is $0.25 \leq Pr_{\mathrm{g}}, Sc_{\mathrm{g}} \leq 100$ and $0 \leq Re_{\mathrm{eff}} \leq 400$, with an error less than 3%	[5]
C3	$Nu^* = \left(2 + 0.552Re_{\mathrm{eff}}^{1/2}Pr_{\mathrm{g}}^{1/3}\right)\left(1 + \frac{1.232}{Re_{\mathrm{eff}}Pr_{\mathrm{g}}^{4/3}}\right)^{-1/2}$ $Sh^* = \left(2 + 0.552Re_{\mathrm{eff}}^{1/2}Sc_{\mathrm{g}}^{1/3}\right)\left(1 + \frac{1.232}{Re_{\mathrm{eff}}Sc_{\mathrm{g}}^{4/3}}\right)^{-1/2}$ where $Re_{\mathrm{eff}} = Re_{\mathrm{d}} + \sqrt{Gr_{\mathrm{d}}}$, $Re_{\mathrm{d}} = \frac{\rho_{\mathrm{g}}\boldsymbol{u}_{\mathrm{rel}}d_{\mathrm{d}}}{\mu_{\mathrm{g}}}$, $Pr_{\mathrm{g}} = \frac{\mu_{\mathrm{g}}C_{\mathrm{g}}}{k}$, and $Sc_{\mathrm{g}} = \frac{v_{\mathrm{g}}}{D_{\mathrm{g}}}$. Range: $0 \leq Re_{\mathrm{eff}} \leq 325$ $0.1\,\mathrm{mm} \leq d_{\mathrm{d}} \leq 1.1\,mm$ with ambient at room temperature to 613 K	[7]
C4	$Nu^* = \frac{2 + 0.87Re_{\mathrm{eff}}^{\frac{1}{2}}Pr_{\mathrm{g}}^{\frac{1}{3}}}{(1 + B_{\mathrm{M}})^{0.7}}$; $Sh^* = \frac{2 + 0.87Re_{\mathrm{eff}}^{1/2}Sc_{\mathrm{g}}^{1/3}}{(1 + B_{\mathrm{M}})^{0.7}}$ where $Re_{\mathrm{eff}} = Re_{\mathrm{d}} + \sqrt{Gr_{\mathrm{d}}}$, $Re_{d} = \frac{\rho_{\mathrm{g}}\boldsymbol{u}_{\mathrm{rel}}d_d}{\mu_{\mathrm{g}}}$, $Pr_{\mathrm{g}} = \frac{\mu_{\mathrm{g}}C_{\mathrm{g}}}{k_{\mathrm{g}}}$, and $Sc_{\mathrm{g}} = \frac{v_{\mathrm{g}}}{D_{\mathrm{g}}}$. Range of validity: $10 \leq Re_{\mathrm{eff}} \leq 100$	[13]
C5	$Nu^* = \frac{2 + 0.39Re_{\mathrm{eff}}^{0.54}Pr_{\mathrm{g}}^{0.76}}{(1 + B_{\mathrm{M}})^{0.7}}$; $Sh^* = \frac{2 + 0.39Re_{\mathrm{eff}}^{0.54}Sc_{\mathrm{g}}^{0.76}}{(1 + B_{\mathrm{M}})^{0.7}}$ where $Re_{\mathrm{eff}} = Re_{\mathrm{r}} + \sqrt{Gr_{\mathrm{d}}}$, $Re_{\mathrm{r}} = \frac{\rho_{\mathrm{g}}\boldsymbol{u}_{\mathrm{rel}}r_{\mathrm{d}}}{\mu_{\mathrm{g}}}$, $Pr_{\mathrm{g}} = \frac{\mu_{\mathrm{g}}C_{\mathrm{g}}}{k_{\mathrm{g}}}$, and $Sc_{\mathrm{g}} = \frac{v_{\mathrm{g}}}{D_{\mathrm{g}}}$. Range of validity: $30 \leq Re_{\mathrm{eff}} \leq 250$	[11]

4 Vaporization: With Droplet Dynamics

4.1 Computational Domain, Boundary Conditions and Initial Conditions

The computational domain of length is 0.05 m and height 0.005 m is considered for ANSYS Fluent simulations (see Fig. 1b). It consists of an inlet (from which mono-dispersed droplets of ethanol enter and subsequently evaporate in the domain), flow passage, outlet, and top and bottom symmetry walls. The governing

equations of two-phase laminar flow are solved using the Eulerian–Lagrangian approach. A second-order accurate convection scheme is used and the system of equations in the continuous phase is solved using the SIMPLE algorithm. In all the simulations, solutions are assumed to be converged when residual in the flow variables is of the order of 10^{-3}. The single droplet vaporization models with gas-phase modeling using correlations mentioned in Table 1 are incorporated in the code via user-defined functions (UDF).

The following boundary conditions are used in the simulation of quasi-2D (see Fig. 1b) laminar droplet evaporation of ethanol: (a) At the left inlet, gas-phase x velocity, $u_g = 1.12$ m/s, gas-phase y velocity, $v_g = 0$ m/s gas-phase temperature, $T_g = 480$ K, mass fraction of gaseous ethanol, $Y_{ethanol} = 0.0$, initial droplet diameter, $d_{d,0} = 30$ μm, droplet x velocity, $u_l = 1.12$ m/s, droplet y velocity, $v_l = 0$ m/s, droplet temperature, $T_{l,0} = 323$ K, and mass flow rate of one drop, $\dot{m}_{fd} = 2.3 \times 10^{-7}$ kg/s is specified; (b) at the right outlet, $\frac{\partial \varphi}{\partial n} = 0$ and $p = 0.0$ are applied where $\varphi = u, v, T, Y,$ and p is the static pressure; (c) at other (top and bottom) boundaries, no diffusive flux i.e. $\frac{\partial \varphi}{\partial n} = 0$ and no convective flux i.e. $v = 0$ are enforced for $\varphi = u, T,$ and Y. At the inlet boundary, the number of droplets is considered equal to the number of grid points. With the specified boundary conditions and arbitrary initial conditions, the converged steady-state solutions are obtained.

4.2 Grid Independence Study

We compare three structured meshes with grid cells of 9501 (coarse), 18,981 (medium), and 40,435 (fine) for the grid independence test. From Fig. 1a, the medium grid is considered as optimum and is used for further simulations. The details of the optimum grid are also shown in Fig. 1b.
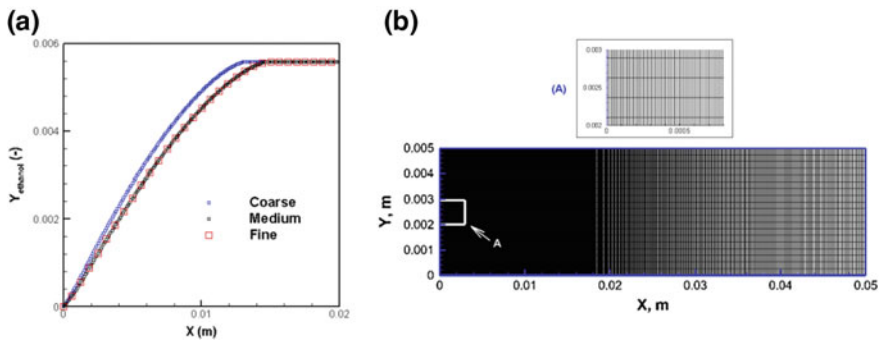
Fig. 1 a Grid independence study [9,501 cells (coarse), 18,981 cells (medium), and 40,435 cells (fine)], b Computational domain with mesh for ethanol spray simulations

5 Results and Discussions

In this section, we show the results of single droplet vaporization models considering mixed convection using the effective *Re* model at ambient pressure for: without droplet dynamics for *n*-decane (initial $Re_d/Gr_d = 0.09$) and *n*-hexane (initial $Re_d/Gr_d = 2.12$); with droplet dynamics for ethanol (initial $Re_d/Gr_d = 60$).

5.1 Initial $Re_d/Gr_d = 0.09$ Case: High Evaporation Rate

Figure 2 shows theoretical results obtained with each of the five correlations C1–C5 (with effective *Re*) for *n*-decane with initial $Re_d/Gr_d = 0.09$ (high evaporation rate). The results are compared with the experimental data of [21] and numerical (classical, rapid mixing model) data of [3] at the droplet Reynolds number, $Re_d = 17$, the free convection droplet Reynolds number, $Gr_d = 195$, ambient air temperature, $T_{amb} = 1000$ K, the initial droplet diameter, $d_{d,0} = 2.0$ mm and initial droplet temperature, $T_{s,0} = 315$ K.

It can be seen from Fig. 2 that with C5 correlation computed results match most closely with the experimental data of droplet-squared diameter, while C4 best matches the results of droplet surface temperature. Further, C5 model predictions of droplet-squared diameter are much better that the numerical results of [3] which uses same gas-phase model, but with forced convection only. This implies that the blowing effect is effectively present in the droplet evaporation process and C5 model is better than C4 in predicting reasonably accurate evaporation rate constants. On the other hand, C4 model predictions of droplet surface temperature

Fig. 2 Comparison of evaporation models without droplet dynamics: temporal history of **a** droplet diameter squared, **b** droplet surface temperature for *n*-decane [$Re_d = 17$; $Gr_d = 195$; ambient air temperature, $T_{amb} = 1000$ K; boiling temperature, $T_{bn} = 446.9$ K; $d_{d,0} = 2.0$ mm; $T_{s,0} = 315$ K]

match well with both experimental and numerical results during initial transients. It is known fact that the effect of convection (this term only appears in the gas-phase model) is to lower the evaporation time and does not affect steady-state evaporation time or duration of heat-up period [22]. Therefore, the effect of the gas-phase model on droplet temperature is absent. The under prediction in droplet temperature by C4 and C5 model could be due to the use of the infinite conductivity assumption in the liquid-phase model. Since the heat from the surroundings penetrates into the droplet, a development of the thermal boundary layer inside a droplet would have a significant effect on heat penetration. It warrants a use of other sophisticated models, viz. finite conductivity liquid-phase model, in situations where accuracy is needed. Nonetheless, C5/C4 model predictions of droplet surface temperature are within the 5% error bars of the experimental data.

5.2   Initial $Re_d/Gr_d = 2.12$ Case: Medium Evaporation Rate

Figure 3 shows theoretical results obtained with each five correlations C1–C5 (with effective Re) for n-hexane with initial $Re_d/Gr_d = 2.12$ (medium evaporation rate case). The results of the history of droplet diameter squared are compared with the experimental data of [6] at the droplet Reynolds number, $Re_d = 17$, the free convection droplet Reynolds number, $Gr_d = 52$, ambient air temperature, $T_{amb} = 1000$ K, the initial droplet diameter, $d_{d,0} = 2.0$ mm and initial droplet temperature, $T_{s,0} = 315$ K. In the absence of experimental data for droplet surface temperature, the results are compared with the numerical (classical, rapid mixing model) data of [3] under the same conditions.

It can be seen from Fig. 3 that the C5 correlation results match more closely with the experimental data of droplet-squared diameter than the C1–C4 models. Although the C4 model had been proposed for blowing effect correction, it is found
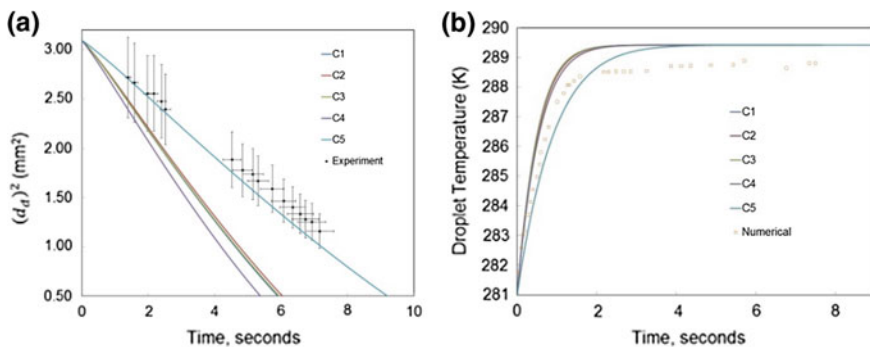
Fig. 3 Comparison of evaporation models without droplet dynamics: temporal evolution of **a** droplet diameter squared, **b** droplet surface temperature for n-hexane [$Re_d = 110$; $Gr_d = 52$; $T_{amb} = 437$ K; $T_{bn} = 344.6$ K; $d_{d,0} = 1.76$ mm; $T_{s,0} = 281$ K]

to be consistently worse than C5. On the other hand, C5 is consistent with the prediction of the history of droplet diameter. This also shows that blowing effects are indeed important and further gas-phase correlations with a wide range of validity of Reynolds number are required. Further, C5 model predictions of initial transients of droplet surface temperature are in better agreement with that of the numerical results of [3] which uses the same liquid-phase model.

It is known that the size of the droplet substantially affects the heat-up period and not the evaporation process. On the other hand, the effect of initial droplet surface temperature (boiling temperature) on evaporation time at high ambient temperature is almost negligible. However, the evaporation rate is different for different fuels due to a difference in thermo-physical properties. Therefore, it is of interest to find out which model best predicts correct evaporation rates preferably for all fuels. It can be observed from these two cases, i.e., pure component fuels, that the blowing effect model (C5 model) is insensitive to the fuel type in the range of the ratio of initial Re_d/Gr_d. However, this needs to be confirmed in the case of biofuels which are multi-component in nature. Therefore, we study ethanol biofuel for low evaporation rate, i.e., initial $Re_d/Gr_d = 60$ case considering the simplest case of laminar flow and mono-dispersed droplets of uniform size including the droplet dynamics.

5.3   Initial $Re_d/Gr_d = 60$ Case: Low Evaporation Rate

Figures 4 and 5 show comparison of theoretical results obtained with each six correlations C0–C5 (with effective Re) for ethanol, with initial $Re_d/Gr_d = 60$ (low evaporation rate), with the data of [23]. Figure 4 shows the comparison of ethanol mass fraction and droplet velocity. Figure 5 shows a comparison of the temporal history of droplet-squared diameter and droplet surface temperature. The results are
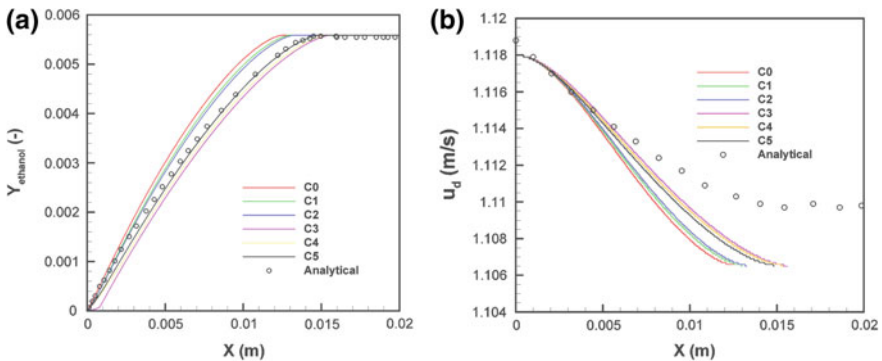
Fig. 4 Comparison of evaporation models with droplet dynamics: **a** ethanol mass fraction, **b** droplet velocity. [$Re_d = 24$; $Gr_d = 0.4$; $T_{amb} = 480$ K, $T_{bn} = 352$ K; $d_{d,0} = 0.03$ mm; $T_{s,0} = 323$ K]
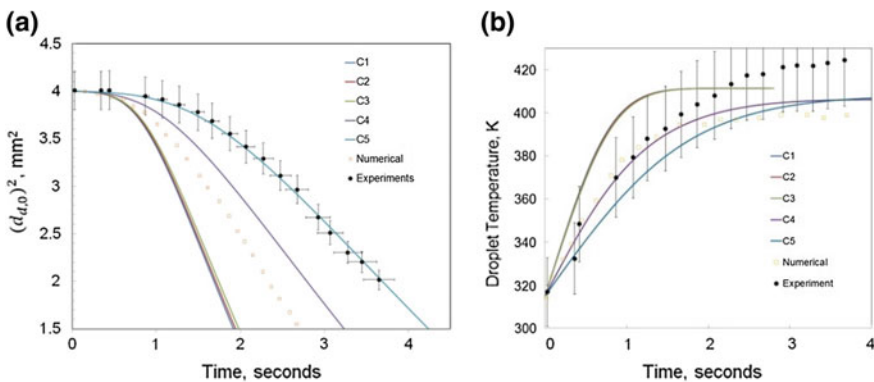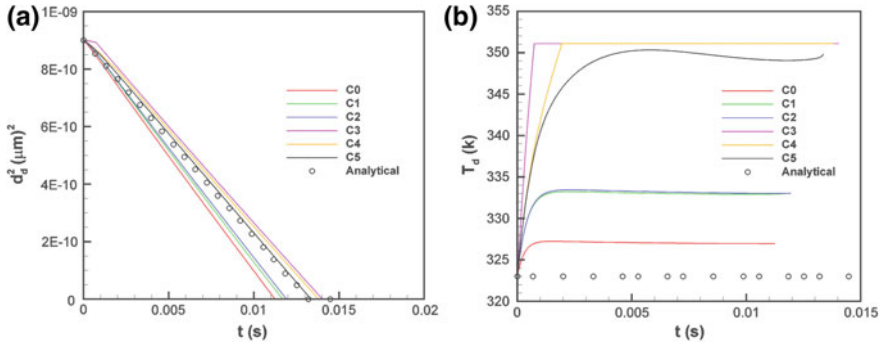
Fig. 5 Comparison of evaporation models with droplet dynamics: temporal history of **a** droplet-squared diameter, **b** droplet surface temperature. [Re_d = 24; Gr_d = 0.4; T_{amb} = 480 K, T_{bn} = 352 K; $d_{d,0}$ = 0.03 mm; $T_{s,0}$ = 323 K]

at droplet Reynolds number, Re_d = 24, free convection droplet Reynolds number, Gr_d = 0.4, ambient temperature, T_{amb} = 480 K, initial uniform droplet diameter, $d_{d,0}$ = 0.03 mm, and initial droplet temperature, $T_{s,0}$ = 323 K. In this case, the effect of natural convection is weak as compared to forced convection.

It can be observed from Fig. 4a that the results reasonably predict the ethanol mass-faction in the inlet section till the ethanol fully evaporates (i.e., after approx. 0.012 m). Among C0–C5 models, C5 performs extremely well in predicting the fuel mass fraction. However, from Fig. 4b, a slight under prediction (maximum difference of approx. 0.2%) in the droplet velocity is observed in the present modeling of droplet dynamics. This difference is essentially observed due to the differences in the drag law used in the computer code and the analytical solution.

Figure 5a shows under predictions (by 0.002 s) in evaporation time by some models. However, all results correctly predict the d-square law nature of droplet evaporation. The evaporation rate can be obtained from Fig. 5a (i.e., slope of the curve).

From the figure, it can be observed that the C5 model predicts the slope very well. It could have been better to discuss critical parameters like droplet distribution, penetration length. However, the droplet distribution is considered as uniform. The penetration length is associated with the droplet velocity and evaporation time. From Fig. 5a, it can be seen that the C5 prediction of penetration length is good. Although the droplet temperature is assumed constant over time in the analytical solution, a comparison of the droplet surface temperature predicted by the various models is shown in Fig. 5b. From this figure, it can be observed that the models C3, C4, and C5 form one group, and C1 and C2 form another. Both these groups do not match with the results of C0 model. However, all the models predict droplet steady-state temperature below its boiling point temperature. In the absence of analytical data which takes into account variation of droplet temperature, it is not possible to conclude which model is best. However, if the majority of the models are considered, the deviation among the C3, C4, and C5 models' results is within

0.85%. Also, the temperature, after 0.005 s, is constant within the error of 0.3%. Therefore, looking at the predictions of the droplet evaporation rate, it can be concluded that the C5 model is reasonably good. It should be noted that in the analytical solutions, the droplet temperature was assumed constant throughout. On the other hand, our models consider that the droplet is spatially constant but varying with time. Since our model is an improved version over the very simple assumption considered in the analytical solution, the transient behavior is predicted very well with our models.

It can be observed from this case (and previous cases) that the blowing effect model (C5 model) is consistent in predicting droplet diameter history at all evaporation rates, i.e., in the range of initial Re_d/Gr_d considered. This shows that blowing effect model (C5) is insensitive to the thermophysical properties of pure- and multi-component fuels in the range of the ratio of initial Re_d/Gr_d considered here. Also, the model predictions (C0–C5) show that the evaporation of ethanol is much like a mono-component droplet. Since the blowing effect model (C5) results are closely matched with the reference data, it is interesting to note that blowing effect is likely significant during the evaporation of fuels/biofuels

6   Conclusions

In this work, the numerical models of single droplet vaporization, i.e., gas phase with effective Re and classical liquid-phase finite conductivity model is studied for n-decane (initial $Re_d/Gr_d = 0.09$) and *n*-hexane (initial $Re_d/Gr_d = 2.12$) without droplet dynamics and ethanol (initial $Re_d/Gr_d = 60$) with droplet dynamics at ambient pressure. The following conclusions are made:

- Mixed convection effects are not negligible in the modeling of vaporization of fuels when the initial Re_d/Gr_d is in the range $0.09 \leq$ initial $Re_d/Gr_d \leq 60$ for the given droplet diameter and ambient conditions at atmospheric pressure.
- For the modeling of vaporization of biofuels, viz. ethanol, the blowing effect is expected to be significant. The biofuel droplets evaporate much like mono-component droplets. However, a further study with multi-component modeling would be helpful for other fuels, for instance, biofuels and diesel blends.
- Blowing effect model C5 is consistent in predicting the history of the droplet-squared diameter of conventional and biofuels in the range $0.09 \leq$ initial $Re_d/Gr_d \leq 60$.
- Blowing effect model C5 is insensitive to the thermophysical properties, i.e., latent heat of vaporization, boiling point temperature, of fuels.
- At intermediate temperature difference between ambient and droplet, and low latent heat of vaporization of bio-fuels, $B > 3$ i.e. the evaporation rate are high. Under these conditions and at high Re_d/Gr_d (of the order of magnitude equals to 1), the C5 model is recommended.

References

1. Sazhin, S.S.: Advanced models of fuel droplet heating and evaporation. Prog. Energy Combust. Sci. **32**, 162–214 (2006)
2. Chen, G., Agarwal, S.K., Jackson, T.A., Switzer, G.L.: Experimental study of pure and multi-component fuel droplet evaporation in a heated air flow. At. Sprays **7**, 317–337 (1997)
3. Miller, R.S., Harstad, K., Bellan, H.J.: Evaluation of equilibrium and non-equilibrium evaporation models for many droplet gas–liquid flow simulations. Int. J. Multiph. Flow **24**, 1025–1055 (1998)
4. Sirignano, W.A.: Fluid Dynamics and Transport of Droplets and Sprays, 2nd edn. Cambridge University Press (2010)
5. Clift, R., Grace, J.R., Weber, M.E.: Bubbles, Drops and Particles. Academic Press, New York (1978)
6. Downing, C.G.: The evaporation of drops of pure liquids at elevated temperatures, rates of evaporation and wet-bulb temperature. AIChE J. **12**(4), 760–766 (1966)
7. Faeth, G.M., Lazar, R.S.: Fuel droplet burning rates in a combustion gas environment. AIAA J. **9**, 2165–2171 (1971)
8. Froessling, N.: Ueber die Verdunstungfallender Tropfen. Gerlands Beitraege. Geophys. **52**, 170–216 (1938)
9. Ranz, W.E., Marshall, W.R. Jr.: Evaporation from drops (Part I and II). Chem. Eng. Progress **48**(3), 141–146, 172–180 (1952)
10. Abramzon, B., Sirignano, W.A.: Droplet vaporization model for spray combustion calculations. Int. J. Heat Mass Transf. **32**(9), 1605–1618 (1989)
11. Chiang, C.H., Raju, M.S., Sirignano, W.A.: Numerical analysis of convecting, vaporizing fuel droplet with variable properties. Int. J. Heat Mass Transf. **35**, 1307–1324 (1992)
12. Haywood, R.J., Nafziger, N., Renksizbulut, M.: A detailed examination of gas and liquid phase transient processes in convective droplet evaporation. ASME J. Heat Transf. **111**, 495–502 (1989)
13. Kolaitis, D.I., Founti, M.A.: A comparative study of numerical models for Eulerian–Lagrangian simulations of turbulent evaporating sprays. Int. J. Heat Mass Transf. **27**, 424–435 (2006)
14. Gollahalli, S.R.: Buoyancy effects on the flame structure in the wakes of burning liquid drops. Combust. Flame **29**, 21–31 (1977)
15. Morin, C., Chauveau, C., Gökalp, I.: Droplet vaporization characteristics of vegetable oil derived bio-fuels at high temperatures. Exp. Thermal Fluid Sci. **21**, 41–50 (2000)
16. Birouk, M., Toth, S.L.: Vaporization and combustion of a soybean biodiesel droplet in a turbulent environment at elevated ambient pressure. Combust. Sci. Technol. **187**(6), 937–952 (2015)
17. Daho, T., Vaitilingom, G., Sanogo, O., Ouiminga, S.K., Segda, B.G., Valette, J., Higelin, P., Koulidiati, J.: A model for predicting evaporation characteristics of vegetable oil droplets based on their fatty acid composition. Int. J. Heat Mass Transf. **55**(11–12), 2864–2871 (2012)
18. Shintre, P., Raghavan, V.: Experimental investigations of burning rates of pure ethanol and ethanol blended fuels. Combust. Flame **156**, 997–1005 (2009)
19. Dirbude, S., Eswaran, V., Kushari, A.: Droplet vaporization modelling of rapeseed and sunflower methyl esters. Fuel **92**(1), 171–179 (2012)
20. Law, C.K., Williams, F.A.: Kinetics and convection in the combustion of alkane droplets. Combust. Flame **19**, 393–405 (1972)
21. Wong, S.C., Lin, A.R.: Internal temperature distributions of droplets vaporizing in high temperature convective flows. J. Fluid Mech. **237**(11), 671–687 (1992)
22. Lefebvre, A.: Atomization and Sprays. Taylor and Francis, NY (1989)
23. Boileau, M.: Simulation numérique de la combustion diphasique. WN/CFD/03/73, July (2003)
24. ANSYS-Fluent UDF, Release 13.0 Manual (2011)

Incremental Sheet Forming: An Experimental Study on the Geometric Accuracy of Formed Parts

Rahul Jagtap and **Shailendra Kumar**

1 Introduction

Over the past few years, research in the area of sheet metal forming is mainly focused on incremental sheet forming (ISF) process because of the advantages it offers [1]. ISF process is still in its early development stages and needs more research efforts to be applied to be a viable option to conventional sheet metal forming process. ISF finds wide variety of applications in many areas ranging from manufacturing of human prosthesis and skull cavity to some very complex parts used in high-end aeronautical and automobile applications. Some researchers from industries are dedicatedly working to develop the ISF process so that it can be used alongside conventional sheet metal forming processes. However, the fact that ISF process cannot produce parts with acceptable quality as per industry standards is a major area of concern. Major limitations of the ISF process are poor geometric accuracy, local thinning leading to fracture, and very long processing time which restricts its application in mass production. Out of the above-listed limitations, geometric accuracy of formed part is one of the major limitations of ISF process. Without the acceptable accuracy, ISF process cannot be used as a sheet metal forming process in industries.

Till date, many researchers have applied research efforts to enhance the quality of parts formed using ISF process. For example, Ambrogio et al. [2] performed preliminary investigation on the accuracy of parts formed in ISF process. It is found that small tool size and small pitch result in good geometric accuracy. Masauka et al. [3] developed tool path in order to compensate the springback in ISF process. Ham and Jeswiet [4] investigated the influence of process parameters on the accuracy of formed parts. Fiorentino et al. [5] conducted experimental study on

R. Jagtap · S. Kumar (✉)
SV National Institute of Technology, Surat 395007, India
e-mail: skbudhwar@gmail.com

83

two-point incremental forming (TPIF) process. It was observed that positive ISF results in forming considerable accurate parts as compared to negative ISF process. Duflou et al. [6] developed a complete taxonomy of relevant features using which matrix of feature interactions has been generated. Radu et al. [7] studied the effect of residual stresses on accuracy of formed parts. Fan and Gao [8] formed titanium alloys using electric hot ISF process. Li et al. [9] studied the influence of process parameters on deformation energy and accuracy of parts formed in ISF process. It was observed that decreasing step depth results in improved geometric accuracy of formed part. Lingham et al. [10] proposed a tool path deflection compensation methodology in TPIF process. Using different tool and sheet compensation methods, the contact between primary and secondary tools was maintained throughout the forming process and accuracy of different geometrical shape was improved. Behera and Ou [11] studied stress-relieving heat treatment of titanium grade 1 parts formed using SPIF process. It was found that heat treatment before and after forming process improves the surface topology of formed part with little or no visible tool marks. Further improvement in accuracy and reduction in the curling effect after unclamping is also observed because of the heat treatment process. Otsu et al. [12] observed that multistage forming results in improved geometric accuracy and two-axis sheet stretching in comparison with single-point incremental forming (SPIF) process. Maqbool and Bambach [13] studied dependence between geometric accuracy and deformation mechanism (membrane stretching, through-thickness shear, and bending deformation).

From the reviewed literature, it is found that very less research efforts have been reported on improving accuracy of parts formed in ISF combined with stretch forming. Further influence of tool radius compensation, one of the major parameters affecting accuracy of formed part, is also not studied. The present paper describes research work focused on studying the influence of four major process parameters namely preforming, preform tool radius (P_rad), wall angle, and tool radius compensation (T_off) on accuracy of parts formed using ISF process combined with stretch forming.

2 Experimental Plan and Methodology

Experiments in the present work are carried out on three-axis CNC machine. A dedicated tooling setup consisting of fixture, clamping plates, and backing plates along with forming tools is fabricated as per geometric specification. In previous research work [2, 14], it is reported that small tool size results in forming accurate parts. Hence, tool size is kept constant at 8 mm. Forming tool made of stainless steel (SS-304) is used to form a conical frustum. Aluminum alloy 1050 blank sheet is used in the present experimental work.

Experiments are designed according to Taguchi's orthogonal array (OA). Influence of four parameters as listed in Table 1 on accuracy of parts formed in ISF process combined with stretch forming (SF) is studied. Each parameter is varied at

Table 1 Process parameters and their levels

Parameter	Unit	Low level	High level
Preforming	mm	10	18
P_Rad	mm	50	90
Wall angle	Degrees	30	70
T_off	mm	0	4

Fig. 1 Formed component having wall angle 50°

three different levels. Formed parts are then trimmed using abrasive water jet cutting machine (AWJM). Parts are scanned using laser scanner, and formed profile is compared with ideal part profile. The error in final part geometry is used as response for further analysis. Figure 1 shows the formed conical frustum.

3 Result and Discussion

The results are analyzed using Minitab 14.0 statistical software. Figure 2 depicts main effects plot for geometric error. From the analysis of variance (ANOVA), it is observed that tool offset is the most significant process parameter followed by wall angle and preforming. Preform tool radius (P_Rad) has small influence on the accuracy of formed part.

As preforming increases, there is a considerable amount of plastic deformation in the blank sheet. This plastic deformation mainly takes place near the clamped edges in the form of sheet bending because there is no support to blank sheet. Due to the hemispherical shape of preforming tool, considerable deformation at the center of cone can also be observed for cones with large wall angles. Hence, increase in preforming causes more bending near clamped edges resulting in increased geometric error. For small preforming, say 10 mm, very small plastic deformation takes place and large part of preforming is restored back due to elastic springback. Hence, small bending near clamed edges is observed which subsequently results in smaller

Main Effects Plot (data means) for Means
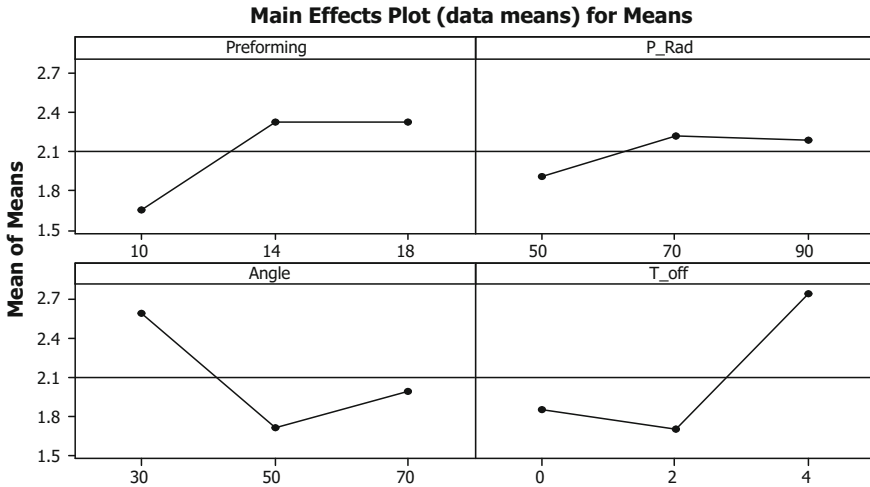
Fig. 2 Main effects plot for geometric error

geometric error. As the preforming increases, more plastic deformation takes place resulting in more geometric error.

The influence of preforming is more on cones with small wall angles, i.e., 30°. As preforming increases, large amount of over-forming is observed which results in increased geometric error. Elastic springback is another major parameter which contributes in increasing geometric error while forming parts with steep wall. The elastic springback in parts with small wall angles is more compared to parts with large wall angles as also reported by [15] which results in increased geometric error. As the wall angle increases from 30° to 50°, amount of plastic deformation increases and the springback is reduced considerably. The decline in springback helps in decreasing geometric error as observed from main effects plot. Increase in geometric error for parts with 70° wall angle is observed because of the preforming process. Due to preforming, considerable plastic deformation takes place at the center of cone. This plastic deformation results in forming a hemispherical shaped bulge at center of cone resulting in more geometric error.

Tool radius compensation or tool offset (T_off) is the most affecting process parameter on the geometric accuracy of formed part. Figure 3 depicts the various tool radius compensation used to investigate its influence on geometric error. From main effects plot, it is revealed that zero tool offset (T_off) results in considerable geometric error. As no tool offset is used, some amount of over-forming takes place which results in geometric error. But some amount of springback reduces the error to some extent. When T_off is increased from zero to 2 mm, amount of over-forming is reduced considerably, resulting in forming fairly accurate parts. The geometric error using 2 mm T_off is minimum as observed from the main effects plot (Fig. 2). While using 4 mm T_off which is equal to tool radius 'r', some amount of under-forming is done because of the tool sheet contact. Forming tool

Fig. 3 Tool radius compensation
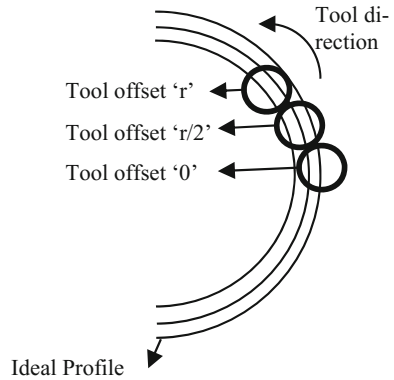
Fig. 4 Percentage contribution of parameters
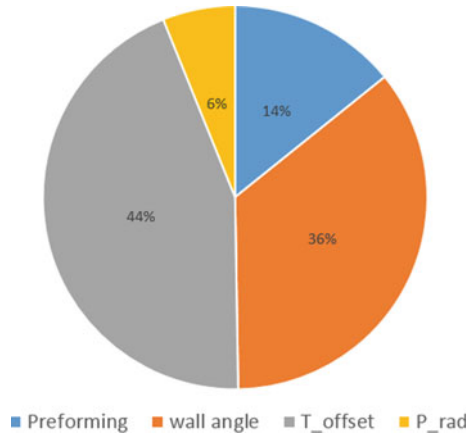
does not have contact with the sheet exactly at periphery of tool, but it is slightly below the periphery where the distance between tool–sheet interface is less than tool radius. In addition to the under-forming, springback also contributes to increase in the geometric error of formed parts. Hence, maximum error can be observed while forming using 4 mm (T_off equal to 'r') tool offset.

Figure 4 depicts the percentage contribution of each parameter in geometric error of formed part. Tool offset is the most affecting parameter in geometric accuracy of formed part with the percentage contribution of 44% followed by wall angle (36%), preforming (14%), and preform tool radius (6%). Hence, the tool offset or tool radius compensation must be wisely selected in order to improve geometric accuracy of parts formed in ISF process combined with stretch forming. Preform tool radius has very small influence on the geometric accuracy.

4   Conclusion

In the present experimental study, influence of four process parameters (preforming, preform tool radius, wall angle, and tool offset) on geometric accuracy of formed parts using ISF combined with stretch forming is studied. The findings of present study are enumerated as under:

1. Tool offset is the most affecting parameter in geometric accuracy of formed part with the percentage contribution of 44% followed by wall angle (36%) and preforming (14%).
2. It is observed that tool offset of half of the tool radius results in minimum geometric error.
3. Parts having small wall angle has poor geometric accuracy compared to parts with steep wall angles.
4. Preforming results in increased geometric error, especially in parts having small wall angles.
5. Preform tool radius does not have any influence on the geometric accuracy of formed parts.

The above findings are certainly useful in improving geometric accuracy of parts formed by ISF process with stretch forming.

References

1. Echrif, S.B.M., Hrairi, M.: Research and progress in incremental sheet forming processes. Mater. Manuf. Processes **26**(11), 1404–1414 (2011)
2. Ambrogio, G., Costantino, I., Napoli, L., Filice, L., Fratini, L., Muzzupappa, M.: Influence of some relevant process parameters on the dimensional accuracy in incremental forming: a numerical and experimental investigation. J. Mater. Process. Technol. **153–154**, 501–507 (2004)
3. Masuku, E.S., Bramley, A.N., Mileham, A.R., Owen, G.W.: Incremental sheet metal forming: a die-less rapid prototyping process for sheetmetal. In: McMahon, C. (ed.) Advances in Integrated Design and Manufacturing in Mechanical Engineering. Springer, Dordrecht (2005)
4. Ham, M., Jeswiet, J.: Dimensional accuracy of single point incremental forming. Int. J. Mater. Form. **1**(1), 1171–1174 (2008)
5. Fiorentino, A., Ceretti, E., Attanasio, A., Mazzoni, L., Giardini, F.: Analysis of forces, accuracy and formability in positive die sheet incremental forming. Int. J. Mater. Form. **2**(1), 805–808 (2009)
6. Duflou, J.R., Clarke, R., Merklein, M., Micari, F., Shirvani, B., Kellens K.: Accuracy improvement in single point incremental forming through systematic study of feature interactions. Key Eng. Mater., 881–888 (2011)
7. Radu, C., Tampu, C., Cristea, I., Chirita, B.: The effect of residual stresses on the accuracy of parts processed by SPIF. Mater. Manuf. Processes **28**, 572–576 (2013)
8. Fan, G., Gao, L.: Numerical simulation and experimental investigation to improve the dimensional accuracy in electric hot incremental forming of Ti–6Al–4V titanium sheet. Int. J. Adv. Manuf. Technol. **72**(5–8), 1133–1141 (2014)

9. Li, Y., Lu, H., Daniel, W., Meehan, P.A.: Investigation and optimization of deformation energy and geometric accuracy in the incremental sheet forming process using response surface methodology. Int. J. Adv. Manuf. Technol. **79**(9–12), 2041–2055 (2014)

10. Lingam, R., Amit, S., Reddy, N.V.: Deflection compensations for tool path to enhance accuracy during double-sided incremental forming. J. Manuf. Sci. Eng. **138**(9), 1–8 (2015)

11. Behera, A., Ou, H.: Effect of stress relieving heat treatment on surface topography and dimensional accuracy of incrementally formed grade 1 titanium sheet parts. Int. J. Adv. Manuf. Technol. **87**(9–12), 3233–3248 (2016)

12. Otsu, M., Ogawa, T., Muranaka, T.: Improvement of forming limit and accuracy in friction stir incremental forming with multistage forming. Procedia Eng. **207**, 807–812 (2017)

13. Maqbool, F., Bambach, M.: Dominant deformation mechanisms in single point incremental forming (SPIF) and their effect on geometrical accuracy. Int. J. Mech. Sci. **136**, 279–292 (2018)

14. Jagtap, R., Kumar, S.: An experimental study on geometric accuracy in hybrid incremental sheet forming. In: 20th International Conference on Materials and Processing Technologies, VIT Chennai (Dec 2017)

15. Behera, A., Lu, B., Ou, H.: Characterization of shape and dimensional accuracy of incrementally formed titanium sheet parts with intermediate curvatures between two feature types. Int. J. Adv. Manuf. Technol. **83**(5–8), 1099–1111 (2015)

Experimental Analysis of Implementing Roughness on NACA 0018 Airfoil

E. Livya, R. Sai Anirudh, V. Vignesh, B. Prasannavenkatesh
and S. Nadaraja Pillai

1 Introduction

Research delving into aerodynamics has always been insistent on finding out methods to improve the aerodynamic performance of a vehicle. This is primarily because aerodynamic performance plays a huge role in fuel economy and the overall running costs of the vehicle. This is clearly observable, especially in the world of F1 racing. We have always heard about F1 cars running out of fuel and their constant need for refueling. This has considerably reduced over the years, due to the consequent improvements in the aerodynamics of cars. The invention of DRS (drag reduction system) in racing has completely transformed the dynamics of the sport. Better overtaking combined with superior fuel economies has been a boon to the sport. It was such a boost to the performance of cars that F1 authorities decided that the usage of the system had to be controlled, for retaining the nail-biting moments the sport is known for.

The studies on drag and its reduction have been an object of focus for the past several decades. As any vehicle subjected against a free stream flow of air (or any fluid) is simultaneously subjected to drag too, every attempt at reducing the drag is essential in improving the aerodynamic performance of a vehicle. Even animals, over millions of years, have evolved to do the same through natural selection, i.e., reducing the drag experienced by them during motion. A very fitting example would be the "shark skin effect" observed in sharks, as shown in Fig. 1 where tiny placoid scales align themselves to form micro-sized riblets on the shark's

E. Livya (✉) · R. Sai Anirudh · V. Vignesh · B. Prasannavenkatesh · S. Nadaraja Pillai
SASTRA Deemed to Be University, Thanjavur, Tamil Nadu, India
e-mail: livya.nasa@gmail.com

S. Nadaraja Pillai
e-mail: nadarajapillai@mech.sastra.edu

Fig. 1 Flow separation in sharks with roughed surface on skin

1. Lamina Boundary Layer over shark surface

2. Boundary Layer separates from skin surface

3. Roughed surface lift off the skin like flaps to hold the Boundayer Layer
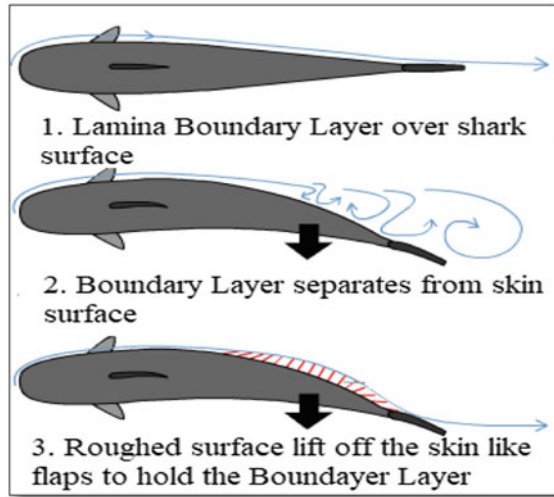
body achieving high amounts of drag reduction in water through delayed flow separation [1].

Early studies on drag reduction were based on inspiration derived from such natural selection phenomena found in animals as [2]. This led to the discovery that the separation of flow from the surface is directly linked to drag, and the delay of flow separation directly led to a reduction in drag [3]. Speeds permitting smooth flow of air over the airfoil and control surfaces must be maintained to control the airplane [4]. This led to further research on methods to delay the flow separation. Also, the effect of surface roughness on the boundary layer development and losses in turbine blades is investigated [5] with different Reynolds numbers, which indicates that the boundary layer is plumper (thicker) on a rough surface than a smooth surface. Current research is primarily focused on non-intervening methods to delay the flow of separation, which means a delay caused by not using wing extensions and other external mechanical or electrical devices on the wing, but by altering the airfoil characteristics (like introducing roughness on the airfoil, as discussed in this paper).

2 Research Methodology

2.1 Tunnel Facility

The experiment was conducted using a low speed, open circuit, suction-type wind tunnel in the Aerospace Laboratory, School of Mechanical Engineering, SASTRA University, India. The tunnel consists of a $300 \times 300 \times 1500$ mm (width $\times$ height $\times$ length) square test section. This wind tunnel is capable of analyzing both

Fig. 2 Wind tunnel facility in SASTRA Deemed to be University
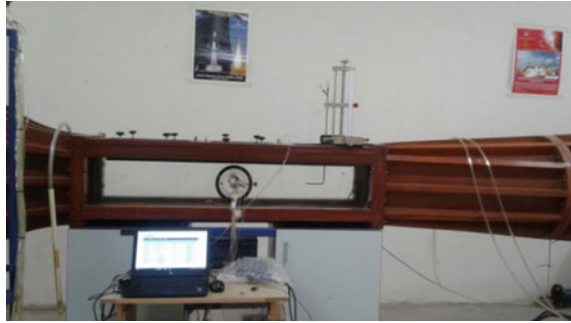
two-dimensional and three-dimensional geometries with the maximum limit of the fan speed being 1500 rpm, corresponding to 60 m/s as shown in Fig. 2. The transverse pitot arrangement is built with the movement along the span-wise and vertical directions, at the downstream of the wind tunnel. The freestream airspeed is varied in the test section by varying the frequency using the frequency drive.

2.2 Selection of Silicon Carbide Sheet

The rough surface was obtained from a silicon carbide (SiC) sheet, commonly known as an emery sheet. The sheet is of grade P180, which corresponds to a roughness index of 80 μm. This sheet was chosen, keeping in mind its surface quality and ready availability. The sheet has an approximate length of 20 mm. The sheet was placed at one-fourth of the total chord length. This arbitrary location was chosen, to take into account the flow separation characteristics of the flow over the airfoil. It was properly glued to the surface without affecting the flow.

2.3 Airfoil

A NACA 0018 symmetric airfoil fabricated from wood was used for this experiment. It has 21 pressure points which were equally spaced with a gap of 9 mm (Δx), point 1 situated at the leading edge, points 2–11 present on the suction surface of the airfoil, and points 12–21, on the pressure surface of the airfoil. These points were connected to a Scanivalve 64-channel pressure scanner via tubes. The chord length of the airfoil is 100 mm. The silicon carbide sheets were glued to the suction surface of the airfoil at pressure points 3 and 4, covering it and creating holes for the points as required at approximately one-fourth of the total chord length as shown in Fig. 3.

Fig. 3 Airfoil model with
introduced roughed surface

Fig. 4 64-Channel pressure
scanner

2.4 Pressure Transducer

The Scanivalve MPS4264 is a unique 64-channel pressure scanner which is capable
of accurately measuring real-time pressure values of 64 points simultaneously and
also measuring the ambient temperature. The 21 probes from the pressure points on
the airfoil along with a 22nd probe (which is connected to the wind tunnel to
measure free stream pressure) were fed to the scanner, which is connected to the
Scanivalve server through a computer using Ethernet cables. The pressure values
were recorded and displayed by the server on the computer. The recorded pressure
values were downloaded in the required format for further calculations. Figure 4
shows the actual model of the MPS4264, depicting its small size with a pen, which
improves its portability and compatibility.

3 Results and Discussion

Initially, the subsonic wind tunnel was calibrated. As the maximum possible free
stream velocity in the wind tunnel is 60 m/s, three optimum velocities were decided
—25, 35, and 45 m/s (Table 1).

Once the wind tunnel was calibrated and the velocities were decided, the airfoil
was selected. A symmetric airfoil (NACA-0018) was selected due to the ease in its
modification. The chosen airfoil was fixed into the wind tunnel, and the wind tunnel
was checked thoroughly for possible leaks. Then, the probes of the Scanivalve
pressure transducer were appropriately connected to the airfoil to measure the
pressure at various points. The pressure was measured for angles of attack ranging

Table 1 Wind tunnel motor fan speed for the desired velocity

S. No.	Motor fan speed (RPM)	Velocity (m/s)	Reynolds number
1	675	25	4.97×10^5
2	915	35	6.95×10^5
3	1155	45	8.95×10^5
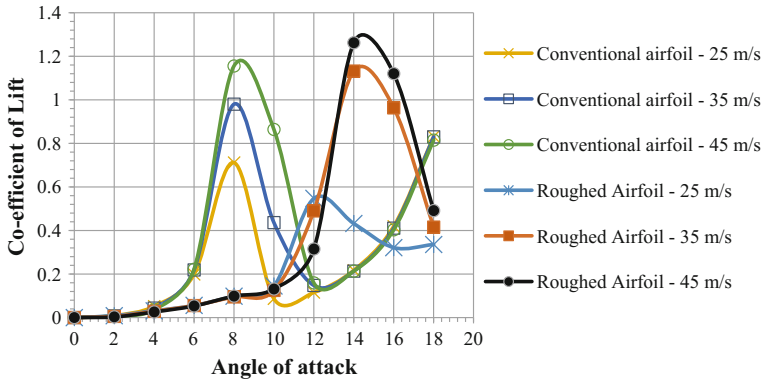
Fig. 5 Coefficient of lift versus angle of attack graph for conventional airfoil

from 0° to 18° in steps of 2° for the three aforementioned speeds. The roughness was introduced on the airfoil surface at one-fourth of the chord length of the airfoil, and the same experimental methodology was followed again; i.e., the pressure values were obtained for the various angles of attack and velocities. The lift coefficient obtained for different velocities are presented. Figure 5 shows stall occurring at an 8° angle of attack for a conventional airfoil, and an increase in lift coefficient is observed with an increase in velocity. A delay in stalling from 8° to 12° has been achieved for the velocity of 25 m/s, by the introduced roughness. On further increasing the velocity to 35 m/s, the stalling angle of attack increases to 14° when roughness is introduced, whereas the stalling angle for the conventional airfoil is about 8°. Further increase in the velocity of airflow to 45 m/s results in a similar increase of 6° in the stalling angle (from 8° to 14°).

The obtained result clearly shows introducing roughness over the airfoil surface decreases the lift coefficient due to an increase in skin friction drag created by the implemented roughness.

4 Conclusion

The concept of introducing roughness is relatively new, with the advantage of no external devices being used to change the flow characteristics. Introduction of roughness on a NACA 0018 airfoil is found to be a more effective way of achieving

stall delay. The critical angle of attack for a conventional NACA 0018 is found to be 8°, and upon introducing roughness on the suction surface of the airfoil, it was delayed to an angle of 12°, in the case of velocity being 25 m/s. This 4° delay is caused by the rough surface which has been introduced where a high energy–low energy air mixing takes places causing the conversion of a laminar boundary layer to a turbulent boundary layer, making the flow more attached to the surface of the airfoil.

  i. A decrease in the coefficient of lift is found, due to a decrease in velocity on the roughened surface of the airfoil. An increase in the coefficient of drag is also found, due to an increase in the skin friction component of drag created by the roughened surface.
 ii. Modification in terms of roughness creates turbulence in order to delay flow separation, which increases the stall angle after which the airfoil is no longer controllable.
iii. The increase in skin friction drag is noticeable; hence, the roughness should be introduced only after the stalling angle for a conventional airfoil is observed.

References

1. Harun, Z., Abbas, A.A., Dheyya Mohammed, R., Ghazali, M.I.: Ordered roughness effects on NACA 0026 Airfoil. In: IOP Conference Series: Material Science and Engineering, vol. 152 (2016)
2. Chen, H., Rao, F., Shang, X., Zhang, D., Ichiro, H.: Biomimetic drag reduction study on herringbone riblets of bird feather. J. Bionic Eng. **10**, 341–349 (2010)
3. Livya, E., Anitha, G., Valli, P.: Aerodynamic analysis of dimple effect on aircraft wing. Int. J. Aerosp. Mech. Eng. **9**(2) (2015)
4. Kojima, H., Kazuyuki, T., Yamamoto, M.: Computation of aerodynamic performance of airfoil with surface roughness. In: 5th International Symposium on Engineering Turbulence Modeling and Measurements, pp. 629–636 (2002)
5. Liu, J., Zhang, W., Zou, Z.: Effect of surface roughness on the aerodynamic performance of turbine blade cascade. Propuls. Power Res. **3**(2), 82–89 (2014)

Numerical Investigation of Siting the Wind Turbine on Vel Tech University Campus

S. M. Vignesh, J. Karthik and R. Jaganraj

1 Introduction

Climate change has made a great impact on society, influenced a vast change in life of species and case an inhabitation for life [1–3]. The world is currently moving towards lower carbon emissions, increased use of renewable energy, and technology that is more energy efficient, with the result that the scientific community is working on sustainable projects such as electric vehicles, solar and wind energy [4, 5]. Wind energy technology is a revolutionary renewable energy generating a global capacity of 486,790 MW in 2015, an increase of 12.5% compared to the previous five years. In India alone, wind power capacity is currently at 32,746 MW and is on target to produce 40% of the country's energy from renewable sources by 2030 [6, 7].

In this paper, we are going to address possible solutions to the problems inherent in the production of energy from wind turbines. The first major problem in wind turbine power plants need greater area of land compared to other sources of energy. Most wind farms are located in forest and agricultural areas, resulting in major deforestation. For example, the Andhra Lake Wind Power Project alone required the cutting down of 300,000 trees [8]. The electrical grid installation itself lead to more cost and ecological loss for power production, and as a result we are investigating an off-grid wind energy source for urban areas. The production of power and its usage will be in the same location. Globally, there are 875 urban areas with a population of 500,000 or more, and in India alone 31.16% of the population is found in urban areas and this is expected to increase to 40.76% by 2030 [8]. The idea of installing wind turbines in existing

S. M. Vignesh (✉) · R. Jaganraj
Vel Tech Rangarajan Dr. Sagunthala R&D Institute of Science and Technology,
Chennai 600062, India
e-mail: emailsmvignesh@gmail.com

J. Karthik
Aerodynamics Laboratory, SMBS, VIT University, Chennai 600127, India

cities and designing future cities with wind turbines will reduce both deforestation and costs to the electricity grid [9]. This paper looks at the possibilities and challenges of installing wind turbines in urban areas.

Computational fluid dynamics [CFD] is widely used tool in the study of wind characteristics in urban locations and wind turbine aerodynamics [10, 11]. In the past, an "observational approach" would be used in such studies, involving field equipment such as an anemometer and wind scanner to study wind characteristics in urban areas. Another method involves the use of a wind tunnel and a scaled-down model of the urban area or wind turbine to be studied. In recent year a "simulation approach" has been used due to the advent of cheap and powerful computational technology leading to a proliferation of CFD studies in fluid and heat transfer research, and especially in the study of wind characteristics in urban areas [12–14]. The main drawback of CFD studies is the accuracy of the result, since the physics of urban areas are highly complex and care must be taken in the validation of results [15, 16].

Wind plays a major role in the effects of pedestrian-level wind conditions, pollutant dispersion, wind-driven rain, natural ventilation and the thermal environment in urban areas [17–21]. In order to produce energy from a wind turbine situated in an urban area, we need to first study the wind and the factors affecting it in urban areas. The wind is affected by the following factors:

- Building arrangement and structure
- Weather conditions
- Radiation from the Sun
- Earth's rotation
- Anthropogenic sources in urban areas
- Roughness around the urban physics.

We are going to study the urban area with its existing buildings and structures without making any changes to their design and location to improve the wind as a resource for energy production. We are also going to ignore small structures and tiny details of the buildings such as windows, balconies and communication masts etc. In terms of weather conditions, we are going to study the wind in normal weather conditions, rejecting the worst weather conditions such as cyclones since they are negligible annually. Thermal radiation from the sun will affect the microclimate in the urban area and the wind resource, but the effect is negligible. Anthropogenic sources from human activities such as vehicles and industry etc. are likewise rejected in the study since their effect is also negligible. The roughness of the surrounding area is studied and the boundary condition in the simulation is fixed according to the roughness data. We have selected the Vel Tech University campus in Avadi as the location for the study because it is easy for us to define the urban area, and to install the wind turbine on the campus. The 1200 m diameter area was chosen as the wind turbine installation study site.

2 Problem Statement and Modelling

We aim to investigate the effective siting of a wind turbine on Vel Tech University campus. The small details (windows, balconies, vehicles, parking areas etc.) are neglected (Fig. 1). The annual wind rose (Fig. 2) of the Avadi region was used in the study and was provided by the Chennai Metrological Center as the boundary condition for the computational analysis [22]. The roughness around the physics in the urban area was studied with the help of Google Maps (Figs. 3 and 4) [23] and the inlet velocity boundary condition is given according to both roughness and wind rose data. The simulation result was used to effectively install two standard ASWT-1 kW and Polaris-20 kW wind turbines and to identify the potential power production from the urban wind resource [24, 25].

The velocity simulation results of the urban physics in different height is measured as normal to fix the wind turbine blades. The urban wind velocity is compared to the wind turbine velocity power curve of two standard ASWT-1 kW and Polaris-20 kW wind turbines and the power produced from the urban wind resource is calculated. The modeling of the urban area is performed using the CATIA V5 image tracing technique with the help of the aerial view from the standard Google Maps (Figs. 5 and 6) [26, 27]. Building height and location are identified by conducting the survey on the campus. The campus consists of the main administration building, department buildings, Vel Murugan auditorium, convention hall, research park, ladies hostel and workshops and laboratories (Fig. 1).

Fig. 1 Geometry of the urban area developed from Google Maps using CATIA V5
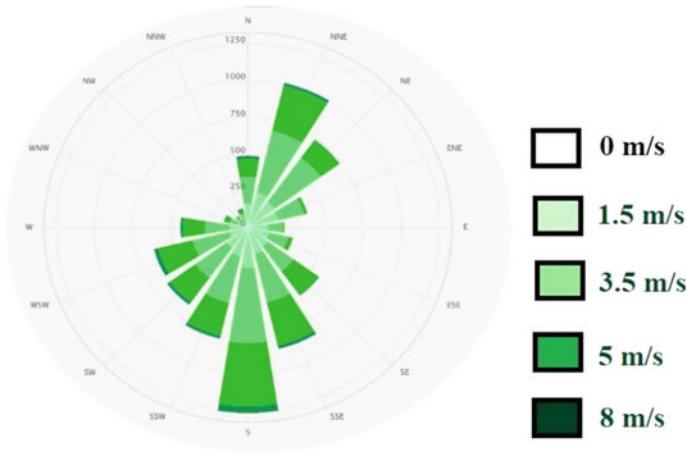
Fig. 2 Wind rose for Avadi, Chennai
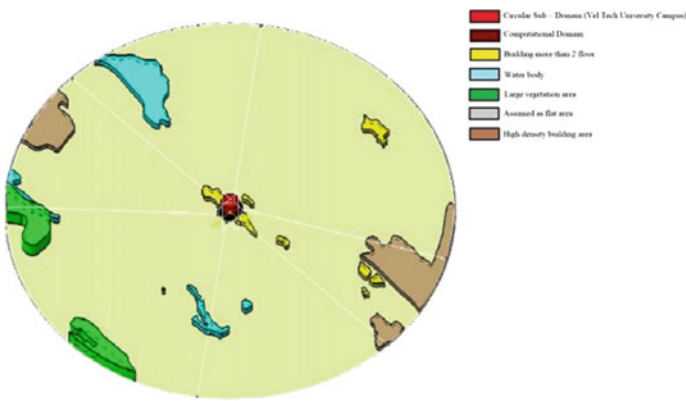
Fig. 3 Isometric view of the roughness terrain model of a 10 km radius area around Vel Tech University campus

3 Computational Study of Urban Physics

3.1 Computational Domain and Grid

In most computational studies of urban areas, a cubic or cuboidal domain is used. However, in this study, a hexagonal domain (Fig. 7) with an edge length of 1200 m and a circular subdomain of 1200 m diameter is used. The domain includes the complete urban area and all campus buildings inside the subdomain [27, 28]. The hexagonal domain reduces computational time and lower number of grids will be generated [28]. The accuracy of the simulation will be increased since the
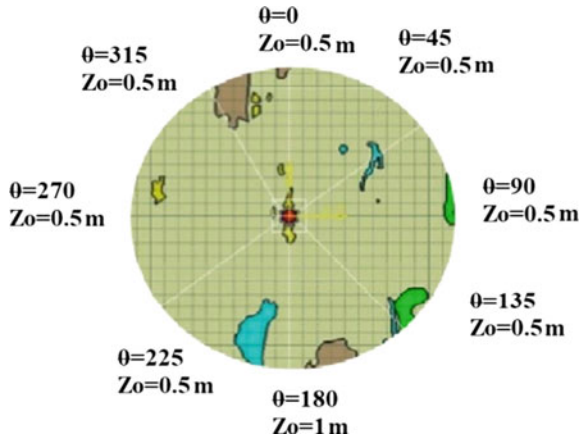
Fig. 4 Aerodynamics roughness around computational domain in different direction
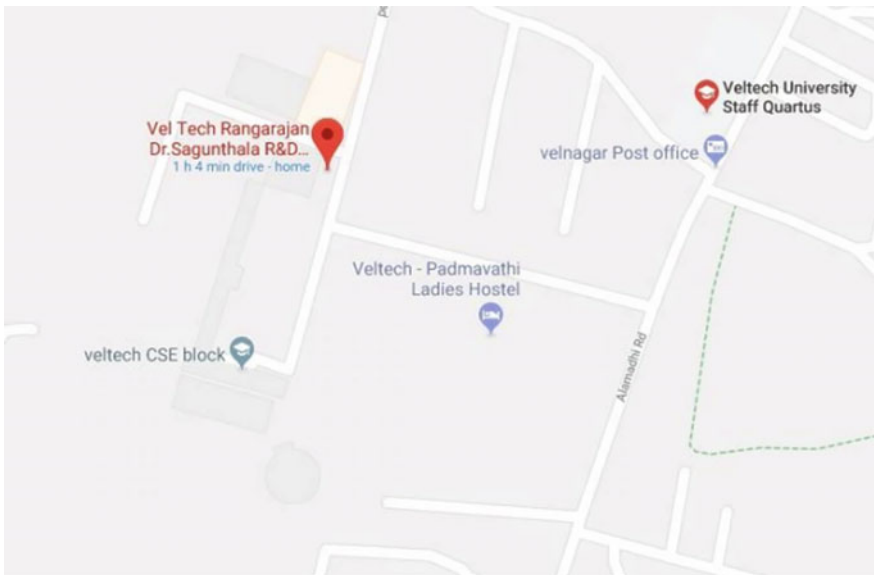
Fig. 5 Aerial view of Vel Tech University campus in Google Maps

hexagonal domain (Fig. 7) has three inlets and outlets, and six roughness areas are identified around the domain. The domain height is 400 m and the maximum blockage ratio is 1.8 [15–17, 27–30].

The computational grid (Fig. 8) is generated based on the recommendation by van Hooff and Blocken to mesh the surface of the domain along the third axis to obtain a three-dimensional grid [15–17]. The fine grid (Fig. 9) is placed inside the

Fig. 6 Satellite image of Vel Tech University campus from Google Maps

Fig. 7 Hexagonal domain
with Vel Tech University
campus in the circular
subdomain
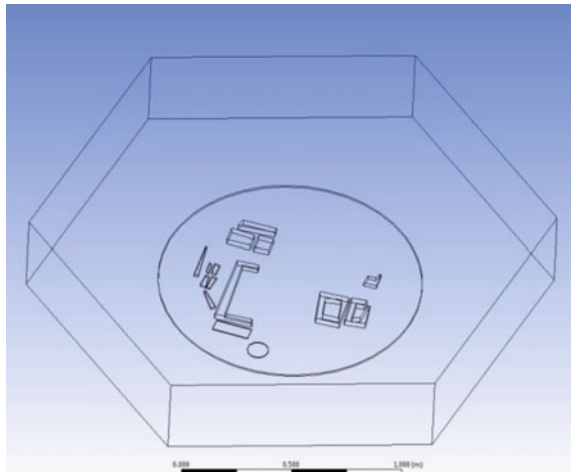
subdomain which is our area of interest and coarser grid with increase in distance
from the center of domain. Based on the building size and the surface area, at
least 10 cells will be on the edge of the building leading to the grid generation
($\sim$10 lakhs hexagonal cells).

Fig. 8 Numerical grid
domain in a wireframe view
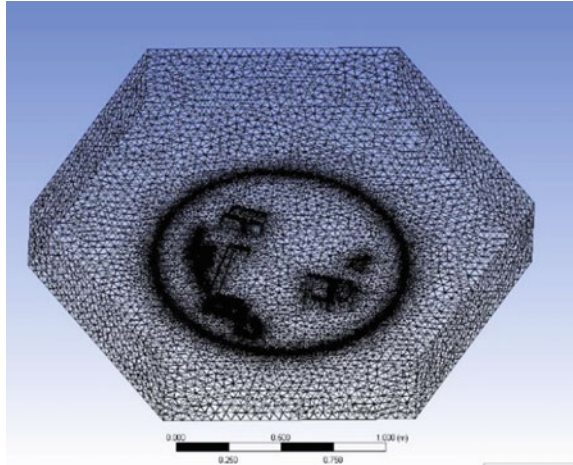
Fig. 9 Grid generated for
Vel Tech University Campus
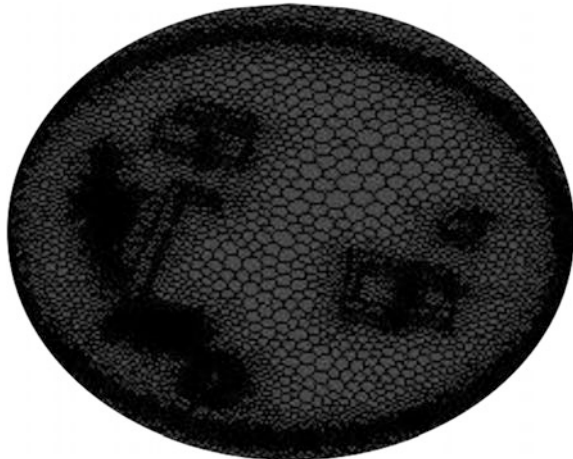
3.2 Boundary Condition

The boundary condition is either the velocity inlet or pressure outlet on each face of
the hexagonal domain. It depends on the wind direction and velocity from the wind
rose of Avadi (Fig. 2) and the installed wind turbine power curve graph (Figs. 10
and 11). In all the simulations, boundary conditions will be three velocity inlet and
remaining will be pressure outlets. The velocity inlet will have parabolic flow due to
the roughness characteristics of the terrain around the urban area and is selected
based on the wind direction [28, 29].
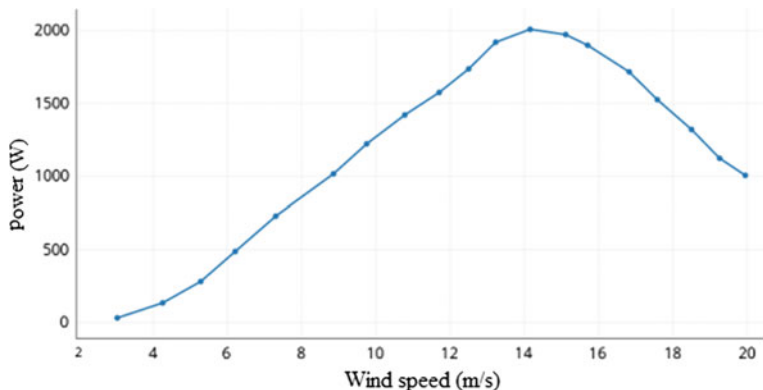
Fig. 10 Power curve for the ASWT-1 kW turbine
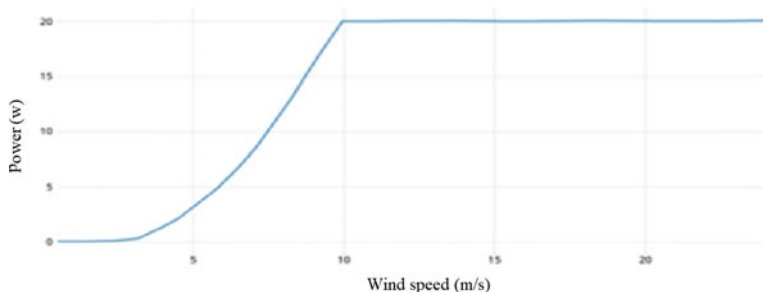
Fig. 11 Power curve for the Polaris-20 kW turbine

At the inlet velocity boundary condition, the logarithmic mean wind speed profile ["U" m/s] will be $Z_0 = 0.5$ m (or) $Z_0 = 1.0$ m depending on wind direction and the variation in wind speed (3–8 m/s).

$$u(z) = \frac{u^*}{k} \ln\left(\frac{z + z_0}{z_0}\right)$$

$$k = \frac{u^{*2}}{k(z + z_0)}$$

$$\varepsilon(z) = \frac{u^{*3}}{k(z + z_0)}$$

The relationship depends on the CFD commercial package software used, and ANSYS Fluent 12 is recommended.

$$k_s = \frac{9.793z_0}{c_s}$$

The wind rose of Avadi indicates three main wind speeds, i.e., 3.5 m/s, 5 m/s and 8 m/s are prevalent (Fig. 2) and they are taken as the inlet velocity for our study. In the case of the wind direction, north-northeast [NNE], northeast [NE], south-southeast [SSE], south [S], south-southwest [SSW], southwest [SW], west-southwest [WSW], and westerly winds are going to contribute 4490 h/year [187 days] (Table 1) of wind resource and eight simulation results will be obtained to install ASWT-1 kW and Polaris-20 kW wind turbine location in the campus (Figs. 10 and 11; Table 2). The location is fixed as black special points on the campus map with height from the ground based on a cut-in wind speed of 3 m/s for the ASWT-1 kW wind turbine and 2.7 m/s for the Polaris-20 kW wind turbine (Figs. 10 and 11; Table 2).

Table 1 CFD simulation details

Direction	Inlet Velocity [m/s]	Hours/year	Average wind velocity [m/s]
North-northeast [NNE]	8	20	5.5
North northeast [NNE]	5	317	
North northeast [NNE]	3.5	431	
Northeast [NE]	5	150	4.25
Northeast [NE]	3.5	371	
South southeast [SSE]	5	304	6.5
South Southeast [SSE]	8	28	
South [S]	8	45	5.5
South [S]	5	432	
South [S]	3.5	512	
South southwest [SSW]	8	21	5.5
South southwest [SSW]	5	230	
South southwest [SSW]	3.5	326	
Southwest [SW]	8	22	5.5
Southwest [SW]	5	205	
Southwest [SW]	3.5	252	
West southwest [WSW]	8	28	5.5
West southwest [WSW]	5	231	
West southwest [WSW]	3.5	246	
West [W]	8	15	5.5
West [W]	5	145	
West [W]	3.5	159	

Specification details	ASWT-1 kW	Polaris-20 kW
Rated power [kW]	10	20
Rotor diameter [m]	3.1	10
Cut-in speed [m/s]	3	2.7
Rated wind speed [m/s]	9	10
Cut-out speed [m/s]	25	25
Survival speed [m/s]	59	50

Table 2 Wind turbine installation details

3.3 Simulation Physics

The governing equations are incompressible flow with continuity, momentum and 3D Reynolds-averaged Navier-Stokes (3D RANS) are solved using k-ε turbulence in ANSYS Fluent version 18 [16, 28, 30]. A SIMPLE algorithm with second order pressure interpolation and discretization schemes in pressure velocity coupling is used for the analysis. The simulation scale residuals are 10^{-4}–10^{-5} for X, Y and Z velocities, 10^{-4} for k and ε, and 10^{-3}–10^{-4} for the continuity equation.

4 Results

There are 8 simulations in total for 8 wind directions and 3 varying average windspeeds to represent the wind velocities and velocity streamline characteristics of the urban area at heights of 10 and 25 m from the ground. The sample points are fixed on the urban area where the wind velocity is more than the cut-in wind speed of both wind turbines.

By comparing the simulation results (Fig. 12), we can fix the sample points at effective locations in the urban area (the ASWT-1 kW wind turbine is denoted by a red dot and the Polaris-20 kW wind turbine by a yellow dot). We have placed 110 red dots (Fig. 13) and 30 yellow dots (Fig. 14) in the urban study area.

In general, it is fair argument that it's possible to fix the exact sampling point in the urban area. The sampling point is not only fixed in the road corners, playground, empty area but also, on the roof of the buildings.

1. ASWT-1 kW wind turbines are placed mostly at the side of roads and in compact areas. It is possible to install the wind turbine on a streetlight.
2. The ASWT-1 kW wind turbine is found to be more effective on the edges of buildings and on the north and east areas of the campus.
3. In total, 110 street light installed wind turbine locations are shown by red dots around the campus buildings and can generate 200 MWh amount of power every year.
4. 30 Polaris-20 kW wind turbines are shown by yellow dots around the campus, mostly on building terraces and can generate 150 MWh of power every year.
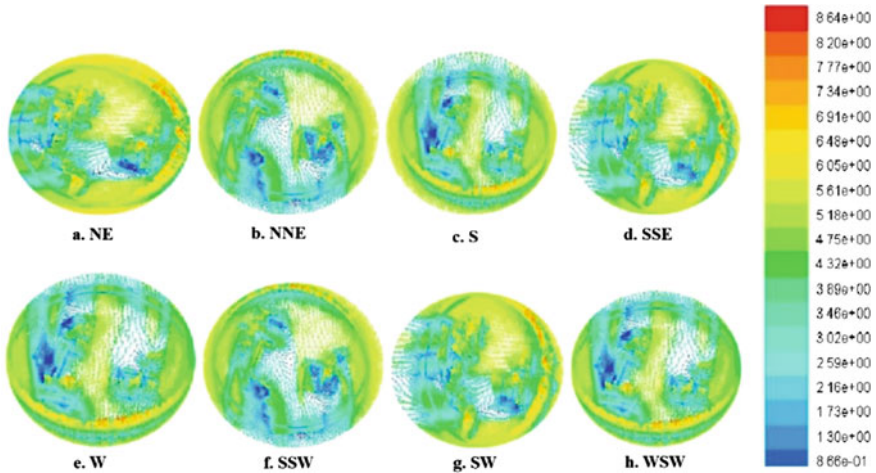
Fig. 12 Simulated result of velocity vector contours
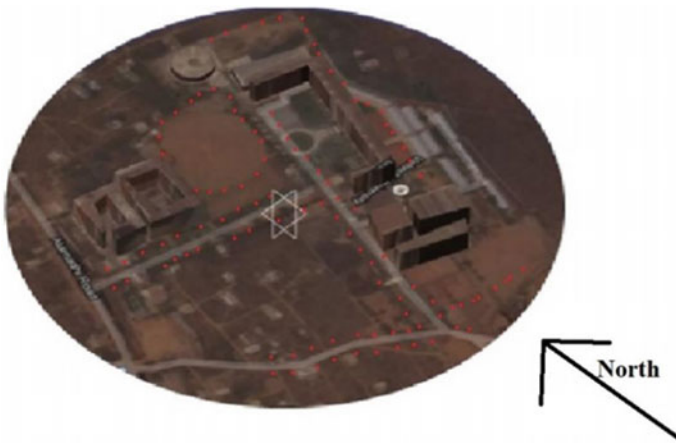
Fig. 13 Location of sample points on Vel Tech University campus for the placement of a 1 kW wind turbine at a height of 10 m. Points identify a street light-installed wind turbine. (Total: 110 points)

5　Discussion

The urban area is modelled using images from the standard Google Maps and processed through CATIA V5. There are few geometrical constraints in this study as we have not included some elements of the terrain in the modelling (trees, telegraph poles, cars, balconies, canopies, windows, etc.). Similarly, we have ignored solar radiation and the local influence of the temperature field as it leads to

Fig. 14 Location of sample points on Vel Tech University campus for the placement of a 20 kW wind turbine at heights of 5 m and 25 m (Total: 30 points)

computational complexity. Due to large scale of the model, there are complication in extracting the information regarding building elevation, material, ground property and building wall detail in this study.

A three-velocity inlet and all others as pressure outlets in a hexagonal domain is created (Fig. 7) considering vertical inlet profiles of the mean velocity (U), turbulent kinetic energy (k) and turbulence dissipation rate (ε) as per the recommendation for urban physics studies in the standard k–ε turbulence model. In the velocity inlet, the atmosphere boundary layer is developed according to the roughness in the direction of the domain. The numerical physics is solved in 3D-RANS problem, in high order grid generation simulation.

In summary, from the simulated results of velocity magnitude of all direction corresponding to the average wind velocity, the effective location of the wind turbine is located on the surface of the campus respect to the height. Altogether, 140 effective location have been identified on Vel Tech University campus.

6 Conclusion

This study shows the importance and the potential for installing wind turbines in urban areas. Previous studies have mostly looked at pedestrian comfort, ventilation, wind turbine optimization and the location of wind turbines in wind farms. This research therefore has potential importance for the future.

This paper is presented with a CFD simulation and numerous approximation to the geometry, leading to the need for an "observation approach" or wind tunnel testing to allow for a more accurate analysis of wind turbine location.

References

1. Amedie, F.A.: Impacts of climate change on plant growth, ecosystem services, biodiversity and potential adaptation measures. Master's Thesis in Atmospheric Science with Orientation towards Environmental Science (2013)
2. Bruhn, D.: Plant respiration and climate change effects. Ph.D. Thesis in Plant Research Department Riső National Laboratory (2002)
3. Chakravarty, S., Ghosh, S.K., Suresh, C.P., Dey, A.N., Shukla, G.: Deforestation: Causes, Effects and Control Strategies. ICAR Research Complex for Eastern Region, Research Center, Plandu, Ranchi, India (2016)
4. Saari, U.A., Baumgartner, R.J., Mäkinen, S.J.: Eco-friendly brands to drive sustainable development: replication and extension of the brand experience scale in a cross-national context. Sustainability **9**, 1286 (2017). https://doi.org/10.3390/su9071286
5. Alankus, O.B.: Technology Forecast for Electrical Vehicle Battery Technology and Future Electric Vehicle Market Estimation. Department of Mechanical Engineering, Okan University, Ballica YoluIstanbul, Tuzla, Turkey, 25 May 2017
6. Chauhan, D., Agarwal, S., Suman, M.K.: Wind power scenario in india: a review. Int. J. Sci. Res. Publ. **3**(9), 1 (2013). ISSN 2250-3153
7. Sangroya, D., Nayak, J. K.: Development of wind energy in India. Int. J. Renew. Energy Res. **5**(1) (2015)
8. Bowen, L., Ebrahim, S., De Stavola, B., Ness, A., Kinra, S., Bharathi, A.V., Prabhakaran, D., Srinath Reddy, K.: Dietary intake and rural-urban migration in India: a cross-sectional study. PLoS One **6**(6), e14822 (2011). https://doi.org/10.1371/journal.pone.0014822
9. Enevoldsen, P.: Managing the risks of wind farms in forested areas: Design principles for Northern Europe. Industrial Ph.D. Dissertation: 4135-00033B (2017)
10. Blocken B.: 50 years of computational wind engineering: past, present and future. J. Wind Eng. Ind. Aerodyn. (in press) (2014)
11. Karthik, J., Vinayagamurthy, G.: Aerodynamic Effect of Vortex Generator in Wind Turbine Blade. In: VIII NCWE 2016
12. Arnfield, J.: Two decades of urban climate research: a review of turbulence, exchanges of energy and water, and the urban heat island. Int. J. Climatol. **23**, 1–26 (2003)
13. Mirzaei, P.A., Haghighat, F.: Approaches to study urban heat Island—abilities and limitations. Build. Environ. **45**, 2192–2201 (2010)
14. Oke, T.R.: The energetic basis of the urban heat island. Q. J. R. Meteorol. Soc. **108**, 1–24 (1982)
15. Casey, M., Wintergerste, T.: ERCOFTAC special interest group on "quality and trust in industrial CFD"—best practice guidelines (2000); Jakeman, A.J., Letcher, R.A., Norton, J.P.: Ten iterative steps in development and evaluation of environmental models. Environ. Model. Softw. **21**, 602–614 (2006)
16. Tominaga, Y., Stathopoulos, T.: CFD simulation of near-field pollutant dispersion in the urban environment: a review of current modeling techniques. Atmos. Environ. **79**, 716–730 (2013)
17. Vos, P.E.J., Maiheu, B., Vankerkom, J., Janssen, S.: Improving local air quality in cities: to tree or not to tree? Environ. Pollut. **183**, 113–122 (2013)
18. Di Sabatino, S., Buccolieri, R., Salizzoni, P.: Recent advancements in numerical modelling of flow and dispersion in urban areas: a short review. Environ. Pollut. **52**, 172–191 (2013)

19. Choi, E.C.: Simulation of wind-driven-rain around a building. J. Wind Eng. Ind. Aerodyn. **46**, 721–729 (1993)
20. Blocken, B., Carmeliet, J.: A review of wind-driven rain research in building science. J. Wind Eng. Ind. Aerodyn. **92**, 1079–1130 (2004)
21. Kato, S., Murakami, S., Mochida, A., Akabayashi, S., Tominaga, Y.: Velocity-pressure field of cross ventilation with open windows analyzed by wind tunnel and numerical simulation. J. Wind Eng. Ind. Aerodyn. **44**, 2575–2586 (1992)
22. www.imdchennai.gov.in/
23. Google Maps: https://www.google.com/maps/
24. Atlantissolar: https://www.atlantissolar.com/turbine_1kw.html
25. Polarisamerica: www.polarisamerica.com/turbines/20kw-wind-turbines/
26. Houda, S., Zemmouri, N., Hasseine, A., Athmani, R., Belarbi, R.: A CFD model for simulating urban flow in complex morphological street network. TOJSAT Online J. Sci. Technol. **2**(1) (2012)
27. Braun, A.L., Awruch, A.M.: Aerodynamic analysis of buildings using numerical tools from computational wind engineering. Maciana Comput. **XXVI**, 1236–1251 (2007)
28. Toparlar, Y., Blocken, B., Vos, P., van Heijst, G.J.F., Janssen, W.D., van Hooff, T., Montazeri, H., Timmermans, H.J.P.: CFD simulation and validation of urban microclimate: a case study for Bergpolder Zuid, Rotterdam. Build. Environ. (2014)
29. Al-Jiboori, M.H., Al-Draji, A.G.: Aerodynamic surface roughness length of Baghdad City. J. Al-Nahrain Univ. **13**(1), 96–102 (2010)
30. Klok, L., Zwart, S., Verhagen, H., Mauri, E.: The surface heat island of Rotterdam and its relationship with urban surface characteristics. Resour. Conserv. Recycl. **64**, 23–29 (2012)

An Improved Unsteady CFD Analysis of Pitching Airfoil Using OpenFOAM

P. Srinivasa Murthy

1 Introduction

There are several methods available to analyze unsteady flow starting from analytical method based on Theodorson [1] to more complex CFD-based Navier–Stokes solvers due to Ashraf et al. [2]. At low Reynolds numbers of the order of insect/birds flight, none of the analytical and quasi-steady methods are useful to predict the flow characteristics which are quite complex involving flow separation, transition, reattachment, unsteadiness. Hence, CFD methods are the right choice although it is more costly and time-consuming and requires high-performance computing systems. Since open-source CFD code "OpenFOAM" becomes more popular for implementing and evaluating on high-performance computing systems, GPU performance has been evaluated for benchmark test case and cavity flow problem and compared with CPU performance. It has been found that from Srinivasa Murthy et al. [3], GPU performance is 1.7 times faster than CPU performance. Also, from another paper of the present author, Srinivasa Murthy et al. [4], it has been found that there was a good comparison with experiment for plunging NACA 0012 airfoil at low Reynolds number. CFD analysis of realistic flapping wing for MICAV application is presented in a paper by Srinivasa Murthy [5], and it has been found that thinner flapping wing produces more lift and thrust than thicker wing. This paper presents the solution of pitching NACA 0012 airfoil at low Reynolds numbers based on open-source CFD code, "OpenFOAM". Results are compared with experiment due to Koochesfahani [6]. It has been found that the comparison of variation of thrust coefficient, CT with reduced frequency, k of OpenFOAM and experiment is quite good, although there are some experimental uncertainties associated in computing CT by wake integration.

P. Srinivasa Murthy (✉)
Scientist 'F' (Retd), Aeronautical Development Establishment, Bengaluru 560075, India
e-mail: dr_ps_murthy@yahoo.co.in

2   Methods

2.1   *Problem Setup and Method of Solution*

Configuration used: NACA 0012 airfoil; pitching motion.

One typical airfoil (symmetric NACA 0012 airfoil) for which experimental data available is considered.

Case analyzed for NACA 0012 airfoil: velocity, $U = 15$ m/s, reduced frequency, $k = 2, 4, 6, 8$, and 10.

Amplitude, alpha = 2 deg, Reynolds number, $R = 12{,}000$.

Solver: simpleFoam, incompressible turbulent flow solver. Laminar flow option is chosen.

CPU: 8 h with 4 parallel processors for one flow simulation for 1.6 s duration.

Grid size: 11,414 cells generated from open-source BlockMesh and snappyHexMesh which are part of the OpenFOAM library.

2.2   *Boundary and Initial Conditions*

At the inflow boundary, the velocity is specified (velocity Dirichlet boundary condition) based on the desired Reynolds number, and the pressure is restricted to the zero-gradient condition (Neumann boundary condition).

At the outflow boundary, the pressure is set to the free stream value (Dirichlet boundary condition), while the velocity is set to the zero-gradient condition (Neumann boundary condition).

The far-field boundary is set to symmetry boundary condition and is placed at an appropriate distance from the moving body surface to minimize its undesired effects on the airfoil's surrounding flow field.

The stationary airfoils are set to no-slip boundary condition with fixed velocity ($U = 0$) and zero-gradient pressure boundary condition.

The unsteady moving airfoils are set to moving wall velocity boundary condition. This boundary condition guarantees the no-slip boundary condition by introducing an extra velocity to keep the flux through the moving boundary equal to zero.

The solution of *N-S* equations also needs the initial fluid properties (velocity, pressure, kinematic viscosity, *k,* and omega) to be specified at the start of the simulations. The steady-state solutions are used as the initial conditions for the time-marching unsteady calculations with free stream velocity.

2.3 Turbulence Model

For most of the low Reynolds number flows k-omega SST turbulence model is used in the incompressible Reynolds-averaged Navier–Stokes solver. But, laminar flow option is chosen for the presented results in this paper.

2.4 New Methodology

A new methodology has been developed by means of numerical experimentation of critical parameters such as relaxation parameters, relative tolerance level, number of sub-iterations, stability parameters (courant numbers), and smoothing parameters to achieve converged solution in cases of severe flow gradients.

In order to get more accurate unsteady solution, one needs to do more rigorous analysis in terms of grid refinement in the region of severe flow gradients with higher-order numerical schemes with better spatial and temporal accuracy. This requires computationally more intensive computing system with large memory and high speed.

3 Results and Discussion

Figure 1 shows mean thrust coefficient versus k for OpenFOAM and experiment due to Koochesfahani [6]. Grid size of 11,414 hexahedral cells is used in OpenFOAM. As reduced frequency k increases, there is an increase in thrust coefficient.
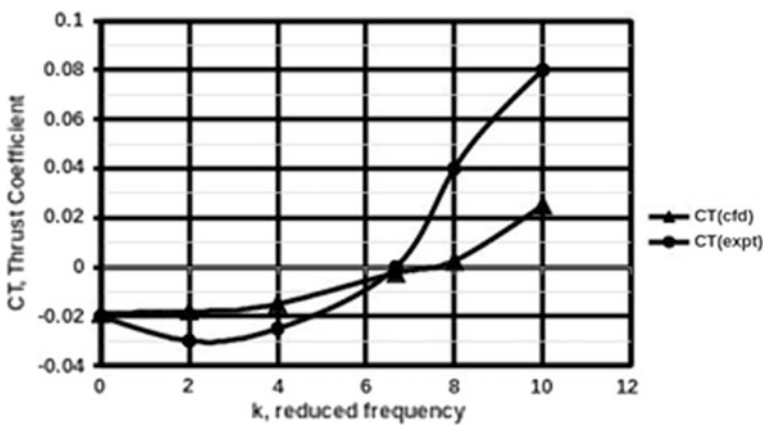
Fig. 1 Time average CT (mean thrust coefficient) versus k (reduced frequency), NACA0012 airfoil, $U = 15$ m/s, $R = 12{,}000$, amplitude $= 2$ deg, grid 11,414 cells
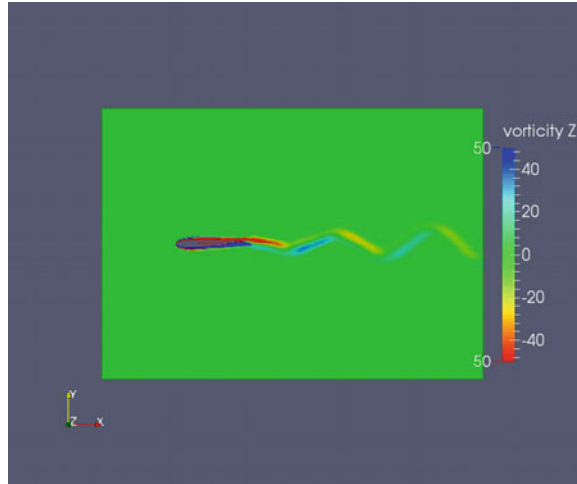
OpenFOAM agreement with experiment is excellent at reduced frequency, $k = 0$ and $k = 6.68$. $k = 0$ corresponds to static case when there is no pitching oscillations, and $k = 6.68$ corresponds to a case when there is no thrust or drag. This is the case where in the clockwise and anticlockwise vortices shed by the pitching airfoil cancels itself to become zero vorticity flow. At $k = 2, 4, 8$, and 10, there are large discrepancies between OpenFOAM and experiment. The reason could be due to the way the thrust coefficient is computed from measured values of local velocity by wake integration.

Figure 2 shows vorticity-Z contours for NACA 0012 airfoil at reduced frequency, $k = 2$. At low frequency, wake is in developing stage, and it appears as sheared vortex with anticlockwise vortex at the top and clockwise vortex at the bottom. This characterizes the drag-producing wake.

Figure 3 shows vorticity-Z contours for NACA 0012 airfoil at reduced frequency, $k = 4$. At this frequency, wake is further developed with clear distinct vortices shed by pitching airfoil. Here anticlockwise vortex is above the clockwise vortex alternately shedding from the trailing edge of pitching airfoil. Here also, vortex wake pattern is a typical characteristic of drag-producing wake.

Figure 4 shows vorticity-Z contours for NACA 0012 airfoil at reduced frequency, $k = 6.68$. At this frequency, wake is further developed with clear distinct vortices shed by pitching airfoil. Here anticlockwise vortex is in line with the clockwise vortex alternately shedding from the trailing edge of the pitching airfoil. So, there is a canceling effect of vortex strengths. There is no thrust or drag, but velocity is uniform in the wake, which means there is no velocity excess or deficit in the wake.

Figure 5 shows vorticity-Z contours for NACA 0012 airfoil at reduced frequency, $k = 8$. At this frequency, wake is further developed with clear distinct vortices shed by pitching airfoil. Here clockwise vortex is above the anticlockwise vortex alternately shedding from the trailing edge of pitching airfoil. This is a case of vortex wake pattern which is a typical characteristic of thrust-producing wake.

Fig. 3 NACA 0012 airfoil, vorticity-Z contours, $t = 1.6$ s, $U = 15$ m/s, amplitude = 2 deg, reduced frequency = 4, $R = 12{,}000$, grid 11,414 cells
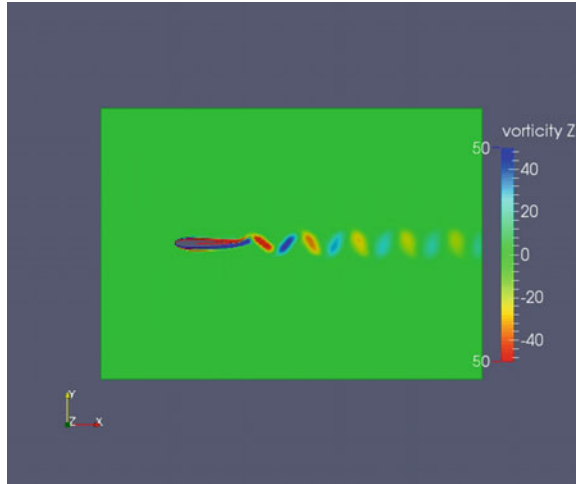
Fig. 4 NACA 0012 airfoil, vorticity-Z contours, $t = 1.6$ s, $U = 15$ m/s, amplitude = 2 deg, reduced frequency = 6.68, $R = 12{,}000$, grid 11,414 cells
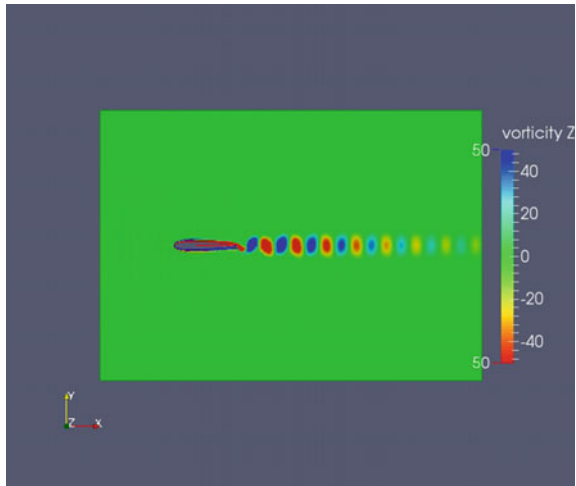
Figure 6 shows vorticity-Z contours for NACA 0012 airfoil at reduced frequency, $k = 10$. At this frequency, wake is further developed with clear distinct vortices shed by pitching airfoil. Here clockwise vortex is above the anticlockwise vortex, which is distinctly clear alternately shedding from the trailing edge of pitching airfoil. This is also a case of vortex wake pattern which is a typical characteristic of thrust-producing wake.

Fig. 5 NACA 0012 airfoil, vorticity-Z contours, $t = 1.6$ s, $U = 15$ m/s, amplitude = 2 deg, reduced frequency = 8, $R = 12,000$, grid 11,414 cells
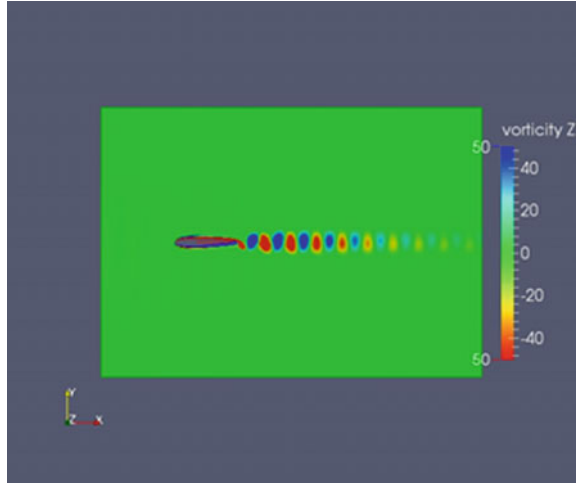
Fig. 6 NACA 0012 airfoil, vorticity-Z contours, $t = 1.6$ s, $U = 15$ m/s, amplitude = 2 deg, reduced frequency = 10, $R = 12,000$, grid 11,414 cells
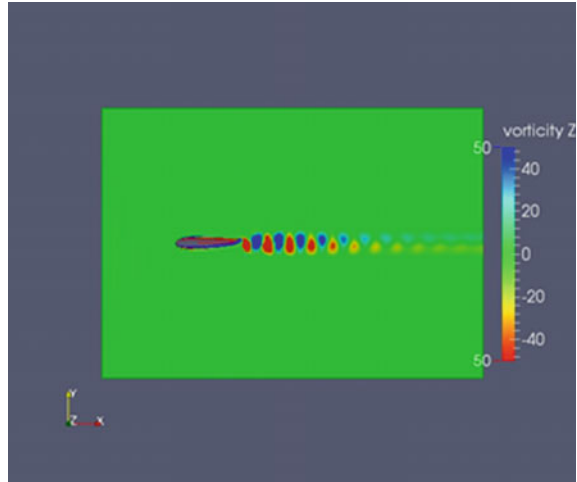
4 Conclusion

CFD analysis of pitching NACA0012 airfoil has been carried out using OpenFOAM incompressible flow solver simpleFoam, and results are compared with experimental data. OpenFOAM solutions are matching close to the experiment at reduced frequency, $k = 0$ and $k = 6.68$ and show good comparison in producing drag and thrust wakes at $k = 2$, 4 and $k = 8$, 10, respectively.

References

1. Theodorsen, T.: General theory of aerodynamic instability and the mechanism of flutter. NASA Report No. 496 (1935)
2. Ashraf, M.A., Lai, J.C.S., Young, J.: Numerical analysis of flapping wing aerodynamics. In: 16th Australasian Fluid Mechanics Conference, Crown Plaza, Gold Coast, Australia, 2–7 Dec 2007
3. Srinivasa Murthy, P., Muralidharan, M.R., Sriramachandra Rao, U., Prasanti, T.: Parallel performance of GPU and CPU in computational fluid dynamics. In: The 14th Asian Congress of Fluid Mechanics—14ACFM, Hanoi and Halong, Vietnam, 15–19 Oct 2013
4. Srinivasa Murthy, P., Muralidharan, M.R.: An improved unsteady CFD analysis of plunging airfoils using OpenFOAM. Int. J. Adv. Thermofluid Res. **2**(1) (2016)
5. Srinivasa Murthy, P.: CFD analysis of flapping wing for MICAV application. In: 2nd International Conference on Innovative Design & Development Practices in Aerospace & Automotive Engineering (IDAD-2016), Chennai, Tamil Nadu, India, 22–24 Feb 2016
6. Koochesfahani, M.M.: Vortical patterns in the wake of an oscillating airfoil. AIAA J. **27**(9), 1200–1205 (1989)

Development of 12 Channel Temperature Acquisition System for Heat Exchanger Using MAX6675 and Arduino Interface

Sandeep P. Nalavade, Abhishek D. Patange, Chandrakant
L. Prabhune, Sharad S. Mulik and Mahesh S. Shewale

1 Introduction

A temperature acquisition performs a significant role in analyzing the performance of heat exchanger equipment used widely in chemical process industry, refrigeration, and air conditioning, etc. [1, 2]. The performance of this heat exchanger device solely depends upon the accurate measurement of temperature of working fluids as well as temperature of surface wall. The rate of heat transfer can be expressed by taking the difference between inlet and exit temperature of working fluid, whereas the heat transfer coefficient and Nusselt number correlate to the difference between surface wall temperature and mean bulk fluid temperature. Also, profile of surface wall temperature between inlet and exit section can be plotted axially [3–5]. Commercial stand-alone data loggers are expensive and are mostly inflexible for adapting in academic research projects and are not tethered to a computer to acquire real-time data [6]. To overcome these limitations, we describe in-house design, development, calibration, and implementation of a 12-channel temperature acquisition system using MAX6675 and Arduino Mega 2560 microcontroller.

S. P. Nalavade
Dr. D. Y. Patil Institute of Technology, Pimpri, Pune, India

A. D. Patange (✉)
Vellore Institute of Technology, Chennai, India
e-mail: abhipatange93@gmail.com

C. L. Prabhune
Zeal College of Engineering & Research, Pune, India

S. S. Mulik
G. H. Raisoni College of Engineering & Management, Pune, India

M. S. Shewale
IUPUI, Indianapolis, IN, USA

2 Literature Review

Due to the huge advancement in data acquisition applications, it necessitates to integrate multiple sensors to any monitoring system to handle the huge data, and evaluating its performance became essential [7, 8]. Heat transfer augmentation techniques like passive, active, or a combination of both are common in various industrial applications. Passive techniques, where inserts are used in the flow passage to enhance the heat transfer rate, offer more benefits as compared with active techniques, because the insert manufacturing is simple and it can be easily engaged [9, 10]. Variety of temperature monitoring instrumentation is available for heat exchanger performance monitoring specifically RTDs, thermistors, and thermocouples are used for temperature sensing [11–13]. Primaa et al. [14] proposed an innovative laboratory kit investigating the heat transfer of a rod. It employs time-dependent measurement with temperature sensors and Arduino. The temperature varies at certain positions of a road while it is being heated, due to the conduction phenomena. The result shows the good inclinations of time-dependent temperature variation. Hinton et al. [15] developed a data acquisition system for automatic temperature measurements of extended surfaces of heat exchanger. Four fins were analyzed and were fitted with thermocouples at one-inch interval so they can be partitioned into eight control volumes. Temperature gradients across the inlet and outlet area for each control volume were determined using recorded thermocouple measurements. The heat transfer coefficients and effectiveness were calculated from recorded data. Tamna et al. [16] investigated heat transfer augmentation in tubular heat exchanger with double V-ribbed twisted tapes with 30° V-shaped ribs using data logger. The experimental results showed the heat transfer and pressure drop in terms of Nusselt number and friction factor.

3 Control System Design and Mechatronics Interface

A novel solution for design and development of temperature acquisition system was formulated using MAX6675 cold-junction compensated K-type thermocouple and Arduino Mega 2560 microcontroller. To design control system and mechatronic integration, the layout of temperature acquisition system is proposed herewith. Figure 1 shows control system design and various components interfaced each other.

Figure 2 shows circuit diagram of 12 channels of MAX6675 and K-type thermocouple interfaced with Arduino microcontroller. Development of temperature acquisition system is shown in Fig. 3.

The microcontroller of used for temperature acquisition system is Arduino ATMega 2560. It has 16 analog inputs and 54 digital I/O pins (14 can be used as PWM). Each of the 54 digital pins on the Arduino Mega 2560 can be used as an
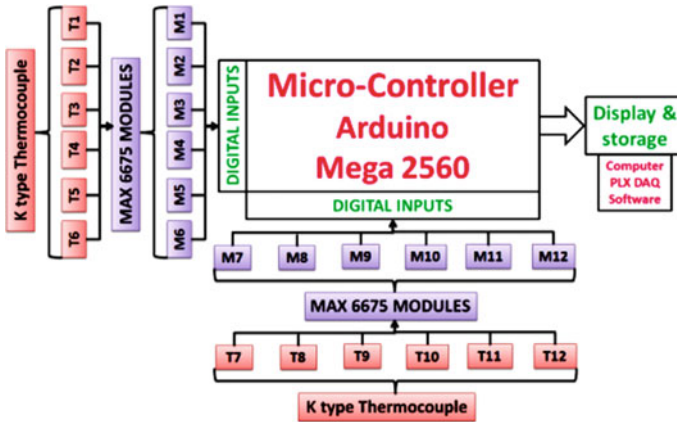
Fig. 1 Control system design
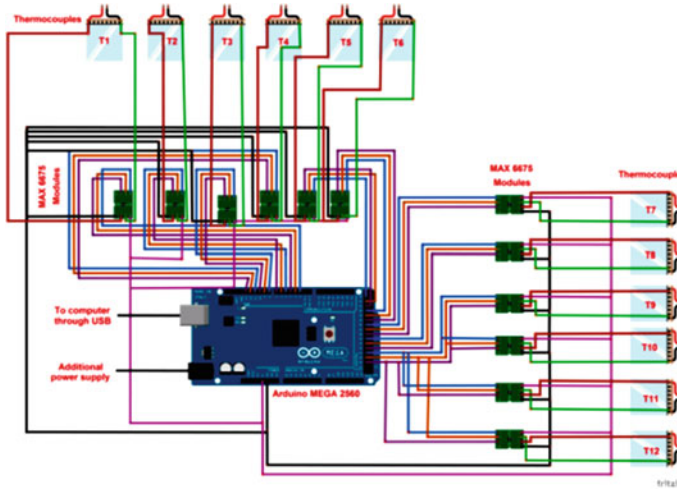
Fig. 2 Mechatronic integration circuit diagram

input or output at 5 V [17, 18]. Here, total 36 digital pins are used and connected to thermocouples through MAX6675 modules. The MAX6675 offers three main functions as conversion of output voltage of thermocouple into temperature, cold-junction compensation and digitizes the signal from a type-*K* thermocouple [19, 20]. Here, 12 *K* type thermocouples have been interfaced to Arduino along with MAX6675 modules.
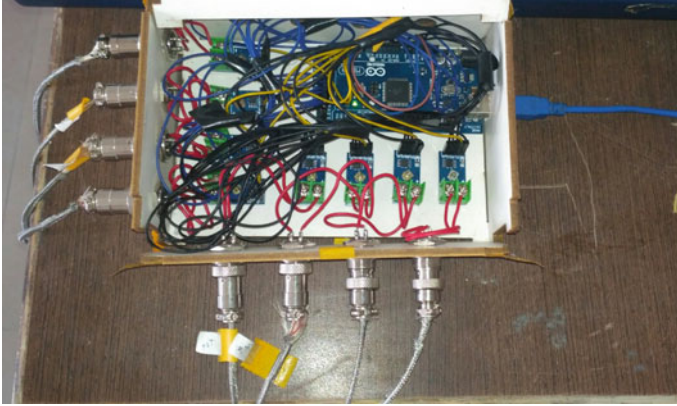
Fig. 3 Development of temperature acquisition system

4   Analysis of Heat Exchanger Device

The developed system is used to record the working fluid inlet (T_1), exit (T_8), and surface wall temperatures (T_w) till steady-state condition attained. Precisely it is heat transferred across the test section Q_{Conv} is equal to heat absorbed by flowing air Q_a.

$$Q_a = Q_{Conv} \tag{1}$$

where;

$$Q_a = mC_p(T_8 - T_1) \tag{2}$$

The convection heat transfer rate from test section can be calculated as

$$Q_{conv} = hA(T_w - T_{mb}) \tag{3}$$

where T_{mb} is mean bulb temperature of air which can be calculated as

$$T_{mb} = \frac{(T_1 + T_8)}{2} \tag{4}$$

The average wall temperature (T_w) was calculated from six points of surface temperatures lined equally between the inlet and the exit of test tube.

$$T_w = \sum \frac{(T_2 + T_3 + T_4 + T_5 + T_6 + T_7)}{6} \tag{5}$$

5 Experimentation and Testing

The experimental setup consists of centrifugal blower, heat exchanger device, U-tube manometer, differential pressure gauge as shown in Fig. 4. Changes in temperature with respect to time at various locations along heat exchanger test section were recorded by developed and commercial systems. The temperature recording is continued till steady-state temperature is achieved which can be verified by plotting time versus temperature graph Fig. 5.
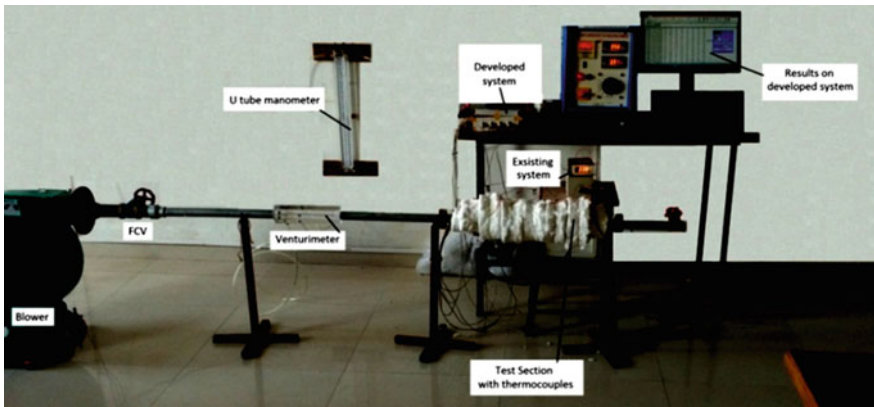
Fig. 4 Experimental setup consisting of heat exchanger device, developed system, etc.
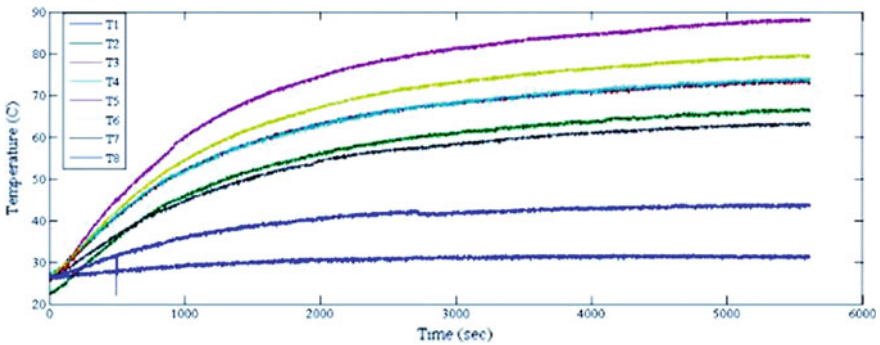
Fig. 5 Variation of temperature with respect to time

Table 1 Observation table and calculations

Systems/ parameters	Re	T_1	T_2	T_3	T_4	T_5	T_6	T_7	T_8	T_w	T_{mb}
Developed system	7000	31	66.5	73.75	74.25	88.75	80.25	63	44.1	74.41667	37.55
Commercial system	7000	30.9	66.6	73.8	74.3	88.8	80.2	63.1	43.9	74.46667	374
										−0.06719	0.399467
										% Error	

6 Results, Validation, and Discussion

The test was conducted using existing commercial system and developed system for fluid flow with Reynolds number 7000 and power input of 50 W. The surface wall temperatures (T_2 to T_7) and working fluid inlet and exit temperature (T_1 and T_8) were recorded, displayed, and stored by MS Excel. Table 1 shows observations.

It has been observed that the steady state has been achieved after 90–100 min, which can be seen from flat temperature profiles as shown in graph Fig. 5.

It has been observed that the recorded temperatures are in good agreement of 99.8% with commercial system. The surface temperature and working fluid temperature varies with respect to time, due to conduction and convection heat transfer from heater surface to working fluid. This flat temperature profiles represents that steady state has been achieved, and hence, data logging has been concluded.

7 Conclusion

A 12-channel temperature acquisition system was developed by using low-cost controller Arduino Mega 2560 and MAX6675 interface. The overall cost of system does not exceed Rs. 6,000/-. *K* type thermocouples were integrated with microcontroller, and a control system was designed to access the real-time input to be acquired from these sensors. Arduino Integrated Development Environment (IDE) is used as back-end software for programming and is integrated with MS Excel to store and display the acquired data. The developed system is calibrated with existing system and was found to have an accuracy of 99.8%. This system is implemented on heat exchanger device for enhancing convective heat transfer rate by incorporating the inserts inside heat exchanger tubes and determining temperatures at various locations.

References

1. Roetzel, W., Luo, X., Xuan, Y.: Measurement of heat transfer coefficient and axial dispersion coefficient using temperature oscillations. Exp. Thermal Fluid Sci. **7**(4), 345–353 (1993)
2. Huang, J., Chen, G., Shu, L., Wang, S.: An experimental study of clogging fault diagnosis in heat exchangers based on vibration signals. IEEE Access 2169–3536 (2016)
3. Lai, Y., Liu, M., Dong, Q.: Dynamic characteristic analysis of heat exchanger tube bundles with external fluid. Pressure Vessel Technol. **21**(12), 22–25 (2004)
4. Su, X.Y.: A research of the on-line monitoring system for the inner leakage of water cooler. M.S. thesis, Dept. Chem. Process Equip., Dalian Univ. Technol., Dalian, China (2005)
5. Gad, H.E., Gad, H.E.: Development of a new temperature data acquisition system for solar energy applications. Renew. Energy **74**, 337e343 (2015)
6. Luo, Y., Bo, C.: Development of on-line monitor for the heat exchanger. J. Nanjing Univ. Technol. **26**(6), 94–97 (2004)
7. Mulik Sharad, S., Deshmukh Suhas, P., Patange Abhishek, D., et al.: Review of vibration monitoring techniques using low cost sensors and microcontrollers. J. Mechatron. Autom. **4** (2), 33–40p (2017)
8. Shewale, M., Mulik, S., Deshmukh, S., Patange, A., Sundare, A., Zambare, H.: Novel machine health monitoring system. In: The 2nd International Conference on Data Engineering and Communication Technology (ICDECT) 2017, Advances in Intelligent Systems and Computing, pp. 153–24. Springer, Berlin (2017)
9. Dewan, A., Mahanta, P., Sumithra Raju, K., Suresh Kumar, P.: Review of passive heat transfer augmentation techniques. Proc. Inst. Mech. Eng. Part A: J. Power Energy **218** (2004)
10. Wakui, T., Yokoyama, R.: On-line model-based performance monitoring of a shell-and-tube type heat exchanger using steam and water. Energy Convers. Manage. **49**(10), 2669–2677 (2008)
11. Primaa, E.C., Karim, S., Utari, S., Ramdani, R., Putri, E.R.R., Darmawati, S.M.: Heat transfer lab kit using temperature sensor based Arduino for educational purpose. Procedia Eng. **170**, 536–540 (2017)
12. Astorga-Zaragoza, C.M., Alvarado-Martínez, V.M., Zavala-Rio, A., Mendez-Ocana, R.M.: Observer-based monitoring of heat exchangers. ISA Trans. **47**(1), 15–24 (2008)
13. Sun, L., Zhang, Y., Saqi, R.: Research on the fouling prediction of heat exchanger based on support vector machine optimized by particle swarm optimization algorithm. In: Proceedings of International Conference on Mechatronics and Automation, pp. 2002–2007, Aug 2009
14. Tatara, R.A., Lupia, G.M.: Assessing heat exchanger performance data using temperature measurement uncertainty. Int. J. Eng. Sci. Technol. **3**(8), 1–12 (2011)
15. Hinton, M.A., Marloth, R., Noorani, R.I.: Data Acquisition System for an Undergraduate Fin Heat Exchanger Experiment. Session 2259, Loyola Marymount University (2002)
16. Tamna, S., Kaewkohkiat, Y., Skullong, S., Promvonge, P.: Heat transfer enhancement in tubular heat exchanger with double V-ribbed twisted-tapes. Case Stud. Thermal Eng. **7**, 14–24 (2016)
17. Datasheet: MAX6675, Cold-Junction-Compensated K-Thermocouples-Digital Converter, 19–2235; Rev 2; 4/14
18. Sobota, J., Pisl, R., Balda, P., et al.: Raspberry Pi and Arduino boards in control education. In: The International Federation of Automatic Control (IFAC) (2013)
19. Looney, M.: An introduction to MEMS. Analog Dialogue **48**(06) (2014)
20. Datasheet: Atmel 2549 QAV R ATmega640/V-1280, 02/2014

Optimization of Clutch Cover Mounting Base Plate Through Twin Threaded Grub Screw

T. V. B. Babu, R. Anbazhagan, V. Sathiyamoorthy, K. Arumugam and R. Suresh

1 Introduction

The successful running of any large-scale manufacturing relies on the compatibility to encourage simple gathering and decrease of unit cost. Large-scale manufacturing strategies request a quick and simple strategy for situating work for precise operations on it. Dances and installations are generation devices used to precisely fabricate copy and exchangeable parts. Dances and installations are uniquely planned with the goal that expansive quantities of segments can be machined or collected indistinguishably and to guarantee compatibility of parts.

T. V. B. Babu (✉) · R. Anbazhagan · V. Sathiyamoorthy
K. Arumugam · R. Suresh
Department of Mechanical Engineering, Vel Tech High Tech
Dr. Rangarajan Dr. Sakunthala Engineering College, Chennai, India
e-mail: prof.tvbbabu@gmail.com

R. Anbazhagan
e-mail: dranbazhagan@velhightech.com

V. Sathiyamoorthy
e-mail: drsathiyamoorthy@velhightech.com

K. Arumugam
e-mail: arumugam@velhightech.com

R. Suresh
e-mail: drsureshr@velhightech.com

2   Problem Identification

Frequent wear in the existing thread in base plate. Changing of base plate due to the wear in thread. Tapping the clutch plate frequently during the time of testing operation. Consumption of time in changing base plate and frequent tapping.

3   Proposed Methodology

The thread gets damaged due to continuous testing of different fixtures in the base plate so to rectify that we are going to introduce a grub screw-like pattern inside the base plate holes. The grub screw-like pattern has internal and external threading so that it can be screwed inside the holes of the base plate where the fixtures are mounted. By fixing this new type of grub screw pattern, the fixture can be fixed in the grub screw so that if it gets worn or gets damaged in the threading, it can be replaced easily; the damage of the base plate can be avoided which will reduce the cost of operation.

4   Scope of Work

- Reconfiguring process plans to minimize change.
- Products and system design innovation.
- Changeable production planning and control enablers.
- Complexity of manufacturing and assembly systems.
- This project can mainly reduce time consumption caused by the issues.
- Cost of the base plate replacement can be cut permanently.

5   Merits of Grub Screw

Fixing of grub screw in base plate is easy. Reduction of work is significant. Reduction in total cost for industry. Frequent wear in base plate is reduced. Consumption of time and man power is reduced. Reliability and adaptability are more.

6 Design

SOFTWARE NAME: CREO 2.0.
See Figs. 1, 2, 3, 4, 5, 6, 7, 8, 9, 10, and 11.
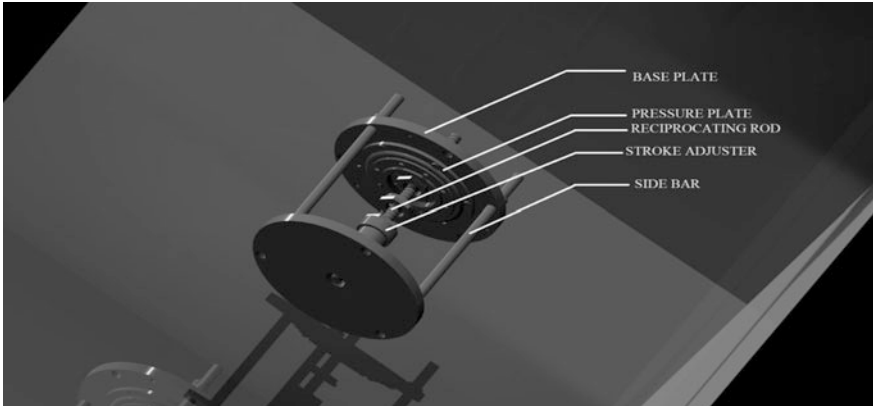
Fig. 1 One workstation of axial fatigue test bench

Fig. 2 Base plate before adding grub screw
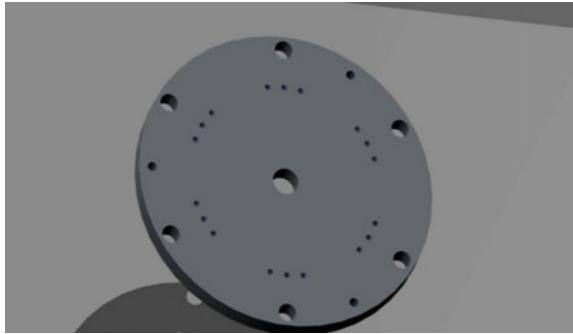
Fig. 3 Internal threading is shown in the base plate
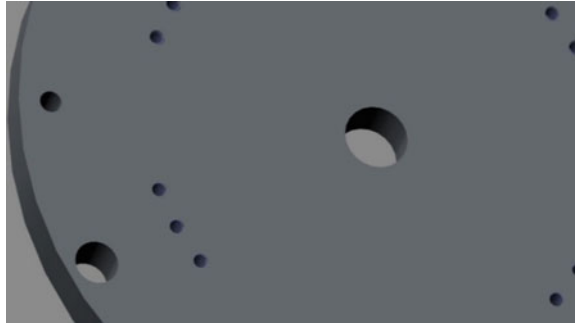
Fig. 4 Draft of base plate
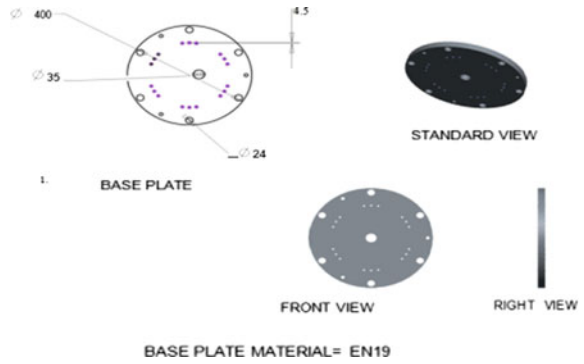
Fig. 5 Modified grub screw with hexagonal key
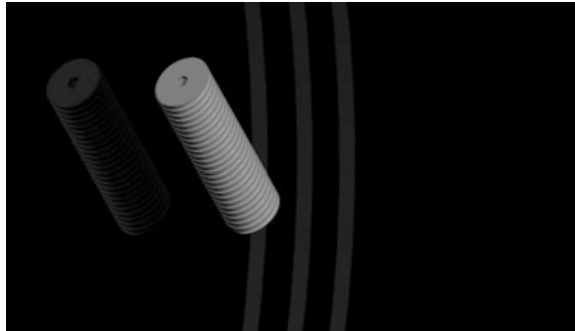
Fig. 6 Grub screw with internal threading
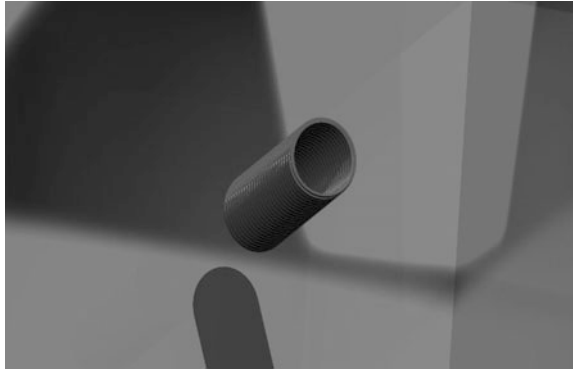
Fig. 7 Draft of grub screw hole at the bottom
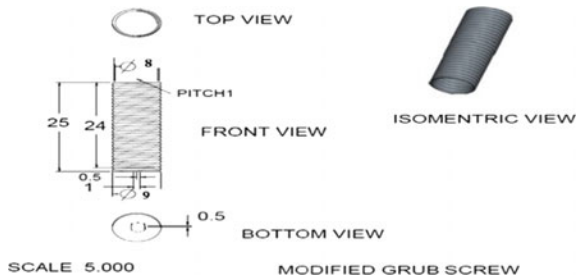
Fig. 8 Base plate before adding grub screw
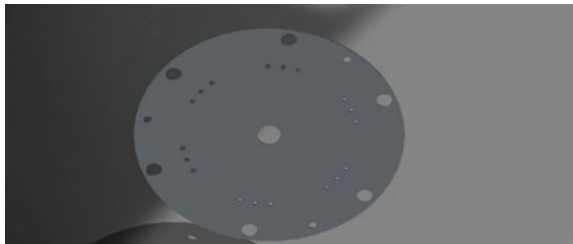
Fig. 9 After adding grub screw
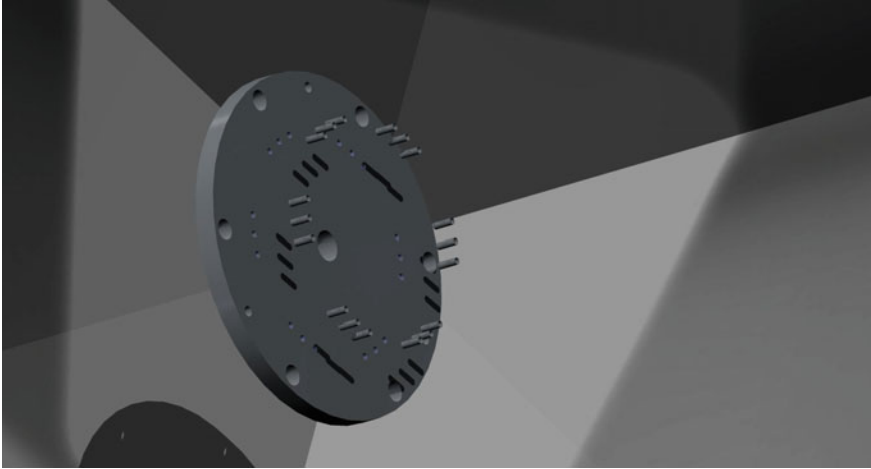
Fig. 10 Exploded view
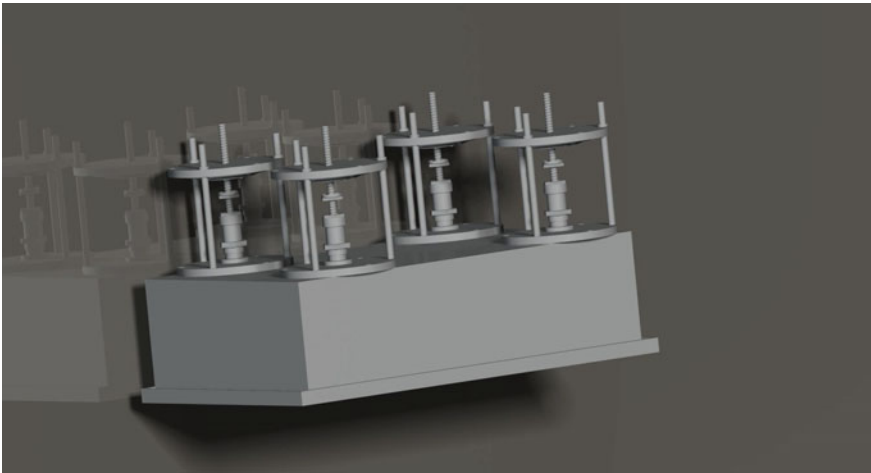
Fig. 11 Overall setup of test bench

7 Conclusion

A detailed study of existing axial fatigue testing machine was studied, and based on the study reports a proposal for optimization of clutch cover mounting base plate through twin threaded grub screw was finished. This modified grub screw is better than the existing working fixtures in the economical and maintenance aspects. Production cost impact through this proposal is 13.5% (approximately) by

implementing this proposed fixture. Thus, the objective of our project has been achieved by design.

The actual valve spent in existing method = 1,60,000 Rs PA.
The valve to be spent in proposed method = 21,600 Rs PA.
Cost impact through this proposal is 13.5%.
Difference between existing and proposed method is 86.5%.

References

1. Shukla, H.M.: Design of jig and fixtures for productivity improvement of stirrup making activity. Int. J. Sci. Res. Dev. **3**(02) (2015). ISSN (online): 2321-0613
2. Umretiya, R., Lakhwani, M.: Design & analysis of self align clutch: a review. Int. J. Sci. Res. Dev. **2**(10) (2014). ISSN (online): 2321-0613
3. Gujja, L.N., Patil, R.D.: Design and analysis of mechanical assembly for the clutch test rig. Int. J. Adv. Res. Sci. Eng. Technol. ISSN: 2350-0328
4. Deb Barma, S., Kumar, R., Kashyap, A., Patel, D., Chaudhari, A.Y.: Modification of grub screw and cam plate for reduction of failure in PMC threading machine. Int. J. Mod. Trends Eng. Res. e-ISSN No.: 2349-9745
5. Purohit, R., Koli, D.: Design and finite element analysis of an automotive clutch assembly. In 3rd International Conference on Materials Processing and Characterisation (2014)

Active Vortex Shedding Control for Flow Over a Circular Cylinder Using Rearward Jet Injection at Low Reynolds Number

S. Karthikeyan, B. T. Kannan and S. Senthilkumar

1 Introduction

Flow control is a hot area of research that spans over decades for fluid dynamics/ aerodynamics researchers [1]. The vortex shedding from the cylinders at certain Reynolds numbers induces vibrations in the structures (bluff bodies), and the phenomenon is called as vortex-induced vibration [2]. This can be a hazardous threat to the structure when the vortex shedding frequency matches the natural frequency of the structure. To reduce this shedding process, many researchers in the past arrived at using active [3–5] and passive [6] control techniques. The present work is an active control of shedding by using jet injection at the aft end of the cylinder, and the study was performed for various injection ratios (IR) by using computational fluid dynamics (CFD) simulations.

2 Computational Methodology

The simulations are performed using commercial CFD tool ANSYS-FLUENT [7]. A large rectangular domain is chosen around the cylinder to capture the shedding process. The jet injection is specified as constant velocity profile. The 2D unsteady laminar flow governing equations are solved numerically, and the solutions are

S. Karthikeyan · S. Senthilkumar (✉)
Department of Aeronautical Engineering, Vel Tech Rangarajan Dr. Sagunthala
R&D Institute of Science and Technology, Chennai 600062, India
e-mail: s.senthilms@gmail.com

B. T. Kannan
Department of Aerospace Engineering, Indian Institute of Technology Madras, Chennai
600036, India

stored at various time intervals. Further details on the methodology and validation are described in the reference literature [6].

3 Results and Discussion

The time series of coefficients of lift and drag are plotted for various injection ratios (see Fig. 1). The base case with no injection shows the oscillations resulting from the vortex shedding process. As the injection ratio increases, the shedding process is suppressed and completely perished above injection ratios 1.5 in the present work.

Figure 2 shows average drag coefficient and Strouhal number for various injection ratios. As the injection ratio increases, the Strouhal number is constant up to a certain range and then decreases to zero around IR = 2. This shows the suppression of shedding from IR = 1.5 and complete suppression for IR = 2 and above. In contrast, the coefficient of drag shows a dip around IR = 1 and then gradually increases.

Figure 3 shows the streamlines for various time instances. At IR = 0.5, the pair of symmetrical vortices evolves at ($t = 1$ s) the wake side of the cylinder and gets
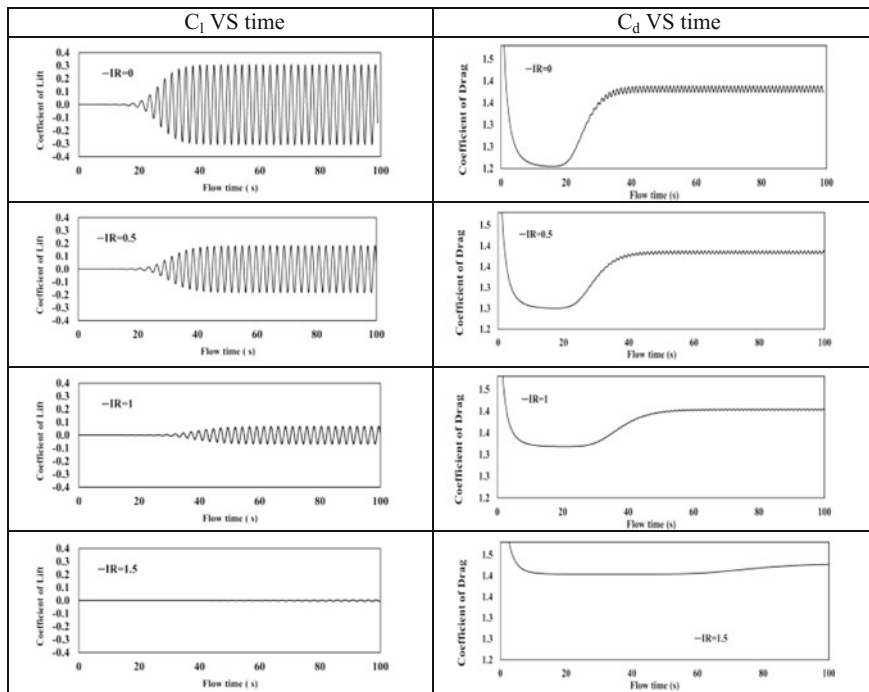
Fig. 1 Time series of lift and drag coefficients
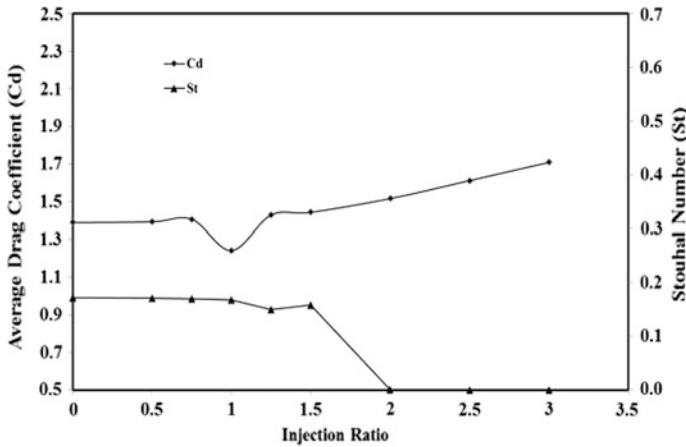
Fig. 2 Average C_d and Strouhal number versus injection ratio

elongated ($t = 10$ s) with the influence of free shear flow and with increased time ($t = 15$ s) the initial vortex breakdown creates a secondary vortex. But the secondary vortex is unstable and diffused in the main stream with time ($t = 40$ s). Then there is an alternative vortex shedding of primary unsymmetrical vortices at wake region. At $t = t_c$, the strong shedding vortex is slightly pushed back due to the intrusive momentum of jet in the wake side, whereas when IR = 0 these alternative shedding vortices are more close to the cylinder aft surface, as shown in Fig. 3. However, there is shift in timing of secondary vortex breakdown, diffused time and periodic shedding time between IR = 0 and IR = 0.5 as clearly seen in Figs. 3 and 1. As shown in Fig. 4, when IR = 1, at $t = 1$ s, the symmetrical primary vortices are pushed further deep into the downstream and there is an attached symmetrical secondary vortices at wake ($t = 10$ s). As the time increases from $t = 20$ s to 40 s, the free shear flow interaction of primary vortices makes the detached primary vortices unstable and breaks as a tertiary vortex. There exists periodic shedding of secondary vortices ($t = 50$ s to 60 s) and the diffused tertiary vortex ($t = 60$ s to 80 s). After this time, shedding of these primary vortices disturbs the size of the secondary vortices, and there is a critical interaction which ultimately makes both the primary and secondary vortices shed periodically ($t = t_c$). In IR = 1.5, as shown in Fig. 4, there is a formation of symmetrical primary vortices ($t = 1$ s) and moved further downstream with larger distance as compared with IR = 1 which is evident from C_l history Fig. 1 and can be attributed to high jet momentum. Then, there are two pairs of stable symmetrical secondary vortices formed ($t = 10$ s) and attached to the rear surface of the cylinder. Free shear layer interaction with detached primary vortices alters and breaks down as a tertiary vortex which is diffused further with time ($t = 60$ s), and then at $t = t_c$, primary vortices shed periodically as happened with IR = 1.

t(s)	IR=0	IR=0.5
1		
10		
15		
20		
30		
40		
45		
tc		
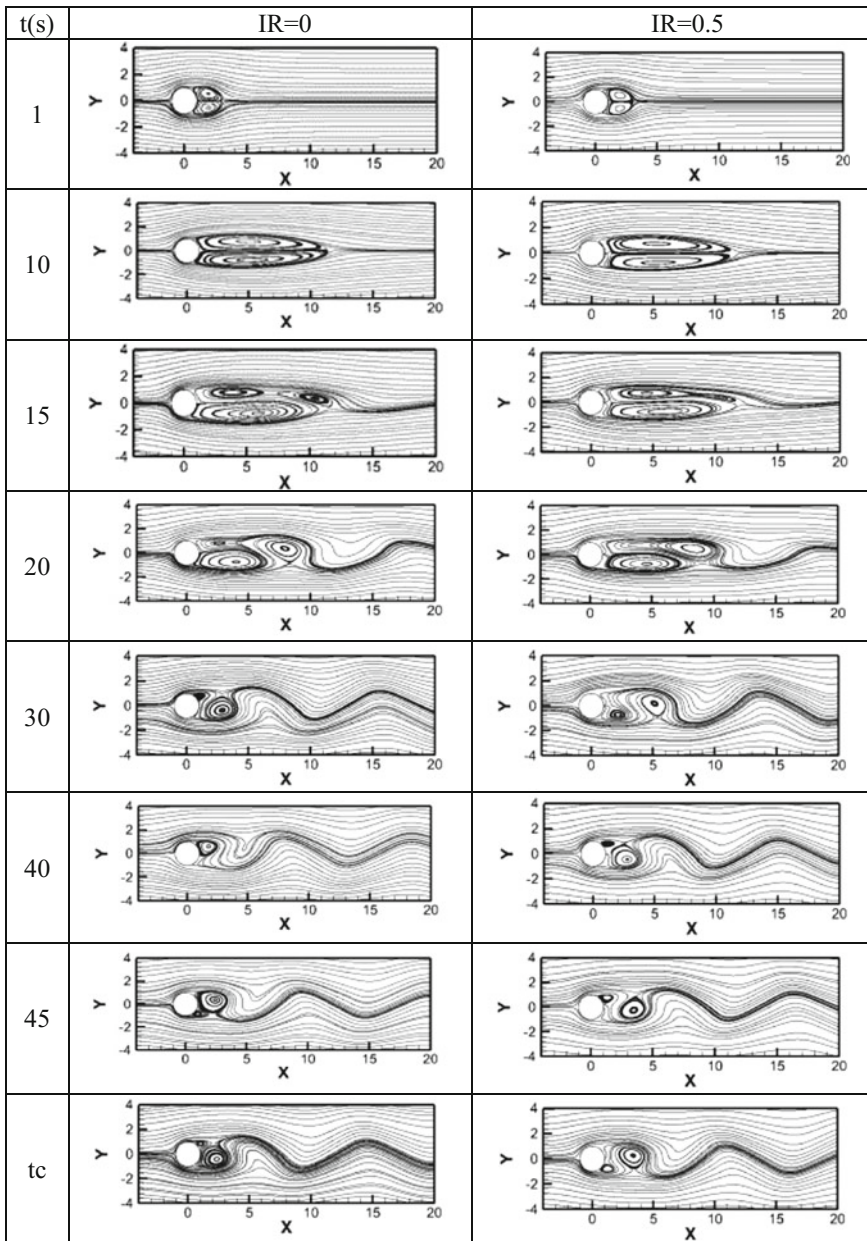
Fig. 3 Streamlines for IR = 0–0.75 at various time instances

t(s)	IR=1	IR=1.5
1		
10		
20		
40		
50		
60		
80		
tc		
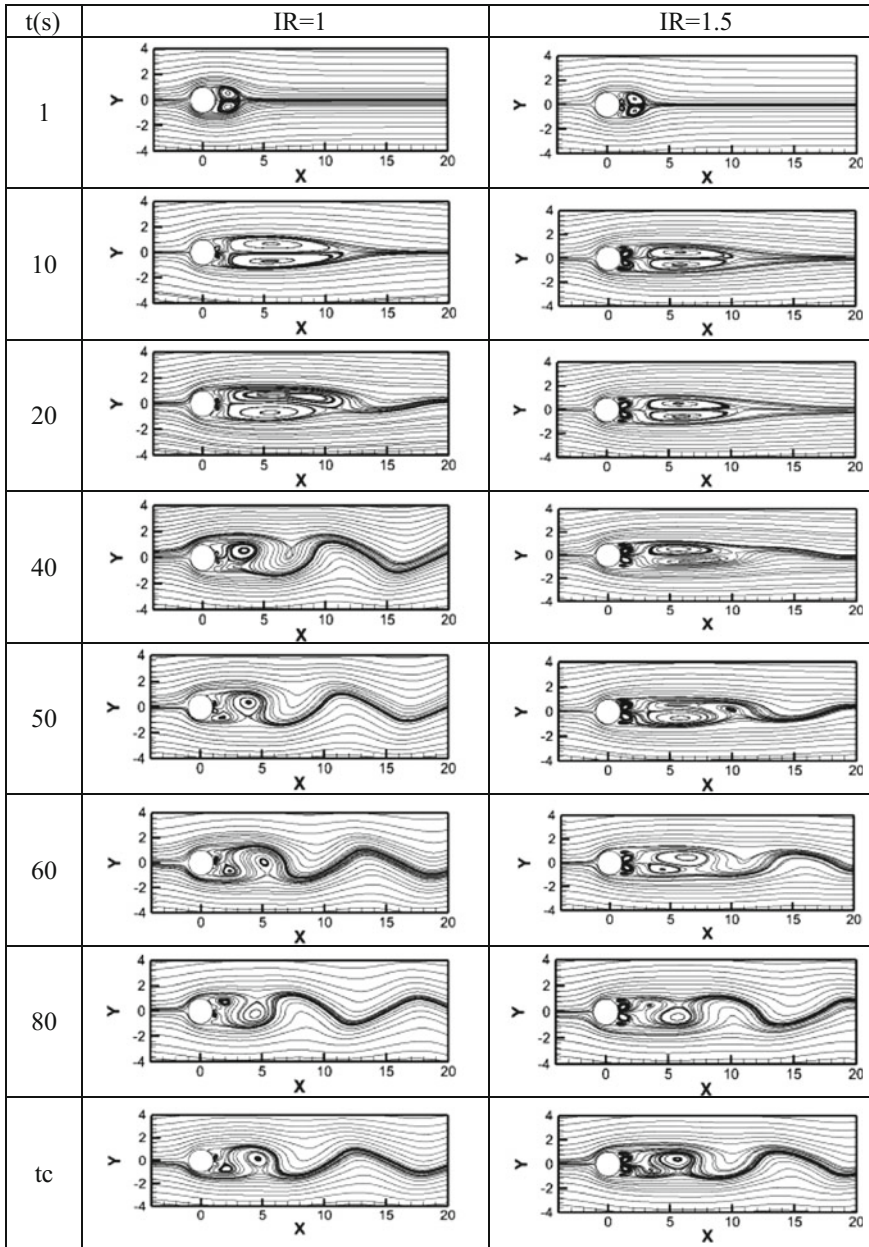
Fig. 4 Streamlines for IR = 1–1.5 at various time instances
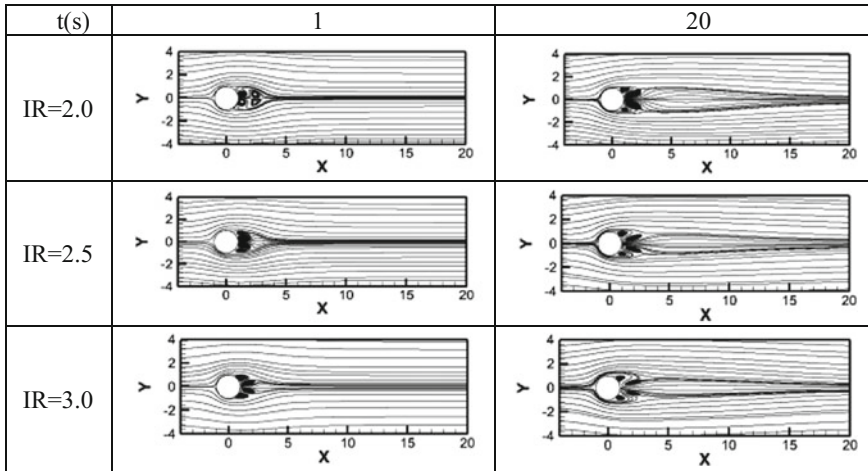
Fig. 5 Streamlines for IR = 2–3 at various time instances

For IR = 2–3, the momentum of jet is very high into the wake, hence there is no shedding of vortices found at wake but there is a formation of two pairs of symmetrical vortices due to jet entrainment which cuts the communication between them completely; one pair of symmetrical vortices located adjacent to the jet core interacts with jet shear layer and stretches downstream. The size and shift in location of the vortices vary with respect to jet strength as shown in Fig. 5.

4 Conclusion

The present work deals with the suppression of vortex shedding with rearward jet injection. The increase in jet momentum results in suppression of vortex shedding but results in the increased drag as penalty. The critical injection ratio is found to be between 1.5 and 2, beyond which the vortex shedding is completely absent.

References

1. Gad-el-Hak, M.: Flow Control: Passive, Active, and Reactive Flow Management, 1st edn. Cambridge University Press, Cambridge (2000)
2. Govardhan, R.N.: Vortex-Induced Vibration of Two and Three-Dimensional Bodies, Cornell University (2000)
3. Ffowcs Williams, J.E., Zhao, B.C.: The active control of vortex shedding. J. Fluids Struct. **3**(2), 115–122 (1989)
4. Saha, A.K., Shrivastava, A.: Suppression of vortex shedding around a square cylinder using blowing. Sadhana **40**(3), 769–785 (2015)

5. Pantokratoras, A.: Laminar flow across an unbounded square cylinder with suction or injection. Z. Angew. Math. Phys. **68**(1) (2017)
6. Karthikeyan, S., Senthilkumar, S.: Control of vortex shedding behind a circular cylinder using a combination of slot and control plates. In: Saha A., Das D., Srivastava R., Panigrahi P., Muralidhar K. (eds.) Fluid Mechanics and Fluid Power—Contemporary Research, LNME, pp. 311–321. Springer, New Delhi (2017)
7. Ansys-Fluent, User Guide Version 14.0 (2011)

Performance Augmentation of Boron–HTPB-Based Solid Fuels by Energetic Additives for Hybrid Gas Generator in Ducted Rocket Applications

Syed Alay Hashim, Sanket Kangle, Srinibas Karmakar and Arnab Roy

1 Introduction

In air-breathing engines, ramjet is dominated due to their higher specific impulse which is higher than rocket engine as well. Because of that, ramjet has been used for medium and high supersonic speed missiles to achieve longer range and endurance [1]. Various modifications have been done in ramjet engines to enhance their ballistic properties. These modifications are realized by changing in working substance (fuels/propellants) as well as internal designs. Among various types of ramjet engines, solid fuel ducted rocket (SFDR) is one which produces higher specific thrust [1, 2]. Therefore, SFDR is considered as an alternative propulsion system to rockets as a means to flying through the atmosphere. Actually, SFDR has two combustion chambers: primary and secondary. In primary combustor (or gas generator), solid fuel/propellant burns and generates fuel-rich high-pressure and high-temperature gas which moves into the secondary combustor and burns further with shock-induced compressed air [3].

The performance of the SFDR is further enhanced by introducing metal particles to the fuel/propellant of the gas generator due to their higher energy release on combustion and also improves density which is beneficial for volume-limited propulsion systems. Some selective energetic fuels (metal/metalloid) which are tested in rocket propulsion application have been compared in Fig. 1 on the basis of their energy release on oxidation. Boron has the highest heat of combustion on both gravimetric (59.3 kJ/g) and volumetric (131.6 kJ/cm^3) basis among the tabulated fuels (Fig. 1) except beryllium which is not used in practice because of its toxic compounds. Although boron particles used in solid fuel/propellant has long been of interest as a fuel especially in ducted rocket applications by many researchers, boron's potential as fuel or a fuel additive has not yet been accomplished thor-

S. A. Hashim · S. Kangle · S. Karmakar (✉) · A. Roy
Indian Institute of Technology Kharagpur, Kharagpur 721302, West Bengal, India
e-mail: skarmakar@aero.iitkgp.ac.in

143
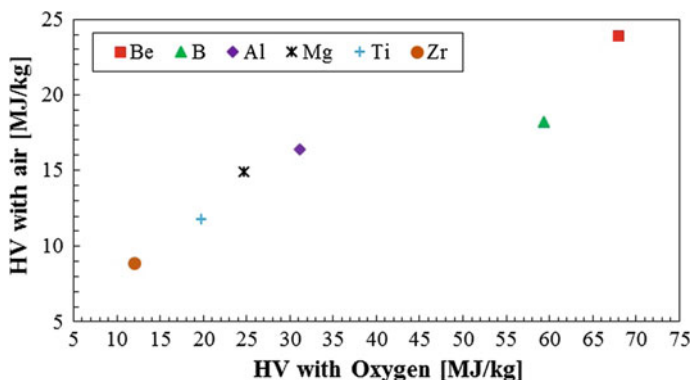
Fig. 1 Heat of combustion of several energetic fuels [3, 15]

oughly, primarily because of the problem associated with its ignition and combustion [4]. Boron forms oxide layer on its surface once it comes in contact with air/oxygen which works as a protective layer due to which the diffusion of oxygen to the boron particle is interrupted and consequently boron ignition is hindered. Actually, the Oxide layer liquefies at relatively low temperatures (450 °C at 1 atm) and covers the surface of the boron particle due to which reaction of oxygen to the core boron becomes slow which in turn affects the overall ignition and combustion performance. About five decades ago, boron had been studied by Macek and Sample [5] where they had analyzed ignition and combustion of a single crystalline boron particle at atmospheric pressure and identified that boron burning happens in two stages. The first stage includes ignition of boron particle covered with a native oxide layer. The second stage comprises the combustion of uncoated boron on heating it above the boiling temperature of B_2O_3 and the oxide layer is completely stripped off by evaporation. Therefore, it is expected that removal of liquid oxide layer from the exterior of boron particle plays a vital role in the ignition and combustion processes [5, 6].

There are several methods to enhance the combustion of boron-contained solid fuels availed either by modifying the propulsion system or by incorporating energetic additives in the fuel. In system-level approach, incorporating aft-burner section or facilitating bypass air steam to the ramjet minimizes the inherent drawback of slow-reacting boron particles due to the two-stage combustion process. However, these modifications have some design complications such as pressure loss and inert weight, which affect the overall performance of the propulsive devices [7, 8]. Balas and Natan [9] observed the condensation of boron oxide using three models with small modifications to judge the performance of boron-based fuel through a two-stage ramjet engine where a part of inlet air is supplied into the secondary chamber. In their investigation, first stage fuel-rich combustible products mixed with bypass air of the secondary combustion chamber and condensed before exhausting through the main nozzle. Recently, it is found that addition of

polytetrafluoroethylene (PTFE) to the boron particles improves boron combustion. This is probably due to effect of their decomposition gases which interact directly with boron oxide and facilitate removal of oxide layer of the boron particles [10]. Among various approaches in boron combustion enhancement, use of nanoparticles in place of micron size performes better due to their higher surface area as well as nanoparticle ignites at lower temperature [11, 12]. Mechanical activation (metal-arresting technique) with other metallic fuels to boron particle is another important approach to enhance the combustion performance of boron-based solid fuels which could be used in high-pressure propulsive systems [13, 14].

Many researchers have recommended metals additives like Mg, Al, and Ti to mix with the boron particles which work as energy booster for favorable combustion of boron-based solid fuel/propellants. Since these particles are easily oxidized, sufficient amount of energy is transferred to the adjacent boron particles to melt the B_2O_3 coating and hence the boron combustion is accelerated [16]. Mixing of magnesium particles with boron is considered to be an effective combination due to its remarkably low melting temperature (650 °C) as well as its high thermal conductivity (156 W/mK) which improves the burning quality. In previous literatures, magnesium content is varied from 0 to 20% by weight, and both ignition temperature and ignition delay times are reduced as the Mg concentration increased [17]. This observation motivates as a solution to endorse boron combustion in SFDR applications, although energy level is slightly affected by using Mg with the boron particles. Thus, the benefits gained by the use of magnesium compensate the reduction of energy density by realizing optimum energy released through the boron–magnesium combination.

In rocket and missile applications, HTPB is a well-known energetic polymer which has been used in the present investigation. This polymer performs a role of a binder for the ingredients (B, Mg, and Ti). In addition to that, it also serves as a solid fuel in hybrid gas generator of SFDR systems. Hybrid gas generator is technically safe and simple, and it offers good control over pressure and mass flow rate of the burned gas [1]. HTPB comes under the category of non-melting fuel which is actually pyrolyzed on heating. Pyrolysis of HTPB has been studied since the 1960s and it is well understood. Numerous techniques have been investigated by various researchers to study the pyrolysis process of polymeric fuels like HTPB. Chiaverini et al. [18] investigated major pyrolysis products of HTPB by mass spectrometer where the temperature had been raised up to around 800 °C. The major species found under that investigation are ethene (C_2H_4), propene (C_3H_6), 1,3-butadiene (C_4H_6), 3-pentene-1-yne (C_5H_6), benzene (C_6H_6), toluene (C_7H_8), and 4-vinyl-cyclohexene (C_8H_{12}) with fluctuating molar concentration depending upon the local temperature assuming comparable heating environments as in a combustion chamber of a propulsive device. The molar concentration of C_4H_6 dominates among the pyrolyzed products of HTPB throughout the temperature range (up to 800 °C) [18]. These volatile fragments might have the carbon and hydrogen atoms in the range of $C_{16}H_{26}$ and higher as well [19]. All these cessation products of HTPB during the pyrolysis process are identified as toxic gases; therefore, protective masks are suggested at the test location throughout the inspection and cleaning of the system [20].

Inside the gas generator of SFDR, a diffusion flame via convection and turbulent diffusion is established on the fuel surface by the pyrolysis species and the oxidizer. This process produces heat to withstand further pyrolysis of the adjacent fuel surface, and regression of fuel takes place which results in species mass, momentum, and energy transfer to the flow region [21]. In that way, it can be conceived that energy generation is a function of heat transportation to the fuel surface through which regression rate is determined. Actually, regression rate is one of the important parameters which decides thrust production, range, and endurance of the propulsive devices.

Generally, a static motor system is used to evaluate the performance of solid fuel or propellants in terms of pressure or thrust-time profile, regression rate, etc. The results obtained from this system are somewhat co-related with the actual rockets by suitable scaling. Similar approach is used for SFDR as well. However, in the present investigation, an opposed flow burner system (OFBS) is used to evaluate B–Mg-HTPB and B–Ti-HTPB fuels where B–HTPB combination has been used as baseline (studied previously [22]). The OFBS is economical small screening device and quite useful for cases where costly nanoparticles are to be tested in the solid fuel composition. The concept of OFBS has been existed in literatures since the 1950s [23–28] and considered to be a suitable tool for screening as well as characterization of hybrid fuels which is analogous to a strand burner test [23, 29]. However, OFBS varies from cross-flow configurations on flame structure, pressure levels, and oxidizer mass fluxes.

The present paper reports an experimental investigation on the effect of Mg and Ti nanoparticles additives on the performance of nB–HTPB-based solid fuel using an OFBS. The OFBS is used to study the regression rate and combustion characteristics of boron-based solid fuels using gaseous oxygen (GOX) as the oxidizer which is impinged on the solid fuel pellet. This setup aids in clear visualization of burning behavior which is not possible with a confined SFDR. The main research objective focuses on the following studies: (i) effects of nMg and nTi on the burning of nB particles and hence the regression rate profile of the solid fuel formulations, (ii) visualization of burning agglomerates using high-speed camera, and (iii) completeness of boron particle combustion with the help of material characterization techniques conducted on the pre- and post-combustion product of the solid fuels.

2 Experimental Methods

2.1 Composition, Characterization, and Preparation of Solid Fuel Sample

Commercially available boron particles (advertised size: <1 µm), magnesium particles (advertised size: <12 nm), titanium particles (advertised size: <70 nm), and

HTPB were procured from Sigma Aldrich (product no. 15580), Nanoshel (Mg/stock no. NS6130-01-169 and Ti/stock no. NS6130-01-146), and Anabond Ltd., Chennai, India, respectively. The solid fuels examined in this investigation include pure HTPB, designated SF1; 90%HTPB/10%nB, designated SF2; 90%HTPB/10%nB with 5%nMg, designated SF3; 90%HTPB/10%nB with 10%nMg, designated SF4; 90%HTPB/10%nB with 5%nTi, designated SF5; and 90%HTPB/10%nB with 10%nTi, designated SF6, respectively. Loading of nMg and nTi particles is 5 and 10% of the total boron mass (10% of total sample weight) contained in the sample.

A Japanese-made (JSM-7610F) field emission scanning electron microscope (FE-SEM) was used to study the morphology of nB, nMg, and nTi particles and burned product of the samples. These feed particles and burned products were sputtered with gold plasma before placing into the FE-SEM in order to minimize the charging effect. X-ray diffraction (XRD) analyses were performed using a Pan analytic system (X'Pert[3] Powder) with Cu Kα ($\lambda = 1.5418$ Å) radiation to check the material crystallinity where angle (2θ) varied from 10 to 60° with a step size of 0.05° and a scanning rate of 5°/min. The active boron content in the as-received boron particles was determined from the thermogravimetric analysis (TGA) in air atmosphere using Pyris Diamond TG/DTA, PerkinElmer Instruments. An alumina (Al_2O_3) crucible of 10–15 mg capacity was used as a sample pan, and a constant air flow of 100 ml/min and a predetermined heating rate of 10 °C/min were used in the experiment to oxidize the sample in the temperature range of 30–1400 °C (approximately). An IKA C200 bomb calorimeter was used to determine the heating values (HV/CV) of the samples. For visualizing and capturing the ejection of particles/agglomerates from the pellet surface, a high-speed video camera (Model: Phantom V7.3) was used at a rate of 1000 fps with a resolution of 800×600 pixels and an image processing software (Image-Pro Plus) was used to study the agglomerates.

Some standard steps were followed in the processing of solid samples. A globe bag (N_2-filled) was used to protect the feed particles from oxidation while measuring and mixing with liquid HTPB. After proper hand mixing (10 min), curative IPDI is mixed (10% of HTPB by wt.) to the mixture and the mixture was stirred again for 10 min. The slurry was then poured into plastic bottles (Ø 12.6 mm) for getting cylindrical shape of the fuel pellets. Finally, bottles were carefully shifted to a vacuum oven to remove air pockets which were trapped inside during mixing/stirring. The oven was set at 60 °C, and at this temperature, the bottles were left for five days continuously for curing. Testing of pellets was not done until 25 days passed at atmospheric temperature after taking them out from oven. Figure 2b, c shows the representative photograph of solid pellet and a pellet loaded in pellet holder for combustion test.

(a) OFB system   **(b)** nB/HTPB sample   **(c)** OFB ignition
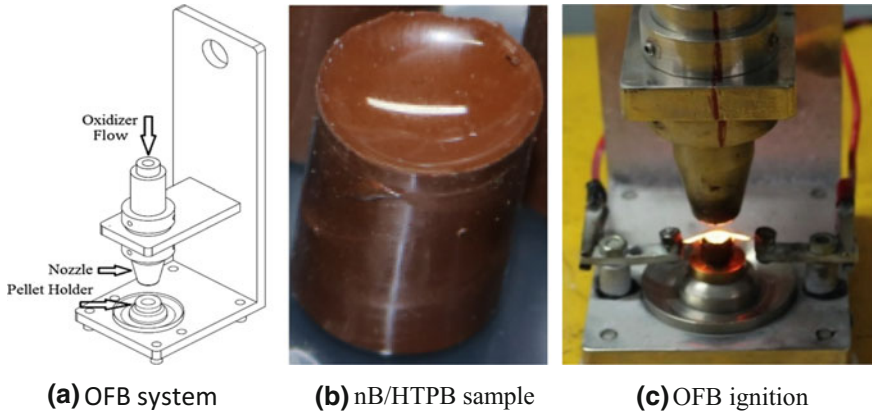
Fig. 2 Representation of design, solid fuel pellet, and real-time ignition [22]

2.2 OFBS Design and Experimental Procedures

Figure 2a shows a schematic representation of an opposed flow burner used in the present study. The major components of the system consist of nozzle ($\varnothing$ 7.5 mm, for oxygen supply), pellet holder, dish, and stand with a nozzle guide. Almost half of the pellet ($\varnothing$ 12.6 mm) length was pushed into the pellet holder, the exposed outer periphery except the top surface coated (thin film) with an inhibitor called silicone gel (Metroark 14 compound) to shield the fuel pellet from fire during the combustion, and the holder was placed at the center of the dish.

The distance between the nozzle exit and the top fuel surface was kept immovable at 10 mm in all the samples tested, tungsten wire ($\varnothing$ 0.25 mm) was connected to sample through a variac for its ignition, and a rotameter was positioned in the oxygen supply line to quantify its flow rate. The oxygen mass flux range in all the experiments varied from 20 to 57 kg/m^2 s where flux is the ratio of oxidizer mass flow rate through the nozzle to its exit cross-sectional area. An in-house LabVIEW program was used to control the oxygen flow and for initiating the ignition process. It was programmed in such a way that oxygen could be supplied first, and after one second, automatically the ignition process could be initiated. A trigger signal from LabVIEW program controls the closing and opening of the solenoid valve for supplying oxygen which runs the system in such a way that after the ignition sample was allowed to burn only for 5 s.

3 Results and Discussion

3.1 Characterization of Boron Particles and Calorific Evaluation of Fuels

Figure 3a, c, and e shows FE-SEM images of nano-boron (nB), nano-magnesium (nMg), and nano-titanium particles (nTi), respectively. All the images have been taken at 50,000 magnifications. The morphology shows that nB is amorphous having lots of fragments on the surface with low degree of crystallinity (size: 150–450 nm and below 1 µm), nMg is in the shape of flakes (thickness: 10–15 nm), and nTi is spherical in shape (size: $\varnothing$10–200 nm). Since no pre-processing of particles has been done before analysis, particles seem to be in agglomerated (or aggregated) and clustered form for nB and nTi cases.

Figure 3b, d, and f shows XRD pattern of the as-received nB, nMg, and nTi powders, respectively. The XRD spectrum of nB reveals that particles are poorly crystalline, since no sharp peak has been seen; however, nMg and nTi seem to have crystals. Since boron particles are keen to react with native oxygen: significant amount of crystalline boron oxide (B_2O_3) is formed while performing XRD; therefore, few B_2O_3 peaks of low intensity can be seen in the pattern; similarly, few MgO and TiO_2 are found in their respective XRD patterns. X'Pert HighScore Plus software has been used to analyze XRD peaks, major peaks of the pattern match with standard data of B (ICDD PDF# 00-011-0617), Mg (ICDD PDF# 98-064-2655), and Ti (ICDD PDF# 98-065-3275), respectively.

Figure 3g shows investigational calorific value results of samples (SF1–SF6). It is observed that maximum calorific value is attained by SF2, although, which is lower than their theoretical value due to the problems associated with boron combustion. Addition of nMg and nTi may improve the combustion inside the bomb, but due to their lower theoretical values than boron, the overall heating values are dropped for SF3–SF6 cases. There is a reduction of 1.3% for SF3 and 1.2% for SF5 as compared to SF2. Reduction in calorific values might be under the influence of degree of purity, particle size, and structure; therefore, these causes cannot be denied as well.

Figure 3h shows a TGA plot between weight gain and temperature. Since, on heating, impurities/moisture existing with particles are evaporated, the curve has dropped a little below 100% weight. The weight % is increased by the sample due to reaction with the oxygen, and eventually, the active content of boron has been estimated as 76.4% by accounting difference of weight gain % of the sample. This analysis indicates that particles are significantly protected by the oxide layer (B_2O_3).
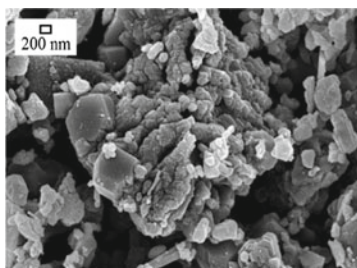
(a) FE-SEM Image (nB-particles) [22]
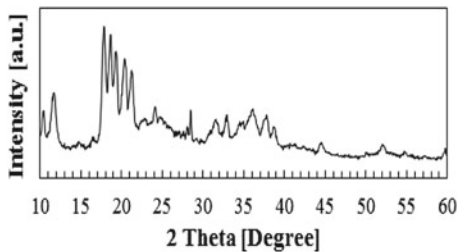
(b) XRD pattern (nB-particles)[22]
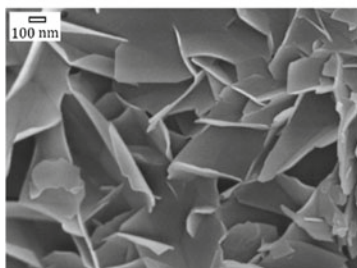
(c) FE-SEM Image (nMg-particles)
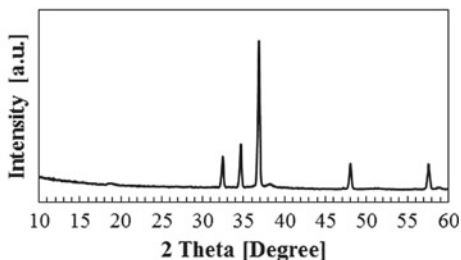
(d) XRD pattern (nMg-particles)
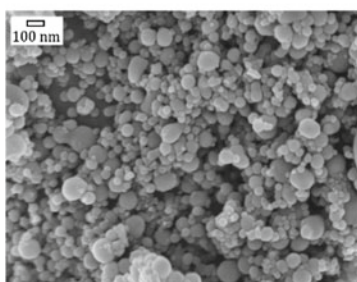
(e) FE-SEM Image (nTi-particles)
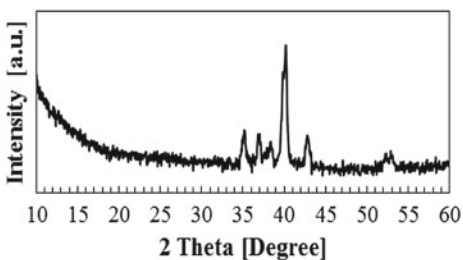
(f) XRD pattern (nTi-particles)
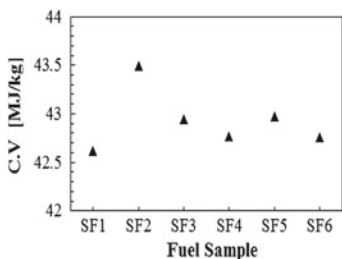
(g) Calorific value of samples
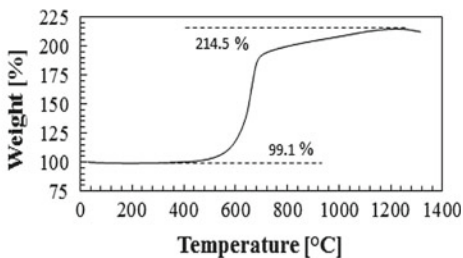
(h) TGA curve (nB-particles) [22]

Fig. 3 Material characterization of feed particles (**a–e**, **f**, **h**) and calorific evaluation of solid fuel samples (**g**)
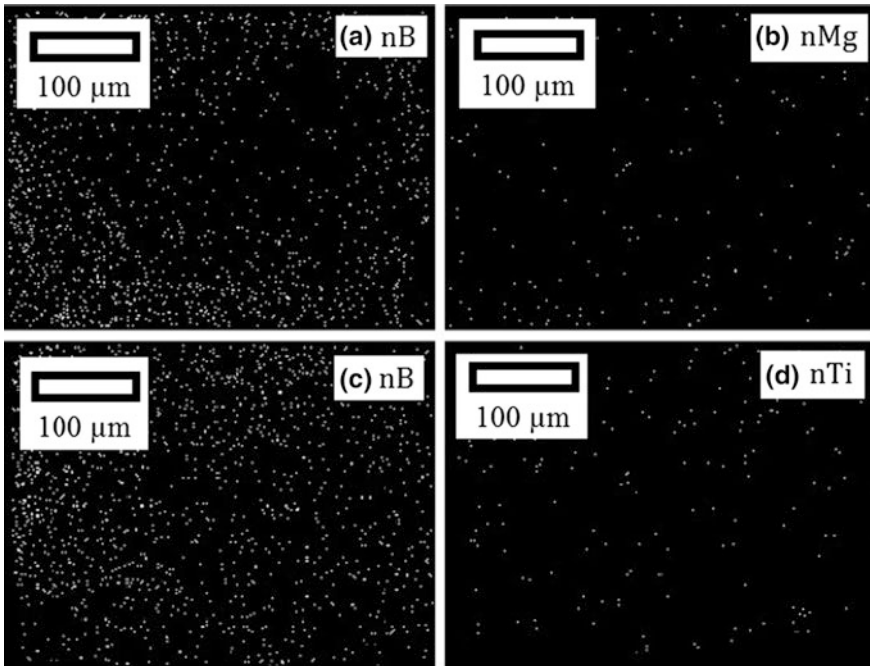
Fig. 4 EDS elemental map of unburned samples SF3 (**a**, **b**) and SF5 (**c**, **d**)

3.2 Sample Homogeneity of B–Mg- and B–Ti-Based Solid Fuel Combinations

Figure 4 shows mapping of cross section of SF3 and SF5 samples by using energy dispersion X-ray spectroscopy (EDS) which is used to check the homogeneity of particles in the sample. These EDS micrographs indicate uniform dispersion of B–Mg and B–Ti particles with the HTPB in SF3 and SF5 samples. It is expected that other samples will also follow the same particle dispersion pattern, since all samples are prepared by similar procedure.

3.3 Flame Visualization and Regression Rate Estimation

The instantaneous flame is visualized by a color camera during combustion (Fig. 5) for pure HTPB- and nB/HTPB-based samples. Bright white flame is observed for pure HTPB and green flame for all nB/HTPB-based fuels (SF2–SF6). The greenish appearance in the flame (SF2–SF6) corresponds to emission of intermediate species (BO_2), which confirms that boron particles participated in the combustion.

(a) SF1   **(b)** SF2 to SF6
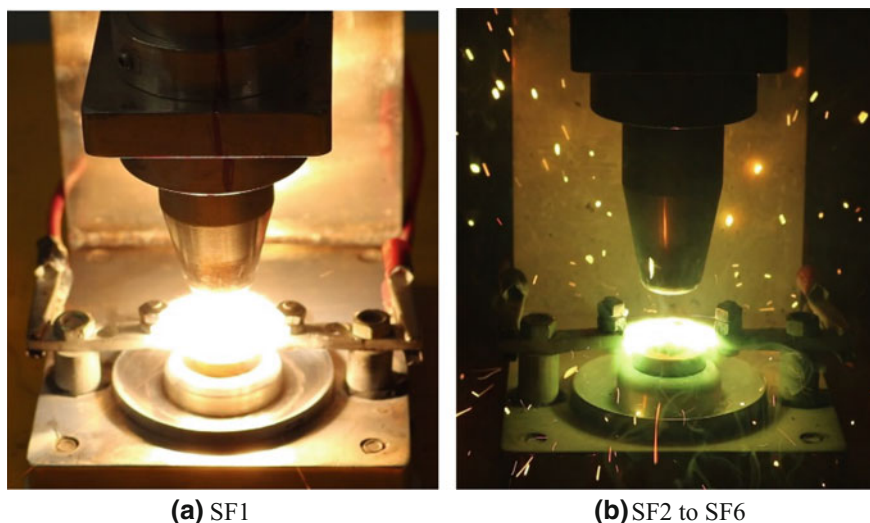
Fig. 5 Visualization of flame color for pure HTPB- and nB/HTPB-based solid fuel [22]

Regression rate trends for pure HTPB- and boron-based samples at several oxidizer fluxes with two different loading (5 and 10%) concentrations of nMg and nTi are shown in Fig. 6. At all fluxes, average regression rate of pure HTPB has higher values compared to any of boron-contained samples, but among boron-contained samples, the regression rate of SF2 has lower values. The drop of regression rate of boron-contained fuels than pure HTPB is caused due to the formation of protective layer of B_2O_3 coating on the surface of boron particles. Since B_2O_3 liquefies at around 450 °C which leads to removal of oxide coating and after that combustion of boron begins, higher temperature on the surface of boron is therefore always necessary for boron combustion. Addition of nMg and nTi to the nB/HTPB-based sample increases the regression rate, although nMg performs better than nTi combination due to the difference in melting and ignition temperatures. Magnesium ignites more quickly than boron, because it reacts with oxidizer quickly and produces sufficient amount of energy to the boron particles, and thus it aids in removal of B_2O_3 layer. Since magnesium reduces the ignition temperature of boron-based solid fuel but certain amount of magnesium is recommended, otherwise, magnesium would consume more amount of oxygen than boron which can increase the ignition delay time of the boron-based fuels [30]. The profiles of the regression rate show that as the concentration of nMg increases the regression rates also increase which is about 12.5% higher (for SF4) compared to SF2 at 57 G_{ox}. Although, for nTi case, the value of regression rate is dropped as the loading increases. However, it is observed that SF5 gives 7% higher regression rate than SF2. In combustor environment either for hybrid rocket or SFDR, heat feedback to the fuel surface is very high which enhances the pyrolysis process of HTPB [31]. The pyrolysis process is further improved by the impregnated metal additives to

HTPB. These metal particles release energy on combustion, and the process of convective and radiative heat transfer to the unburnt fuel is rapidly enhanced due to which regression rate is higher than the pure HTPB [32, 33]. Inclusion of nMg and nTi in the present investigation enhances ignition of the boron particles, which is reflected through regression rates (Fig. 6); however, these values will increase if it is tested in a confined/cross-flow system. Actually, in the cross-flow system, the burning surface is fragmented due to cracks and voids formed on it, because density of these metals has decreased on melting. In this way, burning surface breaks up and produces small clumps of metalized fuel which are readily entrained into the gas flow, and eventually, regression rate of the cross-flow system is enhanced [34]. These types of surface cracks have not been found in the present investigation, due to which there is no significant increase in regression for OFBS cases as compared to cross-flow system.

The other important cause which is responsible for drop of regression rate of the boron-based samples is the phenomenon of ejection of burning agglomerates from

Fig. 6 Regression rate profile for various boron-based solid fuel samples
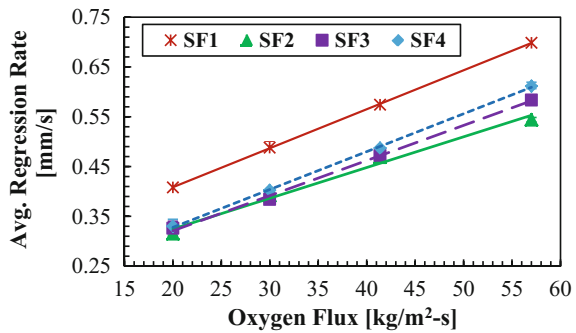
(a) Pure HTPB and nB-nMg-HTPB
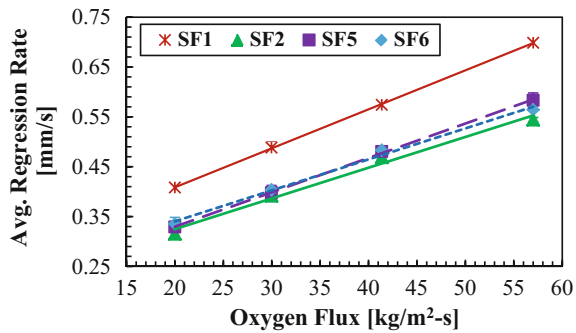
(b) Pure HTPB and nB-nTi-HTPB

the burning surface. Ejection of agglomerates from the burning surface has minimized the release of energy due to inadequate combustion of boron particles on the burning surface. The burning particles/agglomerates release energy throughout their movement, but most of these are far-off from the burning surface or the diffusion flame zone. Therefore, favorable temperature for active boron combustion is not accomplished on the burning surface. Because of this issue, sufficient amount of boron particles could not burn efficiently on the burning surface and it is ultimately reflected through lower regression rate [35]. Though the degree of crystallinity is low in the boron particles, even then it affects the burning as well as regression rate of the fuel samples. Based on the present discussions, regression rate of an OFBS cannot be directly linked with an SFDR. Opposed flow burner is a screening instrument for characterizing the solid fuel at low cost before choosing that fuel for testing in a laboratory-scale/full-scale SFDR systems. It is expected that the lower values of regression rate for boron-based fuel obtained in OFBS would be significantly enhanced in an SFDR system experimentally.

The velocity of the burning agglomerates which move with a flame covering of circular or elliptical profile has been evaluated. The agglomerates expel far away from the burning surface in a chaotic manner. The average velocity of burning agglomerates for all loading concentrations (SF2–SF6) has been found around 6 m/s. It has been noticed that the ejection velocity is not much influenced by loading concentration and oxygen flux. Extensive investigation of burning agglomerates is beyond the scope of the present study.

3.4 Characterization of Condensed Combustion Products

Burned-out residues (condensed combustion products, CCP) of SF2, SF4, and SF6 (at 30 G_{ox}) were examined by FE-SEM as shown in Fig. 7a–c, and it is observed that CCP have various structures like squama and protonema. These structures of reaction products might be formed by the melted B_2O_3. Figure 7d shows the XRD patterns of CCP, investigation of intense XRD peaks (around: $2\theta = 14.5°$ and $28.2°$) shows crystal structure of boric acid (H_3BO_3) which is traced in all the three samples, and along with this, MgO and TiO_2 peaks are also available in SF4 and SF6 residues. Occurrence of H_3BO_3 actually represents B_2O_3 in the sample. Since, during combustion, B_2O_3 is formed which reacts with water vapor (native moisture) and forms H_3BO_3 in the sample [36]. XRD peaks (around: $2\theta = 14.5°$ and $28.2°$) match with the standard data (ICDD PDF# 00-030-0620) which correspond to H_3BO_3.

(a) SF2 [22]

(b) SF4

(c) SF6

(d) XRD pattern
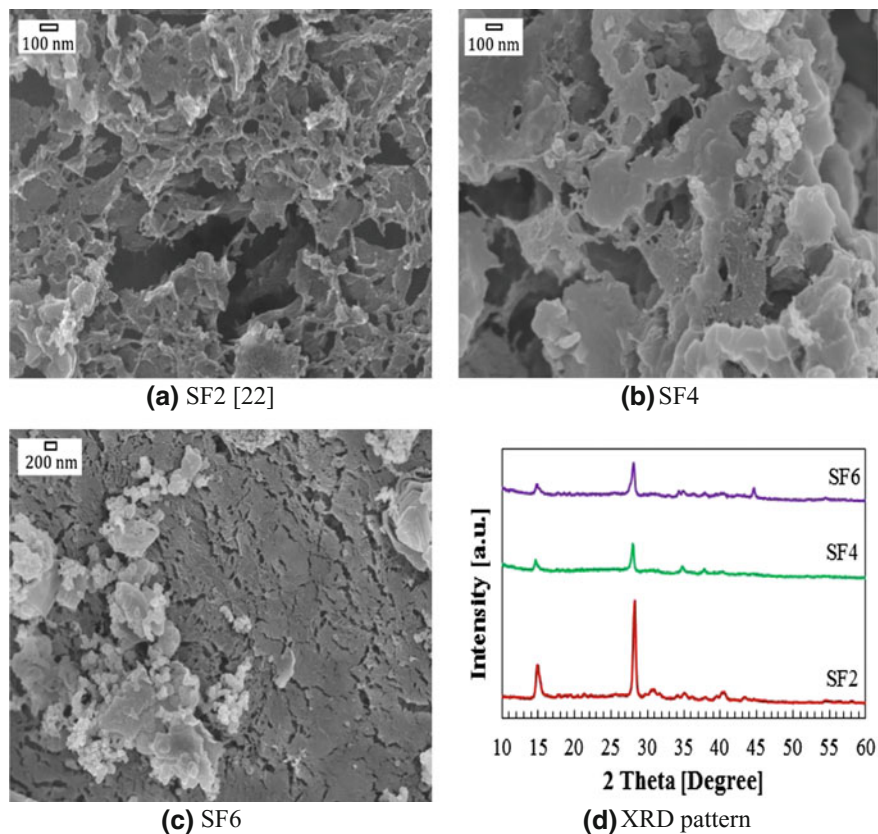
Fig. 7 Characterization of condensed combustion products at 30 G_{ox}

4 Conclusions

The study presented here reveals the effect of magnesium as well as titanium on the burning characteristics of nB-HTPB-based solid fuel by a small OFBS. Addition of nano magnesium or nano titanium influences the combustion mechanism which is reflected through the regression rate. Regression rate for magnesium case is better than the titanium loading to the nB/HTPB mixture. It is found that 10% loading of nMg gives 12.5% increment in regression rate, but for titanium case as the concentration increases regression rate reduces. Addition of magnesium or titanium reduces the calorific values due to lower energy content in both magnesium and titanium particles than boron. Visualization of particles through high-speed videography shows that as particle loading increases, the agglomerate count increases; however, average ejection velocity is nearly identical irrespective of B/Mg/Ti loading in the sample. In the CCPs, elemental B, Mg, or Ti are not identified,

although their compounds exist but boric acid dominates in all the samples (SF2, SF4, and SF6) studied here.

It is concluded that magnesium or titanium is beneficial to nB/HTPB mixture if the ratio between B–Mg and B–Ti is in appropriate quantity. The result obtained in the present opposed flow burner system cannot be compared directly with a laboratory-scale/full-scale hybrid gas generator of an SFDR system, because there is a disparity on their aerothermal environments; nevertheless, these results can be employed as strategies for choice of new solid fuels.

References

1. Komornik, D., Gany, A.: Study of a hybrid gas generator for a ducted rocket. Combust. Explos. Shock Waves **53**(3), 293–297 (2017)
2. Leingang, J.L., Petters, D.P.: Ducted rockets. In: Jensen, G.E., Netzer, D.W. (eds.) Progress in Astronautic and Aeronautic, Tactical Missile Propulsion, vol. 170, pp. 447–468 (1996)
3. Miyayama, T., Oshima, H., Toshiyuki, S., Odawara, T., Tanabe, M., Kuwahara, T.: Improving combustion of boron particles in secondary combustor of ducted rockets. In: 42nd AIAA/ASME/SAE/ASEE Joint Propulsion Conference and Exhibit, California, USA (2006)
4. Yeh, C.L., Kuo, K.K.: Ignition and combustion of boron particles. Prog. Energy Combust. Sci. **22**(6), 511–541 (1996)
5. Macek, A., Sample, J.M.: Combustion of boron particles at atmospheric pressure. Combust. Sci. Technol. **1**(3), 181–191 (1969)
6. King, M.K.: Ignition and combustion of boron particles and clouds. J. Spacecr. Rockets **19**(4), 294–306 (1982)
7. Fink, L.E.: Chronological History of SFRJ Flight Tests. Engineering Technology Boeing Aerospace Company (1981)
8. Natan, B., Gany, A.: Combustion characteristics of a boron fueled solid fuel ramjet with aft-burner. J. Propul. Power **9**(5), 694–701 (1993)
9. Balas, S., Natan, B.: Boron oxide condensation in a hydrocarbon-boron gel fuel ramjet. J. Propul. Power **32**(4), 967–974 (2016)
10. Young, G., Roberts, C.W., Stoltz, C.A.: Ignition and combustion enhancement of boron with polytetrafluoroethylene. J. Propul. Power **31**(1), 386–392 (2015)
11. Kuo, K.K., Risha, G.A., Evans, B.J., Boyer, E.: Potential usage of energetic nano-sized powders for combustion and rocket propulsion. In: Proceeding of Materials Research Society, vol. 800 (2003)
12. Young, G., Sullivan, K., Zachariah, M.R., Yu, K.: Combustion characteristics of boron nanoparticles. Combust. Flame **156**(2), 322–333 (2009)
13. Korchagin, M.A., Grigor'eva, T.F., Bokhonov. B.B., Sharafutdinov, M.R., Barinova, A.P., Lyakhov, N.Z.: Solid-state combustion in mechanically activated SHS systems. I: Effect of activation time on process parameters and combustion product composition. Combust. Explos. Shock Waves **39**(1), 43–50 (2003)
14. Rogachev, A.S., Mukasyan, A.S.: Combustion of heterogeneous nanostructural systems. Combust. Explos. Shock Waves **46**(3), 243–266 (2010)

15. Hashim, S.A., Lahariya, M., Karmakar, S., Roy, A.: Calculation of theoretical performance of boron-based composite solid propellant for the future applications. In: 2nd Innovative Design and Development Practices in Aerospace and Automotive Engineering Conference (International), Springer, New Delhi, pp. 327–335 (2016)
16. Weismiller, M.R., Huba, Z.J., Tuttle, S.G., Epshteyn, A., Fisher, B.T.: Combustion characteristics of high energy Ti–Al–B nanopowders in a decane spray flame. Combust. Flame **176**, 361–369 (2017)
17. Zolotko, A.N., Matsko, A.M., Polishchuk, D.I., Buinovskii, S.N., Gaponenko, L.A.: Ignition of a two-component gas suspension of metal particles. Combust. Explos. Shock Waves **16**(1), 20–23 (1980)
18. Chiaverini, M.J., Harting, G.C., Lu, Y.C., Kuo, K.K., Peretz, A., Jones, H.S., Wygle, B.S., Arves, J.P.: Pyrolysis behavior of hybrid-rocket solid fuels under rapid heating conditions. J. Propul. Power **15**(6), 888–895 (1999)
19. Radhakrishnan, T.S., Rama Rao, M.: Thermal decomposition of polybutadienes by pyrolysis gas chromatography. J. Polym. Sci. Polym. Chem. **19**(12), 3197–3208 (1981)
20. Beck, W.H.: Pyrolysis studies of polymeric materials used as binders in composite propellants: A review. Combust. Flame **70**(2), 171–190 (1987)
21. Sun, X., Tian, H., Li, Y., Yu, N., Cai, G.: Regression rate behaviors of HTPB-based propellant combinations for hybrid rocket motor. Acta Astronaut. **119**, 137–146 (2016)
22. Hashim, S.A., Kangle, S., Karmakar, S., Roy, A.: Combustion characteristics of boron-HTPB based solid fuels for hybrid rocket applications. In: 7th Theoretical, Applied, Computational and Experimental Mechanics Conference (International), Chennai, India (2017)
23. Schlichting, H., Gersten, K.: Boundary-layer theory, 9th edn. Springer, Germany (2017)
24. T'ien, J.S., Singhal, S.N., Harrold, D.P., Prahl, J.M.: Combustion and extinction in the stagnation-point boundary layer of a condensed fuel. Combust. Flame **33**, 55–68 (1978)
25. Krishnamurthy, L., Williams, F.A.: A flame sheet in the stagnation-point boundary layer of a condensed fuel. Acta Astronaut. **1**, 711–736 (1974)
26. Nakoryakov, V.E., Pokusaev, B.G., Troyan, E.N.: Impingement of an axisymmetric liquid jet on a barrier. Int. J. Heat Mass Transf. **21**(9), 1175–1184 (1978)
27. Glauert, M.B.: The wall jet. J. Fluid Mech. **1**(6), 625–643 (1956)
28. Watson, E.J.: The radial spread of a liquid jet over a horizontal plane. J. Fluid Mech. **20**(3), 481–499 (1964)
29. Shark, S.C., Zaseck, C.R., Pourpoint, T.L., Son, S.F.: Solid-fuel regression rates and flame characteristics in an opposed flow burner. J. Propul. Power **30**(6), 1675–1682 (2014)
30. Liu, J.Z., Xi, J.F., Yang, W.J., Hu, Y.R., Zhang, Y.W., Wang, Y., Zhou, J.H.: Effect of magnesium on the burning characteristics of boron particles. Acta Astronaut. **96**, 89–96 (2014)
31. Chaturvedi, S., Dave, P.N.: Solid propellants: AP/HTPB composite propellants. Arab. J. Chem., 1–8 (2015)
32. Beckstead, M.W.: A summary of aluminum combustion. Paper Presented at the RTO/VKI Special Course on Internal Aerodynamics in Solid Rocket Propulsion, vol. 32, no. 6, pp. 2107–2114 (2002)
33. King, M.K.: Aluminum combustion in a solid rocket motor environment. Proc. Combust. Inst. **32**(2), 2107–2114 (2009)
34. Sandall, E., Kalman, J., Quigley, J.N., Munro, S., Hedman, T.D.: A study of solid ramjet fuel containing boron–magnesium mixtures. Propuls. Power Res. **6**(4), 243–252 (2017)
35. Hashim, S.A., Karmakar, S., Roy, A., Srivastava, S.K.: Regression rates and burning characteristics of boron-loaded paraffin-wax solid fuels in ducted rocket applications. Combust. Flame **191**, 287–297 (2018)
36. Liu, D., Xia, Z., Huang, L., Hu, J.: Boron particle combustion in solid rocket ramjet. J. Aerosp. Eng. **28**(4), 04014112 (2015)

Experimental Investigation of Wear and Hardness Test Over AA2219 with Reinforcement of Tungsten Carbide

R. Rohith Renish, M. Arun Pranesh, K. Karthik and Vasavi Vanarasi

1 Introduction

The innovative materials provide unlimited prospects for modern material science and for their development. The specific characteristics of MMCs which can be used in the process of design of material like custom made dependent based on its application [1–3]. Due to the potential property exhibited by the composites of metal matrix which helps us to achieve the desired conceptions of the designer. This type of material group becomes more interesting to conduct the experiment for constructional and functional property of the materials, if the conventional materials characteristics do not reach the increased standards of their specific demands, or give the solution for the problem [4–6]. Though the present material technologies available in the MMCs are been compared with other modern material technologies like powder metallurgy. Hence, the advantages produced by these composite materials can be analysed only when there is a relationship between reasonable cost-performance and the component production of that particular material [7]. The usage of a composite material is mandatory if its special property can only be attained by application of these materials.

R. Rohith Renish · K. Karthik · V. Vanarasi
Department of Mechanical Engineering, Vel Tech Rangarajan
Dr. Sagunthala R&D Institute of Science and Technology, Chennai 600040, India

M. Arun Pranesh (✉)
Department of Mechanical Engineering, Kathir College of Engineering,
Coimbatore 641062, India
e-mail: mspranesh@gmail.com

159

2 Materials and Methodology

This method of stir casting can be initiated by placing an empty crucible in the muffle. At initial, the temperature is set to 500 °C in order to get heated up, and then, it is gradually increased up to 900 °C. In the process of stir casting, the matrix material used is Aluminium alloy AA2219. To remove the dust particles present in the Aluminium alloy, it is cleaned, then weighed and poured into the crucible for melting [8, 9]. Thus, the nitrogen gas is used to create an inert atmosphere during the melting process. Particles of WC (tungsten carbide) are used as reinforcement; 2% by weight of pure WC powder is used as wetting agent. The molten composite of 750 g can be processed at a single stage of the crucible. Therefore, the reinforcement tungsten carbide powder of required quantity is weighed on the weighing machine. Reinforcements are heated for half hour and at temperature of 500 °C. When the entire matrix reaches its molten state, stirring of the matrix is started. The speed controller is used to control the rpm of Stirrer. Therefore, the speed is increased from 0 to 300 rpm. But the temperature of heater is kept at 630 °C which is below the melting point of the matrix temperature. At a particular stage, a uniform semisolid molten matrix is obtained due to the continuous stirring of matrix at 630 °C. This semisolid preheated matrix is poured into the crucible enhances the weldability of the reinforcement and reduces the settling of the particle in the bottom [10]. The conical hopper is used to pour the reinforcements, and the rate of flow is measured as 0.5 g/s. Dispersion time taken by the matrix is noted as 5 min. After a continuous stirring, the resulted semisolid-stage slurry is again reheated at a temperature 900 °C to obtain a liquid state of the slurry. Then, the RPM of the Stirrer is then gradually decreased to zero. This experimental set-up of stir casting is then kept aside, and the composite of molten slurry is then poured into the metallic mould which is preheated at 500 °C. The slurry is used in molten state in this entire process. The slurry is poured uniformly into mould in order to avoid trapping of gas. It is reduced by air to reduce the particle settling time in the matrix.

3 Result and Discussion

3.1 Hardness

Hardness is defined as one of the essential properties of a material that supports it to resist from plastic deformation, penetration, indentation, and scratching. Here, in this test, indentation hardness is measured by making use of Brinell hardness method. Thus, from Fig. 1a, the hardness of different percentages of reinforcement in the composite materials, it is observed that the presence of higher amount of tungsten carbide particles in the material resulted in higher indentation value. This is due to the fact that tungsten carbide has high scratch resistance. It is also seen that increase in the percentage of reinforcement increased the hardness until 6%.
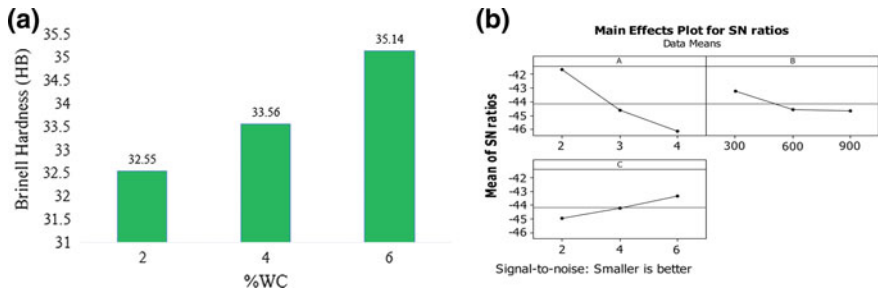
Fig. 1 a Hardness graph, b main effects plot for means

Table 1 Tabulation for hardness

S. No.	Specimen	Load-P (kgf)	Dia of steel ball (D) (mm)	Dia of indentation (mm)	Brinell hardness number (BHN)
1	2% WC	250	5	2.65	32.55
2	4% WC	250	5	2.6	33.56
3	6% WC	250	5	2.4	35.14

Beyond that when the reinforcement is added dispersion is occurred due to agglomeration of the reinforcement. This can reduce the scratch resistance, but beyond a range of 6% of tungsten carbide the hardness value may drop gradually. However, this property is yet to be experimentally verified (Table 1).

3.2 Wear Test

The factors which are required to conduct the experiments are identified as load, speed and % of WC—here three level and three factors. The specimen for hardness and wear tests was prepared, and they were tested in a testing machine. The results of the properties for different compositions of sample are obtained from the wear testing machine.

From the preceding literatures, it has been observed that Taguchi's quality concept is a well-known procedure for optimizing the wear of the material. The tentative values are taken for investigation. Taguchi's method is based on orthogonal array experiments that give much compact variance of the testing values with optimum settings. For analysis, a statistical software Minitab 16 is used for getting the result like mean graphs with corresponding responses. These responses are then used for choosing the influenced parameters. The L9 orthogonal array issued only for understanding the effects of mixed level factor.

Table 2 SN ratio table

Load (kg)	Speed (rpm)	% WC	Wear (μm)	SN values
2	300	2	132	−42.41
2	600	4	121	−41.65
2	900	6	112	−40.98
3	300	2	147	−43.34
3	600	4	179	−45.05
3	900	6	188	−45.48
4	300	2	157	−43.91
4	600	4	224	−47.00
4	900	6	239	−47.56

Figure 1b shows the main effects plot. In the figure mentioned the signal-to-noise ratio was chosen to be smaller is said to be better which means the wear rate of the AA2219–WC composites is to be as minimum as possible so that the wear resistance will be greater. Also, the following plot was made between the mean of the SN ratios and the considered factors like load, speed and percentage of reinforcement. It could be inferred that if the means drop along with the *X*-axis the objective is achieved in least and if *X*-axis raises the objective is satisfied. Percentage of tungsten carbide is contributing more towards the wear resistance of the MMC which is observed from the figure (Table 2).

3.3 Characterization

The samples manufactured by the process of stir casting and it is used for testing the wear properties are then characterized by Energy Dispersive Spectroscopy (EDX) and Scanning Electron Microscopy (SEM). The results of EDX analysis can be used for the chemical characterization of AA2219–WC metal matrix composites based on the constituents present in it. Figure 2 shows EDX analysis graph for AA2219–6% of WC sample. Generally, aluminium alloy AA2219 consists of aluminium as a major element followed by copper. Other alloying elements constitute meagre composition. As the alloy is reinforced with tungsten carbide, Fig. 2 peak showing carbon is higher and constitutes 15.5% of weight overall. Copper constitutes 3.88% of weight which is the inherent alloying element of the base metal. Due to the nature of manufacturing process, formation of oxide also happens to be a part of the final composition (Table 3).

Fig. 2 EDX spectroscopy of AA2219–6% WC composite
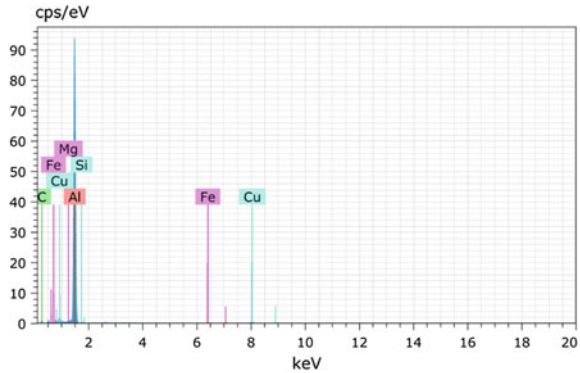
Table 3 EDX analysis of elements AA2219–6% WC composite

Element	Norm C (wt%)	Atom C (at.%)
Al	74	61.60
C	15	28.99
O	5.03	7.06
Cu	3.88	1.37
Fe	0.69	0.28
Si	0.33	0.26
Mg	0.31	0.29
Cl	0.19	0.12
K	0.07	0.04

3.4 Characterization by SEM

Scanning electron microscopic images are taken for the wear test samples in order to study the profile nature of the wear tracks. The images are taken by exposing the worn-out surfaces of each sample to electron beam, and the inferences were drawn.

SEM micrograph of 2% WC composite sample is shown in Fig. 3a. Wear tracks clearly show less wear resistance towards the counter-facing disc due to presence of more amounts of softer aluminium and less amount of harder carbide particles. It can also be seen that the mechanism of wear is abrasive wear as the tracks tend to break in the middle as loose fragments. Formation of these broken and loose fragments was due to poor surface bonding and less interaction between the base metal and reinforcement. Cavities and large grooves were also a part of the worn surface with irregular profile indicating non-uniformly distributed bonding between the matrix and reinforcement. Delamination was less predominant in carbide particles which can be observed from the micrograph.

Similarly, from the SEM micrograph of the 4% WC composites shown in Fig. 3b, the depth of wear tracks was shallow due to presence of hard carbide particles. Interaction between the matrix and reinforcement improved and so the
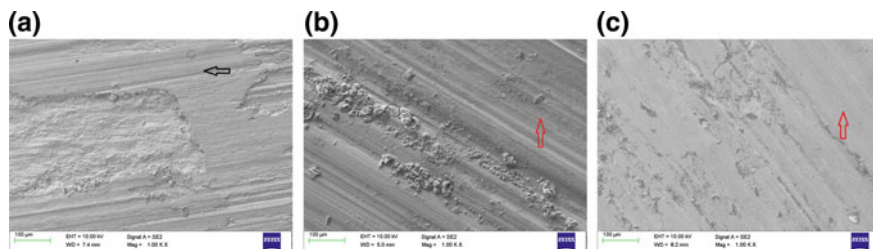
Fig. 3 **a** SEM micrograph of AA2219–2% WC composite, **b** SEM micrograph of AA2219–4% WC composite, **c** SEM micrograph of AA2219–6% WC composite

flakes formation could be seen along the wear direction but the loose fragments were found to be lesser. Carbide particles tend to resist the scratch induced by counter-facing disc but due to insufficient harder particles flake formation occurs. Uniformly dispersed tungsten carbide particles amongst the matrix could also be observed from the micrograph. No evidence of cavities and large grooves were observed.

Figure 3c shows the SEM micrograph of 6% WC composites. Due to presence of higher amount of carbide particles, wear rate was very low which is evident from the track width. Grooves, broken and loose fragments could not be seen in any part of the image. This is due to good surface bonding and interaction between matrix and reinforcement. Tracks were discontinuous as the hard counter-facing disc could not be able to scratch the composite fully. Lower amount flakes could be seen, and the dispersion of reinforcement is uniform along the matrix.

From the SEM micrographs, it could be seen that when the presence of carbide particles increases the wear resistance of the composite increases and the surface abnormalities due to sliding wear decreases. As studied from the literatures when 8% of tungsten carbide reinforced with AA2219, no appreciable change in wear behaviour could be observed which is yet to be confirmed physically.

4   Conclusion

Composite of AA2219 reinforced with WC was manufactured successfully by using aluminium stir casting machine. Hardness test was conducted successfully using Brinell Hardness machine and obtained hardness was high for 6% of WC. Taguchi L9 array was followed to design the experiment, and the optimized wear rate is 150 μm; ANOVA analysis was used to optimize the statistical data obtained for wear test. The actual wear rate was 140 μm. There is no third composition formation during stir casting process which was proved by EDX analysis, and the wear rate was found to be very less on AA2219 with 6% of tungsten carbide, when analysed using SEM.

References

1. Kala, H., Mer, K.K.S., Kumar, S.: A review on mechanical and tribological behaviors of stir cast aluminum matrix composites. J. Mater. Process. Charact. **200**, 373–384 (2014)
2. P, Srinivasa Rao, Sivadasan, K.G., Balasubramanian, P.K.: Structure-property correlation on AA 2219 aluminum alloy weldments. Bull. Mater. Sci. **19**, 549–557 (2008)
3. Mathan Kumar, N., Senthil Kumaran, S., Kumaraswamidhas, L.A.: Wear behaviour of Al 2618 alloy reinforced with Si_3N_4, AlN and ZrB_2 in situ composites at elevated temperatures. J. Mater. Process. Technol. **208**(1–3), 532–541 (2008)
4. Saravanan, S.D., Senthil Kumar, M.: Effect of mechanical properties on rice husk ash reinforced aluminum alloy (AlSi10Mg) matrix composites. Int. Conf. Des. Manuf. **206**(1–3), 167–179 (2013)
5. Padmavathi, K.R., He, C.: Tribological behaviour of aluminium hybrid metal matrix composite. Int. Conf. Des. Manuf. **97**, 660–667 (2014)
6. Ahmed, I., Renish, R.R., Karthik, K., Karthik, M.: Experimental investigation of polymer matrix composite for heat distortion temperature test. Int. J. Mech. Eng. Technol. **08**(8), 520–528 (2017)
7. Rahmana, H., Al Rashed, H.M.M.: Characterization of silicon carbide reinforced aluminium matrix composites. Int. Conf. Mech. Eng. **90**, 103–109 (2014)
8. Sharma, P., Sharma, S., Khanduja, D.: A study on microstructure of aluminium matrix composites. Int. Conf. Des. Manuf. **19**(2), 209–220 (2012)
9. Surekha, K., Murty, B.S., Rao, K.P.: Microstructure and pitting corrosion of friction stir welded joints in 2219-O aluminium alloy thick plate. Corros. Sci. **202**, 4057–4068 (2008)
10. Sharma, P., Khanduja, D, Sharma, S.: Dry sliding wear investigation of Al6082/Gr metal matrix composites by response surface methodology. J. Mater. Res. Technol. **209**, 3278–3489 (2009)

Pedagogical Evaluation of Mechanical Engineering Education Using Additive Manufacturing

Saurabh Srivastava and Sarang Pande

1 Introduction

Additive manufacturing (AM) is a novel technique which implies the addition of material layer by layer such that there is no waste of raw material, and complex geometries can be made easily. AM uses different materials such as polymers, metals, alloys and ceramics for making patterns, models and prototypes within time and which can be used for various purposes. AM is gaining importance day by day as lots of new industries are using this technology for various works related to AM. With the use of AM, various products related to aerospace like sophisticated parts are produced which can be used for various types of applications.

Additive manufacturing in today's time is considered to be one of the powerful techniques or the tool with the help of which various complex objects can be built easily. Various types of complex models are made and applied into various forms. AM includes the process of creating a CAD model and converting the CAD models into STL file format, and then, that STL file is used for creating the solid prototype. Various materials like ABS and PLA as well as alloys are being used for producing the prototypes. AM is classified according to the processes and the state of the raw material used. First classification is solid based in which material used is in solid form. Second classification is liquid based as liquid in the form of resins is used. Third form is the powdered form in which powder is used for AM.

Additive manufacturing is used in various fields such as aerospace, automobile, biomedical and jewellery manufacturing. In medical implants like hip replacement, plastic surgery and tissue engineering, AM plays a big role as the study as well as the actual models has nonlinear geometry which can only be made by the help of AM, and it can be used for various types of transplants and medical surgery.

S. Srivastava (✉) · S. Pande
Mechanical Engineering Department, Marwadi Education Foundation Group of Institutions, Rajkot, India
e-mail: saurabh159a@gmail.com

In jewellery application also, AM is used for making patterns for the jewels. Complex geometries can be manufactured easily, and varieties of jewels are being made for the people to use it for wearing. AM is also used in shoemaking industries as for the shoe soles and also for making toys for the kids.

2 Scenario of Additive Manufacturing in Engineering Education

Engineering education is one of the types of education where engineers are made through different studies and subjects, and the in-depth knowledge helps the engineers to solve all engineering problems. Various types of engineering areas are there such as mechanical engineering, electrical and electronics, computer science and information technology, and civil engineering which provide a platform for the people to use their knowledge for the upliftment of society.

Engineering education includes the basic tools of Bloom's taxonomy which has different parameters such as remembering, understanding, application, evaluate and create with the help of which the education of mechanical engineering subject can be carried out in a proper manner and students can not only learn the subject in a best possible way but also apply their knowledge in a better manner.

The work done by various people in this field is by experimenting the class for a subject with and without the use of AM [1]; the technological challenges truly overcome in making 3D printing truly available [2]; project-oriented teaching and learning using AM [3]; creating learning environment using engineering design and 3D printing [4]; digital 3D printing used in teaching education [5]; and 3D technologies in design education [6].

3 Additive Manufacturing in Mechanical Engineering Education

Additive manufacturing proves to be one of the major tools in providing a good knowledge of mechanical engineering by helping the students to learn about various aspects of the mechanical engineering in an easy and proper manner. Various aspects of mechanical engineering include the knowledge of various types of mechanisms which are the part of kinematics of machines and dynamics of machines such as inversions of mechanism and various other things like gear and cam mechanisms for which the models and prototypes are made by using AM technology as well as it will be beneficial for the teachers to understand the subject in a better way.

Various models of gears which were made by the use of AM technology helps teachers to teach the students each and every aspect of the topic in a correct manner.

Apart from mechanisms, various other things like the study and utilisation of materials and their properties as well as all the measurement and calibrations of different aspects can easily be learned by application and understanding of the models and prototypes made from AM process.

4 Additive Manufacturing Case Study

Product development is one of the main areas where AM plays an important role as new products are being developed and can be used according to the needs of the customers.

Regarding the use of AM in new product development, project is being carried out for making new design and AM of paper punching machine which is being used by various users in various fields like officers and students and academicians for documentation purpose. The first step is to prepare a CAD model for the new design through calculations, and then, with the help of proper dimension of each and every aspect of the punch, new model is created in Creo software which is being physically made by printing it in 3D printer. The material which is being used for the modelling in AM is ABS which will provide a good solution for the new design concept (Fig. 1).

A new design is made which is of low weight and high accuracy. Model is fabricated with the help of AM (fused deposition modelling technique). Through this project students have learnet the concepts of AM in a right manner. Thus, purpose of outcome based learning is achieved.

New design of paper punching machine helps the student to innovate something on their own by following the product development process (Fig. 2).
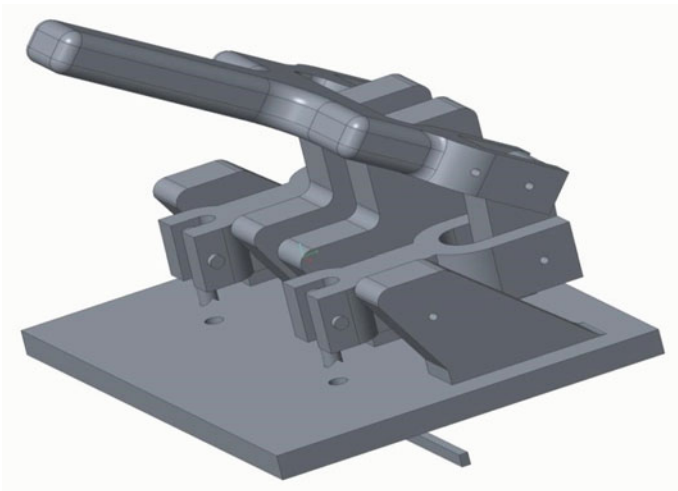
Fig. 1 CAD model of punching machine made by students
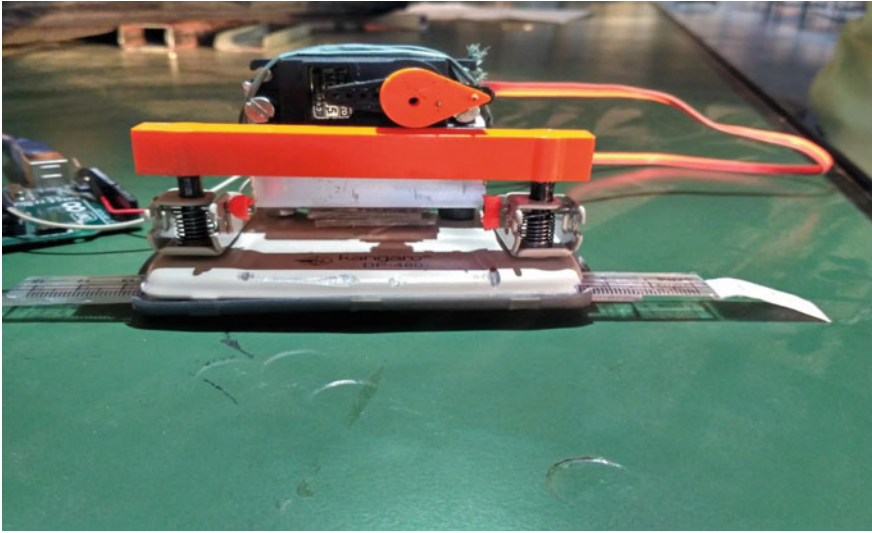
Fig. 2 Additive manufactured model of paper punching machine

5 Comparison of Parameters

Engineering education in modern days requires continuous development in didactics, pedagogical and used practical methods, which include project-based learning so as to satisfy outcome-based education. Various parameters are used like project management where if a group of students work for a task, then they understand how to complete and manage all the activities. Time management relates to how the activities are carried out in proper schedule according to the correct time allotted. Then, working in a group realises the students about how to work as a team; for proper working, proper communication is needed which needs self-confidence, and according to that, there should be flexibility and adaptability of new methods to be adapted; and for a task to be done, the work should be reliable to be processed, product development is done, and the work should be innovative in nature. English is used as a language for communication and presentation.

Example: An experiment was done for 30 students in the subject of Design of Machine Element; for 30 students, project-based learning method is done, rubrics are set for each stage, and accordingly, students are being graded (Fig. 3).

This observation of different parameters is without the use of AM in which marks are given in hit and trial manner and according to that analysis is done such that what are the levels of students according to the different parameters and defines the needs of AM to increase the levels.

After the application of AM technology, the effectiveness of knowledge and other various parameters is measured and it got increased which is shown in the statistical analysis with respect to different parameters. The average rate of creativity and knowledge of the students got increased, and a comparison is done for the application of AM in engineering education (Figs. 4 and 5).

FACTORS	MARKS
PROJECT MANAGEMENT	1.2
TIME MANAGEMENT	0
TEAM WORK	1.1
COMMUNICATION	1.3
SELF CONFIDENCE	1.1
FLEXIBILITY AND ADAPTABILITY	1
ENGAGEMENT RELIABILITY	1.5
PROCESS DEVELOPMENT AND DESIGN	0
PRODUCT DEVELOPMENT AND DESIGN	1.1
ENGLISH LANGUAGE	1.5
SUSTAINABILITY	1.7
PROBLEM SOLVING AND INNOVATION	1.3
PRESENTATION	1

Fig. 3 Radar diagram for different parameters

FACTORS	MARKS
PROJECT MANAGEMENT	4
TIME MANAGEMENT	3
TEAM WORK	3
COMMUNICATION	3
SELF CONFIDENCE	4
FLEXIBILITY AND ADAPTABILITY	4
ENGAGEMENT RELIABILITY	4
PROCESS DEVELOPMENT AND DESIGN	4
PRODUCT DEVELOPMENT AND DESIGN	3
ENGLISH LANGUAGE	3
SUSTAINABILITY	2
PROBLEM SOLVING AND INNOVATION	3
PRESENTATION	3

Fig. 4 Radar diagram of various parameters of AM
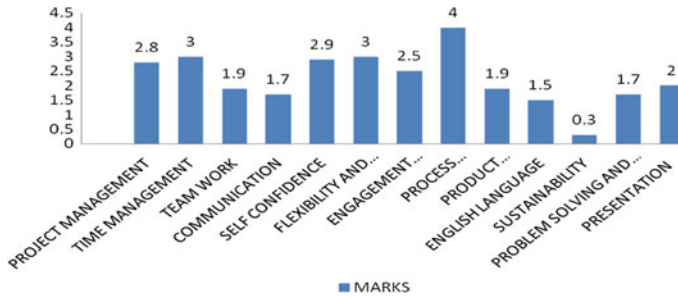
Fig. 5 Improvement in graphical diagram using AM

6 Conclusion

AM plays a vital role in providing a right direction to the students about how to learn the engineering concepts and how to utilise that concept in order to make a product which is useful for the society. Projects done with the help of different parameters play a vital role in shaping up the carrier of the students, and thus, using different analytical skills like design and analysis help the students to learn the concept in a proper manner.

References

1. Kostakis, V., Niaros, V., Giotitsas, C.: Open source 3D printing as a means of learning: An educational experiment in two high schools in Greece, Telematics. Inform. **32**(1), 118–128, February (2015)
2. Eisenberg, M.: 3D printing for children: what to build next? Int. J. Child Comput. Interact. 7–13 (2013)
3. Gladysz, B., Urgo, M., Gaspari, L., Pozzan, G., Kohl, H.: Perspectives for international engineering education. Procedia Manuf. (2017)
4. Pikkarainen, A., Salminen, A., Piili, H.: Creating learning environment connecting engineering design and 3D printing. Phys. Procedia 122–130 (2017)
5. Vernera, I., Merksamerb, A.: Digital design and 3D printing in technology teacher education. Procedia CIRP **36**, 182–186 (2015)
6. Junk, S., Matt, R.: A new approach to introduction of 3D digital technologies in design education. Procedia CIRP 35–40 (2015)

Numerical Investigation of Cu–H$_2$O Nanofluid in a Differentially Heated Square Cavity with Conducting Square Cylinder Placed at Arbitrary Locations

Basant Kumar, Bishwajit Sharma and Rabindra Nath Barman

1   Introduction

For viscous incompressible fluid flows, lid-driven cavity is a well-established yardstick problem. Various investigations have been carried out in the past with various combinations of cavity configurations and temperature gradients. Many factors mainly encourage the investigation of a lid-driven cavity. Well-posed boundary conditions and regular geometry have made this flow a favored test case for the computational schemes, arising the need for an accurate database against which such schemes can be validated. It also offers an opportunity to study a "stationary, captive" primary vortex Roshiko [1], along with complex secondary phenomenon such as Taylor-Goertier vortices. Also, we can say the flow is an ideal representation of many engineering situations like the flow over repeated slots on the heat exchanger walls or on the surface of aircraft body or also flow over cutoffs.

In heat transfer equipment, fluids are often used as heat carriers. Conventional fluids, such as mineral oil and water, have low thermal conductivity resulting low heat conduction. To tackle this situation, nano-sized metal particles in base fluid have been introduced, and in the recent years, it has drawn the attention toward cooling of industrial applications. Using of these nano-sized particles with high thermal conductivity in the base fluid will notably increase the thermal conductivity of the fluid. The model proposed by Maxwell [2] predicted the thermal conductivity of mixtures which had solid particles in it. He showed that effective thermal conductivity of these suspensions increased with the increase of volume fraction of the solid particles, though his model was valid for micro-sized particles and low dense mixtures. The numerical investigation was carried out by Sharma et al. [3] considering the parameters like Ri, ϕ, and different size of the heaters. It was found that

B. Kumar · B. Sharma · R. N. Barman (✉)
Department of Mechanical Engineering, National Institute of Technology
Durgapur (NITD), West Bengal 713209, India
e-mail: rn.barman@me.nitdgp.ac.in

173
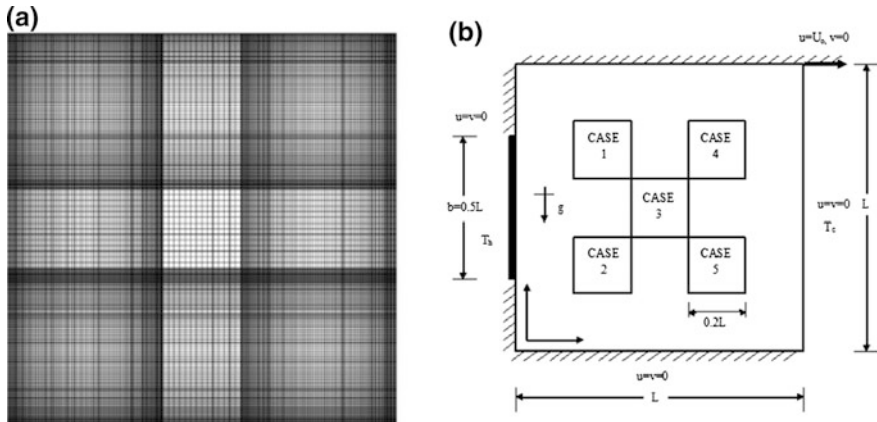
Fig. 1 **a** Grid distribution for case 3, **b** schematic of cavity with different locations of conducting cylinder

the natural convection significantly affect flow field at higher Ri, and the governing parameter is the size of the heaters. Experimental results of Xie et al. [4] also showed higher thermal conductivities for nanofluid with an increase in solid volume fraction. Nondimensional parameters such as Reynolds number, Prandtl number, Richardson number and Grashof number play a consequential role in heat transfer-related applications. Oztop [5] varied the Rayleigh number $1000 < Ra < 10,000$, different heater size with different locations and aspect ratio of cavity 0.5–2 and observed that cavity with low aspect ratio was more efficient than with the higher one. Chatterjee [6] investigated the heat transfer inside the cavity with a thermally insulated rotating circular cylinder placed centrally within the enclosure and $1 \leq Ri \leq 10$, dimensionless rotational speed $0 \leq \Omega \leq 5$ and nanoparticle concentration $0 \leq \varphi \leq 0.20$. He observed the heat transfer greatly depended on the rotational speed of the cylinder and the nanoparticle concentration. Aydin [7] investigated with a centrally located heat source at the bottom wall whereas Nasr [8] used heater length equal to $0.37H$ on the vertical wall. Further, investigations have been carried out with different heater sizes and locations [9–12].

The objective of this paper is to determine the thermal performance of nanofluid which is analyzed by the location of the solid cylinder Fig. 1b, percentage volume of Cu nanoparticles (0, 3, 5%) and Richardson number (0.01, 1). Grashof number and Prandtl number in this work are fixed to 10^4 and 6.2, respectively.

2 Mathematical Formulation

A square cavity of height and length L with an aspect ratio of 1 unit is considered for the present study. A two-dimensional steady flow is considered with the boundary conditions as shown in Fig. 1b. A solid square cylinder of size $0.2L$ is placed inside the cavity which is filled with Cu–H₂O nanofluid. The center of cylinders is located at a distance of $0.2L$ from adjacent sides (case 1, 2, 4, and 5) and at the center of cavity (case 3). Nanofluid properties are calculated as mathematical formulation shown by Talebi et al. [13] using the thermo-physical property nanoparticle and water. The governing equations subjected to the above-mentioned boundary conditions, shown in Fig. 1b, are discretized and solved by FVM-based CFD package FLUENT [14]. QUICK schemes along with SIMPLE algorithm are used for spatial discretize and solving the pressure velocity couplings of RANS equations. The convergence criteria are set as 10^{-10} and 10^{-12} for continuity and energy equations, respectively.

Figure 1a shows the non-uniform grid generated with refined mesh closer to the walls. The grid independence test is checked by varying the number of grids and calculating the Nusselt number at those grids. The case is solved with six different mesh sizes and $Ri = 0.1$ and $Gr = 10^4$. The Nusselt number distribution is represented as different grid count. It seems to vary with 0.003% at 125×125 grids. All further investigations are performed at 125×125 grid configuration. The present numerical scheme and a good agreement with de Vahl Davis [15] are shown in Table 1.

3 Results and Discussions

The flow and thermal fields for different parameters like the nanoparticle concentration, different cylinder location, and Ri are depicted in the form of streamlines and isotherms in Fig. 2. As Ri increases Re decreases making natural convection dominant in the fluid domain. Similarly, when Ri decreases the forced convection is dominant. The lid movement is in positive x-direction which causes the clockwise (CW) rotation of the fluid inside the cavity. The conducting solid cylinder though restricts the fluid flow but do allow the heat to pass through. As a result of the blockage provided by the cylinder, the fluid flow gets accelerated. For case 1, at low

Table 1 Comparison of local and average Nusselt number with de Vahl Davis [15]

Ra	de Vahl Davis [15] Average Nusselt number (Nu)	Present study	Error %
1×10^4	2.242	2.27	1.42
1×10^5	4.523	4.62	2.16
1×10^6	8.928	9.06	1.51
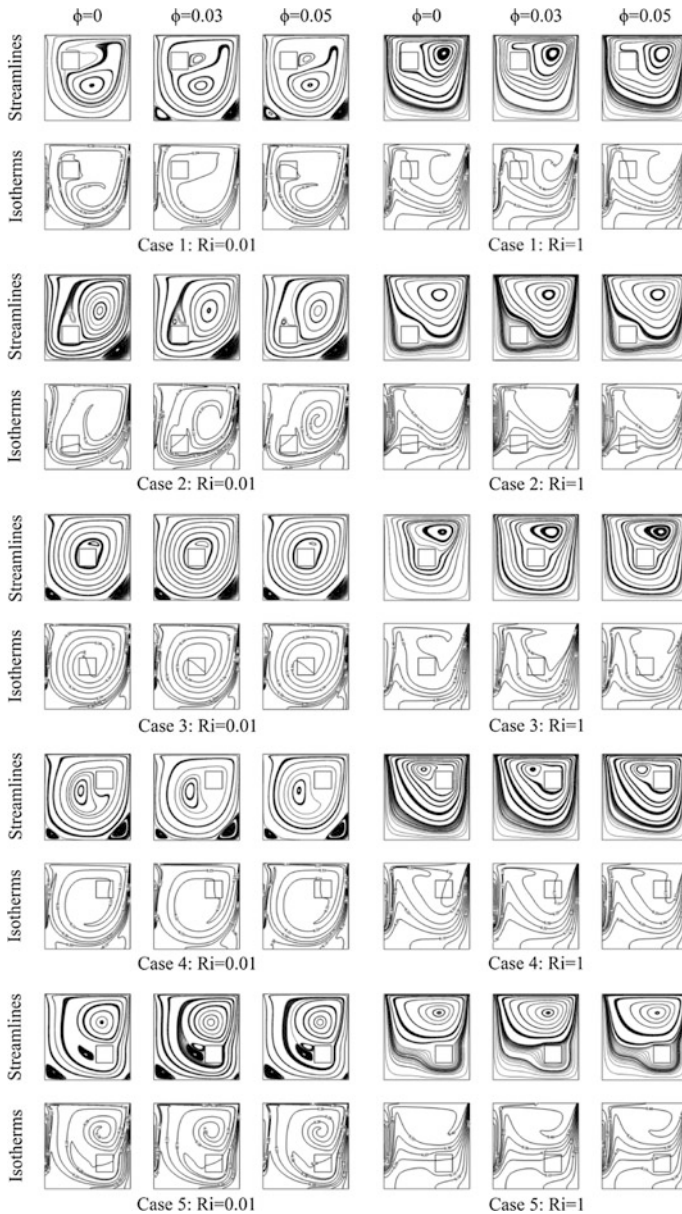
Fig. 2 Streamlines and isotherms for different location and for Ri = 0.01 and 1

Ri, two counterclockwise eddies are formed at the right and left of the bottom corner. One smaller and the other relatively larger than the former clockwise rotating eddies are formed on the right side of the cylinder. At higher Ri, one big eddy is seen on the right side but away from the cylinder. The isotherms near the
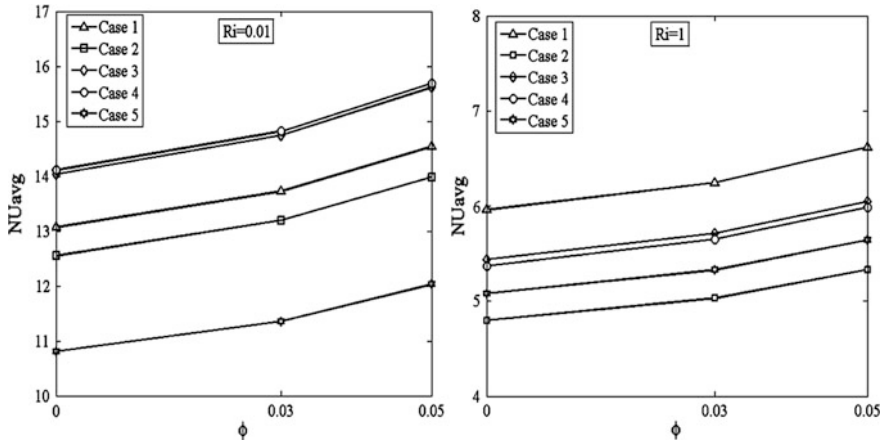
Fig. 3 Variation of average Nusselt number of the right cold wall with ϕ for different Ri and cylinder location

heated and cold walls are denser in case of higher Ri because of the natural convection effect. In case 2, a similar trend as in case 1 is observed but at Ri = 0.01 one counterclockwise (CCW) eddy is eliminated and the two clockwise (CW) eddies are now combined into a single large eddy.

At Ri = 1, the eddy as in case 1 has grown bigger. Isotherms too show a similar trend. In case 3, at Ri = 0.01, one small clockwise (CW) eddy is formed above the top wall of the cylinder and the remaining counterclockwise (CCW) eddies are almost identical to case 1. At Ri = 1, streamlines are almost similar to case 1. Isotherms in Ri = 0.01 are more regular as compared to Ri = 1. In case 4, the clockwise (CW) eddy has shifted toward the left wall of the conducting cylinder. At Ri = 0.01, the isocontours are same as in cases 1 and 3 which is because of the dominance of forced convection. In case 5, the counterclockwise (CCW) eddy at the bottom right corner is smaller as compared to all other cases. Near the left wall of the square cylinder two eddies both in opposite direction are observed and a clockwise (CW) eddy is seen above the square cylinder. At Ri = 1, one clockwise (CW) eddy is observed above the cylinder. It is found that the heat transfer rate is affected notably by mixed convective strength, the location of the conducting cylinder, and volume fraction of the nanoparticles. The variation of the average Nusselt number on the cold right wall of the enclosure to the nanoparticle concentration for different Ri and the location of the cylinders are given in Fig. 3. With the increase of nanoparticle concentration, there is a linear increase of the average Nusselt number. The increase of ϕ increases the effective thermal conductivity of the nanofluid which in turn escalates the average Nusselt number. For both Ri, as ϕ increases by 3%, Nu increases approximately by 5%. When ϕ increases by 5%, Nu increases by 11%.

4   Conclusion

At lower Ri, forced convection is dominant in fluid and thermal transport. As Ri increases, natural convection comes into effect but is subdued with the increase in nanoparticle concentration. For Ri = 0.01, Nu is highest for case 4, i.e., conducting solid cylinder is placed near the cold and moving wall and lowest for case 5. For Ri = 1, Nu is highest for case 1, i.e., conducting solid cylinder is placed near the heated and moving wall and lowest for case 2. Heat transfer rate is affected notably by mixed convective strength, the location of the conducting cylinder, and the volume fraction of the nanoparticles. With the increase of nanoparticle concentration, there is a linear increase of the average Nusselt number. For both Ri, as ϕ increases by 3%, Nu increases approximately by 5%. When ϕ increases by 5%, Nu increases by 11%.

References

1. Roshko, A.: Some measurements of flow in a rectangular cutout. No. naca-tn-3488. California Inst of Tech, Pasadena (1955)
2. Maxwell, J.C.: A Treatise on Electricity and Magnetism, vol. 1. Clarendon Press (1881)
3. Sharma, B., et al.: Numerical investigation of Cu-water nanofluid in a differentially heated square cavity with conducting solid square cylinder at center. Int. J. Heat Technol. (2018) Accepted
4. Xie, H., et al.: Dependence of the thermal conductivity of nanoparticle-fluid mixture on the base fluid. J. Mater. Sci. Lett. **21**(19), 1469–1471 (2002)
5. Oztop, H.F., Abu-Nada, E.: Numerical study of natural convection in partially heated rectangular enclosures filled with nanofluids. Int. J. Heat Fluid Flow **29**(5), 1326–1336 (2008)
6. Chatterjee, D., Gupta, S.K., Mondal, B.: Mixed convective transport in a lid-driven cavity containing a nanofluid and a rotating circular cylinder at the center. Int. Commun. Heat Mass Transfer **56**, 71–78 (2014)
7. Aydin, O., Yang, W.-J.: Natural convection in enclosures with localized heating from below and symmetrical cooling from sides. Int. J. Numer. Meth. Heat Fluid Flow **10**(5), 518–529 (2000)
8. Nasr, K.B., et al.: Numerical study of the natural convection in cavity heated from the lower corner and cooled from the ceiling. Appl. Therm. Eng. **26**(7), 772–775 (2006)
9. Hasnaoui, M., Bilgen, E., Vasseur, P.: Natural convection heat transfer in rectangular cavities partially heated from below. J. Thermophys. Heat Transfer (U.S.) **6** (1992)
10. Ahmed, G.R., Yovanovich, M.: Numerical study of natural convection from discrete heat sources in a vertical square enclosure. J. Thermophys. Heat Transfer **6**(1), 121–127 (1992)
11. Türkoglu, H., Yücel, N.: Effect of heater and cooler locations on natural convection in square cavities. Numer. Heat Transfer Part A Appl. **27**(3), 351–358 (1995)

12. Koca, A., Oztop, H.F., Varol, Y.: The effects of Prandtl number on natural convection in triangular enclosures with localized heating from below. Int. Commun. Heat Mass Transfer **34** (4), 511–519 (2007)
13. Talebi, F., Mahmoudi, A.H., Shahi, M.: Numerical study of mixed convection flows in a square lid-driven cavity utilizing nanofluid. Int. Commun. Heat Mass Transfer **37**(1), 79–90 (2010)
14. Fluent, Ansys.: 12.0 theory guide. AnsysInc 5 (2009)
15. de Vahl Davis, G.: Natural convection of air in a square cavity: a bench mark numerical solution. Int. J. Numer. Meth. Fluids **3**(3), 249–264 (1983)

Numerical Investigation of Single Ramp Scramjet Inlet Characteristics at Mach Number 5.96 Due to Shock Wave–Boundary Layer Interaction

K. Raja Sekar, S. Jegadheeswaran, R. Kannan, P. Vadivelu and G. Prasad

1 Introduction

The future of the high-speed flight depends on the development of air-breathing propulsion system without rotating components. The major advantage of air-breathing propulsion system is the ability to generate high specific impulse compared to rockets. The design of the inlet compression system decides the performance of the hypersonic space propulsion system, and the optimized inlet is able to increase the payload capacity of the whole system. The scramjet engine employs dual-mode compression system to achieve the effective pressure recovery [1]. The problems associated with the supersonic compression using oblique shock wave are the shock wave–boundary layer interaction and shock wave reflection [2, 3]. The oblique shock generated by the ramp interacts with the turbulent boundary layer on the cowl surface and produces subsonic separation bubble; further, the unsteady subsonic bubble grows faster and reduces the mass flow rate in the outlet [4]. The number of studies was conducted experimentally as well as computational fluid dynamics [5–8] to control the shock wave–boundary layer interaction and the subsonic bubble formation in the inlet. The characteristics of a single ramp inlet for both steady and unsteady conditions are studied in this paper.

K. Raja Sekar (✉) · S. Jegadheeswaran · P. Vadivelu · G. Prasad
Bannari Amman Institute of Technology, Sathyamangalam 638401, India
e-mail: rajasekark@bitsathy.ac.in

R. Kannan
Amrita School of Engineering, Amrita Vishwa Vidyapeetham, Coimbatore 641112, India

181

2 Inlet Model and Computational Method

2.1 Inlet Model

The 2D inlet model is used for the computational study as shown in Fig. 1 with 38.7° ramp angle to generate the shock at the Mach number of 5.96, the produced shock wave had a wave angle of 54.5°, and the distance between the ramp and the cowl is maintained as 60 mm.

2.2 Computational Methods

The flow field properties are calculated by solving Navier–Stokes equations. An implicit scheme with second-order accuracy is used for both steady and unsteady flow field computation. The flow field is treated as ideal gas, and for turbulence modeling, the two-equation k–ω shear–stress transport (SST) Reynolds-averaged Navier–Stokes (RANS) model is used. To capture the boundary layer behavior, the y plus is maintained below 1. The inlet is assumed to be pressure far-field and outlet of the computational model as pressure outlet. The computational model is solved for continuity, momentum and energy, and the corresponding residuals are monitored up to the convergence criterion for these residuals to drop below 10^3.

3 Results and Discussion

3.1 Steady Analysis

The static pressure distribution on the lower lip follows the same trend as the experimental work done by Sriram [9]; where the subsonic bubble occurs, the static
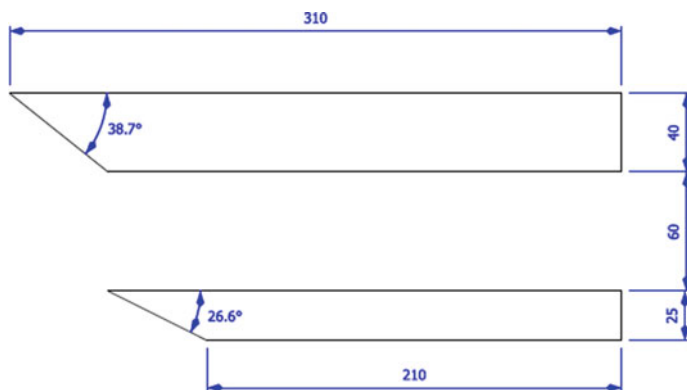
Fig. 1 Computational geometry of the supersonic inlet
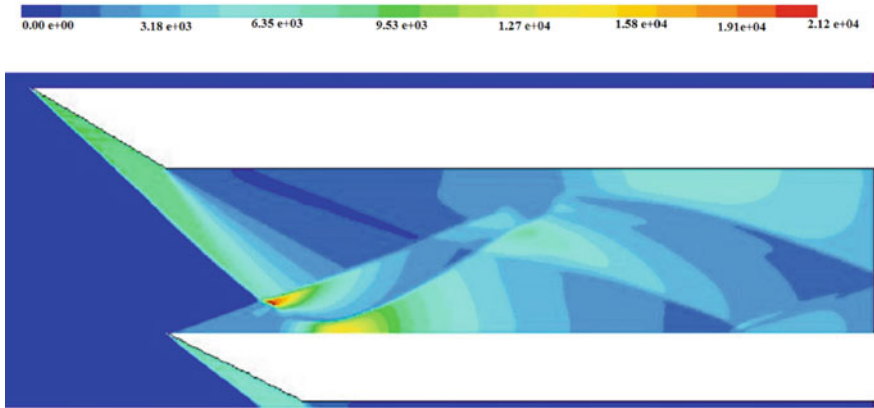
Fig. 2 Static pressure distribution in the scramjet inlet

Fig. 3 Static pressure in the lower lip
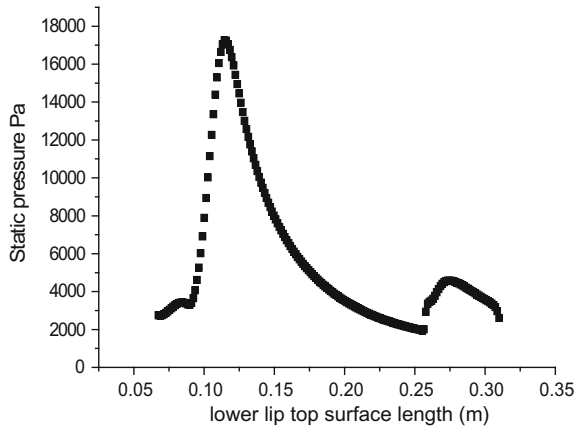
pressure increases and the peak pressure on the lower lip occurs at 110 mm from the leading edge and the pressure computed is 1800 Pa and the pressure measured experimentally by Sriram is about 3400 Pa; the pressure drop in the computational result is due the difference in the experimental model and the computational model. In the experimental model, they used ramp only to generate shock, but in the computational model the same ramp is used as the inlet of the scramjet. The reflected shock wave interacts with the boundary layer of the ramp wall and reflected again so that the pressure drop occurs in the computational model (Figs. 2 and 3).

Mach number distribution shown in Fig. 4 shows the interaction of the shock wave from the ramp and lower lip and creates two reflected shock wave leads to subsonic bubble in the lower lip; this can be avoided by designing the shock system
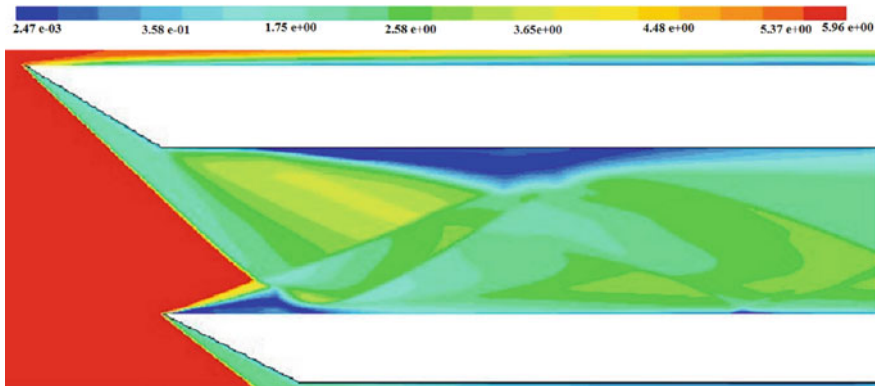
Fig. 4 Mach number distribution in the inlet

to hit the leading edge of the lower lip, but the experiment done by Sriram and Jagadeesh [10] intentionally created this subsonic bubble to study the control mechanism. The bubble size measured experimentally is 14 mm also same as computed using the computational fluid dynamics studies. In the ramp wall, bigger subsonic bubble occurs due to the reflected shock wave and boundary layer interaction, and the size of the bubble is measured as 135 mm width and maximum height of 14 mm using ImageJ.

3.2 Unsteady Analysis

To understand the behavior of the subsonic bubble, transient analysis was conducted with a time step size of 0.1 ms with 3000 iterations for each time step and the solution becomes steady after 2.1 ms. During the starting time, the no separation bubble exists and shock wave reflects due to the normal reflection over a time the shock wave reflection changed as Mach reflection, and shock wave–boundary layer interaction (SWBL) leads to the formation of subsonic bubble. When the size of the bubble increases, the mass flow at the exit also reduces correspondingly. Figure 5 shows the variation of the subsonic bubble size over the time. The static pressure of the intake varies according to the subsonic bubble size as indicated in Fig. 6.
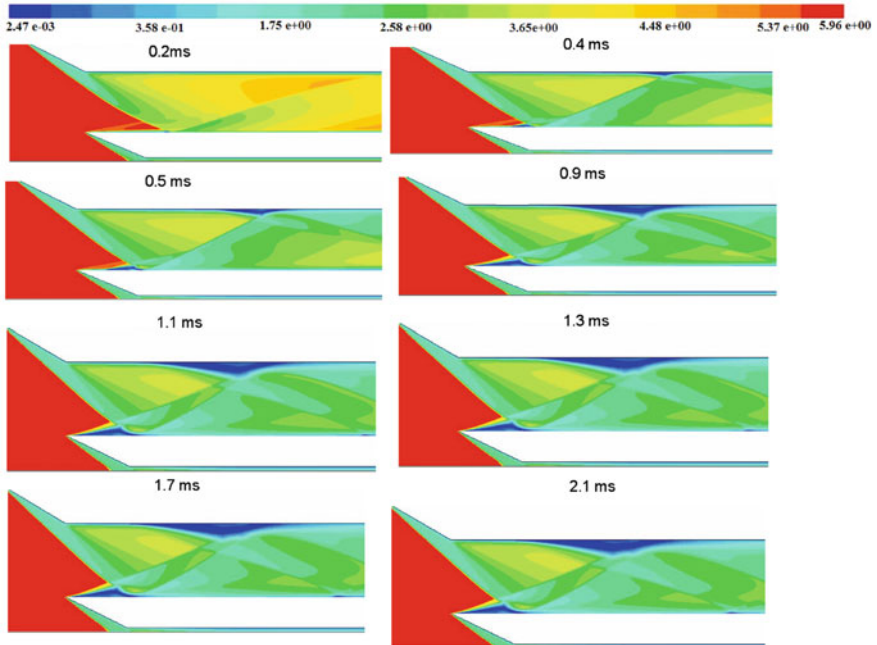
Fig. 5 Mach contour for different time steps

4 Conclusion

The characteristics of the single scramjet inlet under steady and transient conditions were studied numerically and validated with the experimental investigation. The accuracy of the numerical results had a good match with the experimental results. The analysis shows that the shock strength increases due to the shock wave–boundary layer interaction (SWBL)-induced subsonic bubble formation and the mass flow rate reduces with respect to the bubble size.
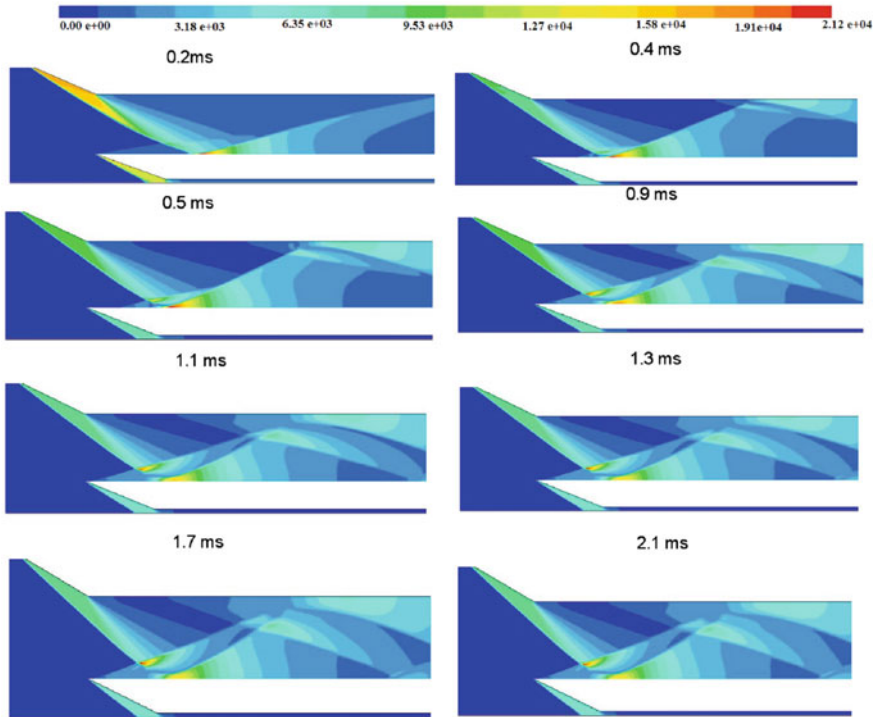
Fig. 6 Static pressure distribution for different time steps

References

1. Deng, R., Jin, Y., Dong Kim, H.: Numerical simulation of the unstart process of dual-mode scramjet. Int. J. Heat Mass Transf. **105**, 394–400 (2017)
2. Ben-Dor, G.: Shockwave Reflection Phenomena, 2nd edn. Springer (2007)
3. Tan, H., Sun, S.: Oscillatory flows of rectangular hypersonic inlet unstart caused by downstream mass-flow choking. J. Propul. Power **25**(1) (2009)
4. Weixing, W., Rongwei, G.: Numerical study of unsteady starting characteristics of a hypersonic inlet. Chin. J. Aeronaut. **26**(3), 563–577 (2013)
5. Van Wie, D.M., Aultt, D.A.: Internal flow field characteristics of a scramjet inlet at Mach 10. J. Propul. Power **12**(1) (1996)
6. Barber, T.J., Hiett, D., Fastenberg, S.: CFD modeling of the hypersonic inlet starting problem. In: 44th AIAA Aerospace Sciences Meeting and Exhibit, Reno, Nevada (2006)
7. Schulte, D., Henckels, A., Wepler, U.: Reduction of shock induced boundary layer separation in hypersonic inlets using bleed. Aerosp. Sci. Technol. **4**, 231–239 (1998)
8. John, B., Kulkarni, V.N., Natarajan, G.: Shock wave boundary layer interactions in hypersonic flows. Int. J. Heat Mass Transf. **70**, 81–90 (2014)
9. Sriram, R.: Shock tunnel investigation on hypersonic impinging shockwave boundary layer interaction. PhD Thesis, Indian Institute of Science (2013)
10. Sriram, R., Jagadeesh, G.: Shock tunnel experiments on control of shock induced large separation bubble using boundary layer bleed. Aerosp. Sci. Technol. (2014)

Numerical Analysis of Discrete Element Camber Morphing Airfoil in the Reynolds Number of Conventional Flyers

T. Rajesh Senthil Kumar ⬤**, Nikitha Narayanaprasad, Yashmitha Kumaran, V. Sivakumar** ⬤ **and Balajee Ramakrishnananda** ⬤

1 Introduction

Increasing air travel is contributing to pollution due to fuel consumption. Fuel consumption also increases the cost for airlines. National Aeronautics and Space Administration (NASA) states that the US fleet can save up to 140 million dollars per year, if the airfoil drag is reduced by 1% [1]. One of the ways to decrease fuel consumption is to decrease the drag and increase the aerodynamic efficiency of aircrafts. A possible solution to this would be to adopt morphing technologies on aircraft lifting surfaces.

While aircrafts are usually designed for particular mission requirements, their performance would inevitably be sub-optimal over other segments and off-design conditions of a mission profile. To mitigate this issue, different morphing solutions were proposed by various researchers [1, 2]. Poonsang discusses multi-section variable camber wing for small unmanned aerial vehicles (SUAV) [3]. Rajesh et al. studied the performance of a two-element morphed airfoil at Reynolds numbers corresponding to SUAVs [4]. Miller studied the performance of variable camber compliant wing by conducting wind tunnel testing and simulations [5]. The aim of the current work is to morph the camber of an airfoil in the Reynolds number of conventional flyers (3×10^6) using discrete element method. Numerical simulations are conducted using ANSYS Fluent V15.0.

T. Rajesh Senthil Kumar (✉) · N. Narayanaprasad · Y. Kumaran
V. Sivakumar · B. Ramakrishnananda
Department of Aerospace Engineering, Amrita School of Engineering,
Amrita Vishwa Vidyapeetham, Coimbatore, India
e-mail: t_rajesh@cb.amrita.edu

2 Geometry of Airfoils and Computational Setup

2.1 Camber Morphing

Discrete element method for morphing airfoils modifies the camber/mean line of the airfoil at different locations [3, 4]. The baseline airfoil selected is NACA 0012 which has a straight camber line. NACA 0012 has a maximum thickness of 12% at 30% of the chord. The target airfoil NACA 23012 has a maximum thickness of 12% at 30% of the chord and a maximum camber of 2% at 15% of the chord.

The camber line of baseline airfoil is morphed using discrete morphing concept at three locations, namely, at maximum camber position of target airfoil, maximum thickness position of target airfoil and at a typical position of a plain flap, which are at 15%, 30%, and 80% of the chord, respectively, as shown in Fig. 1.

In order to distinguish between the morphed airfoils, the following nomenclature is adopted. The first two alphabets "MA" indicate that it is a morphed airfoil. The next digit represents the number of discrete morphing positions in the mean line of the baseline airfoil. The suffix alphabets describe the various configurations based on geometric variations as listed in Table 1.
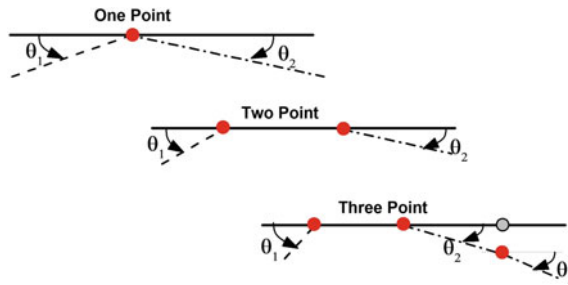
Fig. 1 Discrete morphing concept

Table 1 Nomenclature of morphed airfoil and morphing details

Morphed config.	Airfoil	Location of morphing	Angle (θ) at morphed location		
			15% c	30% c	80% c
One point	MA_1A	15% chord	LE: 7.59°		
			TE: 1.35°		
	MA_1B	30% chord		LE: 3.81°	
				TE: 1.64°	
Two point	MA_2A	15% chord and 30% chord	7.59°	1.64°	–
Three point	MA_3A	15% chord, 30% chord and 80% chord	7.59°	1.72°	1.43°
	MA_3B		7.59°	1.15°	2.86°
	MA_3C		7.59°	0.57°	4.29°

Fig. 2 Validation of results
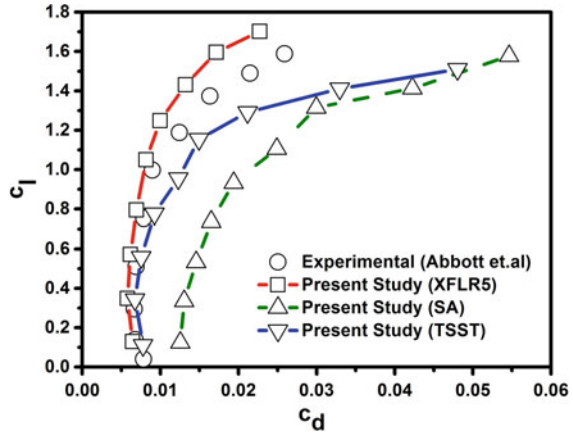
2.2 Computational Model and Validation

A quadrilateral structured grid in a C–H domain of radius 20 times of the chord of the airfoil was created in ANSYS Fluent [6]. The airfoil's chord was set to be 0.305 m. Grid independent solutions were attained with 1.4 million cells in the simulation domain. Wall y+ was maintained to be less than 3. The boundary conditions are specified as velocity inlet and pressure outlet. Spalart–Allmaras (S-A) [7] and transitional shear stress transport models (TSST) [8] were used. Along with this, XFLR5 V. 6.14 is used to simulate the flow over airfoils [9].

Experimental results available for NACA 23012 [10] were used to validate and compare the numerical results obtained from XFLR5 and ANSYS Fluent. From this validation study, it was seen that the Spalart–Allmaras model over predicted the drag coefficients and the TSST model captured the drag coefficient closer to the experimental value, as shown in Fig. 2. Hence, TSST model is selected to capture the performance characteristics of morphed airfoils. Interestingly, the results obtained from XFLR5 closely matched with the experimental values although XFLR5 is more approximate. The same has also been observed in earlier works [4].

3 Results and Discussion

3.1 Aerodynamic Performance of Morphed Airfoils

To quickly get an initial idea, the performance of the six morphed airfoils shown in Table 1 was estimated using XFLR5 for Reynolds number of 3×10^6. The performances of the six morphed airfoils were compared with NACA 23012. The morphed airfoils were then ordered as three sets which are classified as producing

Table 2 Combinations of morphed airfoils based on their performance

AoA (°)	Airfoil		
	MA_l (c_l)	MA_d (c_d)	MA_ld (c_l/c_d)
0	MA_3C	MA_1B	MA_3C
2	MA_3C	MA_1B	MA_3C
4	MA_3C	MA_1B	MA_3C
6	MA_3C	MA_3C	MA_3C
8	MA_3B	MA_1B	MA_3B
10	MA_3B	MA_1B	MA_3B
12	MA_2A	MA_1B	MA_3B
14	MA_2A	MA_1B	MA_3C
16	MA_3C	MA_3C	MA_3C

high lift, low drag, and high c_l/c_d at that particular AoA. These sets are labeled as MA_l, MA_d, and MA_ld, respectively, in Table 2.

The above airfoils were then analyzed in ANSYS Fluent using TSST model for a Reynolds Number of 3×10^6. The results obtained were compared with those for NACA 0012 and NACA 23012. Figure 3 shows that MA_l set of airfoils have high lift coefficient and c_l/c_d ratio, but poor drag characteristics. The lift coefficient of MA_3C airfoil belonging to the MA_l set was higher by 3.27–25.12% and 16–68.12% compared to NACA 23012 and NACA 0012, respectively, over the range of AoA. MA_d gives minimum drag coefficient values compared to other classes, but the lift and c_l/c_d characteristics are comparatively less. Figure 3b shows that drag coefficient of MA_1B belonging to the set MA_d drops by 39.84 and 37.6% compared to NACA 23012 and NACA 0012, respectively, at 0° AoA. In the MA_ld set, MA_3C airfoil shows high c_l/c_d in the AoA range of 0°–6°, which is the usual operating AoA range. The c_l/c_d of this airfoil is 57.14% more than NACA 23012 at 0° AoA. After 6° AoA, the aerodynamic efficiency of NACA 0012 exceeds the other airfoils.

To minimize the drag, the surface curvatures of morphed airfoils were modified near the morphing location to have a smooth profile. Fourth-order surface smoothening at the morphing locations were done using MATLAB. The

(a) Lift coefficient   (b) Drag coefficient   (c) Lift/Drag ratio
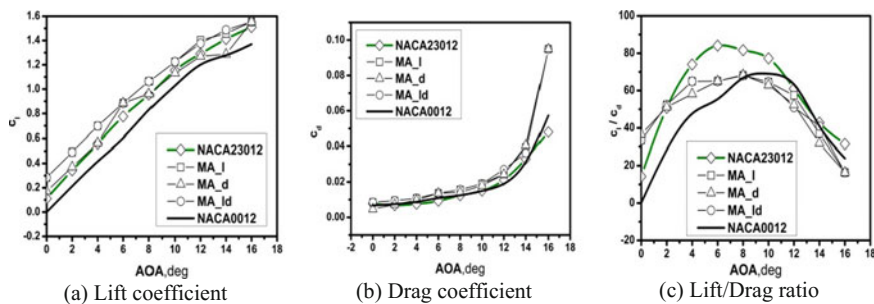
Fig. 3 Aerodynamic performance of combinations of morphed airfoils
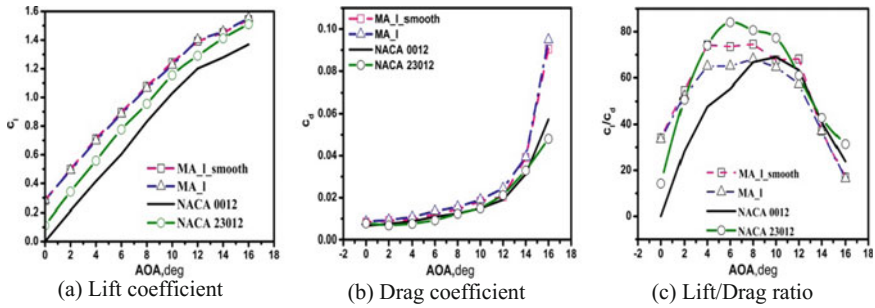
Fig. 4 Aerodynamic performance of smoothed MA_l
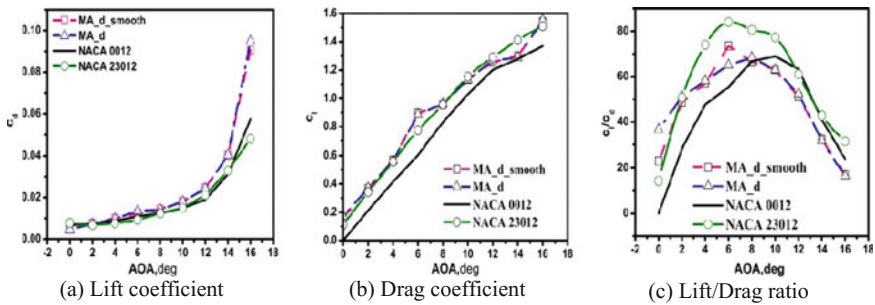
Fig. 5 Aerodynamic performance of smoothed MA_d
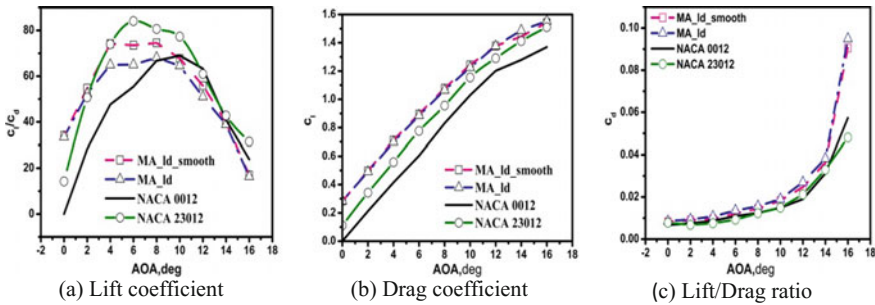
Fig. 6 Aerodynamic performance of smoothed MA_ld

performances of these airfoils were computed using TSST model in ANSYS Fluent. The performance of smoothened airfoils were compared with other airfoils as shown in Figs. 4, 5, and 6.

At 12° AoA, MA_l_smooth shows a maximum drop in c_d by 1.64% and a maximum rise in c_l/c_d ratio by 18.73% compared to MA_l. At 6° AoA, MA_d_smooth shows a maximum rise in c_l/c_d ratio by 11.5% compared to MA_d

as shown in Figs. 4 and 5. At 12° AOA, MA_ld_smooth shows a maximum reduction in drag by 12% and a maximum rise in c_l/c_d ratio by 14.2% compared to MA_ld, as shown in Fig. 6. Lift coefficients seem to be more or less insensitive to smoothing.

4   Conclusions

From the XFLR5 results, three classifications of the airfoils were formed based on lift coefficient, drag coefficient, and c_l/c_d ratio. These airfoils were then analyzed in ANSYS Fluent using TSST model and following conclusions are made:

- MA_l gives an average of 14% increase in c_l with respect to NACA 23012 in the angle of attack range 0°–16°. This class of morphed airfoils can be used where there is demand for high lift, like takeoff, landing, climbing flight, etc. MA_d produced minimum drag values but the lift and c_l/c_d characteristics were not better than NACA 23012. MA_d could reduce the drag by 39% at 0° AoA, implying that this configuration can be deployed during taxiing. MA_ld can be used during cruise where the angle of attack usually ranges from 0° to 6°. In all three classes, after 6° AoA, the base airfoil shows better c_l/c_d values compared to morphed airfoils.
- For smoothened morphing, the morphing locations were assumed to be covered with flexible material. Reduction in drag and increase in c_l/c_d ratios were observed while the lift coefficient seemed to be more or less unaffected by smoothing. This study provides hope toward adoption of morphing solutions for practical use. Further, investigation is needed in the direction of material selection and simplified mechanism to actuate this type of design that can be used in realistic applications.

References

1. Barbarino, S., Bilgen, O., Ajaj, R.M., Friswell, M.I., Inman, D.J.: A review of morphing aircraft. J. Intell. Mater. Syst. Struct. **22**, 823–877 (2011)
2. Vasista, S., Tong, L., Wong, K.C.: Realization of morphing wings: a multidisciplinary challenge. J. Aircr. **49**, 11–28 (2012)
3. Poonsong, P.: Design and analysis of a multi-section variable camber wing. MS Thesis, University of Maryland, United States (2004)
4. Rajesh Senthil Kumar, T., Sivakumar, V., Ramakrishnananda, B., Arjhun, A.K., Pandian, S.: Numerical investigation of two-element camber morphing airfoil in low Reynolds number flow. J. Eng. Sci. Technol. **12**(7), 1939–1955 (2017)
5. Miller, S.C.: Fluid structure interaction of a variable camber complaint wing. MS Thesis, University of Dayton, Unites states (2015)
6. ANSYS FLUENT 12.0/12.1 Documentation. http://www.afs.enea.it/project/neptunius/docs/fluent/html/th/node50.htm. Last accessed 2017/7/21

7. Spalart, P.R., Allmaras, S.R.: A one-equation turbulence model for aerodynamic flows. AIAA paper 92-0439 (1992)
8. Menter, F.R., Langtry, R.B., Likki, S.R., Suzen, Y.B., Hungang, P.G., Volker, S.: A correlation based transition model using local variables part 1—model formulation. ASME J. Turbomach. **128**, 413–422 (2006)
9. XFLR5. http://www.xflr5.com/xflr5.htm. Last accessed 2017/3/18
10. Abbott, I.H., Von Doenhoff, A.E.: Theory of Wing Sections including Summary of Airfoil, 1st edn. Dover Publications Inc., New York (1959)

Comparison of Quarter Car Suspension Model Using Two Different Controllers

**Arivazhagan Anandan, Arunachalam Kandavel
and Arockia Suthan Soosairaj**

1 Introduction

Suspension plays a major role in automotive vehicles to attain safety and ride comfort. But by using a conventional type of suspension system, attainment of aforementioned behavior at the same level is not possible. This is due to the fact, in the passive type of suspension system, parameters like spring stiffness and damping coefficient are fixed. There is always a trade-off between comfort and vehicle handling in the passive system as shown in Fig. 1. For having good comfort, soft damping is required, and to have a good safety in vehicle, hard damping is needed. Due to this, suspension performance is limited. The above-mentioned limitation is reduced by the innovation of active and semi-active system which was lightened in the year during 1960s. Compare with semi-active type, active suspension produces improved performance. It is because of that active system has energy adding elements and controllers. At the same time, it needs more components like actuators and sensors, simultaneously the cost of this active suspension is high when compared with other types. This is the reason why this type of suspension is not implemented in conventional cars but to luxury cars.

By using quarter car model, most of the properties like ride comfort, load carrying capacity, and road holding properties are analyzed [1]. This was the reason, most of the researchers considering quarter car model instead of full car model for their work, and also it is simple to develop the mathematical equation in the quarter car. Some authors have done work on the optimal controller to improve the performance of the suspension [2–4], and some have made on PID controller [5–8]. In paper [2], authors had considered passenger seat dynamics along with quarter car suspension for their system representation and acceleration dependent method (ADM)-based LQR to reduce the passenger seat acceleration. In [3], authors

---

A. Anandan (✉) · A. Kandavel · A. S. Soosairaj
Department of Automobile Engineering, M.I.T, Anna University, Chennai 600044, India
e-mail: arivazhagan_arul@yahoo.com

195

Fig. 1 Passive suspension trade-off
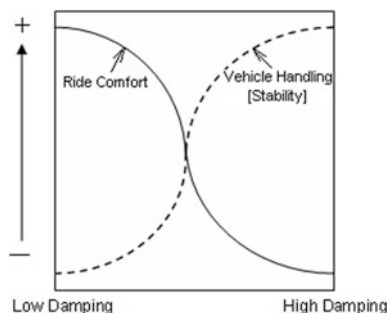
concluded that LQR controller-based active suspension provides better performance than the passive system. In an article [4], authors had considered 2 DOF quarter car model and found that settling time and peak value for various suspension characteristics are reduced by the use of LQR. In paper [5], authors found that ride comfort of the vehicle was increased by two-fold using PID-controlled suspension than by passive. In [6], authors had developed quarter car model using identification technique and proposed a PID-type H∞ controller to the active system and concludes that proposed controller does not have any deviation in the simulation and application phase. PID state feedback controller for the quarter car model is developed in [7], and they attained significant improvement in the performance than the passive. In an article [8], authors had developed PID controller based on Zeigler–Nichols method for the quarter car active suspension system and achieved better performance. Form the above studies, it is clearly understood that by using quarter car suspension, most of the suspension characteristics are analyzed, and better performance is attained by using active than the passive system. The main aim of this work is to identify suitable controller for different road profiles to a quarter car suspension model, and this work is limited to a comparison between only two controllers, namely linear quadratic regulator and proportional integral derivative controller.

This paper is organized as follows; Sect. 2 presents with mathematical modelling of a quarter car suspension system for passive and hydraulic actuated active system. Section 3 gives with designing of PID and LQR controller. Section 4 discusses the simulation results, and finally, Sect. 5 deals with the conclusion.

2 Mathematical Modeling

The governing equation of motion for the system shown in Fig. 2 is developed by using Lagrange's principle. For simplicity, the system is assumed to have only heave motion, and nonlinearity of the springs and dampers are neglected.

Mathematical modelling of Fig. 2 is developed using Lagrange's energy principle. The Lagrangian equation is the difference of total kinetic energy of the system

Fig. 2 Quarter car model
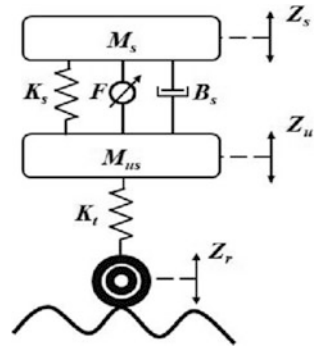
and the total potential energy of the system. The generalized form of Lagrangian equation is given in (1)

$$\frac{\mathrm{d}}{\mathrm{d}t}\left(\frac{\partial L}{\partial \dot{q}_i}\right) - \frac{\partial L}{\partial q_i} + \frac{\partial D}{\partial \dot{q}_i} = Q_i \tag{1}$$

where Lagrangian term $(L) = T - V$; T—total kinetic energy; V—total potential energy; D—dissipative energy of the system; q_i—generalized ith coordinate; Q_i—force on the ith coordinate; and the energy equations of the system are given in (2), (3), and (4), respectively.

$$T = \frac{1}{2}M_s(\dot{z}_s)^2 + \frac{1}{2}M_u(\dot{z}_u)^2 \tag{2}$$

$$V = \frac{1}{2}K_s(z_s - z_u)^2 + \frac{1}{2}K_t(z_u - z_r)^2 \tag{3}$$

$$D = \frac{1}{2}B_s(\dot{z}_s - \dot{z}_u)^2 \tag{4}$$

$$q_i = \begin{bmatrix} z_s & z_u \end{bmatrix}^{\mathrm{T}}$$

$$Q_i = \begin{bmatrix} F & z_r \end{bmatrix}^{\mathrm{T}}$$

The governing equation for the given system is derived from the above equations and is represented in (5) and (6)

$$M_s\ddot{z}_s + K_s(z_s - z_u) + B_s(\dot{z}_s - \dot{z}_u) = F \tag{5}$$

$$M_u\ddot{z}_u + K_s(z_u - z_s) + K_t(z_u - z_r) + B_s(\dot{z}_u - \dot{z}_s) = -F \tag{6}$$

2.1 Passive System

A mathematical model of the passive system is developed using state space model. With the use of state space representation, higher order derivatives of the system are reduced to first-order derivative in matrix form as shown in (7) and (8).

State space equation

$$\dot{x}(t) = Ax(t) + Lw(t) \tag{7}$$

$$y(t) = Cx(t) + Du(t) \tag{8}$$

Let state vectors,

$$x(t) = [x_1 \ x_2 \ x_3 \ x_4]^T$$

where

$$x_1 = Z_s - Z_u; \quad x_2 = \dot{Z}_s; \quad x_3 = Z_u - Z_r; \quad x_4 = \dot{Z}_u;$$

$$A = \begin{bmatrix} 0 & 1 & 0 & -1 \\ \frac{-K_s}{M_s} & \frac{-B_s}{M_s} & 0 & \frac{B_s}{M_s} \\ 0 & 0 & 0 & 1 \\ \frac{K_s}{M_u} & \frac{B_s}{M_u} & \frac{-K_t}{M_u} & \frac{-B_s}{M_u} \end{bmatrix};$$

$$L = \begin{bmatrix} 0 \\ 0 \\ -1 \\ 0 \end{bmatrix}; \quad C = I_4; \quad D = (0)_{1X4}; \quad w(t) = \{\dot{Z}_r\};$$

2.2 Active System

State space model of the active suspension system is represented in (9) and (10).

$$\dot{x}(t) = Ax(t) + Bu(t) + Lw(t) \tag{9}$$

$$y(t) = Cx(t) + Du(t) \tag{10}$$

Let state vectors,

$$x(t) = [x_1 \ x_2 \ x_3 \ x_4]^T$$

$$\dot{x}_1 = \dot{Z}_s - \dot{Z}_u; \quad \dot{x}_2 = \ddot{Z}_s; \quad \dot{x}_3 = \dot{Z}_u - \dot{Z}_r; \quad \dot{x}_4 = \ddot{Z}_u;$$

$$A = \begin{bmatrix} 0 & 1 & 0 & -1 \\ \frac{-K_s}{M_s} & \frac{-B_s}{M_s} & 0 & \frac{B_s}{M_s} \\ 0 & 0 & 0 & 1 \\ \frac{K_s}{M_u} & \frac{B_s}{M_u} & \frac{-K_t}{M_u} & \frac{-B_s}{M_u} \end{bmatrix} \quad B = \begin{bmatrix} 0 \\ \frac{1}{M_s} \\ 0 \\ \frac{-1}{M_u} \end{bmatrix} \quad L = \begin{bmatrix} 0 \\ 0 \\ -1 \\ 0 \end{bmatrix}$$

$$C = I_6; \quad D = (0)_{1X6};$$

$$u(t) = \{F\}; \quad w(t) = \{\dot{Z}_r\};$$

3 Controller Design

Performance of the suspension system is improved by using active suspension. In active suspension, the system response is feedback to the controller which converts the open-loop system to closed loop. With the use of this closed-loop controller, suspension performs better than the passive by minimizing the oscillations and settling time of the suspension responses. In this work, two different controllers are designed and compared to achieve the better performance of the suspension system.

3.1 PID

It is a combination of three different controllers, namely proportional, integral, and derivative. It is a closed-loop feedback controller. The proportional controller is used to reduce the rise time of the system response during the transient period, but at the same time, it increases steady-state error. Steady-state error of the system is reduced by introducing integral controller to the system, but it leads the system to oscillatory response. This makes the system unstable. The aforementioned oscillatory response will be reduced by implementing a derivative controller to the above-mentioned controller combination. By reducing the peak amplitude, steady-state error, and settling time of the suspension system, the performance of the suspension system is improved. The mathematical expression for PID controller is given in (11).

$$u(t) = K_p e(t) + \frac{K_p}{T_i} \int_0^T e(t)dt + K_p T_d \frac{de(t)}{dt} \tag{11}$$

In this work, PID controller is designed using Zeigler–Nicholas tuning method. Proportional gain—K_p of the system is calculated by using critical gain K_{cr}. Critical gain value of the system is calculated based on the closed-loop system subjected to unit step response. It is the gain value at which the system sustained its oscillation, and the respective period is called as critical time period P_{cr}. Beyond this gain

Table 1 Zeigler–Nicholas tuning rules

Controller	K_p	T_i	T_d
P	0.5 K_{cr}	∞	0
PI	0.45 K_{cr}	0.83 P_{cr}	0
PID	0.6 K_{cr}	0.5 P_{cr}	0.125 P_{cr}
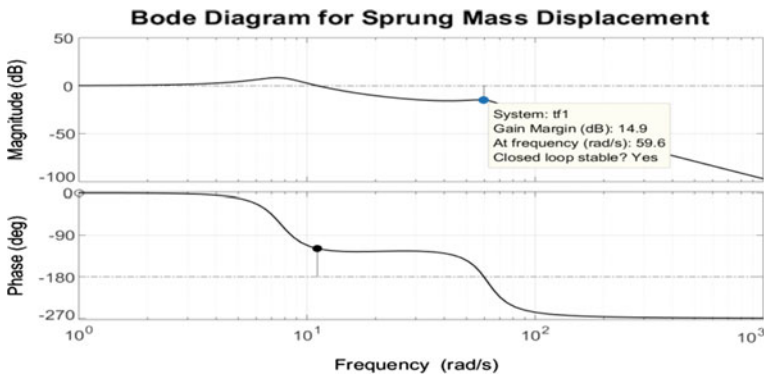
Fig. 3 Bode plot for passive suspension system

value, system becomes unstable. The integral time constant—T_i and derivative time constant—T_d are determined from Zeigler–Nicholas tuning rules as shown in Table 1.

The gain margin of the passive system is obtained as 14.9 dB from Fig. 3.

By using Bode plot, gain margin of the system is determined. Simultaneously critical gain K_{cr} value of the system which is equal to 5.56 is calculated from (12), and corresponding P_{cr} value is obtained as 0.103 s from Fig. 4.

$$20 \log K_{cr} = 14.9 \tag{12}$$

3.2 LQR

In this portion, LQR controller is considered to analyze the performance of the active suspension system. LQR is a full state feedback controller which provides an optimal solution to the system by reducing the performance index (J)

$$J = \frac{1}{2} \int_0^\infty \left(x^T Q x + u^T R u \right) dt \tag{13}$$
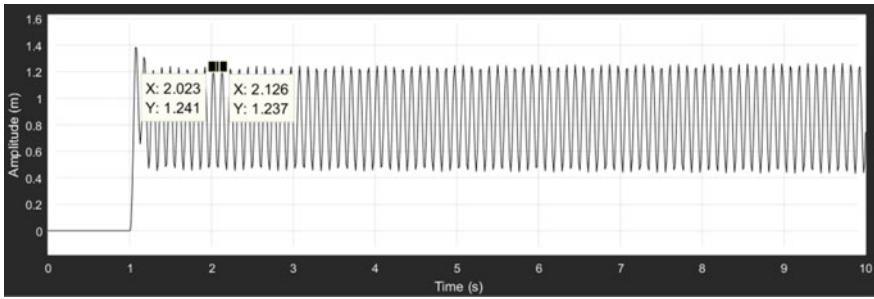
Fig. 4 Unity step response of the closed-loop system with $K_{cr} = 5.56$

Table 2 LQR controller parameters

Cost function	Parameters
Q	$\begin{bmatrix} 200 & 0 & 0 & 0 \\ 0 & 250 & 0 & 0 \\ 0 & 0 & 5 & 0 \\ 0 & 0 & 0 & 0.01 \end{bmatrix}$
R	0.01

The control law which used to minimize the above cost function (13) is

$$u = -Kx \tag{14}$$

where K is LQR gain and is given by

$$K = R^{-1}B^{\mathrm{T}}P \tag{15}$$

The value of P is calculated by solving algebraic Riccati equation as given as

$$A^{\mathrm{T}}P + PA + Q - PBR^{-1}B^{\mathrm{T}}P = 0 \tag{16}$$

In Eq. (13), the term Q is considered as state weighting factor which is a positive semi-definite matrix, while the term R is considered as input weighting factor which is a positive definite matrix. The values of Q and R which are used in this LQR controller are given in Table 2.

4 Results and Discussion

This portion is mainly consisted of with the performance of the suspension system excited with single bump road input. Road input has been modelled as shown in Fig. 5. The frequency of sinusoidal bump is 8 Hz, which has been characterized by,

$$r(t) = \frac{a(1-\cos(8\pi t))}{2}, \quad \text{for } 0.5 \leq t \geq 0.75$$
$$r(t) = 0, \qquad \text{otherwise}$$

where $a = 0.10$ (road bump height 10 cm) [9].

Suspension performance is analyzed by using the parameters which are given in Table 3. This work is mainly concentrated on ride comfort of the vehicle. So, accordingly sprung mass acceleration performance is carried out with different controller techniques.

Based on the road input and the vehicle modelled using aforementioned parameters, the sprung mass acceleration of the passive system is compared with PID-controlled active system and is shown in Fig. 6. Similarly, the performance of the passive suspension is compared with the LQR-controlled active system, and the system response is shown in Fig. 7.

From Fig. 6, it is clearly understood that the response of the sprung mass acceleration of the passive suspension system is reduced by implementing PID
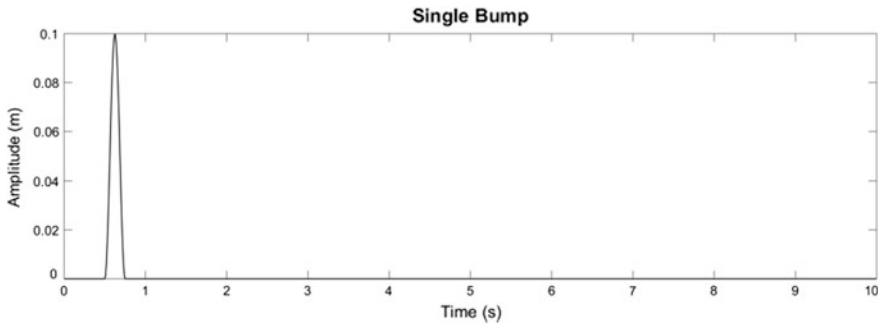
Fig. 5 Single bump road input

Table 3 2 DOF quarter car model parameters [1]

Description	Parameter	Quantities
Sprung mass	M_s	250 kg
Unsprung mass	M_u	45 kg
Suspension stiffness	K_s	16,000 N/m
Tire stiffness	K_t	160,000 N/m
Suspension damping coefficient	B_s	1000 Ns/m
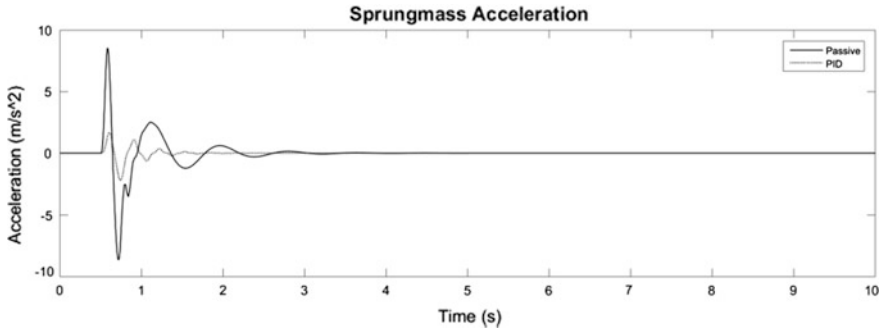
Fig. 6 Sprung mass acceleration for passive and PID-controlled suspension system
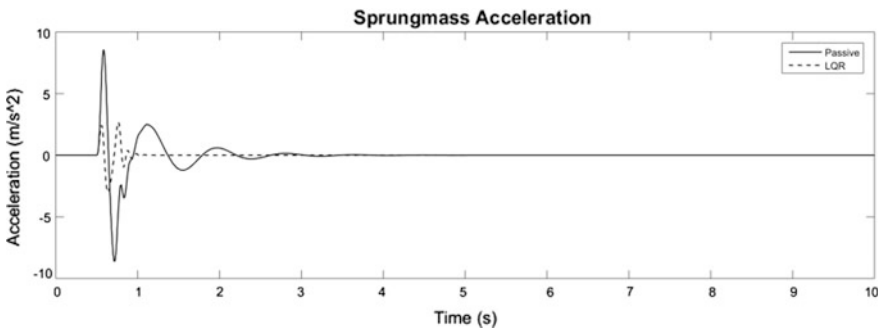
Fig. 7 Sprung mass acceleration for passive and LQR-controlled suspension system

Table 4 Time domain specifications of the sprung mass acceleration response using passive, PID, and LQR suspension systems

Specifications	Passive	PID	LQR	% of reduction in passive response with PID-based active system	% of reduction in passive response with LQR-based active system
Peak value	8.541	1.659	2.683	80.58	68.58
RMS	2.943	0.6262	1.037	78.72	64.76

controller in the system. The RMS and peak value of the passive and PID-used active systems are mentioned in Table 4.

From Fig. 7, it is clearly identified that the response of the sprung mass acceleration of the passive suspension is reduced by introducing LQR-based active suspension system in the vehicle model. Similarly, the peak value and RMS of the two are mentioned in Table 4.

From Table 4, it is observed that the peak value and RMS of the passive suspension are reduced by using active suspension system. The peak value of the

sprung mass acceleration of the passive suspension system is reduced to 80.58% by PID-based active suspension, and for LQR it is reduced to 68.58%. The ride comfort of the suspension system is quantified by using the RMS value. The RMS value of the sprung mass acceleration of the passive system is 2.943 which is 78.72% higher than the suspension using PID, and while comparing with LQR, it is about 64.76% lower than the passive system.

5   Conclusion

In this paper, ride comfort of the passive suspension system is compared with LQR-based active suspension and PID-based active system. PID controller gain value is obtained using Zeigler–Nicholas tuning method. LQR gain value is optimized by fixing the Q and R values. Then the performance index of the suspension system is minimized using LQR controller. Ride comfort of the suspension system is quantified with respect to the sprung mass acceleration RMS value. From the results and discussion, the RMS value of the PID is comparatively minimum than the LQR and passive. So, it is concluded that ride comfort of the suspension system is improved in a much better way by using the PID-controlled suspension than the LQR-based control system for the given road input. This work can be further extended for simulation of different road profiles with different controllers.

References

1. Rajamani, R.: Vehicle Dynamics and Control. Springer, New York (2012)
2. Senthil Kumar, M., & Vijayarangan, S.: Design of LQR controller for active suspension system. Indian J. Eng. Mater. Sci. **13**, 173–179 (2006)
3. Sam, Y.M., et al.: LQR Controller for Active Car Suspension. IEEE (2000)
4. Agharkakli, A., et al.: Simulation and analysis of passive and active suspension system using quarter car model for different road profile. Int. J. Eng. Trends Technol. **3**(5) (2012)
5. Tandel, Anand, et al.: Modeling, analysis and PID controller implementation on double wishbone suspension using SimMechanics and Simulink. Procedia Eng. **97**, 1274–1281 (2014)
6. Erol, B., Delibasi, A.: Proportional integral derivative type H infinity controller for quarter car active suspension system. J. Vib. Control (2016)
7. Nusantoro, G.D., Priyandoko, G.: PID state feedback controller of a quarter car active suspension system. J. Basic Appl. Sci. Res. **1** (2011)
8. Kumar, M.S.: Development of active suspension system for automobiles using PID controller. In: Proceedings of the World Congress on Engineering 2008, vol. II (2008)
9. Sam, Y.M., Osman, H.S.O., Ghani, M.R.A.: A class of proportional-integral sliding ode control with application to active suspension system. Syst. Control Lett. **51**, 217–223 (2004)

Hot Forging Characteristics of Powder Metallurgy Duplex Stainless Steels Developed from 304L and 430L Pre-alloyed Powders

C. Rajkumar, R. Mariappan, S. Jayavelu, M. Arun Prasad and Ankam Vinod Kumar

1 Introduction

In recent years, a need for duplex stainless steel is increasing day by day. So a thrust is developed in industry persons and academic researchers for developing duplex stainless steels. Properties such as corrosion resistance, mechanical properties, and stubbornness have an ideal stability in duplex stainless steels [1]. The above properties are bringing down in the austenitic and ferrite stainless steels.

Duplex stainless steel can be produced by several modes. However, manufacturing of duplex stainless steel by using powder metallurgy process is economic and near net shape. The first mode of attaining duplex structure was made by using pre-alloyed powders [2]. The second approach was mixing elemental powders Chromium, Nickel, Molybdenum with austenitic, and ferrite powders in an appropriate ratio to get duplex microstructure [3]. Typical applications of powder metallurgy duplex stainless steel are offshore, marine, nuclear applications, and the tone wheels for anti-lock braking system [4].

Garcia et al. (2007) studied pitting corrosion behavior of powder metallurgy austenitic stainless steels sintered in nitrogen-hydrogen atmosphere. Powder metallurgy 304L and 316L stainless steels have been compacted at 400, 600, and 800 MPa and sintered in vacuum and nitrogen-hydrogen atmosphere. They determined that pitting resistance is higher for powder metallurgy 316L austenitic [5].

The sintering atmosphere plays an indispensable role on structure and properties of Austeno-ferritic stainless steels. The densification of stainless steels sintered in N_2 environment is 8–14%. The microstructure of DSS sintered in N_2 atmosphere showed the presence of Cr_2N, apart from duplex structure and lead to increase in tensile strength and lower elongation was reported by Mariappan et al.

C. Rajkumar (✉) · R. Mariappan · S. Jayavelu · M. Arun Prasad · A. V. Kumar
Department of Mechanical Engineering, Vel Tech Rangarajan
Dr. Sagunthala R&D Institute of Science and Technology, Avadi, Chennai, India
e-mail: crajkumar77@rediffmail.com

(2009) [6]. Apart from sintering atmosphere, sintering time also influences the traits of powder metallurgy duplex stainless steels. Brytan et al. (2009) observed that duplex stainless steels sintered for longer duration of time, i.e., for 4 h enhanced the tensile strength, density, toughness, and influence strength [7]. The sinter cooling rate influences the microstructure and mechanical properties of powder metallurgy austenitic, ferrite, and duplex stainless steels. Duplex stainless steels subjected to furnace cooling consist of austenite, ferrite grains, and mixed constituent. On the other hand in case of water cooling, duplex stainless steels have austenite, ferrite island and rich in martensitic [8]. The slow cooling rate causes the formation of intermetallic phase and leads to decrease in mechanical properties [9].

Parts made by sintering process will always have pores. So the density values of sintered samples at all times are decreased in contrast to the theoretical density. Pores present in the sintered part may be the initiator of crack throughout the application. Hot forging is the suitable metal forming process and having advantages such as low cost, achieving same undeformed structure, high density, attaining good toughness, and saving material [10]. The disadvantages of hot forging are viable of reacting between the atmosphere and component, and need of subsequent heat treatment process. From the careful study of literature survey, many investigators have made the contributions in cold forging process and find the advantages such as attainable dimensional accuracy, incredible surface quality, and weight of the workpiece equals the ultimate weight of the cold forged component [11,12].

In the present research work, two different compacts of duplex stainless steel were prepared from 304L, 310L, and 430L blended with elemental powders such as chromium, molybdenum, nickel, and manganese. The samples underwent compaction and sintering at a temperature of 1300 ± 100 °C. Forging operation is to be carried out at 1150 °C. The characterization techniques such as microstructure analysis, hardness measurement, and ferrite count were done for the forged duplex stainless steel.

2 Experimental Procedure

Water atomized powders such as 304L, 310L, and 430L were procured from M/s Hoganas India Ltd. These powders were properly combined with chromium, nickel, molybdenum, and manganese to get two compositions, i.e., DSS Sample 1 and DSS Sample 2. The chemical compositions of 304L, 310L, and 430L powders are given in Table 1.

Table 1 Chemical composition of pre-alloyed powders

Powder grade	Cr	C	Ni	Si	Mn	Mo	Fe	Flow rate/50 g (s)
304L	17	0.03	9	0.6	2.00	_	Bal	25.4
310L	24	0.02	10	0.30	2.00	0.30	Bal	25.4
430L	16.6	0.02	_	1.20	0.10	_	Bal	25.4

Table 2 Composition of duplex stainless steel powder mix

Composition	Elements %									
	Cr	C	Ni	Si	Mn	Mo	Fe	N	Ni_{eq}	Cr_{eq}
DSS Sample 1	21	0.02	5	0.846	2	3	Bal	0.1	6.6	25.29
DSS Sample 2	21	0.02	9	0.705	2	3	Bal	–	10.56	25.05
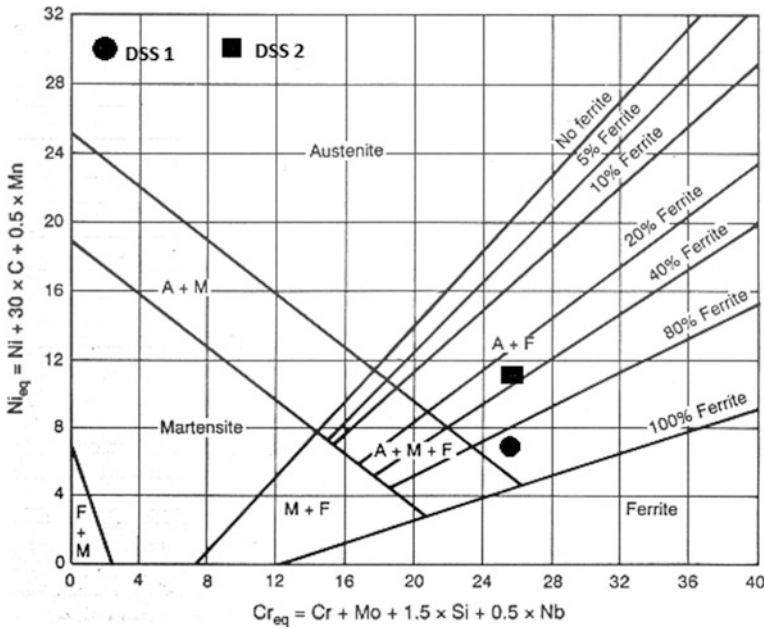
Fig. 1 Schaffler's diagram

The chemical compositions of two different duplex stainless steel samples having nickel and chromium equivalent are shown in Table 2. The Schaffler diagram (Fig. 1) was used for preparing powder mix. Even though, Schaffler's diagram has been used for welding. In theoretical point of view the diagram can be used for powder metallurgy stainless compositions also. The nickel and chromium equivalent can be calculated by using the formula (Ni_{eq} = %Ni + 30% C + 0.5% Mn) and (Cr_{eq} = % Cr + % Mo + 1.5% Si + 0.5% Nb) and located in schaffler's diagram. Green compacts of size having diameter 30 and 12 mm height were compacted at a pressure of 560 ± 10 MPa. The compacts were sintered at a temperature of 1300 ± 10 °C in vacuum and hydrogen atmosphere for 2 h. The sintered samples were kept in an electrical furnace for 2 h and underwent metal forming operation at a temperature of 1150 °C followed by water quenching.

3   Results and Discussions

3.1   *Density of Duplex Stainless Steel*

The density of the green compacts was evaluated by using mass and physical dimensions. Lump of the compacts and external dimensions were used to find out the sintered density. Lever arm rule is used to find the theoretical density value of duplex stainless steels. From the careful review of experimental outcomes, sintering surrounding plays a vital role on sintered density. Figure 2 shows the density values of two sintered cum forged duplex stainless steels. The green density of DSS1 is 6.3 g/cc, and its sintered density is 6.92 g/cc, i.e., 91% of theoretical density. The sintered density of DSS 1 is raised 8% from green density. While the green density value of DSS 2 is 6.1 g/cc and sintered density value is 7.218 g/cc, i.e., 96% of theoretical density. The sintered density is enhanced 15% from green density. The sintered duplex stainless steel Sample 2 shows better density than DSS 1. This is due to the reason that duplex stainless steel sintered in vacuum atmosphere prevented the interaction of air with the interior particle leading to densification, i.e., increasing in packing density. On the other hand, duplex stainless steels sintered in hydrogen atmosphere exhibited minimum densification because gas attracts the inner part of the pores will prevent densification.

3.2   *Microstructure*

Before samples underwent microstructural studies, they should be made smooth and glossy, etched with Beraha's etchant. Energy dispersive spectrum with the help of scanning electron microscope is carefully cut from the part of austenite and ferrite phases.
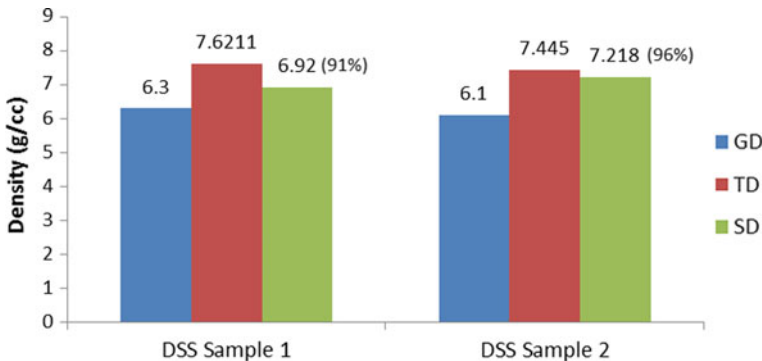
Fig. 2 Density values of DSS sintered in vacuum, hydrogen atmosphere

Fig. 3 Microstructure of
DSS 1
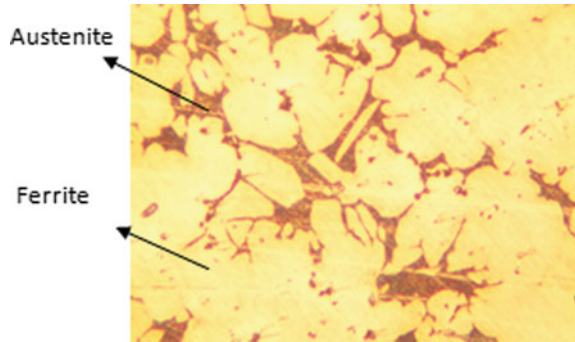
Fig. 4 Microstructure of
DSS 2
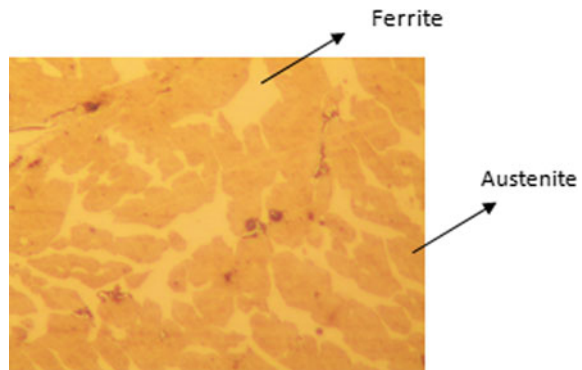
The microstructures of duplex stainless steels Sample 1 and Sample 2 are shown in Figs. 3 and 4, respectively. From the microstructure, it is observed that duplex stainless steel sintered in vacuum (DSS Sample 2) shows clear fine grains of austenite and ferrite and confirms the duplex structure. The microstructure also shows the low porosity level for vacuum sintered duplex stainless steels than hydrogen atmosphere. The cause for this is no gas is trapped inside the pores during sintering [13].

But the duplex stainless steels sintered in hydrogen atmosphere (DSS Sample 1) also consist of austenite and ferrite grains but in larger size.

3.3 Tensile Strength and Hardness Evaluation

Tensile strength of forged duplex stainless steels was determined by using Hounsfield Tensometer. Rockwell hardness tester (Model VV 3000 J) was used to find the hardness of forged duplex stainless steels. The tensile strength and Rockwell hardness values of duplex stainless steel for samples DSS 1 and DSS 2 were evaluated by using Hounsfield Tensometer and Rockwell hardness tester.

Table 3 Mechanical properties of duplex stainless steels sintered in various atmospheres

Duplex stainless steels composition	Sintering environment	Tensile strength	Rockwell hardness
DSS Sample 1	Hydrogen	685 MPa	60 HRC
DSS Sample 2	Vacuum	723 MPa	62 HRC

The tensile strength and Rockwell hardness value of forged DSS Sample 2 were more than DSS Sample 1. This is due to the fact that the density of duplex stainless steel of Sample 2 was more than duplex stainless steel of Sample 1. Apart from the above reason, duplex stainless steels sintered in reducing environment were not able to take away the surface of oxides fully. The perfect phase balance was achieved for duplex stainless steels sintered in vacuum environment and exhibited better tensile strength. Table 3 shows the tensile strength and hardness values of duplex stainless steel Sample 1 and Sample 2. Highest tensile strength of 723 MPa has been obtained for vacuum sintered duplex stainless Steels.

4   Conclusions

The sintered stainless steels in vacuum environment show better densification than steels sintered in hydrogen environment.

DSS 2 sintered in the presence of partial vacuum shows higher tensile strength of 723 MPa and hardness value of about 62 HRC than DSS 1.

Duplex stainless steel sintered in vacuum (DSS Sample 2) shows clear fine grains of austenite and ferrite and confirms the duplex structure.

The microstructure also shows the low porosity level for vacuum sintered duplex stainless steels than hydrogen atmosphere. The cause for this is no gas is trapped inside the pores during sintering.

References

1. Datta, P., Upadhaya, G.S.: Sintered duplex stainless steels from premixes of 316L and 434L powders. Mater. Chem. Phys. **67**, 234–242 (2001)
2. Munez, C.J., Utrilla, M.V., Urena, A.: Effect of temperature on sintered austeno-ferritic stainless steel microstructure. J. Alloy. Compd. **463**(1-2), 552–558 (2008)
3. Smuk, O.: Microstructures and properties of modern P/M duplex stainless steels. Doctoral thesis, Department of Material Science Engineering, Royal Institute of Technology, Sweden, pp. 1–5 (2004)
4. Velasco, F., Bautista, A., González-Centeno, A.: High-temperature oxidation and aqueous corrosion performance of ferritic, vacuum-sintered stainless steels prealloyed with Si. Corros. Sci. **51**(1), 21–27 (2009)

5. García, C., Martín, F., de Tiedra, P., Cambronero, L.G.: Pitting corrosion behaviour of PM austenitic stainless steels sintered in nitrogen-hydrogen atmosphere. Corros. Sci **49**(4), 1718–1736 (2007)
6. Mariappan, R., Kumaran, S., Rao, T.S.: Effect of sintering atmosphere on structure and properties of austeno-ferritic stainless steels. Mater. Sci. Eng. A **517**(1–2), 328–333 (2009)
7. Brytan, Z., Dobrzanski, L.A., Actis Grande, M., Rosso, M.: The influence of sintering time on the properties of PM duplex stainless steel. J. Achiev. Mater. Manuf. Eng **37**(2), 387–396 (2009)
8. Martín, F., et al.: Influence of sinter-cooling rate on the mechanical properties of powder metallurgy austenitic, ferritic, and duplex stainless steels sintered in vacuum. Mater. Sci. Eng. A **642**, 360–365 (2015)
9. Brytan, Z., et al.: Stainless steels sintered form the mixture of prealloyed stainless steel and alloying element powders. Mater. Sci. Forum **672**. Trans Tech Publications, (2011)
10. Abdel-Rahman, M., El-Sheikh, M.N.: Workability in forging of powder metallurgy compacts. J. Mater. Process. Technol. **54**(1–4), 97–102 (1995)
11. Huppmann, W.J., Brown, G.T.: The steel powder-forging process—a general review. Powder Metall. **21**(2), 105–114 (1978)
12. Das, J., et al.: Hardness and tensile properties of Fe–P based alloys made through powder forging technique. Mater. Sci. Eng. A **479** (1–2), 164–170 (2008)
13. Ji, C.H., et al.: Sintering study of 316L stainless steel metal injection molding parts using Taguchi method: final density. Mater Sci Engineering. A **311** (1–2), 74–82 (2001)

Machinability Studies of TiAlN-/AlCrN-Coated and Uncoated Tungsten Carbide Tools on Turning EN25 Alloy Steel

T. Sampath Kumar, A. Vinoth Jebaraj, K. Sivakumar and P. Mathivanan

1 Introduction

Nowadays tool manufacturing industries are very intense in developing new cutting tools materials and coatings. Generally, machinability of the cutting tool material depends on surface properties such as hot strength, wear behavior, surface hardness, and fracture toughness. The tungsten carbide (WC) tools are commonly used for machining hard materials such as alloy steels [1] and high-speed steels [2]. But the tool wear reported is higher in WC tools while machining hard materials. So, the development of suitable coating technique and identifying suitable coating material are the prime challenges faced by the tool developers.

The coated tools have shown advantages such as greater wear resistance and lesser heat generation, even at exciting cutting conditions. The various monolayer coatings such as TiN, TiCN, TiC, and Al_2O_3 [3] are deposited on WC cutting tools, in order to enhance the tool surface hardness, and thereby increasing the tool life and improving the surface finish of the work material. However, the high-speed machining is performed in industries for achieving better surface quality and optimum material removal rate [4]. In recent years, the turning of hard materials has been done using TiAlN-coated cutting tools [5]. These hard coatings can withstand heavy stresses during operation. Further, AlTiN-based coatings form a protective alumina-like tribo-film during cutting operation and prevent intensive sticking of workpiece material with coating at higher speed cutting condition [6]. The uncoated carbide, ceramic, and CrTiAlN nanostructured composite coated tools were used for

T. Sampath Kumar (✉) · A. Vinoth Jebaraj
School of Mechanical Engineering, Vellore Institute of Technology,
VIT University, Vellore, India
e-mail: sampathtpp@gmail.com

K. Sivakumar · P. Mathivanan
Department of Mechanical Engineering, Valliammai Engineering College,
SRM Nagar, Kattankulathur, India

machining of heavy tungsten alloys. The CrTiAlN coating has shown better tool life than other tools [7]. The hard coatings such as TiAlN, TiCN, TiN (PVD coatings) have shown increase in tool life and productivity [8]. Maan [9] has conducted experiments on AISI 1045 steel workpiece using TiN-, TiN-/TiC-, and TiN-/Al_2O_3-/TiC-coated tools and reported that the better surface quality was obtained when the tool cutting speed was high with minimum feed rate as well as low depth of cut. Among the tested cutting tools, TiN-/TiC-coated tool has provided better surface quality. Ali [10] has developed the regression model and conducted the experiments using PVD-coated ceramic tools for turning of AISI 8660 hardened alloy steel. Surface roughness analysis showed that the feed rate was a dominant factor when compared to cutting speed, depth of cut, and nose radius on the surface roughness. In the present study, TiAlN/AlCrN coating was done on the WC tool and its machining performance on EN25 alloy steel workpiece has been investigated and compared with uncoated WC tool. Various tests have been performed using three levels of cutting speed, feed rate, and depth of cut on the coated and uncoated WC tools.

2 Experimental Details

The experiments were conducted using the coated inserts and EN25 alloy steel as workpiece material in a conventional lathe machine with dry environment. The experiments were planned based on the L_9 orthogonal array using Taguchi method. The samples were extracted from the EN25 alloy steel rods with a diameter of 100 mm and a length of 500 mm. The cutting tool nomenclature has triangular insert of 60°, clearance angle of 7°, insert grade of K10, and a corner radius 0.8 mm. The TiAlN/AlCrN coating was developed on WC inserts using PVD process. The coated tool has a surface hardness of 33 GPa and an adhesive strength of 42 N. Fine grains between 30 and 50 nm and the dense structure were formed during the coating process which led to increase in surface hardness. The surface roughness value (120 nm) for the TiAlN/AlCrN bilayer coating was lesser due to less surface irregularities and pits. Therefore, the coating characteristic for TiAlN/AlCrN bilayer coating was better to carry out the experimental work. Turning experiments were carried out at three different levels using the design of experiments. The turning process was performed for a length of 100 mm using both coated and uncoated tools. The design of experiments for the main factors and levels is shown in Table 1. The L_9 orthogonal array was used for the investigation

Table 1 Design of experiment for the main factors and levels

Main factors	Levels		
	1	2	3
Cutting speed (m/min)	50	100	150
Feed rate (mm/rev)	0.118	0.314	0.457
Depth of cut (mm)	0.3	0.7	1.0

Table 2 L_9 orthogonal array

Experiment trails	Cutting speed (m/min)	Feed rate (mm/rev)	Depth of cut (mm)
L1	1	1	1
L2	1	2	2
L3	1	3	3
L4	2	1	2
L5	2	2	3
L6	2	3	1
L7	3	1	3
L8	3	2	1
L9	3	3	2

and is shown in Table 2. The experiment trails were conducted to find the optimized turning parameters by having constraints such as minimum tool wear and minimum surface roughness from the output values. The tool maker's microscope was used to measure the tool wear on the flank face. Further, surface roughness parameters were measured using 2D Mahr's surface roughness tester. The turning parameters were analyzed using Minitab 15 software for both tool life and roughness parameters.

3   Result and Discussions

3.1   Tool Wear Analysis

Figure 1a–d shows the optical images of minimum and maximum tool flank wear images observed on TiAlN-/AlCrN-coated and uncoated tools, respectively. The flank wear was found to be minimum for the coated tool. It was around 0.035 mm (L8 trail) for the coated tool and 0.09 mm (L5 trail) for the uncoated tool, respectively. The maximum amount of flank wear measured for the coated tool was 0.315 mm (L2 trail) and for the uncoated tool was 0.57 mm (L7 trail), respectively. The tool flank wear graphs obtained from the L_9 orthogonal array trials for TiAlN-/AlCrN-coated tools and uncoated tools are shown in Fig. 2. The reduction in tool wear for the TiAlN-/AlCrN-coated tool was measured at L8 trail (i.e., V_3, f_2, d_1). The minimum tool wear for the uncoated tool was measured at L5 trail (i.e., V_2, f_2, d_3). The built-up edge adhered with the tool during the chip movement. The built-up edge is observed in L2 (i.e., $V_1 f_2 d_2$), L3 (i.e., $V_1 f_3 d_3$), and L5 (i.e., $V_2 f_2 d_3$) experimental trails for TiAlN-/AlCrN-coated tools. But, the built-up edge is evident at all the experimental trails in the uncoated tools. The formation of built-up edge increases the cutting forces and significantly affects the surface finish of the machined workpiece [11].
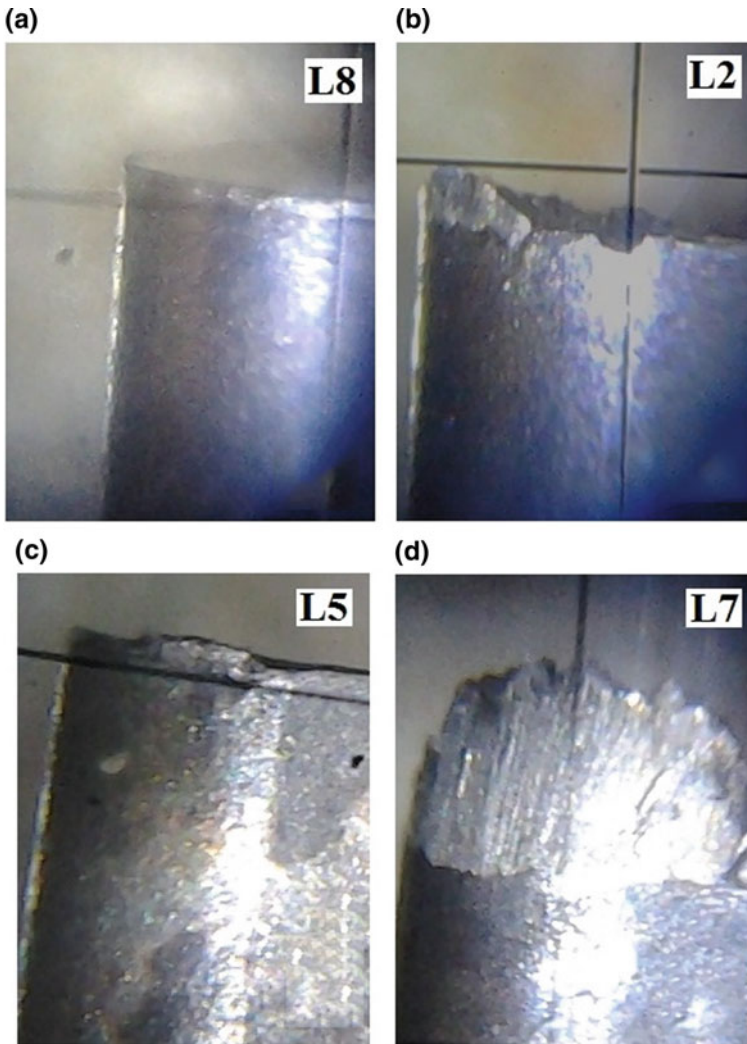
Fig. 1 Minimum and maximum tool flank wear images obtained from the L_9 orthogonal array trials for TiAlN-/AlCrN-coated tools (**a**, **b**) and uncoated tools (**c**, **d**)

3.2 Surface Roughness Analysis

From the output results obtained, the minimum value of surface roughness parameter (Ra) observed for the coated tool as 1.43 μm and for the uncoated tool as 2.65 μm. The maximum value of surface roughness parameters (Ra) for the coated tool and uncoated tool is 4.15 and 5.75 μm, respectively. The surface roughness graphs obtained from the L_9 orthogonal array trials for TiAlN-/AlCrN-coated tools and uncoated tools are shown in Fig. 3. The optimized surface roughness for the
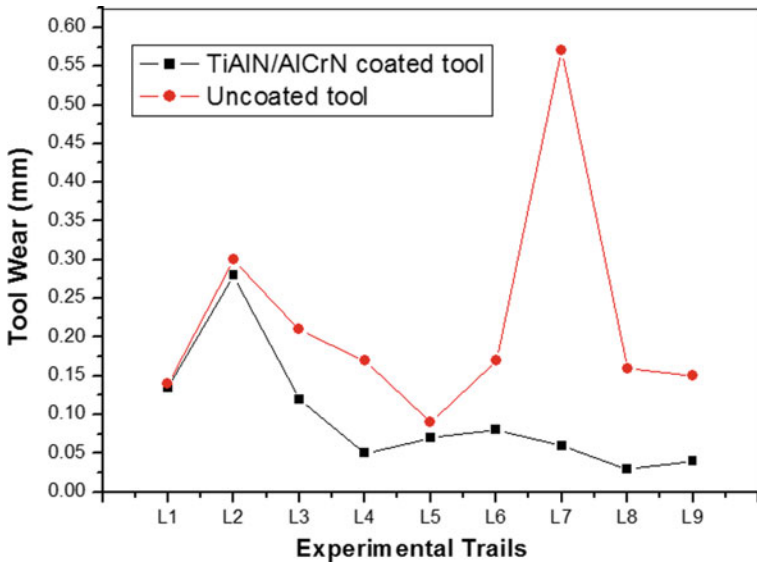
Fig. 2 Tool flank wear graphs obtained from the L_9 orthogonal array trials for TiAlN-/AlCrN-coated tools and uncoated tools
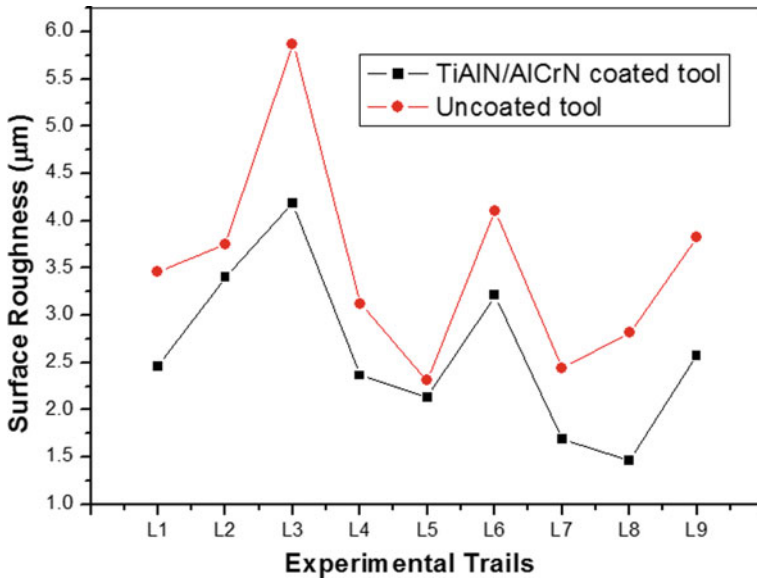
Fig. 3 Surface roughness graphs obtained from the L_9 orthogonal array trials for TiAlN-/AlCrN-coated tools and uncoated tools

coated tool was obtained at L8 trail (i.e., V_3, f_2, d_1), and the same for uncoated tool was obtained at L5 trail (i.e., V_2, f_2, d_3). Normally, higher feed rate results in more surface roughness. In general, the large nose radius tool gives better surface finish. Existing literature shows that the surface finish of the workpiece in turning process can be influenced by various factors such as cutting speed, feed rate, depth of cut, workpiece hardness, cutting edge angle, tool nose radius, workpiece, and tool material [12]. In the present work, both lower cutting speed as well as moderate cutting speed results in higher surface roughness with increasing feed rate. But the surface roughness decreases at higher cutting speeds, with increasing feed rate and lower depth of cut.

3.3 The Taguchi Method Evaluation Results

Main effect and S/N analysis for tool wear in TiAlN-/AlCrN-coated and uncoated tools

The main effect strategies were implemented to find the optimized design conditions to obtain better cutting tool characteristics. Table 3 indicates the response tables for TiAlN-/AlCrN-coated tool wear of signal-to-noise ratio and mean. The results of Taguchi method revealed that the cutting speed has played a major role in deciding the tool wear, when compared to feed rate and depth of cut. The response table reveals feed rate has moderate effect on the tool wear and the depth of cut has less significance on tool wear for the coated tool [13].

Table 4 indicates the response table for uncoated tool wears of signal-to-noise ratio and mean. The cutting speed is the highly responsible factor for the tool wear, when compared to feed rate and depth of cut for the uncoated WC tool. The feed rate is the moderate responsible factor, but the depth of cut is the least responsible factor for the tool wear in uncoated tool [14].

Table 3 Response table for tool wear in TiAlN-/AlCrN-coated tools

	Levels	Cutting speed	Feed rate	Depth of cut
S/N values	1	13.75	22.62	22.43
	2	23.69	20.46	22.26
	3	27.62	21.98	20.36
	Delta	13.86	2.16	2.07
Mean values	1	0.21667	0.08167	0.08500
	2	0.06667	0.13833	0.12833
	3	0.04333	0.10667	0.11333
	Delta	0.17333	0.05667	0.04333
	Rank	1	2	3

Table 4 Response table for tool wear in uncoated tools

	Levels	Cutting speed	Feed rate	Depth of cut
S/N values	1	15.52	12.45	16.13
	2	17.23	15.96	14.31
	3	12.43	16.76	14.74
	Delta	4.81	4.31	1.82
Mean values	1	0.1800	0.2933	0.1567
	2	0.1433	0.1767	0.2000
	3	0.2933	0.1467	0.2600
	Delta	0.1500	0.1467	0.1033
	Rank	1	2	3

Table 5 Response table for surface roughness of workpiece in TiAlN-/AlCrN-coated tools

	Levels	Cutting speed	Feed rate	Depth of cut
S/N values	1	−10.302	−6.622	−7.090
	2	−8.066	−6.847	−8.778
	3	−5.362	−10.261	−7.863
	Delta	4.941	3.639	1.688
Mean values	1	3.351	2.173	2.379
	2	2.571	2.335	2.782
	3	1.910	3.324	2.671
	Delta	1.442	1.151	0.402
	Rank	1	2	3

Main effect and S/N analysis for surface roughness of workpiece in TiAlN-/AlCrN-coated tools and uncoated tools

Table 5 indicates the response table for roughness parameters of the work material EN25 steel in coated WC tools of signal-to-noise ratio and mean. The turning speed has more influence on the surface roughness than the feed rate and depth of cut. The depth of cut has the least dominating factor, and the feed rate has the moderate dominating factor for surface roughness in TiAlN-/AlCrN-coated tool [15].

Table 6 indicates the response table for roughness parameters of the work material in uncoated WC tools of signal-to-noise ratio and mean. For the uncoated carbide tool, feed rate has more effect on the surface roughness parameters than the cutting speed and depth of cut. Further, uncoated carbide tool exhibited less significant effect on the depth of cut, and the cutting speed has moderate effect on the surface roughness. The findings observed in the present work are similar to the existing literature which shows the increasing trend of surface roughness when the feed rate increases [16].

Table 6 Response table for surface roughness of workpiece in uncoated tools

	Levels	Cutting speed	Feed rate	Depth of cut
S/N values	1	−12.550	−9.478	−10.682
	2	−9.809	−9.239	−11.007
	3	−9.461	−13.104	−10.130
	Delta	3.088	3.865	0.877
Mean values	1	4.362	3.009	3.462
	2	3.179	2.955	3.566
	3	3.026	4.603	3.541
	Delta	1.336	1.648	0.104
	Rank	2	1	3

4 Conclusion

In the present investigation, the machinability of EN25 alloy steel was studied using TiAlN-/AlCrN-coated tools and the results are compared with the uncoated cemented carbide tools. The conclusions are as follows:

The minimum flank wear measured in the coated WC tool and uncoated tool was 0.035 and 0.09 mm, respectively. The reduction in tool wear in coated tool was observed at the cutting speed $(V_3) = 150$ m/min, feed rate $(f_2) = 0.314$ mm/rev, and depth of cut $(d_1) = 0.3$ mm. From the main effect analysis using S/N ratio and mean, the variable cutting speed has played a predominant role and highly influenced in the tool wear for both coated and uncoated WC tools. The minimum flank wear attributes due to the high hardness of the coating.

The minimum surface roughness measured in the workpiece was 1.43 µm for the coated tool and 2.65 µm for the uncoated tool. The optimum surface roughness was measured at $V_3 = 150$ m/min, $f_2 = 0.314$ mm/rev, and $d_1 = 0.3$ mm for the coated tool. From the main effect analysis using S/N ratio and mean, it was found that the cutting speed and feed rate are highly dominated in the resulting roughness parameters for the coated and uncoated tool. The coating minimizes the friction between the tool–workpiece interface, which results in minimum surface roughness.

The optimal cutting condition is obtained when $V = 150$ m/min, $f = 0.314$ mm/rev, and $d = 0.3$ mm, which resulted in better roughness parameters and maximum tool life for the coated tool. The optimal cutting condition is obtained when $V = 100$ m/min, $f = 0.314$ mm/rev, and $d = 1.0$ mm, which resulted in better surface finish and minimum tool wear for uncoated tool.

References

1. Dhiman, S., Sehgal, R., Sharma, S.K., Sharma, V.S.: Machining behaviour of AISI 1018 steel during turning. J. Sci. Ind. Res. **67**, 355–360 (2008)
2. Sahoo, A.K., Sahoo, B.: Surface roughness model and parametric optimization in finish turning using coated carbide insert: response surface methodology and Taguchi approach. Int. J. Ind. Eng. Comput. **02**, 819–830 (2011)
3. Hao, Z., Gao, D., Fan, Y., Han, R.: New observations on tool wear mechanism in dry machining Inconel718. Int. J. Mach. Tools Manuf. **51**, 973–979 (2011)
4. Singh, H.: Optimizing tool life of carbide inserts for turned parts using Taguchis design of experiments approach. In: Proceedings of the International MultiConference of Engineers and Computer Scientists, vol. II, IMECS 2008, pp. 19–21 (2008)
5. Fox-Rabinovich, G.S., Yamamoto, K., Aguirre, M.H., Cahill, D.G., Veldhuis, S.C., Biksa, A., Dosbaeva, G., Shuster, L.S.: Multi-functional nano-multilayered AlTiN/Cu PVD coating for machining of Inconel 718 superalloy. Surface Coatings Technol. **204**, 2465–2471 (2010)
6. Mativenga, P.T., Abukhshim, N.A., Sheikh, M.A., Hon, B.K.K.: An investigation of tool chip contact phenomena in high speed turning using coated tools. Proc. IMech Part B: J. Eng. Manuf. **220**, 657–667 (2005)
7. Sert, H., Can, A., Habali, K., Okay, F.: Wear behaviour of PVD TiAlN, CVD TiN coated and cermet cutting tools. Tribol. Ind. **27**(3–4), 03–09 (2005)
8. Gokkaya, H., Nalbant, M.: The effects of cutting tool coating on the surface roughness of AISI 1015 steel depending on cutting parameters. Turkish J. Eng. Env. Sci. **30**, 307–316 (2006)
9. Tawfiq, M.A.: Effect of multi-coats of cutting tools on surface roughness in machining AISI 1045 steel. Eng. Tech. **26**(12), 01–11 (2008)
10. Motorcu, A.R.: The optimization of machining parameters using the Taguchi method for surface roughness of AISI 8660 hardened alloy steel. J. Mech. Eng. **56**(6), 391–401 (2010)
11. Bakkal, M., Shih, A.J., Scattergood, R.O.: Chip formation, cutting forces, and tool wear in turning of Zr-based bulk metallic glass. Int. J. Mach. Tools Manuf. **44**, 915–925 (2004)
12. Sahoo, A.K., Orra, K., Routra, B.C.: Application of response surface methodology on investigating flank wear in machining hardened steel using PVD TiN coated mixed ceramic insert. Int. J. Ind. Eng. Comput. **04**, 01–10 (2013)
13. Pathade, H.P., Wakchaure, V.D.: Experimental investigation of flank wear in coated carbide tipped tool for machining AISI 304. Int. J. Mech. Prod. Eng. Res. Dev. **03**, 63–86 (2013)
14. Kumbhar, Y.B., Waghmare, C.A.: Tool life and surface roughness optimization of PVD TiAlN/TiN multilayer coated carbide inserts in semi hard turning of hardened EN31 alloy steel under dry cutting conditions. Int. J. Adv. Eng. Res. Stud. **02–04**, 22–27 (2013)
15. Kaladhar, M., Venkata Subbaiah, K., Srinivasa Rao, C.: Performance evaluation of coating materials and process parameters optimization for surface quality during turning of AISI 304 austenitic stainless steel. Int. J. Eng. Sci. Technol. **03**, 89–102 (2011)
16. Gunay, M., Yucel, E.: Application of Taguchi method for determining optimum surface roughness in turning of high-alloy white cast iron. Measurements **46**, 913–919 (2013)

Study on Temperature Indicating Paint for Surface Temperature Measurement—A Review

**P. L. Rupesh, M. Arul Prakasajothi, U. Chandrasekhar,
Rajendra Mycherla and M. Bhanu Teja**

1 Introduction

Aircraft propulsion systems and the land-based power generation systems use gas turbines in an effective and extensive way. In aircraft propulsion systems, the temperature of the operational engine components must be optimized by the aeronautical manufacturers to increase the lifespan of the turboshaft and its thermal efficiency[1–3]. The energy output of gas turbine may be maximized through the rise in turbine entry or inlet temperature. Increase in turbine inlet temperature from 1700 to 2200 K may lead to high thermal efficiency and increase in power output. Increase in turbine entry temperature also increases the heat load to the turbine blade. As a consequence, the turbine blade material may undergo thermal stress as it exceeds the melting temperature of blade material. Thermal mapping is essential for the health monitoring of gas turbine blade. In the combustion chamber of gas turbine, heat load on the combustor liner is maximum due to convection and the liner walls are exposed to a large proportion of total heat flux due to radiation from flame [4–7]. This excessive heat load may reduce the durability of liner wall. Therefore, it is necessary to keep the temperatures and temperature gradient down to an acceptable level. In order to determine the temperature profile of combustor liner or turbine blade, several measurement techniques are available globally. Some of the techniques such as discrete sensor arrays, liquid crystal thermometers and IR thermography have been described below in brief.

P. L. Rupesh (✉) · M. Arul Prakasajothi · R. Mycherla · M. Bhanu Teja
Department of Mechanical Engineering, Vel Tech Rangarajan
Dr. Sagunthala R&D Institute of Science & Technology, Chennai, India
e-mail: rupeshkumar221@gmail.com

U. Chandrasekhar
Department of Aeronautical Engineering, Vel Tech Rangarajan
Dr. Sagunthala R&D Institute of Science & Technology,
Avadi, Chennai 600062, Tamil Nadu, India

223

2   Global Temperature Measurement Techniques

2.1   *Discrete Sensor Arrays*

The heating rates and structural temperatures are normally obtained by few number of temperature indicating sensors like thermocouples or RTDs which may be placed at certain locations of interest. To attain maximum resolution, the sensors should be operated in dense arrays.

2.2   *Liquid Crystal Thermometers or TLC*

The thermochromic coating on liquid crystals provides reversible history of temperature continuously on the surface. These coatings were mostly practised in laboratories to study the transfer of heat in the research of gas turbines. These are not suitable for hypersonic flight tests due to the reversibility obtained by continuous visualization at the time of flight which is not practical, at elevated temperatures.

2.3   *IR Thermography*

The distribution of spatial temperature obtained by infrared thermography is opposed by radiometer measurements. The pyrometers are being carried to check the history of temperature in flights and an IR camera to check the distribution of transient temperature on inner surface of a vehicle. This can be influenced by solar reflection when it is used to examine the external surfaces, and it is also more expensive.

2.4   *Thermal Phosphors*

The luminescent coatings which are based on phosphor can be classified into temperature indicating paints (TIPs) and inorganic ceramic coatings of thermographic phosphor. A certain shorter wavelength light illuminates these coatings which can luminescent at longer wavelengths. The luminescent intensity of light is a function of temperature. These inorganic thermographic phosphors have the application of measuring the surface temperature up to a range 2000 K in a ground-based test rigs.

   The thermal measurement technique which has been described above has their own limitations in measuring the temperature profile of the gas turbine combustors

and turbine blades [8, 9]. Due to the harsh environment associated with turboshaft engines, the above-described temperature measurement techniques will be challenging. For example, the thermal measurement of a turbine blade which is subjected to 1000 °C is very difficult. The allowable limit of the high thermal stress that the turbine blade can withstand is evaluated through the thermal mapping. In this case, thermal paint or temperature indicating paint can be chosen as the efficient thermal measurement technique.

3 Irreversible Thermal Paints or Temperature Indicating Paints (TIPs)

The most commonly used technique for testing gas turbine components in industrial application is the usage of temperature indicating paints which allows global mapping of distribution of peak temperatures on the blades of turbine and cans of combustor which avoid difficulties faced with traditionally used electrical and electronic-based temperature indicating sensors [10]. The visible colour changes are the result of chemical reactions that these special paint mixtures undergo at particular elevated temperatures. The main attraction of using thermal paints to model the distribution of temperature over a surface is the ability to obtain a global temperature profile of the component under examination, where thermocouples and other such methods can only give point temperatures.

These TIPs have found its unique position in the following practical applications.

1. Usage of TIPs for combustor and turbine components to know the temperature profiles since late 1950s by Rolls-Royce.
2. Testing of gas turbine and many aero-engines for the validation and confirmation of the engine and its component's design.
3. TIP plays a very important role in thermal mapping of components during hypersonic flight tests.

4 Thermal Paint Chemistry

Thermal paints can be employed as either single-change or multiple-change colour transition paints. In the thermal paint, the colour starts to appear by the interaction of electrons which are present in matter with light. The thermochromism is a property of a material where the colour can be changed in relation to temperature. As the name suggests, single-change thermal paints undergo only one transition of colour, where multi-change can transit through several different colours.
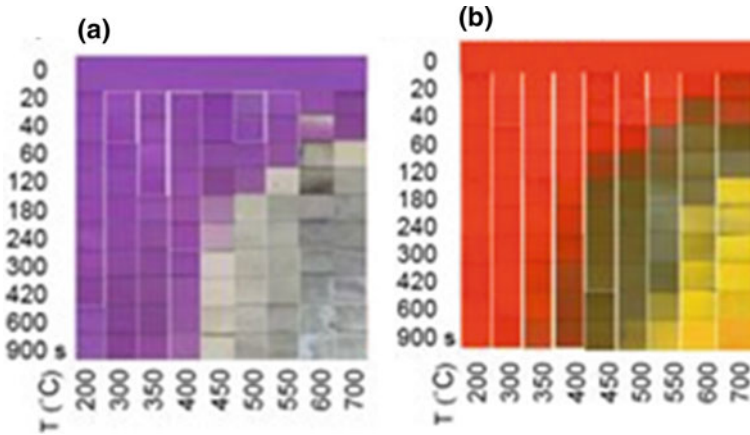
Fig. 1 Colour map of single-change and multi-change TIP. **a** SC 400; **b** MC 490-10

The colour maps for TIP SC 400 and MC 490-10 [11–13] shown in Fig. 1a, b, respectively, indicates that the colour change occurs when the temperature crosses the threshold. The figure also indicates that (a) undergoes a single colour transition after it crosses 400 °C and (b) undergoes 10 colour transitions with an interval of 50 °C.

Thermal indicating paints change colour in response to both time and temperature. In effect, this means when thermal paints are subjected at temperature to a time duration, the longer the time, the lower the temperature required to change the paint to the next colour. The test strips should be the same material and thickness as the engine component. Exposure time must be the same.

5   Chemistry Behind Colour Transition

Thermal paints consist of a resin (or a binder solution) and a transition metal pigment which is contained within the resin. The resin must be sufficiently stable enough to withstand elevated temperatures without changing structure. It is the pigment that changes colour at different temperatures. Resins used in industrial applications are acrylic based and a commonly used solution is polymethylacrylate (PMA). PMA resin is able to be heated to high temperatures and remains stable.

When the colour change occurs, this indicates that a physical change in the chemistry has also occurred [14] such that light is reflected at a different wavelength which appears as a different colour as shown in Fig. 2. The driving force of the colour change in the thermal paint is the ability of the transition metals to change energy states and to form complex ions.

Fig. 2 Colour change at
different wavelengths of light
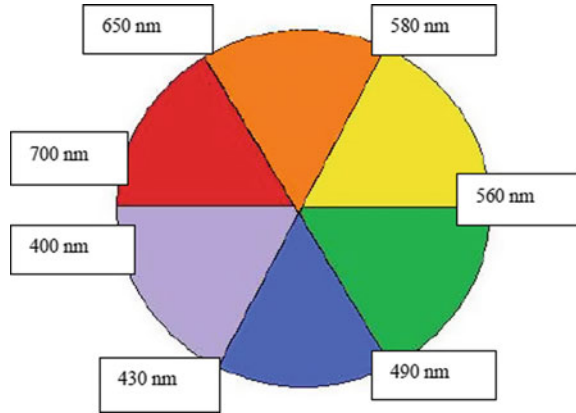
6　Calibration Methodology

The calibration method for the thermal paints is briefed in Fig. 3. To examine a
colour change of the paint, the metal coupons should undergo a proper surface
treatment and then the metal coupons are heated at different temperatures for every
10 min [2, 3].

Calibration Methodology
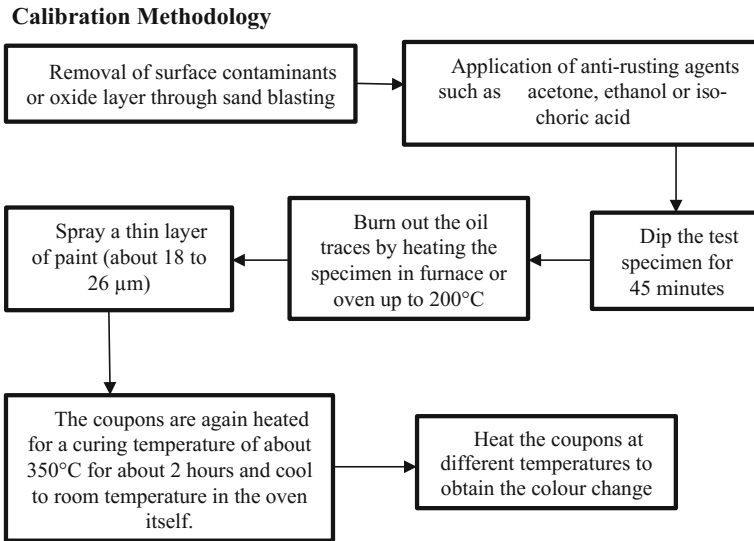
Fig. 3 Methodology for calibration

7   Recent Research Works Using TIP

Table 1 indicates few research works which includes the usage of TIP in various applications. Some of the research works carried with the TIP have been described in brief to exhibit its practical applications.

Mandavkar et al. [15] focused on the health monitoring of gas turbine blades through focusing the critical zone and hot spot along the temperature distribution using thermal paints. The effect of internal cooling through the holes in the blades has been studied by capturing the images of thermal contours. A turbine blade prototype has been manufactured and painted with TIP as shown in Fig. 4a. Colour change as shown in Fig. 4b has been examined on heating of gas turbine blade through LPG flame ignited through nozzle. A digital image processing technique (image pixel method) has been developed, and each image pixel is assigned with corresponding temperature value. Thermal mapping was done by comparing the calibrated data with image pixel temperature contours.

The work presented by Lempereur et al. [16] indicates an accurate measurement of temperature from colour (produced by thermal paint TP96) through the image processing technique [conversion of RGB colour space into HLS (hue, lightness and saturation)].

Table 1 Research works on TIP

S. No.	Author	Ref. no.	Remarks
1	Mandavkar et al.	[15]	Health monitoring of gas turbine blades through hot spots (from TIP)
2	Lempereur et al.	[16]	Relation between colour and temperature value through different image processing techniques
3	Yang et al.	[17]	Research of TIP
4	Lee et al.	[18]	Whole field temperature distributions in heat transfer enhancement applications
5	Andrew et al.	[19]	Mapping the structural heating during the process of hypersonic flight tests
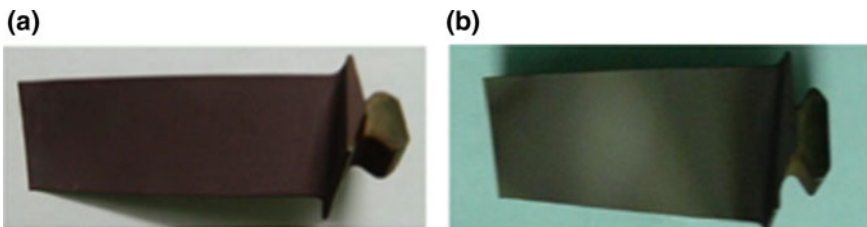
Fig. 4 **a** Painted component, **b** heated component

In order to avoid the accuracy error with isotherm evaluation on a surface with thermal paint, the above image processing technique has been implemented. Figure 5a shows the identification of isotherm using HLS method. A 3D scanner has been used to digitize the outer shape of the component with the insertion of determined temperature levels as shown in Fig. 5b.

Yang and Zhi-Min [17] have observed the temperature profile of the hot-end components through the judgement of colour change of thermal paint films. The author has made a new thermal paint with a unique formula design and has explained the preparation and painting process. An efficient calibration system was studied for isotherm identification as shown in Fig. 6a. This paint has been applied to an aero-turbine engine component, and the temperature profile has been recorded [20] with the flow of high-velocity gas on the component's surface as depicted in Fig. 6b .

Structural heating during hypersonic flight tests [21, 11, 12] has been mapped using permanent change thermal paints by Neely and Riesen [19]. The paint response along with the pressure dependence has been investigated as shown in
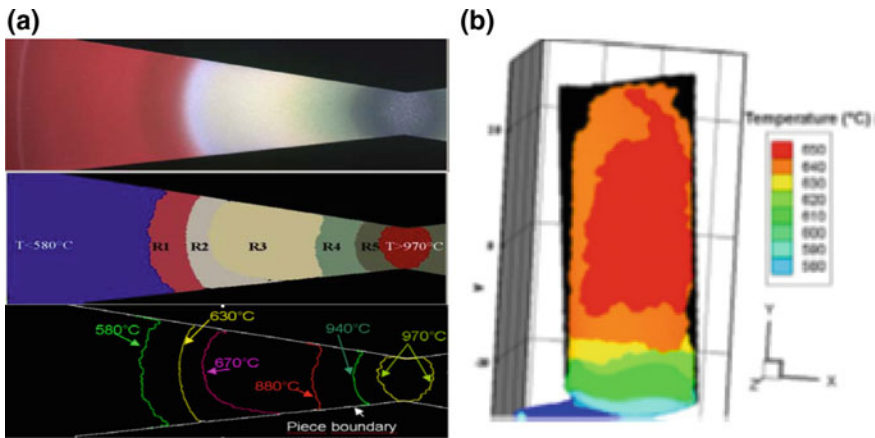
Fig. 5 **a** Isotherm identification, **b** 3D scanned thermal map
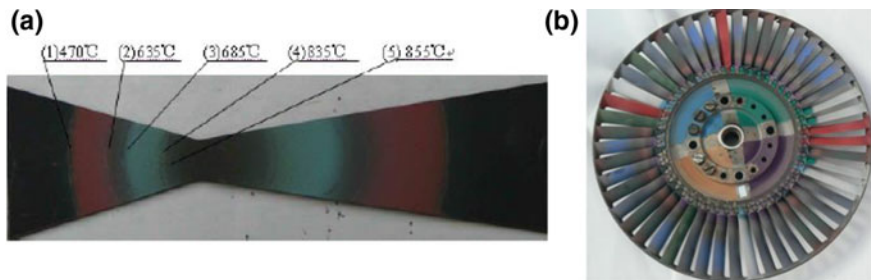
Fig. 6 **a** Temperature measurement, **b** test engine component
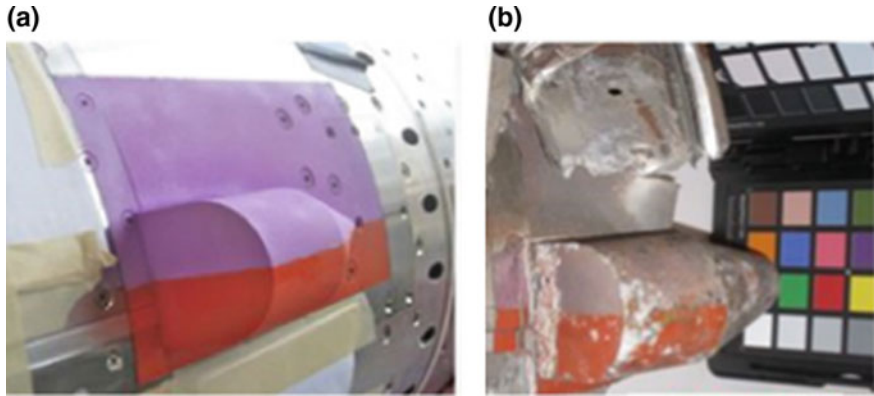
Fig. 7 Colour change of MC 165-2 and MC 450-10. **a** preflight, **b** postflight

Fig. 7a. The colour change of thermal paints as shown in Fig. 7b indicates the full transient heating of the vehicle across its trajectory. The structural response of the hypersonic flight (HI Fire 0) has been studied with aerodynamic heating.

8   Conclusion

The measurement of temperature and its indication at all the points on the surface of high-temperature application components like aero-engine combustor, turbine and compressor blades is essential for validating their life. Though there are various techniques and devices available for measuring the temperature, they are not suitable for the above applications as they cannot helpful in framing the thermal mapping. On the other hand, the TIPs are able to indicate the variations in temperature profiles from one point to other on the surface of a component, and they enable us in creating the thermal mapping for various temperature profiles.

References

1. Cowling, J.E., King, P., Alexander, A.L.: Temperature-indicating paints. Ind. Eng. Chem. **45** (10), 2317–2320 (1953)
2. Bird, C., Mutton, J.E., Shepherd, R., Smith, M.D.W., Watson, H.M.L.: Surface temperature measurement in turbines. In: AGARD-CP-598 (1998)
3. Bown, N.W., Cain, T.M., Jones, T.V., Shipley, P.P., Barry, B.: In flight heat transfer measurements on an aero-engine nacelle. In: ASME 94-GT-244 (1994)
4. Connolly, M.: Temperature measurement using thermal paints. Rolls-Royce Deutschland, Germany (2009)
5. Bird, C., Mutton, J.E., Shepherd, R., Smith, M.D.W.: Surface temperature measurement in turbines. In: AGARD Conference Proceedings, vol. 598, 21.421.10 (1998)

6. Liu, T., Sullivan, J.P.: Pressure and Temperature Sensitive Paint. Springer, Heidelberg (2004)
7. Liu, T., Campbell, B.T., Bums, S.P., Sullivan, 1.P.: Temperature and pressure-sensitive paints in aerodynamics. Appl. lvfechanics Rev. **50**, 227–246 (1997)
8. Dolvin, D.J.: Hypersonic international flight research and experimentation (HIFiRE) fundamental sciences and technology development strategy. In: AIAA-2008–2581 (2008)
9. Griffin, A., Kittler, J., Windeatt, T., Matas, G.: Techniques for the interpretation of thermal paint coated samples. In: Proceedings of the 1996 Conference on Pattern Recognition. IEEE, New York, pp. 959–963 (1996)
10. Iliff, K.W., Shafer, M.: A comparison of hypersonic vehicle flight and prediction results. AIAA-93-0311 (1993)
11. Neely, A.J., Tjong, W.C.: Calibration of thermal paints for hypersonic flight test. In: AIAA-2008-2664 (2008)
12. Neely, A.J., Tracy, P.J.: Transient response of thermal paints for use on short-duration hypersonic flight tests. In: AIAA-2006-8000 (2006)
13. Padgham, C.A., Saunders, J.E.: The perception of light and colour. G. Bell and Sons Limited, London (1975)
14. Jones, R.A., Hunt, J.L.: Use of temperature-sensitive coatings for obtaining quantitative aerodynamic heat transfer data. AIAA J. **2**(7), 1354–1356 (1964)
15. Mandavkar, P.S., Sawane, S.M.S.R.D., Dongre, D.G.: Study of thermal mapping for health monitoring of gas turbine blade. Int. J. Res. Sci. Eng. **1**, 1–6
16. Lempereur, C., Andral, R., Prudhomme, J.Y.: Surface temperature measurement on engine components by means of irreversible thermal coatings. IOP Sci. Measur. Sci. Technol. **105501**, 4–5 (2008)
17. Yang, L., Zhi-Min, L.: The research of temperature indicating paints and its application in aero-engine temperature measurement. In: Asia-Pacific International Symposium on Aerospace Technology (APISAT 2014), Procedia Engineering, pp. 1154–1155 (2014)
18. Lee, J.J., Craig Dutton, J., Jacobi, A.M.: Application of temperature-sensitive paint for surface temperature measurement in heat transfer enhancement applications. J. Mech. Sci. Technol, **21**, pp. 1254, 1257 (2007)
19. Neely, A.J., Riesen, H.: Permanent-change thermal paints for hypersonic flight-test. In 15th AIAA International Space Planes and Hypersonic Systems and Technologies Conference 2008, pp. 2–3, 5–8, 14–15 (2008)
20. Taniguchi, T., Sanbonsugi, K., Ozaki, Y., Norimoto, A: Temperature measurement of high speed rotating turbine blades using a pyrometer. In: ASME-GT2006-90247 (2006)
21. Kojima, F., Fukuda, S., Asai, K., Nakakita, K.A.: Identification of time and spacial varying heat flux from surface measurements based on TSP technology. In: Proceedings of the SICE Annual Conference (2004)

Inflight Parameter Estimation Framework for Fixed-Wing UAV

R. Jaganraj, R. Velu and P. Gokul Raj

1 Introduction

Parameter estimation is the complicated process in system identification. System identification is the key to establish the desired control architecture for any system including aircraft. The researchers were published many articles targeted on system identification of aircraft. Parameter estimation is the process of estimating unknown parameters available in mathematical modeling. The process is widely classified by the nature of the system which is physics based or black box model. Output error method and equation error method are the examples for physics-based model and artificial intelligence; fuzzy are the black box model. Very few researchers were working on development on autopilot for UAV due to its complexity of instrumentation and data collecting pedagogy. The UAV becomes versatile in nature based on the application and a way it is being deployed. Automobile sector is moving toward the autonomous operation of vehicle and incorporating non-fossil energy applications. This development provides the subsystems required for UAV which was not available during past decades. Developing this kind of UAV requires robust autopilots which could bring the UAV from laboratory to commercial platform. As part of developing such robust autopilots, the initial step is estimating the associated parameters and handling, tuning of those parameters during inflight is mandatory. Because these parameters are determines constrains of UAV deployment, operation and autonomous missions in background. The basic classification, design, and applications of UAV and its potential were described by Austin [1] and Gundlach [2]. Anyway, the design and fabrication of UAV is not the scope of this paper.

R. Jaganraj (✉) · R. Velu · P. Gokul Raj
Vel Tech Rangarajan Dr. Sagunthala R&D Institute
of Science and Technology, Chennai, India
e-mail: aerojagan@live.com

The autopilot design of an aircraft requires systematic process of starting from UAV dynamical modeling which includes parameter estimation and system identification followed by Vepa [3] selecting desired functions of autopilot, choosing structure scheme and choosing appropriate autopilot architecture. The entire process depends on the robust dynamical model of the aircraft. The dynamical modeling of the aircraft is derived from set of linearized/nonlinear equations of motion which requires the aerodynamic, stability, and inertial parameters of an aircraft. The process of system identification [4] is establishing the dynamical model of the aircraft by observing input and corresponding output then relating this observation based on appropriate physical system model. The identification process [5] is simply establishing the relationship between stick inputs to the actuators to the state of an aircraft from sensors. System identification process done by flight test observed parameters whereas principle identification process is done by wind tunnel observed parameters. Parameter estimation is limiting the functions of the fault-tolerant flight control system [6] based on the methodology being adapted. Recursive algorithm was developed [7] to estimate thrust and power coefficients of propeller-driven UAV using Kalman filter. Parameter estimation and identification is compared for recursive [8] and least square method. The parameters of 25% left wing missing UAV was obtained [9] and used to model the linearized 6 DOF dynamics of 25% missing wing aircraft.

This paper explains the experimental investigation of instrumentation of UAV to convert RC aircraft into inflight parameter estimation framework using commercial autopilot and telemetry. Further, the process of system identification and selection of sensors was explained.

2 Flight Instrumentation: Airframe Assembly

Flight mechanics and control laboratory (FMC laboratory) of Vel Tech University has 1 kg fixed wing airframe—Sky surfer. Presently, this laboratory develops in-house custom autopilot and fault detection and identification system for Sky surfer. As a part of this work, present work aims to develop VAF-01 airframe for implementation of inflight parameter estimation framework. VAF-01 is the in-house custom-build UAV which can be incorporated initial instrumentation trail for the selected UAV airframe. The design, geometry, and inertial characteristics of VAF-01 are given in Table 1.

Table 1 VAF-01 airframe

S. No	Description	Value
1	Fuselage length (l)	100 cm
2	Fuselage cross-sectional area (A)	3 cm^2
3	Span (b)	160 cm

3 Flight Instrumentation: DAQ System Integration

Flight mechanics and control laboratory was established inflight data gathering facility using commercial autopilot Pixhawk as DAQ. The primary code for autopilot was customized to get the values of different flight data. The DAQ has the onboard memory SD card for avoiding data loss due to connectivity error. In addition to the available onboard sensor, additional sensors were incorporated to measure control surface deflection and then calibrated for stick input followed by autopilot input to actuators. Figure 1 shows the complete integration of flight instrumentation and inflight test (Fig. 2).

The primary sensors required for estimating state of the UAV is IMU, digital gyroscope, magnetometer, and digital accelerometer. The selected autopilot DAQ system consists of these primary sensors on board. In addition to this, for obtaining airspeed and digital pitot probe was installed on the airframe. For dual redundancy GPS also installed on board and connected with DAQ system. The airframe is

Fig. 1 Flight instrumentation and inflight testing

Fig. 2 Complete integration of DAQ system using commercial autopilot
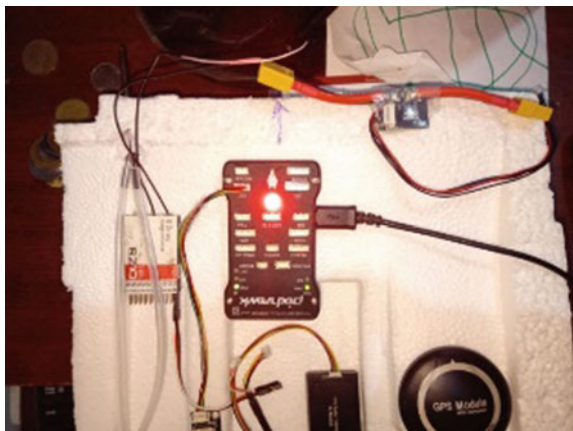
powered by 1000 kV motor which makes the UAV to fly with 0.5 T/W. The airframe has three primary control surfaces, elevator, aileron, and rudder. To measure this control surface deflection, initially flexible force sensor (Fig. 3) was chosen. The calibration of flexi sensor is given below. This calibration was done to obtain the relationship between control surface deflection with respect to the change in resistant.

Figure 4 shows the calibration curve of the flexible force sensor. The curve shows that the sensor has linearity between −5° and −30° deflection. The calibration was done several times to check the linearity. Note this calibration was done starting from −5° to −30° in single direction. Figure 5 shows the hysteresis curve of flexible sensor starting from 30° to −30° and vice versa in a single trail. This curve clearly shows the output deviation at a certain input pressure, when that input is approached first by increasing and then by decreasing pressure. So, this kind of sensors which depend on loading and unloading nature could not be used for measuring deflection of the control surface. The reason is loading and unloading strain will not be linear which cause the sensor to show different output on a same point when loading cycle varies.

Fig. 3 Flexible force sensor calibration setup

Fig. 4 Calibration curve of flexible force sensor (0° to −35° deflection vs. resistance)
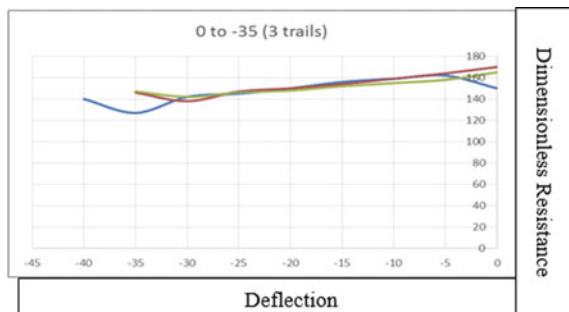
Fig. 5 Hysteresis curve of flexible force sensor
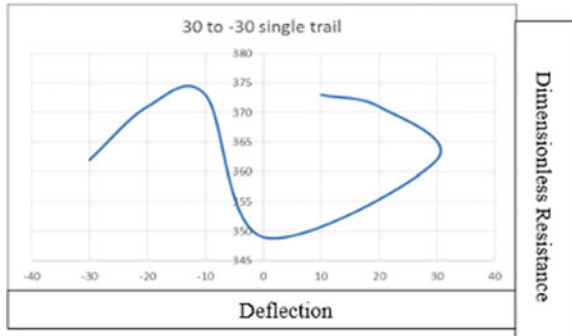
4　Flight Instrumentation: Selection of Sensors

Aerodynamics and Moment Parameter model of fixed wing Aircraft—The longitudinal aerodynamic and moment parameter model of fixed wing aircraft can be represented as below in Eq. (1). The α and q terms are stability derivatives, and δe terms are control derivatives. We can represent the above Eq. (1) as below where Y is the output, X is the input and θ is the state-dependent parameters.

$$
\begin{bmatrix} C_L \\ C_D \\ C_m \end{bmatrix} = \begin{bmatrix} C_{LO} & C_{L\alpha} & C_{L\delta e} & C_{Lq} \\ C_{DO} & C_{DO} & C_{D\delta e} & C_{Dq} \\ C_{mO} & C_{m\alpha} & C_{m\delta e} & C_{mq} \end{bmatrix} \begin{bmatrix} 1 \\ \alpha \\ \delta e \\ Qc/2v \end{bmatrix} \tag{1}
$$

$$
Y = \theta X \tag{2}
$$

　　Input design—Input design is important component in flight test preparations. Even though, the parameters were obtained during steady-level flight condition or trimmed condition, the proper input design only will leads to healthy parameter estimation. Because, each algorithm have its own assumptions which may leads to several errors. So, proper input design will give healthy flight data. The motivation of input design is to excite aircraft on its natural frequency by different input. The commonly used input design is 3211. The sample input for elevator was given in Fig. 6.
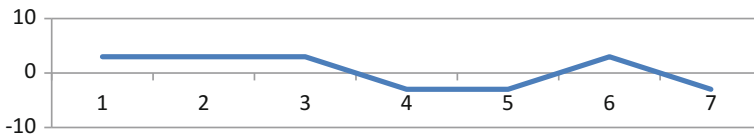
Fig. 6　Sample 3211 input design for elevator

System identification methodology—In general, system identification is the process of defining unknown parameters present in mathematical model of the system which is structured with unknown parameters. System identification process is classified based on the nature of the system (physics-based model and black box model). General types of parameter estimation methods are equation error method, output error method, filter error method, artificial neural network, fuzzy logic, etc. The selection of method is based on the quality of the quantification sensors and data acquisition system. Least square method is one of the parameter estimations
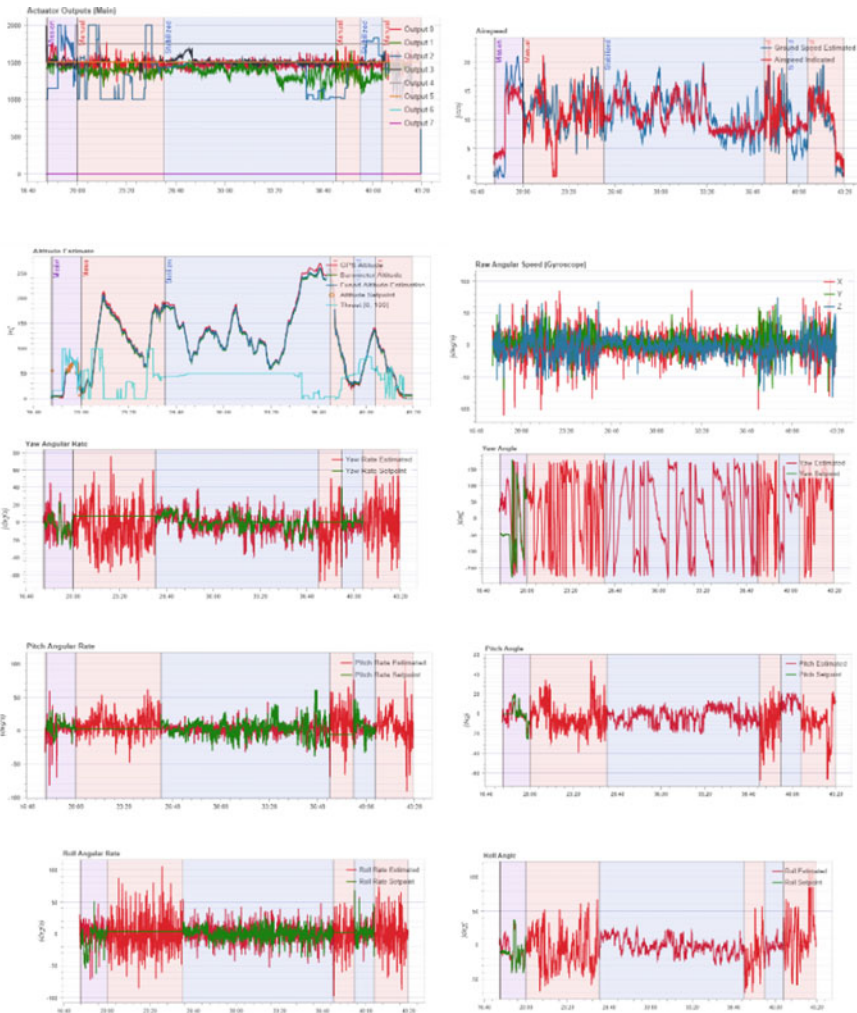
Fig. 7 Inflight test results

and solutions for Eq. (1) which can be represented as below in Eq. (3) where squares of errors is minimum for the system as given below in Eq. (4) (Є is the error in parameters).

$$\Theta = (X^T X^{-1})(X^T(Y))$$ (3)

$$Y = \theta X + Є$$ (4)

5 Inflight Test Results

The flight test was conducted, and real-time data were recorded and further processed to get values of *Y* and *X* of Eq. (2). The parameter estimation was done for further research on fault detection system architecture. The sample results of flight test are given below. All results were obtained in GCS via telemetry link. Figure 7 shows the input, altitude, pitch, roll, and yaw data.

6 Conclusion

The methodology of framework for parameter estimation was explained and process of conversion of RC airframe into parameter estimation was explained. The selection of sensor for measuring control surface deflection was given, and result for flexi sensor is shown that strain-based flexi sensor hysteresis characteristics is not suitable for measuring the deflection. The sample results of flight test were presented, and system identification method was discussed. The flight was conducted, and parameter identification platform was developed for further research on fault detection and identification of fixed-wing UAV.

References

1. Austin, R.: Unmanned Aircraft Systems: UAVS Design, Development and Deployment. Willey, New York (2010). ISBN 978-0-470-05819-0
2. Gundlach, J.: Designing Unmanned Aircraft Systems: A Comprehensive Approach. AIAA Education Series (2012)
3. Vepa, R.: Flight Dynamics, Simulation, and Control for Rigid and Flexible Aircraft. Taylor & Francis Group (2015)
4. Jategaonkar, R.V.: Flight Vehicle System Identification: A Time Domain Methodology. Progress in Astronautics and Aeronautics, AIAA (2015)
5. Cai, G., Dias, J., Seneviratne, L.: Survey of small-scale unmanned aerial vehicles: recent advances and future development trends. Unmanned Syst. **2**(2), 1–25 (2014)
6. Zhang, Y., Jiang, J.: Bibliographical review on reconfigurable fault-tolerant control systems. Ann. Rev. Control **32**, 229–252 (2008)

7. Ahsun, U., Badar, T., Tahir, S., Aldosari, S.: Real-time identification of propeller-engine parameters for fixed wing UAVs. IFAC-PapersOnLine **48–28**, 1082–1087 (2015)
8. Amelin, K., Tomashevich, S., Andrievsky, B.: Recursive identification of motion model parameters for ultralight UAV. IFAC-PapersOnLine **48–11**, 233–237 (2015)
9. Chowdhary, G., DeBusk, W.M., Johnson, E.N.: Real-time system identification of a small multi-engine aircraft with structural damage. In: AIAA Infotech@Aerospace 2010, Atlanta, Georgia, 20–22 Apr 2010
10. Nelson, R.C.: Flight stability and automatic control, 2nd edn. McGraw Hill (1998)

Experimental Studies on Surface Roughness of H12 Tool Steel in EDM Using Different Tool Materials

T. N. Valarmathi⬤**, S. Sekar, G. Anthony, R. Suresh and K. N. Balan**

1 Introduction

In EDM, the heat produced between the electrode and work by the spark is used to machine the work material. Hence, the properties of electrode decide the quality of machining. To analyze the electrode material, more research is carried out in EDM. Research works report that the tool material, current, pulse duration, and voltage have significant effect on surface roughness and material removal rate [1–7].

Guu et al. [8] studied the surface behavior of tool steel during EDM and reported that the tensile residual stress developed affects the machined surface. Kiak and Cakir [9] studied the behavior of tool steel machining using EDM with pure copper electrode and reported that pulse time and pulse current have more effect and the increase of these parameters increases the roughness value. Kumar et al. [10]

T. N. Valarmathi (✉) · G. Anthony · R. Suresh
School of Mechanical Engineering, Sathyabama Institute of Science and Technology,
Deemed to be University, Chennai 600119, Tamil Nadu, India
e-mail: valarmathi.tn@gmail.com

G. Anthony
e-mail: journacantony@gmail.com

R. Suresh
e-mail: suresh8r8@gmail.com

S. Sekar
Department of Mechanical Engineering, Rajalakshmi Engineering College,
Anna University, Chennai 602105, Tamil Nadu, India
e-mail: sekarsarav@gmail.com

K. N. Balan
Department of Automobile Engineering, Hindustan Institute of Technology
and Science, Deemed to be University, Chennai 603103, Tamil Nadu, India
e-mail: knb5463@gmail.com

reported a review of the surface quality of the machined component using EDM. Kumar and Batra [11] investigated the different types of die steel and reported that surface modification using EDM is promising and the more considerable parameter is peak current. Abbasi et al. [12] studied the influence of parameters on surface roughness in machining of HSLA steel with molybdenum wire and reported that the contribution is more by pulse on time. In the present work, the behavior of electrode material and process parameters in machining of H12 tool steel using EDM on surface roughness is investigated.

2   Experimental Work

In this study, H12 steel is used because it has high strength and wear resistance properties, and hence, it is extremely used in casting, forging, and extrusion applications. As it contains 5% chromium and 1.5% molybdenum, it is hard to machine by conventional machining methods. Hence, EDM is used to perform machining operations. The electrode materials selected are copper and copper–tungsten (75 and 25%). The CuW electrode is made by mixing the powders by powder metallurgy, and then, it is compacted in the die. EDM is performed using milling machine (Fig. 1).

3   Method of Analysis

3.1   Taguchi and ANOVA Method

The experiments have been designed and performed using Taguchi L_9 orthogonal array approach. Duty cycle, gap voltage, and peak current are considered as

Fig. 1 EDM milling machine during machining of H12 tool steel with copper and copper–tungsten electrodes

parameters, and surface roughness is the response variable. As the R_a value has to be reduced, smaller the better is considered.

3.2 Measurement of Surface Roughness

The surface roughness (R_a) is an important factor in machining. If the roughness is more, the wear and friction will be more. Hence, it must be minimized to avoid cracks and other defects. The R_a can be measured using surface roughness tester. The R_a is determined using the Eq. (1)

$$R_a = \frac{1}{n} \sum_{i=1}^{n} |y_i| \tag{1}$$

4 Results and Discussion

In this study, EDM is done on H12 steel with copper and copper–tungsten electrodes using Taguchi L_9 orthogonal array. The input control parameters are varied to analyze and optimize the response variable R_a and to compare the effectiveness of the tool materials. The results obtained using two electrodes are reported in Table 1.

4.1 Analysis of Surface Roughness

Surface Roughness for Copper Electrode As the response variable, surface roughness has to be minimized, the smaller is the better option is selected under

Table 1 Experimental results of surface roughness (R_a)

Expt. runs	Control factors			Surface roughness (R_a)	
	Peak current	Gap voltage	Duty cycle	Cu electrode	Cu–tungsten electrode
1	8	40	0.6	6.361	4.967
2	8	50	0.7	6.056	6.539
3	8	60	0.8	7.184	6.784
4	10	40	0.7	8.294	6.317
5	10	50	0.8	7.591	6.008
6	10	60	0.6	8.341	6.671
7	12	40	0.8	6.843	6.381
8	12	50	0.6	6.845	6.223
9	12	50	0.7	6.765	6.614

Table 2 S/N ratio for R_a with copper electrode

Level	Peak current (A)	Gap voltage (B)	Duty cycle (C)
1	−16.28	−17.05	−17.07
2	−18.14	−16.65	−16.87
3	−16.67	−17.39	−17.15
Delta	1.85	0.73	0.27
Rank	1	2	3

Table 3 Results of ANOVA for R_a for copper electrode

Source	DOF	Sum of square	Mean square	F value	P value	Contribution %
Peak current	2	5.7329	2.86643	8.56	0.105	78.24
Gap voltage	2	0.8085	0.40426	1.21	0.453	11.03
Duty cycle	2	0.1169	0.05845	0.17	0.851	1.60
Error	2	0.6694	0.33469			9.13
Total	8	7.3277				100.00

S/N ratios. The response table for R_a in machining using a copper electrode is reported in Table 2. The ANOVA results of each parameter are reported in Table 3. From the tables, it is identified that the peak current has more influence on R_a. Figure 2 shows the S/N ratio plots. From the S/N ratio plots, it is identified that the combination of A2, B1, and C3 gives the minimum surface roughness (R_a) values. That is, the combination of minimum gap voltage (40 V), medium peak current (10 A), and maximum duty cycle (0.8) shows optimum surface roughness values.

Surface Roughness for Copper–Tungsten Electrode The response table for surface roughness in machining using copper–tungsten electrode is reported in Table 4. From the table, it is identified that the gap voltage has more influence followed by duty cycle and peak current. The ANOVA results of each parameter are reported in Table 5. From table, it is noted that the contribution of gap voltage is more on surface roughness.

Figure 3 shows the S/N ratio plots. From the S/N ratio plots, it is identified that the combination of A1, B1, and C1 gives the minimum surface roughness (R_a) values. That is, the combination of minimum peak current, minimum gap voltage, and minimum duty cycle shows optimum results.

Comparison of R_a Comparison of R_a values obtained using the two electrodes in machining is reported in Fig. 4. From the comparison graph, it is observed that the R_a is small while using tungsten copper electrode in the machining of H12 steel.
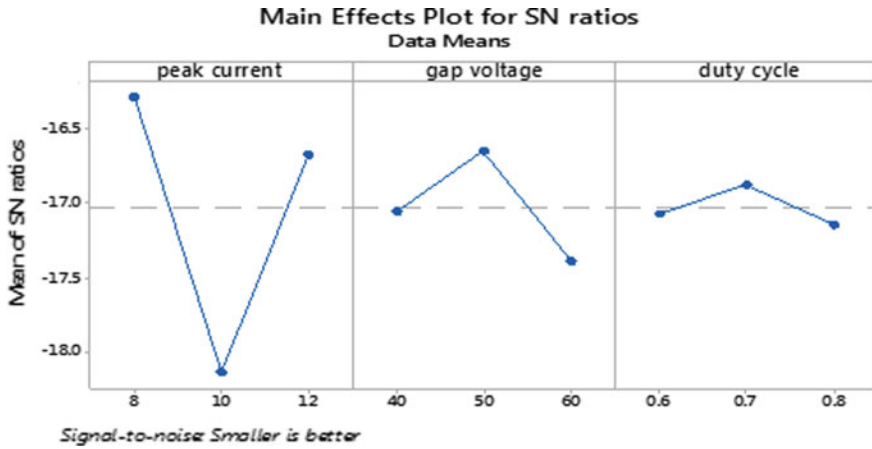
Fig. 2 *S/N* ratio plots for surface roughness with copper electrode

Table 4 *S/N* ratio for R_a with copper–tungsten electrode

Level	Peak current	Gap voltage	Duty cycle
1	−15.62	−15.34	−15.43
2	−16.02	−15.92	−16.24
3	−16.13	−16.51	−16.10
Delta	0.51	1.16	0.81
Rank	3	1	2

Table 5 Results of ANOVA for R_a for copper–tungsten electrode

Source	DOF	Sum of square	Mean square	*F* value	*P* value	Contribution %
Peak current	2	0.4316	0.2158	0.24	0.804	8.04
Gap voltage	2	2.0335	1.0167	1.15	0.465	37.89
Duty cycle	2	1.1358	0.5679	0.64	0.609	21.17
Error	2	1.7654	0.8827			32.90
Total	8	5.3662				100.00

5   Conclusions

EDM machining using two different electrodes on H12 steel is carried out to optimize the machining conditions for minimizing the R_a. The final conclusions arrived are as follows:

Main Effects Plot for SN ratios
Data Means

Signal-to-noise: Smaller is better
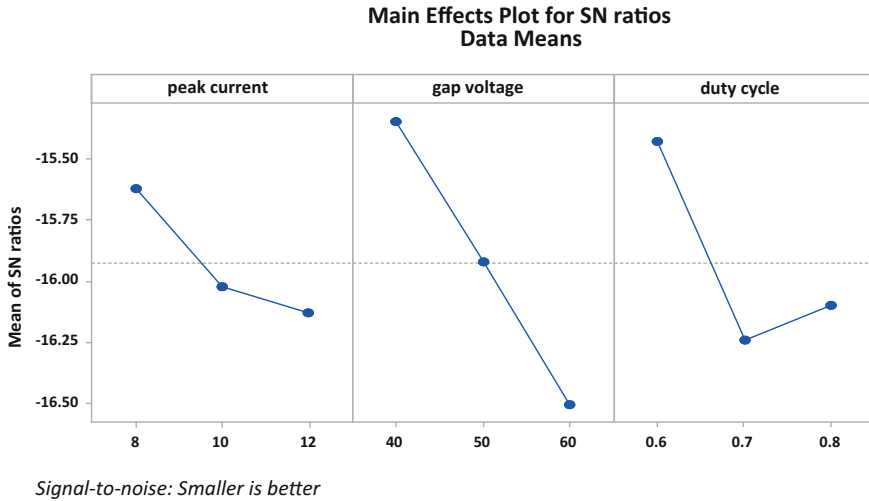
Fig. 3 *S/N* ratio plots for R_a with copper–tungsten electrode
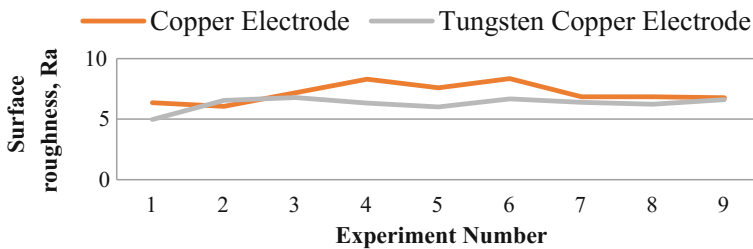
Fig. 4 Comparison of surface roughness values of copper electrode and copper–tungsten electrode

- From the experimental results, it is observed that the R_a is less in machining with tungsten copper electrode.
- From response tables for *S/N* ratio and means and ANOVA results, it is revealed that the peak current has more influence on R_a followed by gap voltage and duty cycle with copper electrode and gap voltage has a significant effect on R_a followed by duty cycle and peak current with copper–tungsten electrode.

References

1. Kumar, D., Beri, N., Kumar, A., Sharma, S.: Some studies on electric discharge machining of hastelloy using copper chromium powder metallurgy electrode using reverse polarity. Int. J. Adv. Eng. Tech. **1**(3), 74–84 (2010)
2. Kocher, G., Chopra, K., Kumar, S.: Investigation of surface integrity of AISI D3 tool steel after EDM. Int. J. Emerg. Technol. Adv. Eng. **2**(4), 160–162 (2012)

3. Lajis, M.A.: The implementation of Taguchi method on EDM process of tungstencarbide. Eur. J. Sci. Res. **26**(4), 609–617 (2009)
4. Beri, N., Maheshwari, S., Sharrna, C., Kumar, A.: Performance evaluation of powder metallurgy electrode in electrical discharge machining of AISI D2 steel using Taguchi method. Int. J. Mech. Ind. Aerosp. Eng. **2**(2), 225–229 (2008)
5. Rizvi, S.A.H., Agarwal, S.: An investigation on surface integrity in EDM process with a copper tungsten electrode. Proc. CIRP **42**, 612–617 (2016)
6. Nakagawa, T., Sampei, M., Hirata, A.: Improvement in machining speed with working gap control in EDM milling. Precis. Eng. **47**, 303–310 (2017)
7. Torres, A., Luis, C.J., Puertas, I.: EDM Machinability and surface roughness analysis of TiB2 using copper electrodes. J. Alloy. Compd. **690**, 337–347 (2017)
8. Guu, Y.H., Hocheng, H., Chou, C.Y., Deng, C.S.: Effect of electrical discharge machining on surface characteristics and machining damage of AISI D2 tool steel. Mater. Sci. Eng., A **358** (1–2), 37–43 (2003)
9. Kiyak, M., Cakır, O.: Examination of machining parameters on surface roughness in EDM of tool steel. J. Mater. Process. Technol. **191**(1–3), 141–144 (2007)
10. Kumar, S., Singh, R., Singh, T.P., Sethi, B.L.: Surface modification by electrical discharge machining: a review. J. Mater. Process. Technol. **209**(8), 3675–3687 (2009)
11. Kumar, S., Batra, U.: Surface modification of die steel materials by EDM method using tungsten powder-mixed dielectric. J. Manuf. Process. **14**(1), 35–40 (2012)
12. Abbasi, J.A., Jahanzaib, M., Azam, M., Hussain, S., Wasim, A., Abbas, M.: Effects of wire-cut EDM process parameters on surface roughness of HSLA steel. Int. J. Adv. Manuf. Technol. **91**(5–8), 1867–1878 (2017)

Effect of Equivalence Ratio on Parameters of Coal-Fired Updraft Gasifier

Bhargav Manek and Hardik Ramani

1 Introduction

In today's era, fossil fuel is a major source of energy. The direct combustion of coal for heating purpose is a serious reason for pollution as it emits carbon dioxide. Therefore, utilization of coal in a safer way is a major task in industry. Gasification process has benefits to produce clean energy by converting coal into syngas (H_2 + CO) [1]. Gasifier is a standard device for generation of syngas. It has been classified according to the flow of gas like co-current (downdraft), counter-current (updraft), and entrained flow. Fluidized bed is a new technology to provide suspension to coal particles in reactor. Different zones are generated in fixed bed gasifier due to gasification process called drying, devolatilization, reduction, and oxidation [2]. For medium-scale applications like ceramic industries, updraft gasifier has been used for many years. Simple geometry, versatility in fuel, and less cost are major advantages of updraft gasifier. For the requirement of more energy, coal has been used as fuel, but it creates more pollution than other petroleum hydrocarbons. Ceramic product industries have been using updraft gasifier for many years. In the ceramic product industries, major purpose of gasifier is to generate heat in furnace. So, gasifier operators are not considering the syngas composition which was made after coal gasification. When flame temperature inside the furnace became lower then required value of temperature, the gasifier operators fed more amount of coal inside the gasifier. Due to varying amount of coal feeding against constant amount of air and steam feeding, the constant amount of syngas can not be generated. For generating the best syngas composition, experimental methods are too much costly and time-consuming. Numerical simulation is a technological boost to improve syngas quality by computational work without any experiments. Several authors have been worked on numerical study of gasifier with

B. Manek (✉) · H. Ramani
Department of Mechanical Engineering, Marwadi Education Foundation
Group of Institutions, Rajkot 360003, India
e-mail: bhargavmanek94@gmail.com

different modeling methods and different commercial solvers. Chen et al. [1] investigated the effect of equivalence ratio of three different fuels for entrained flow gasifier and also showed benefits of torrefaction. Murugan and Joseph [3] examined the effect of E.R. on rice husk in downdraft gasifier. Fernando and Narayana [4] used Euler–Euler approach for fixed bed condition to find optimum airflow rate. Jeong et al. [5] used Euler–Lagrange approach to find optimum coal particle size. Zogala and Jenoszek [6] analyzed the underground coal gasification (UCG) process under different oxidizer. Murgia et al. [7] used Euler multiphase approach for fixed bed operation in updraft gasifier. From above observation, it is notified that continuous feed in updraft gasifier is rarely observed. It is also observed that equivalence ratio is a major parameter for the performance of gasifier. Also, Euler–Lagrange frame is very useful to simulate continuous feed operation.

2 Mathematical Modeling

2.1 Geometry

Updraft gasifier in the present study is sketched in Fig. 1. This updraft gasifier is cylindrical in shape having two ports on top. The height of gasifier is 5600 mm,

Fig. 1 Schematic of updraft gasifier
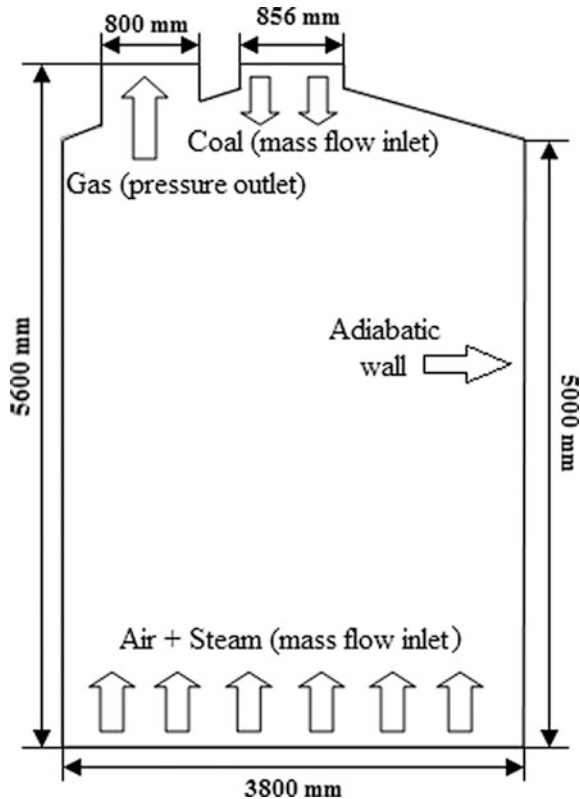
Table 1 List of governing equation

Continuity equation	$\nabla \cdot (\rho \vec{V}) = S_m$	(1)
Momentum equation	$\nabla \cdot (\rho \vec{v} \cdot \vec{v}) = -\nabla P + \nabla \tau + \rho \vec{g} + \vec{F}$	(2)
Energy equation	$\nabla \cdot (\rho \vec{V} \cdot T) = \nabla(\lambda(\nabla T)) + S_h$	(3)
Species transfer equation	$\nabla \cdot (\rho \vec{V} \cdot Y_i) = \nabla(\rho D \cdot (\nabla Y)) + S_r + R_i$	(4)
Turbulent kinetic energy	$\nabla \cdot \left(\rho \vec{V} \cdot k\right) = \nabla\left[\left(\mu + \frac{\mu_t}{\sigma_k}\right) \cdot \nabla k\right] + G_k - \rho\varepsilon$	(5)
Turbulent dissipation rate	$\nabla \cdot (\rho \vec{V} \cdot \varepsilon) = \nabla\left[\left(\mu + \frac{\mu_t}{\sigma_\varepsilon}\right) \cdot \nabla\varepsilon\right] + C_{1\varepsilon}G_k\frac{\varepsilon}{k} - C_{2\varepsilon}G_k\rho\frac{\varepsilon^2}{k}$	(6)
Kinematic viscosity	$\mu_t = \left(\rho C_\mu k^2\right)/\varepsilon$	(7)

Constants : $C_{1\varepsilon} = 1.44$ $C_{2\varepsilon} = 1.92$ $\sigma_k = 1$ $\sigma_\varepsilon = 1.3$ $C_\mu = 0.09$

and diameter of cylinder is 3800 mm. Dry coal is fed from the top center hole through hopper having a diameter of 856 mm. Outlet is just aside of coal inlet having diameter of 800 mm with center distance of 1172 mm. Mixture of air and steam is fed from the bottom inlet.

2.2 Assumptions

Actual reactions in gasifier involve too much complicated chemistry. In the present numerical work, few assumptions are taken: (1) steady-state, incompressible, and turbulent flow field has been chosen. (2) Thermal radiation is ignored, and gasifier wall is considered as adiabatic. (3) Pollutants like NO_x, SO_x are not generated in the process. (4) Coal particle size is constant, and also, air and steam flows are uniform at bottom. The governing equations [3] are shown in Table 1.

2.3 Discrete Phase Modeling

The modeling of fuel particle in fluid is modeled by Euler–Lagrange frame that considers inertia and hydrodynamic force coupled to mass, momentum, and energy. Discrete phase modeling is useful to track the particle trajectories in continuum. Velocity change can be written by Chen et al. [1],

$$m_p \frac{dV_p}{dt} = F_d \tag{8}$$

where, V_p is particle velocity and F_d is drag force on fuel particle by the surrounding fluid. Drag force can be represented by

$$F_d = \frac{\left(\rho A_c C_d V_r^2\right)}{2} \tag{9}$$

where ρ is density of fluid, A_c is cross-sectional area of solid particle, C_d is drag coefficient, and V_r is relative velocity of the solid particle and surrounding fluid. Some heat and mass transfer processes also happened on particle surface. They are considered as source terms in governing equations. These processes includes evaporation of moisture, devolatilization of particle in volatile matter, char and ash. After that char and volatiles were converted into gases.

2.4 Chemical Reactions

Devolatilization
At high temperature, coal particles are decomposed into char, volatiles, and ash. The equilibrium condition of volatile release of dry ash-free fuel is described by two-step devolatilization model known as Kobayashi model.

$$\text{Fuel} \xrightarrow{k_l} (1 - Y_l)\text{Char}_l + (Y_l)\text{Volatile (For low temperature)} \tag{10}$$

$$\text{Fuel} \xrightarrow{k_h} (1 - Y_h)\text{Char}_h + (Y_h)\text{Volatile (For high temperature)} \tag{11}$$
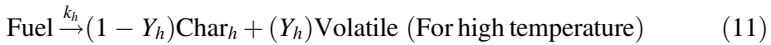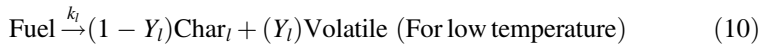
where Y is stochiometric coefficient and k is reaction rate. l and h stand for high and low temperatures. Combined reaction kinetics is given by

$$\frac{dV}{dt} = (k_l Y_l + k_h Y_h)\ \text{Fuel} \tag{12}$$

$$k_l = A_l e^{\left(-\frac{E_{a,l}}{RT}\right)} \tag{13}$$

$$k_h = A_h e^{\left(-\frac{E_{a,h}}{RT}\right)} \tag{14}$$

where V is mass fraction of species, R is universal gas constant, A is Arrhenius-type pre-exponential factor, E_a is activation energy of reaction, and T stands for temperature. The values of Y_l, Y_h, A_l, A_h, $E_{a,l}$, $E_{a,h}$ [1] is denoted in Table 2.

Table 2 Kinetic parameter of devolatilization equations

Y_l	0.3
Y_h	1
A_l (1/s)	2×10^6
A_h (1/s)	1.3×10^7
$E_{a,l}$ (J/kmol)	1.046×10^8
$E_{a,h}$ (J/kmol)	1.674×10^8

Solid-Phase Reaction

$$C_s + 0.5O_2 \xrightarrow{k_1} CO \tag{15}$$

$$C_s + H_2O \xrightarrow{k_2} CO + H_2 \tag{16}$$

$$C_s + CO_2 \xrightarrow{k_3} 2CO \tag{17}$$

Gaseous-Phase Reaction

$$H_2 + 0.5O_2 \xrightarrow{k_4} H_2O \tag{18}$$

$$CO + 0.5O_2 \xrightarrow{k_5} CO_2 \tag{19}$$

$$CO + H_2O \xrightarrow{k_6} CO_2 + H_2 \tag{20}$$

$$CH_4 + 0.5O_2 \xrightarrow{k_7} CO + 2H_2 \tag{21}$$

$$CH_4 + H_2O \xrightarrow{k_8} CO + 3H_2 \tag{22}$$
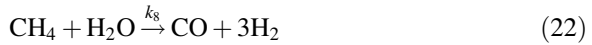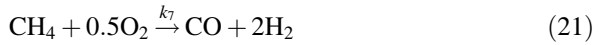
where k is reaction rate, and it can be represented by

$$k = AT^b e^{\left(\frac{-E_a}{RT}\right)} \tag{23}$$

A is Arrhenius-type pre-exponential factor; T is temperature; b is temperature exponent; E_a is activation energy; and R is universal gas constant. Values of these parameters [5] are listed in Table 3.

Table 3 Kinetic parameter of solid- and gaseous-phase reactions

K	A	b	E_a(J/kmol)
k_1	0.052 kg/m^2/s/Pa$^{0.5}$	0	6.1×10^7
k_2	0.0732 kg/m^2/s/Pa$^{0.5}$	0	1.125×10^8
k_3	0.0782 kg/m^2/s/Pa$^{0.5}$	0	1.15×10^8
k_4	6.8×10^{15} (m^3/kmol)$^{0.75}$/K^{-1}/s	-1	1.67×10^8
k_5	2.239×10^{12} (m^3/kmol)$^{0.75}$/s	0	1.674×10^8
k_6	2.34×10^{10} (m^3/kmol)$^{0.5}$/s	0	2.883×10^8
k_7	4.4×10^{11} (m^3/kmol)$^{0.75}$/s	0	1.25×10^8
k_8	8.7×10^7 (m^3/kmol)$^{0.5}$/s	0	2.51×10^8

Table 4 Proximate and ultimate analysis of coal	Proximate analysis (wt% dry basis)		Ultimate analysis (wt% dry basis)	
	F.C.	0.41	C	0.76
	V.M.	0.28	H	0.06
	Ash	0.31	O	0.17
	HHV	32.12 MJ/kg	N	0.01

2.5 Boundary Conditions

The boundary conditions are set as per the operating conditions at ceramic industry defined by gasifier producers (Radhe Renewable Energy Development Pvt. Ltd). Coal was fed from the top at 300 K atmospheric temperature at 0.25 kg/s. Standard Indian bituminous-type coal has been used. Coal parametric data like proximate and ultimate analysis is given in Table 4. Air was fed from the bottom with steam at nearly 400 K temperature at rate of 0.50 kg/s. Steam was added to produce more hydrogen at rate of 0.122 kg/s. Gauge pressure at inlet was nearly 200 mm of water. The outlet of gasifier was with gauge pressure of 120 mm of water column. The wall of gasifier was considered as adiabatic wall with no-slip condition. Figure 1 also indicates all boundary conditions.

2.6 Numerical Considerations

The commercial software ANSYS Fluent was used in this study for numerical simulation. SIMPLE algorithm is used to solve the governing equations with first-order upwind scheme implemented for calculating various convection and diffusion fluxes. Grid independency test has been carried out with same boundary conditions. It has been noted that grid with 30.7 k cells shows maximum temperature inside the gasifier. After generating more finer grid, there has been no change in maximun temperature inside the gasifier. So, grid with 30.7 k cells was considered as optimum grid for simulation.

3 Results and Discussion

In the present study, numerical simulation has been carried out first in experimental operating condition as per ceramic industry. At E.R. value 0.29, the case is validated with gasifier wall temperature at ceramic industry. In actual gasifier,
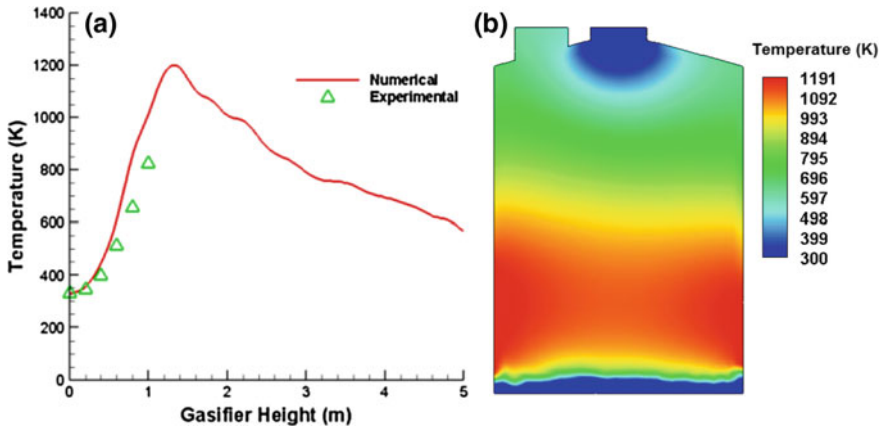
Fig. 2 **a** Temperature distribution on gasfier wall and **b** temperature contour at E.R. value 0.29

six thermocouples are attached at bottom part of wall over 1 m with 0.2 m distance between each of them. Figure 2a shows that within 1 m gasifier height, temperature continuously rises approaching to oxidation zone. Simulation result for temperature distribution shows good agreement with industrial readings. Also, the temperature in the gasifier has been noticed to decrease in reduction and pyrolysis zones.

3.1 Gasification Phenomena

Figure 2b demonstrates static temperature profile of gasifier at E.R. value 0.29. It shows that high temperature is located inside the oxidation zone which is just above the ash zone. From oxidation zone, going upward; temperature is decreasing in reduction and pyrolysis zone simultaneously. Figure 3a–d shows molar fraction profile of CO_2, H_2O, CO, H_2. According to gasification phenomena, we can clearly see that at bottom in oxidation zone, coal particles react with air due to complete combustion; high carbon dioxide and water vapor are formed. In reduction zone, that products again react with oxidizers and form carbon monoxide and hydrogen, i.e., syngas. Near outlet, syngas is carried out at nearly 594 K temperature with gas component molar fraction as CO—28.1%, CO_2—8.4%, H_2—17.7%, H_2O—19.3%, CH_4—0.3%, and N_2—rest.
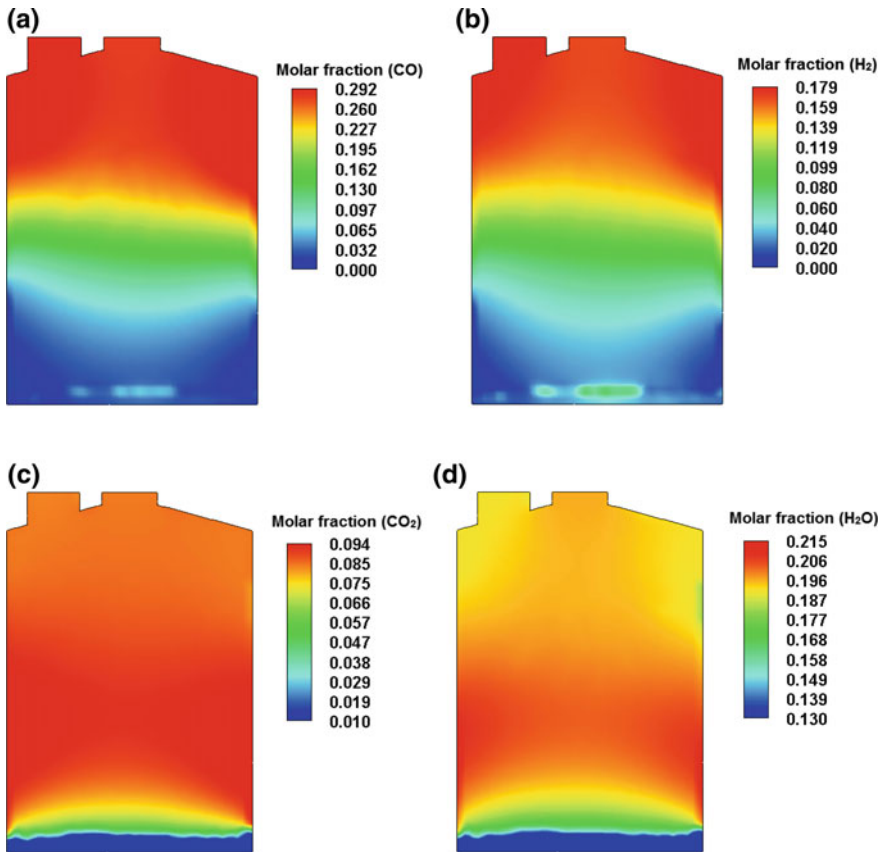
Fig. 3 **a** Molar fraction contour of carbon monoxide at E.R. value 0.29 **b** Molar fraction contour of hydrogen at E.R. value 0.29 **c** Molar fraction contour of carbon dioxide at E.R. value 0.29 and **d** Molar fraction contour of water vapor at E.R. value 0.29

3.2 Effect of Equivalence Ratio

E.R. values are taken as 0.2, 0.24, 0.28, 0.32, 0.36, 0.4 for simulations. E.R. value 0.28 gives the maximum amount of CO. After the increment in E.R. value, CO and H_2 molar fractions are reduced and CO_2 and H_2O molar fractions are increased. This is due to the phenomena that increase in E.R. value leads to complete combustion. Also, with the increase in E.R., outlet syngas mean temperature also increases (Fig. 4).
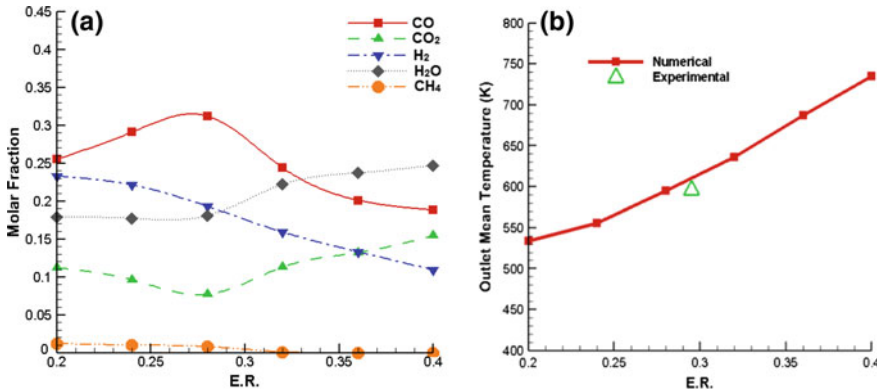
Fig. 4 a Molar fractions of different species at different E.R. values and **b** Outlet mean temperature of syngas at different E.R. values

4   Conclusion

The gasification phenomena of coal in updraft gasifier are explored using a numerical method. From the present study, it has been observed that ceramic industry is working on E.R. value 0.29, while syngas fraction is maximized at E.R. value 0.28. This ensures the optimal running condition of industry working with good prediction.

References

1. Chen, W.-H., Chen, C.-J., Hung, C.-I., Shen, C.–I, Hsu, H.-W.: A comparison of gasification phenomena among raw biomass, torrefied biomass and coal in an entrained-flow reactor. Appl. Energy (112), 421–430 (2013)
2. Higman, C., van der Burgt, M.J.: Gasification, 2nd edn. Gulf Publishing Press (2007)
3. Murugan, P.C., Joseph Sekhar, S.: Species—transport CFD model for the gasification of rice husk (Oryza Sativa) using downdraft gasifier. Comput. Electron. Agric. (139), 33–4 (2017)
4. Fernando, N., Narayana, M.: A comprehensive two dimensional computational fluid dynamics model for an updraft biomass gasifier. Renew. Energy (99), 698–710 (2016)
5. Jeong, H.J., Seo, D.K., Hwang, J.: CFD modeling for coal size effect on coal gasification in a two-stage commercial entrained-bed gasifier with an improved char gasification model. Appl. Energy (123), 29–36 (2014)
6. Zogała, A., Janoszek, T.: CFD simulations of influence of steam in gasification agent on parameters of UCG process. J. Sustain. Min. (14), 2–11 (2015)
7. Murgia, S., Vascellari, M., Cau, G.: Comprehensive CFD model of an air-blown coal-fired updraft gasifier. Fuel (101), 129–138 (2012)

Numerical Analysis of Two-Phase Blood Flow in Idealized Artery with Blockage

Krunal Joisar, Ramesh Bhoraniya and Atal Harichandan

1 Introduction

Hemodynamic is the study of dynamics of blood. The diseases related to the blood circulation mainly depend on the dynamics of blood. Atherosclerosis, the disease in which the diameter of artery reduces due to the plaque formation, is related to blood circulation. This reduction of diameter of artery behaves as a blockage to the blood flow. Blood is non-Newtonian fluid with shear thinning property which is non-homogeneous in nature. Blood mainly consists of plasma, red blood cells (RBCs), and white blood cells (WBCs). In blood, RBCs and WBCs are suspended in the plasma. Plasma is made of 95% by water and rest is the minerals, ions, etc. RBCs are biconcave in shape and their percentage in blood varies from 40 to 50% in male and from 36 to 46% in female [1]. WBCs are roughly spherical in shape; the constitution of WBCs in blood is less than 1%. Non-Newtonian behavior of blood is mainly due to the RBCs and WBCs. For the low shear rates, blood can be considered as Newtonian fluid because non-Newtonian behavior affects very less to the flow characteristics in the large arteries. For the better analysis, non-Newtonian behavior of blood must be considered. In spite of such complexities, blood flow can be efficiently modeled with the use of the computational fluid dynamics (CFD). The abnormal flow conditions such as sudden pressure drop, reduction in flow rate, and high shear stress due to atherosclerosis can be efficiently analyzed using the CFD. Hemodynamics has become topic of interest due to its usefulness in medical science. Many researchers have shown interest in study of hemodynamics which has led to better understanding the blood flow characteristics. Blood flow has been modeled using the Newtonian model of viscosity by many researchers. There are many models of viscosity available in open literature to define the shear thinning

K. Joisar (✉) · R. Bhoraniya · A. Harichandan
Department of Mechanical Engineering, Marwadi Education Foundation
Group of Institution, Rajkot 360003, Gujarat, India
e-mail: Krunal753@gmail.com

behavior of blood. Barbara et al. [2] compared various models for blood viscosity. In many literatures, plasma is considered as Newtonian fluid because it is 95% water [3, 4]. Gidaspow and Huang [5] performed kinetic theory-based simulation of blood flow. Goldsmith and Karino [6] analyzed experimentally the behavior of red blood cells in annular vertex formed due to sudden concentric expansion. The diameter of artery in body varies from 2.5 cm to a few microns. The flow behavior of blood in micro-channel has been addressed by Wu et al. [7]. The cell transport is analyzed into intracranial aneurysm by Chubin et al. [8]. Due to various difficulties in modeling blood flow, many areas such as blood flow with blockage is not addressed properly yet. Thus, present study aims to simulate the blood flow with blockage in order to increase understanding of flow conditions occur due to blockage.

2 Mathematical Modeling

The blood has been simulated as two-phase fluid considering blood as non-Newtonian fluid. In blood, RBCs (dispersed phase) are suspended in plasma (continuous). Eulerian–Eulerian approach of multiphase was used because of its applicability to wide range of volume fraction [9]. The governing equations describing the multiphase model of blood can be summarized as.

2.1 Continuity Equation

Continuity equation for each phase (c = plasma, RBCs) is given by,

$$\frac{\partial(\rho_c \varepsilon_c)}{\partial t} + \nabla \cdot \left(\rho_c \varepsilon_c \overrightarrow{v_c}\right) = 0 \tag{1}$$

where ρ is density, ε is the volume fraction, t is time, and v is velocity.

2.2 Momentum Equation

Momentum equation for each phase is given by:

$$\frac{\partial(\rho_c \varepsilon_c \vec{v}_c)}{\partial t} + \nabla \cdot (\rho_c \varepsilon_c \vec{v}_c \vec{v}_c) = -\varepsilon_c \nabla p + \nabla \cdot \overline{\overline{\tau}}_c + \rho_c \varepsilon_c \vec{g} \\ + \sum_{l \neq c} \alpha_{\mathrm{pq}} (\overrightarrow{v_q} - \overrightarrow{v_p}) + \overrightarrow{F_c} \tag{2}$$

where p is the pressure, τ is stress–strain tensor, F is the external forces such as virtual mass, rotational, and shear lift. In drag force, the subscripts p and q represent the plasma and RBCs, respectively.

2.3 Blood Rheology

The mixture viscosity of blood is the function of shear rate and hematocrit (volume fraction of RBCs). The Quemada viscosity model [10, 11] was used to simulate the blood flow. The viscosity of blood is given by,

$$\mu = \mu_p \left[1 - \frac{\varepsilon_q}{2} \left(k_\infty + \frac{k_0 - k_\infty}{1 + (\dot{\gamma}/\dot{\gamma}_c)^b} \right) \right]^{-2} \tag{3}$$

where k_∞ and k_0 are the intrinsic viscosities. $\dot{\gamma}$ is local shear rate. $\dot{\gamma}_c$ is critical shear rate.

These parameters are given as,

$$b = 0.5 \tag{4}$$

$$k_0 = 55\,\varepsilon_q.e^{-6\varepsilon_q} + 1.9 \tag{5}$$

$$k_\infty = 1.65\left(\varepsilon_q + 0.05\right)^{-0.3} \tag{6}$$

$$\dot{\gamma}_c = 1 \tag{7}$$

3 Numerical Considerations

The present numerical solution has been obtained using multiphase Eulerian–Eulerian method by using ANSYS Fluent software. No slip boundary condition is applied at walls. For outlet boundary, pressure outlet condition with zero static pressure is selected. Velocity inlet boundary condition is applied at inlet for all the cases. For non-Newtonian behavior of blood, Quemada viscosity model is customized by a user-defined function (UDF) in ANSYS Fluent. The convergence was achieved with maximum 10^{-5} residual level. The grid independent study for the computational mesh in the present numerical simulation of blood flow over a sudden expansion geometry has been carried out. The results show that the mesh with 22,184 elements provides optimum results in terms of maximum velocity in the geometry. Therefore, all simulations attributing to the present work were carried out with that particular mesh.

4 Results

In the present research work, the blood flow has been modeled by using a sudden expansion model as shown in Fig. 1 with two different blood flow conditions.

Case 1 Blood with 1% hardened red blood cells (diameter = 7.5 µm, density = 1.13 g/cm^3) suspended in water (density = 1.0 g/cm^3, dynamic viscosity = 0.001 Pa.s) simulated at two different steady velocities of 7.57 and 23.3 cm/s.

For case 1 with 1% hardened RBCs at two steady-state velocities of 7.57 and 23.3 cm/s, the location of reattachment of flow was found to be in good agreement with the experimental results [6] (Table 1).

The contours for velocity distribution and velocities at various locations in vertex region are shown in Fig. 2 and Table 2, respectively. The comparison of
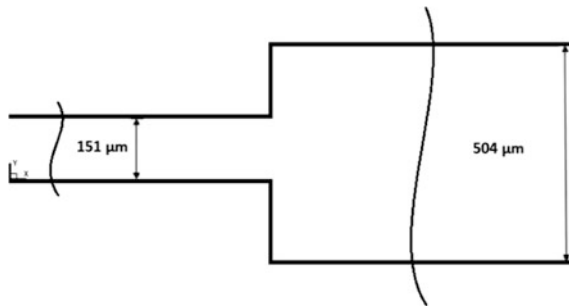
Fig. 1 Sudden expansion geometry

Table 1 Reattachment length

Velocity (cm/s)	Experimental results (µm) [6]	Present work (µm)
7.57	222	210
23.3	638	600
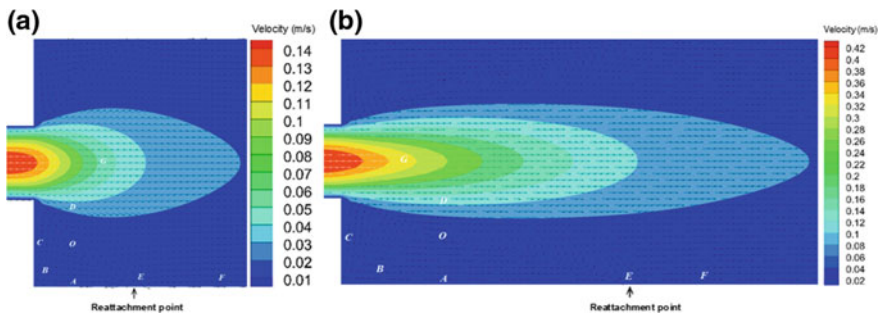
Fig. 2 Velocity contours for **a** 7.57 cm/s and **b** 23.3 cm/s steady velocities

Table 2 Comparison of velocities (m/s) in vertex region

Locations	Velocity = 0.0757 m/s			Velocity = 0.233 m/s		
	Karino and Goldsmith [6]	Jung et al. [9]	Present work	Karino and Goldsmith [6]	Jung et al. [9]	Present work
O	0.54	0.825	0.92	2.44	4.426	5.17
A	0.64	0.375	0.36	3.59	5.313	3.88
B	0.36	0.522	0.26	3.03	6.122	1.41
C	1.46	1.567	0.82	6.93	12.082	4.05
D	11.8	24.399	13.7	94.1	89.646	92.1
E	0.3	0.328	0.27	0.84	0.573	1.29
F	3.3	0.7	2.61	0.95	2.947	3.73
G	48.6	52.339	50.97	272	314.423	283

velocities shows good agreement with the experimental results [6] and numerical results [9] as shown in Table 2.

Case 2 Blood with 45% red blood cells (diameter = 8 µm, density = 1096 kg/m^3) suspended in plasma (density = 1020 kg/m^3, dynamic viscosity = 0.0011 Pa.s). Simulations were performed at 40.3 and 55 cm/s steady velocities.

The distribution of RBCs for both the velocities is presented in Fig. 3. The contour shows that the vertex region becomes more RBC depleted as the velocity increases, which shows consistency of multiphase model with the experimental results and numerical results [6, 9].
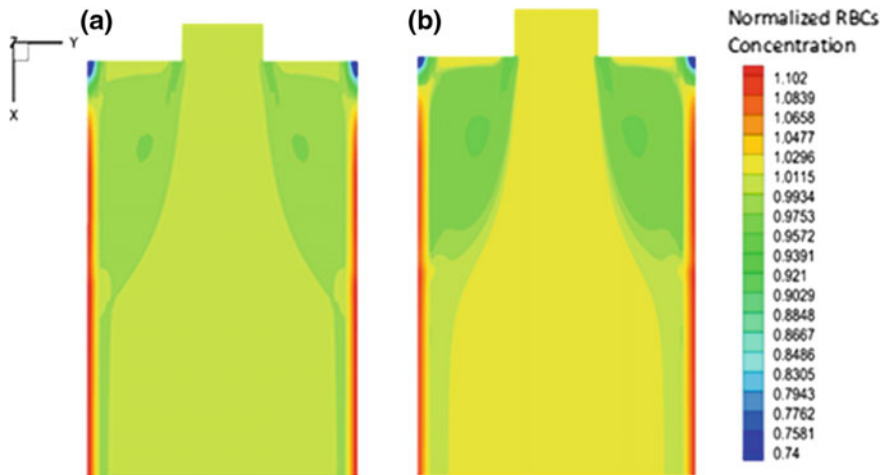
Fig. 3 **a** RBCs distribution at 40.3 cm/s with 45% RBCs volume fraction, **b** RBCs distribution at 55 cm/s velocity with 45% RBCs volume fraction
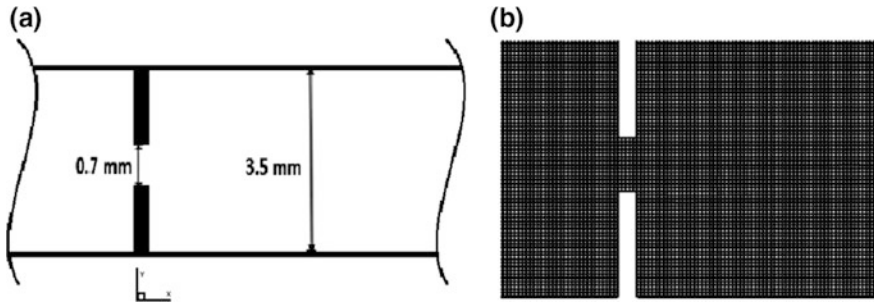
Fig. 4 **a** Geometry of idealized artery with blockage, **b** enlargement of mesh of idealized artery near blockage
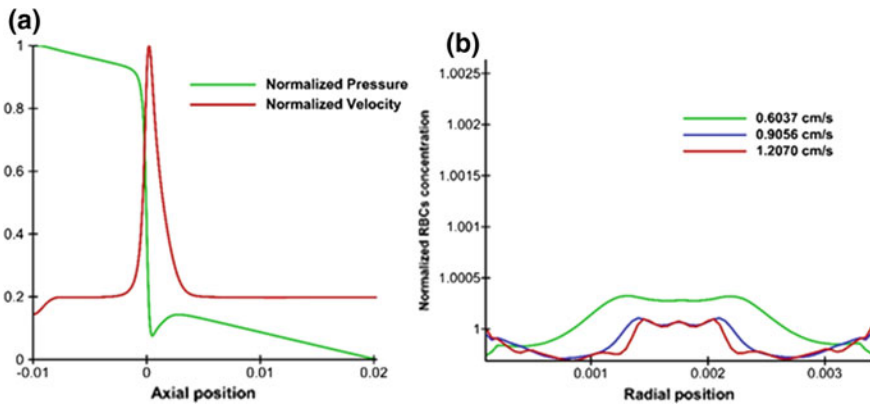
Fig. 5 **a** The variation of normalize pressure and normalized velocity along centerline of artery for 45% RBCs volume fractions at 1.2070 cm/s, **b** normalized distribution of RBCs along radial direction at 2 mm after blockage for three steady velocities of 0.6037, 0.9056, and 1.2070 cm/s

The validation of the present numerical model for multiphase blood flow through a sudden expansion geometry ensures the accurate selection of numerical model parameters. Therefore, authors intend to use the same model for a two-dimensional geometry of idealized artery with significant blockage (80% in present case) as shown in Fig. 4 with the inlet and outlet diameters of 3.5 mm, and the blockage diameter of 2.8 mm with the 0.25 mm thickness of blockage.

The simulations on the idealized artery with blockage were carried out considering 45, 40, and 30% of RBCs volume fraction for three steady velocities of 0.6037, 0.9056, and 1.2070 cm/s. The reduction in pressure with the increase in velocity due to blockage is plotted at 45% of RBCs volume fraction as shown in Fig. 5a. It is observed that pressure reduces significantly due to blockage. Figure 5b shows the distribution of RBC at the section of 2 mm after blockage for three

steady velocities. The trend of migration of RBCs toward center increases as the velocity increases.

The contour for RBCs distribution across artery geometry is plotted for three different steady velocities at 45% RBCs volume fraction as shown in Fig. 6. From the contour, it is observed that the vertex region become more RBC depleted as the velocity increases. For the area before blockage, RBCs concentration reduces as the velocity increases.

However, the pressure reduction at various RBCs concentration for three velocities is shown in Fig. 7a. The total pressure increases with increase in RBCs
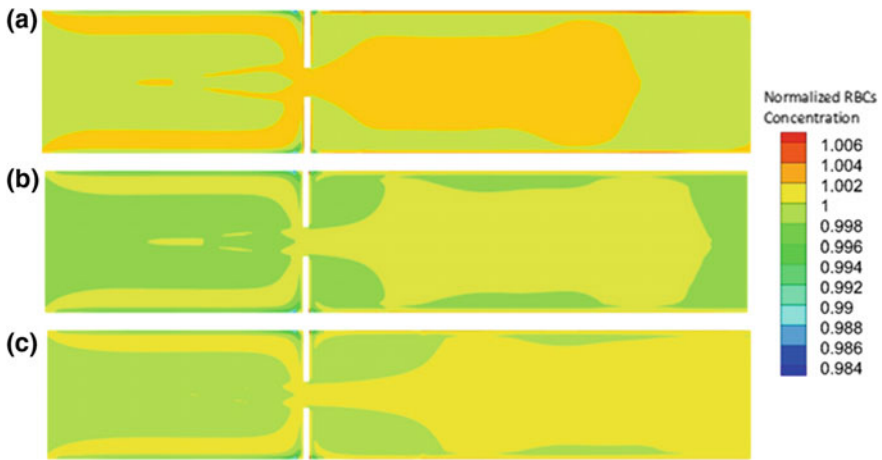
Fig. 6 **a** Normalized RBCs concentration at 0.6037 cm/s, **b** normalized RBCs concentration at 0.9056 cm/s, **c** NORMALIZED RBCs concentration at 1.2070 cm/s. All at 45% RBC volume fraction
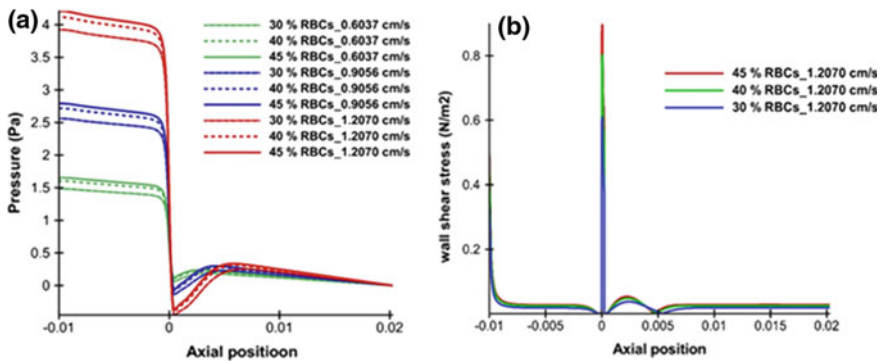
Fig. 7 **a** Pressure variation along center of artery for 30, 40, and 45% of RBCs volume fraction at 0.6037, 0.9056, and 1.2070 cm/s velocities. **b** Wall shear stress variation with RBCs volume fraction at 1.2070 cm/s velocity

volume fraction and the maximum velocity in the artery decreases. Although the effect of increase in RBCs volume fraction on the reduction of pressure is very less, the wall shear stress increases considerably with increases in the RBCs volume fraction which can be observed from Fig. 7b.

5   Conclusion

The multiphase model of blood flow with steady velocity is validated and used to simulate the blood flow in idealized artery with 80% blockage. From the present study, it is observed that the abnormal pressure reduction occurs due to blockage and pressure reduction increases as the velocity of flow increases but the reduction in pressure is very less affected by change in RBCs volume fraction. The shear stress abnormally increases due to blockage and increase in shear stress is significantly affected by the RBCs volume fraction in blood. As the volume fraction of RBCs in blood increases, the shear stress also increases significantly. The vertex region has been observed to be RBC depleted region and it increases with the velocity of flow. This study can become base to the analysis of various diseases related to blood flow. The results from present work can further be used to analyze the effect of blockage in blood flow in realistic artery. The present study can also be carried out with consideration of WBCs in blood flow. Also, simulation of pulsating blood flow can be considered that will provide more details about vivo flow and the effect of blockages on atherosclerosis.

References

1. Lewis, S.M., Dacie, J.V.: Practical Haematology, pp. 12–17. Churchill livinstone, London (1995)
2. Barbara, M.J., Peter, R.J., Stuart, C., David, K.: Non-Newtonian blood flow in human right coronary arteries: transient simulations. J. Biomech. **39**, 1116–1128 (2006)
3. Lightfoot, E.N.: Transport phenomena and living systems. In: Biomedical Aspects of Momentum and Mass Transport. Wiley, New York (1974)
4. Strang, K.T., Widmaier, E.P., Raff, H., Sherman.: Luciano's human physiology. In: The Mechanisms of Body Functions. McGrow-Hill, New York (2004)
5. Gidaspow, D., Huang, J.: Kinetic theory based model for blood and its viscosity. Ann. Biomed. Eng. **37**, 1534–1545 (2009)
6. Karino, T., Goldsmith, H.L.: Flow behaviour of blood cells and rigid spheres in an annular vortex. Philos. Trans. R Soc. London B **279**, 413–445 (1977)
7. Wu, W.T., Kim, J., et al.: A numerical study of blood flow using mixture theory. Int. J. Eng. Sci. **76**, 56–72 (2014)
8. Chubin, O., Huang, W., Matthew, M.Y., Qian, Y.: Hemodynamic modeling of leukocyte and erythrocyte transport and interactions in intracranial aneurysms by a multiphase approach. J. Biomech. **49**, 3476–3484 (2016)
9. Jung, J., Hassanein, A., Lyczkowski, R.: Three-phase CFD analytical modeling of blood flow. Med. Eng. Phys. **30**, 91–103 (2008)

10. Quemada, D.: Rheology of concentrated disperse system II: a model for non-newtonian shear viscosity in steady flows. Rheol. Acta **17**, 632–642 (1978)
11. Buchanan, J.R., Kleinstreuer, C., Comer, J.K.: Rheological effects on pulsatile hemodynamics in a stenosed tube. Comput. Fluids **29**, 695–724 (2000)

Generalized Design of Experiments for Structural Optimization

A. V. Pavan Kumar, Karandas Kornaya, Srihari Bharadwaj and S. Sanjeev

1 Introduction

Mechanically, optimization is choosing the best solution without being under-designed or over-designed. It is also true that the analysis and optimization go hand in hand. The constraint equations are applied to the analysis data, and the iterative analysis is carried out to get the exact analysis results. Reduction of the stress in the analysis is not only the sole purpose of analysis. Instead, reduction of mass with considerable stress without being under-designed or over-designed should be the purpose for optimization.

Any mechanical design can be explicitly considered for optimization using design of experiments (DOEs). Software such as ANSYS has now got the capability to do the DOE. This DOE uses a technique such as the MOGA algorithm which is specially designed for multiple-input multiple-output systems. The results from screening algorithm for the initial approximation can be used as design points or candidate points in some cases. But those algorithms fail to work when the structure is 1D which spans in three dimensions, the software tries to mesh the structure as 3D mesh, and hence, the time for solving them drastically increases. The proposed method for DOE and optimization methods follow sensitivity analysis, getting design points, regression analysis, creation of surface response,

A. V. Pavan Kumar (✉)
Erasmus Mundus, Mathematical Modelling in Engineering, L'Aquila, Italy
e-mail: pavanku222@gmail.com

K. Kornaya
Nitte Meenakshi Institute of Technology, Bengaluru, India

S. Bharadwaj
Sathyabama Institute of Science and Technology, Chennai, India

S. Sanjeev
JSS Science and Technological University, Mysore, India

269

equation of surface, finding best solution by constraint equation. We use interpolation model to create the optimum solution and is explained in the subsequent sections.

2 Pre-optimization Analysis

Referring to Suraj et al. [1] for the material selection, frame design, methodology, loading conditions, assumptions during analysis are exactly same, but for Fig. 1 with mesh size 60 division per line and type of convergence H type, results of the analysis are given in Table 1. Throughout the paper, only eight inputs are considered (also possible to consider more).

1. $R1$ and $T1$ are the outer radius and the thickness of the main roll hoop.
2. $R2$ and $T2$ are the outer radius and the thickness of the front roll hoop.
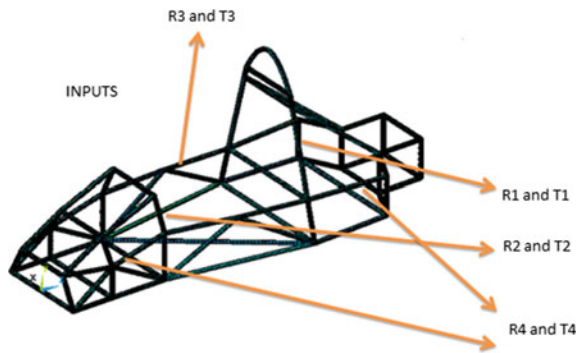
Fig. 1 DOE break up

Table 1 Initial value for the analysis results

Results	Front impact	Rear impact	Side impact	Roll over
Force acting (N)	35,312	8829	7357.5	8829
Type	To the front four nodes	To the rear four key points	To the side impact members	Front and main roll hoop
Fixing points	Suspension pickup points	Front pickup points	Opposite side impact members	Bottom of the chassis
Max von Mises stress (MPa)	202.87	272.391	193.112	101.66
Factor of safety	1.897	1.413	1.99	3.787
Max deflection (mm)	1.224	4.957	3.863	0.4602

3. $R3$ and $T3$ are the outer radius and the thickness of the side impact members.
4. $R4$ and $T4$ are the radius diameter and the thickness of all other members including bracings, front impact members, side supports.

The initial values for the analysis results showed in Table 1 are $R1 = R2 = R3 = R4 = 12.7$ mm and $T1 = 2.4$ mm, $T2 = 2.7$ mm, $T3 = 1.7$ mm and $T4 = 1.4$ mm. The values are just the best guess, and there is no special reason for the consideration. In fact, there is no mistake in considering any other values and still getting the exact same result at the end.

3 Sensitivity Analysis

It is very important to know the factors which affect the stress. As mentioned earlier, eight-dimensional variations are considered as inputs and the stress is the output, since there are four different loads acting on the same structure at different places of different types at different times. It is easy for one to think to do an explicit dynamic analysis for the system. But if the system has been broken down to small parts and each result is controlled by the factor which can be bounded by some value of output, then the need of explicit analysis is ruled out and can be done just by using static analysis.

For all four kinds of analysis, a common radius of 12.7 mm and thickness of 1.4 mm is considered for sensitivity analysis (again the choice of a person can be varied). And by changing the thickness, if the stress changes, this indicates the sensitivity of the member involved. To be precise, it is to be noted that $T(i)$ is changed keeping the $R(i)$ constant that means outer radius is kept constant and the thickness varies. This changes the dimension of the section (i). It is very important to realize that the principal stress acts in a plane. In the whole car chassis, it acts only in one part and in one single plane. It is very important to locate these stress positions in the chassis. Usually, the position will be the position of maximum principal stress. Changing the dimensions of these stress positions highly affects the system and can be called as sensitivity. In other words, changing the dimensions of the position having maximum stress or the principal stress leads to change in the stresses drastically and the changed dimensions are sensitive to the input.

Considering the von Mises stress would be appropriate as the maximum stresses as they are always located in the principal plane. But in case, if the maximum stress occurs in the weld joint, there exits multiple sensitivity where the problem has to be handled differently. From the results, it can be inferred that the first principal stress is always positive which in turn means that the first principal stress always tries to create the crack. Von Mises stress will not be always equal to the principal stress. If the middle and minimum principal stresses are trying to oppose the first principal

Table 2 Front impact analysis sensitivity

Section 1		Section 2		Section 3		Section 4		Stress (MPa)
R1	T1	R2	T2	R3	T3	R4	T4	
12.7	1.4	12.7	1.4	12.7	1.4	12.7	1.4	206.859
12.7	1.7	12.7	1.4	12.7	1.4	12.7	1.4	205.665
12.7	1.4	12.7	1.7	12.7	1.4	12.7	1.4	206.859
12.7	1.4	12.7	1.4	12.7	1.7	12.7	1.4	206.641
12.7	1.4	12.7	1.4	12.7	1.4	12.7	1.7	177.765

Table 3 Report of analysis

Type of analysis	Sensitivity
Front impact analysis	Section 4 (S4)
Side impact analysis	Section 1 (S1)
Rear impact analysis	Section 4 (S4)
Roll over	Section 1 (S1)
Torsional rigidity	Section 2 (S2)

stress, the maximum von Mises stress will be lesser than the principal stress. If middle and minimum principal stresses are trying to support the first principal stress, then von Mises stress is greater than the first principal stress. Hence, for this reason, von Mises stress which is the deviatoric stress or the equivalent stress of all the principal stresses is taken as the output to monitor the results in all analysis.

For the sake of reducing huge calculations, a sample for front impact sensitivity is given in Table 2, similar procedure is adopted for all other forces, and the results are tabulated in Table 3.

3.1 Observation from Sensitivity Analysis

S4 (front), S4 (rear) and S1 are sensitive to the loads. But it is also observed that the deflection in the torsional rigidity is affected by S2. Hence, S2 and S1 are considered same. S3 is not sensitive to any kind of analysis. It is not that S3 is least considered. It only means that the dimensions of section 3 are not creating considerable changes in the stress in any analysis. Hence, a least value according to SAE rules 12.7 mm radius and 1.4 mm diameter is considered as S3.

R4 front (mm)	10.7	12.7	14.7	16.7
T4(mm)	Stress (MPa)			
1	383.31	272.906	204.651	159.436
1.2	330.627	234.409	175.283	136.259
1.4	292.984	206.859	154.231	123.712
1.6	264.815	186.195	138.411	123.54

Table 4 Design points of front impact

3.2 Design Points and Response Surfaces

While creating a response surface, it is more than usual to consider the response surface of dimension 9, in our case, that is, 8 dimensions of input and 1 dimension of output. But the creation takes a lot of time and large sampling, and the root mean square error (RMSE) of the model significantly increases due to the fewer number of design points. In order to get good regression [2] it is recommended to use a large number of design points with various combinations of the order of 2^n combination where n is the number of inputs.

Design points can be constructed as per the requirement. Orthogonal arrays were proved to be more efficient compared to the other arrays used in screening but are more tedious. $L9$, $L16$, $L25$, $L36$, etc., can be used for the optimization [1] purpose depending on the inputs. It is noted that the design points are again iterations carried out in FEM software. An $L16$ array would be good and sufficient enough to determine the equation of third order to find the best solution with least error and residuals. Hence, $L16$ array is considered, and each of the design samples for each type of analysis is tabulated here.

Surface response is plotted subsequently, and the surface equation by interpolation model is created for each of the analyses. Here, only front impact design points are presented in detail in Table 4 and all the other corresponding tables are omitted but graphs for all others are given with their surface equations.

4 Interpolation Model

MATLAB is used to create a continuous and differentiable equation in the bounded domain of $R4 \times T4$ keeping $R4$ is the x-axis, $T4$ in y-axis and stress in z-axis. MATLAB uses the bi-variant interpolation method [2, 3] to fit the surface from the given points. The extension to multi-variate interpolation is not trivial, but is not hard. Figure 2 shows the graph for front impact and also includes the equation and the statistical parameters for the evaluation of goodness of fit. The obtained equation for the impact analysis is written in (1).
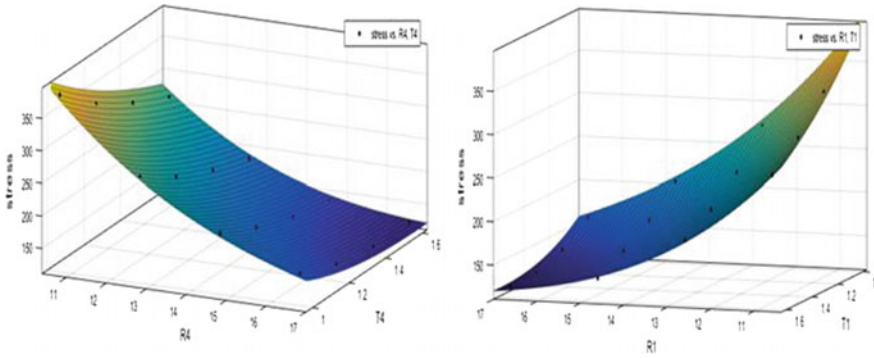
Fig. 2 Response surface for front impact (left) and side impact (right) with R square values 0.9996 and 0.9997, respectively

$$\begin{aligned} \text{Stress} = {}& 2885 - 304.8 \times R - 1168 \times T + 13.74 \times R^2 + 34.38 \times R \times T \\ & + 383.8 \times T^2 - 0.2365 \times R^3 - 0.1846 \times R^2 \times T \\ & - 2.754 \times R \times T^2 - 57.11 \times T^3. \end{aligned} \tag{1}$$

All the figures are created by the polynomials of order three in x and y keeping 95% confidence interval. A similar plot for read impact and roll over can be plotted, and the values of R square are 0.9999 and 0.9998, respectively.

4.1 Multidimensional Bi-section

The response surface is a three-dimensional surface (not 2 D, it is not plane!) as it has length, breadth and height. Implicit equations are found out. These equations are chopped by using another two-dimensional plane [1]. The intersection of these curves is a dimension lesser than the lower order of the intersecting plane, i.e. two-dimensional curve [1, 2].

The intersection of any two curves is the solution to system of two equations by equating them together [3]. Similarly, if two surfaces intersect then equating two surfaces leads to the solution.

If $Z = f(x, y)$ is a surface, and $z = g(x, y)$ is a plane [3]. Then, the intersecting plane is solved as $f(x, y) = g(x, y)$ or it can be combined to solve.

$f(x, y) - g(x, y) = 0$ [3], and this equation is solved to get possible points. These points are used to create the curves. Below plot shows the combination of response surface having $D4$ and $T4$ as the inputs and the $z = 200$ curve (Fig. 3).
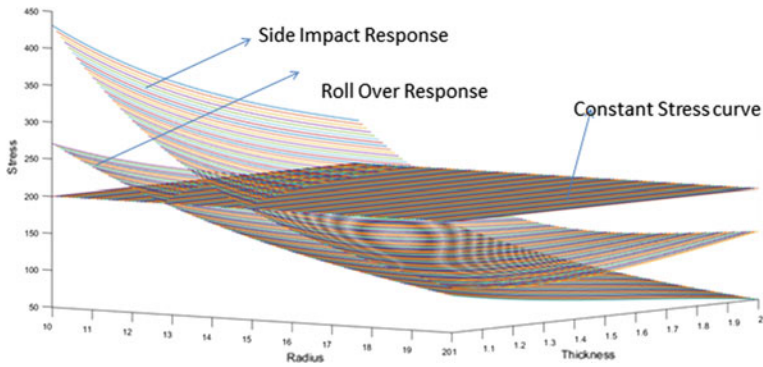
Fig. 3 Combined response surfaces

5 Results and Conclusion

The optimization solutions we obtain from this are not just points but, in fact, an infinite number of points collected as a continuous line. The results are obtained by taking the surface $Z(x, y)$ and cutting the whole surface by the method of characteristics with another surface that is the constant surface of $G(x, y) = 200$. The reason why 200 is chosen is according to the design consideration, and the same can be done for any value of stress. A MATLAB code is constructed based on the linear algebra and the statistics to obtain the results (Fig. 4).

Table 5 represents the optimum solution of the problem. It is also noted that when there are infinite solutions, the medium of the intersecting continuous curve is
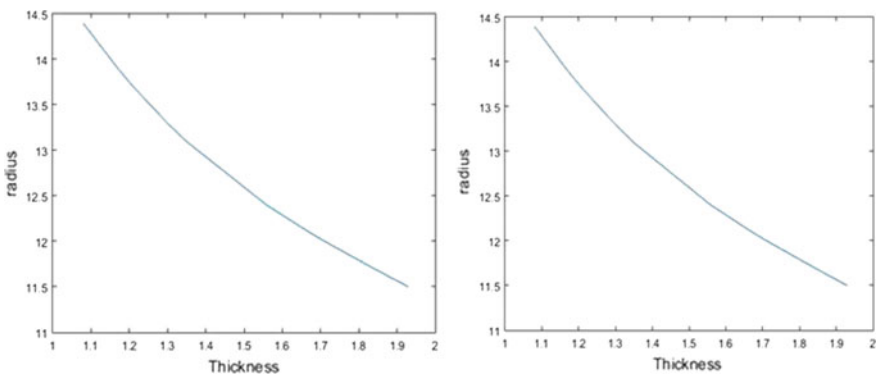
Fig. 4 Intersecting curves of $R4$, $T4$ (left) and $R1$, $T1$ (right)

Table 5 Optimum solution of the problem

Radius	Value (mm)	Thickness	Value (mm)
R4 (front)	13.30	T4 (front)	1.35
R4 (rear)	13.10	T4 (rear)	1.98
R1	13.10	T1	1.45
R2	13.10	T2	1.4
R3	12.7	T3	1.4

taken as the solution. If there is a mass constraint along with the problem, then the solution with least mass is considered as an optimum solution.

References

1. Suraj, R., Pavan Kumar, A.V., Kulkarni, A.P., Kiran, Aithal S., Vinutha, R.: Optimization technique applied for method of evaluation of a controllable factor of FSAE car chassis. In: Bajpai, R., Chandrasekhar, U. (eds.) Innovative Design and Development Practices in Aerospace and Automotive Engineering. Lecture Notes in Mechanical Engineering. Springer, Singapore (2017)
2. Pavan Kumar, A.V., Yeshodhara, B., Vinayaka, N. Dr., Banerjee, N.: Effective optimisation technique using bivariate interpolation methods. Int. J. Advancements Mech. Aeronaut. Eng. IJAMAE **2**(2). ISSN: 2372-4153
3. Kiusalaas, J.: Numerical Methods in Engineering with Matlab. Cambridge Publications, Cambridge

Numerical Prediction of Performance of a Double-Acting α-Type Stirling Engine

Hsi-Yao Yang, Yi-Han Tan and Chin-Hsiang Cheng

1 Introduction

Sources of renewable energy come in many different types, where solar thermal energy technology is one of the most feasible energy sources in Taiwan. The central and south Taiwan is sunshine resource-rich region. Therefore, solar thermal energy can be utilized in a combination of concentrating dish solar power system [1] and Stirling engine for power generation with efficiency of 22–28% [2]. Other than that, the north-east and east Taiwan region are located on the Pacific Ocean Ring of Fire, providing an abundant source of geothermal energy, predicted to have power generation potential of 730 MW [3]. This heat energy source can be applied in Stirling engine power generation to provide clean energy. Stirling engine is made of compression space at cold end, expansion space at hot end, regenerator connecting both spaces and its linked mechanisms. The ideal Stirling cycle is made of two isochoric processes and two isothermal processes.

A multiple cylinder engine can provide higher power output with a smaller size of cylinder diameter, stroke and lower charged pressure. Double acting means the expansion space and compression space are located at both sides of pistons, thus working fluid of both chambers apply force on the piston at the same time. The working fluid expansion in expansion space pushes the piston, while compression in compression space pulls the piston. Both forces acting in the same direction can increase the overall efficiency of engine. The phase angle of the pistons is to be a

H.-Y. Yang · Y.-H. Tan (✉) · C.-H. Cheng
Department of Aeronautics and Astronautics, National Cheng Kung University,
Tainan, Taiwan
e-mail: yihan0205@gmail.com

H.-Y. Yang
e-mail: n794590@gmail.com

C.-H. Cheng
e-mail: chcheng@mail.ncku.edu.tw

cycle divided by the number of cylinders. In this case, the four-cylinder engine has a phase angle of 90°. The basic concept of a four-cylinder double-acting Stirling engine is to connect the expansion space of one α-type Stirling engine to the compression space of another forming four engine cylinders. This engine has a total of four expansion spaces, four compression spaces and four regenerator channels. Comparing the four-cylinder double-acting α-type Stirling engine to conventional α-type Stirling engine, this engine is much simpler in terms of its mechanism and maintenance as four pistons are removed from its configuration. The non-explosive nature of Stirling engine also gives a silent and environmentally friendly operation.

Following the advancement of computing technology, computer-aided design and computer-aided engineering, computational fluid dynamics becomes so widely in use in many industrial prototype design and analysis. Computational fluid dynamics is an effective tool in visualizing physical phenomenon of fluid while overcoming the downside of experiments, which include excessive time and high cost. This research develops the engine's thermal and flow field numerical simulation model using Fluent software to predict its power output and thermal efficiency. Parametric analysis is carried out to study the effects of varying charged mass, heating temperature and porosity on engine performance. These results are useful in predicting the optimum operating condition for the engine to perform at its best.

The numerical simulation in this research is based on the four-cylinder double-acting α-type Stirling engine designed by Fung [4]. His engine design is based on the double-acting Stirling engine by Whisper Gen Technology company [5]. A prototype of four-cylinder double-acting Stirling engine is designed and built. A wobble yoke mechanism is chosen for its simplicity and easy to manufacture traits. With reference to this engine design and geometry, this research looks forward to validate the simulation results with its future thermodynamic model simulation or experimental results.

In addition, in Nguyen's study, the computational fluid dynamics (CFD) simulation of four-cylinder double-acting α-type Stirling engine is carried out in Fluent software. User-defined functions (UDFs) are adapted to the software to model to piston motion in all four cylinders of engine. His simulation result shows that all four cylinders have similar thermal and flow fields. Each cylinder also produces similar power output [6]. Therefore, it can be concluded that only simulation of one cylinder of engine is necessary. This helps to save a lot of computational resources. In the CFD simulation of Stirling engine, one important consideration is the modelling of regenerator. The regenerator in Stirling engine absorbs heat from working gas when gas flows from heater to cooler and releases heat during the reverse process. Relations for calculating heat transfer and pressure drop characteristics in oscillatory flow of regenerator, such as Darcy permeability, Forchheimer's inertial coefficient needs to be applied in CFD modelling [7, 8]. The viscous resistance coefficient and inertial resistance coefficient can be calculated from the wire mesh geometry and regenerator's porosity.

2 Numerical Simulation Methods and Theory

2.1 Basic Assumptions

A few basic assumptions are made for the numerical simulation:

1. The engine working fluid domain is modelled as three-dimensional transient turbulent flow field.
2. Working fluid is assumed as ideal gas.
3. Working fluid is assumed as compressible gas.
4. Gravity effects are neglected.

2.2 Governing Equations

The governing equations implemented in the CFD analysis include mass conservation equation, momentum conservation equation and energy conservation equation. The equations are shown as below.

Mass conservation equation:

$$\nabla \cdot \rho \vec{V} + \frac{\partial \rho}{\partial t} = 0 \tag{1}$$

Momentum conservation equation:
x-direction:

$$
\nabla \cdot (\rho \vec{V} u) + \frac{\partial(\rho u)}{\partial t} = -\frac{\partial P}{\partial x} + \frac{\partial \sigma_{xx}}{\partial x} + \frac{\partial \tau_{yx}}{\partial y} + \frac{\partial \tau_{zx}}{\partial z} \\
+ \frac{\partial(-\rho \overline{u'u'})}{\partial x} + \frac{\partial(-\rho \overline{u'v'})}{\partial y} + \frac{\partial(-\rho \overline{u'w'})}{\partial z} + F_x \tag{2}
$$

y-direction:

$$
\nabla \cdot (\rho \vec{V} v) + \frac{\partial(\rho v)}{\partial t} = -\frac{\partial P}{\partial z} + \frac{\partial \tau_{xy}}{\partial x} + \frac{\partial \sigma_{yy}}{\partial y} + \frac{\partial \tau_{zy}}{\partial z} \\
+ \frac{\partial(-\rho \overline{v'u'})}{\partial x} + \frac{\partial(-\rho \overline{v'v'})}{\partial y} + \frac{\partial(-\rho \overline{v'w'})}{\partial z} + F_y \tag{3}
$$

z-direction:

$$\nabla \cdot (\rho \vec{V} w) + \frac{\partial(\rho w)}{\partial t} = -\frac{\partial P}{\partial z} + \frac{\partial \tau_{xz}}{\partial x} + \frac{\partial \tau_{yz}}{\partial y} + \frac{\partial \sigma_{zz}}{\partial z}$$
$$+ \frac{\partial(-\rho \overline{w'u'})}{\partial x} + \frac{\partial(-\rho \overline{w'v'})}{\partial y} + \frac{\partial(-\rho \overline{w'w'})}{\partial z} + F_z \qquad (4)$$

Energy conservation equation:

$$\frac{\partial(\rho h)}{\partial t} + \nabla \cdot (\rho \vec{V} h) = \frac{DP}{Dt} + \frac{\partial}{\partial x}\left[\left(k_{\text{th}} + \frac{c_p \mu_t}{\text{Pr}_t}\right)\frac{\partial T}{\partial x}\right]$$
$$+ \frac{\partial}{\partial y}\left[\left(k_{\text{th}} + \frac{c_p \mu_t}{\text{Pr}_t}\right)\frac{\partial T}{\partial y}\right] + \frac{\partial}{\partial z}\left[\left(k_{\text{th}} + \frac{c_p \mu_t}{\text{Pr}_t}\right)\frac{\partial T}{\partial z}\right] \qquad (5)$$

2.3 Porous Medium Theory

In the simulation, the regenerator channel is modelled as wire mesh porous medium, whereby two additional source terms need to be added into the momentum equation as in (2–4) [7, 8]. The source terms are viscous resistance coefficient, calculated from Darcy's law and inertial resistance coefficient calculated from Darcy-Forchheimer law. The source terms can be defined as below:

$$F_i = -\left(D\mu\vec{V} + \frac{1}{2}C\rho|\vec{V}|\vec{V}\right) \qquad (6)$$

Based on the geometry, the viscous resistance coefficient and inertial resistance coefficient can be calculated using the equations below.

$$\Gamma = \frac{d_w}{\phi}, \quad 0 < \Gamma < 1 \qquad (7)$$

$$\varphi = 1 - \frac{\pi}{4}\Gamma \qquad (8)$$

$$K_f = \frac{4}{33.6}d_w^2\frac{(1-\Gamma)^3}{\Gamma} \qquad (9)$$

$$c_f = \frac{0.337}{2\sqrt{33.6\Gamma(1-\Gamma)^5}} \qquad (10)$$

Based on (7–10), viscous resistance coefficient and inertial resistance coefficient can be calculated.

$$D = \frac{\varphi^2}{K_f} \tag{11}$$

$$C = \frac{2c_f\varphi^3}{\sqrt{K_f}} \tag{12}$$

2.4 Computation Model

In this research, the realizable k-ε turbulence model is implemented for simulating the thermal and flow fields of engine. This turbulence model satisfies certain mathematical constraints on the Reynolds stresses and is consistent with the physics of turbulent flows. The realizable k-ε turbulence model differs from the standard k-ε model in two important ways:

1. The realizable k-ε model contains a new formulation for turbulent viscosity.
2. A new transport equation for the dissipation rate, ε has been derived from an exact equation for the transport of the mean-square vorticity.

This model is more suitable for predicting flows involving rotation, boundary layers under strong adverse pressure gradients, separation and recirculation. As the gravity and buoyancy effects are affected, the transport equations for k and ε in realizable k-ε turbulence model can be simplified as below:

$$\frac{\partial}{\partial t}(\rho k) + \frac{\partial}{\partial X_j}(\rho k V_j) = \frac{\partial}{\partial X_j}\left[\left(\mu + \frac{\mu_t}{\mathrm{Pr}_k}\right)\frac{\partial k}{\partial X_j}\right]$$
$$+ G_k + G_b - \rho\varepsilon - Y_M + S_k \tag{13}$$

$$\frac{\partial}{\partial t}(\rho\varepsilon) + \frac{\partial}{\partial X_j}(\rho\varepsilon V_j) = \frac{\partial}{\partial X_j}\left[\left(\mu + \frac{\mu_t}{\mathrm{Pr}_\varepsilon}\right)\frac{\partial\varepsilon}{\partial X_j}\right]$$
$$+ \rho C_1 S\varepsilon - \rho C_2\frac{\varepsilon^2}{k + \sqrt{v_g\varepsilon}} + C_{1\varepsilon}\frac{\varepsilon}{k}C_{3\varepsilon}G_b + S_\varepsilon \tag{14}$$

The pressure implicit with splitting of operator (PISO) algorithm is implemented for the pressure–velocity calculation procedure. This algorithm is originally developed for non-iterative computation of unsteady compressible flow.

3 Numerical Simulation Model

3.1 Working Fluid Domain Geometry and Mesh Model

The schematic of the engine geometry is shown in Fig. 1. For the mesh model, the expansion and compression chambers are made of hexahedron mesh, while regions with more complex geometry are finely meshed. The mesh model has 348,923 nodes and 475,283 elements. The mesh has minimum orthogonal quality of 0.221 and maximum skewness of 0.837 which is an acceptable quality of mesh.

3.2 Piston Displacement Function

The wobble yoke mechanism is adapted as mechanism of the four-cylinder double-acting Stirling engine. The wobble yoke angle variation with the tilted plate angle is shown as below:

$$\theta_i = \theta_{\text{plate}} \sin\left(\varpi t - \frac{(i-3)\pi}{2}\right), \quad i = 1, 2, 3, 4 \tag{15}$$

Equation (15) calculates the wobble yoke angle for all four pistons. Taking in the effects of wobble yoke arm and link, the piston displacement function can be defined. In the simulation setup in ANSYS Fluent, the piston motion is modelled
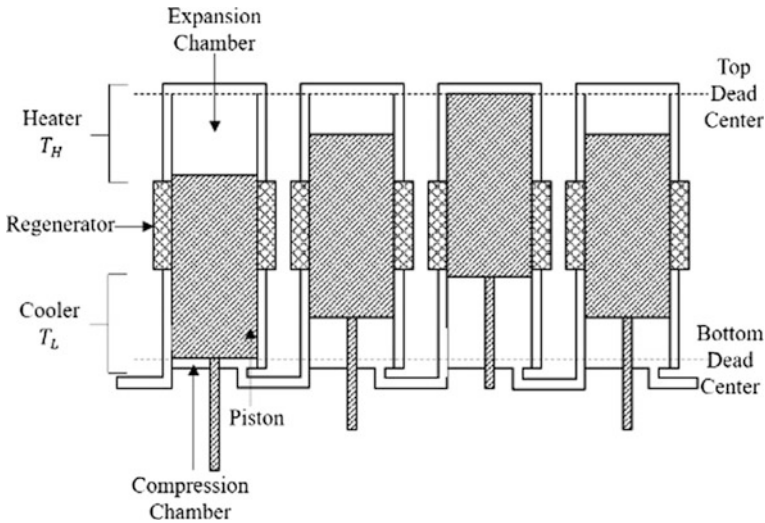
Fig. 1 Schematic of engine geometry

using piston velocity function, which is the differential of piston displacement function. The piston velocity function is shown below. Figure 3 shows the piston velocity profile.

$$
V_{\text{pi}} = 10^{-3} \times \theta_{\text{plate}} \varpi \cos\left(\varpi t - \frac{(i-3)\pi}{2} \right)
$$

$$
\left\{ L_{\text{arm}} \cos \theta_i + L_{\text{link}} \left[\frac{-\xi^2 (1 - \cos \theta_i) \sin \theta_i}{\sqrt{1 - \xi^2 (1 - \cos \theta_i)^2}} \right] \right\} \tag{16}
$$

$$
i = 1, 2, 3, 4
$$

whereby

$$
\xi = \frac{L_{\text{arm}}}{L_{\text{link}}} \tag{17}
$$

3.3 Boundary Conditions Setup

All wall boundaries are set up as no-slip wall. Heating temperature is set as 1000, 1100 and 1200 K for parametric analysis. The cold end temperature is held at constant temperature of 300 K. The walls of regenerator channels, flow channels, expansion and compression chamber are assumed adiabatic and no slip. Both sides of pistons are periodic moving boundaries, modelled using the piston velocity function.

3.4 Charged Mass Setup

The initial total volume of working fluid in all four cylinders is different. Thus, equal charged pressure means unequal mass of working fluid in all four chambers which will produce different power output for each cylinder, leading to vibration in engine and causing damage to the mechanical parts. Therefore, the initial charged pressure has to be determined from the initial total volume of the chamber for equal amount of mass for each of all four cylinders.

3.5 Engine Performance Evaluation

The expansion and compression power can be calculated using (18). The power output of one cylinder is the sum of expansion and compression power. The engine

total power output can be calculated as 4 times of one cylinder power output. Engine thermal efficiency is the ratio of work output and heat input.

$$\dot{W}_{e,c} = \frac{\omega}{60} \oint P_{e,c} dV_{e,c} \tag{18}$$

4 Simulation Results and Discussion

4.1 Baseline Case Results and Discussion

Table 1 shows the engine design parameters. The engine's baseline operating condition is tabulated in Table 2. Figure 2 shows the baseline case *p-V* diagram of expansion and compression chamber in ZONE 1. ZONE 1 is the working chamber between the expansion chamber in cylinder 1 and compression chamber in cylinder 4 as in Fig. 1. One cylinder of the Stirling engine's expansion chamber produces positive power output of 915.24 W, while the compression chamber produces negative power output of −579.74 W. The net power output is 335.50 W. Thus, the engine total power output is 1342 W.

Figure 3 shows the effects of variation of engine speed on ZONE 1 *p-V* diagram which are 1000, 2500 and 3500 rpm. The charged mass in all these cases is 63.4 mg. As the engine speed increases, the area enclosed by the *p-V* diagram decreases. Thus, increasing the engine speed does not necessarily increase the engine power output.

Table 1 Engine design parameters

Cylinder diameter, D_{bore} (mm)	62
Stroke (mm)	37.424
Piston link diameter (mm)	12
Expansion chamber swept volume (c.c.)	451.94
Compression chamber swept volume (c.c.)	387.22

Table 2 Baseline case operating condition

Operating condition	
Hot end temperature	1000 K
Cold end temperature	300 K
Regenerator's initial temperature	650 K
Working fluid charged mass	$m_i = 63.4$ mg
Regenerator's porosity	0.691
Engine speed	2500 rpm
Working fluid	Helium

Fig. 2 Baseline case ZONE
1 *p-V* diagram
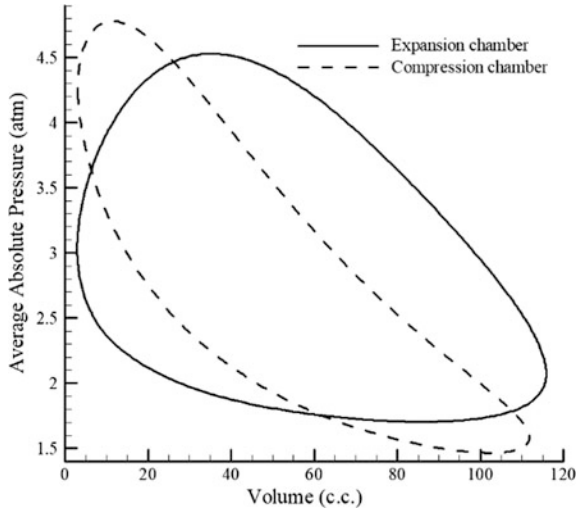
Fig. 3 Effects of engine
speed on ZONE 1
p-V diagram
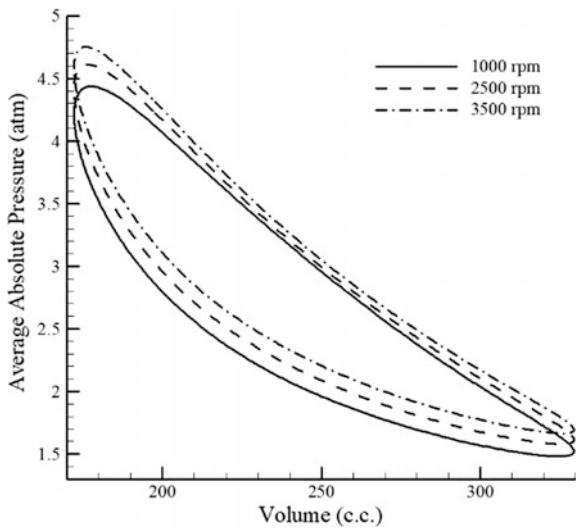
4.2 Effects of Heating Temperature and Engine Speed on Engine Performance

The effects of heating temperature and engine speed on power output and thermal efficiency of engine is shown in Figs. 4 and 5. In all these cases, the charged mass is 317.0 mg. With higher heating temperature, working fluid absorbs more heat per unit time, thus the power output and its corresponding engine speed increases. Besides, thermal efficiency also increases. Meanwhile, with lower heating

Fig. 4 Effects of heating
temperature and engine speed
on power output
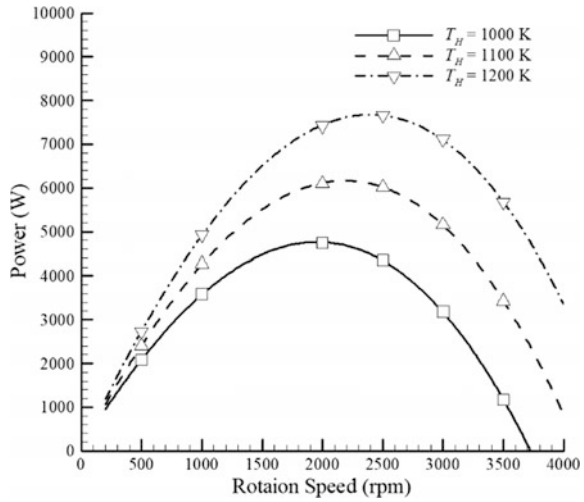
Fig. 5 Effects of heating
temperature and engine speed
on thermal efficiency
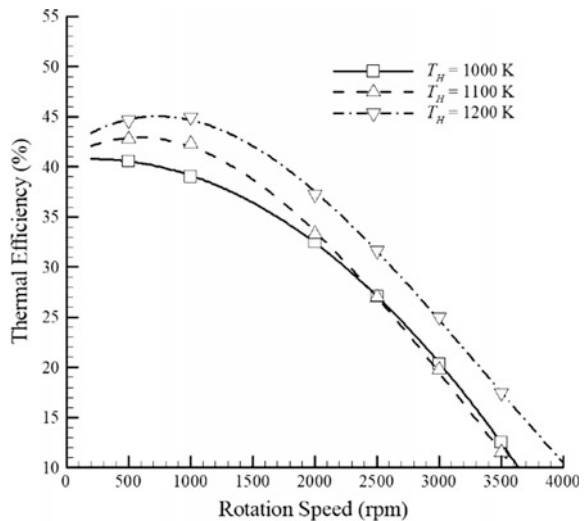
temperature, the working fluid takes longer time to carry out heat exchange with the
heater, thus highest thermal efficiency is achieved at lower engine speed.

4.3 Effects of Regenerator's Porosity on Engine Performance

Figure 6 shows the relationship between power output and the regenerator's porosity,
while Fig. 7 shows the relationship between thermal efficiency and the regenerator's

Fig. 6 Effects of
regenerator's porosity on
power output
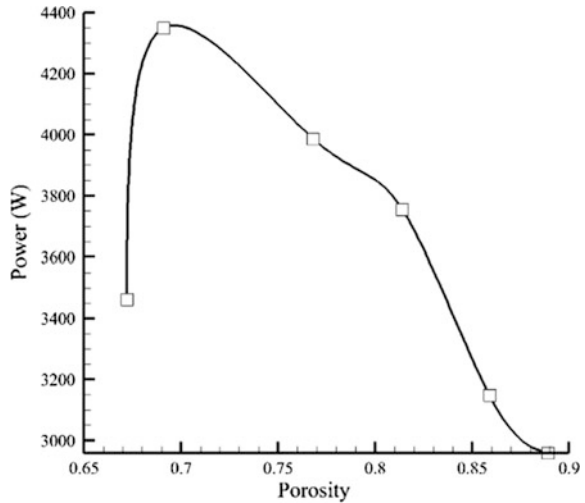
Fig. 7 Effects of
regenerator's porosity on
thermal efficiency
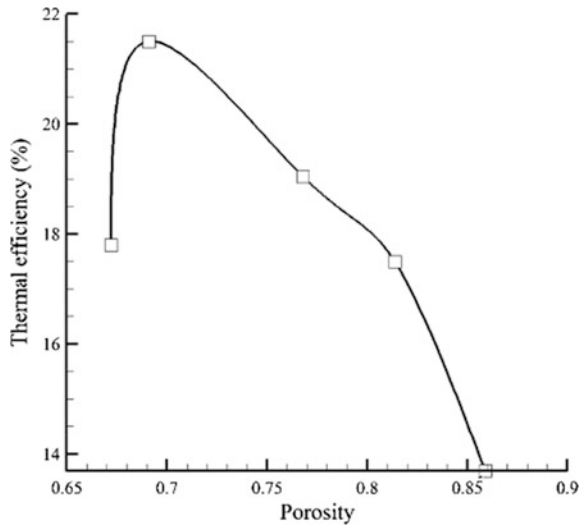
porosity. The operating conditions include charged mass of 317.0 mg, heating temperature of 1000 K, engine speed of 2500 rpm. As regenerator's porosity increases, the regenerator's surface area in contact with working fluid reduces causing thermal efficiency to decrease. On the other hand, as regenerator's porosity increases, the pressure loss also decreases. Therefore, there has to be an optimum regenerator's porosity to produce highest power output. Based on Fig. 7, the regenerator's porosity of 0.691 corresponds to the optimum thermal efficiency of 21.5%. The higher the regenerator's porosity, thermal efficiency and pressure loss will both decrease, thus an optimum regenerator's porosity for optimum thermal efficiency exists.

5   Conclusions

In this paper, the method and results of four-cylinder double-acting Stirling engine numerical simulation are discussed. Parametric analysis is also carried out to study the engine's optimum operating conditions. The baseline case simulation results yield a total power output of 1350 W and thermal efficiency of 25.09%. Based on the results, the optimum operating condition for achieving highest power output can be found. Besides, increasing heating temperature from 1000 to 1200 K at 500 rpm with charged mass of 317.0 mg, the power output increases from 2000 to 2785 W. The optimum regenerator's porosity for best engine performance under baseline operating condition is 0.691 which produces power output of 4248 W.

References

1. Abbas, M., Boumeddane, B., Said, N., Chikouche, A.: Dish stirling technology: a 100 MW solar power plant using hydrogen for Algeria. Int. J. Hydrogen Energy **36**, 4305–4314 (2011)
2. Kolin, I., Koscak-Kolin, S., Golub, M.: Geothermal electricity production by means of the low temperature difference stirling engine. World Geotherm. Congress **2000**, 3199–3203 (2000)
3. Janowski, M.: Alternative Ways of Utilising Geothermal Energy by Means of a Module Based on the Stirling Engine for Electricity Production. World Geothermal Congress, Australia (2015)
4. Fung, T.Y.: Theoretical analysis and design of double acting four-cylinder stirling engine. Master thesis, Department of Aeronautics and Astronautics, National Cheng Kung University, 2017
5. Clucas, D., Raine, J.: The WhisperGen: a strategy for commercial production. In: International Stirling Engine Conference and Exhibition, pp. 159–168 (1997)
6. Nguyen, T.: Numerical simulation of thermal and flow field in a double-acting alpha-type stirling engine. Master thesis, Department of Aeronautics and Astronautics, National Cheng Kung University (2015)
7. Boroujerdi, A., Esmaeili, M.: Characterization of The frictional losses and heat transfer of oscillatory viscous flow through wire-mesh regenerators. Alex. Eng. J. **54**, 787–794 (2015)
8. Landrum, E., Conrad, T., Ghiaasiaan, S., Kirkconnell, C.S.: hydrodynamic parameters of mesh fillers relevant to miniature regenerative cryocoolers. Cryogenics **50**, 373–380 (2010)

Design Optimization, Automation and Testing Analysis of Dust Cleaning Mechanism for Solar Photovoltaic Power Plant

P. A. Patil, J. S. Bagi, M. M. Wagh and G. S. Patil

1 Introduction

Indian energy has come to be known as a "strategic commodity," and any uncertainty about its supply can threaten the functioning of the entire economy, particularly like a developing countries. The energy demand of earth can be easily fulfilled by solar energy. The main method for harnessing solar power is with arrays made up of photovoltaic (PV) cells. Electricity generated using solar photovoltaic (SPV) technology can only be economical if the PV modules operate reliably for 25–30 years under field conditions [1].

Solar photovoltaic conversion technique is largely used as a pioneer and efficient conversion of solar energy. Many factors govern SPV energy conversions efficiency like solar intensity, area of module, semiconductor, tracking mechanisms, dust, and dirt [2, 3]. The dust and other accumulation significantly affect solar cell performance, and by implementing dust cleaning mechanism, it overcomes these problems. Because photovoltaic energy is an accessible technology, it has become a popular investment for companies as well as for residential users. Consequently, this demand has stimulated the research for increasing the overall output power of PV systems causing laboratories all over the globe [4]. The study of different locations data shows that the amount of reduction in power varies from some 30 to 50%. So the cleaning of PV panels is one of the necessary steps for improving the efficiency of the panel.

P. A. Patil (✉) · J. S. Bagi · M. M. Wagh · G. S. Patil
Energy Technology, Department of Technology, Shivaji University, Kolhapur, India
e-mail: pruthvirajpatil135@gmail.com

289

2   Design Optimizations of Dust Cleaning Mechanism

Design Optimization of Brush
So, from Table 1, by comparing we can say that **Synthetic Brush Materials** are optimized material for the brush manufacturing [5, 6].

Design of Drive Motors

$$\textbf{Torque (T) = Force} \times \textbf{Distance}$$

$$\text{Force} = \text{Weight of brush} = 8.0\,\text{kg} = 78.4\,\text{N}$$

$$\text{Distance} = \text{Radius of roller brush} = 60\,\text{mm}$$
$$= 78.4 \times 60 = 4704 \text{ N-mm}$$

This torque is only for idle roller, now roller with contact or considering friction on glass force due to friction is **F = μ.N**.
Where

μ = kinetic coefficient of friction between glass and nylon = 0.17
N = normal reaction = 78.4 N
$F = 0.17 \times 78.4 = 13.32$ N

Table 1 Design optimization of brush

Properties	Natural brush materials	Synthetic brush materials	Antistatic brush materials	Fiber brush materials	Wire brush materials
Shape	Level	**Level or Crimp**	Level	Level	….
Flex life	E	**E**	E	F	P
Springiness or flicking	F	**E**	G	G	P
Bend recovery	F	**E**	G	G	P
Resistance to set	G	**G**	F	F	F
Abrasion resistance	F	**E**	G	P	G
Water absorption	–	**9%**	7%	5%	–
Stiffness in water	F	**F**	G	P	P
Cost	High	**Low**	Avg.	Low	Very High

E = Excellent, G = Good, F = Fair, P = Poor

So total force required = 78.4 + 13.32 = **91.72 N**.
Now total torque required = 91.72 × 60 **= 5503.2 N-mm**.

Design Optimization of Shaft

In this application, the shaft is subjected to combined tensile and bending force and is given by,

$$\tau = \frac{16te}{\pi d^3} \tag{A}$$

where $\tau = \frac{0.5 Syt}{\text{Factor of safety}} = 17.5$

$te = \sqrt{m^2 + T^2} = \sqrt{110^2 + 5503^2} = 5504.09 \text{ N mm}$

So, putting the values in Eq. (A)

$17.5 = \frac{16(5504)}{\pi d^3}, d^3 = \frac{88064}{17.5\pi}$. So $d = \phi$ **= 12.70 mm**.

Design of Coupling

Muff Coupling

Outer diameter of the sleeve, $D = 2d + 13 = 2 \times 12.70 + 13 = $ **38.4 mm**.
Length of the sleeve, $L = 3.5d = 3.5 \times 12.70 = $ **44.45 mm**.

Design of Rack and Pinion Gear

The rubber belt is selected as rack drive [7].

Pitch of belt = 9.525, $9.525/\pi = 3$, so **Module (m) = 3**.

The required load to be travel is approximately 10 kg and 8 number of teeth is selected for the pinion.

For outer diameter of the pinion, we have $D = m(T + 2)$ so **O.D. = 30 mm**.
We have depth of cut $= m \times 2.25$. So, **depth of cut = 6.75 mm**.
Shaft of motor which is used to rotate the gear is 6 mm So, **I.D. = 6 mm**.

Drive Supporting Bracket Assembly

Drive supporting assembling is designed after assembling all designed part as a complete mechanism. The supporting assembly should sustain all forces of mechanism and moves the mechanism as per required directions (Figs. 1 and 2).

3 Drawing of Dust Cleaning Mechanism

See Fig. 3.
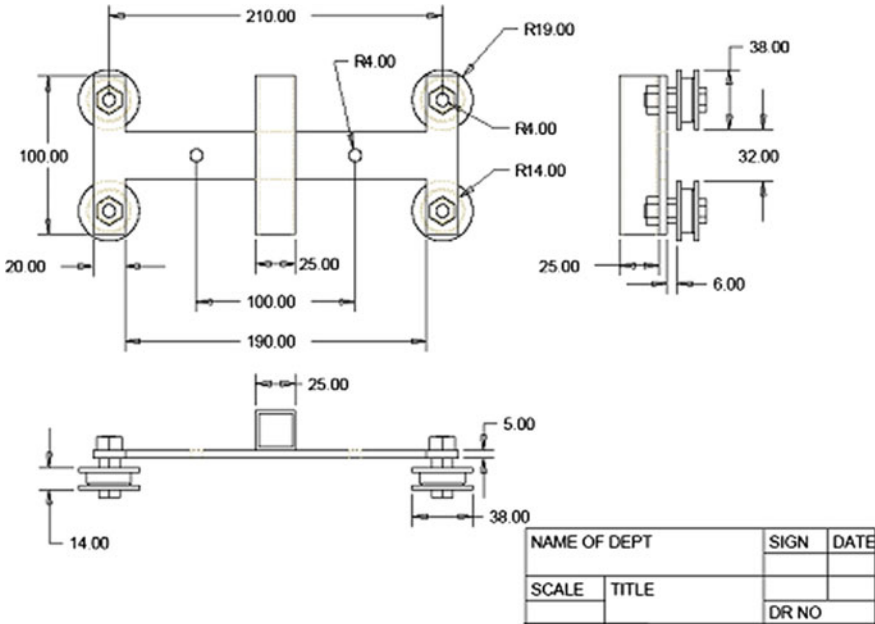
Fig. 1 Drawing of drive supporting bracket assembly

4 Automation of Dust Cleaning Mechanism

4.1 Selection of Electronic and Electrical Components and Brief History

Locomotion

Motors: DC geared motors (1) rated 12 V and 500 rpm for brush rotations. (2) Rated 12 V and 60 rpm for assembly locomotion.

Electronics circuit: Supply 1: 12 V 5 A switched-mode power supply (SMPS) to convert AC to DC. Supply 2: 9 V batteries to power the microcontroller.

Motor Drivers: L298n IC operated motor driver to control the direction and speed of motors according to microcontroller signals. Suitable for 12 V and 0.5 mA driving operations and also has inbuilt circuit protection [8].

Microcontroller: Atmega328p IC attached to the Arduino UNO development board. It is 8-bit microcontroller having analog and digital signal processing functionality according to the program [9, 10].

Sensors: Limit switches to act as edge detectors of the solar panel. Best efforts are made to get RoHS compliant components (Figs. 4, 5, and 6).

Fig. 2 Drive supporting assembly

5 Test Setup and Testing

See Fig. 7.

The above testing setup used to test the performance of solar panel while removing the dust from solar panel. The numerical analysis consists of determination of absolute efficiency, relative loss of panel generation, relative efficiency, and total power output. This determination is found out by following equations

Absolute Efficiency of Solar Panel with Dust

$$\eta_{\text{Absoulute}} = \frac{V_{\text{oc.}}I_{\text{sc.}}\text{ff}}{\text{AI}} = \frac{78.8 \times 4.41 \times 0.7}{3.1 \times 838} = 9\%$$
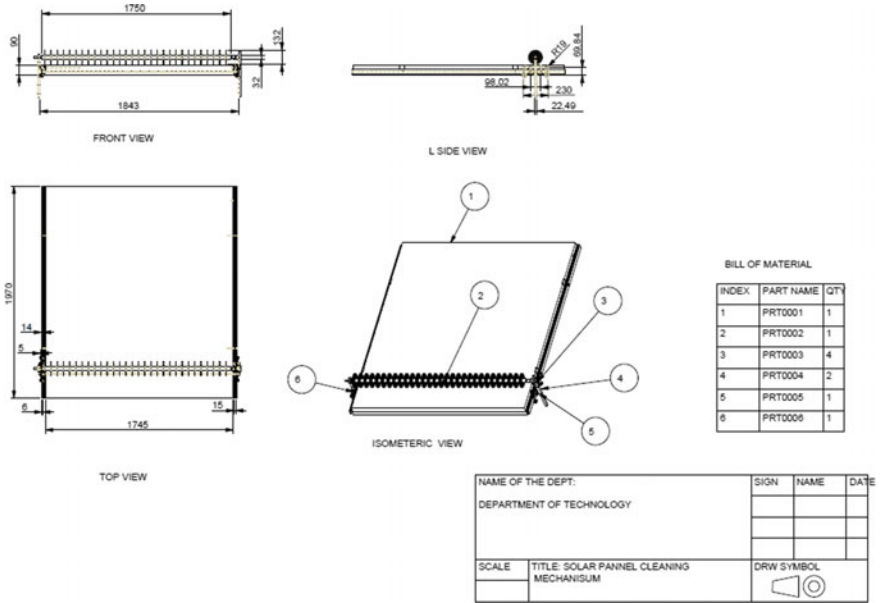
Fig. 3 Drawing of dust cleaning mechanism
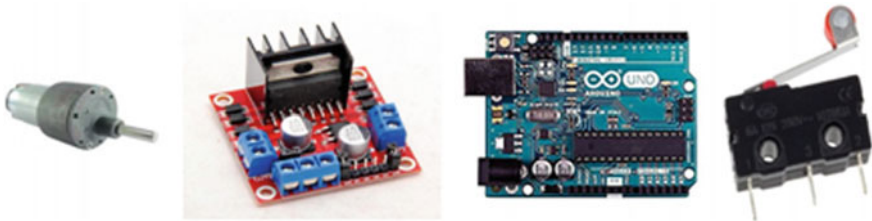
Fig. 4 Motor, motor driver, microcontroller, limit switch

Absolute Efficiency of Solar Panel Without Dust

$$\eta_{\text{Absoulute}} = \frac{V_{\text{oc.}}I_{\text{sc.}}\text{ff}}{\text{AI}} = \frac{81.8 \times 4.58 \times 0.7}{3.1 \times 710} = 11.92\%$$

$$\text{Reduction in absolute efficiency} = 11.92\% \ - 9\%$$
$$= 2.92\%$$
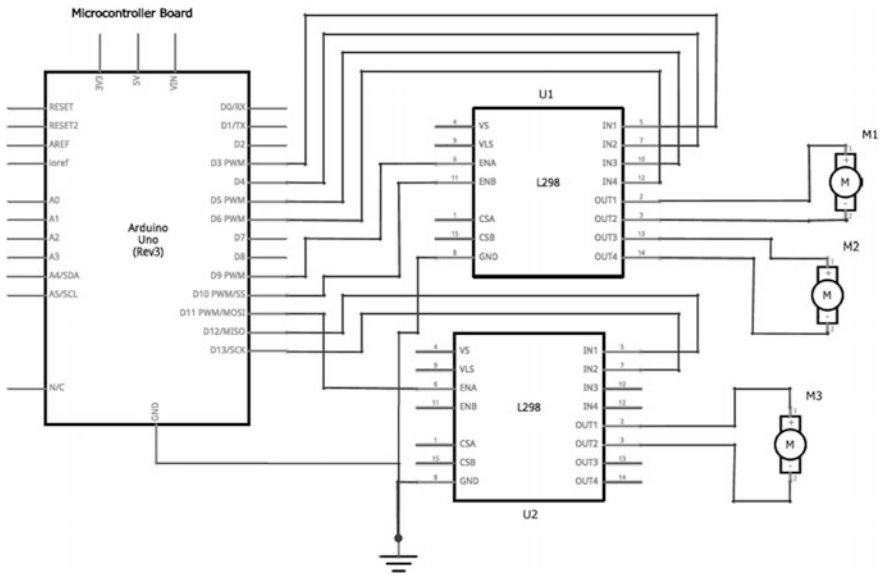
Fig. 5 Circuit diagram for electronic component and connections [11, 12]
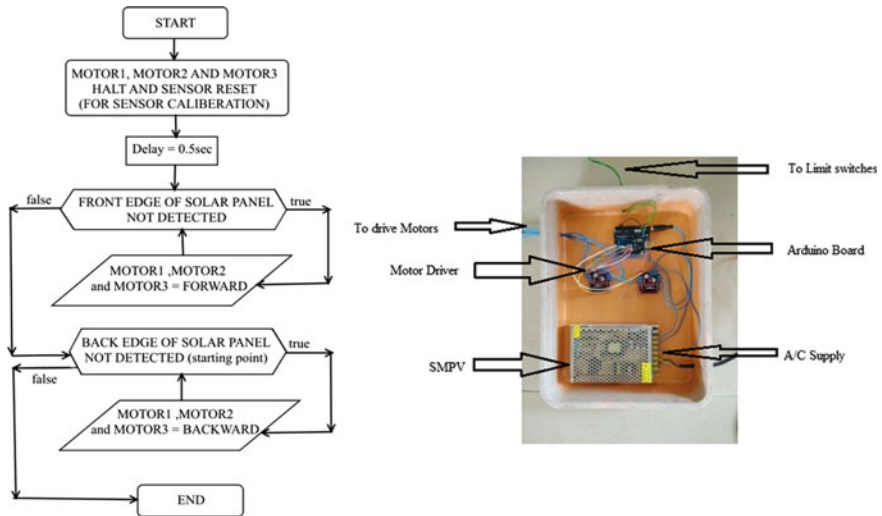
Fig. 6 Program and assembly of automation kit

Fig. 7 Test setup of solar PV

$$\text{Reduction in relative efficiency} = \frac{\text{eff. without dust} - \text{eff. with dust}}{\text{eff. without dust}}$$
$$= 24.49\%$$

$$\text{Relative efficiency of plant} = 100 - \text{Relative loss of panel generation}$$
$$= 75.51\%$$

$$\text{Total Power} = V_{\text{oc}} \times I_{\text{sc}}.$$

So, by comparing both efficiencies, the reduction in absolute efficiency is 2.92%. So the testing is carried out by taking the experiments to reduce dust and measurement of different parameters with every swept of the mechanism and lastly compare all the readings with solar panel without dust which is the calibrated reading taken immediately after washing the panel (Table 2).

6 Result and Discussion

6.1 Energy Required for Dust Cleaning Mechanism

The efficiency of solar panel without dust (solar panel with zero dust) is 11.92%. So the power output is 374.64 $\frac{\text{W}}{\text{m}^2}$. There is need to determine the how much energy can use for mechanism. All calculation and required data are described below.

Table 2 Performance of cleaning mechanism

No. of swept	Absolute panel efficiency (%)	Relative loss of panel generation (%)	Relative efficiency (%)	Total power output (W)	Dust density (g/m^2)
0	9	24.49	75.51	338.68	395.14
1	9.3	21.97	78.03	340.78	371.23
2	9.4	21.14	78.86	344.31	350.12
–	–	–	–	–	–
–	–	–	–	–	–
19	11.5	3.52	96.48	368.19	61.89
20	11.6	2.68	97.32	369.91	44.52

Table 3 Total energy required for dust cleaning mechanism

No. of cycle	1	2	3	4	5	6	7	8	9	10
Power (Wh)	0.3198	0.6399	0.96	1.27	1.599	1.92	2.238	2.559	2.88	3.198

- Total distance in both swept—196 cm
- Time required for forward swept—32 s
- Time required for reverse swept—32 s
- Total current drawn to motor drive—0.5 A
- Voltage between two terminals—12 V
- So total power = 12 × 0.5 = 6 W

  - Power required for single swept—$\frac{6 \times 32}{60 \times 60} = 0.05333$ Wh
  - Power required for single cycle (two swept) = 64 s
  - Power required for one cycle—$\frac{6 \times 64}{60 \times 60} = 0.1066$ Wh

- There are three numbers of motors, viz. one for brush and other two for gear drive. All motors have same voltage of 12 V and 0.5 A current. The working time for motor is also same so the energy required for all motors is same as that of calculated.
- So total power required for mechanism = 3 × 0.1066 Wh

  = **0.3198 Wh** (Table 3).

- Dust accumulation degrades its conversion efficiency up to 24.49%.
- After 20 sweeps, the absolute efficiency increases from 9 to 11.62%.
- Succeed to reduce the loss of efficiency from 2.68 to 24.49%.
- Relative efficiency increases from 75.51 to 97.32%.
- By removing dust, production of panel increases from 338.68 W to 369.91 W.
- Dust density reduces after 20 sweeps of cleaning 395.14–44.52 g/m^2

Table 4 Result summary

Clean panel	Dusty panel	Observed loss by dust	After clean gain of power	Power requires for cleaning	Net power gain
2.1 kWh	1.59 kWh	510 Wh	450 Wh	3.198 Wh	446.80 Wh

- So the average radiation at the department of technology = 10 h/ day = 210 W/m^2
- Total generated power = 10 × 210 = 2.1 kWh
- Loss of power by dust = 2.1 × 24.49/100 = 0.51 kWh
- So power generated by dusty panel = 2.1 − 0.51 = 1.59 kWh
- Power achieved after cleaning of 20 sweeps = 2.04 kWh
- Increase of power production = 2.04 − 1.59 = 0.45 kW = 450 Wh
- Power required for cleaning = 3.198 Wh
- Net gain of power by mechanism = 450 − 3.198 = **446.80 Wh**

So the total energy saving by whole system is 446.80 Wh (Table 4).

7 Conclusion

The dust accumulation on the solar panel is one of the most important causes to Detroit efficiency of solar PV panel. This project discusses the dust accumulation and analyzes the effect of dust by experimental setup. Theoretically observed efficiency loss from 10 to 50% while by practical conclude that the dust reduces the power output up to 24.49%.

The design optimization of components is done in this project. The optimum material is selected for manufacturing. The manufacturing of mechanism is done as per design and drawings of each component.

In this project, the automation of project is done by use of electronics part like microcontroller, Arduino board, motor driver, limit switch.

After the testing of performances of panel, cleaning shows the absolute efficiency of panel which increases from 9 to 11.6%, whereas the cleaned panel has 11.92%. So it can say that mechanism succeed to clean panel up to 97.32% by its power output. Along with this also other parameter of performance such as relative efficiency, relative loss of panel generation and total power output are consider with respect to cleaning cycles.

References

1. Patil, S., Mallaradhya, H.M.: Design and implementation of microcontroller based Automatic dust cleaning system for solar panel. Int. J. Eng. Res. Adv. Technol. (IJERAT), 02(01), 187–190. ISSN: 2454-6135 (May 2016)
2. Mekhilef, S., Saidur, R., Kamalisarvestani, M.: Effect of dust, humidity and air velocity on efficiency of photovoltaic cells. Renew. Sustain. Energy Rev. **16**, 2920–2925 (2012)
3. Monto Mani, and Rohit Pillai: Impact of dust on solar photovoltaic (PV) performance: research status, challenges and recommendations. Renew. Sustain. Energy Rev. **14**, 3124–3131 (2010)
4. Introduction—Ministry of New and Renewable Energy. Retrieved from http://mnre.gov.in/mission-and-vision-2/mission-and-vision
5. Selecting the right brush. https://www.sealeze.com/selecting-the-right-brush
6. Properties of various plastic materials. http://www.plasticsintl.com/sortable_materials.php
7. Bhandari, V.B.: Design of Machine Element
8. MOTOR DRIVER IC L298: http://www.nex-robotics.com/images/downloads/l298.pdf
9. Al-Qubaisi, E., Al-Ameri, M., Al-Obaidi, A., Rabia, M., ElChaar, L., Lamont, L.A.: Microcontroller based dust cleaning system for a standalone photovoltaic system. In: Proceedings of the 2009 Electric Power and Energy Conversion Systems, Abu Dhabi (2009)
10. Microcontroller ATMEGA328P: http://www.atmel.com/Images/Atmel-42735-8-bit-AVR-Microcontroller-ATmega328-328P_Datasheet.pdf
11. ARDUINO UNO: http://download.arduino.org/products/UNO/Arduino-UNO-Rev3e-SCH.pdf[3]
12. ARDUINO SOFTWARE: http://www.arduino.org/

Optimization of a Dual-Stepped Cone Inlet for Scramjet Applications

Subramanian Suryanarayanan, Nivetha Shyam, G. Devi and Giri Revanth Ravish

1 Introduction

Scramjet engines operate on high supersonic flow regimes wherein combustion chamber has supersonic flow throughout. The scramjet engines are usually employed for sustained hypersonic flows [1]. Scramjets work efficiently between Mach 3 and 12. Compared to this, ramjet operates with little efficiency when the free stream reaches beyond Mach 3.

Intake is the most vital component of the engine. It converts the kinetic energy of the airflow into a static pressure rise that helps in deceleration of flow at lower speeds. This deceleration takes place as the flow passes through a series of oblique shocks that are formed due to the presence of ramps in the inlet, also called as staged compression [2]. Among the possible options of external deceleration, double-stepped cone is selected because of its efficiency in pressure recovery with minimal total pressure loss when compared to a normal shock system or a multiple shock train system [3].

The general shock theta beta Mach (θ–β–M) relation calculates the physical properties of airflow through the shock waves. The assumed condition is fixed that the Mach number is achieved at altitude of 10 km. By this, we could initially get the atmospheric conditions at 10 km altitude from an international standard atmosphere [4]. By using the oblique shock relations, we can get the variation in their properties of fluid medium air ahead and behind the shock wave can be calculated. They are detailed below.

S. Suryanarayanan · N. Shyam (✉) · G. Devi · G. R. Ravish
Department of Aeronautical Engineering, Veltech Rangarajan Dr. Sagunthala R&D Institute of Science & Technology, Avadi, Chennai 600062, Tamil Nadu, India
e-mail: Nivetha293@gmail.com

2 Ramp Selections

2.1 Ramp 1 Selection

The values are calculated using the oblique shock relations. The excel worksheet is used for calculation purpose. It is calculated in a random variation of cone deflection angle θ from $8°$ to $15°$. The calculated flow properties are given for Mach 2 and Mach 7.

- For Mach 7

Thus, the oblique shock relations are used here and calculated the variation of Mach number from ahead of the oblique shock wave to behind the oblique shock wave. Various cone deflection angles are ranging from 8 to 15. These are the initial step calculations done (Table 1 corresponds to Mach 7).

- For Mach 2 (Table 2).

2.2 Ramp 2 Selections

The above values give the Mach variation behind the shock waves. The variations of flow properties are assumed to be linear with change in cone angle.

Table 1 Normal Mach for $M = 7$

M_1	θ_1	β_1	$M_{n,1}$
7	8	15.7254	1.89719
7	9	15.409	1.859953
7	10	16.3818	1.974257
7	11	17.3805	2.091012
7	12	18.4035	2.209949
7	13	19.4481	2.33067
7	14	20.5136	2.453008
7	15	21.598	2.576645

Table 2 Normal Mach for $M = 2$

M_1	θ_1	β_1	$M_{n,1}$
2	8	36.84	1.199165
2	9	38.2436	1.238012
2	10	39.3134	1.267124
2	11	40.423	1.296851
2	12	41.5752	1.327205
2	13	42.775	1.358242
2	14	44.0285	1.390032
2	15	45.3436	1.422669

Table 3 Ramp 2 selection with oblique shock relations

M_1	θ_1	β_1	$M_{n,1}$	$M_{n,2}$	M_2
2	10	39.31	1.267032	0.803248	1.64084
3	10	27.38	1.37967	0.74843	2.505559
4	10	22.23	1.513302	0.696431	3.287589
5	10	19.37	1.658336	0.651651	4.00254
6	10	17.58	1.812223	0.613791	4.653093
7	10	16.38	1.974046	0.581865	5.236269

By fixing the first step angle in the dual-step spike, the Mach number behind first oblique shock are tabulated in Table 3.

These are the property changes due to the single oblique shock formed at the tip of the spike. There will be another step cone after first step cone. This could be formed with a rule of cone deflection angle $\theta_1 < \theta_2$. The θ_2 will be increased from θ_1 value so by that mass flow rate of air is calculated for a different set of values of θ_2. For second step, angle of the spike is varied from 5°, 6°, 7° and 12°.

From these above data, linear variation of the velocity raise will be obtained by the step calculation of cone deflection angle. θ_2 and θ_1 are defined by this result. Here we conclude the values of cone deflection angles as a geometrically first step of the spike is about 10°, and the second step of the conical spike will be having 22° from the horizontal axis. This geometry of the inlet spike is defined by above results; so from here $\theta_1 = 10°$; $\theta_2 = 12°$ are fixed.

3 CFD Analysis

The mathematical calculations are done to find the intersection of oblique shock waves to the inlet cowl lip by the trigonometrical relations. These values are being verified by this computational fluid dynamics results for several Mach number variations from Mach 2 to 7.

This design was made in geometry part of the fluent module with the mentioned geometry dimensions. The result can be verified if the oblique shock waves exactly place on the inlet cowl lip. They could form the shock reflection by the cowl lip position so by this there could be a formation of an isolator behind the inlet area. In this case, the geometry is considered to be right.

For Mach number, the analysis is done and listed down in an order.

In the computational analysis, axisymmetric flow is assumed and the unknowns are solved using an implicit solver.

3.1 CFD Analysis—Mach 7

The analytical is further verified by doing CFD analysis for the same 2D wedge geometry as above. The shock on lip condition is achieved at Mach 7 for the same geometry.

This figure shows the pressure variation before and after the shock interaction over the wedge (Fig. 1). The contour image for Mach number variation along the geometry of the cowl and cone of the ramjet engine in 2D section was drawn as an axisymmetric swirl to form a conical section. For Mach no: 7, inlet velocities fixed and their results are shown above.

The isolator length is selected based on the velocity drop locations in the curve. The isolator extends to the point where the velocity is dropped in the inlet for 2 times from the lip of the inlet. From the pressure contours, it can be inferred that optimal pressure rise occurs for the selected cone angles. The pressure rise are similar to that obtained by the analytical equations.

3.2 Mach 2

The CFD analysis is carried out with the same geometry at Mach 2. The various contours were obtained, and the pressure contour shows that there is a minimum
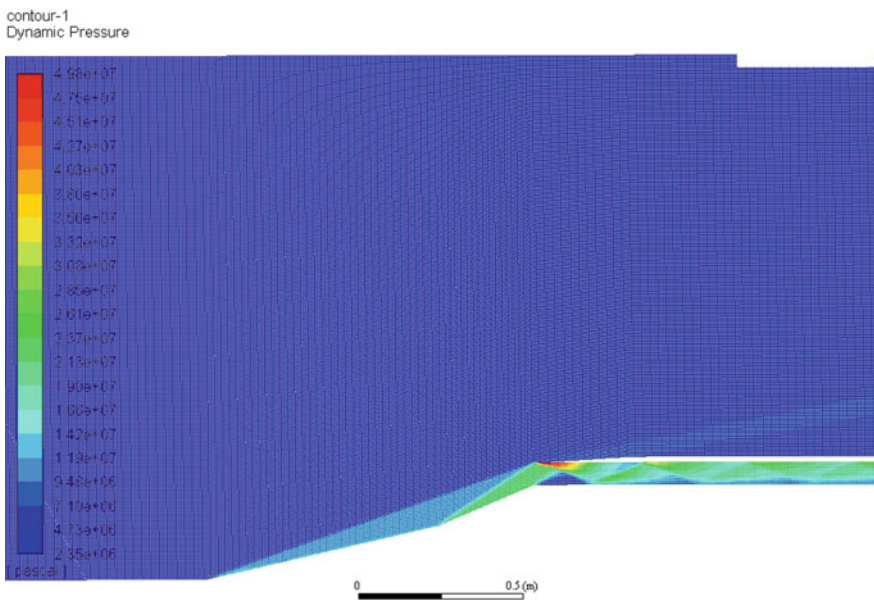
Fig. 1 Pressure contour for Mach 7
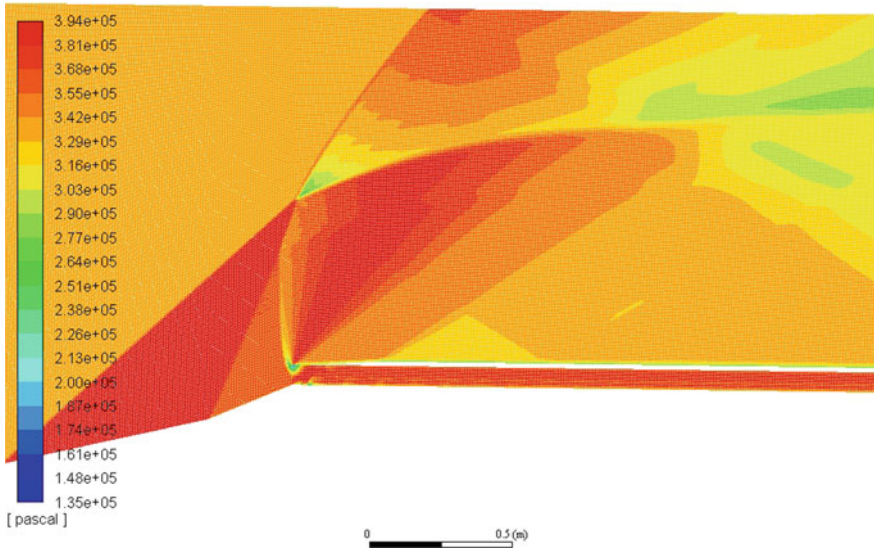
Fig. 2 Pressure contour for Mach 2

spillage at the given specific conditions. The pressure contour for Mach 2 is shown below (Fig. 2).

Here the oblique shock wave formed at the step 1 of the spike will be intersected by the next oblique shock wave formed by the second step of the spike. It has to be placed at the inlet cowl lip to form an isolator with reflected shock waves.

The contour image for Mach number variation along the geometry of the cowl and cone of the ramjet engine in 2D section drawn as an axisymmetric swirl to form a conical section. For Mach 2, inlet velocity is fixed and their results are shown above.

From the above analysis, we have finalized the performance characteristics of the ramjet engine for Mach number 2–7. Thus, the characteristics of fluid medium air will be analysed for variation of oblique shock angles and cone deflection angle selected. As per the data acquired by above will be used here for further calculations of the optimization of the ramjet engine will be done with those data obtained by the general shock relations.

4   Conclusion

The geometry of inlet is optimized with the design of a dual-stepped cone for scramjet operations. The design calculations are done analytically and the performance of the design is validated by during numerical analysis for the inlet. No spillage condition is achieved for the inlet at Mach 7, and it is ensured that for other

Mach numbers, the inlet operates with minimum spillage throughout the operating regime. The effects of boundary layer are taken into consideration in the analytical relations but are neglected in the CFD analysis. The future work has scope to include boundary layer effects in CFD analysis. The inlet design is optimized for the entire operating regime.

References

1. Falempin, F.: Design and experimental evaluation of a Mach 2-Mach 8 inlet. In: 10th AIAA/NAL-NASDA-ISAS International Space Planes and Hypersonic Systems and Technologies Conference. https://doi.org/10.2514/6.2001-1890
2. Derek, D., Torrez, S.: Performance analysis of variable-geometry scramjet inlets using a low-order model. In: 47th AIAA/ASME/SAE/ASEE Joint Propulsion Conference & Exhibit 31 July–03 August 2011, San Diego, California, AIAA, pp. 2011–5756
3. Drayna, T.W., Shoreview.: Self-Starting Supersonic Inlet. US 20130213481A1 http://patentimages.storage.googleapis.com/pdfs/US20130213481.pdf
4. Advanced Aircraft Design: Conceptual Design, Analysis and Optimization of Subsonic Civil Airplanes, First Edition. Egbert Torenbeek. © 2013 by Egbert Torenbeek. Published 2013 by John Wiley & Sons, Ltd

Experimental Investigations for Improving the Strength of Parts Manufactured Using FDM Process

N. V. S. S. Sagar and K. S. Vepa

1 Introduction

1.1 Fused Deposition Modeling (FDM)

With the increase in the need for customizable and reliable production of functional parts, automation of manufacturing became a priority for the industry. Many processes have been developed to achieve this goal and are grouped under a category called rapid prototyping (RP) which is synonymous with additive manufacturing (AM) and 3D printing (3DP). In rapid prototyping, functional parts are fabricated using various materials through an additive process, one layer over the other, starting from a CAD model. This allows the design engineer to visualize their designs even before they are manufactured [1, 2]. Some of the RP methods that are developed in the recent past are: fused deposition modeling (FDM), selective inhibition sintering (SIS), 3D inkjet printing (3DP), selective laser sintering (SLS), stereolithography (STL), and stereo-thermo-lithography, etc. [3, 4]. Choice of the method depends on the application.

In fused deposition modeling (FDM) process, a nozzle conveys in the x–y-directions, i.e., the bed of the machine, and extrudes the molten materials in the z-direction, i.e., perpendicular to the bed of the machine. The schematic of FDM process is shown in Fig. 1.

N. V. S. S. Sagar (✉)
Veltech University, Avadi, Chennai 600062, India
e-mail: nvsssagar@gmail.com

K. S. Vepa
VEPA Technologies LLP, Hyderabad, India
e-mail: sridhar.v.k@gmail.com

Fig. 1 FDM process [5]
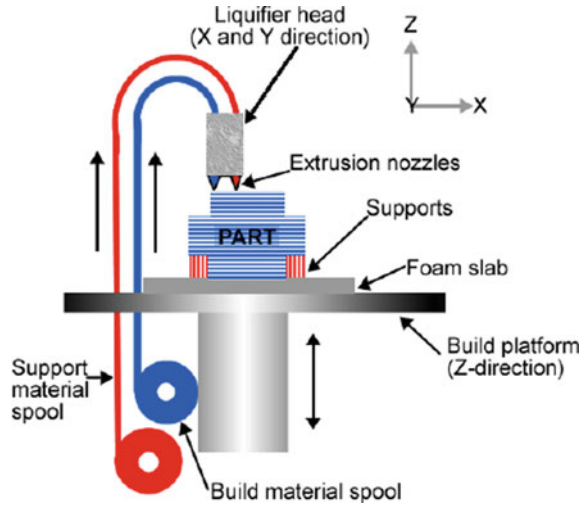
1.2   Machine Used for FDM Process

Technical specifications of the machine used for FDM process are provided in Table 1. It is a fully enclosed industrial grade 3D printer which assures a consistently high print quality and repeatability. The following steps are followed for manufacturing functional parts using this machine:

a. Preparing 3D CAD model for the part and converting it into STL format.
b. STL file has to be checked for errors like gaps, dangling edges, and flip triangles, and if present take necessary actions.
c. Generate sliced layer data for the model followed by generation of g-code.
d. Post-processing the specimen for the required surface finish.

Table 1 Printer technical specifications

Parameter	Value
Maximum printable area	500 mm × 500 mm × 500 mm
Extruder temperature	Up to 270 °C
Layer precision	0.1–0.25 mm
Positioning accuracy	20 μ
Layer thickness ranges	range1: 0.1–0.15 mm, range2: 0.15–0.25 mm, and range3: 0.25–0.3 mm
Bed temperature	Up to 90 °C
Maximum print speed	200 mm/s

2 Materials Used for Printing Test Specimens

In this work, bronze PLA, wood PLA, and TPU materials are tested. Table 2 shows the printing specifications of these materials. It is important to understand the relation between the response behavior of these materials and the process parameters so that a right combination of process parameters for a material is identified.

3 Experimental Testing

For ascertaining the mechanical strength properties of these materials, three different tests have been conducted, viz., tensile test, flexural test, and impact test. Figure 2 shows the shape of the specimen and the corresponding test along with the dimensions.

Table 2 Printing specifications of the materials

Property	Bronze PLA	Wood PLA	TPU
Print temperature (°C)	190–210	210–220	225–235
Bed temperature (°C)	60–65	50	40

Fig. 2 Specimens for testing

(a) Tensile Test

(b) Flexural Test

(c) Impact Test
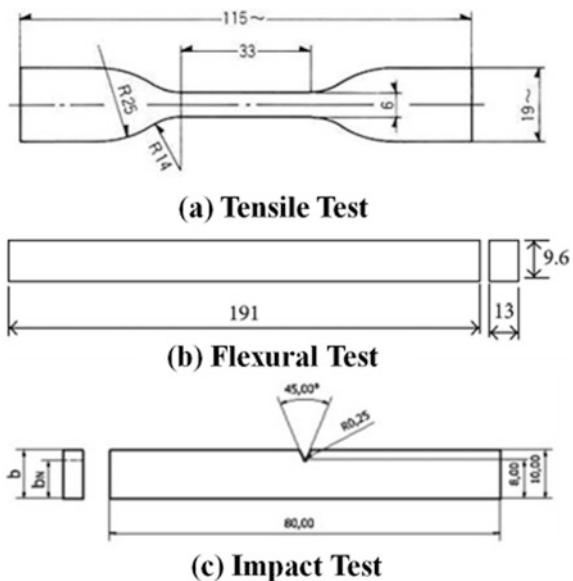
3.1 Printing/Preparation of Specimens for Experimental Testing

The following steps are followed in preparing the specimen for the mechanical testing:

a. CAD models for the test specimens are first modeled in CATIA (a commercially available CAD package) and then converted into .stl format.
b. Using KISSlicer PRO v1.5 (a commercially available slicing package), slicing (process of dividing the 3D model into layers and assigning thickness to these layers) of the model is done.
c. G-codes are then generated for the sliced model using another package called Repetier-Host.
d. The g-code file is then used by the FDM machine for manufacturing the part.

3.2 Tests and Results

The following steps are followed in preparing the specimen for the mechanical testing:

In the current work, two process parameters, viz., layer thickness and build orientation, are tested. Three layer thicknesses, viz., 0.1, 0.15, and 0.2 mm, and three orientations, viz., *XY*, *X*, and *Y,* are chosen. For each combination of layer thickness and build orientation, three individual test specimens for tensile, flexural, and impact tests have been manufactured. Tensile and flexural tests have been performed on UTES 60-TS machine with a capacity of 600 kN and a least count of 0.05 kN. Impact test has been performed on Qualitest QPI machine with a range of 0.5–50 J and a least count of 0.05 J.

Results of all the tests are shown in Fig. 3. It is clear that bronze PLA has shown higher flexural strength, TPU material has shown higher impact strength, and wood PLA has shown higher tensile strength. Figure 4 shows the summarized results of the experimental tests. Tensile strength decreases with increase in layer thickness, and flexural strength increases with increase in layer thickness. *X* orientation has always yielded better tensile and flexural strength, but impact strength is fluctuating. Also, it can be concluded that neither layer thickness nor orientation is independent parameters and the strength of the functional parts is dependent on a combination of these two parameters. To calculate the best possible combination of these parameters, gray relational analysis has been carried out using MATLAB.

(a)

(b)

(c)
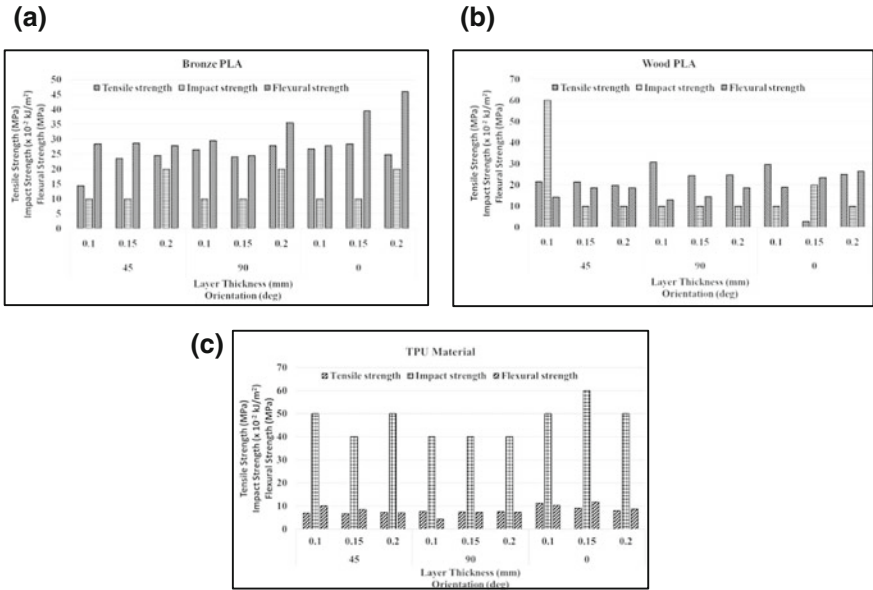
Fig. 3 Test results for different specimens with three different materials

(a)

(b)
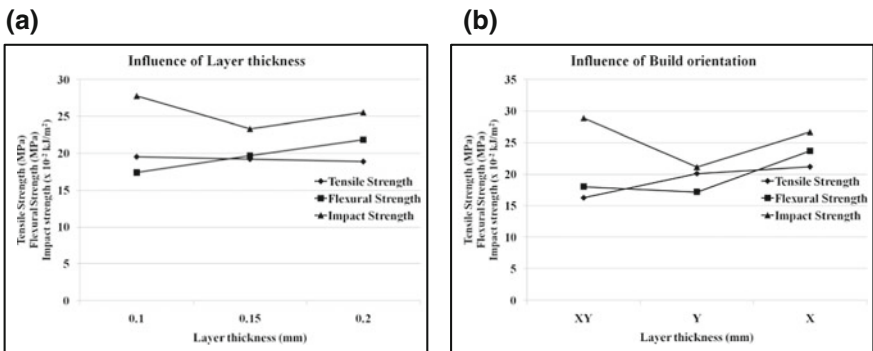
Fig. 4 Influence of layer thickness and build orientation

4 Gray Relational Analysis (GRA)

GRA is a sequential method that results in the optimization of the experimental data. Following steps are carried out for achieving the required optimization [6]:

(a) Normalization of output response,

(b) Calculation of gray relational coefficients based on the normalized output, and

Table 3 GRA ranking for different materials

Sample No.	Tensile strength (MPa)	Flexural strength (MPa)	Impact Strength ($\times 10^{-2}$ kJ/m^2)	Grade	Rank
(a) Bronze PLA					
1	14.39	28.4	10	0.3487	9
2	23.5	28.71	10	0.4353	7
3	24.5	27.85	20	0.6717	3
4	26.45	29.49	10	0.5037	6
5	24.02	24.44	10	0.4274	8
6	27.87	35.5	20	0.8122	2
7	26.71	27.77	10	0.5037	5
8	28.39	39.56	10	0.6526	4
9	24.81	46.05	20	0.8872	1
(b) Wood PLA					
10	21.59	14.2	60	0.5756	2
11	21.44	18.71	10	0.3887	7
12	19.9	18.68	10	0.3768	9
13	30.85	12.93	10	0.5555	4
14	24.36	14.5	10	0.384	8
15	24.85	18.75	10	0.4255	6
16	29.7	18.99	10	0.5446	5
17	2.71	23.56	20	0.5578	3
18	25.02	26.54	10	0.6058	1
(c) TPU material					
19	6.98	10.08	50	0.5108	3
20	6.77	8.52	40	0.4002	6
21	7.22	7.16	50	0.4346	5
22	7.73	4.33	40	0.3517	9
23	7.44	7.31	40	0.3861	8
24	7.65	7.37	40	0.3916	7
25	11.27	10.31	50	0.7397	2
26	9.13	11.76	60	0.8375	1
27	8.06	8.85	50	0.4909	4

(c) Calculation of gray relational grade that decides the optimized combination.

MATLAB code has been generated to carry out the gray relational analysis. Table 3 shows the results of this analysis. Results from GRA show that sample no. 9 is the best possible combination for bronze PLA which means a combination of *X* orientation and 0.2-mm layer thickness yields best results, sample no. 17 is the best possible combination for wood PLA which means a combination of *X* orientation and 0.15-mm layer thickness yields best results, and sample no. 27 is

the best possible combination for TPU material which means a combination of *X* orientation and 0.2-mm layer thickness yields best results. In general, build orientation in the direction of loading always yields better strength properties for the functional parts.

References

1. Burns, M.: Automated Fabrication: Improving Productivity in Manufacturing. Prentice-Hall Inc. (1993)
2. Chua, C.K., et al.: Rapid Prototyping: Principles and Applications. World Scientific (2003)
3. Jacobs, P.F.: Stereolithography and Other RP&M Technologies: From rapid Prototyping to Rapid Tooling. Society of Manufacturing Engineers (1995)
4. Pham, D., Dimov, S.S.: Rapid Manufacturing: The Technologies and Applications of Rapid Prototyping and Rapid Tooling. Springer Science & Business Media (2012)
5. Sidambe, A.T.: Biocompatibility of advanced manufactured titanium implants—a review. Materials **7**(12), 8168–8188 (2014)
6. Pannerselvam, R.: Design and Analysis of Experiments. PHI Learning Pvt. Ltd. (2012)

Effects of Wall Thinning Behaviour During Pipe Bending Process—An Experimental Study

M. Karthikeyan, M. P. Jenarthanan, R. Giridharan and S. J. Anirudh

1 Introduction

For boiler and pipeline applications, bent pipes are preferred to maintain the uniform flow of steam/fuel. Pipe, which is formed by any of the forming process, especially extrusion, can be bent in many ways like welding pipes together and by deforming plastically into any angle by using respective dies. Pipe bending can be done by either hot work or cold work, depending on its applications and need. A pipe will bent in multiple directions and angles. Common simple bends consist of forming elbows, which are bends that range from 2° to 90°, and U-bends, which are 180° bends.

Depending on the dimensions of the pipe and angle to be bent and bend radius, the type of bending and bender will be chosen in industries. The most preferable bending methods are rotary die bending, hydraulic bending for small pipes up to 200-mm diameter and for big pipes more than 200-mm diameter; incremental induction bending is preferred in which plastic deformation is done at re-crystallization temperature. During bending the pipe, its wall thickness tends to change, the wall along the inner radius of the tube becomes thicker due to the compression force, and the outer wall becomes thinner due to tensile force. Depending on the bend angle, wall thickness, and bending process, the inside of the wall may wrinkle.

In the past, wall thickness variations have been studied at different angles from 1° to 180° by Lynn [1]; also, wall thinning ratio and wall thickening ratio were calculated once the bending was done. Kale and Thorat [2] controlled the ovality in pipe bending by providing support on tension and compression sides in such a way that wall thinning or flattening is also controlled in the bend area. Agarwal [3]

M. Karthikeyan (✉) · M. P. Jenarthanan · R. Giridharan · S. J. Anirudh
School of Mechanical Engineering, SASTRA Deemed University,
Thanjavur 613401, Tamil Nadu, India
e-mail: karthikeyan@mech.sastra.edu

conducted a parametric study for the case of bending with combined internal pressure and axial pull, and it shows that with proper selection of the pressure and axial pull, wrinkling is eliminated, thickness distribution around the tube can be optimized, and cross-sectional distortion of the tube can be reduced. Sedighi [4] studied the variation in wall thinning by using fillers, rubber and lead. Also, comparison of results is obtained with the usual bending and bending which is done with fillers. Thinvongpituk et al. [5] have studied the circular tubes collapse behaviour by focusing on its energy absorption characteristics and collapse mechanism. In order to predict the collapse behaviour of tubes and ovality, various diameter to wall thickness ratio (D/t) pipes as been bent using three roller bender, respective moment, buckling and wall thickness variation studied. Li et al. [6] described analytically the deformation behaviours of thin-walled tube NC bending with large diameter D/t and small bending radius R_d/D with respect to wrinkling, wall thinning and cross-sectional deformation. Hu and Li [7] conducted a study on pipe bending with small bend radius in induction bending for analysing the stress state and deformation of pipe bending along with an FE modelling. Tang [8] conducted an experiment to study the plastic deformation theory in pipe bending, and also various pipe bending phenomena were theoretically solved to compare with the experimental results. Yang et al. [9] studied the wall thinning effects of rotary bending by applying axial push force under different conditions, with the pipe of having wall thickness and smaller bend radii. Kim et al. [10] conducted an experiment to study the effect of local wall thinning on the collapse behaviour of pipe elbows subjected to a combined internal pressure and in-plane bending load. In this work, experimental work is carried out to study the effects of wall thinning due to bending of boiler pipes. Cold bending and hot bending process are done. Various fillers are used in cold bending, and increasing radius of bending is used in incremental bending, hot bending.

2 Wall Thinning

Wall thickness is the main criteria which governs the strength of the pipe, especially when the pipes are handled for high-pressure operations like boilers. To direct the flow of steam/fuel in different directions, bent pipes are preferred to avoid turbulence. Life of the pipe mainly depends on the wall thickness at the extrados region, that is, when a high-pressure steam flows inside the pipe for a prolonged period of time, it leads to wear. Hence, thicker the wall, the longer it will serve. It was observed that while bending the pipe there was excess wall thinning in most of the pipes, especially for smaller bend radius. This excess wall thinning may lead to develop a few bending defects such as wrinkles, ovality and shrinkage in length. Figure 1 shows the defects of wall thinning in pipes. Therefore, by controlling this excess wall thinning, defects are reduced and pipe strength will be increased. To study about the wall thickness variation in pipes, a number of experiments were carried out in both hydraulic bending and incremental bending.

Fig. 1 Defects due to excess wall thinning

Flattening   Kinking   Wrinkling

2.1 Control of Wall Thinning

Excess wall thinning occurs mainly because of force acting on the tension side of the bend, that is, when the force is not distributed uniformly throughout the bend area. In normal bending, due to the excess tensile force acting on the extrados region, wall tends to thin; since the pipe is hollow, the force cannot be countered. If additional fillers are packed tightly inside the pipe and undergo the same procedure, the tension force will be balanced and directed throughout the bend area; therefore, adding of fillers inside the pipe will help to decrease the wall thinning to certain extent.

Adding fillers in case of smaller pipes is convenient; however for pipes with greater diameter and length, it is not feasible. Especially for induction bending, since the deformation is done in incremental manner addition of fillers does no good to the bending operation. One of the greater advantages of incremental bending is its bend radius can be altered (before starting), since there is no separate die is used. So, pipes with various bend radiuses can be done in single bender machine. It was observed that for smaller bend radius, deformation happened more. Hence by varying the bend radius of a pipe for the same bend angle, wall thinning can be reduced.

3 Bending at Atmospheric (Cold) and Elevated (Hot) Temperature

The pipe specimen parameters as shown in Table 1 are used for cold and hot bending process.

Table 1 Pipe parameters

Pipe parameters	Type of bending	
	Cold bending	Incremental hot bending
Diameter and wall thickness	(1) 33.8 and 1.8 mm and (2) 30 and 5 mm	762 and 27 mm
Length	460 mm	7500 mm
Bend angle	60°	90°

3.1 Cold Bending

Cold bending experiments were carried out to study and analyse the percentage of wall thinning and its effect towards other bending defects like ovality, wrinkling, waviness formation which are interconnected with wall thinning.

It is well known that when the amount of wall thinning is controlled the above-stated defects can also be controlled and reduced to certain extent. So, in order to control and rationalize wall thinning it is necessary to control and guide tension force acting at extrados (see Appendix 1) in certain manner so that wall thinning is maintained in correct proportions.

In case of normal bending when it is Cold (DIE Used), only outer portion of the intrados region is in contact with the die and is guided by die whereas in other regions (Inner and outer side of extrados region along with inner side of intrados region) is left free. Due to this, forces will not be distributed uniformly at above mentioned portions lead the wall thinning to take place in undetermined manner, thereby leads to non-uniform bending. Therefore, a pipe bent normally can be taken for reference and it can be used for comparing percentage change of wall thinning with pipe bent with fillers.

Since the pipe is not supported at the extrados (inside and outside) region of a pipe, wall thinning happens at an undetermined manner. Bending a pipe with fillers, such as fine sand, green sand and wax, will tend to reduce the effect of tension force acting at tensile side by absorbing excessive tension force and distribute the same in uniform manner.

Filler being an additional element when filled in a pipe acts as a controlling agent at inner side of a pipe which absorbs excessive tension force acting at inner side. So thereby, tension force is controlled which in turn reduces wall thinning. Pipe dimension (wall thickness) was measured before and after bending using portable ultrasonic thickness tester. The results are given in Table 2.

Table 2 Cold bending, wall thinning, wall thickening and % of wall thinning

Pipe (specimen)	Thinning (% of change in WT[a])				Thickening (% of change in WT)			
	Without filler	With fillers			Without filler	With fillers		
		Fine sand	Green sand	Wax		Fine sand	Green sand	Wax
1	1.4 (22.22)	1.475 (18.05)	1.465 (18.6)	1.43 (20.55)	2.11 (17.22)	1.99 (10.5)	1.965 (9.16)	2.12 (17.77)
2	4.235 (15.3)	4.34 (13.2)	4.255 (14.9)	4.27 (14.6)	5.70 (14)	5.45 (9)	5.72 (14.4)	5.805 (16.1)

[a]*WT* Wall Thickness

3.2 Incremental Hot Bending

Pipe bend radius can be increased by altering the push force and the movable support (see Appendix 2). Bend radius for the same bend angle can also be altered. By taking advantage of this, bend radius for the same set of pipes having the same bend angle was varied and variation in wall thinning was studied. For inspection purpose, set of readings were taken before the bending operation at both extrados and intrados regions of the pipe.

Thickness of pipe was measured manually with help of ultrasonic thickness tester. Thickness at the tension and compression sides of pipe was measured before and after bending, and their values are given in Table 3.

The measurements are recorded and shown in Table 4 which is generated by the incremental bender with condition monitoring control.

From the above table, graph is plotted to visualize the change in wall thinning for different bend radiuses (Fig. 2).

Table 3 Parameters of pipe in incremental bending

Bend radius	Initial thickness (at tension side)	Final thickness (at tension side)	% of WT
1600	29.78	24.44	17.93
1900	29.63	25.11	15.25
2300	29.60	26.32	11.08

Table 4 Change in wall thinning at corresponding bend angle for different bend radiuses

Bend angle (°)	Bend radius (mm)		
	1600 (% of WT)	1900 (% of WT)	2300 (% of WT)
10	15.1	11.7	11.6
20	15.2	11.6	11.9
30	16.4	13.6	12.2
40	14.5	12.3	11.2
50	16.1	14.4	11.9
60	16.1	15.1	12.1
70	14.7	12.8	10.9
80	15.1	13.6	10.6
90	16.3	15.8	11.6
Average % of WT	13.95	12.09	10.4
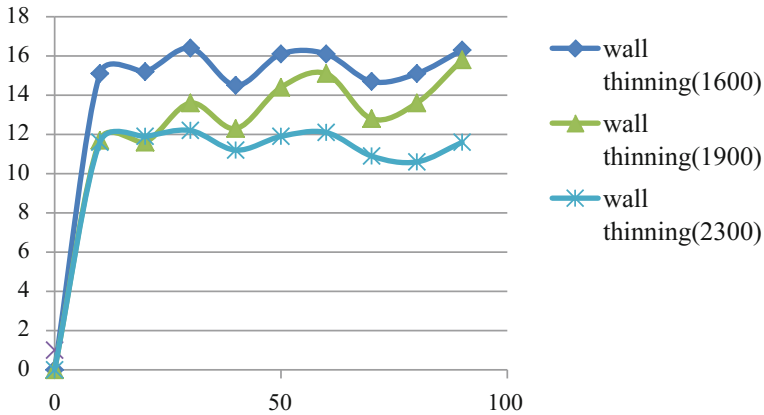
Fig. 2 Graph between bend angle and wall thinning

4 Results and Discussion

It is preferred to bend a pipe using fine sand as filler, since difference in % of wall thinning between normal bend and filler (fine sand—best of all) is nearly 2.5% with respect to wall thinning. Average wall thinning at bend radius 1600 mm was 13.95 and 13.04%, and average wall thinning was reduced to 12.09% at bend radius 1900 mm. Average wall thinning was reduced to 10.40% at bend radius 2300 mm. Therefore, reduction of wall thinning from 13.95 to 10.40% was obtained by increasing the bend radius from 1600 to 2300 mm. Wall thinning was reduced from 17.93 to 11.08% while measuring thickness manually on tension side. Therefore by increasing bend radius, wall thinning can be reduced. This method of increasing bend radius to reduce wall thinning is preferred when die availability is not there and even after availability of die using filler is highly dangerous and risky.

5 Conclusion

In this work, experimental work has been carried out to study the effects of wall thinning due to bending of boiler pipes. Cold bending and hot bending processes have been done. Various fillers have been used in cold bending, and increasing radius of bending has been used in incremental bending, hot bending. The results showed that there is considerable improvement in wall thinning effects during bending of boiler pipes.

Appendix 1: Pipe Bending Terminologies and Types

The terminologies and abbreviations which are involved in pipe bending process are given as follows (also refer Fig. 3)

- **DOB**—degree of bend.
- **WT**—wall thickness.
- **Inside radius (ISR) and outside radius (OSR)** are nominal references defining the extreme inner and outer limits of the tube arc.
- **The centreline radius (CLR)** is, of course, the average of the ISR and OSR.
- **Plane of bend** is the plane defined by the inside radius and outside radius.
- **Line of tangency** is actually a plane, perpendicular to the plane of bend, passing through the origin of the bend and the beginning point of the bend (in other words, it separates the arc of the bend from the tangent section). Before the line of tangency, the tube is straight. Past the line of tangency, it is bent. In draw bending, the line of tangency is fixed in space, through which the tube is drawn around the bend die as it rotates.
- **Neutral axis versus centreline radius**: As shown in Fig. 4, the neutral axis is physically close to the centreline radius, but these terms are not synonymous. The neutral axis is a narrow region, lying inside of the centreline radius, separating the zone of compression from the zone of stretching. At the neutral axis, the tube wall neither compresses nor stretches.
- **Intrados versus inside radius**: The intrados is the zone of compression, bounded by the inside radius and the neutral axis.
- **Extrados versus outside radius**: The extrados is the zone of stretching, bounded by the outside radius and the neutral axis.
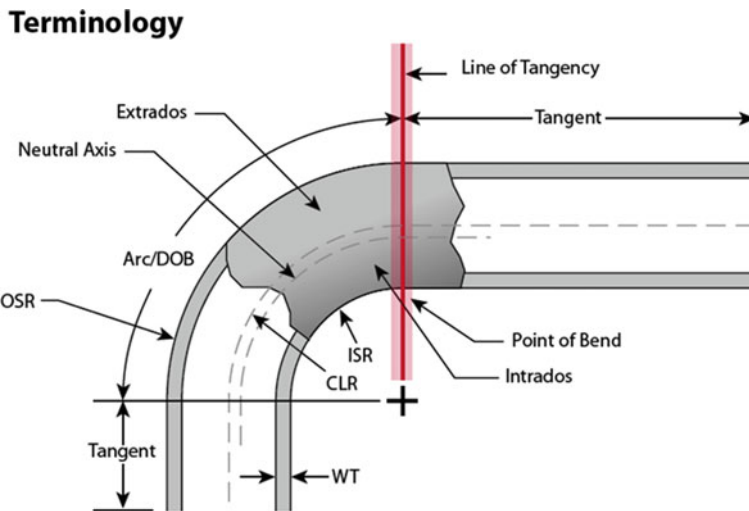
Fig. 3 Terminologies
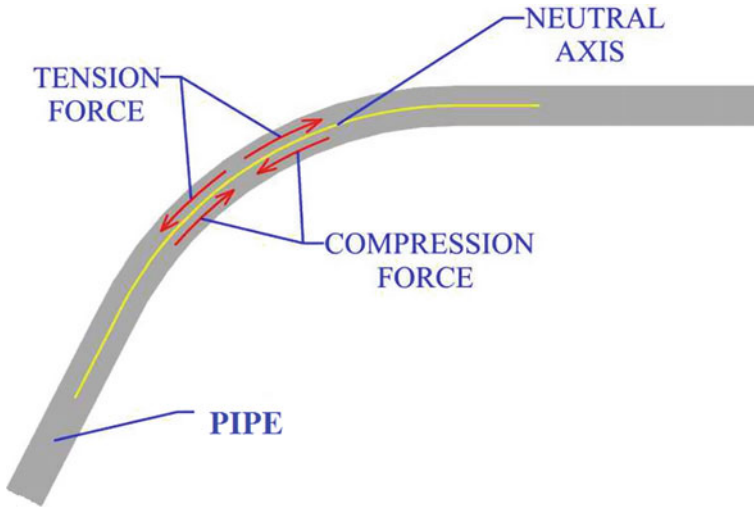
Fig. 4 Force distribution in bend area

Types of Pipe Bending

Commonly used pipe bending methods are

1. Rotary die bending.
2. Rollers bending.
3. Hydraulic bending.
4. Incremental bending.
5. Conduit bending.

Above methods are done in either hot bending or cold bending.

Appendix 2: Pipe Benders

Hydraulic Bender

A hydraulic pipe bender set-up entails of a pressure die, which is connected to the piston of cylinder from which the required pressure is given. The cylinder is filled with hydraulic oil and placed horizontally, with pressure lever at the other end. The pipe is placed perpendicular to the cylinder position, and two supports are placed just beside the pipe at respective ends. The pressure is given in the form of stroke by the lever. For every stroke, the piston will move forward, hence pushing the die until it makes contact with the pipe and to be carried out until the required bend is achieved. The pressure die will push the pipe at the centre, but the two
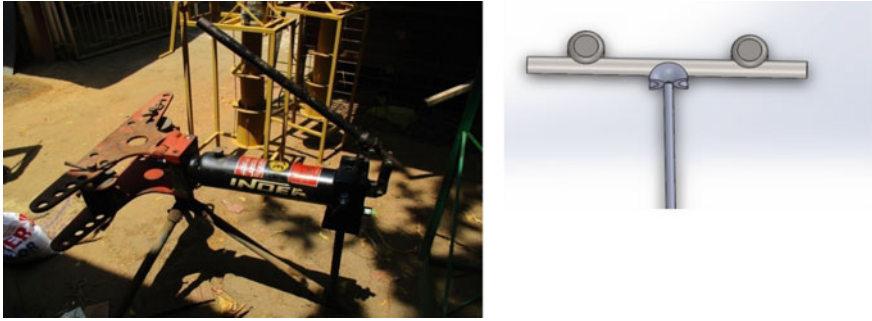
Fig. 5 Hydraulic bender and solid model

supports will prevent the pipe to move forward along with the die; hence, bending is achieved for different bend radiuses and die can be selected accordingly (Fig. 5).

Incremental Bender

This type of bending comes under hot working. In incremental bending, the pipe is fixed in horizontal position. Bender has one fixed support, one movable support and an inductor. Fixed support is stationary with inductor which is used to heat the pipe and pusher which is used to move the pipe for respective bend radius. Pipe is clutched into movable hand jaws and drew onto forcing spine. The position of jaws
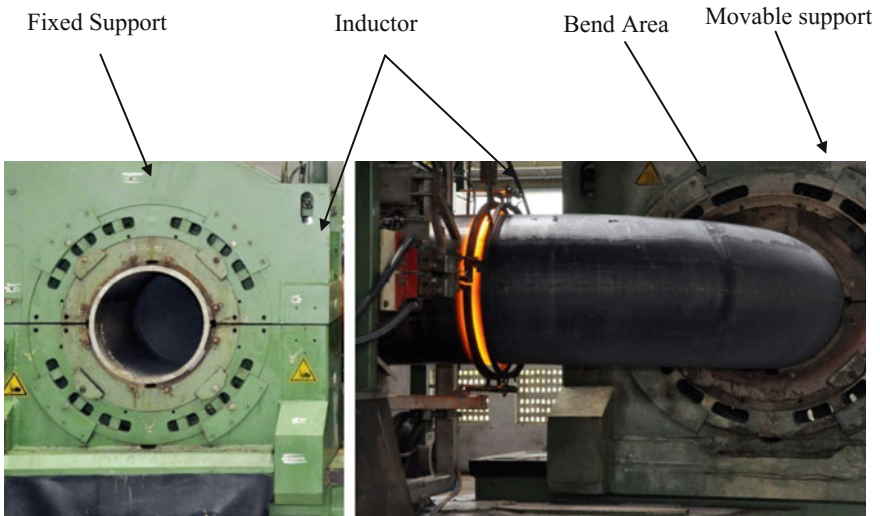
Fig. 6 Incremental bending parts

is determined by demanded bending radius. Tube heater (inductor) is activated and starts heating the bent pipe zone. Turning on a machine drive, the forcing spine is moved, and it is pushing a tube which is now bent around centre of rotation of the moving hand. Bent part of a tube is cooled using water jets (Fig. 6).

References

1. Lynn, F.B.: Wall thinning during tube bending. Pines Technol. **1**, 26–31 (2009)
2. Kale, A.V., Thorat, H.T.: Control of ovality in pipe bending. Paper presented at 5th international & 26th all india manufacturing technology, design and research conference (AIMTDR 2014), IIT Guwahati, Assam, India, Dec 12–14 2014
3. Agarwal, R.: Tube bending with axial pull and internal pressure. Ph.D. dissertation, Texas A&M University (2004)
4. Sedighi, M.: Role of filling material on defects of thin-walled tube bending process. J. Theoret. Appl. Mech. **52**(1), 227–233 (2014)
5. Thinvongpituk, C., Poonaya, S., Choksawadee, S., Lee, M.: The ovalisation of thin-walled circular tubes subjected to bending. In: World Congress on Engineering, vol. 2, pp.2–4 (2008)
6. Li, H., Yang, H., Yan, J., Zhan, M.: Numerical study on deformation behaviours of thin-walled tube NC bending with large diameter and small bending radius. Comput. Mater. Sci. 45, 921–934 (2009)
7. Hu, Z., Li, J.Q.: Computer simulation of pipe-bending processes with small bending radius using local induction heating. J. Mater. Process. Technol. **91**, 75–79 (2000)
8. Tang, N.C.: Plastic-deformation analysis in tube bending. Int. J. Press. Vessels Pip. **77**, 751–759 (2000)
9. Yang, M., Zhan, M., Kou, Y.L.: Deformation behaviours of thin-walled tube in rotary draw bending under push assistant loading conditions. J. Mater. Process. Technol. **210**, 143–158 (2010)
10. Kim, J.W., Naa, M.G., Park, C.Y.: Effect of local wall thinning on the collapse behaviour of pipe elbows subjected to a combined internal pressure and in-plane bending load. Nucl. Eng. Des. **238**, 1275–1285 (2008)

Computational Simulation of Wind Flow Behavior Around a Building Structure

K. B. Rajasekarababu and G. Vinayagamurthy

1 Introduction

The growth of population has led to increase of vertical structures like tall buildings. Tall buildings are mainly affected by lateral forces of strong turbulent wind. Due to the upstream wind conditions, the intensity and magnitude of these strong wind loads effect on tall building structures. These wind load exposed structures are drafted according to the wind standards since most of the tall structures are exposed to different upstream boundary layer flows. In the present study, the effect of upstream wind on tall buildings is computationally simulated and measured using IDDES turbulence model. Basically, computational simulations are used to study three-dimensional physical flow phenomena associated with turbulences, stagnations, recirculation (wake regions), separations, and wind shear layers. These flow features around the building are difficult to model and capture precisely with instruments. Most of the previous literature studies have reported the wind load effect on the height to width ratio, wind-induced angle, side ratios, and slenderness on tall rectangle building. Only a few researchers have reported upstream effects, wake profile, and recirculation zones on isolated tall structures using computational simulation. Liu and Niu [1] evaluated the Steady Reynolds-Averaged Navier–Stokes (SRANS), Large Eddy Simulation (LES), and Detached Eddy Simulation (DES) turbulence models and assessed computational parameters including the grid resolution for all cases. The discretization time step (Δt) and non-dimensional sampling time (t^*) for the LES and DES cases are also evaluated. Further, they demonstrated that the DES can produce wind velocity field similar to those of LES.

K. B. Rajasekarababu · G. Vinayagamurthy (✉)
Aerodynamics Laboratory, School of Mechanical and Building Sciences (SMBS),
VIT-University, Chennai 600127, India
e-mail: vinayagamurthy.g@vit.ac.in

K. B. Rajasekarababu
e-mail: kb.rajasekarababu2014@vit.ac.in

Tominaga [2] studied the effect of fluctuations on the velocity statistics in SRANS and URANS turbulence models using 1:1:2 rectangular buildings. Joubert et al. [3] measured the up and downstream velocity profiles, side wall recirculation zones around the rectangular prism using IDDES turbulence models. Rajasekarababu et al. [4] simulated a setback building using IDDES and DDES turbulence models and have reported that the application of IDDES turbulence model is preferable for wind engineering problems in terms of velocity profiles, side wall recirculation, and aerodynamic pressure coefficient. Kar and Dalui [5] reported a pressure distribution on isolated octagonal tall building using k–epsilon model. Most of the studies stated in the literature are corresponding to RANS, Unsteady Reynolds-Averaged Navier–Stokes (URANS), and LES turbulence models. The effect of turbulence model is significant in simulating wind flow around the tall buildings. The RANS models are efficient and widely used for attached boundary layers flows, but it has less accuracy in stagnation and separation zones. Furthermore, LES model is highly accurate and better than RANS for resolving complex turbulence around the building, but it requires highly fine mesh in the near wall and demands large computation resources and time (LES requires 20 times longer computational time than other turbulence models).

The hybrid turbulence model, DES is considered to be a middle ground between RANS and LES in terms of efficiency and accuracy respectively by Spalart et al. [6] and have examined highly separated flow regions. Shur et al. [7] have discussed some developments in Delayed Detached Eddy Simulation (DDES) which is shield against grid-induced separation (GIS). And other additional developments provide Improved Delayed Detached Eddy Simulation (IDDES) which corporate wall-modeled LES (WMLES). This turbulence model makes it applicable to an extensive range of applications. IDDES can provide both the accuracy of LES and efficiency of RANS. This hybrid (IDDES) turbulence model is well suited for wall region and highly separated flow regions making it as a choice of turbulence model for the upstream applications.

2 Methodology

2.1 Setup Description

This study is adopted by CSIR-SERC's wind tunnel test section as computational domain and is shown in Fig. 1 [8]. The focused building geometry having scale of 1:300, *L/D* of 2, *H/D* of 3 and blockage ratio of 1.5% is used for the computational simulation study to investigate upstream wind flow characteristic and aerodynamic pressure coefficients. These parameters are monitored at different levels, namely *H/D* = 1, 2, and 3. The pressure coefficient is validated with experiment at *H/D* = 2, the wind flow incidences acting on the shorter side of the building at 0° and longer

Fig. 1 Conceptual representation of the computational domain
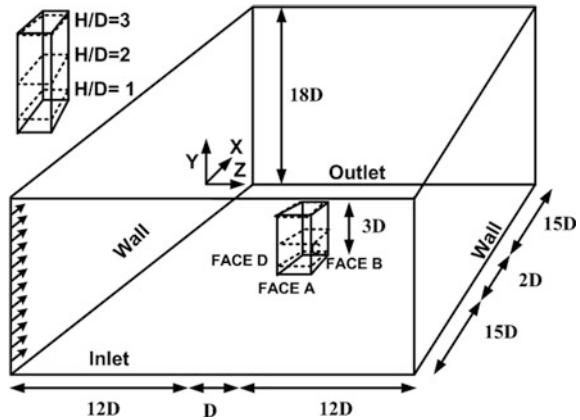
side at 90°. The simulation has been conducted at a mean wind speed of $U_x = 15.3$ m/s at the height of the model ($H = 300$ mm).

3   Numerical Model

3.1   Turbulence Model

Hybrid (RANS/LES) IDDES turbulence model is used for this validation study. RANS Shear Stress Transport (SST) turbulence model runs in the background of IDDES turbulence model. Menter et al. [9] and Shur et al. [7] have used SST model, substituting the length scale destruction in k transport equation by replacing the length scale as a subgrid-scale model for fabricating hybrid turbulence model. This function helps to transit the wind flow smoothly in inner and outer layers of the region. When using WALES method, IDDES length scale elevates and prevents the reduction of eddy viscosity in RANS region. This interface acts as WALES on the inner edge of log layer based on sets maximum grid length scale.

3.2   Computational Setting and Parameters

The constructed computational domain exactly resembles the wind tunnel test section. The domain is deployed with universal boundary layer (uniform) and ensures fully developed flow. It follows the best practice guidelines by Frank et al. [10]. In computational domain, an adaptive meshing technique is used for meshing with fully structured hex cells as grid. This simulation is performed with the ANSYS Fluent 18 solver settings using SIMPLE algorithm for pressure–velocity coupling and second-order discretization. Convergence is assumed and obtained in

the residuals of 10^{-6} for continuity and momentum for *XYZ,* and $K\omega$ residuals are leveled off at 10^{-6}. The residuals are monitored over a considerable time period of an approximate1.3 s.

4   Results

In the simulation, 3D rectangular building structure is simulated subjected to uniform terrain condition at angle of incidences 0° and 90°. In Fig. 2, the data of the upstream stagnation and downstream recirculation zones are calculated in terms of three different heights. In Fig. 2a, upstream stagnation effects are visible at 3D width and height building. The upstream stagnation at the top of the building (3D) increases the velocity due to strong viscous stress. Upstream stagnation initiates scoop effect (upstream wind decelerates toward ground) and standing vortex on upstream of the building. In downstream recirculation region, the velocity fluctuates dramatically due to vortex. Figure 2b shows that the flow restored to free stream velocity at 12D width and 1D and 2D heights of the building. The velocity gradients are high near the building due to strong ground-level corner wind reattachment. This originates wake recirculation on the downstream. At 3D height, the recirculation due to free stream shear flow initiates small vortices behind the building.

Figure 3 shows the variation of aerodynamic coefficient of mean pressure distribution under uniform terrain as the function of FACES of the building at 0° and 90° of wind incidences. The Cp mean extracted on *H/D* = 2 (mid-width) of the building is validated against experimental data [8].

At 0° incidence on FACE A, a positive pressure is experienced due to flow stagnated in the windward which is being distributed parabolically due to sharp edges (without any fillet or chamfer on the corners of the building). FACE B and D
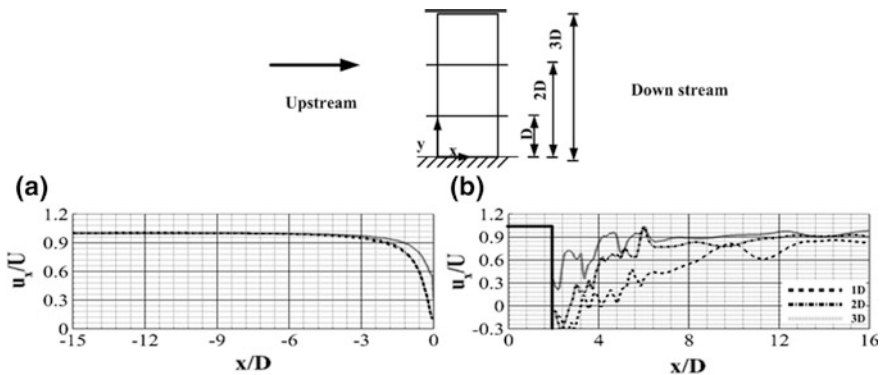
Fig. 2 Velocity profile: **a** upstream stagnation and **b** downstream recirculation
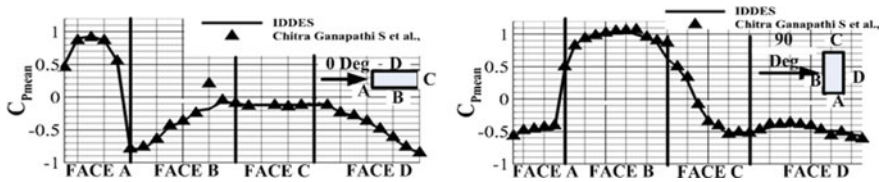
Fig. 3 Variation of Cp_{mean} distribution for 0° and 90°

experienced a peak negative pressure in the presence of strong shear flow due to velocity gradient near the building. FACE C shows a negative pressure with slight variation due to standing wake behind the building. Now at 90° incidence on FACE B, the building physics follows some pressure variations like the 0° incidence on FACE A. In FACE A and C, pressure starts with negative peak and ends with positive peaks, respectively, because of the reattachment of circulation of flow due to sharp in the building. FACE D having a little difference at 90° compared with 0° evidences the presence of circulation flow on free stream.

The instantaneous time-averaged iso-surface contours are displayed in Fig. 4. This shows complex flow patterns, wake streams, side wall circulation, and vortices on the iso-surface. Figure 4c shows a decrease of wake height and an increase of width in the downstream zone referred to as a wake funnel effect. The top and side views show that oscillation of vortex from higher to the lower frequency originates harping vortices driven by way of wake drag parts behind the building. The standing vortex (horseshoe vortex) is permanently attached in the upstream of the building due to stagnation and scoop effect. The presence of sharp edges in the building creates strong viscous shear flow, and leading-edge vortices are driven by the downstream along with velocity gradients. The upstream corner flow creates dissipation due to shear off by small vortices and expands the growth of funnel it is driven by vortex stretching.

5 Conclusion

This paper studied the computational simulation of the upstream effect of wind on a tall building structure. The purpose of this study is to understand better knowledge of wind upstream stagnation and downstream recirculation flow around the building. The results indicate the occurrence of scoop effect on upstream in terms of D (width) and velocity gradient on downstream. The accuracy of computation is validated with Cp_{mean}. This shows the choice of turbulence model (IDDES) for this application is good and reproduces the aerodynamic coefficients with minor
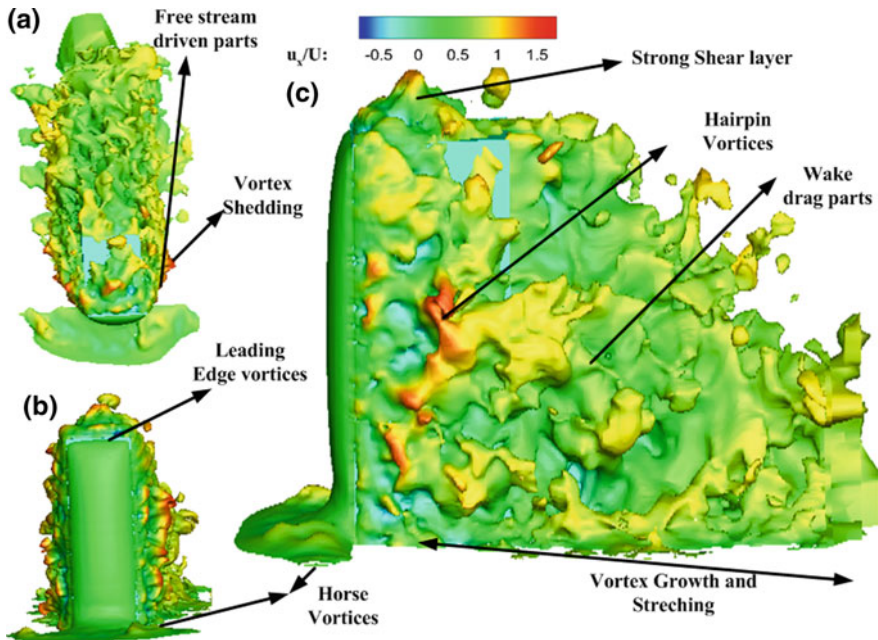
Fig. 4 Iso-surface for 0°, **a** top view, **b** front view, and **c** side view

dispenses. Overall, the IDDES turbulence model made possible to visualize wind flow around the building with less computational time and requirements.

References

1. Liu, J., Niu, J.: CFD simulation of the wind environment around an isolated high-rise building: an evaluation of SRANS, LES and DES models. Build. Environ. **96**, 91–106 (2016)
2. Tominaga, Y.: Flow around a high-rise building using steady and unsteady RANS CFD: effect of large-scale fluctuations on the velocity statistics. J. Wind Eng. Ind. Aerodyn. **142**, 93–103 (2015)
3. Joubert, E.C., Harms, T.M., Venter, G.: Computational simulation of the turbulent flow around a surface mounted rectangular prism. J. Wind Eng. Ind. Aerodyn. **142**, 173–187 (2015)
4. Rajasekarababu, K.B., Vinayagamurthy, G., Selvi Rajan, S.: The Eighth National Conference on Wind Engineering, vol. 8, pp. 151–160, ISWE, IIT(BHU), Varanasi, India (2016)
5. Kar, R., Dalui, S.K.: Wind interference effect on an octagonal plan shaped tall building due to square plan shaped tall buildings. Int. J. Adv. Struct. Eng. (IJASE) **8**(1), 73–86 (2016)
6. Spalart, P., Allmaras, S.: A one-equation turbulence model for aerodynamic flows. In: 30th Aerospace Sciences Meeting and Exhibit. (1992)
7. Shur, M.L., et al.: A hybrid RANS-LES approach with delayed-DES and wall-modelled LES capabilities. Int. J. Heat Fluid Flow **29**(6), 1638–1649 (2008)

8. Chitra Ganapathi, S., Harikrishna, P., Selvi Rajan, S.: Effects of upstream terrain characteristics on aerodynamic coefficients of structures. Arch. Civ. Mech. Eng. **17**(4), 776–785 (2017)
9. Menter, F. R., Kuntz, M., Langtry, R.: Ten years of industrial experience with the SST turbulence model. Turbulence, heat and mass transfer. **4**(1), 625–632 (2003)
10. Frank, J., et al.: Best Practice Guideline for the CFD Simulation of Flows in the Urban Environment. In the COST Action 732. Quality Assurance and Improvement of Meteorological Models. University of Hamburg, Meteorological Institute, Center of Marine and Atmospheric Sciences (2007)

Numerical Analysis of Bubble Hydrodynamics in a Steam Reactor Chemical Looping Reforming System

Akash Chavda and Atal Harichandan

1 Introduction

In today's ever-growing world economy, every sector required energy and that energy is produced by combustion of fossil fuels like coal, natural gas and they produce harmful byproducts like nitrogen oxide, sulfur oxide, and carbon dioxide which are responsible for greenhouse effect and global warming. However, hydrogen as fuel of the future addresses to the environmental concerns as conversion of hydrogen into the energy produces only water as a product with no negative impact on environment. In every ton of hydrogen production, 9–10 tons of CO_2 are likely to be produced from natural gas, oil, coal, and electrolysis [1, 2]. Chemical looping reforming (CLR), an efficient hydrogen production and 100% CO_2 capture, has been investigated by many researchers recently [3–5]. A CLR system consists of three separate reactors: air reactor, fuel reactor, and steam reactor. A suitable oxygen carrier is oxidized in the air reactor and transferred into the fuel reactor using cyclone where oxygen carrier (metal oxide) is reduced and oxygen released from the metal oxide reacts with fuel. Water vapor and CO_2 are produced at fuel reactor outlet where water vapor is condensed and 100% of CO_2 is captured and stored for later use. The reduced metal oxide from fuel reactor is transferred into the steam reactor where it reacts with oxygen from the water vapor and forms partially oxidized metal oxide and hydrogen. Figure 1 shows the schematic of CLR process.

The fluid dynamics and reaction kinetics between gas- and solid-phase particles are highly complex in a CLR process in which a fluidized bed reactor is considered.

A. Chavda (✉) · A. Harichandan
Marwadi Education Foundation Group of Institutions, Rajkot, Gujarat 360003, India
e-mail: akashdchavda@gmail.com

A. Harichandan
e-mail: harichandan.iitkgp@gmail.com

Fig. 1 Schematic of chemical looping reforming process
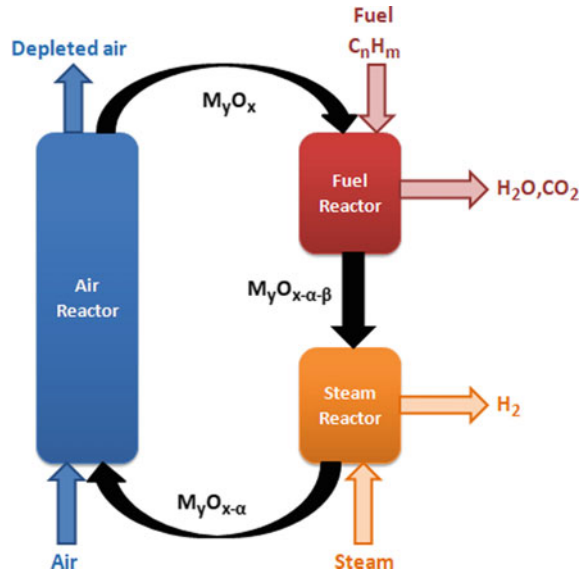
Computational fluid dynamics (CFD), which works with the principles of conversion of mass, momentum, energy, and species transport, has been used by many researchers for capturing the real-time flow physics [6–14]. However, very less numerical work has been carried out on investigation of unsteady aspect of bubble generation, rise, growth, and rupture in the steam reactor. In the present paper, authors intend to understand the chronological development of bubbles inside the steam reactor which is significant particularly at the beginning of reaction and in the following stages before attaining quasi-steady state. Also, it was intended to understand the fuel conversion rate for different particle sizes of the oxygen carrier in a CLR process.

The present numerical simulation of CLR process is carried out with iron oxide as oxygen carrier and water vapor as fuel for steam reactor to study the bubble hydrodynamics and the effect of various oxygen carrier particle sizes on the conversion of vapor into hydrogen. The present investigation of CLR process involves three interconnected reactors in which Fe_3O_4 is oxidized into Fe_2O_3 in the air reactor followed by reduction of Fe_2O_3 to FeO in the fuel reactor and oxidation of FeO to Fe_3O_4 in the steam reactor. Equations (1)–(3) describe low temperature (700–1100 K) exothermic reaction in air reactor, high temperature (800–1600 K) endothermic reaction in the fuel reactor, and low temperature (700–1200 K) exothermic reaction in steam reactor, respectively.

$$4Fe_3O_4 + O_2 \rightarrow 6Fe_2O_3 \text{ (Air reactor)} \tag{1}$$

$$4Fe_2O_3 + CH_4 \rightarrow 8FeO + CO_2 + 2H_2O \text{ (Fuel reactor)} \tag{2}$$

$$3FeO + H_2O(g) \rightarrow Fe_3O_4 + H_2 \text{ (Steam reactor)} \tag{3}$$
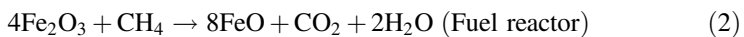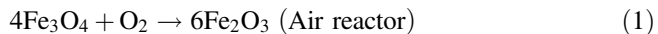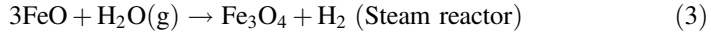
2 Numerical Considerations

The commercial CFD code FLUENT based on finite volume method and phase coupled (PC-SIMPLE) has been used to solve unsteady multiphase flow physics by considering second-order upwind scheme for coupled equations. The convergence criterion for given unsteady flow physics is 10^{-6} for scaled residual components, and time step is 10^{-4} s. Figure 2 shows the two-dimensional geometry and grid cells of the steam reactor. The height and width of the reactor are 1 and 0.25 m, respectively. Grid independence test has not been carried out explicitly for the present numerical work. However, authors ensure the numerical cell size to be ten times greater than oxygen carrier particle sizes so as to capture bubble hydrodynamics in circulating fluidized bed reactor accurately [15]. The steam reactor is divided into 2500 rectangular numerical cells for simulation. Steam reactor is divided into static bed region (0.4 m) and dense bed region (0.6 m). Metal oxide particles are patched with volume fraction of 0.48 in static bed region, and no metal oxide particles are considered to be present in free bed region initially. The heat transfer coefficient between the gas phase and solid phase used for the present simulation was reported by Gunn [2]. The collision coefficient of 0.88 was taken for solid particles. Velocity inlet for the bottom distributor plate and pressure outlet for the outlet of the steam reactor was used as boundary conditions. No slip condition was used on the wall for both the phases. Fluidization velocity is provided to the solid particles for better mixing of gas and solid phases. Second-order QUICK scheme was used to evaluate the convective terms. The model parameters used for the base case in the present study are similar to those used by Deng et al. [6].

Fig. 2 Schematic and grid of the steam reactor
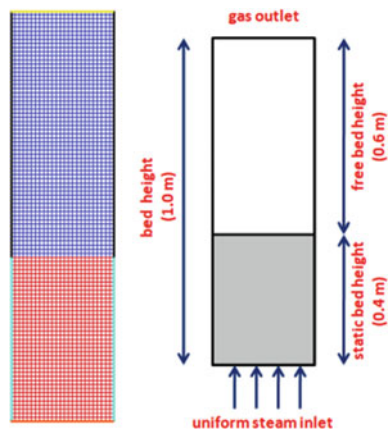
3 Results and Discussions

The gas and solid mixtures were numerically simulated by multiphase CFD model based on kinetic theory of granular flow to study the bubble hydrodynamics of chemical reaction in steam reactor. A user-defined function (UDF) has been incorporated into the ANSYS Fluent model for customizing proper chemical reaction between steam and iron oxide. The oxygen carrier granules are assumed to be spherical, uniform in size, smooth, inelastic, and mono-dispersed spheres. The chemical reaction between gas and solid phases was considered at 1073 K. The fuel (100% wt. of H_2O) in the steam reactor is fed with uniform inlet velocity from the bottom distributor plate. The iron oxide as oxygen carrier with certain fluidization velocity is kept in static bed region. The fuel, supplied at the distributor plate, transfers the momentum to the oxygen carrier, and an activation site or nucleation reaction temperature 1073 K will be created at reaction temperature of 1073 K in the reactor [16]. Chemical reaction between reduced oxygen carrier and oxygen present in the steam will produce H_2 as gaseous product. Due to variation in reactor temperature, uneven formation of active sites emphasizes the study of unsteady bubble hydrodynamics in the reactor. The simulations are carried out under various oxygen carrier particle sizes.

Figure 3 shows the results of numerical simulation carried out considering similar parameters as Deng et al. [6] by considering hydrogen as fuel and calcium sulfate as oxygen carrier in a similar geometrical model and computational grid. Figure 3 shows variation in molar fraction of gaseous phase along the centerline of the reactor ($x = 0$ cm) and at a height of ($y = 30$ cm) from the inlet in static bed region and at the outlet. The difference between present results and Deng et al. [6] are due to two major changes in the present model as second order discretization scheme instead of first order scheme and pressure outlet boundary condition at
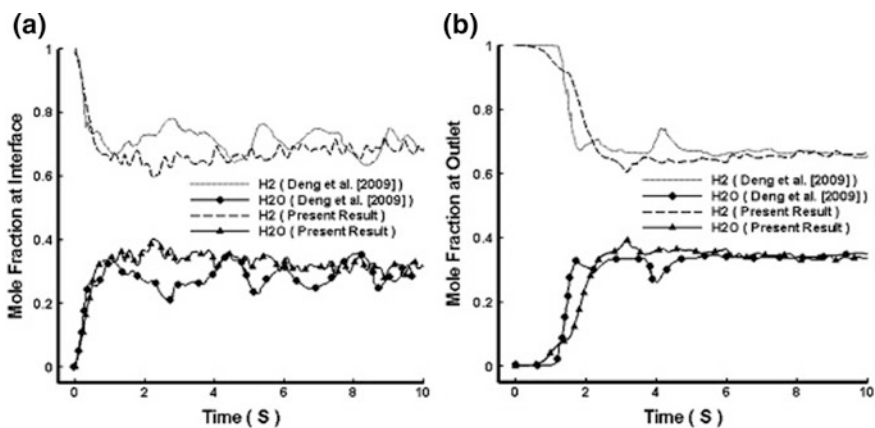
Fig. 3 Molar fraction in gas phase along the centerline of the reactor ($x = 0$ cm) and **a** at height of 30 cm of inlet and at **b** outlet

outlet of the reactor against outflow condition are used by Deng et al. [6]. Figure 3a shows a sudden decrease in the molar fraction of gaseous reactant (hydrogen) from unity to oscillate around 0.68 in the initial period up to 1.0 s. However, the opposite trend has been seen with molar fraction of gaseous product (water vapor) increasing from zero and oscillating around 0.32. After 1.0 s, reaction reached to the quasi-steady state and molar fraction of H_2 and H_2O which are 0.7 and 0.32, respectively. At the outlet, quasi-steady state is achieved after 3.8 s with 0.65 and 0.35 molar fraction of gaseous reactant (H_2) and product (H_2O), respectively. Good agreement between the present results with Deng et al. [6] allows authors to further carry out the simulation by considering steam as fuel and iron oxide as oxygen carrier to study the bubble hydrodynamics and the effect of different oxygen carrier particle size in a CLR system.

3.1 Unsteady and Quasi-steady Bubble Hydrodynamics

Figure 4 shows solid volume fraction contour of chemical reaction between steam and iron oxide inside the steam reactor from 0 to 2 s for better understanding of hydrodynamics. The reaction kinetics inside the steam reactor has been considered by the shrinking core model [16]. Steam was fed with uniform velocity from the distributor plate, whereas iron oxide granules were initially patched in static bed region with fluidization velocity lower than the inlet velocity of steam.
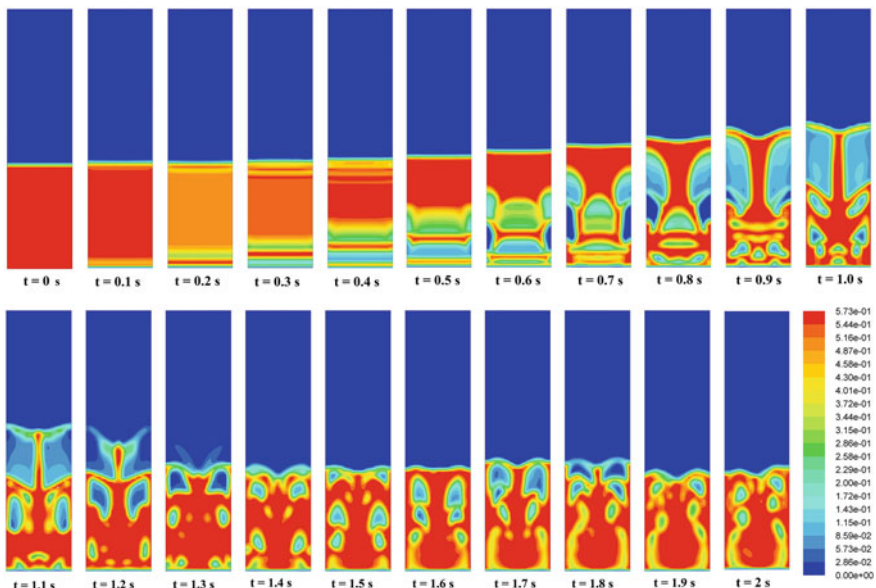
Fig. 4 Solid volume fraction contour from 0 to 2 s
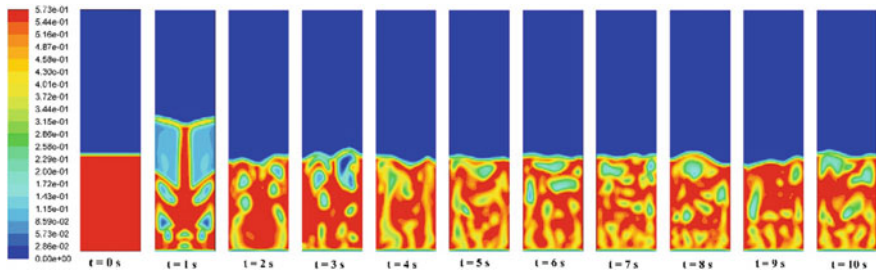
Fig. 5 Unsteady and quasi-steady development of solid volume fraction contour

The momentum transfers from steam to iron oxide at suitable reaction temperature and allows ignition of reaction in the steam reactor. Figure 4 illustrates generation, rise, growth, and rapture regime of bubble hydrodynamics in steam reactor. As the reaction ignites, smaller bubbles are created near the distributor plate in the static bed region between 0.0 and 0.5 s. The smaller bubbles trail behind the larger bubbles due to the low-pressure zone created in the wake of larger bubbles. These pressure differences accelerate the smaller bubbles toward the larger bubbles and coalesce with larger bubbles. In this process, velocity of larger bubbles will increase quickly. As a result, bubble size will grow quickly in narrow flow passage area and slug is formed in the steam reactor which in turn creates two vertical offset columnar structures. The solid oxygen carrier particles are pushed upward by the rising slug and due to the gravity and differential density of gas–solid particles; solid particles are pushed downward along the center and the wall of the steam reactor. This regime is noticeable from 0.5 to 1.5 s. This upward movement of solid particles due to rising slugs followed by falling down along the wall of reactor forming a core annulus structure is similar to that reported by Clift and Grace [17] using rectangular cross-sectional reactor similar to the present geometrical model.

Figure 5 shows the evolution of solid volume fraction profile from 0 to 10 s. It gives a good understanding of the unsteady and quasi-steady bubble dynamics and chemical reaction in the steam reactor. The reaction rate has been observed to be different inside the reactor due to fluidization velocity of solid particles and the difference in gas velocities inside the bubble and slug. The global intermixing of gas and solid phase inside the reactor with the continuous bubble formation, rise, growth, and burst is achieved by the continuous supply of the fed steam through distributer plate. The unsteady nature of the reaction is observed within 1.5 s after that reaction progresses toward the quasi-steady state. After that, core annulus structure no longer exists and global intermixing between gas and solid particles achieves quasi-steady state.
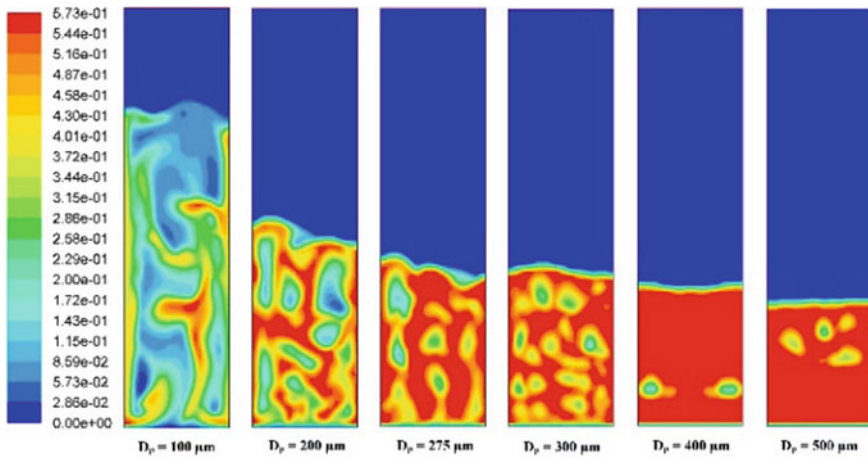
Fig. 6 Solid volume fraction contour with different particle sizes of oxygen carrier at quasi-steady state ($t = 10$ s)

3.2 *Effect of Particle Size of Oxygen Carrier*

Figure 6 shows solid volume fraction contour in steam reactor using different sizes of iron oxide particles. Geometry and numerical cell size of the steam reactor are same for all the cases. It is noticeable that as particle size of oxygen carrier increases from 100 to 500 µm the global intimate mixing between gas and solid phases will be lower in quasi-steady state. Due to that, higher conversion rate of steam to hydrogen is seen with smaller particle size of iron oxide. As the particle size increases in the steam reactor, there is less formation of activation sites which are responsible for proper conversion of steam into the hydrogen due to lower mixing of gas and solid phase in the steam reactor.

Figure 7 shows molar fraction and conversion rate of steam with respect to time and particle size of iron oxide. As the particle size of the iron oxide is reduced, total surface area required for the chemical reaction of the oxygen carrier is increased so more steam will come into direct contact with iron oxide which results in better chemical reaction and higher conversion rate of steam.

4 Conclusion

A numerical model has been developed to carry out simulation of steam reactor in chemical looping reforming with steam as a fuel and iron oxide (FeO) as an oxygen carrier. The numerical model was developed to study the temporal development of bubble hydrodynamics, unsteady state, and quasi-steady state. The molar fraction and conversion rate of steam have been also studied with different particle sizes of
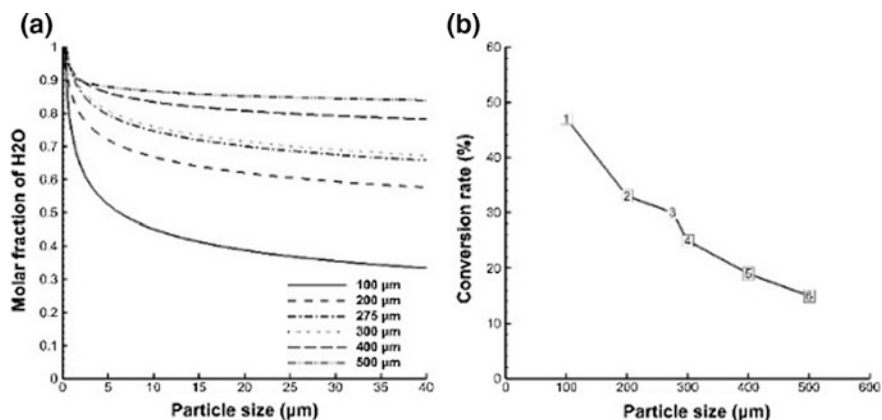
Fig. 7 **a** Molar fraction of H_2O and **b** conversion rate for different particle sizes at quasi-steady state

oxygen carrier. In the present simulation, it is noticeable that unsteady bubble hydrodynamics lies in 0–2 s. After that, columnar bubble structure will collapse due to difference in density between gas and solid phases. The conversion rate in the steam reactor has been observed to decrease due to increase in the particle size of oxygen carrier that results in less intimate mixing between gas and solid phases as the particle sizes varied from 100 to 500 µm.

This simulation work of chemical looping reforming can also be considered in future work by changing the fuel, oxygen carrier, and operating parameters.

References

1. Momirlan, M., Veziroglu, T.: Recent directions in world hydrogen production. Renew. Sustain. Rev. **3**, 219–231 (1999)
2. Gunn, D.J.: Transfer of heat or mass to particles in fixed and fluidized beds. Int. J. Heat Mass Transfer **21**, 467–476 (1978)
3. Richter, H.J., Knoche, K.F.: Reversibility of combustion processes. In: ACS Symposium Series, vol. 235, pp. 71–85 (1983)
4. Harichandan, A.B., Shamim, T.: CFD analysis of bubble hydrodynamics in a fuel reactor for a hydrogen-fueled chemical looping combustion system. Energy Conserv. Manag. **86**, 1010–1022 (2014)
5. Rydén, M., Lyngfelt, A., Mattisson, T.: Production of H_2 and synthesis gas by chemical-looping reforming. In: The Eight International Conference on Greenhouse Gas Control Technologies, Trondheim, Norway (2006)
6. Deng, Z., Xiao, R., Jin, B., Song, Q.: Numerical simulation of chemical looping combustion process with $CaSO_4$ oxygen carrier. Int. J. Greenhouse Gas Control **3**, 368–375 (2009)
7. Khan, M.N., Shamim, T.: Investigation of hydrogen in a three reactor chemical looping reforming process. Appl. Energy (2015)

8. Fan, L.-S., Zeng, L., Wang, W., Luo, S.: Chemical looping processes for CO_2 capture and carbonaceous fuel conversion - prospect and opportunity. Energy Environ. Sci. **5**, 7254–7280 (2012)

9. Tang, M., Xu, L., Fan, M.: Progress in oxygen carrier development of methane-based chemical-looping reforming: a review. Appl. Energy **151**, 143–156 (2015)

10. Protasova, L., Snijkers, F.: Recent developments in oxygen carrier materials for hydrogen production via chemical looping processes. Fuel **181**, 75–93 (2016)

11. Mattisson, T., Lyngfelt, A., Cho, P.: The use of iron oxide as an oxygen carrier in chemical-looping combustion of methane with inherent separation of CO_2. Fuel **80**, 1953–1962 (2001)

12. Ryu, H.J., Gin, G.T.: Chemical-looping hydrogen generation system: performance estimation and process selection. Korean J. Chem. Eng. **24**(3), 527–531 (2007)

13. Mahalatkar, K., Kuhlman, J., Huckaby, E.D., O'Brien, T.: Computational fluid dynamic simulation of chemical looping fuel reactors utilizing gaseous fuels. Chem. Eng. Sci. **66**, 469–479 (2011)

14. Cho, W.C., SeO, M.W., Kim, S.D., Kang, K.S., Bae, K.K., Kim, S.H., et al.: Reactivity of iron oxide as an oxygen carrier for chemical-looping hydrogen production. Int. J. Hydrogen Energy **37**, 16852–16863 (2012)

15. Gelderbloom, S.J., Gidaspow, D., Lyczkowski, R.W.: CFD simulations of bubbling/collapsing fluidized beds for three Geldart groups. AlChE J. **49**, 844–858 (2003)

16. Hossain, M.: Fluidized bed chemical looping combustion: development of a bimetallic oxygen carrier and kinetic modeling. Ph.D. Dissertation, The University of Western Ontario, London, Ontario, Canada (2007)

17. Clift, R., Grace, J.R.: Continuous Bubbling and Slugging. Academic Press, London (1985)

Numerical Study of Flow Field Investigation of Air Jet Impingement on Different Solid Block Size

M. Muthukannan, P. Rajesh Kanna, P. Ganesan, V. Ganesh Moorthy and V. Dineshkumar

1 Introduction

The jet impingement cooling technique is used in industries like turbine blade cooling, rocket launcher cooling, electrical, metal annealing, and textile drying and electronic equipments in order to confiscate a huge amount of heat. The most common types of impingement are confined and unconfined jets. The design and fabrication of confined jets are very complicated compared to unconfined jets. There are many numerical and experimental investigations conducted to find out the effect of confinement wall on jet impingement. The experimental and numerical predictions are mostly related to turbulent jet impingement to have fast cooling. But in the case of cooling of electronic equipments, the area which needs to be cooled is small and also the velocity. In order to consider the present situation, the laminar regime is considered for the entire computational domain.

The Reynolds number (Re) is also confined to 200 in order to avail the laminar flow for the present investigation. Previously, the researchers found out that up to the Re of 500, the flow is considered as laminar in the jet impingement. When the jet impinges on the block, it induces more turbulence. Jambunathan et al. [1] reported a review on single jet impingement in detailed manner. Sivasamy et al. [2] predicted the flow patterns for various situations. They predicted that with the increase of Re, the size of the vortexes increases. Gao and Ewing [3] investigated numerically to find out the effect of confinement surface on heat transfer. When H/D is greater or equal to

M. Muthukannan (✉) · V. Ganesh Moorthy · V. Dineshkumar
Kalasalingam Academy of Research and Education, Krishnankoil 626126, Tamil Nadu, India
e-mail: mmk.mech@gmail.com

P. Rajesh Kanna
Alghurair University, 37374, Dubai, UAE

P. Ganesan
Bahir Dar University, Bahir Dar, Ethiopia

343

one, the confinement surface was not influencing factor on heat transfer. Yang and Shyu [4] numerically predicted on the fluid flow and heat transfer characteristics of multiple impinging slot jets with an inclined confinement surface. They concluded that the inclination angle has more effect compared to entrance *Re* on recirculation region. Choo and kim [5] proved that thermal performance of unconfined jets is nearly 20–30% lower than confined jets. Ravi et al. [6] conducted visualization study on flow dynamics of round jet impinging on a porous medium. They suggested a mathematical relationship between the reattachment length and *H/d*. Colucci and Viskanta [7] analyzed the local heat transfer characteristics of a confined nozzle at nozzle-to-plate spacing $(0.25 < H/d < 6)$ using a thermochromatic liquid crystal technique. They have shown that the unconfined impinging jet leads 20–30% higher thermal performance compared to the confined impinging jet under the fixed flow rate condition. Shukla and Dewan [8] presented a comprehensive review on flow and thermal characteristics of jet impingement. Zhang et al. confirmed that there was increase in average Nusselt number with the increase of protrusion relative depth and the Reynolds number.

2 Mathematical Formulation

In this section, description of the problem under investigation is shown in Fig. 1. Mathematical formulations, boundary conditions adopted for the present investigation, and solution methodology have been shortly described.

2.1 Problem Description

In the present numerical investigation, the authors focused on single-slot jet impingement on a solid block. The fluid used is air. The density and viscosity of the fluid are maintained as a constant one. For the sake of simplicity, 2D is approached for the entire computational domain. In this computational domain, the symmetry
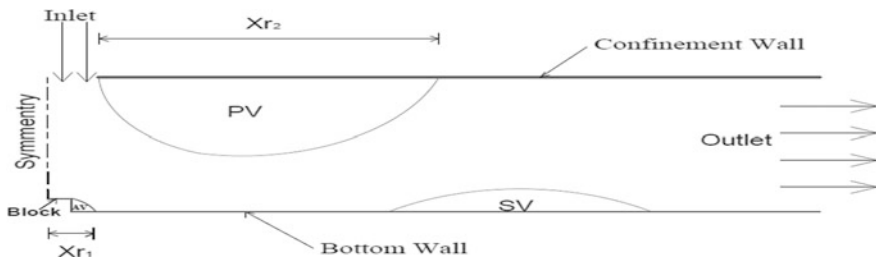
Fig. 1 Schematic diagram of the physical model and the coordinate system

condition is adopted in order to acquire the solution for half of the computational domain. In the present investigation, the block is considered as a square one and the size of the block is considered as 0.75 * 0.75 and 0.75 * 1.50. In the computational domain, the jet n impinges (u) on the block and turns into the right hand of the computational domain. The hydraulic diameter (D_h) of the jet is considered as 1. The horizontal distance of the computational domain is considered as L_x and in vertical as L_y. The length of the computational domain is considered as 20 D_h in order to obtain the fully developed flow.

2.2 Governing Equations

Continuity equation: $\quad \frac{\partial \mathbf{U}}{\partial \mathbf{X}} + \frac{\partial \mathbf{V}}{\partial \mathbf{Y}} = 0$

X-momentum equation: $\quad \mathbf{U}\left(\frac{\partial \mathbf{U}}{\partial \mathbf{X}}\right) + \mathbf{V}\frac{\partial \mathbf{U}}{\partial \mathbf{Y}} = -\frac{\partial \mathbf{P}}{\partial \mathbf{X}} + \frac{1}{\mathbf{Re}}\left(\frac{\partial^2 \mathbf{U}}{\partial \mathbf{X}^2} + \frac{\partial^2 \mathbf{U}}{\partial \mathbf{Y}^2}\right)$

Y-momentum equation: $\quad \mathbf{U}\frac{\partial \mathbf{V}}{\partial \mathbf{X}} + \mathbf{V}\frac{\partial \mathbf{V}}{\partial \mathbf{Y}} = -\frac{\partial \mathbf{P}}{\partial \mathbf{Y}} + \frac{1}{\mathbf{Re}}\left(\frac{\partial^2 \mathbf{V}}{\partial \mathbf{X}^2} + \frac{\partial^2 \mathbf{V}}{\partial \mathbf{Y}^2}\right)$

2.3 Numerical Procedure

The present numerical investigation is done to find out the flow field characteristics like reattachment length, vortex center, and horizontal velocity profile. In this numerical study, SIMPLE algorithm is employed to solve the governing equations. Pressure-based solver is adopted, and momentum equation is solved by second-order upwind scheme discretization. Gambit is used as the modeling software, ANSYS Fluent is used as the analysis purpose, and Tecplot is used to view streamlines and formation of vortexes for the present computational domain.

2.4 Validation Work

The validation work is done against Sivasamy et al. [2] to prove the adopted present algorithm as a correct one. In this validation work, the AR = 2, Re = 100 is taken, and the vortex centers are compared with the Sivasamy et al. [2] (Fig. 2).

Fig. 2 Streamlines of Sivasamy et al. for Re = 200 and AR = 2
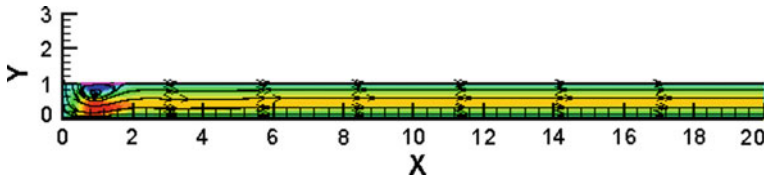
Fig. 3 Streamlines for $Re = 200$ and AR = 2 using present algorithm

Table 1 Validation work against Sivasamy et al. [2]

		X-coordinate		Y-coordinate	
S. No.	Re No.	Present algorithm	Sivasamy	Present algorithm	Sivasamy
1	200	0.90	0.87	0.73	0.70

Figure 3 reproducing the same vortex center like Sivasamy et al. with maximum of 5% error in *X*-coordinate and 2% error in *Y*-coordinate. The following Table 1 enables the present algorithm as a correct one, and it can be adopted for the present investigation.

2.5 Parameters Affecting the Flow Field

(a) Reynolds number (*Re*)

Reynolds number is defined as the ratio between inertia force and viscous force. Reynolds number is signifying the velocity of flow which will be varied from 100 to 300 with a step of $Re = 100$.

(b) Block Size

In the present investigation, the block is considered as a square one and the size of the block is considered as 0.25 * 0.25, 0.50 * 0.50, 0.75 * 0.75, and 0.75 * 1.5.

3 Results and Discussion

In the present numerical investigation, the flow field characteristics like reattachment length, vortex center, and horizontal velocity profile are predicted for various ARs. The above flow field properties are found out because of its importance. From previous research work, it is concluded that at the reattachment or nearer to the reattachment point the heat transfer will attain as a maximum one. So the above flow field properties are predicted for various ARs and *Re*'s in the present investigation. Properties are found out because of its importance. From previous research

work, it is concluded that at the reattachment or nearer to the reattachment point, the heat transfer will attain as a maximum one. So the above flow field properties are predicted for various square block sizes and for various Reynolds numbers in the present investigation.

3.1   Effect of Re on Flow Field for Block Size 0.75 * 0.75

Figure 4 depicts the flow field for various *Re's* for the block size 0.75 * 0.75. It is confirmed that the vortex is formed nearer to the block is called adjacent vortex, and another vortex formed on the top wall is called as primary vortex. Due to increased frictional force along the bottom wall and holding the effect of primary vortex, secondary vortex is also formed. It is important to note that formation of secondary vortex occurs for the higher Reynolds number only.

3.2   Effect of Re on Flow Field for Block Size 0.75 * 1.50

Figure 5 shows the flow field investigation for the block size 0.75 * 1.50. From Fig. 5, it is predicted that for the block size 0.75 * 1.50 the size of the primary vortex increases with the increase of Reynolds number. In the present case, the size
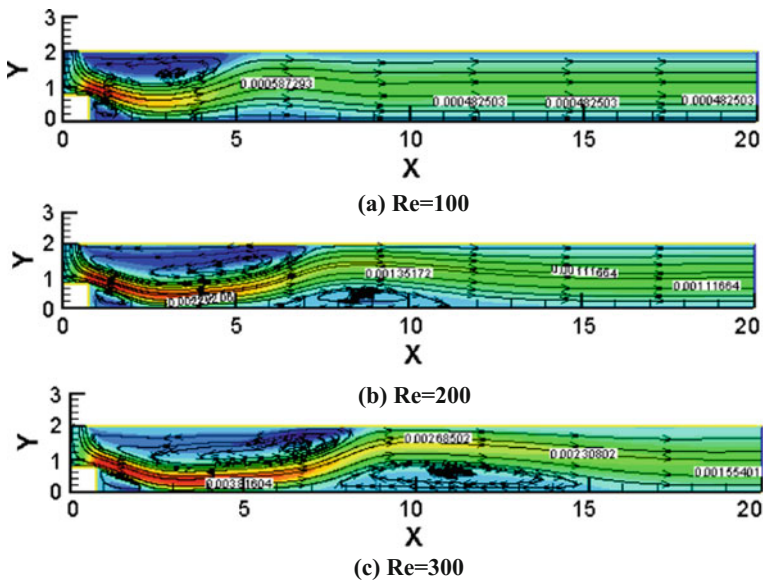
Fig. 4 Flow field investigation for various Re of block size 0.75 * 0.75

(a) Re=100

(b) Re=200

(c) Re=300
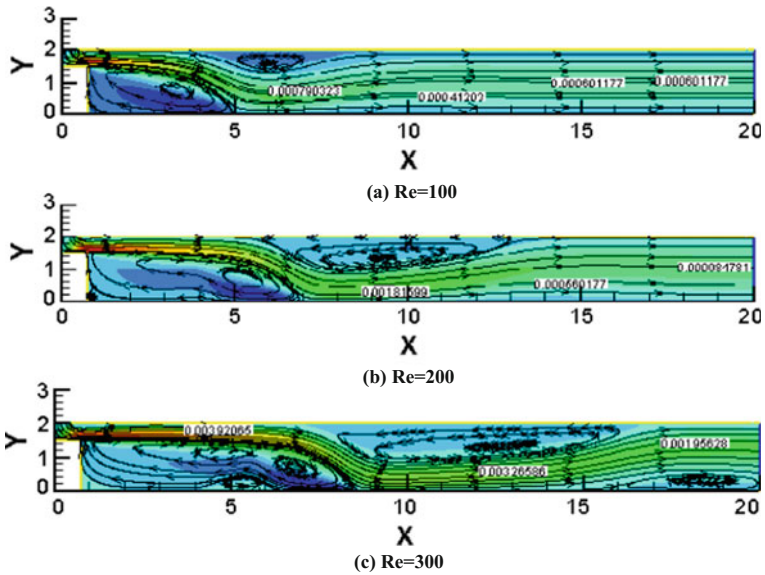
Fig. 5 Flow field investigation for various *Re's* of block size 0.75 * 1.50

of the adjacent vortex is not increasing in significant manner. For the Reynolds numbers of 300, two vortices are merged to form primary vortex. From the previous studies, it is confirmed that merging of vortices leads to the turbulent flow. For the Reynolds number of 300, another vortex is formed in addition to adjacent, primary, and secondary vortices.

3.3 Effect of Re on Vortex Center for Block Size 0.75 * 0.75

For the block 0.75 * 0.75, it is inferred that the vortices are moving significantly in *X*-direction compared to *Y*-direction. In case of primary vortex center, there is 113% increase in *X*-coordinate and in the case of secondary vortex center, there is 28.23% increase in *X*-coordinate (Table 2).

Table 2 Effect of *Re* on vortex center for block size 0.75 * 0.75

S. No.	Re	Primary vortex center		Secondary vortex center	
		X-coordinate	Y-coordinate	X-coordinate	Y-coordinate
1	100	3.0695	1.3706	–	–
2	200	5.2288	1.353	8.6407	0.4027
3	300	6.5435	1.4291	11.0801	0.5665

3.4   Effect of Re on Vortex Center for Block Size 0.75 * 1.50

In case of primary vortex center, there is 112.29% increase in X-coordinate and in the case of secondary vortex center, there is 01.23% increase in X-coordinate (Table 3).

3.5   Horizontal Velocity Profile for Different Block Size

Figures 6 and 7 are predicting where the flow gets fully developed. From Figs. 6 and 7, it is concluded that if the block size increases, the place at flow gets convergence also increases.

Table 3   Effect of Re on vortex center for block size 0.75 * 1.50

S. No.	Re	Primary vortex center		Secondary vortex center	
		X-coordinate	Y-coordinate	X-coordinate	Y-coordinate
1	100	5.9870	1.5844	3.2835	0.7220
2	200	6.01	1.57	3.3481	0.7080
3	300	12.71	1.30	–	–
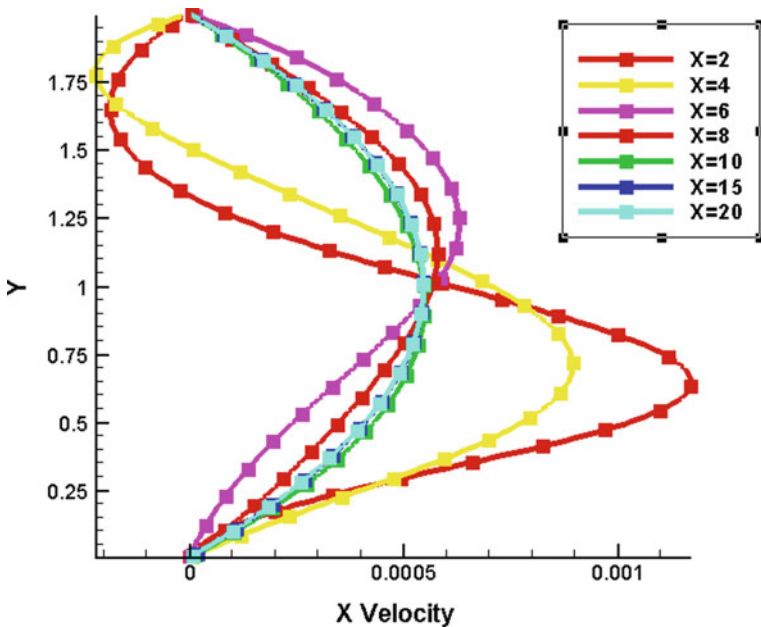
Fig. 6   Horizontal velocity profile for block size 0.75 * 0.75 for $Re = 100$
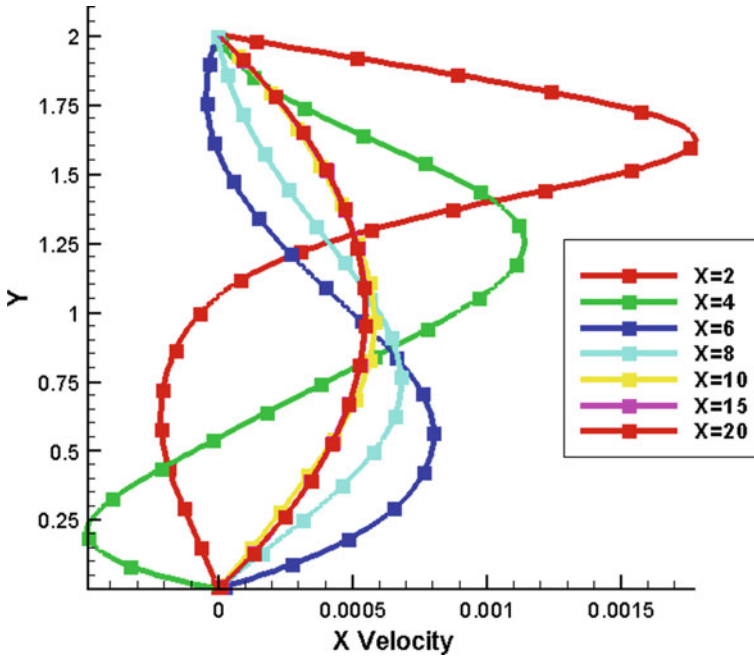
Fig. 7 Horizontal velocity profile for block size 0.75 * 1.50 for *Re* = 100

4 Conclusion

The present numerical study investigates the effect of jet impinging on a different block size. The flow parameters vortex center and horizontal velocity profile are predicted for various flow situations. It is concluded that when *Re* increases, the size of the vortices also increases and the vortex centers also move in downstream direction. For the block width 0.75 * 0.75 up to the *Re* = 300, there is no indication of starting turbulence flow. But in the case of 0.75 * 1.5 block size for the Reynolds number of 300, tow vortices are merged to form primary vortex. This merging of two vortices forming primary vortex is the starting of turbulence flow. Horizontal velocity profile predicting that for the block size 0.75 * 1.5 at *X* = 15 only flow gets developed. From the investigation, it is proved that the size of the block played a major role in jet impingement.

References

1. Jambunathan, Lai, Moss, Button: A review of heat transfer data for single circular jet impingement. Int. J. Heat Fluid Flow **12**, 106–115 (1992)
2. Sivasamy, A., Selladurai, V., Rajesh Kanna, P.: Numerical simulation of two-dimensional laminar slot-jet impingement flows confined by a parallel wall. Int. J. Numer. Methods Fluids **55**, 965–983 (2007)
3. Gao, N., Ewing, D.: Investigation of the effect of confinement on the heat transfer to round impinging jets exiting a long pipe. Int. J. Heat Fluid Flow **27**, 33–41 (2006)
4. Yang, Shyu, C.-H.: Numerical study of multiple impinging slot jets with an inclined confinement surface. Numer. Heat Transfer A **33**(1), 23–37 (1998)
5. Choo, K.S., Kim, S.J.: Comparison of thermal characteristics of confined and unconfined impinging jets. Int. J. Heat Mass Transfer **53**(15–16), 3366–3371 (2010)
6. Yakkatelli, R., Wu, Q., Fleischer, A.S.: A visualization study of the flow dynamics of a single round jet impinging on porous media. Exp. Therm. Fluid Sci. **34**, 1008–1015 (2010)
7. Colucci, D.W., Viskanta, R.: Effect of nozzle geometry on local convective heat transfer to a confined impinging air jet. Exp. Therm. Fluid Sci. **13**, 71–80 (1996)
8. Shukla, A.K., Dewan, A.: Flow and thermal characteristics of jet impingement: comprehensive review. Int. J. Heat Technol. **35**, 153–166 (2017)
9. Zhang, D., Qu, H., Lan, J., Chen, J., Xie, Y.: Flow and heat transfer characteristics of single jet Impinging on protrusioned surface. Int. J. Heat Mass Transfer **58**(1–2), 18–28 (2013)

Stress Intensity Factors for a Plate with Slant Edge Crack Built with Rapid Manufacturing Process

M. Afzal Bhat and **A. A. Shaikh**

1 Introduction

Additive Manufacturing has contributed significantly to the field of commercial manufacturing practices from the last three decades [1]. Initially termed as Rapid Prototyping (RP), it was developed merely to build prototypes of the new products, and later with the advances in technology and materials emerged for producing tooling (Rapid Tooling/RT), currently the application has extended for production of end-use parts or whole products (Additive Manufacturing/AM). AM has a wide range of applications in different fields [2–10], yet various authors have predicted its influence on new industrial revolution [11, 12], and in near future, the annual global economic impact of $200 bn–$600 bn is projected [13].

Unlike machining process where usually material is removed, rapid manufacturing is the fabrication technology in which parts are built in an additive manner by stacking of layers [12]. A three-dimensional CAD model is created and exported as STL file to the RP machining interface software which slices the whole model into layers. Depending upon the nature of RP process, either material deposition path or laser guiding paths are traced for each individual layer. These layers are stacked together to get the build part or assembly.

Fracture properties are important in such products where inherent cracks are unavoidably present. While applying a load, the crack surfaces may open and displace normal to each other, or slide in plane or tearing action may take place. These three loading conditions are known as mode I, mode II, and mode III as

M. A. Bhat (✉)
Chhotubhai Gopalbhai Patel Institute of Technology, Uka Tarsadia University,
Gopal-Vidyanagar, Maliba Campus, Surat, Gujarat 394350, India
e-mail: bhatafzal@gmail.com

A. A. Shaikh
Sardar Vallabhbhai National Institute of Technology, Surat, India
e-mail: aas@med.svnit.ac.in
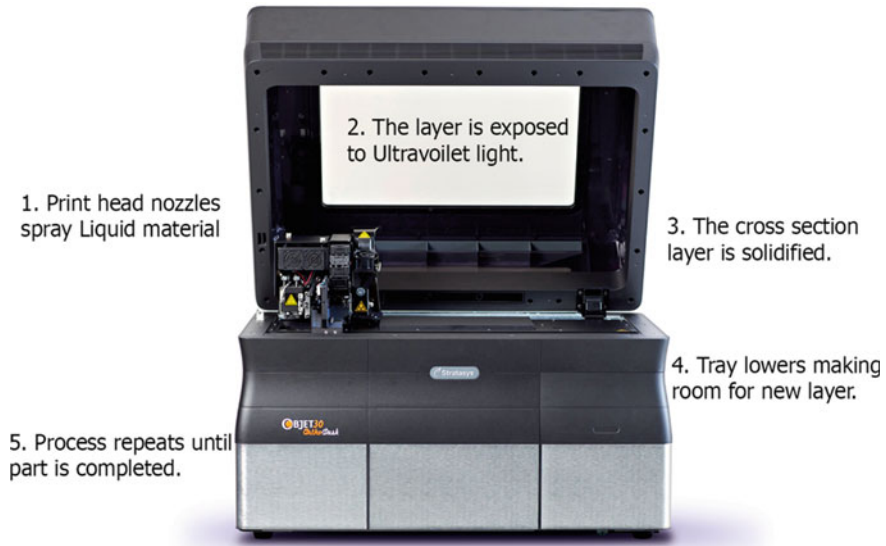
Fig. 1 Objet 30 3D printer and its working

shown in Fig. 1 [14]. Complex behavior is reported for mixed-mode conditions, previous work for mode I and mode II fields under small-scale yielding conditions, with the in-plane stresses having a different asymptotic functional form than the out-of-plane stresses [15]. Pure mode I, II and mixed-mode I/II are mostly possible in engineering problems, and slant cracks are in mixed-mode loading conditions. Several tests have been used for measuring mixed-mode fracture toughness in the mode I/II range. These tests include the edge-delamination tension [16], the crack-lap shear [17], the mixed-mode bending (MMB) test [18], the asymmetric double cantilever beam [19], the mixed-mode flexure [20], and the variable mixed-mode [21] test.

In the present work, mode I and mode II stress intensity factors are studied for slant edge crack specimen built by Polyjet-based rapid manufacturing process. Also, the effect of layer-built angle, crack length ratio, and crack angle is studied and compared with finite element analysis results. It has been observed that the layer-built angle, crack length ratio, and crack angle have a significant effect on stress intensity factors as will be discussed in later sections.

2 Experimentation

2.1 Material Description

The materials used for the specimen are Verowhiteplus RGD835 as main material and Objet support SUP705 as support material supplied as cartridges. The material

is in liquid form which gets solidified upon exposure to the ultraviolet (UV) light. The present work is carried out using 3D printer (Objet 30) to build the specimen of RP material. It is one of the 3D printers which uses Polyjet 3D printing technology for Additive Manufacturing method patented by Stratasys to produce components. Polyjet 3D printers spray jet layers of liquid photopolymer to build tray and instantly cure them with UV light. The layer thickness sprayed is 16-μ with accuracy as high as 0.1 mm. The composition of the Verowhiteplus RGD835 material [22] and Objet support SUP705 [23] material is shown in Tables 1 and 2, respectively.

2.2 Fabrication

Full factorial design of experiments is incorporated to plan experiments for two replications by which 36 (18 each) specimens were fabricated by choosing three factors, i.e., layer-built angle (0°, 45°, 90°), crack length ratio (0.3, 0.5), and crack angle (30°, 45°, 60°). The specimens are fabricated by Objet 30 3D printer employing Polyjet process. The fabrication was initiated by preparing a three-dimensional (3D) CAD model in CAD package. This 3D model was then exported as STL (STereoLithography) file format and submitted to the printer's interfacing software Objet Studio for slicing. This interfacing software also calculates the material deposition paths for main material as well as for support material where necessary. The Objet 30 3D printer system and its process to make parts are shown in Fig. 1.

The dimensions of the slant edge crack specimen are shown in Fig. 2. Two symmetrical holes of 8 mm diameter are placed 56 mm apart to grip the specimen in the clevis. The thickness of the specimen is 6 mm. The length L of the specimen is 80 mm, width W is 30 mm, crack length ratio a/W is either 0.3 or 0.5, and the value of crack angle is 30°, 45°, and 60°.

Table 1 Composition of Verowhiteplus FullCure 835 material

Component	Approximate % by weight
Acrylic monomer	<30
Isobornyl acrylate	<25
Phenol, 4,4'-(1-methylethylidene)bis-, polymer with (chloromethyl) oxirane, 2-propenoate	<15
Diphenyl-2,4,6-trimethylbenzoyl phosphine oxide	<2
Titanium dioxide	<0.8
Acrylic acid ester	<0.3
Propylene glycol monomethyl ether acetate	0.1–0.125
Phosphoric acid	0.002–0.015

Table 2 Composition of Objet support SUP705 material

Component	Approximate % by weight
Poly(oxy-1,2-ethanediyl),α-(1-oxo-2-propenyl)-ω-hydroxy-	<50
1,2-Propylene glycol	<35
Polyethylene glycol	<30
Glycerin	<25
Phosphine oxide, phenylbis(2,4,6-trimethylbenzoyl)-	<0.5
Acrylic acid ester	<0.3

Fig. 2 Slant edge crack specimen sketch
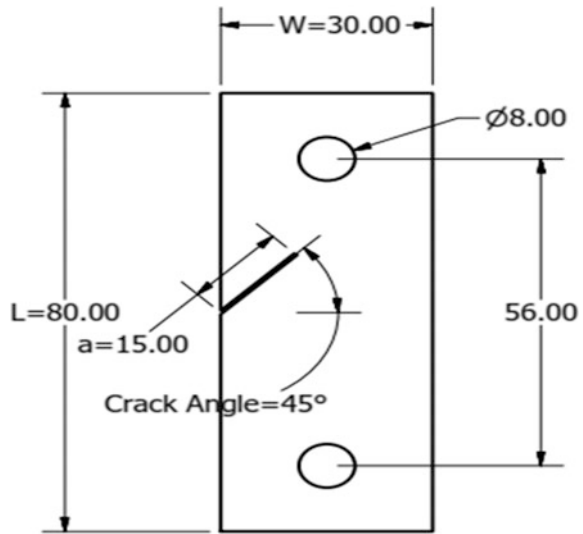
2.3 Testing

Tests are performed by applying tensile load using electronic Tensometer PC 2000 made by Kudale. The tests were conducted in a displacement control mode with a rate of 2 mm/min using 5 kN load cell. The specimens are fractured to obtain load versus load line displacement curves from which peak load was identified for each specimen.

3 Finite Element Analysis

A two-dimensional plane strain model is analyzed in Abacus/CAE. The dimensions of the plate are shown in Fig. 2 with edge crack originating at center of left edge of the plate. The length L of the specimen is 80 mm, width W is 30 mm, crack length

ratio a/W is either 0.3 or 0.5, and the angle α of the slant edge is varied at 30°, 45°, and 60°. The loading pins are modeled as rigid bodies. The plate is loaded by applying a concentrated load at the center of upper pin in the vertical direction. The center of lower pin is constrained as fixed to restrict all motions. However, the center of the upper pin is allowed to move in vertical direction only. Two analysis steps are used. In the first step, the lower and upper pins are constrained. In the second step, controlled load is applied gradually on the upper pin. The crack is introduced into the model with a seam. From the crack editor, the virtual crack extension direction is specified with the q-vector. The crack tip is meshed using a ring of collapsed quadratic quadrilateral elements. Second-order elements are generally used to obtain a mesh singularity at the crack tip.

For a sharp crack, the strain field becomes singular at the crack tip. Including the singularity at the crack tip for a small-strain analysis improves the accuracy of the J-integral, stress intensity factors, and the stress and strain calculations. The geometry is partitioned by defining the circular lines centered on the crack tip for facilitating the generation of a focused mesh. The crack tip is meshed using a ring of collapsed quadratic quadrilateral elements. Second-order elements are generally used to obtain a mesh singularity at the crack tip. In the present analysis, a value of 0.25 is used for the midside node parameter which moves the midside nodes on the element sides adjoining the collapsed edge to the 1/4 points of the elements. At the crack tip, the element sides are collapsed with single-node-type degenerate element control. The circular partitioned areas are meshed using the swept meshing technique which allows the mesh to be regular and focused. The remaining portion of the model is free meshed using the medial axis meshing algorithm. The edge-based tools for specifying mesh seeding facilitate the development of a focused mesh around the crack tip. In the second analysis step, contour integral output is requested for 10 contours.

4   Result and Discussion

Slant edge crack specimens are fabricated at layer-built angle of 0°, 45°, and 90° with the variation of crack length ratio (0.3 and 0.5) and crack angle at 30°, 45°, and 60°. Design of experiments is used to plan experiments by keeping the levels of these three factors at different levels which gave 18 runs for single replicate. The experiment was repeated for each run to have second replication. Mode I and mode II stress intensity factors are calculated using the empirical formula given in [24]. It is observed (Fig. 3) that the values of mode I and mode II stress intensity factors change with the variation of layer-built angle of the specimen. The values first increase with an increase in layer-built angle, and then with further increase in layer-built angle, the values of mode I and mode II stress intensity factors decrease. The peak values of mode I and mode II stress intensity factor are observed for slant edge crack specimens with layer orientation of 45°. The value of mode I stress intensity factor decreases as the crack angle changes from 30° to 60°, while the

value of mode II stress intensity factor increases as the crack angle changes from
30° to 60°. As the crack angle is increased from 30° to 60°, the mode I loading
condition decreases while mode II loading condition increases which results in an
increased value of mode I stress intensity factor with crack angle and vice versa for
mode II stress intensity factor.

A relation is developed which correlates mode I stress intensity factor (K_I) and
mode II stress intensity factor (K_{II}) of slant edge crack specimen with crack length
ratio (a/W), crack angle (θ), and layer-built angle (ϕ) of the specimen. The
developed models are presented by Eqs. 1 and 2 for mode I and mode II stress
intensity factors of slant edge crack specimens, respectively.
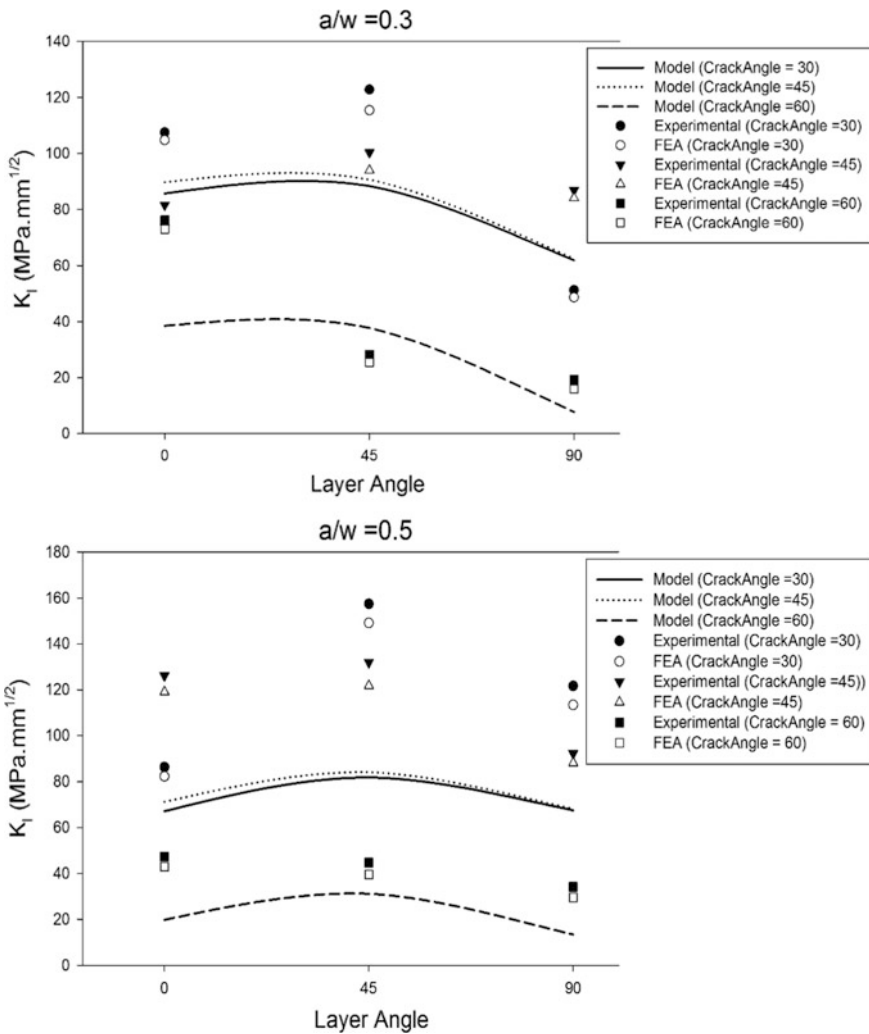
Fig. 3 Variation of mode I stress intensity factor with change of layer-built angle
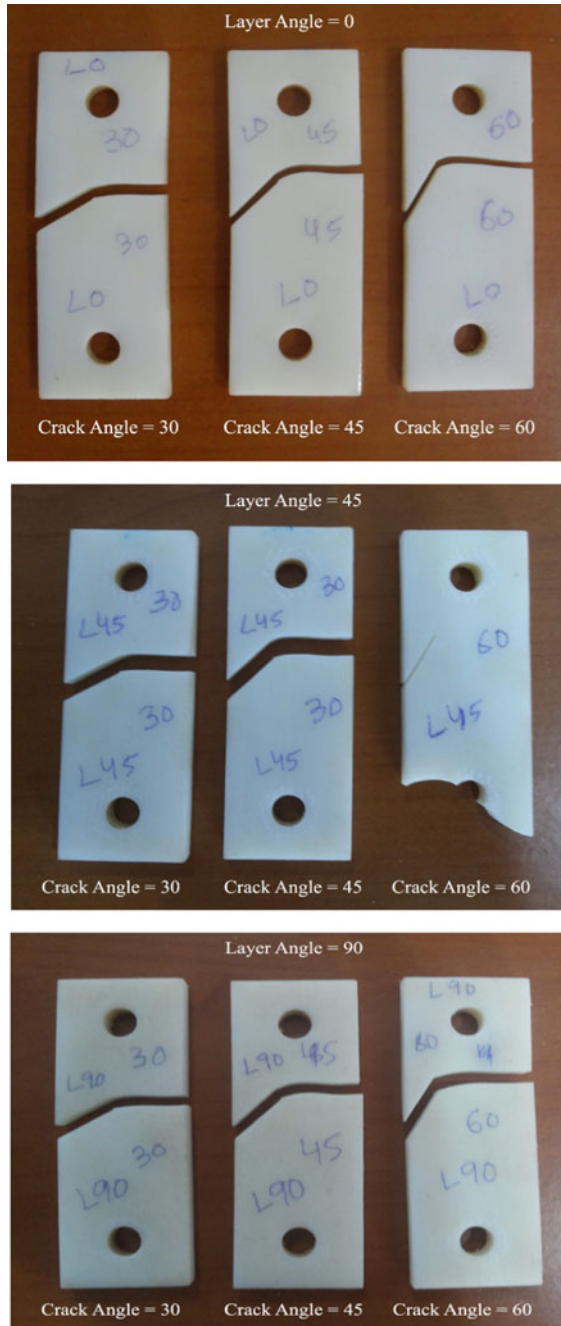
Fig. 4 Fractured slant edge crack specimens with different layer-built angle

$$K_{\mathrm{I}} = -60.30 - 93.43(a/w) + 0.055\theta + 9.49\phi + 1.35(a/w)\theta$$
$$- 0.007\theta^2 - 0.003\theta\phi - 0.123\phi^2 \tag{1}$$

$$K_{\mathrm{II}} = -136.71 - 101.43(a/w) + 0.146\theta + 9.25\phi + 1.55(a/w)\theta$$
$$- 0.002\theta^2 - 0.019\theta\phi - 0.81\phi^2 \tag{2}$$

The R-Square (R-Sq) values of the fitted model are 83.87 and 74.67% for mode I stress intensity factor and mode II stress intensity factor of slant edge crack specimen which show that the fitted models are a good fit of the data for both developed models.

Finite element analysis is carried out to obtain mode I and mode II stress intensity factors for each slant edge crack specimen by taking average value of respective peak loads obtained for two replicas for each run with respective crack length ratio, crack angle, and layer-built angle. The values of mode I and mode II stress intensity factors thus obtained are compared to the values observed by experimentation by bias error calculated by Eq. 3, where K_{actual} is the experimental value of stress intensity factor and K_{FEA} is the value of stress intensity factor obtained by finite element analysis. The average bias error of mode I stress intensity factor and mode II stress intensity factor for slant edge crack specimen is 7.30 and 6.91%, respectively.

$$\mathrm{error} = \left| \frac{K_{\mathrm{actual}} - K_{\mathrm{FEA}}}{K_{\mathrm{actual}}} \right| \times 100 \tag{3}$$

Figure 4 shows some of the fractured slant edge crack specimens at 0°, 45°, and 90° layer orientation, respectively. By examining the crack propagation profiles, it is observed that almost in all the specimens the crack is propagated in straight line in the direction of width of the specimen, in other words, in the direction perpendicular to load applied due to minimum projected area ahead of crack tip. Also, in some of the specimens the failure occurred at the load pinhole which is mostly seen in 45° layer-built angle specimens.

5   Conclusion

The slant edge crack specimen was fabricated using Polyjet 3D printing rapid manufacturing technology and tested for stress intensity factors by varying layer-built angle, crack length ratio, and crack angle. Finite element analysis was carried out and predicted models were developed. From the results, it is revealed that there is adequate closeness of the results obtained with predictive models and finite element analysis with the experimental observations. In general, it is observed that the values of mode I and mode II stress intensity factors change with the

variation of layer-built angle of the specimen. The values of mode I and mode II stress intensity factors increase as the layer-built angle increases from 0° to 45° and then decrease with further increase of layer-built angle from 45° to 90°; i.e., the peak value of mode I and mode II stress intensity factors is obtained when the layer-built angle of the specimen is 45°. The deflection of crack path profiles (waviness) in all slant edge crack specimens increases as the layer-built angle increases. However, it is observed that crack angle of the slant crack does not affect the crack deflection angle and the crack is propagated in straight line in the direction of width of the specimen, i.e., in the direction perpendicular to load applied angle due to the minimum area of projection. The variation of layer-built angle, crack length ratio, and crack angle has a significant effect on the variation of stress intensity factor of the slant edge crack specimen built by rapid manufacturing technology.

References

1. Levy, G.N., Schindel, R., Kruth, J.-P.: Rapid manufacturing and rapid tooling with layer manufacturing (LM) technologies, state of the art and future perspectives. CIRP Ann. Manuf. Technol. **52**(2), 589–609 (2003)
2. Wong, K.V., Hernandez, A.: A review of additive manufacturing. ISRN Mech. Eng. **2012**, 10 (2012)
3. Horn, T.J., Harrysson, O.L.A.: Overview of current additive manufacturing technologies and selected applications. Sci. Prog. **95**(3), 255–282 (2012)
4. Gibson, I., Rosen, D., Stucker, B.: Additive Manufacturing Technologies, 3D Printing, Rapid Prototyping, and Direct Digital Manufacturing. Springer, New York (2010)
5. Petrovic, V., Vicente Haro Gonzalez, J., Jordá Ferrando, O., Delgado Gordillo, J., Ramón Blasco Puchades, J., Portolés Griñan, L.: Additive layered manufacturing: sectors of industrial application shown through case studies. Int. J. Prod. Res. **49**(4), 1061–1079 (2011)
6. Eyers, D., Dotchev, K.: Technology review for mass customisation using rapid manufacturing. Assem. Autom. **30**(1), 39–46 (2010)
7. Khajavi, S.H., Partanen, J., Holmström, J.: Additive manufacturing in the spare parts supply chain. Comput. Ind. **65**(1), 50–63 (2014)
8. Khajavi, S.H., Partanen, J., Holmström, J., Tuomi, J.: Risk reduction in new product launch: a hybrid approach combining direct digital and tool-based manufacturing. Comput. Ind. **74**, 29–42 (2015)
9. Davia-Aracil, M., Jimeno-Morenilla, A., Salas, F.: A new methodological approach for shoe sole design and validation. Int. J. Adv. Manuf. Technol. **86**(9–12), 3495–3516 (2016)
10. Chimento, J., Jason Highsmith, M., Crane, N.: 3D printed tooling for thermoforming of medical devices. Rapid Prototyp. J. **17**(5), 387–392 (2011)
11. Berman, B.: 3-D printing: the new industrial revolution. Bus. Horiz. **55**(2), 155–162 (2012)
12. Hopkinson, N., Hague, R., Dickens, P.: Rapid Manufacturing: An Industrial Revolution for the Digital Age. Wiley (2006)
13. Manyika, J., Chui, M., Bughin, J., Dobbs, R., Bisson, P., Marrs, A.: Disruptive Technologies: Advances that will Transform Life, Business, and the Global Economy. McKinsey Global Institute, San Francisco, CA, 180 (2013)
14. Anderson, T.L.: Fracture Mechanics: Fundamentals and Applications. CRC press (2017)

15. Sutton, M.A., Boone, M.L., Ma, F., Helm, J.D.: A combined modeling–experimental study of the crack opening displacement fracture criterion for characterization of stable crack growth under mixed mode I/II loading in thin sheet materials. Eng. Fract. Mech. **66**(2), 171–185 (2000)
16. American Society for Testing and Materials: Standard E399-06, Standard Test Method for Linear-Elastic Plane-Strain Fracture Toughness KIC of Metallic Materials. Annual Book of ASTM Standards. ASTM, Philadelphia (2007)
17. O'Brien, T.K.: Mixed-mode strain-energy-release rate effects on edge delamination of composites. In: Wilkins, D.J. (ed.) Effects of Defects in Composite Materials, pp. 125–142. ASTM STP 836, American Society for Testing and Materials, Philadelphia (1984)
18. Johnson, W.S.: Stress analysis of the crack-lap-shear specimen: an ASTM round-robin. J. Test. Eval. **15**(6), 303–324 (1987)
19. Reeder, J.R., Crews, J.H.Jr.: The mixed-mode bending method for delamination testing. AIAA J. **28**(7), 1270–1276 (1990)
20. Bradley, W.L.; Cohen, R.N.: Matrix deformation and fracture in graphite-reinforced epoxies. In: Johnson, W.S. (ed.) Delamination and Debonding of Materials, pp. 389–410. ASTM STP 876, American Society for Testing and Materials, Philadelphia (1985)
21. Russell, A.J., Street, K.N.: Moisture and temperature effects on the mixed-mode delamination fracture of unidirectional graphite/epoxy. In: Delamination and Debonding of Materials. ASTM International (1985)
22. Waterman, N.A., Dickens, P.: Rapid product development in the USA, Europe and Japan. World Class Des. Manuf. **1**(3), 27–36 (1994)
23. Kai, C.C.: Three-dimensional rapid prototyping technologies and key development areas. Comput. Control Eng. J. **5**(4), 200–206 (1994)
24. Bechtle, S., et al.: Mixed-mode stress intensity factors for kink cracks with finite kink length loaded in tension and bending: application to dentin and enamel. J. Mech. Behav. Biomed. Mater. **3**(4), 303–312 (2010)

Design, Analyze, and Develop a Hybrid Silencer for 250 kVA DG Set

Saurabh Palnitkar, Loash Suri, Chandrabhushan Sugandhi and Prashant Anerao

1 Introduction

All internal combustion engines when in operation produce noise. This noise often exceeds the safe limit of 80 dBA, which is a constant source of hindrance to the environment and also humans. This noise is mainly due to mechanical vibrations or exhaust noise.

Due to significant advancement in engineering, the mechanical vibrations have been curtailed to an extent where they now have negligible contribution to noise. However, the exhaust noise has remained almost the same. Significant advances in damping materials and acoustic filters have been made in the past decades. Hence, the design of a silencer able to optimally attenuate exhaust noise and generate minimal back pressure across all engine speeds has gained importance.

Normally, silencer design using numerical techniques is an iterative method requiring a lot of trial and error. This is not an acceptable methodology in today's day and age.

The design of silencer was strictly as per the stringent regulations and also the space available within the generator canopy. R. Ramganesh and G. Devaradjane have given back pressure higher preference than noise attenuation while considering a design. Back pressure has a much more deteriorating impact on the overall system performance [1]. Selection of muffler is based upon attenuation requirement and the noise characteristics of the source. The types of silencer have been broadly classified into three categories namely: absorptive silencer, reactive silencer, and hybrid silencer by T. Sharmin and his colleagues. In an absorptive silencer, the attenuation is only due to the acoustic filters present. While the reactive silencer dampens noise due the provision of baffles within the silencer. Whereas a hybrid silencer provides a combination of both to achieve required attenuation [2].

S. Palnitkar (✉) · L. Suri · C. Sugandhi · P. Anerao
Vishwakarma Institute of Information Technology, Pune 411040, India
e-mail: palnitkarsaurabh@yahoo.com

The various components of any silencer like baffles, resonators, and baffle pipes have been addressed at length by Kingston Barnabas et al. [3]. Followed by the selection of the type of silencer required, the design parameters like number of chambers, location and size of inlet and outlet pipes, diameter of holes of the inner surface have been discussed by Chaudhri et al. [4].

Vinod Sherekar and P. R. Dhamangaonkar state the requirements like adequate insertion loss, cost and weight of silencer that need to be fulfilled by the selected design [5]. To calculate the losses across the silencer COMSOL AB has applied Helmholtz equation to the flow of gases through silencer. Shital Shah and her colleagues stated different parameters for minimum volume of silencer required to have an acceptable performance [6]. C. G. Puneetha, H. Manjunath, and M. R. Shashidhar have studied the variation of different parameters such as the pressure and velocity along the length of silencer and demonstrated the same using CFD analysis [7].

1.1 Problem Statement and Objectives

The scope of this paper is to establish a design methodology to make design process easier and streamline by making use of wave theories, in short practical approach to get better design. Also, this approach will predict design quality at an earlier stage of silencer design, evaluate quality of the design, and improve the same throughout the product design steps and reduce cost of prototype development.

A hybrid silencer for a 250 kVA diesel generator set is developed, which restricts the sound pressure to 75 dBA at a distance of 1 m and the back pressure should be below 600 mm of water column

- To evolve a methodology for designing and manufacturing of a silencer suitable for an engine any capacity
- Restrict the sound pressure to 75 dBA
- The back pressure generated because of the silencer should not be more than 600 mm of water column
- Avoid knocking in the silencer as this would augment the sound created by the engine

2 Designing of Component

2.1 Design for Sound Pressure

Sound pressure is the pressure generated by the waves exiting the silencer at a distance of 1 m (Table 1).

Table 1 Chamber lengths for various frequencies	Firing frequencies (Hz)	Respective chamber length (m)
	100	1.1
	200	0.55
	300	0.366
	400	0.275
	500	0.222

Firing Frequencies

$$\text{Cylinder firing rate (CFR)} = \frac{N}{120} = 12.5 \tag{1}$$

Therefore, firing frequencies for first five harmonics are 100, 200, 300, 400, and 500 Hz.

Chamber Length

For firing frequencies, the chamber lengths are calculated using following equation:

$$\lambda = \frac{c}{f} \tag{2}$$

$$L = \frac{\lambda}{4} \tag{3}$$

where C = speed of sound in air = 440 m, λ = wavelength.

Resonator Length

Resonator Minimum frequency = 450 Hz, Resonator Maximum frequency = 550 Hz. Based on the above frequencies, the wavelengths and corresponding resonator lengths are given in Table 2.

$$\text{Total Length of Resonator} = L_{\text{max}} + (L_{\text{max}} - L_{\text{min}}) + 0.01 = 0.295 \text{ m}$$

We have decided to select chamber L_2, L_3, and L_4 and to tackle the frequencies between 450 and 550 Hz, a resonator has been added

$$\text{Total Length} = 0.55 + 0.366 + 0.275 + 0.295 = 1.489 \text{ m}$$

Table 2 Wavelengths and length of resonating chamber		Wavelength (λ)	Resonator length (L)
	Maximum	0.97 m	0.2425 m
	Minimum	0.8 m	0.2 m

Thickness of rock wool:

$$C = f \times \lambda \tag{4}$$

f = Frequency 4000 Hz.

Thickness of rock wool $= \frac{\lambda}{4} \times 3 = 72$ mm.

Dimensions of Silencer

Diameter of inlet/outlet pipe = 169 mm (Based on engine outlet)

- Assuming diameter of outer shell three times diameter of inlet pipe = 3 169 = 507 mm (As per ASHRAE specifications)
- Assuming diameter of baffle pipes half of diameter of inlet pipe = 0.5 × 169 = 84.5 mm (As per ASHRAE specifications)
- **Sound Pressure Loss**

Pressure loss is the reduction in sound pressure when the gases travel through the silencer

1. Transmission loss due to perforated sheet (TL_{prf})

$$W = L \times \pi \times t_1 \times d_1 \times \rho = 16.69 \text{ kg} \tag{5}$$

$$TL_{prf} = 20 \log_{10}(f \times w) - 47 = 50.51 \text{ dBA} \tag{6}$$

Due to 60% porosity, transmission loss is $0.6 \times 50.51 = TL_{prf} = 30.30$ dBA. Where t_1 and d_1 are the thickness and diameter, respectively, of perforated sheet.

2. Transmission loss due to MS sheet 1.2 mm thick (TL_{out})

$$\begin{aligned} W &= L \times \pi \times t_2 \times d_2 \times \rho = 22.4 \text{ kg} \\ TL_{out} &= 53.01 \text{ dBA} \end{aligned} \tag{7}$$

where t_2 and d_2 are the thickness and diameter, respectively, of outer shell.

3. Transmission loss due to rock wool = TL_a = 3 dBA
4. Transmission loss due to expansion and contraction of gas

$$\text{Area ratio} = \frac{\text{chamber dia}^2}{\text{baffle pipe dia}^2} = 36 \tag{8}$$

$$TL_{ec} = 10 \times 10 \log_{10}\left[1 + 0.25\left\{\text{Area ratio} - \left(\frac{1}{\text{Area ratio}}\right)\right\}^2\right] = 25.11 \text{ dBA} \tag{9}$$

$$\text{Total transmission loss} = \frac{2 \times \text{TL}_{ec} + \text{TL}_{out} + \text{TL}_{prf}}{3}$$
$$= 51.24 \text{ dBA (Calibrated for DG set)} \qquad (10)$$

Total transmission loss expected with rockwool is 54.24 dBA.

2.2 Design for Back Pressure

$$\text{Dynamic head in chamber} = \frac{(l \times Q^2 \times \rho \times 3.6)}{\text{baffle pipe dia}^5 \times 10^5} \qquad (11)$$

Using the above formula the dynamic head in every chamber is as follows as in Table 3.

Actual dynamic head is $\dfrac{2209}{1.17}$ = 1877.85 pa (Calibrated for 2 baffle system).

3 Numerical Verification

Analytically obtained values of both sound pressure and back pressure were verified using different simulation techniques.

3.1 Sound Pressure

Transmission loss as expected from the MATLAB program is 58.881 dBA (Fig. 1).

Table 3 Back pressure in each chamber

Dynamic head (1st chamber)	1.013 kPa
Dynamic head (2nd chamber)	1.013 kPa
Dynamic head (3rd chamber)	0.429 kPa
Dynamic head (Total)	2.075 kPa
Water column	208.454 mm of water column
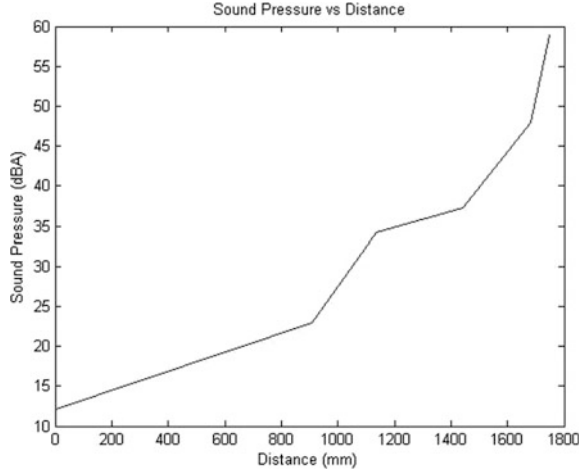
3.2 Back Pressure

The flow pattern of exhaust gases has been studied using CFD and the corresponding back pressure due to restriction to flow has been evaluated. The back pressure is essentially the pressure rise through each chamber caused as a result of restriction to flow of exhaust gases by the baffles. Thus, proper balancing of confliction parameters such as noise and back pressure is to be carried out. The assumptions for the analysis are as follows (Figs. 2, 3 and 4):

- The flow is considered to be steady
- The properties of fuel oil vapor have been attributed to the exhaust gases

However, the impact of every parameter varies. The effect of each of these parameters has been discussed in Table 4.

Fig. 2 Velocity distribution
(streamlines)
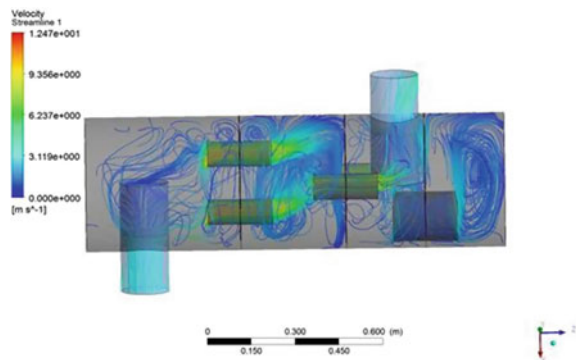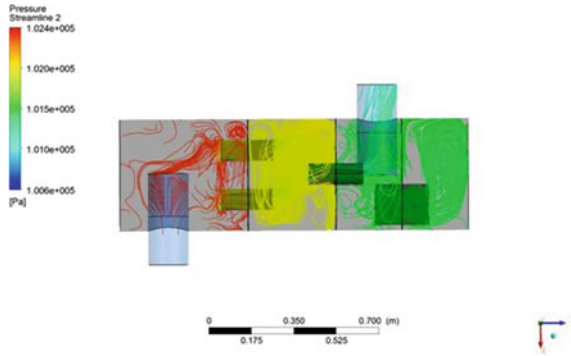
Fig. 3 Pressure distribution (streamlines)
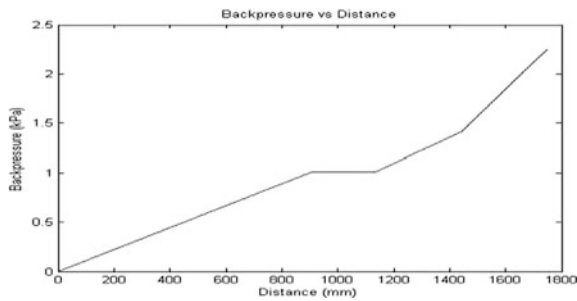
Fig. 4 Pressure variation versus distance (MATLAB)

Table 4 Effect of various parameters on back pressure

Parameter	Variation in back pressure due to 1% change in parameter (%)
Pipe diameter	6.1
Velocity	3.48
Mass flow rate	4.13
Length	1.8

3.3 Inference

The results achieved through analytical calculations and CFD are very close to each other with a minimal error of 14.31%. Thus, we are expecting a total back pressure of 186 mm of water and an insertion loss of 51 dBA which meets our initial design requirements.

We also conclude that reduction in baffle pipe diameter increases transmission loss but has a more significant increase in back pressure. For 1% change in pipe

Table 5 Comparison between analytical and numerical values

Parameter	Analytical value	Numerical value
Back pressure	191.42 mm of water column	208.45 mm of water column
Transmission loss	54.24 dBA	58.88 dBA

diameter, there is a variation of 6.1% in back pressure. Hence, we will proceed for manufacturing of the above design.

4 Results

The final values obtained from the methodologies showed minimal errors and are well within the initial design considerations. The back pressure and transmission loss results have been tabulated in Table 5.

5 Conclusion

A hybrid silencer has inherent advantages over a simple reflective or absorptive silencer since it provides effective noise attenuation through both destructive interference and sound absorption. The governing equations for sound pressure level and back pressure are Helmholtz equation and Bernoulli's equation, respectively.

It can also be concluded that transmission loss and back pressure are two conflicting parameters. The parameter having most significant effect on back pressure is the diameter of the baffle pipe. With increase in baffle pipe diameter, the back pressure reduces but the output sound pressure level increases. Thus, back pressure is inversely proportional to pipe diameter.

References

1. Ramganesh, R., Devaradjane, G.: Simulation of flow and prediction of back pressure of the silencer using CFD. In: National Conference on Recent Trends and Developments in Sustainable Green Technologies. ISSN: 0974–2115. J. Chem. Pharm. Sci. (2015)
2. Rahman, M., Sharmin, T., Hassan, A.F.M.E., Al Nur, M.: Design and construction of a muffler for engine exhaust noise reduction. In: International Conference on Mechanical Engineering, ICME05-TH-47 (2005)
3. Kingston Barnabas, J., Ayyappan, R., Devaraj, M.R.: Design and fabrication of exhaust silencer for construction equipment. In: National Conference on Emerging Trends in Mechanical Engineering (2013)

4. Chaudhri, J.H., Patel, B.S., Shah, SA.: Muffler design for automotive exhaust noise attenuation—a review. Int. J. Eng. Res. Appl. **4**(1), 220–223 (Version 2) (2014). ISSN: 2248-9622
5. Sherekar, V., Dhamangaonkar, P.R.: Design principles for an automotive muffler. Int. J. Appl. Eng. Res. **9**(4), 483–489 (2014). ISSN 0973-4562
6. Shah, S., Kalyankumar, S.K., Hatti, S., Thombare, D.G.: A practical approach towards muffler design. Dev. Prototype Valid. SAE 2010-032-0021
7. Puneetha, C.G., Manjunath, H., Shashidhar, M.R.: Backpressure study in exhaust muffler of single cylinder diesel engine using CFD analysis. In: Altair Technology Conference, India (2015)

Design, Analysis, and Simulation of a Power-Split Device for Hybrid Two-Wheeler

Enanko Moulick, Kiran P. Wani and Sanjay A. Patil

1 Introduction

The main function of automobile transmission is to adapt the traction available from the engine to suit the vehicle, the road profile, the driver, and the environment. Since Panhard developed the first sliding gear transmission in 1895, transmission has evolved a long way. Earl. A Thompson invented synchromesh gearbox and sold it to GM, who first offered them in Cadillac in 1928. CVT, which is preferred for scooters, was invented by Daimler in 1896 [2]. Planetary gear train, which is generally used in Automatic transmission, has two degrees of freedom have been known about since 1000 BC. These days, they are used as power-split device in hybrid vehicle to take power from two sources (see Fig. 1).

Parallel hybrid vehicle, like Toyota Prius, generally uses a power-split device to combine the power from two sources, engine and electric motor (Toyota Hybrid Synergy) [4]. Many other original equipment manufacturers (OEMs) like Ford, GM, BMW, Renault also uses similar kind of configuration for their hybrid vehicles. Changle Xiang, Kun Huang and Reza Langari described the model architecture, operational mode analysis, the mathematical modeling, energy management

E. Moulick (✉)
College of Engineering Pune, ARAI Academy, Pune, India
e-mail: enankoscentury@gmail.com

K. P. Wani · S. A. Patil
ARAI Academy Pune, Pune, India
e-mail: wani.pga@araiindia.com

S. A. Patil
e-mail: sapatil.pga@araiindia.com

373

Fig. 1 Configuration of power-split HEV [3]
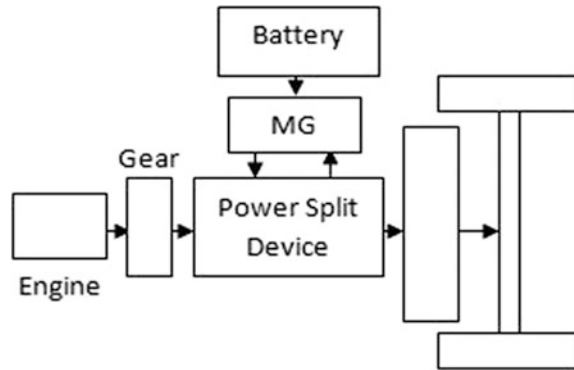
design, simulation and validation of an electromechanical transmission (EMT)-based power-split HEV with three planetary gear trains [3]. Xiaolen Ai, Terry Mohr, and Scott Anderson came up with the concept of a power-split electrome-chanical infinitely variable transmission that can be used as a direct replacement for existing conventional stepwise transmission [5]. Later, Ai along with Anderson modeled and simulated this for an electric vehicle and found that the electrome-chanical infinitely variable transmission not only enhances the vehicle's accelera-tion performance but also delivers up to 2.5 times fuel economy improvement [6]. N. S. Gopi Krishnan and Kiran P. Wani described their design, methodology, simulation, and testing of their hybrid two-wheeler. For integration of the two power sources, they used a cam clutch as a freewheel mechanism which isolates the action of one powertrain virtually [7].

In the hybrid two-wheeler (H2W) segment, none of the OEMs are still able to come up with a reliable product mostly due to the bigger size of the batteries. Most H2Ws deployed on the roads are series type where the motor receives power from the gasoline-powered generator. Using this, configuration restricts the vehicle speed up to a very low limit, that's why customers are reluctant to adopt it. In 2005, Kuen-Bao Sheu and Tsung-Hua Hsu presented a novel hybrid electric motorcycle transmission whose primary feature is a mechanical-type rubber V-belt CVT and chain drives to combine the power of two power sources. They proposed that when the vehicle speed is low, it should run on the motor but once it increases then the engine power is transmitted through the V-belt CVT [8].

This paper focuses on the need, design, and simulation of a power-split device, which can be used to replace conventional gearbox, where it will receive power from two sources, optimize it, and then deliver it to the wheels. This technology also helps the vehicle to shift from electric mode to hybrid mode. The core behind this system is an epicyclic gear train which performs the job of power-spilt device.

2 Design of H2W with Power-Split Device

2.1 Selection of Base Vehicle

The base vehicle chosen for design of this system is Bajaj Pulsar 220Fi. The ratio span of this vehicle is 3.115, so this factor is considered while selecting the number of teeth for power-split device. Some specifications of the engine are:

Engine Type: Spark Ignition
Maximum Power: 15.6 KW
Speed at Maximum Power: 8500 RPM
Maximum Speed: 12,000 RPM
Idle Speed: 800 RPM

2.2 Selection of DC Motor

The system is designed in such a manner that the vehicle initially runs on the motor as the starting torque of the motor is much more than of an IC engine. For this mode, the engine needs to be disconnected which is done with help of clutch.

Now, the motor is supposed to be used for the following two purposes:

1. To run the vehicle in pure electric mode initially until it attains specific velocity and
2. To vary the speed of the output of the gearbox when the vehicle runs in hybrid mode. In this mode, the vehicle will take its power from the engine and the motor speed will be varied to get different speed.

Keeping these things in mind, specifications of the engine, the vehicle requirement, and cost variable a 24 V 1 kW DC motor was selected which can rev up to 3000 RPM having a Rated speed of 2400 RPM.

2.3 Design of Epicyclic Gear Train

In the conventional vehicle, there is primary reduction of 3.47 between the engine and the gearbox, followed by the reduction in the gearbox and finally a reduction of 2.57 in the chain drive. These two reductions were kept unchanged and only the gearbox is modified for this purpose. Now, as already discussed, an epicyclic gear train is used as a power-split device. A simple epicyclic gear train can have max six possible configurations considering input, output, and braking. All the possible configurations were explored, calculations were done for all of them considering motor speed to vary within 20% of the engine speed using the below formulae [9]:

$$\omega_s Z_s + \omega_p Z_p - \omega_c \left(Z_s + Z_p \right) = 0 \tag{i}$$

$$\omega_s Z_s + \omega_p Z_p - \omega_c \left(Z_s + Z_p \right) = 0 \tag{ii}$$

where,

ω_s, ω_p, and ω_r = speed of sun gear, planet carrier, and ring gear, respectively.
Z_s, Z_p, and Z_r = Number of teeth on the sun gear, planet carrier, and ring gear, respectively.

Size of the gear is a considerable factor here as the size of the conventional gearbox is very compact, so keeping that in mind, the smallest possible gear configuration was used for the above calculation. So Z_s = 22, Z_p = 18, and Z_r = 58.

From the calculations as shown in Table 1, it is observed that using the below configuration and varying the motor speed within 20% of the engine speed, the range of speed ratios comes as 3.23.

Engine connected to sun gear; motor connected to ring gear; output taken from carrier.

2.4   Clutch Actuation Algorithm

There are two clutches (C1 and C2) used in this configuration (see Fig. 2). Initially, the vehicle runs only on the IC engine and C1 is used to disconnect engine from the

Table 1 All possible configurations for power-split device

S. No.	Sun gear	Ring gear	Carrier	ratio Span	Remarks
1	Engine	Motor	Output	3.23	Best range
2	Motor	Engine	Output	1.16	Not suitable
3	Output	Motor	Engine	1.33	Not suitable
4	Output	Engine	Motor	1.766	Not suitable
5	Engine	Output	Motor	1.116	Not suitable
6	Motor	Output	Engine	−6.33	Negative
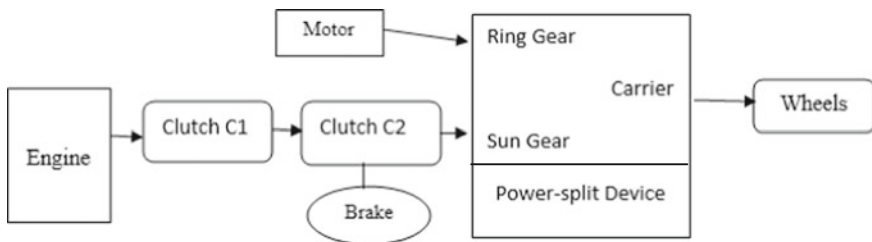
Fig. 2 Block diagram of the design

transmission system whereas simultaneously C2 is used for breaking the sun gear. Now, once the speed of the vehicle goes beyond 12 kmph, the engine is throttled and when the engine speed reaches 1200 rpm the C2 is disengaged, thereby disengaging the sun gear and the engine power is transmitted to the sun gear by engaging the C1.

3   Simulation

The whole system is simulated in MATLAB and Simulink software, which already has predefined blocks for almost all components for a vehicle in the Simscape toolbox. Parameters of the blocks like engine, gears, clutches are modified as per the given data of the vehicle. At first, a conventional vehicle is simulated. Once its result is within the limit, the model is then further modified to make it as a hybrid vehicle with power-split device (see Appendices 1 and 2).

   The DC motor is connected across a variable resistor to control its speed. Two clutches are connected in series which were controlled by the algorithm driven by the function, where inputs from the vehicle speed and engine RPM are taken in. These functions are coded to serve for the engagement and disengagement of the clutches as per the way discussed in the previous paragraph above. Engine is given full throttle, when required, to keep the things simple for this simulation. To observe the performance of the vehicle on this configuration, various outputs are captured like motor RPM versus time (see Fig. 3), engine RPM versus time (see Fig. 4), engine power versus time (see Fig. 5), and vehicle speed versus time (see Fig. 6).

Fig. 3 Motor rpm versus time (s)
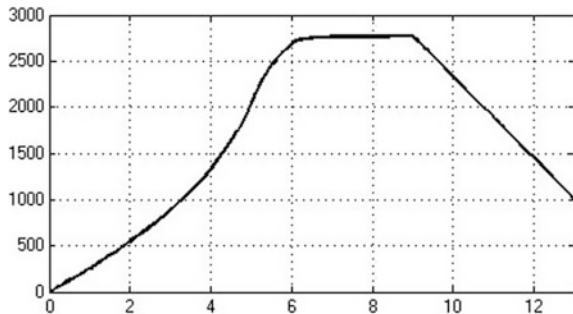
Fig. 4 Engine rpm versus
time (s)
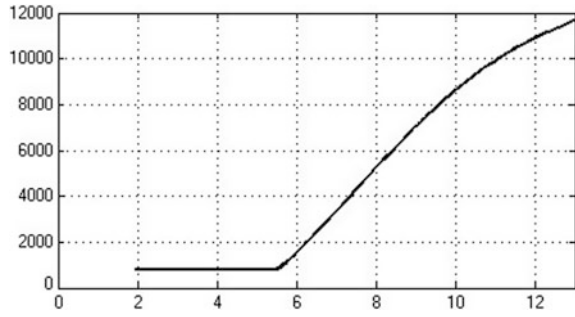
Fig. 5 Engine power
(W) versus time (s)
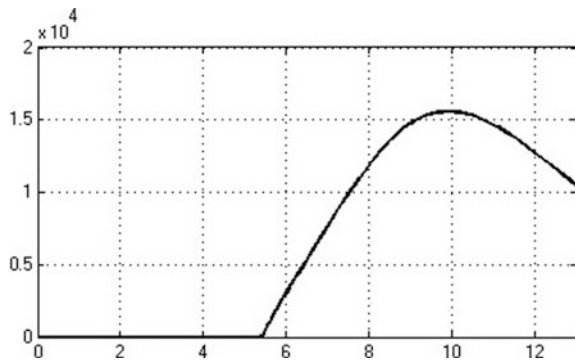
Fig. 6 Vehicle speed (kmph)
versus time (s)
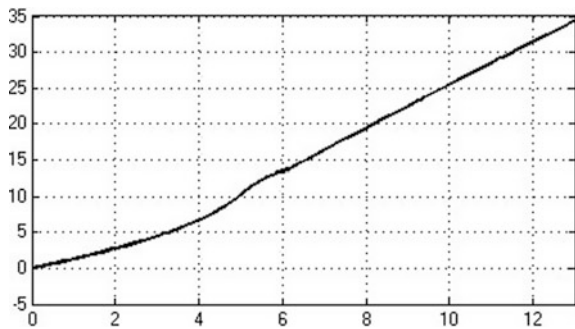
4   Results

Figure 3, 4, 5, and 6 depict the results of the simulations. We can see that initially
vehicle is driven by the motor as engine is kept in idle, and it is also disconnected
from the power-split device. Once the vehicle speed reaches 12 kmph, then the
engine is throttled, clutch is engaged, now, the power-split device receives power

from both the sources, and the vehicle speed continues to increase. Further, when the motor speed is reduced the vehicle speed continues to rise. This way motor works as a variator and only varies the output speed. It can be further reduced and even polarity may be reversed to attain higher speed.

Figure 3 indicates how motor speed initially increases. In this phase, vehicle is in pure electric mode. In Fig. 6, it can be noticed that around 5 s mark, there is slight variation in the slope of the curve. It is that phase where the engine is throttled (see Fig. 4) and power is transmitted (see Fig. 5) to the power-split device through the clutch.

5 Conclusion

The following conclusions can be drawn on the basis of these results:

- Power-split device can be used for H2Ws to get power from two sources, optimize it, and then send it to the wheels.
- It can also help in utilizing the advantages of one of the sources over a range, for example, motor for initial torque.
- Motor can be used to work as a variator when engine is throttled just to vary the output speed.
- Using this, hybrid vehicle can also be tuned for better power or economy.

6 Future Work

Developing a more advanced algorithm that can control the electric motor which when used a variator will help in further optimize the performance of the engine. The vehicle can be tuned for more power or better economy.

Appendix 1: Transmission Block of the Simulation

Appendix 2: Simulink Blocks in MATLAB
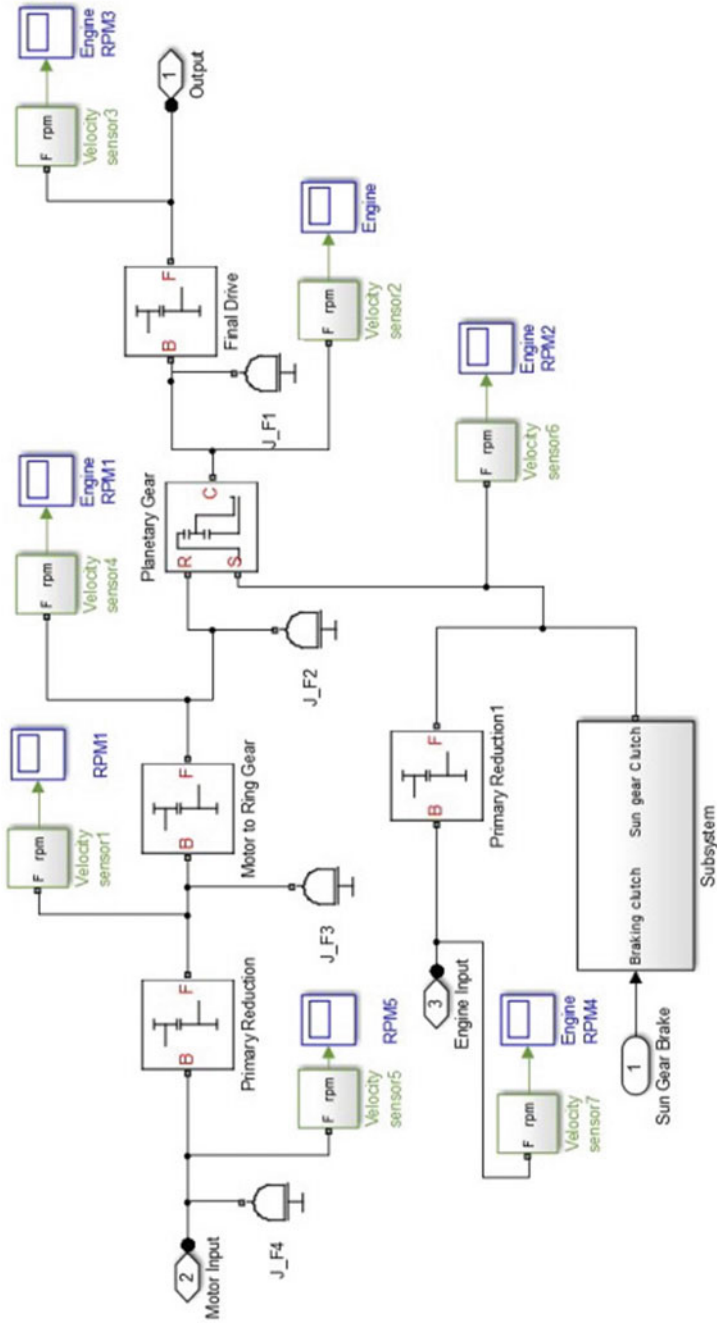
References

1. SIAM homepage, http://www.siamindia.com, last accessed 28/01/2018
2. Nortan, R.L.: Automotive Milestones; The Technological Development of the Automobile. Industrial Press, Inc. (July 2015)
3. Xiang, C., Huang, K., Langari, R.: Power-split electromechanical transmission design and validation with three planetary gears for heavy-duty vehicle. Iran J. Sci. Technol. Trans. Mech. Eng. (2017). https://doi.org/10.1007/s40997-017-0105-1
4. Yang, Y., Emadi, A.: Integrated Electro-Mechanical transmission Systems in Hybrid Electric Vehicles (2011)
5. Ai, X., Mohr, T., Anderson, S.: An electro-mechanical infinitely variable speed transmission. In: SAE-Transmission & Driveline Symposium 2004 (SP-1817), 2004-01-0354
6. Ai, X., Anderson, S.: An electro-mechanical infinitely variable transmission for hybrid electric vehicles. In: SAE-Advanced Hybrid Vehicle Powertrains 2005 (SP-1973), 2005-01-0281
7. Gopi Krishnan, N., K. Wani: Design and Development of a Hybrid Electric Two-Wheeler. SAE Technical Paper 2015-26-0118 (2015). https://doi.org/10.4271/2015-26-0118
8. Sheu, K.-B., Hsu, T.-H.: Design and implementation of a novel hybrid-electric-motorcycle transmission. Appl. Energy **83**, 959–974 (2006)
9. A. Kahraman, H. Ligata, K. Kienzie, D.M. Zini, A kinematics and power flow analysis methodology for automatic transmission planetary gear trains. J. Mech. Des. **126**, 1071–1101 (Nov 2004)

Development of Inhibition System for SIS Process

G. Bhuvaneshwaran, Mesfin Sisay, R. Manivannan, P. Arunkumar
and M. Silambarasan

1 Introduction

Additive manufacturing (AM) is an advanced rapid prototyping (RP) process to fabricate the complex shapes from various materials such as thermoplastics, metals and wax [1]. The AM technologies can be divided into a solid-based method (fused deposition modelling and laminated object manufacturing), liquid-based method (stereolithography) and powder-based method (selective laser sintering) which are among the well-established techniques in the commercial market [2]. Selective inhibition sintering (SIS) process is a novel powder-based technique, and it is performed on the basis of sintering and inhibition phenomena [3]. Asiabanpour et al. [4] developed an alpha machine to perform SIS process and investigated the specific printer path generation method in SIS process. They also experimented with various polymer powders and inhibition materials. The inhibition process plays the major role in fabricating the 3D parts with fine geometric details and good surface finish in SIS process [5]. Yoozbashizadeh et al. [6] have studied four theories for the inhibition process such as microscopic mechanical and macroscopic

G. Bhuvaneshwaran (✉) · M. Sisay · R. Manivannan · P. Arunkumar · M. Silambarasan
Centre for Autonomous System Research (CASR), Veltech Rangarajan
Dr Sagunthala R&D Institute of Science and Technology,
Avadi, Chennai 600062, India
e-mail: gd.bhuvanesh1@gmail.com

M. Sisay
e-mail: mesfins245@gmail.com

R. Manivannan
e-mail: manivannanrangasamy@gmail.com

P. Arunkumar
e-mail: arunmech198@gmail.com

M. Silambarasan
e-mail: silambu.friends@gmail.com

mechanical, thermal and chemical inhibition process. Each theory can be applicable for the specific inhibitor and operating conditions. Asiabanpour et al. [7] have been prepared the inhibition solution by mixing saturated aqueous potassium iodide solution with alcohol for fabricating parts from polystyrene powders. Khoshnevis et al. [8] used a single-orifice nozzle which is activated by an electromagnetic solenoid valve for depositing inhibition solution. Also, it can handle various inhibition solutions with the wide range of liquid characteristics such as viscosity and surface tension. Torabi et al. [9] worked in SIS process for metallic part fabrication, and they used high-resolution, high-performance piezoelectric print head (WF30) for the inhibition process. From the literature studies, it is observed that the controlling of inhibition droplets and penetration into the powder layer by inhibitor droplets are to be concerned in SIS process. In the present paper, the inhibition mechanism is developed to produce the fine geometric details with good surface finish of part in SIS process. In addition, the fluid properties of inhibitor are key concern in achieving desirable geometry. Hence, the various salts are considered for inhibitor preparation and observed that potassium iodide has better inhibition effect.

2 SIS Machine

The SIS process works by sintering in the parts body and inhibition at the selective areas of powder bed. The following process is involved in the fabrication of SIS part. (i) The polymer powder is initially spread over the build platform through roller mechanism to make the first layer. (ii) The inhibitor is deposited at the selected boundaries of build part through print head nozzle that moves along the X-Y plane. (iii) The pre-processed layer is heated through an inexpensive heating system to perform sintering. (iv) The above sequence is repeated until the desired part is obtained. Finally, the fabricated part is extracted from the build tank and the post-processing including removal of inhibitor, and cleaning of surplus materials from the part, completes the SIS process. The details of SIS machine are shown in Fig. 1.

The build tank (200 × 200 mm) and feed tank (250 × 200 mm) are moving along Z-axis using NEMA 23 stepper motor. The roller mechanism and tool path generation using inhibition mechanism are coupled with X-Y-axis, which are realized by belt and pulley drive. The limit switches are connected in the maximum and minimum positions of X- and Y-direction to control the movements. The infrared heater mechanism is moving Y-axis for sintering the polymer powders. The part bed is maintained at 100 °C using surface plate heater to avoid the curling of sintered part. The solid state relay is used to switch the heater and to maintain the temperature settings. The thermistors are used to measure the temperature of IR heater and bed heater. The ATMEGA 2560 with RAMPS 1.4 board acts as the controller of the SIS system. The SMPS system is connected with the controller which will supply the input DC. The controller sends the signals to five stepper motors for X,

Fig. 1 SIS machine

Y, *Z*, Extrusion 1 and Extrusion 2. The A4988 and Tb6600 stepper drivers are used to actuate NEMA 17 and 23 stepper motors, respectively. The LCD monitor is used to provide information and to control the motions.

3 Inhibition Mechanism Modelling

The inhibition mechanism is developed through actuating syringe pump, which is coupled with stepper motor, and it is shown in Fig. 2. In this mechanism, the rotational motion of stepper motor is being converted into reciprocated motion of syringe. The stepper motor is in series connection with screw rod and parallel connection with syringe. The two smooth rods are attached at two sides of stepper motor, and it is fixed at both ends.

The inhibition deposition is mainly influenced by parameters such as droplet size and volumetric flow rate, which are controlled by nozzle diameter and specification of stepper motor (steps per mm, speed and acceleration). The multiple iterations were carried out by varying nozzle diameter to get effective inhibition process that is mentioned in Table 1. The optimal conditions of extrusion length are being measured at syringe diameter of 27 mm from six experiments. The extrusion length is the movement of plunger to achieve 1 mm of distance in *X*- or *Y*-direction. The feed rate is also varied for each iteration to achieve the flow as required.
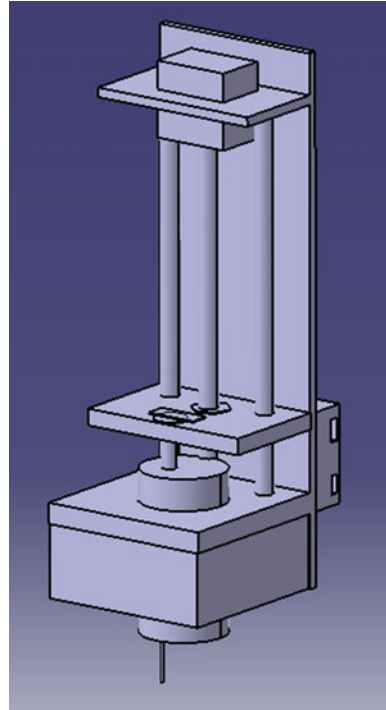
Table 1 Optimal conditions for various nozzle diameters

S. No.	Nozzle diameter (mm)	Extrusion length (mm)
1	0.26 (25G)	0.000037
2	0.413 (22G)	0.000043
3	0.603 (20G)	0.00005
4	0.838 (18G)	0.000059
5	1.194 (16G)	0.00007
6	1.6 (14G)	0.000088

The regression equation is developed for the output responses of extrusion length, which is shown below:

$$\text{Extrusion length} = (1 \times e - 5)x + (2 \times e - 5) \tag{1}$$

where x is nozzle diameter.

Since the inhibition material has higher fluidity and due to hydrostatic pressure, it is not possible to stop the flow of inhibition immediately. To overcome this difficulty, it is needed to retract the plunger by small distance to counteract the pressure generated during extrusion. This effect affects the succeeding stage of inhibiter extrusion that has to be prevented by adding the same retraction distance.

4 Inhibition Preparation and Comparative Studies

Inhibitors are used to prevent selected region of the powder layer from sintering. Asiabanpour et al. [4] identified four inhibition phenomena, i.e. impact cutting, cooling, chemical reaction and separation. Separation phenomena cause prevention of cohesion of powder particles by creating physical barrier between them. This can be achieved by adding a large amount of salt in the selected region of the powder layer. For effective inhibition process during sintering, the salt in the inhibition solution must have relatively high-water solubility and high melting point.

In this study, the inhibition ability of four types of salt which has high solubility in water at ambient temperature and high melting point has been examined. These salts and their solubility in water and melting point are given in Table 2. Isopropyl alcohol is added to the solution to reduce its surface tension in such a way that it can penetrate the powder layer and avoid the formation of the droplet.

The parts fabricated through applying various inhibition solutions are shown in Fig. 3. The result of the investigation shows that KI and $BaCl_2$ are found to be effective in inhibiting the selected region of the powder layer from sintering. Further investigation has been carried out to see the effect of barium chloride inhibitor on dimensional tolerance. Part is fabricated from a 40 mm × 40 mm rectangular CAD model. The dimension of the part produced by SIS process is found to be 38 mm × 38 mm which is 1-mm reduction from each side. This dimensional variation has come from the dispersion of the inhibition solution to either side of the boundary on which it is applied and some contraction. In general from this study, it is found that barium chloride inhibitor is good in providing the part with good dimensional accuracy (Fig. 4).

5 Conclusion

In the paper, the inhibition mechanism is developed using cost-effective screw-type actuator. The optimal condition for the regulated flow is iterated through various parameter studies during the SIS process. The syringe diameter and nozzle diameter

Table 2 Solubility and melting points of inhibitor salts

S. no	Salt	Solubility in water at ambient temperature	Melting point (°C)
1	Potassium iodide (KI)	135 g/100 ml	681
2	Barium chloride ($BaCl_2$)	35.8 g/100 ml	962
3	Magnesium sulphate ($MgSO_4$)	35.1 g/100 ml	1124
4	Sodium sulphate ($Na_2SO_{4)}$)	13.9 g/100 ml	884

(a) KI (potassium chloride)

(b) BaCl$_2$ (Barium chloride)

(c) MgSO$_4$ (Magnesium Sulphate)

(d) NaSO$_4$ (Sodium Sulphate)
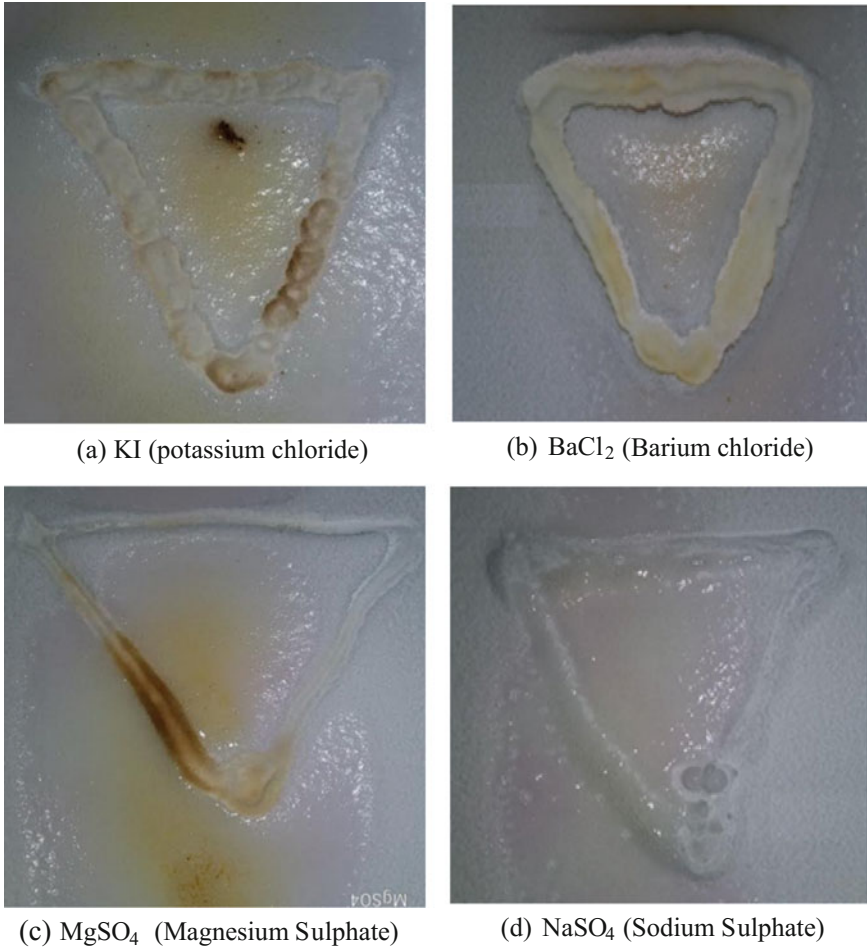
Fig. 3 Comparison of various inhibitor solutions

are controlled to obtain smooth flow of inhibition. In addition, the experimental study on various inhibitors is performed to investigate inhibition effects on powder layer during sintering process. The result of the investigation shows that KI and BaCl$_2$ are found to be effective in inhibiting the selected region of the powder layer from sintering. The ratio of saturated salt solution and alcohol is obtained through performing multiple iterations. Experimental results reveal that the developed mechanism is able to deposit thin inhibition layer on the powder surface to inhibit regions for effective sintering.
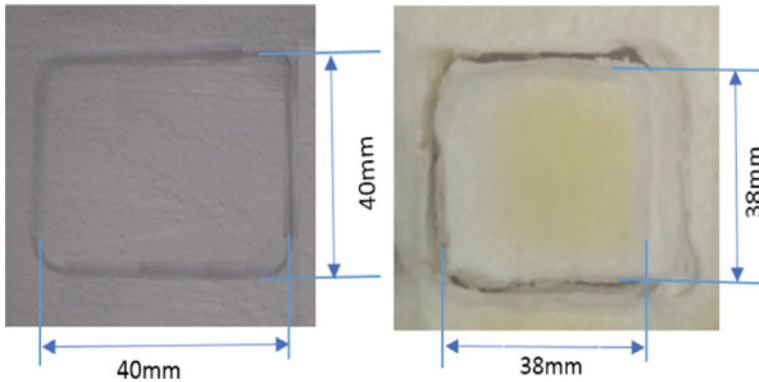
Fig. 4 Effect of barium chloride inhibitor on dimensional tolerance of a part

References

1. Chua, C.K., Chou, S.M., Wong, T.S.: A study of the state-of-the-art rapid prototyping technologies. Int. J. Adv. Manuf. Technol. **14**(2), 146–152 (1998)
2. Huang, S.H., Liu, P., Mokasdar, A., Hou, L.: Additive manufacturing and its societal impact: a literature review. Int. J. Adv. Manuf. Technol. **67**(5), 1191–1203 (2013)
3. Khoshnevis, B., Asiabanpour, B., Mojdeh, M., Palmer, K.: SIS— a new SFF method based on powder sintering. Rapid Prototyp. J. **9**(1), 30–36 (2003)
4. Asiabanpour, B., Khoshnevis, B.: Machine path generation for the SIS process. Robot. Comput. Integr. Manuf. **20**(3), 167–175 (2004)
5. Khoshnevis, B., Yoozbashizadeh, M., Chen, Y.: Metallic part fabrication using selective inhibition sintering (SIS). Rapid Prototyp. J. **18**(2), 144–153 (2012)
6. Yoozbashizadeh, M.: Metallic Part Fabrication with Selective Inhibition Sintering (SIS) Based on Microscopic Mechanical Inhibition. University of Southern California (2012)
7. Asiabanpour, B., Khoshnevis, B., Palmer, K., Mojdeh, M.: Advancements in the SIS process. In: 14th International Symposium on Solid Freeform Fabrication, Austin, TX
8. Khoshnevis., B., Asiabanpour, B.: Selective Inhibition of Sintering, Rapid Prototyping, pp. 197–220. Springer, Boston (2006)
9. Torabi, P., Petros, M., Khoshnevis, B.: Enhancing the resolution of selective inhibition sintering (sis) for metallic part fabrication. Rapid Prototyp. J. **21**(2), 186–192 (2015)

Finite Element Analysis of Lifting Lugs Under Actual Factory Conditions

Mir Aamir Abbas

1 Introduction

The lifting lug design is mostly performed in the industry by considering the vertical load [1]. The lateral loads are generally not considered for structural design evaluation. It may be noted that if the lifting ropes are vertical, then such calculations would be valid, but such conditions are not available in general. The wire ropes from the pulley connected to the lifting lug are, in general, not vertical but inclined. This inclination causes lateral loads to act on the lug. The effect of these lateral loads on the lugs must be evaluated to ensure the structural integrity of the design. The analysis is generally performed currently in the industry using analytical calculations followed by finite element analysis. A method is developed for calculating the lateral loads on the lug in the practical situation using basic mechanics and mathematics, and then stresses are calculated by both finite element method and analytical calculations. The comparison of the analytical stress calculations and FEA results shows a remarkable correlation, thus validating the results. A general lifting lug arrangement in a factory is shown in Fig. 1.

2 Modelling and Calculations

From the design, the values of *a* and *b* are known but the values of *c* are not known. The problem may be solved by measuring the length of lifting rope. Using Pythagorean theorem,

M. A. Abbas (✉)
Aadyah Aerospace, Bengaluru, India
e-mail: friendabbas@gmail.com

Fig. 1 General lifting lug
arrangement
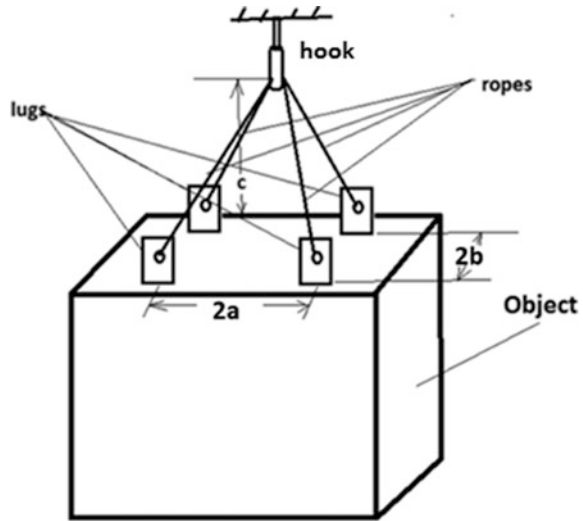
Fig. 2 Free body diagram of
the rope
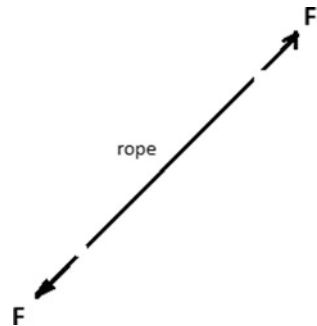
$$a^2 + b^2 + c^2 = l^2$$
$$\Rightarrow c = \sqrt{l^2 - a^2 - b^2} \tag{1}$$

The wire rope generally has low bending stiffness and for load calculation it may
be considered as a string. A free body diagram of the rope is shown in Fig. 2.

The rope experiences axial pull. The vector force F is transmitted to the lug by
contact. To calculate the force F, it may be noted that the rope and the axial force
have the same inclination. Therefore, force vector and the distance vector of the
pulley with respect to the lug hole form similar triangles OAB and O′A′B′ with the
force with respect to the components a, b and c and F_x, F_y and F_z as in Fig. 3.

Let the weight of the assembly be 4 W. However, F_z = weight, W,

Fig. 3 Force with respect to
the components a, b and c
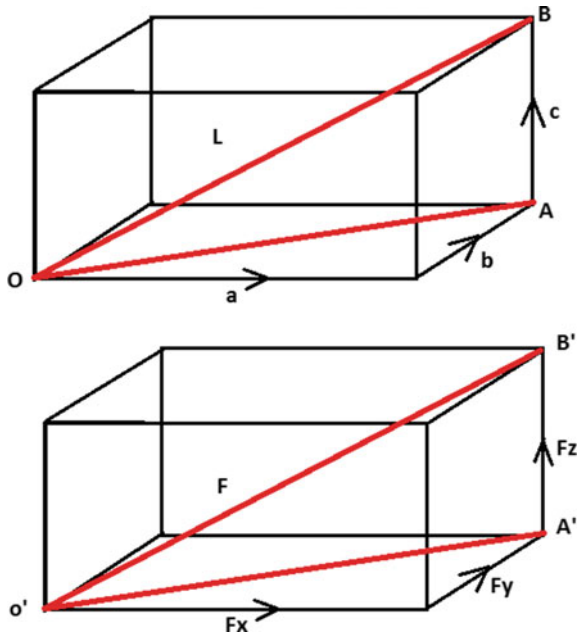
F_x, F_y and F_z obtained as

$$F_y = \frac{W.b}{\sqrt{l^2 - a^2 - b^2}}$$ (2)

$$F_x = \frac{W.a}{\sqrt{l^2 - a^2 - b^2}}$$ (3)

These loads F_x, F_y and F_z may be taken as loads acting on the lug.

The location of the action of these loads on the lug is found by considering the lug–rope surface interaction as being frictionless. The point of action is located by the intersection of the projection of force vector on the *XZ*-plane with the boundary of the hole (Fig. 4).

$$m = r.\frac{a}{l} \quad \text{and} \quad n = r.\frac{c}{l}$$ (4)

Analytical stress calculation

The lug is idealized as a beam. F_x and F_z are the in-plane loads. F_y is the out of plane load. The in-plane load causes in-plane deformation including in-plane bending. The out of plane loads cause out of plane bending.

Fig. 4 Point of action on the
XZ-plane
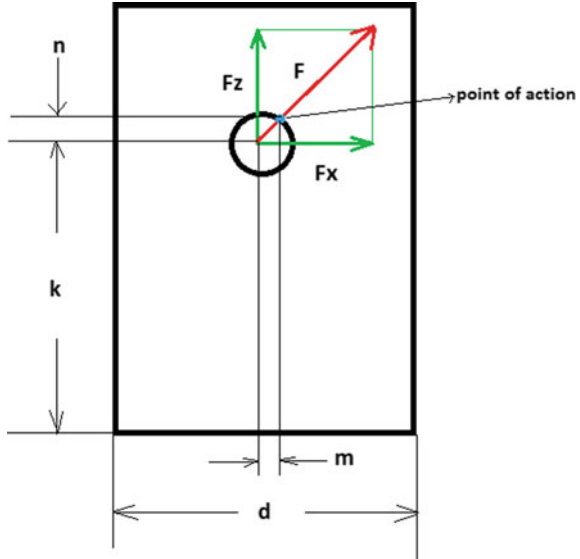
The bending moment about the *y*-axis is

$$M_y = F_x(K+n) - F_z m; M_x = F_y(K+n)$$

The twisting of the lug is not considered in this calculation.
Bending stress in the lug is calculated by the [2] beam formula:

$$\sigma_b = \frac{M}{Z} \quad \text{where,} \quad Z = \frac{I}{Y}$$

The maximum bending stress due to M_y is $\sigma_{b1} = \frac{6.M}{t.d^2}$.
The maximum bending stress due to M_x is $\sigma_{b2} = \frac{6.M}{t^2.d}$.
The tensile stress due to the force F_z is $\sigma_t = \frac{W}{t.d}$.

The combination of worst stresses occurs at the lug bottom corner where all the stresses are tensile. Therefore, the maximum stress induced in the lug is given by

$$\sigma_{\max} = \frac{6M_y}{td^2} + \frac{6M_x}{t^2 d} + \frac{w}{td} \tag{5}$$

2.1 Case Study: Factory Lifting Conditions

A lug of thickness, $t = 8$ mm, width, $d = 60$ mm and height 100 mm with a hole of diameter 10 mm was analysed for a load of $W = 10{,}000$ N, $a = 4000$ mm, $b = 3000$ mm, $l = 10{,}000$ mm.

von Mises stress in response to vertical load
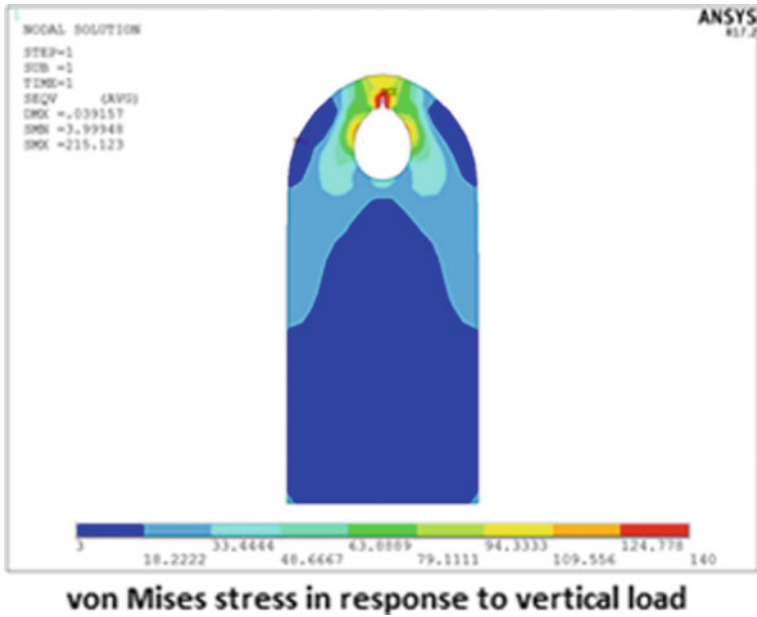
Fig. 5 von Mises stress by FEA for vertical load

We get

$$M = 4\,\text{mm}, \quad n = 8.66\,\text{mm}, \quad Fx = 4618, Fy = 3464,$$
$$M_x = 376,410\,\text{N mm}, \quad M_y = 461,880\,\text{N mm}$$
$$\sigma_{b1} = 76.98\,\text{MPa}, \quad \sigma_{b2} = 376.41\,\text{MPa}, \quad \sigma_t = 16.67\,\text{MPa}$$

The maximum principal stresses obtained by analytical calculation by the derived formulae and FEA were 470.05 and 472.885 MPa, respectively, for the total loads. The von Mises stress by FEA for vertical load was 140 MPa while that for the total loads was 435 MPa. The FEA results are shown in Figs. 5 and 6.

2.2 Dynamic Considerations

The weight represents only the static load, and it must be scaled by the dynamic factor for the design calculations. The worst dynamic loads occur on the lug while moving the load along the factory. The dynamic magnification factor is found by [3] using the expression:

von Mises stress in response to complete load

Maximum Principal stress in response to total loads
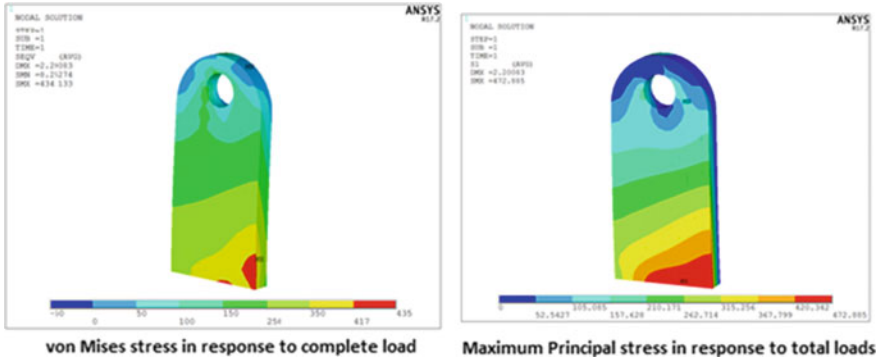
Fig. 6 von Mises stress by FEA for total load

$$\text{Dynamic magnification factor}, A = 1 + \frac{V^2}{gk} \tag{6}$$

where

V is the horizontal velocity with which the object is being moved;

g is the acceleration due to gravity;

k is the distance from the point of suspension from the crane hook to the centre of gravity of the object being lifted.

The maximum speed at which the load is carried is limited to 10 m/s. The value of k for this case is about 10 m. The dynamic magnification factor is about 2.69. Thus, the maximum von Mises stress induced is:

$$\sigma_{\max} = \sigma_{\text{static}} \cdot A = 2.02 \times 435 = 878 \text{ MPa}$$

For rupture of ductile materials, the failure criterion used is strain. Since the induced stress is greater than the yield stress, the value of strain accounting fort the plastic deformation can be found by the following expression [4] derived using Neuber's rule:

$$\sigma = \left\{ \frac{\sigma_{yp}}{T} - \frac{\sigma_{yp}}{E} \pm \sqrt{\left(\frac{\sigma_{yp}}{E} - \frac{\sigma_{yp}}{T} \right)^2 + 4 \frac{s^2}{TE}} \right\} \cdot \frac{T}{2};$$

$$\varepsilon = \sigma_{yp}/E + (\sigma - \sigma_{yp})/T$$

where

T is the tangent modulus of the material = 6500 MPa;

σ_{yp} = yield stress = 250 MPa;

Young's modulus = 200 GPa;
We get materially nonlinear stress = 320.1349 MPa;
And the corresponding strain = 0.012 or 1.2%.

3 Discussion

The finite element analysis of the actual factory condition was performed both analytically and by finite element method. The results showed good correlation, and the finite element analysis also showed solution convergence. It was found that the stresses were well beyond the yield point and also the lug may not rupture but will undergo significant plastic deformation causing design failure. The finite element analysis for vertical load also showed solution convergence. Although the stresses were beyond the yield point, the localized plasticity might relieve stresses and the component may not fail. An evaluation using the Neuber's rule indicates that the strain is well below the rupture strain, but it does cause a violation of the design intent.

It may be noted that the above problem when solved by the two different approaches gives drastically different result. If the latter approach is followed, it would give unsafe results and is not recommended. Thus, the consideration of the actual factory lateral lifting loads is necessary.

4 Conclusion

The results of the calculations both analytical and numerical reveal that considering the actual factory condition lateral lifting loads is necessary. Failure to do so may result in violation of the design intent.

References

1. Kulkarni, S.V., Khaparde, S.A.: Transformer Engineering: Design and Practice. CRC Press, Boca Raton (2004)
2. Timoshenko, S.: Strength of Materials-Part 1: Elementary Theory and Problems, 3rd edn. CBS Publishers and Distributors (2000)
3. Aamir Abbas, M., et al.: Finite element analysis of crane hook. IOSRD J. Eng. **1**(2), 118–123 (2014)
4. Abbas, M., et al.: Structural finite element analysis of an electrical lug. In: IEEE Conference Proceedings ICSEMR (2015)

Numerical Simulation of High Velocity Impact on Composite Targets Using Advanced Computational Techniques

K. Subramani and I. Vinoth kanna

1 Introduction

Propelled earthenware materials have been produced over the past 50 years [1–3]. These materials normally connected as warm obstruction coatings to secure metal structures, wearing surfaces or as necessary parts independent from anyone else [4–6]. High quality, hardness, high-temperature protection, concoction latency, wear protection and low thickness properties have prompt the improvement of strategies to toughen the material by support with filaments and hairs opening up more applications for pottery [7–9]. Lightweight ceramic-based defensive frameworks were produced for workforce, flying machine and vehicle security. In the nearby battle and policing circumstance, they have demonstrated against high speed and shield puncturing rounds [10–12].

2 Methodology

A ceramic metal composite system subjected to high velocity impact is taken up for study. Analytical and experimental treatments for such type of problem are very difficult, and hence, numerical solution using finite element method is attempted for the analysis. The finite element analysis software, AUTODYN is used for the analysis. Efficient configurations of ceramic/metal composite system are proposed. Performances of the various configurations are compared and best case is chosen

K. Subramani (✉) · I. Vinoth kanna
Department of Mechanical Engineering, Vel Tech Rangarajan
Dr. Sagunthala R&D Institute of Science and Technology, Chennai, India
e-mail: subbumecad@gmail.com

399

for further study. Response of the ceramic/metal composite system with best
configuration having high ballistic limit and low areal density is studied by varying
the parameters such as front- and backplate thickness.

3 Numerical Models

3.1 Modelling of Ceramic/Metal Composite System

Two-dimensional and three-dimensional finite models are developed using
AUTODYN for investigating the impact response of ceramic/metal composite
target as shown in Figs. 1 and 2. Ogive nose steel projectile with impact velocity at
the range of (660–750 m/s)[13, 6, 10, 14]. Projectile has total length of 29.11 mm,
diameter 7.62 mm and mass 8.32 g [11, 15, 16]. Lagrangian grid-based finite
element model is investigated for impact resistance of ceramic/metal composite
panels [16–18].

In this chapter, a brief introduction to finite element method, its applications,
advantages and disadvantages are discussed [15, 17]. An introduction to
AUTODYN, two-dimensional modelling, three-dimensional modelling and mate-
rial modelling of ceramic/metal composite system are also explained [1, 19, 20].

4 Simulation of High Velocity Impact

In this chapter, an experimental study reported in the literature is adopted for the
validation of constitutive and material models used in simulations of high velocity
impact [15, 19, 21].

Fig. 1 2D finite element
model of target and projectile
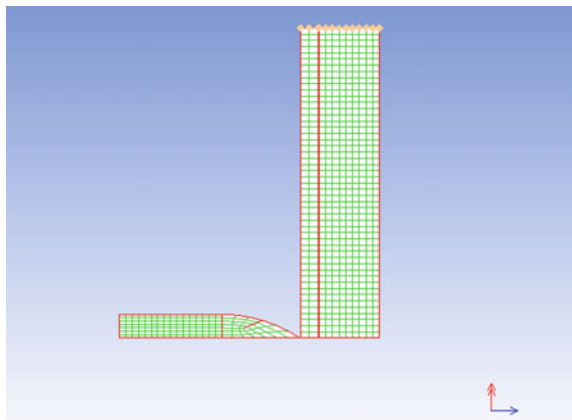
Fig. 2 3D finite element
model of target and projectile
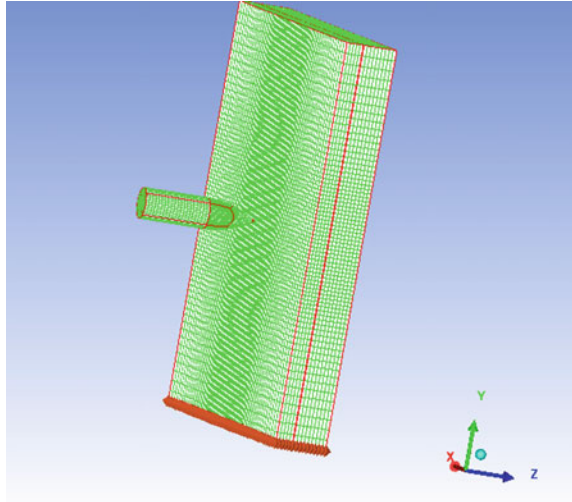
4.1 STUDY-1: Determining the Ballistic Limit Velocity for Given Target and Projectile

Impact response of amours of silicon carbide backed by aluminium against hard steel projectile was simulated to determine ballistic limit velocity [22–24]. An axis symmetric finite element (FE) model of composite target and projectile was created using AUTODYN software (Figs. 2 and 3). The problem has been analysed in the literature [5, 25]. Details of steel projectile and target plate are given in Table 1. Ballistic limit velocity was reported as 660 m/s for the target plate. Material properties available in material library of AUTODYN were used with small modification to account for erosion of the materials [26, 7, 8].

Since erosion criterion was not mentioned in the reported reference, reasonable values are used instantaneously for geometric strain values used in the (FE) model

Fig. 3 Axisymmetric
geometry of FE model
($h1/h2 = 1.0$)
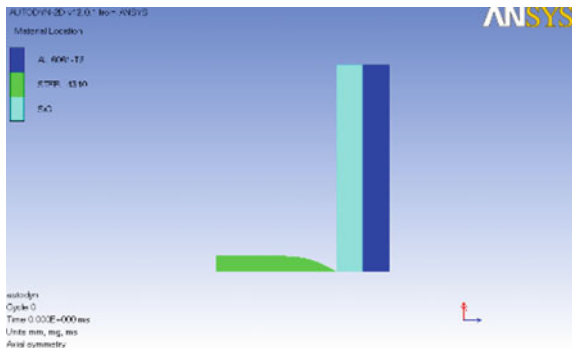
Fig. 4 Axisymmetric
geometry of FE model
($h1/h2 = 1.0$)—Finite element
mesh
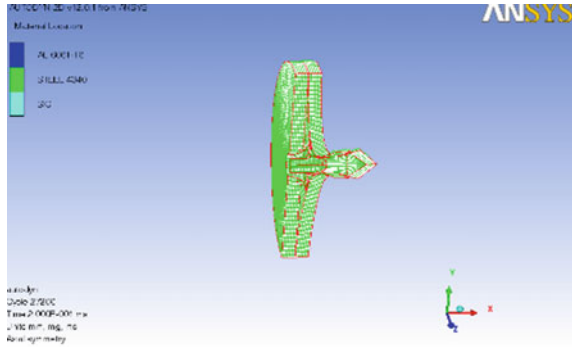
Table 1 Geometric details of
impact problems

Details	Value
Diameter	7.62 mm
Length	29.11 mm
Mass	8.32 g
Nose shape	Ogive
Front plate thickness	6.35 mm
Backplate thickness	6.35 mm

Table 2 Material model for
steel-4340

Equation of state	Linear
Strength	Johnson Cook
Failure	Johnson Cook
Erosion criteria	Geometric strain
Geometric strain	1.90
Type of geometric strain	Instantaneous
Material cutoff	Defaults

Table 3 Material model for
silicon carbide (SIC)

Equation of state	Polynomial
Strength	Johnson–Holmquist
Failure	Johnson–Holmquist
Erosion criteria	Geometric strain
Geometric strain	1.80
Type of geometric strain	Instantaneous
Material cutoff	defaults

are 190, 180 and 150% for steel projectile, front target plate (SIC, ceramic) and
backplate (Al6061-T6, aluminium alloy), respectively [27, 12, 28]. Details of
material models used in the simulation are available in Tables 2, 3 and 4.

Table 4 Material model for aluminium (Al6061-T6)

Equation of state	Shock
Strength	Steinberg
Failure	Johnson Cook
Erosion criteria	Geometric strain
Geometric strain	1.50
Type of geometric strain	Instantaneous
Material cutoff	defaults

The target plates were unbonded as per the problem given in the literature. Therefore, the target plates were not joined at the interface [29, 3, 30]. The free edges of target plates are provided with the velocity boundary condition as (general 2d velocity zero) available with AUTODYN. It was observed that instantaneous geometric strain value affects the amount of erosion of the material. Higher value of geometric strain generally indicates lesser erosion of the material. Residual velocity of the projectile was observed to vary with respect to change in geometric strain value [31, 32, 9].

4.2 Results

Output of finite element analysis is plotted for residual velocities, perforation status as shown in Figs. 5, 7 and 4, 6 for initial velocities of 660 and 670 m/s [2, 12], respectively. The simulated velocities of projectile at 200 μs after impact are compared in Table 5. Ballistic limit velocity was found as 660 m/s similar to that reported in the literature [33, 34]. Energy summary of projectile status as shown in Figs. 8, 9, 10 and 11.

Ballistic limit velocity is found as 660 m/s for which the projectile was defeated.

Fig. 5 Projectile defeated by the target (VI = 660 m/s)
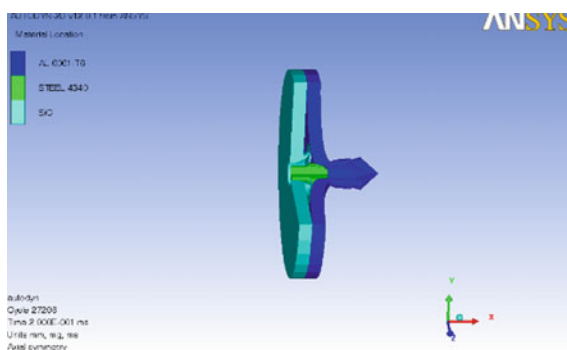
Fig. 6 Velocity history of projectile in *X*-direction (at VI = 660 m/s)
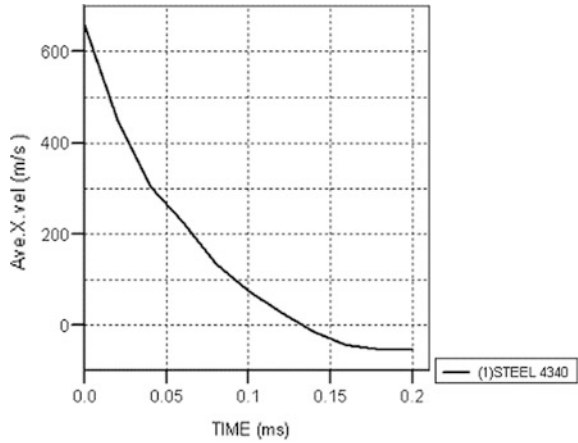
Fig. 7 Projectile perforated the target (VI = 670 m/s)
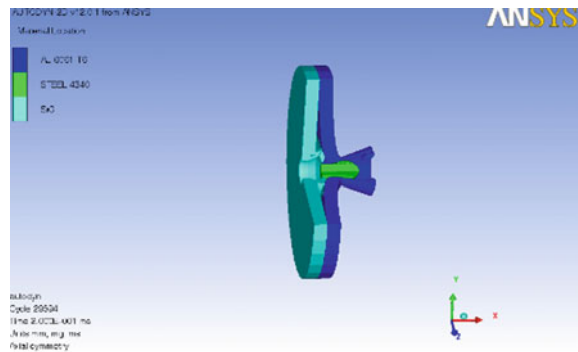
Table 5 Validation of Autodyn model

Initial velocity	Velocity at 200 μs		Remarks
	Literature	Present study	
660	0.00	0.00	Projectile defeated
670	80.00	56.4	Target perforated

5 Results and Discussions

In this chapter, results of the numerical study are analysed. Validation of the numerical model is given at the beginning [23, 8, 27, 12], followed by the responses of the ceramic/metal composite system. Result of parametric study is carried out the

Fig. 8 Velocity history of projectile in *X*-direction (at VI = 670 m/s)
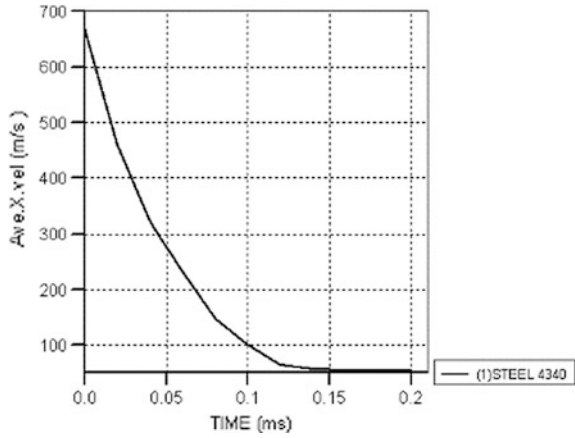
Fig. 9 Kinetic energy of projectile
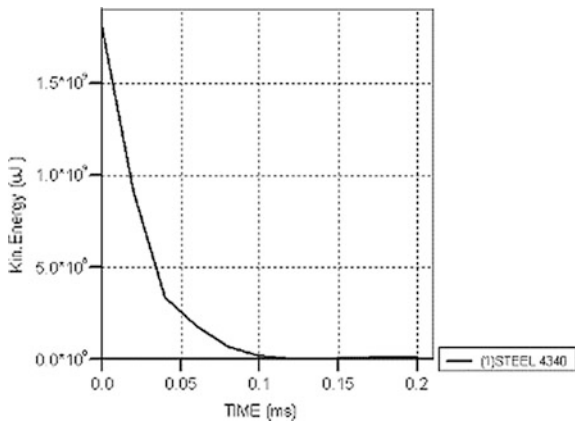
Fig. 10 Total energy of projectile

Fig. 11 Energy summery of projectile

best configuration and optimum thickness ratios for ($h1/h2 = 0.5, 0.6$ mm) [20, 21, 35]. Effect of the best thickness ratios for ceramic/metal composite system analysis of 3D model under high velocity impact.

5.1   Simulation of 3D Model Ceramic/Metal Composite Under High Velocity Impact

CASE 1 Plate thickness ratio ($h1/h2 = 0.5$)

Axisymmetric geometry of finite element (FE) model is shown in Fig. 12. Finite element mesh of this model is shown in Fig. 13. Front plate thickness is 4.23 mm [15, 36]and backplate thickness is 8.47 mm [21, 37] by a hard steel projectile. The impact velocity is considered as 715 m/s [25, 38].

It was found that the target gets defeated by the 7.62 AP [19, 25, 38, 35] projectile (velocity at 715 m/s) [13]. By stretching back surface in the circular region, fracture occurs and hence it causes in the front of the projectile a plug to be detached, which happened only because of tensile stress developed due to its large

Fig. 12 Axisymmetric geometry of FE model ($h1/h2 = 0.5$)
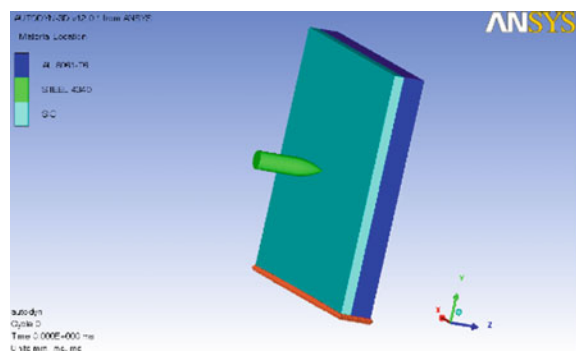
Fig. 13 Axisymmetric geometry of FE model (h1/h2 = 0.5)—Finite element mesh
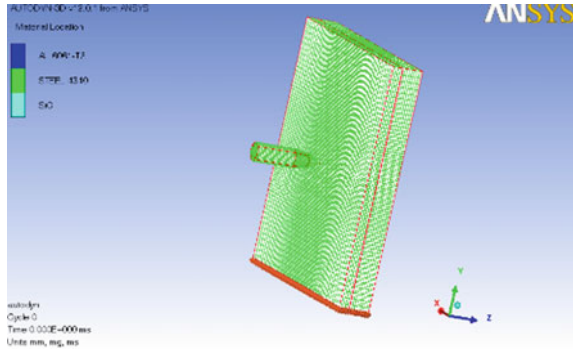
Fig. 14 Projectile defeated by the target (at VI = 715 m/s)
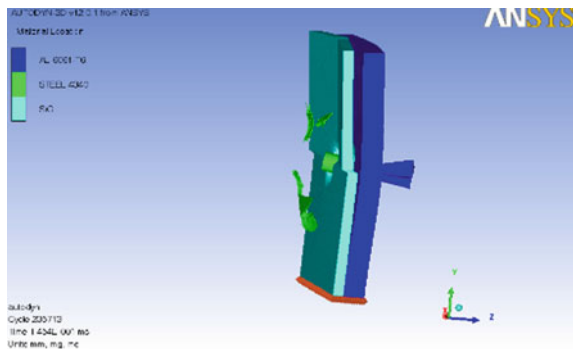
strains around the periphery of the projectile [17, 38, 29]. There is no significant bending of the backing plate is observed because of the force the projectile applies on the target is distributed over a quite small area of the metal plate [39, 10, 40]. In this configuration [41, 11, 42], the projectile can fully erode thin ceramic tile with experiencing less deceleration, such that it can defeat the target shown in Fig. 14. Residual velocities as 0 m/s [26, 23, 24], respectively, as shown in Fig. 15. Various energy histories, namely internal, kinetic are provided for the projectile in Figs. 17 and 18. Finally, summary of all energies is summarized in Fig. 19. Total mass of the projectile as shown in Fig. 16.

5.2 Simulated Results for 2D Model

Two-dimensional analysis of ceramic/metal composite targets different ratios for (h1/h2 = 0.3, 0.4, 0.5, 0.6, 0.7, 1.0) and different plate thickness. Analysis after getting the results for various parameter residual velocities, ballistic limit, remarks as shown in Table 6 (Figs. 20 and 21).

Fig. 15 Velocity history of
projectile in *Z*-direction
(at VI = 715 m/s)
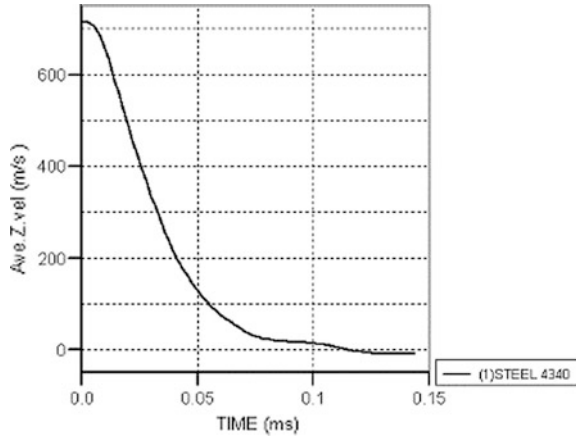
Fig. 16 Total mass of the
projectile
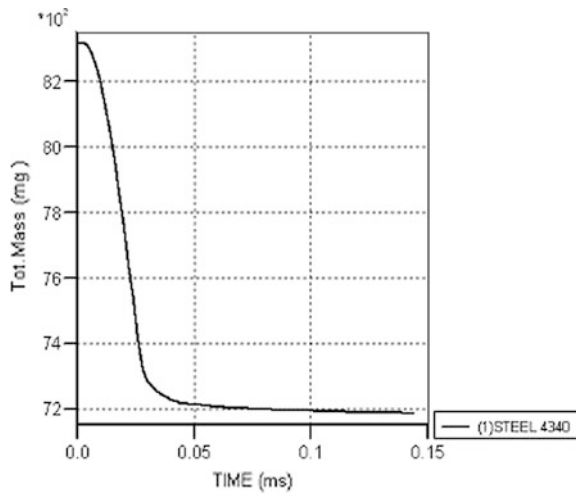
5.3   Comparison of 2D Model and 3D Model

The numerical simulations were performed using both 2D and 3D models. The
results from the 2D model were shown to compare well with that of the 3D model
as shown in Table 7.

Fig. 17 Internal energy of the projectile
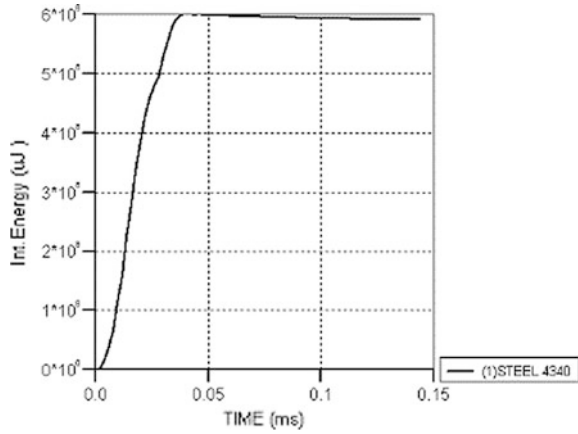
Fig. 18 Kinetic energy of the projectile
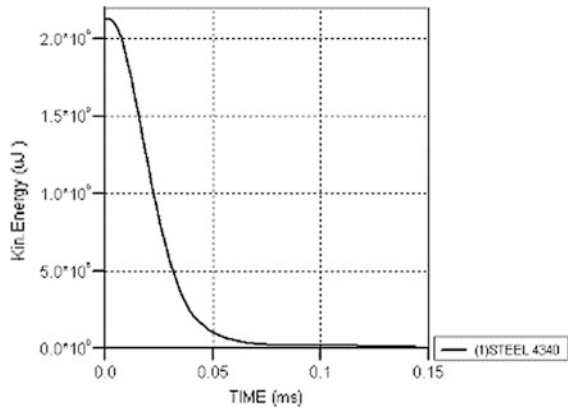
Fig. 19 Energy summary of the projectile
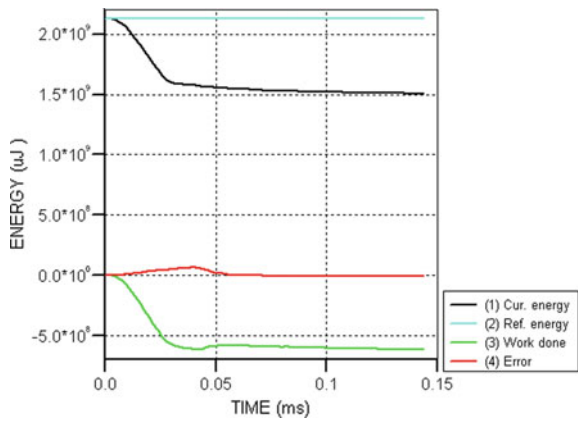
Table 6 Simulated results for 2D model

h1/h2 ratio (mm)	Initial velocity (m/s)	Residual velocity (m/s)	Remarks	Ballistic limit (m/s)
1.0	660	0	Projectile defeated	660
1.0	670	54.63	Projectile perforated	–
0.3	660	381.46	Projectile perforated	–
0.3	670	391.86	Projectile perforated	–
0.4	660	483.10	Projectile perforated	–
0.4	670	456.72	Projectile perforated	–
0.5	715	0	Projectile defeated	715
0.5	725	20.87	Projectile perforated	–
0.6	725	0	Projectile defeated	725
0.6	730	239	Projectile perforated	–
0.7	690	0	Projectile defeated	690
0.7	700	50.41	Projectile perforated	–
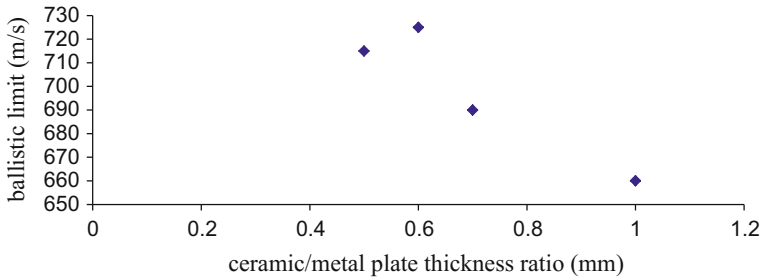
Fig. 20 Ballistic limit (m/s) versus Ceramic/metal plate thickness ratio (mm)
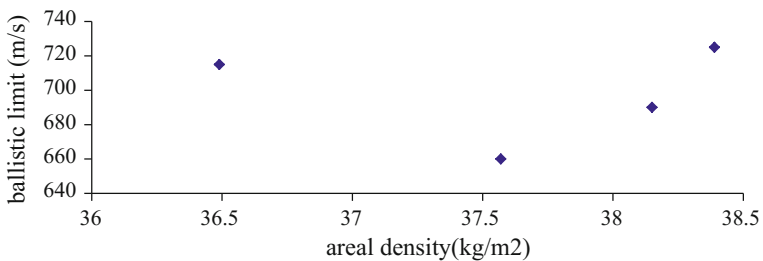
Fig. 21 Ballistic limit (m/s) versus Areal density (kg/m^2)

Table 7 Comparison of 2D and 3D model

h1/h2 ratio (mm)	Initial velocity (m/s)	Velocity at 200 μs		Remarks
		2D model	3D model	
0.5	715	0	0	Projectile defeated
0.6	725	0	0	Projectile defeated

6 Conclusion

The material models for ceramic materials and metals reported in the literature are critically reviewed [43, 36, 14]. It is found that the Johnson–Holmquist models JH-1 and JH-2 models are extensively used in numerical simulations. JHB material model is an improved model and more suitable to the computations [44, 16, 17]. The Johnson–Cook model is the most commonly used model for metals and experimental results reported in the literature are in close agreement with numerical results. In this report, numerical studies on high velocity impact on ceramic/metal targets are carried out [18, 2].

The numerical study using AUTODYN software simulated successfully, the experimental study reported in the literature. The FE model predicated the ballistic limit velocity 660 m/s as reported in the literature. However, the erosion model for material is included and the erosion criterion was kept based on the instantaneous geometric strain values. Maximum geometric strain for steel projectile was obtained based on various trails as 190% with which reported results were obtained and compared as well.

The ballistic productivity of fired/metal composite love framework against 7.62 AP and 8.32 g [19, 2, 21] steel shots has been explored by a numerical approach. The noteworthy wonders, for example, shot disintegrating, shot puncturing, vanquished, development of clay disappointment, are very much caught by Lagrange conspire. Simulation of the existence of optimum value of the front plate to back plate thickness for a given areal density. The ideal thickness for earthenware/metal composite framework proportion for estimations of ($h1/h2 = 0.5, 0.6$). In any case, ballistic execution of two-component composite levels indicates huge contrast. (0.5) proportions for level of ballistic point of confinement 8.333% and areal thickness 2.187% reductions, contrast with (0.6) proportions for level of ballistic farthest point 9.848% and areal thickness 2.182% increments. Correlation regarding areal thickness, in this way best arrangement of clay/metal thickness proportions for (0.5). It can be reasoned that the present re-enactment technique, which is perceptive than explore.

References

1. Wikipedia.org/wki/chobham-armour
2. Fawaz, Z., Zheng, R., Behdinan, K.: Numerical simulation of normal and oblique ballistic impact on ceramic composite armors. Compos. Struct. **63**, 387–395 (2003)
3. Nagappan, M., Vinoth Kanna, I: A novel technique and detailed analysis of cars in Indian roads to adopt low ground clearance. Int. J. Ambient Energy, 1–7 (2018)
4. AmarPrakash, J.: Influence of adhesive thickness on high velocity impact performance of ceramic/metal composite targets. Int. J. Adhes. Adhes. **41**, 186–197 (March 2013)
5. Holmquist, T.J., Johnson, G.R.: Characterisation and evaluation of silicon carbide for high-velocity impact. J. Appl. Phys. **31**, 113–127 (2005)

 6. Tytler, I.F.B., Thompson, N.H., Jones, B.E., Wormell, P.J.H., Ryley C.E.S.: Vehicles and Bridging. METU Library, UG446.5 V37 (1985)
 7. Johnson, G.R., Holmquist, T.J., Beissel, J.: Appl. Phys. **94**, 1639 (2003)
 8. Holmquist, T.J., Templeton, D.W.A.N.D., Bishoni, K.D.: Constitutive modeling of aluminum nitride for large strain, high strain rate and high pressure applications. Int. J. Impact Eng. **25**, 211–231 (2001)
 9. Subramani, K., Logesh, K., Kolappan, S., Karthik, S.: Experimental investigation on heat transfer characteristics of heat exchanger with bubble fin assistance. Int. J. Ambient Energy, 1–4 (2018)
10. Guden, M., Yildirim, U., Hall, I.W.: Effect of strain rate on the compression behavior of a woven glass fiber/SC-15 composite (2003)
11. Smith, P.D, Hetherington, J.G.: Blast and Ballistic Loading of Structures. Butterworth-Heinemann Ltd (1994)
12. Vinoth Kanna, I., Devaraj, A., Subramani, K.: Bio diesel production by using Jatropha: the fuel for future. Int. J. Ambient Energy, 1–7 (2018)
13. CIAR Homepage. www.ciar.org
14. Achenbach, J.D.: Wave Propagation in Elastic Solids. American Elsevier, New York (1975)
15. Florence, A.L.: Interaction of Projectiles and Composite Armor, Part II. Standford Research Institute, Menlo Park, California, AMMRC-CR-69-15 (1969)
16. Faik, S., Witteman, H.: Modeling of impact dynamics: a literature survey. In: International ADAMS User Conference (2000)
17. Goldsmith, W.: Impact. Edward Arnold Publishers, London (1960)
18. Science. how stuff works.com
19. Arias, A., Zaera, R.: Numerical modeling of the impact behaviour of new particulate-loaded composite materials. Compos. Struct. **61**, 151–159 (2003)
20. Goncalves, D.J., de Melo, F.C.L.: Analysis and investigation of ballistic impact on ceramic/metal composite armour. IJMATOOL **44**, 307–316 (2003)
21. Mahdi, S., Gillespie Jr., J.W.: Finite element analysis of tile-reinforced composite structural armor subjected to bending loads. Compos. B Eng. **35**, 57–71 (2004)
22. Vicente, S.G., Laura, S.P.: Analysis of failure of add-on armour for vehicle protection against ballistic impact. Int J. Impact Eng. **16**, 1837–1845 (2009)
23. Johnson, G.R., Holmquist, T.J.: A Computational Constitutive Model For Brittle Materials, pp. 1075–1081 (1992)
24. Johnson, G.R., Holmquist, T.J.: An improved computational constitutive model for brittle materials (1994)
25. Holmquist, T.J., Johnson, G.R.: Characterisation and Evaluation of Silicon Carbide for High-Velocity Impact, p. 97. JI, Appl. Phys. (2005)
26. AUTODYN, Century Dynamics, www.century-dynamics.com
27. Vinoth Kanna, I.: Optimisation of the evaporator of a refrigerator employing hydrocarbon as a refrigerant. Int. J. Ambient Energy, 1–8 (2018)
28. Vinoth Kanna, I., Paturu, P.: A study of hydrogen as an alternative fuel. Int. J. Ambient Energy, 1–4 (2018)
29. Vinoth kanna, I., Pinky, D.: Automatic seat level control using MEMS programmed with Lab VIEW. Int. J. Ambient Energy, 1–4 (2018)
30. Vinoth Kanna, I., Vasudevan, A, Subramani, K.: Internal combustion engine efficiency enhancer by using hydrogen. Int. J. Ambient Energy, 1–4 (2018)
31. Vinoth Kanna, I.: Modelling and thermal analysis of air-cooling system with fin pitch in IC engines. Int. J. Ambient Energy, 1–9 (2018)
32. Devaraj, A., Yuvarajan, D., Vinoth Kanna, I.: Study on the outcome of a cetane improver on the emission characteristics of a diesel engine. Int. J. Ambient Energy, 1–4 (2018)
33. Paturu, P., Vinoth kanna, I.: Experimental investigation of performance and emissions characteristics on single-cylinder direct-injection diesel engine with PSZ coating using radish biodiesel. Int. J. Ambient Energy, 1–10 (2018)

34. Vinoth Kanna, I., Pinky, D.: Investigation of the effects of exhaust and power loss in dual-fuel six-stroke engine with EGR technology. Int. J. Ambient Energy, 1–6 (2018)
35. Grujicic, M., Pandurangan, B., Zecevic, U., Koudela, K.L., Cheeseman, B.A.: Ballistic performance of alumina/S-2 glass-reinforced polymer-matrix composite hybrid lightweight armor against armor piercing (AP) and non-AP projectiles. Multidiscip. Model. Mater. Struct. **3**(3), 287–312 (2007)
36. Zhou, G., Reid, S.R.: Impact Behavior of Fiber-Reinforced Composite Materials and Structures. CRC (2000)
37. Aydınel, A., Yıldırım, R.O., Ögel, B.: Numerical and analytical investigations of Al_2O_3 ceramic-GFRP composite armor systems against 7.62 mm AP. USMOS, ODTÜ, Ankara (2005)
38. Bulent, R.J., Basaran, K.: Computational analysis of advanced composite armour systems. Int. J. Impact Eng. **25**, 211–231 (2007)
39. Ogorkiewicz, R.: Armored Fighting Vehicles (AFV). Seminar, UK (2006)
40. Silva, M.A.G, Cismasiu, C., Chiorean, C.G.: Numerical simulation of impact on composite laminates (2003)
41. Wang, B., Chou, S.M.: The behavior of laminated composite plates As armor. J. Mater. Process. Technol. **68**(3), 279–287 (1997)
42. Zukas, J.A., Nicholas, T., Swift, H.F., Greszczuk, L.B., Curran, D.: Impact Dynamics. Wiley (1982)
43. Zouheir, F., Kamran, B., Yigui, X.: Optimum design of two-component composite armors against high-speed impact. Compos. Struct. **73**(3), 253–262 (2006)
44. Sung, H.A., Woo, K.J., Hee, J.K.: Development trends of ceramic composite armors for combat vehicles. J. Korean Soc. Precis. Eng. **22**(7) (2005)
45. Zaera, R.: Modeling of the adhesive layer in mixed ceramic/metal armours subjected to impact. Compos. A **31**, 823–833 (2000)
46. Lee, M., Yoo, Y.H.: Analysis of ceramic/metal armour systems. Int. JI. Impact Eng. **25**, 819–829 (2001)
47. Yen, C.F.: Ballistic impact modeling of composite materials. In: 7th International autodyne, Users Conference (2002)

Study of Future Refrigerant for Vapor Compression Refrigeration Systems

I. Vinoth kanna and **K. Subramani**

1 Introduction

In the early days, natural refrigerants were used, but there was little to no safety regulations so systems ended up using very dangerous refrigerants. Some were highly flammable, and some were even toxic. Soon scientists realized the markets need for better and safer refrigerants [1, 2].

Then, in the 1930s they developed CFCs, which were scientifically tested and were safer to use. They were nonflammable, nontoxic, and a non-corroding gas, which was cheap to produce, so they seemed ideal [3, 4]. However, in the 1970s they realized that the chlorine molecules within these were completely destroying our ozone layer and were banned.

In the late 1970s and early 1980s, experts developed HCFCs which had far less damaging effects on the ozone; however, HCFCs were still able to damage the ozone layer because they contained chlorine molecules [5].

To solve the issue of ozone destruction, scientists came up with HFCs, which did not contain chlorine; this meant they would not destroy the ozone layer [6, 7]. However, they later realized HFCs still damage the environment because they are greenhouse gases and so these are beginning to be phased out also.

I. Vinoth kanna (✉) · K. Subramani
Department of Mechanical Engineering, Vel Tech Rangarajan
Dr. Sagunthala R&D Institute of Science and Technology, Chennai, India
e-mail: vinothkanna.research@gmail.com

2   Ozone Layer Depletion

The ozone-depleting chemicals rise up into the stratosphere, and the chemicals are swept into the winds of the polar vortex, which is a ring of fast-moving air that circles the South Pole, and the chemicals have been building up here since CFC refrigerants first started being used [8].

This buildup in the South Pole has been destroying the ozone layer by burning a hole through it [9, 10]. The laws and regulations on the use of chemicals in refrigerants have been increasingly tightened over the years and as this continues, the plant will have time to repair this hole. Let us just briefly learn why and how this has been burning a hole in our ozone layer [11].

In our planet first, we have the troposphere, and then, we have the stratosphere [12, 13]. The ozone layer exists within the stratosphere. The ozone layer protects us from the suns UV rays that are very harmful and cause cancer.

Within the ozone layer, we have the ozone molecule, which has three oxygen atoms; these absorb the UV rays [14]. The CFC molecules rise up into the stratosphere, and the UV rays cause the chlorine atoms to break off [15, 16].

This separation of the chlorine atom causes a chemical reaction, resulting in the chlorine atom stealing an oxygen atom from the ozone molecule [7, 17]. This creates a chlorine monoxide molecule and a separate oxygen molecule. The ozone layer is unable to support these new molecules and so a gap is formed in the stratosphere [6, 12, 18]. The bigger the hole gets, the more UV rays will be able to reach us.

3   Global Warming Potential

The other problem with the refrigerants is their global warming potential (GWP) [3, 6, 10, 12, 14, 19–21]. If the infrared rays pass through our atmosphere, it will hit the earth surface and most are rebounded back into space with a few rebounding and staying within the atmosphere [14].

Scientists since discovered that many of the chemicals in the refrigerants prevented infrared rays from pass through them, so as they build up in the atmosphere they prevent the rays from leaving which causes heat treatment and this is leading to climate change. Although there are many contributors to this and many are man-made [8].

4   History of Refrigerants

Refrigerants have been introduced since the 1800s, a variety of changes made by the scientist in order to meet required GWP and ODP [22, 23]. Figure 1 shows the periodic changes of refrigerant in history.
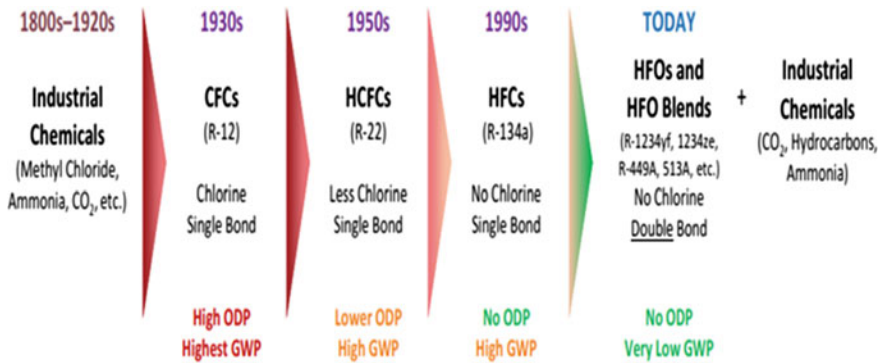
Fig. 1 History of refrigerants

Selection of refrigerants for the future will need to balance performance (capacity and efficiency), safety and sustainability, and total cost of system ownership [24].

5 Industrial Gases as Refrigerants

Industrial gases were introduced in the year 1800, and it has been used up to the year 1920 [25].

- Not new, some of the earliest refrigerants.
- Used currently where they make sense (safety and efficiency concerns).
- Rebranding as "natural" products, but:
  - The so-called natural refrigerants are actually industrial gases produced in large chemical processing facilities [26, 27].
  - These facilities use energy to create or isolate, purify CO_2, hydrocarbons, and ammonia [26, 28].
  - They also use feedstocks and generate wastes similar to other chemical manufacturing processes [27, 29].

6 Hydrocarbon Manufacture

Hydrocarbons are produced in an oil refinery or natural gas processing plant [2, 9]. There are several process steps to produce high purity refrigerants such as propane and isobutane. Figure 2 shows the details of natural gas production steps.
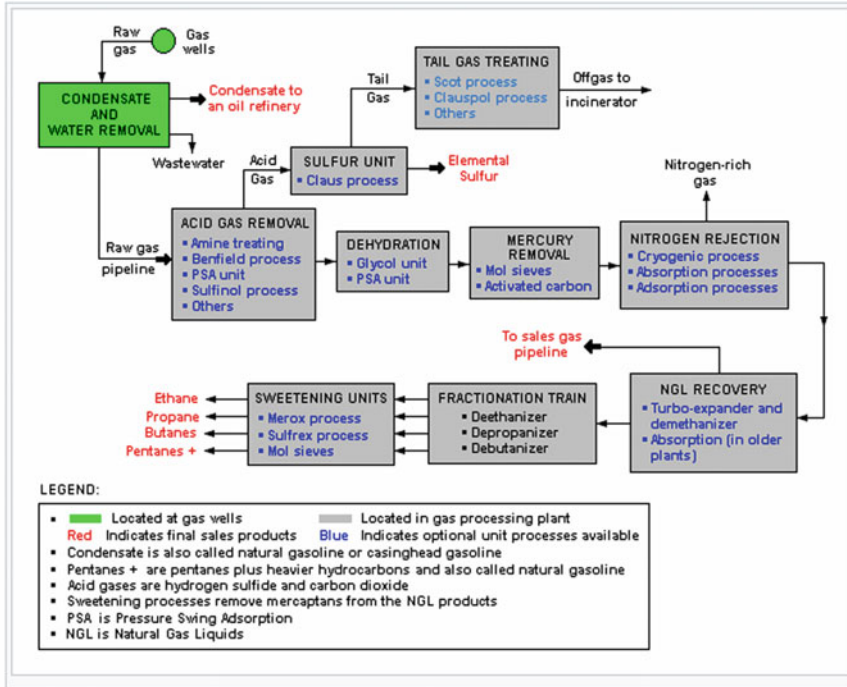
Fig. 2 Natural gas process steps

6.1 Example Processing Steps

- Condensate and water removal,
- Mercury removal,
- Nitrogen removal,
- Natural gas liquid recovery,
- Fractionation,
- and Sweetening purification units

7 Ammonia Manufacture

Ammonia is primarily produced by the reaction of nitrogen with hydrogen. However, there are several steps preceding this, starting with natural gas feedstock (Fig. 3):
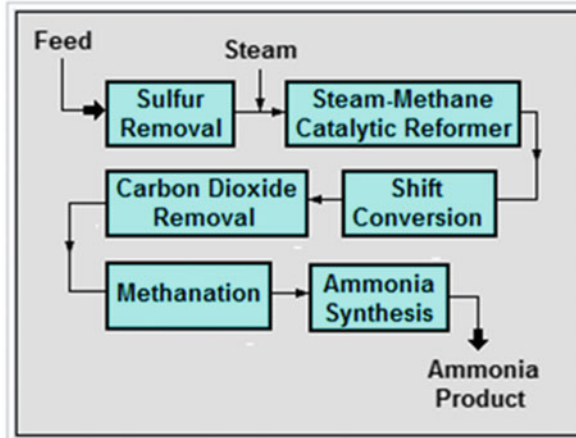
Fig. 3 Block flow diagram of the ammonia synthesis process
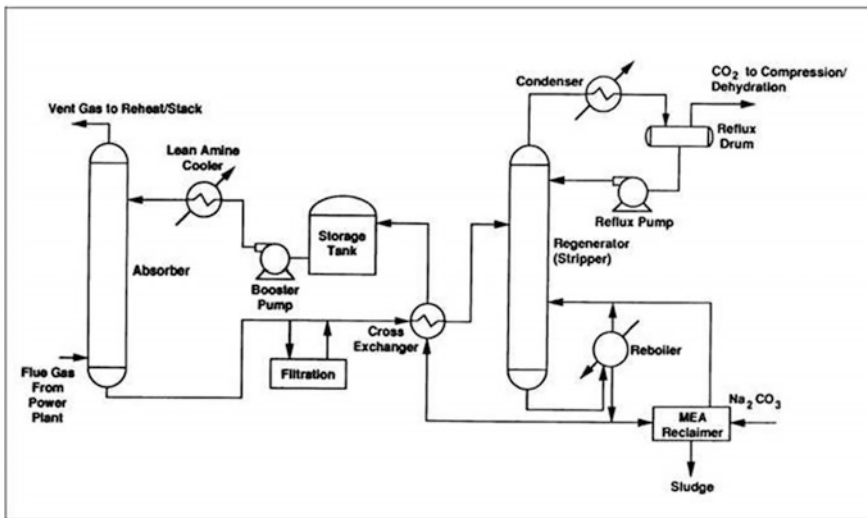
Fig. 4 Schematic diagram of the amine separation process

- Sulfur removal from natural gas feedstock:

$$H_2 + RSH \rightarrow RH + H_2S \ (gas)$$

- Hydrogen sulfide absorption through beds of zinc oxide:

$$H_2S + ZnO \rightarrow ZnS + H_2O$$
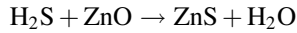
- Catalytic steam reforming to form hydrogen plus carbon monoxide:

$$CH_4 + H_2O \rightarrow CO + 3H_2$$
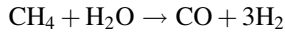
- Catalytic shift conversion to carbon dioxide and more hydrogen:

$$CO + H_2O \rightarrow CO_2 + H_2$$
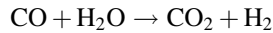
- Carbon dioxide is then removed by absorption.
- Catalytic methanation to remove small amounts of CO and CO_2

$$CO + 3H_2 \rightarrow CH_4 + H_2O$$
$$CO_2 + 4H_2 \rightarrow CH_4 + 2H_2O$$
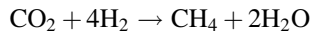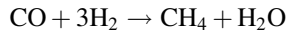
- Hydrogen is then catalytically reacted with nitrogen to form anhydrous liquid ammonia and purified

$$3H_2 + N_2 \rightarrow 2NH_3$$
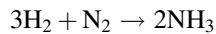
8 CO_2 Manufacture

CO_2 is primarily produced (Fig. 5) by:

- Combustion of fossil fuel (e.g., coal, oil, and gas)
- Separation of the CO_2 from the combustion product stream (e.g., flue gas—Fig. 4)
- Several purification steps

9 Future Refrigerant

9.1 Evaluation of Working Fluids in Refrigeration Systems

In general, we have a plenty of refrigerants in the universe, but we cannot use all as refrigerants in refrigerator, it should satisfy the following phenomenon [7, 13, 21].

Measurable data and objective chemical, physical, thermodynamic and environmental properties [4, 17].
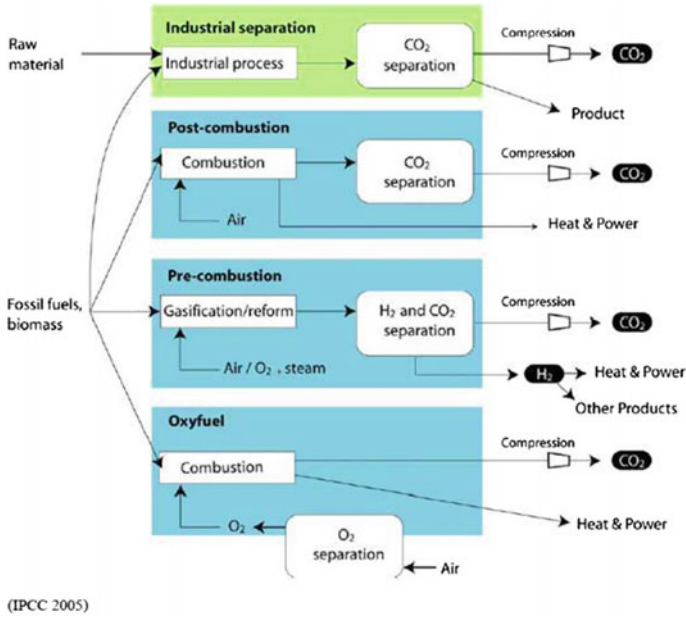
Fig. 5 CO_2 production options

Standard and reproducible engineering principles, measurements and testing [20, 23, 26].
For example:

- Boiling point,
- Vapor pressure,
- Heat capacity,
- Ozone depletion potential,
- Atmospheric lifetime,
- Global warming potential,
- Toxicity (acute, chronic, etc.),
- Flammability (LFL, UFL, and burning velocity) [3, 30],
- Heat of combustion [6, 18, 28],
- and Energy efficiency [7, 10, 16]

Table 1 Designing a low GWP molecule

Molecule	Structure	Atmospheric lifetime	GWP	Status
PFC-116	CF3–CF3 No hydrogen	10,000 years	11,100	No long used
HFC-134a	CH2F–CF3 2-H atoms	13 years	1300	Current refrigerator runs by using "HFC-134a" as a refrigerant
HFO-1234yf	CH2=CF– CF3 "Olefin"	10 days	<1	Future refrigerant to replace HFC-134a.

9.2 Exact Meaning of Global Warming Potential (GWP)

GWP = Atmospheric Lifetime $\times$ Infrared Absorbance [5, 6, 23, 24]
    Atmospheric Life $\rightarrow$ rates of destruction reactions (hydroxyl radical) (Table 1)

$$HFC = \frac{[OH-]}{k}$$

9.3 Designing a Low GWP Molecule

HFC (Fig. 6a) has only single bond whereas double bond in HFOs (Fig. 6b) quicker breakdown in the atmosphere, yet stable in systems [18] (Table 2).

9.4 Comparison of HFC Versus HFO

- Same operating conditions as 134a (similar P/T curve) (Graph 1 and Table 3).
- Capacity and efficiency is similar to HFC-134a.
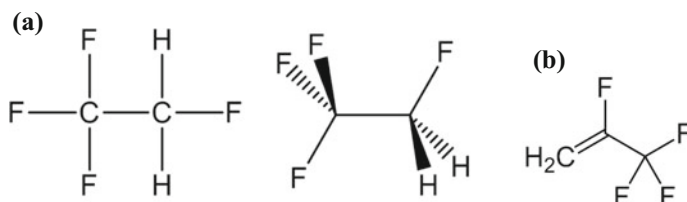
Fig. 6 a HFC, **b** HFO

Table 2 HFC versus HFO

	HFC-R 134a	HFO-R 1234yf
Formula	CH2FCF3	CF3CF=CH2
Molecular weight	102	114
ODP	0	0
GWP100 (ARS)	1300	<1
T, Critical point	102 °C	95 °C
Boiling point	−26 °C	−29 °C

Graph 1 P/T curve for R 134a and R 1234yf
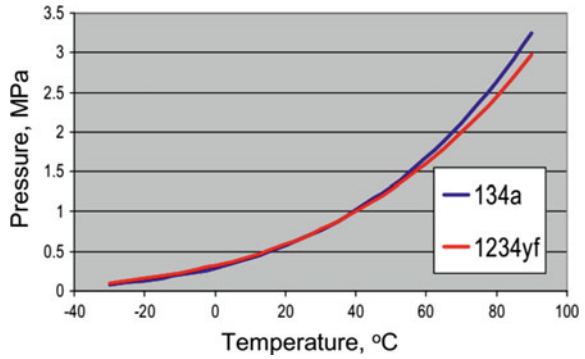
Table 3 Refrigerant flammability classification

Highly flammable	3	Propane, Isobutane
Moderately flammable	2	R-152a
Mildly flammable	2L	R-1234yf, R-452B
Nonflammable	1	R-134a, R-410A

9.5 Refrigerant Flammability Classifications

To meet 2L flammability, burning velocity must be ≤ 10 cm/s [4, 7, 16, 28].

9.6 Primary Flammability Parameters

Parameter	Risk Trend
Lower LFL	⬆
Larger (UFL − LFL)	⬆
Lower MIE	⬆
Higher UFL	⬆
Higher HOC	⬆

- **Lower/Upper Flammability Limits (LFL/UFL)**
  Minimum/maximum concentrations of a substance in air that exhibit flame propagation (usually shown as volume percentage in air) [3, 4, 30].
- **Minimum Ignition Energy (MIE)**
  Minimum energy required to ignite a flammable gas/air mixture. Sources with energy levels below this value will not result in an ignition [17, 18, 28].
- **Burning Velocity (BV)**
  Burning velocity is the velocity of a laminar flame under given values of composition, temperature, and pressure of a refrigerant [1, 13, 27].
- **Heat of Combustion (HOC)**
  While combustion, the amount of heat released per unit mass (or mole) of a substance is called Heat of Combustion [15, 19, 22].

9.7 Flammable Property Comparison

See Table 4.

10 Optimizing for the Future

Following balanced properties are needed to introduce a new refrigerant in the global market [3] (Fig. 7)

- Zero ODP
- Low GWP

Table 4 Flammable property comparison

	R-290 (Propane)	R-152a	R-717 (Ammonia)	R-1234yf
Safety rating	A3	A2	B2L	A2L
LFL (vol. %)	2.2	3.9	15.0	6.2
UFL (vol. %)	10.0	16.9	28.0	12.3
UFL – LFL (vol. %)	7.8	13.0	13.0	6.1
MIE (mJ)	0.25	0.38	100–300	>5000
BV (cm/s)	46	23	7.2	1.5
HOC (kJ/g)	46.3	16.5	18.6	10.7
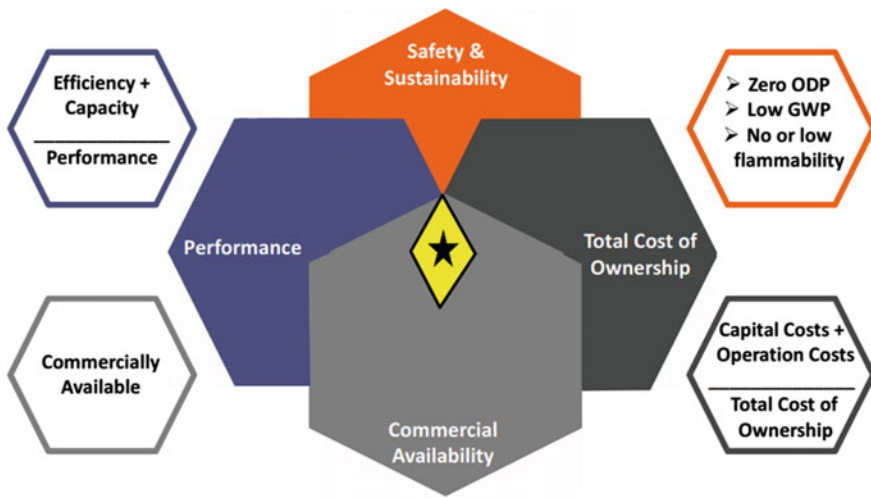
Fig. 7 Optimal balance properties [2, 6, 7, 30]

- No or low flammability
- Total cost of ownership
- Commercially available
- Performance
- Safety and sustainability

11   Low GWP HFO Products for Refrigeration
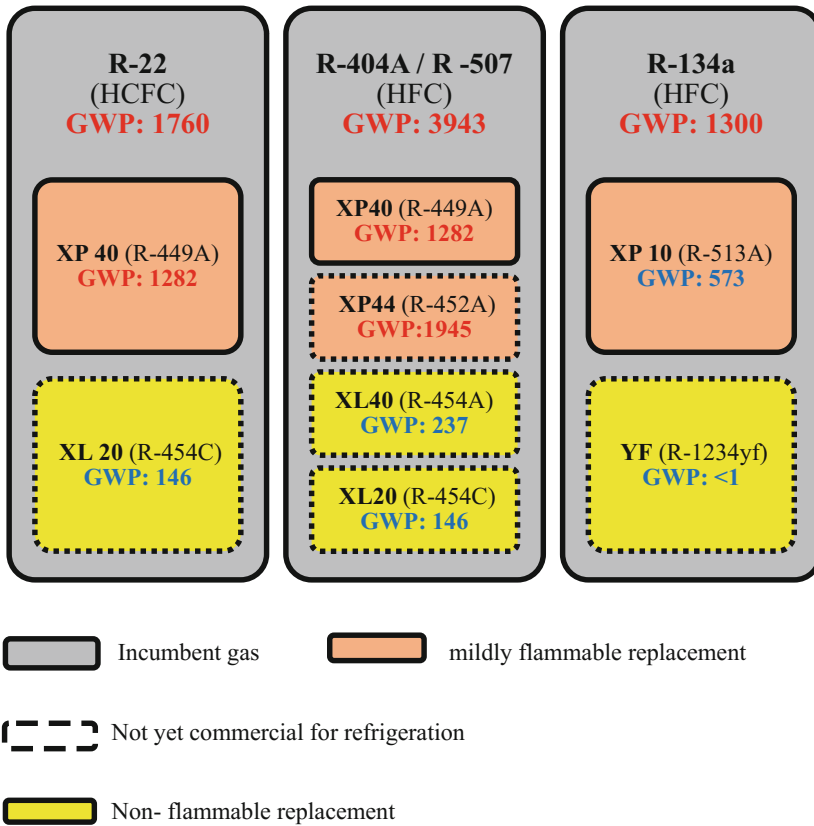
12   Conclusion

Refrigerants are greenhouse gases that contribute to global warming and many environmental metrics. Hence, a substitution is very much needed. Our motivation is to find substitute for refrigerant thereby reducing environmental problem like ozone depletion, GWP. In addition, hereby we conclude that R1234yf as a refrigerant for future refrigerator to meet our needs.

References

1. Vinoth Kanna, I.: Optimisation of the evaporator of a refrigerator employing hydrocarbon as a refrigerant. Int. J. Ambient Energy, 1–8 (2018)
2. Gill, J., Singh, J.: Energy analysis of vapor compression refrigeration system using mixture of R134a and LPG as refrigerant. Int. J. Refrig. **84**, 287–299 (2017)
3. Chapter 3: Refrigerants—SciTech Connect. Elsevier. http://scitechconnect.elsevier.com/wp-content/uploads/2016/05/main-15
4. Bayrakçi, H.C., Özgür, A.E.: Energy and exergy analysis of vapor compression refrigeration system using pure hydrocarbon refrigerants. Int. J. Energy Res. **33**(12), 1070–1075 (2009)
5. Du, K., Calautit, J., Wang, Z., Wu, Y., Liu, H.: A review of the applications of phase change materials in cooling, heating and power generation in different temperature ranges. Appl. Energy **220**, 242–273 (2018). Online publication date: 1-June-2018
6. Devaraj, A., Yuvarajan, D., Vinoth Kanna, I.: Study on the outcome of a cetane improver on the emission characteristics of a diesel engine. Int. J. Ambient Energy, 1–4 (2018)
7. Punia, S.S., Singh, J.: An experimental study of the flow of LPG as refrigerant inside an adiabatic helical coiled capillary tube in vapour compression refrigeration system. Heat Mass Transf. **51**(11), 1571–1577 (2015)
8. Ecosystem—Encyclopedia of earth: www.eoearth.org
9. Vinoth Kanna, I., Devaraj, A., Subramani, K.: Bio diesel production by using Jatropha: the fuel for future. Int. J. Ambient Energy, 1–7 (2018)
10. Vinoth Kanna, I.: Modelling and thermal analysis of air-cooling system with fin pitch in IC engines. Int. J. Ambient Energy, 1–9 (2018)
11. Imperial Brown—home: sp.imperialmfg.info
12. Vinoth Kanna, I., Paturu, P.: A study of hydrogen as an alternative fuel. Int. J. Ambient Energy, 1–4 (2018)
13. HONGO, K.: Air conditioning and refrigeration systems by water vapor compression: refrigeration systems utilizing a water refrigerant turbo-refrigerator. In: Proceedings of Conference of Kanto Branch 2002.8(0), pp 123–124 (2002)
14. Chopra, K., Sahni, V., Mishra, R.S.: Thermodynamic analyses of multiple evaporators vapor compression refrigeration systems with R410A, R290, R1234YF, R502, R404A, R152A and R134A. Int. J. Air-Cond. Ref. **22**, 1450003 (2014)
15. Vinoth Kanna, I., Vasudevan, A., Subramani, K.: Internal combustion engine efficiency enhancer by using hydrogen. Int. J. Ambient Energy, 1–4 (2018)
16. Kılıç, B.: Exergy analysis of vapor compression refrigeration cycle with two-stage and intercooler. Heat Mass Transfer **48**(7), 1207–1217 (2012)
17. Bair, S., Baker, M., Pallister, D.M.: The high-pressure viscosity of refrigerant/oil systems. Lubr. Sci. **29**(6), 377–394 (2017)
18. Brown, J.S., Zilio, C., Cavallini, A.: The fluorinated olefin R-1234ze (Z) as a high-temperature heat pumping refrigerant. Int. J. Refrig. **32**(6), 1412–1422 (2009)
19. Gill, J., Singh, J.: Use of artificial neural network approach for depicting mass flow rate of R134a/LPG refrigerant through straight and helical coiled adiabatic capillary tubes of vapor compression refrigeration system. Int. J. Refrig. **86**, 228–238 (2018)
20. Hermes, C.J.L.: Refrigerant charge reduction in vapor compression refrigeration cycles via liquid-to-suction heat exchange. Int. J. Refrig. **52**, 93–99 (2015)
21. Mbarek, W.H., Tahar, K., Ammar, B.B.: Energy efficiencies of three configurations of two-stage vapor compression refrigeration systems. Arab. J. Sci. Eng. **41**(7), 2465–2477 (2016)
22. Paturu, P., Vinoth kanna, I.: Experimental investigation of performance and emissions characteristics on single-cylinder direct-injection diesel engine with PSZ coating using radish biodiesel. Int. J. Ambient Energy, 1–10 (2018)

23. Colorado, D., Rivera, W.: Performance comparison between a conventional vapor compression and compression-absorption single-stage and double-stage systems used for refrigeration. Appl. Therm. Eng. **87**, 273–285 (2015)
24. A. Kitanovski: Present and future caloric refrigeration and heat-pump technologies. Int. J. Refrig. **57**, 288–298 (Sept 2015)
25. A Future Refrigerant—Aranca: http://context.aranca.com/hubfs/Aranca_Reports/CO2-As-A-Future-Refrigerant
26. Nagappan, M., Vinoth Kanna, I.: A novel technique and detailed analysis of cars in Indian roads to adopt low ground clearance. Int. J. Ambient Energy, 1–7 (2018)
27. Vinoth kanna, I., Pinky, D.: Automatic seat level control using MEMS programmed with Lab VIEW. Int. J. Ambient Energy, 1–4 (2018)
28. Vinoth Kanna, I., Pinky, D.: Investigation of the effects of exhaust and power loss in dual-fuel six-stroke engine with EGR technology. Int. J. Ambient Energy, 1–6 (2018)
29. Qureshi, B.A., Zubair, S.M.: The effect of refrigerant combinations on performance of a vapor compression refrigeration system with dedicated mechanical sub-cooling. Int. J. Refrig **35**(1), 47–57 (2012)
30. Gill, J., Singh, J.: Component-wise exergy and energy analysis of vapor compression refrigeration system using mixture of R134a and LPG as refrigerant. Heat Mass Transf. **54**(5), 1367–1380 (2018)

Numerical Simulation of Viscous Flow Past Elliptic Cylinder

Ranjith Maniyeri

1 Introduction

A study on steady and viscous fluid flow over stationary cylinder has got significant attention in fluid mechanics over long years. Most of the research works were devoted to circular and square cylinder, and only limited study were reported for elliptic cylinder [1–4]. Elliptical cylinders are best models for heat exchanger fitted with elliptical tubes, airfoils, blades, etc. Further, flow over cylinder is a fluid–structure interaction (FSI) problem which is of fundamental and research interest in computational fluid dynamics (CFD). FSI problems can be effectively handled by immersed boundary (IB) method. The origin of IB method was devoted to Charles Peskin [5, 6]. Recently, many versions of IB methods were developed by researchers which can simulate both rigid and deforming structures interacting with fluid flow. In the present paper, an improved version of IB method developed by Shin et al. [7] is used to demonstrate viscous fluid flow behavior over a stationary elliptic cylinder for fixed aspect ratio for a range of Reynolds number varying from 10 to 80. Here, the elliptic cylinder is modeled as an IB, and the viscous fluid flow is labeled by continuity and momentum equations. The streamline pattern near the cylinder is identified for different Reynolds numbers. Further, through numerical simulations, steady-state values of average drag coefficients are calculated.

R. Maniyeri (✉)
Department of Mechanical Engineering, National Institute of Technology
Karnataka (NITK), Surathkal, Mangalore 575025, Karnataka, India
e-mail: mranji1@nitk.edu.in

2 Numerical Strategy

In this paper, dimensionless Navier–Stokes and continuity equations are used which is given by

$$\left(\frac{\partial \mathbf{u}}{\partial t} + \mathbf{u} \cdot \nabla \mathbf{u}\right) = -\nabla p + \frac{1}{Re}\nabla^2 \mathbf{u} + \mathbf{f}(x, t) \tag{1}$$

where $\mathbf{u}$ is the fluid velocity, p is the fluid pressure, and $\mathbf{f}$ is the force used to impose no-slip condition on the elliptic cylinder termed as Eulerian force density.

$$\nabla \cdot \mathbf{u} = 0 \tag{2}$$

The force $\mathbf{f}$ acts on the fluid and can be computed as below

$$\mathbf{f}(x, t) = \int \mathbf{F}(s, t)\,\delta(x - X(s, t))\mathrm{d}s \tag{3}$$

where $\mathbf{F}$ is the force exerted by the fluid on the elliptic cylinder designated as Lagrangian force density. The Lagrangian force $\mathbf{F}$ is calculated using the feedback forcing method of virtual boundary method explained in [7] which is described as

$$\mathbf{F}(s, t) = \alpha \int_0^t (\mathbf{U}_b - \mathbf{U})\mathrm{d}t + \beta(\mathbf{U}_b - \mathbf{U}) \tag{4}$$

where α and β are the feedback forcing coefficients. The velocity of an IB point on the elliptic cylinder is determined as below

$$\mathbf{U}_b(s, t) = \int \mathbf{u}(x, t)\,\delta(\mathbf{x} - \mathbf{X}(s, t))\mathrm{d}x \tag{5}$$

where $\delta(x)$ is Peskin's regularized Dirac delta function given by,

$$\delta(\mathbf{x}) = \frac{1}{h^2}\emptyset\left(\frac{x_k - x_i}{h}\right)\emptyset\left(\frac{y_k - y_i}{h}\right) \tag{6}$$

where (x_k, y_k) and (x_i, y_i) are Lagrangian and Eulerian coordinates. The present work employed the below Dirac delta function [6–9],

$$\emptyset(r) = \begin{cases} \frac{1}{8}\left(3 - 2|r| + \sqrt{1 + 4|r| - 4r^2}\right), & 0 \le |r| < 1 \\ \frac{1}{8}\left(5 - 2|r| + \sqrt{1 + 4|r| - 4r^2}\right), & 1 \le |r| < 2 \\ 0, & 2 \le |r| \end{cases} \tag{7}$$

Here, the discretization is performed on a Cartesian grid system with staggered grid arrangements [9]. Further, finite volume method is utilized to obtain the discretized form of Eqs. (1) and (2) by incorporating fractional-step scheme [10]. Successive over-relaxation (SOR) scheme is used to obtain the velocities, whereas incomplete Cholesky conjugate gradient (ICCG) is used as the pressure solver.

3 Results and Discussion

In the present study, a two-dimensional numerical model is built using Fortran in which an elliptical cylinder at rest in a viscous uniform fluid flow domain of 50×30 is considered. The elliptic cylinder with aspect ratio (ratio of length of minor axis to major axis) 0.5 is considered at the center of the domain. Here, nonuniform grid system is used everywhere except near and inside the elliptic cylinder. Numerical simulations are performed for different Reynolds number, $Re = 10, 30, 40, 60$, and 80. The length of major axis of the ellipse is taken as the characteristic length for defining the Reynolds number. The feedback forcing coefficients chosen for present work are $\alpha = -4000.0$, $\beta = -40.0$, and the time step is $\Delta t = 0.01$. The advantage of present IB method over Peskin's IB method [6] is that higher time step can be selected in this scheme.

Through the developed numerical model, first of all streamline pattern exhibiting phenomena of fluid–structure interaction is well captured. Figure 1 shows the streamlines for five different values of Reynolds numbers ($Re = 10, 30, 40, 60$, and 80). The streamlines are plotted when the flow became fully developed and steady state. First of all, it is clear from all the cases that no-slip boundary condition is well satisfied on the surface of the cylinder which is implemented through the IB formulation employed. Again, for $Re = 10$, there is no recirculation observed behind the cylinder. But, from $Re = 30$ to 80, vortices are formed behind the cylinder which are in pair one above and one below about the centerline of the elliptic cylinder along the major axis. It can be seen that, in all the cases of Re considered, a pair of stationary recirculating vortices is formed behind the cylinder.

It is known from available research works [11, 12] and the previous work of the present author [13] that for circular cylinder under the same flow and geometric conditions, for $Re \geq 45$, unsteadiness arises spontaneously with vortex shedding behind the cylinder. But, in the present work for the case of elliptic cylinder even up to $Re = 80$, unsteadiness does not appear. This is primarily due to the effect of low aspect ratio (0.5) compared to 1.0 for the cylinder under the same flow conditions. Hence, it can be mentioned that elliptic cylinders offer less flow resistance than circular cylinders.

Here, drag forces are computed from the values of momentum forcing as explained in [8]. Using the drag forces, average values of drag coefficients are calculated for each Reynolds numbers and tabulated in Table 1. It is then compared for the cases of $Re = 10$ and $Re = 40$ with that of Sivakumar et al. [4] and Sen et al. [14]. The values of drag coefficients for other values of Re is not available in the
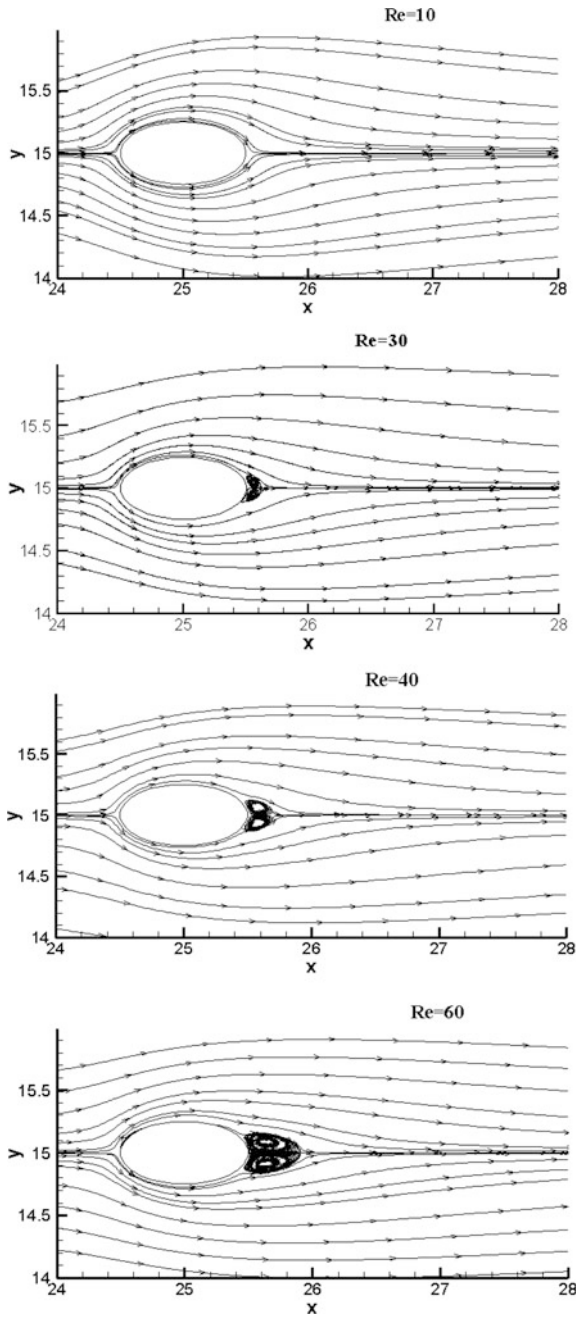
Fig. 1 Streamline pattern for different Reynolds number
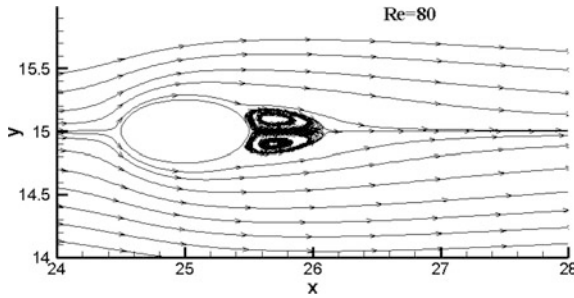
Fig. 1 (continued)

Table 1 Comparison of average drag coefficient

Reynolds number (*Re*)	Present	Sivakumar et al. [4]	Sen et al. [14]
10	2.262	2.1238	2.1305
30	1.254	–	–
40	1.087	1.0314	1.0328
60	0.894	–	–
80	0.782	–	–

literature. From Table 1, it is evident that the present values of average drag coefficient and those of Sivakumar et al. [4] and Sen et al. [14] are in reasonable agreement. This shows the validity of the proposed numerical model.

4 Conclusion

Uniform viscous flow past an elliptical cylinder at rest is investigated using an improved version of immersed boundary method on a finite volume framework. A numerical model is built in which the elliptic cylinder is constructed using Lagrangian coordinates, and fluid flow is described using Eulerian coordinates. The variables in these two coordinates are interconnected using a regularized Dirac delta function. The Navier–Stokes and continuous equations characterizing the fluid dynamics are solved using a fractional-step method. Using the computational model, numerical simulations are done for Reynolds numbers ranging from 10 to 80 for a fixed aspect ratio of the elliptic cylinder. The steady-state streamline patterns are observed using the numerical model. The average values of drag coefficients are calculated and verified with those of other available literature results to prove the accuracy of the developed scheme. It is believed that the developed numerical scheme and the obtained results will be highly helpful for understanding the fluid dynamic behavior of elliptical-shaped objects in a uniform flow under low Reynolds number conditions.

References

1. Mittal, R., Balachandar, S.: Direct Numerical Simulation of flow past elliptic cylinders. J. Comput. Phys. **124**, 351–367 (1996)
2. Shintani, K., Umemura, A., Takano.: A low-Reynolds-number flow past an elliptic cylinder. J. Fluid. Mech. **136**, 277–289 (1983)
3. Faruquee, Z., Ting, D.S.-K., Fartaj, A., Barron, R.M., Carriveau, R.: The effects of axis ratio on laminar fluid flow around an elliptic cylinder. Int. J. Heat Fluid Flow **28**, 1178–1189 (2007)
4. Sivakumar, P., Bharti, R.P., Chhabra, R.P.: Steady flow of power-law fluids across an unconfined elliptic cylinder. Chem. Eng. Sci. **62**, 1682–1702 (2007)
5. Peskin, C.S.: Numerical analysis of blood flow in the heart. J. Comput. Phys. **25**, 221–249 (1997)
6. Peskin, C.S.: Immersed boundary method. Acta Numer. **11**, 1–39 (2002)
7. Shin, S.J., Huang, W.-H., Sung, H.J.: Assessment of regularized delta functions and feedback forcing schemes for an immersed boundary method. Int. J. Numer. Meth. Fluids **58**, 263–286 (2008)
8. Lai, M.C., Peskin, C.S.: An immersed boundary with formal second-order accuracy and reduced numerical viscosity. J. Comput. Phys. **160**, 705–719 (2000)
9. Maniyeri, R., Kang, S.: Numerical study on the rotation of an elastic rod in a viscous fluid using an immersed boundary method. J. Mech. Sci. Technol. **26**, 1515–1522 (2012)
10. Kim, J., Kim, D., Choi, H.: An immersed boundary finite volume method for simulations of flow in complex geometries. J. Comput. Phys. **25**, 132–150 (2001)
11. Fornberg, B.: A numerical study of steady viscous flow past a circular cylinder. J. Fluid Mech. **98**, 819–855 (1980)
12. Tritton, D.J.: Experiments on the flow past a circular cylinder at low Reynolds numbers. J. Fluid Mech. **6**, 547–555 (1959)
13. Maniyeri, R.: Numerical study of flow over a cylinder using an immersed boundary finite volume method. IJER. **3**, 213–216 (2014)
14. Sen, S., Mittal, S., Biswas, G.: Steady separated flow past elliptic cylinders using a stabilized finite-element method. Comput Model Eng Sci. **86**, 1–27 (2012)

Processing and Evaluation of Mechanical Properties of Sisal and Bamboo Chemically Treated Hybrid Composite

R. Siva, T. N. Valarmathi, B. Siddardha, Kallat Sanjana and Bhasker Dakshin

1 Introduction

A composite is usually made up of at least two materials out of which one is the binding material known as matrix and another is known as reinforcing material. Ku et al. [1] have found that natural fibres when compared with the artificial fibres have the better properties like low weight, less density, eco-friendly, more specific strength, but it has few disadvantages like uneven surface characteristics, high moisture absorption, and variation in quality. Maya Jacob John et al. [2] have explained that recently because of developments of environmental issues, composites using natural fibre have given a tremendous growth of interest due to their eco-friendly characteristics like biodegradability and recyclability. Joshi et al. [3] explain that another advantage of natural fibre over synthetic fibre is that natural fibre after its lifetime can be disposed or thrown out by the process of composting or by the process of recovering the calorific value of natural fibre in the furnace. Amada et al. [4] say about the bamboo fibre that it is a natural fibre which is extracted from plants through several processes. These fibres are used for several processes, they are used in construction to increase the strength, and it is used for fabrics and for decorative purposes. Bamboo fibre when treated with different chemicals shows various improvements in its properties. Biswas et al. [5] explain that natural fibre-reinforced composites (NFRCs) can be used instead of a synthetic fibre like glass and carbon fibre-reinforced polymer composite. The advantages of this are non-abrasive in nature and are low cost. Khalil et al. [6] said the bamboo

R. Siva (✉) · B. Siddardha · K. Sanjana · B. Dakshin
Department of Mechanical Engineering, Sathyabama Institute
of Science and Technology, Chennai, India
e-mail: rsivapsg@gmail.com

T. N. Valarmathi
School of Mechanical Engineering, Sathyabama Institute
of Science and Technology, Chennai, India

fibre composites that have good mechanical properties are used in construction. Kabir et al. [7] shown that poor compatibility between the polymer matrix and fibre could be improved by surface modification by using many chemical treatments. This improves the property of the fibre. Gomes et al. [8] claimed that many researchers have shown the alkali treatments because it increases the properties of the fibre, it is widely used method and less expensive. This treatment given to the natural fibre in order to remove the little percentage of wax, oil, etc., that is covering the outer surface of the fibre cell wall. This will lead to the increase in roughness of the surface of the fibre. This increases the strength of bonding between the matrix and the fibre and in turn increases the mechanical properties of the composites. Ramesh et al. [9] says sisal fibre composites are eco-friendly because they are degradable and they also have a very good property of elasticity. It is chosen sisal fibre as one of the best reinforcing material for composites due to its low density, no health hazard, high specific strength. This is also used in making of mats, ropes, carpets, etc. Mayandi et al. [10] say that alkali treatment with $Ca(OH)_2$ solution on sisal fibre increases the tensile strength. The solution of alkaline treatment with 15% $Ca(OH)_2$ shows better mechanical properties of composite. Many papers have proven that alkali treatment with NaOH solution treated fibres has increased mechanical properties of required composites. Here, we are going to study about the effect of fibres when treated with another chemical treatment of calcium hydroxide $Ca(OH)_2$ solution.

2 Experimental Procedures

2.1 Materials and Methods

The natural sisal and bamboo fibre are extracted out from sisal plant and bamboo through a manual process. The alkali treatment is a process in which the fibres are dipped in a solution about an hour and then it is taken out then washed and dried. This increases the strength of the fibre. The bamboo and sisal fibre were dipped in $Ca(OH)_2$ solution with 15%, and the composites were made with matrix material epoxy resins by compression moulding method. The fibres were randomly arranged as 40 vol.% with epoxy matrix material by the compression moulding process. The composites were made with the size 300 mm × 300 mm × 3 mm. There were three types of laminates: (1) epoxy matrix + untreated sisal/bamboo/sisal (S/B/S), (2) epoxy matrix + 15% $Ca(OH)_2$-treated sisal/bamboo/sisal (S/B/S) and (3) epoxy matrix + 15% $Ca(OH)_2$-treated bamboo/sisal/bamboo (B/S/B) were made by compression moulding technique with the size 300 mm × 300 mm × 3 mm. Fabrication of laminates has been done with untreated sisal fibers and untreated bamboo fibers by three layers. The layer arrangement has two outer untreated sisal fibers with untreated bamboo fibers in the middle. The matrix epoxy mixed with hardener is poured over the fibre layers, and the load is applied, and it is left to cure

for 24 h. Similarly, two outer layers of treated bamboo with one middle layer of treated sisal and two outer layers of treated sisal with one middle layer of treated bamboo laminates were prepared by the same method. Three types of laminates are shown in Figs. 1, 2 and 3.

2.2 Testing

The tensile samples of 250 and 25 mm width of sisal–bamboo hybrid laminates were prepared according to ASTM D 3039. The tensile test was performed on the computerized universal testing machine TUECN-200, Hitech India. The flexural test was performed according to ASTM D 790 on the computerized universal

Fig. 1 Untreated S/B/S composite

Fig. 2 Treated B/S/B composite
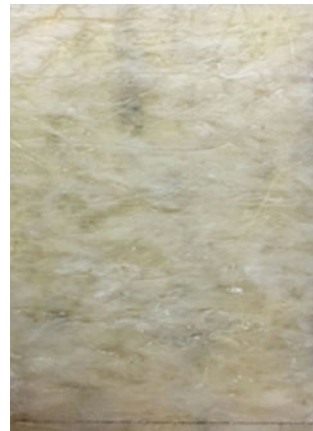
Fig. 3 Treated S/B/S
composite

testing machine TUECN-200, Hitech India, in a three-point bend configuration. The
size of the flexural test samples was 125 mm length and 12.7 mm width with the
span length of 75 mm. Tensile and flexural testing were performed at a cross head
speed of 3 mm/min cross head speed. The impact test was performed according to
the ASTM 4812 by the hammer AIT 300 N, FASNE. The sample size for impact
tests was 64 mm length and 12.7 mm width.

3 Results and Discussion

3.1 Tensile Test

The tensile test is conducted on the different laminate specimen by using a universal
testing machine. Table 1 shows the results of the different laminates that are
prepared. The tensile test specimen for treated Sisal/Bamboo/Sisal, untreated
Sisal/Bamboo/Sisal and treated Bamboo/Sisal/Bamboo were shownin Fig. 4.

T1, T2 and T3 in Fig. 4 represent S/B/S (treated), S/B/S (untreated) and B/S/B
(treated).

Table 1 Tensile strength test on laminates

Specimen	S/B/S (treated)	S/B/S (untreated)	B/S/B (treated)
Gauge thickness (mm)	8.36	10.84	11.36
Gauge width (mm)	29.46	27.86	29.40
Original cross-sectional area (mm^2)	246.29	302.28	334.12
Ultimate tensile load (kN)	4.98	4.44	4.60
Ultimate tensile strength (MPa)	20.00	18.00	17.00

Fig. 4 Tensile specimens
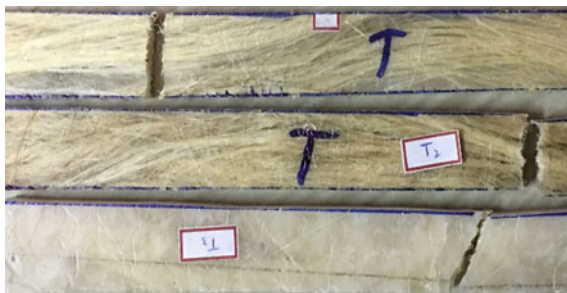
The S/B/S (treated) fibre-reinforced polymer shows better tensile properties (20 MPa) than the other B/S/B (treated) (17 MPa) and S/B/S (untreated) (18 MPa) laminates.

3.2 Impact Test

The Charpy impact test is conducted on the different laminate specimen, and the results were made in Table 2. The tested specimens are shown in Fig. 5.

I1, I2 and I3 in Fig. 5 represent S/B/S (treated), S/B/S (untreated) and B/S/B (treated).

The S/B/S (treated) fibre-reinforced polymer shows better impact properties, i.e. 14 J, than the other B/S/B (treated) 12 J and S/B/S (untreated) 10 J laminates.

Table 2 Impact test on laminates

Notch type	Test temperature (°C)	Sample ID	Absorbed energy (J)
Unnotched	240	S/B/S (treated)	14
Unnotched	240	S/B/S (untreated)	10
Unnotched	240	B/S/B (treated)	12

Fig. 5 Impact-tested laminates

Table 3 Flexural strength on laminates

Test parameters	S/B/S (treated)	S/B/S (untreated)	B/S/B (treated)
Flexural strength (N/mm^2 or MPa)	44.79	111.92	26.77

Fig. 6 Flexural
strength-tested laminates
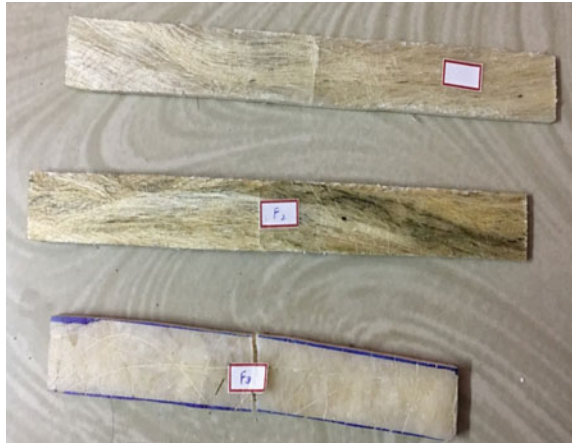
3.3 Flexural Test

The flexural tests are done on the specimen of the different laminates, and the results are shown in Table 3.

The tested specimens are shown in Fig. 6.

F1, F2 and F3 in Fig. 6 represent S/B/S (treated), S/B/S (untreated) and B/S/B (treated).

The S/B/S (untreated) laminate shows better properties than that of the other two laminates. The S/B/S (treated) laminate shows the property that is superior to that of the B/S/B (treated) laminate.

4 Conclusion

The mechanical properties of untreated S/B/S laminate, $Ca(OH)_2$ chemically treated S/B/S laminate and chemically treated B/S/B laminate have been investigated in detail. The effects and important findings from the present work are as follows:

- The $Ca(OH)_2$ chemically treated S/B/S laminates are found 10% improvement in tensile than untreated S/B/S laminates and 15% improvement in treated B/S/B laminates.
- The $Ca(OH)_2$ treatment modifies and cleans the fibre surface through OH-functional groups to make better bonding which improve tensile test.

- The Ca(OH)$_2$ chemically treated S/B/S laminates are found 29% improvement in impact than untreated S/B/S laminates and 14% improvement in treated B/S/B laminates.
- The untreated S/B/S laminates are found 60% improvement in impact than Ca(OH)$_2$ chemically treated S/B/S laminates and 76% improvement in treated B/S/B laminates.
- It is concluded that Ca(OH)$_2$ chemical treatment decides the surface condition of the fibre. The outer sisal fibre laminates show greater mechanical properties than outer bamboo fibre laminates. From the flexural test, the fibre debonding is more in the treated fibre than untreated fibre.

References

1. Ku, H., Wang, H., Pattarachaiyakoop, N., Trada, M.: A review on the tensile properties of natural fibre reinforced polymer composites. Compos Part B **42**, 856–873 (2011)
2. Maya Jacob John, S.T.: Biofibers and composites. Carbohydr. Polym. **71**, 343–364 (2008)
3. Joshi, S.V., Drzal, L.T., Mohanty, A.K., Arora, S.: Are natural fibre composites environmentally superior to glass fibre reinforced composites. Compos. A Appl. Sci. Manuf. **35**, 371–376 (2004)
4. Amada, S., Munekata, T., Nagase, Y., Ichikawa, Y., Kirigai, A., Zhifei, Y.: The mechanical structures of bamboos in viewpoint of functionally gradient and composite materials. J. Compos. Mater. **30**, 800–819 (1996)
5. Biswas, S., Ahsan, Q., Cenna, A., Hasan, M., Hassan, A.: Physical and mechanical properties of jute, bamboo and coir natural fibre. Fibres Polym **14**(10), 1762–1767 (2013)
6. Khalil, H.P.S., Bhat, I.U.H., Jawaid, M., Zaidon, A., Hermawan, D., Hadi, Y.S.: Bamboo fibre reinforced bio composites: a review. Mater. Des. **42**, 353–368 (2012)
7. Kabir, M.M., Wang, H., Lau, K.T., Cardona, F.: Chemical treatments on plant-based natural fibre reinforced polymer composites: an overview. Compos. B: Eng. **43**, 2883–2892 (2012)
8. Gomes, A., Matsuo, T., Goda, K., Ohgi, J.: Development and effect of alkali treatment on tensile of curaua fibres green composites. Compos. A Appl. Sci. Manuf. **38**(8), 1811–1820 (2007)
9. Ramesh, M., Palanikumar, K., Hemachandra, Reddy K.: Comparative evaluation on properties of hybrid glass fibre-Sisal/Jute reinforced epoxy composites. Procedia. Eng **51**, 745–750 (2013)
10. Mayandi, K., Rajini, N., Pitchipoo, P., Winowlin Jappes, J.T., Varada Rajulu, A.: Properties of untreated and chemically treated *Cissus quadrangularis* natural fibres and their composites with polyester as the matrix. Polym. Compos. (2016)

On the Surface Finish Improvement in Hybrid Additive Subtractive Manufacturing Process

Mayur Vispute, Narendra Kumar, Prashant K. Jain, Puneet Tandon and Pulak M. Pandey

1 Introduction

Additive manufacturing (AM) also known as 3D printing has shown worth due to its complex part fabrication capabilities without any specific tools and fixtures. In AM, part is fabricated directly from its CAD model by adding material in a layer-by-layer manner. The part fabrication process is started with the generation of CAD model of required geometry using any modeling software which is then converted into the STL file format [1, 2]. The STL model is exported to the corresponding software where it is sliced to extract the contour information. After that, the printing toolpath is generated for each slice. This information is then loaded into the machine controller for fabricating parts. Due to the layer-by-layer stacking of material, surface finish and dimensional accuracy of fabricated parts are affected. Therefore, some post-processing techniques are employed to provide the better surface finish. The typical steps followed in AM are shown in Fig. 1a. Various AM processes have been developed over the time, and the fabricated parts have been used for prototyping and end-use applications. These processes can be categorized based on the form of raw material used for processing such as liquid, solid, and powder. Among all, solid-based AM processes are more popular due to its low cost. Fused deposition modeling process is one of them in which a solid filament wire is fed into the liquefier head of the extruder head.

In FDM, different polymers and their composites are available in the form of filament for fabricating prototypes or functional parts. As discussed, the material is deposited in the filament form on the built platform in layer-by-layer form, which

M. Vispute · N. Kumar (✉) · P. K. Jain · P. Tandon
PDPM Indian Institute of Information Technology,
Design and Manufacturing, Jabalpur, Madhya Pradesh, India
e-mail: nyiiitj@gmail.com

P. M. Pandey
Indian Institute of Technology, Delhi, India
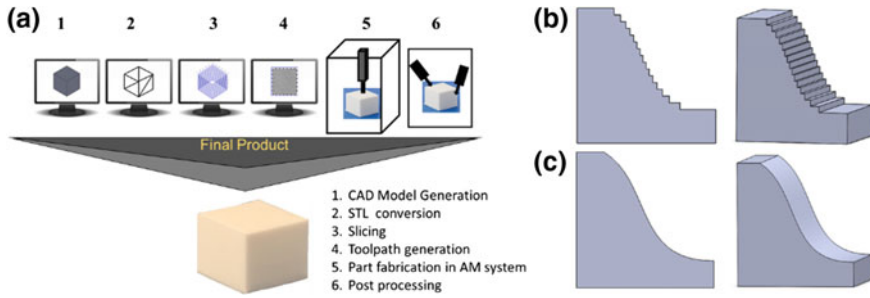
Fig. 1 **a** Typical AM cycle, **b** actual, and **c** desired part

affects the surface finish causes the development of cusp and staircase effects [3]. Figure 1b, c shows the actual and desired FDM fabricated part, respectively. Staircase effect can be seen clearly. In order to improve the surface finish and dimensional accuracy, post-processing operation is required.

Enormous literature has been reported in the post-processing domain for FDM in which researchers have developed the various techniques to improve the surface finish of the fabricated parts. Galantucci et al. performed chemical finishing technique on FDM parts at various process parameters by dipping ABS part in dimethyl ketone (90%)–water (10%) solution [4]. Slice height and raster width were the most influenced parameters for surface roughness of part. In another work, they compared tensile and compressive properties of chemically treated and untreated FDM part [5]. Little reduction was observed in the tensile strength of part. Kuo et al. carried out vapor polishing by striking acetone vapors of FDM processed parts [6]. They also developed regression equation for determining required polishing time based on polishing area. Results showed the effectiveness of the acetone-vapor polishing system with high polishing efficiency and little chemical waste. Boschetto et al. performed machining operation on FDM-fabricated part for various cutting depths at each build orientation angle [7]. They developed equation between build orientation angle and cutting depth for minimization of surface roughness. Another attempt made by the Taufik and Jain to improve the surface finish in which the adjacent valleys were filled by semi-solidified material using a CNC-selective melting tool [8]. A novel barrel finishing technique was developed by Boschetto and Bottini [9]. They rotated the barrel consisting of part, powder, media, and water at specific speed and time for improving surface finish of part.

The presented literature shows that each post-processing technique has their own advantages and limitations. Although chemical, vapor, and barrel finishing techniques are economically viable but unsuitable for localized finishing. Further, the addition of chemical solvent ruins the mechanical properties of parts. On the other side, post-processing through machining can be cost-effective and suitable for localized finishing without affecting the mechanical properties of the parts. However, machining has also its limitations due to location error effect. A hybrid process can be developed in order to overcome the said limitations by merging

additive and subtractive manufacturing processes. With the development of the hybrid process, location error effect will be reduced. The present study aims to develop a hybrid additive subtractive manufacturing process (HASM) on the same platform for improving surface finish. A CNC milling machine has been used as the machining center, while a customized material deposition tool has been developed for additive manufacturing of the parts. A customized software module has also been developed to generate a required toolpath for additive and subtractive manufacturing. Feasibility of the developed process has been analyzed by performing printing and finishing operations on the same setup. In this setup, firstly, additive manufacturing is carried out followed by subtractive manufacturing is carried out on the same station without changing the position of the part. In order to retain good dimensional accuracy, part is fabricated with optimum oversize dimensions.

2   Development of HASM Process Set Up

HASM setup has been developed with the help of existing three axes CNC milling machine for improving the surface finish of fabricated parts as shown in Fig. 2. On this setup, two operations can be performed such as additive manufacturing for oversize part fabrication and subtractive manufacturing for improving surface finish. An indigenous material deposition tool (MDT) has been developed for performing additive manufacturing, which works on the screw extrusion principle. Instead of the filament, the developed process uses the material in pellet form, which makes it cost-effective as compared to commercial FDM printers. The developed MDT can be attached to the CNC milling machine with the help of existing tool holder, which shows its compatibility with the machine. The developed MDT is designed in such a way that it can be replaced at any time by milling cutter when machining operation needs to be performed. The MDT consists of a barrel, screw, heating elements, nozzle, hopper, and supporting frame. Pellets enter

Fig. 2 Developed HASM setup

in the barrel with the help of screw rotation where heating elements provide the heat energy and convert them into the semi-molten state.

Pellets of acrylonitrile butadiene styrene (ABS) material are taken in the study due to frequent use in commercial FDM process. This semi-molten material extrudes from a tiny nozzle on the heated build platform in a layer-by-layer fashion. By joining deposited layers, 3D part is formed. After completion of part fabrication through additive manufacturing, MDT has been replaced by ball nose milling cutter for performing subtractive manufacturing. Milling cutter performs the machining operation on the fabricated part and removes the extra material deposited during additive manufacturing. It results in the good surface finish of part after machining operation.

3 Development of Toolpath for HASM

An indigenous toolpath has been developed for HASM to ensure the proper part fabrication. First, the parts are fabricated in an additive manner, and then the subtractive approach is used to remove the material. An in-house developed program has been written in MATLAB by implementing various algorithms in which the cad model of the part is imported in STL format and sliced to extract the contour information of each layer. Then, part is oversized with increasing dimensions optimally to reduce material loss during machining. After that, toolpath is generated for each layer with the help of the extracted data. Raster- and contour-based approach has been employed for additive manufacturing while for subtractive manufacturing; a novel approach has been implemented based on STL triangles and contour offsetting. All the steps required for HASM are merged by developing a graphical user interface (GUI) as shown in Fig. 3.
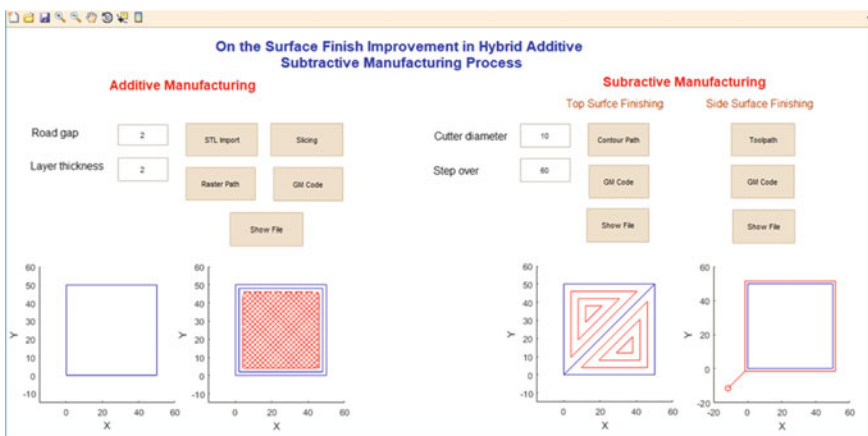
Fig. 3 Developed graphical user interface

in which the user can change the value of each parameter as per the requirement. For additive manufacturing, the parameters such as road gap, layer thickness can be altered by just clicking in the corresponding edit box, and then again, the whole toolpath can be rewritten with a new set of altered parameters. In the same way, the user can also change the parameters related to the machining such as cutter diameter, step over. NC part programs are generated for HASM, which is compatible with CNC machine. Those part programs of HASM are exported to CNC machine for experimentation.

4 Case Study

In order to validate proposed work, a primitive shape, the cube has been considered for a case study. All the operations are performed from toolpath generation to machining of the additive manufactured parts. Figure 4a, b shows CAD and STL model of cube generated from modeling software. Sliced layers of STL model obtained from MATLAB is shown in Fig. 4c. Then, raster- and contour-based toolpath is generated for each sliced layer. Figure 4d shows generated a toolpath of additive manufacturing for one layer. After that, toolpath is generated for subtractive manufacturing as shown in Fig. 4e. NC part programs are generated for additive and subtractive manufacturing. The generated part programs are exported to three axes CNC milling machine. After that, part fabrication is carried out with
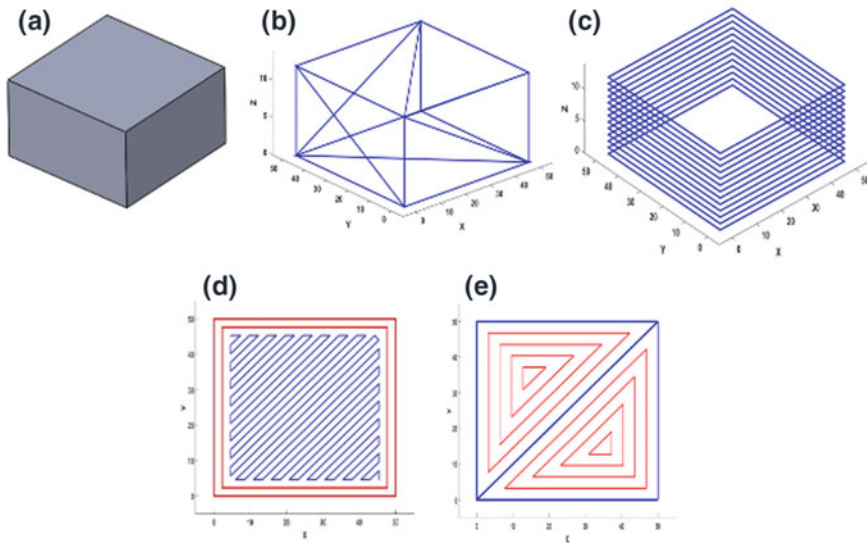
Fig. 4 **a** CAD model, **b** STL model, **c** sliced data of STL model, **d** additive toolpath for one layer, **e** subtractive toolpath
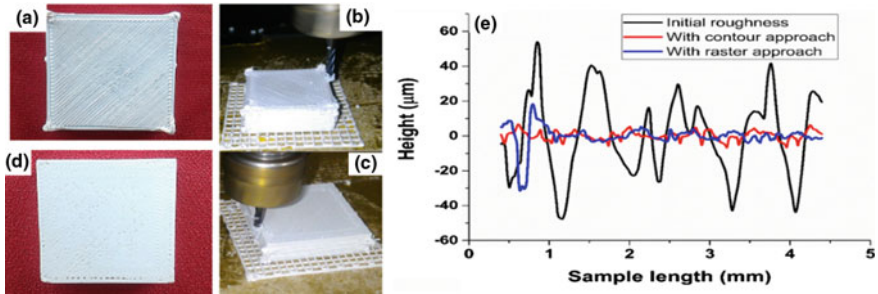
Fig. 5 **a** Fabricated part, **b** top surface finishing being performed, **c** side surface finishing being performed, **d** finished part, and **e** corresponding surface roughness profiles

the help of developed AM setup, and then, machining operation is performed using ball nose milling cutter of radius 1.5 mm. The nozzle of diameter 0.4 mm is used for part fabrication. Figure 5 shows the different stages of HASM process.

The surface roughness of unfinished and finished part is measured in order to see the improvement. Tesa Rugosurf 10G-roughness tester is used for measuring roughness profiles. The considered cutoff length has been taken 0.8 mm. The obtained surface roughness profiles of the unfinished and finished part are shown in Fig. 5e.

It can be observed that there is a significant reduction in surface roughness value after performing machining on the AM part. The obtained surface roughness value of additive manufactured part is 19.495 µm while it reaches to 2.068 µm after performing machining. During the machining, extra-oversize dimensions of the parts are also reduced to improve the dimensional accuracy. It shows that HASM is very effective for improving surface finish and dimensional accuracy of the printed parts.

5 Conclusion

A new printing and post-finishing approach based on hybrid additive subtractive manufacturing process is presented. Three axes CNC milling machine is employed for conducting the study. The developed process fabricates 3D parts using novel MDT and improves the surface finish of the fabricated parts by performing machining on the same setup. The part surface quality of the fabricated parts is improved by removing peaks in the form of chips using ball nose milling cutter. An indigenous software module is also developed and presented to generate a toolpath for additive and subtractive manufacturing. A case study is presented which shows the feasibility and viability of the developed process. The obtained results of case study show the significant improvement in the surface finish after applying machining operation on the fabricated part.

References

1. Kumar, N., Shaikh, S., Jain, P.K., Tandon, P.: Effect of fractal curve based toolpath on part strength in fused deposition modelling. Int. J. Rapid Manuf. **5**, 186–198 (2015)
2. Shaikh, S., Kumar, N., Jain, P.K., Tandon, P.: Hilbert Curve Based Toolpath for FDM Process. In CAD/CAM, Robotics and Factories of the Future, Springer, New Delhi, pp. 751–759 (2016)
3. Taufik, M., Jain, P.K.: Laser assisted finishing process for improved surface finish of fused deposition modelled parts. J. Manuf. Process. **30**, 161–177 (2017)
4. Galantucci, L.M., Lavecchia, F., Percoco, G.: Experimental study aiming to enhance the surface finish of fused deposition modeled parts. CIRP Ann. Manuf. Technol. **58**, 189–192 (2009)
5. Galantucci, L.M., Lavecchia, F., Percoco, G.: Quantitative analysis of a chemical treatment to reduce roughness of parts fabricated using fused deposition modeling. CIRP Ann. Manuf. Technol. **59**, 247–250 (2010)
6. Kuo, C.-C., Mao, R.-C.: Development of a precision surface polishing system for parts fabricated by fused deposition modeling. Mater. Manuf. Process. **31**, 1113–1118 (2016)
7. Boschetto, A., Bottini, L., Veniali, F.: Finishing of fused deposition modeling parts by CNC machining. Robot. Comput. Integr. Manuf. **41**, 92–101 (2016)
8. Taufik, M., Jain, P.K.: CNC-assisted selective melting for improved surface finish of FDM parts. Virtual Phys. Prototyp., **11**, 319–341 (2016)
9. Boschetto, A., Bottini, L.: Surface improvement of fused deposition modeling parts by barrel finishing. Rapid Prototyp. J. **21**, 686–696 (2015)

Impact of Control Unit Gains on Noise Mitigation in Swash Plate Pump Pumping Systems

Molham H. Chikhalsouk, Khalid Zhouri, Chandra Somayaji and Monsif Shinneeb

1 Introduction

In the recent years, several studies have been conducted on the swash plate pump. Akers [1] has modelled the early models which were named as the barrel block. He controlled the pressure by using a pressure regulator. The input was a step increase, and he has investigated the transient response by simplifying the mathematical model and opting the open loop model and then applying the optimum control theory. There was an improvement in the pump transient response. Kalafatis in [2] has another interest as he has modelled and investigated the pump characteristics. He has also implemented a pressure regulator, and the results were obtained numerically and compared with the pump curves.

Manring [3] has studied the influence of some parameters on the pump performance. The new design of the pump comes with an inclination between the piston axis and the rotational axis. The new inclination angle reduces the detachment force that tries to detach the piston from its socket, and increases the piston stroke which increases the pump overall specific power. Khalil [4] has modelled and simulated the inclined model and investigated the pump kinematics. Also, Khalil in [5] has proposed a single PD control unit to simplify the design and reduce the cost. The proposed control strategy was compared with several proposes an existing strategy. However, the study did not include any investigation for the noise and vibration outcomes. Chikhalsouk [6] has derived simplified expressions for the pump kinematic and has extended to pressure, flow rate and pump power. These results were compared with the ones were developed by Khalil; the new expressions have shown good agreement with the other expressions.

M. H. Chikhalsouk (✉) · K. Zhouri · C. Somayaji · M. Shinneeb
Mechanical Department, ADM, Higher Colleges of Technology, Abu Dhabi, UAE
e-mail: malsouk@hct.ac.ae

Another interesting study was done by Backe [8] to improve the dynamics of load sensing systems. In that study, the pump was equipped with an electro-hydraulic valve to adjust the pump flow rate. The load sensing control unit has shown an acceptable stability but it was a quite quick response, which is not very desirable in the most of the hydraulic applications. The simple structure of the control unit can increase the pump overall efficiency, and it can be up to 80% [7]. The prime mover rotational velocity determined the pump efficiency, and its always recommended to run at high speed [8, 9]. The improvement of the pump power efficiency was investigated for the variable pump operating conditions to match the variable load requirements [10]. This is the condition of the variable displacement pump such as the swash plate pump. In [11], Mansouri has used a different approach to controlling the pump flow. This approach is based on using a latching valve to on/off the flow. Where in the on position, the flow is directed to the hydraulic rail and generating the high-pressure flow. However, in the off position, the flow is redirected to the short path and sends back to the pump inlet. This approach has led to a great energy saving in the pump, especially in the partial load requirements. Another study was conducted by Martin [12]. Where a servo valve was presented and simplified by eliminating the factors, they have a little impact on the performance and by linearizing the nonlinear model. Martin has developed two novel models for the servo valve, which are the torque motor electrical model that correlates the torque motor electric current to the coil voltage, and the second one was the hydraulic model that correlates the pump flow rate to the coils' current. The pump flow rate is affected by the quality of the mating components that affect the amount of the leakage in the pump. The leakage value is proportional to the pressure drop in the leakage line. The pump rotational speed affects the leakage value in hydraulic motors and pumps (Merritt, 1967). In several studies, the effect pump/motor line is neglected. Compressibility is approximated to be a constant value [13].

In this work, a novel control scheme is presented to effectively control the swash plate pump inclination angle, and hence, the pump flow rate. The new strategy implements a single PID control strategy to obtain certain advantages such as simplifying the design, lowering the production costs, improving the pump overall static and dynamic characteristics, and smoothening the pump performance to increase the pump service life. The paper is divided into several parts. It starts with a brief introduction that includes the literature review about the swash plate pump in general and its control-related studies, then the structure of the swash plate pump is introduced, the different control strategies of the swash plate pump are explained, then, the mathematical model of the used control strategies is presented, the experimental set-up and the obtained findings are listed in Sects. 5 and 6. The work conclusion is summarized in Sect. 7.

2 Axial Piston Pump's Construction

The fundamental parts of a conical swash plate pump are illustrated in Fig. 1. A specific number of pistons/cylinders are arranged in a circular arrangement and in the conical design, the pistons axis is inclined with respect to the rotational axis. This angle is named as the conical angle. The Pistons' housing is maintained firmly against the port plate by the aid of the cylinder block spring keeps the pistons' housing. A hydrodynamic bearing between the port plate and the cylinders' block is generated by filling the existing gap with a thin film of oil. A joint connects the individual pistons' bases to the slipper through a ball/socket joints. Both the swash plate and the slippers are maintained at the predetermined touch by the aid of thin film oil, which plays the role of the hydrodynamic bearing surface. The swash plate inclination angle is adjusted by control piston, which is external to the pump.

3 Control Unit

In order to maintain the hydraulic oil properties and optimize the pump power utilization, the present model of the swash plate pump is equipped with a control unit. The function of the control system is to calculate the swash plate inclination angle, i.e. to determine the piston stroke and the pump flow rate. In order to displace the swash plate and generate the needed angle, two inputs are required, which are a
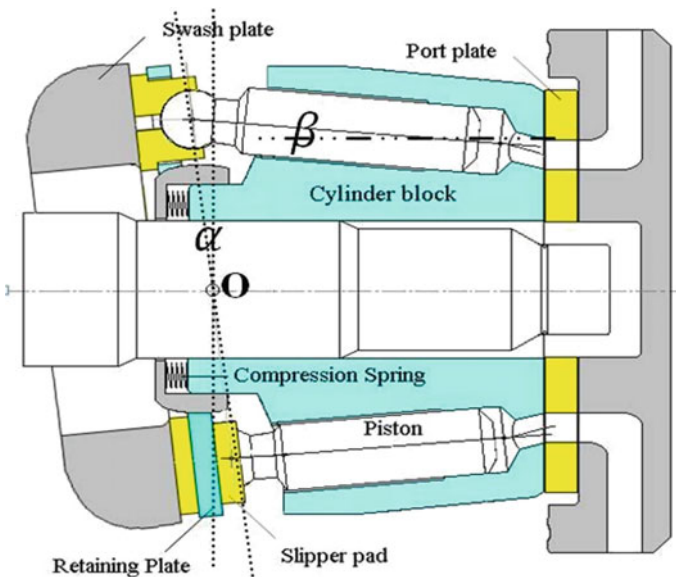
Fig. 1 Swash plate pump general structure

hydraulic input and an electronic input. The hydraulic unit produces the required hydraulic input. The structure of the hydraulic subsystem consists of a secondary pump to generate the pressurized fluid on the control cylinder, and it is connected to the inlet of a hydraulic proportional valve. The valve has a moving part (spool), it's housing (sleeve), and two restoring springs that push the spool against a solenoid. The solenoid is activated by the control current, which is generated by the electronic part of the control unit.

4   Control Unit and Noise

There is a relationship between the noise and the control unit, where the type of the controller influences the noise generated by the pump. The control unit follows different strategies such as proportional derivative (PD), proportional-integrative and derivative (PID), proportional and integrative (PI), or a combination of them. It is known that the operation of the pump causes noise, and that noise can be expressed in the sinusoidal form, where it has small amplitude and high frequency, as follows:

$$y = A.\sin(\omega t) \tag{1}$$

where y is the noise, A is the amplitude of the noise, ω is the noise frequency, and t is time.

Accordingly, in PD controller, the derivative gain amplifies the noise amplitude, while the PID suppresses the noise.

5   Control Strategies

The current swash plate pump model comes with two negative feedback control system/loops.

The swash plate control system scheme with two negative loops is shown in Fig. 2. The inner loop controls the spool movement, and this control is achieved by
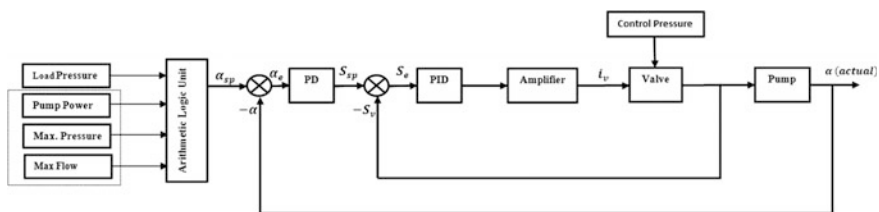
Fig. 2 Swash plate pump with two negative feedback control system/loops
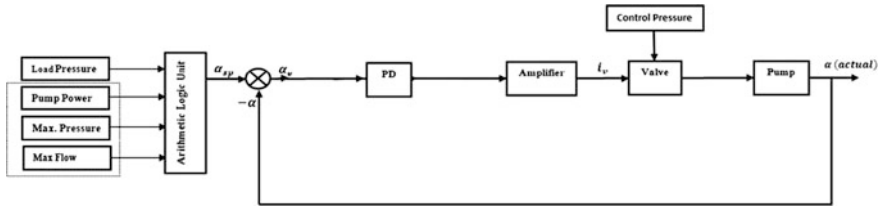
Fig. 3 Swash plate pump with double feedback control loop representation

the aid of LVDT position sensor to monitor the position of the spool. The inner loop is equipped with a PID controller. However, the outer loop is equipped with a PD controller, and its function is to control the swash plate inclination angle. The current model has some disadvantages and backdrops such as slow response which makes it inconvenient to most of the applications that require a quick response. Medhat Khalil [14] has proposed a single PD controller to control the swash plate inclination angle and left the spool motion uncontrolled. This modification can be achieved by removing the electrical feedback wire from the inner loop. The new control strategy can be illustrated in Fig. 3.

The PD controller gains were determined by applying the Ultimate Sensitivity method. The new PD gains have given a better pump performance (in comparison to the conventional two negative feedback). For example, the rise time has dropped from 120 to 50 ms. However, this proposed single controller has not measured the vibration and noise levels. Chikhalsouk [15] has studied the vibration levels for the proposed single PD controller and concluded the high levels of the vibration and noise levels, which are not acceptable in hydraulic systems. In the same study [15], Chikhalsouk has proposed a single PID controller as the PID controller gains were recalculated and determined to ensure the smooth operation.

The proposed control scheme is illustrated in Fig. 4. The control unit controls the piston displaces through controlling the swash plate inclination angle which is the control variable. There are considerations should be respect in the PID tuning such as the maximum and minimum pressure, maximum and minimum flow rate and lastly the pump power. In [15], Chikhalsouk has applied Ultimate Sensitivity method to calculate and tune the PID controller gains. According to this method, there was more reduction in the rise time and ultimately there was a great impact on
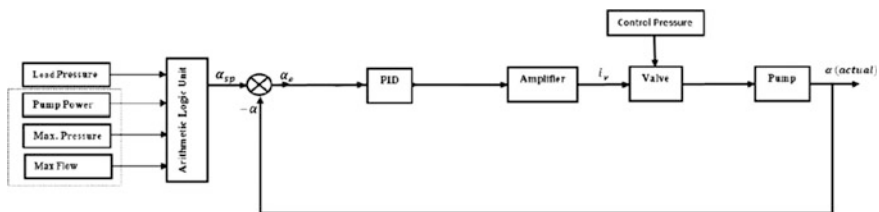
Fig. 4 Swash plate pump with single PID controller representation

the noise and vibration levels, which makes this design is more optimum and preferable in the hydraulic systems that driven by swash plate pumps. Experimental investigations were conducted to investigate the of the system noise levels with PD and PID single controllers.

6 Experimental Set-up

The experimental set-up representation is shown in Fig. 5, which consists of the hydraulic subsystem and the control subsystem.

6.1 The Hydraulic Subsystem

The hydraulic subsystem has the flowing components: the primary swash plate pump, the secondary control pump, a disturbance unit, oil filtration and conditioner, and accessories.

The Primary Swash plate Pump:

The pump (1) is driven by an electric motor (2). The electric motor has 10 HP in power and enough to produce the required torque and rpm for the pump.
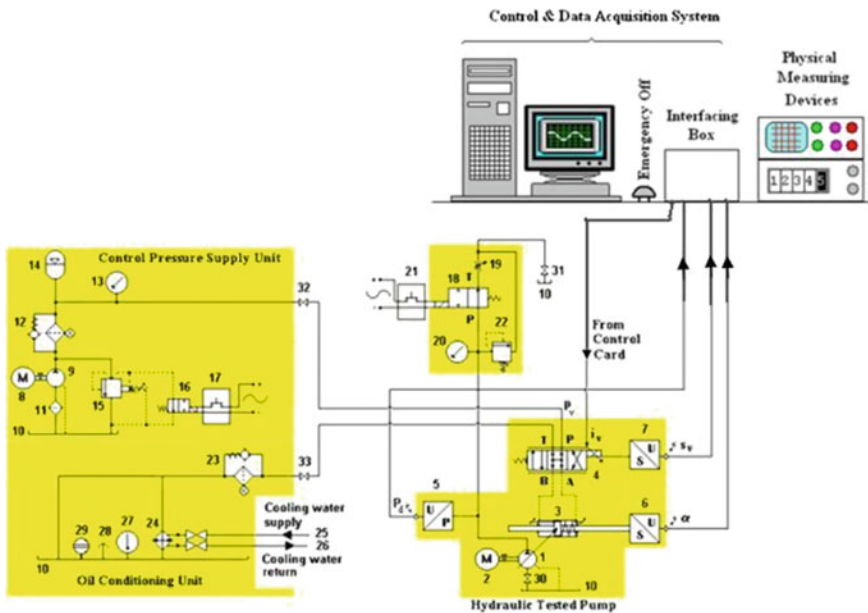
Fig. 5 Hydraulic and control subsystems schematic experimental set-up

The control cylinder (3) controls pump inclination angle. This control piston is mechanically connected to the swash plate. In the two negative loops, the proportional valve (4) gets the electrical signal from the PID controller to produce the pre-calculated pressure value in the input of the hydraulic subsystem line and pushes the control piston. Several transducers are needed to supply the arithmetic unit and then calculate the required swash plate inclination angle. The inputs are the inclination angle, the load of the pressure and the spool position.

The Secondary Control Pump:

A 15 MPa separate pump is used to generate the control pressure. The pressure is needed to move the control piston (3) by the aid of the proportional valve (4). The control pump (9) uses the same hydraulic oil tank (10) and driven by a separate electric motor (10). Two oil filters are used to maintain the quality of the oil. The first filter (11) is installed on the pump supply line; however, the second filter (12) is installed on the bypass pipe. In order to read the delivered pressure values, a dial gauge (13) is installed on the pump delivery line. To keep the pressure constant, a pressure accumulator (14) is installed on the delivery line. Also, for safety reason, a pressure relief valve is installed (15) to bleed the excessive pressure.

Load Simulation Subsystem:

A load simulation subsystem is used to mimic different operating loads. This subsystem is a two-way loading valve (18) that is installed on pump delivery line (31) to the reservoir (10), and it cuts off or connects the pump to the load or to the reservoir. Also, a throttle valve (19) is equipped to manually adjust the loading pressure. Another dial gauge (20) is equipped to show the pressure value. Also, a relief valve is installed to relieve the pressure as it reaches the maximum allowable value.

Oil Conditioning Subsystem:

It is vital in the hydraulic system to avoid the oil overheating that affects the oil physical and chemical properties. For this purpose, a filter (23) is used to trap the oil contamination from dust and fine particles, also an oil cooler (24) is added to cool off the oil temperature and keep it at the recommended temperature. In order to read the temperature value, a thermostat (27) is installed measure the oil temperature. Also, two valves (25, 26) are added to link/cut off this subsystem.

   Accessories: To pump the air off the hydraulic system, an oil breather (28) is added to the hydraulic system, and two cut-off valves (30–33) are installed to isolate the hydraulic system form the control pump and the swash plate. To simulate the piping system, a simply supported pipe is linked to pump; and the pipe was as follows: length is 3.5 (m), the inner radius is 0.011 (m), while the outer radius is 0.0127 (m).

6.2 The Control Subsystem

The newly proposed control subsystem was parameterized, built and tested based on Simulink 7-1 R. The compositions of the control subsystem are shown in Fig. 6. An I/O card is linked to a computer. The input/output card transfers the readings from electrical signals; these values can be read via the multimeter and then convert them into numerical values and fed them to the Simulink. The software manipulates the readings and simulates the physical control unit and then re-fed them to the input/output card and then to the pump.

In the real world, the physical components of the control unit contain the logical unit, the PID controller to control the swash plate inclination angle, and there is a control signal conditioner. These components are installed on the green board. The role of the logic element is to determine the value of the inclination angle based on the pressure value transmitted by the pressure transducer. The calculated value comes as an electrical value and fed to the PID controller. There are some limitations for the computed values to ensure the maximum pump pressure and flow rate and the respecting the pump power. The control unit is powered by two 12 DC power supply. LabVIEW is used to handle the analog signals and fed it to the I/O card.
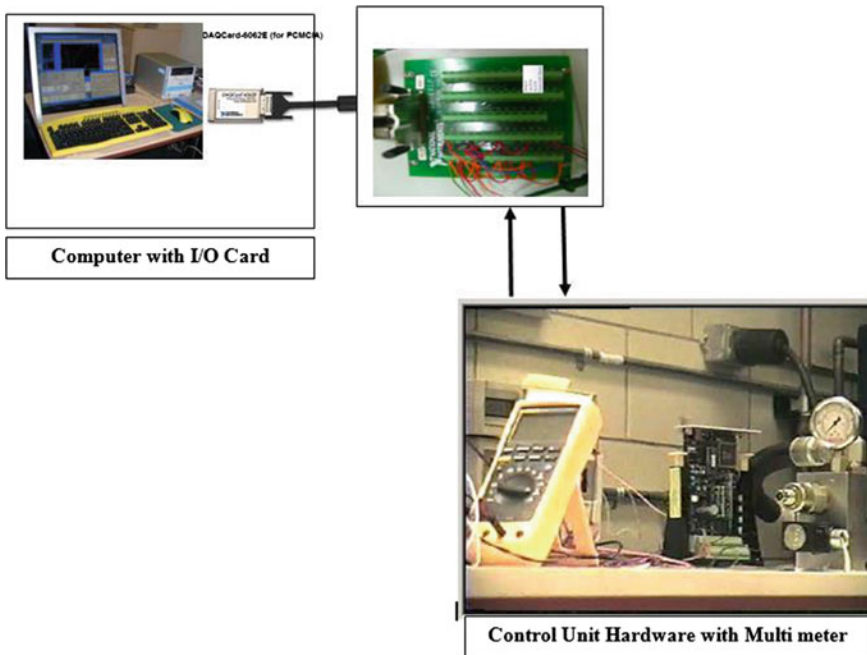
Fig. 6 Components of control subsystem

7   Results

The newly proposed control strategy noise level is examined and compared to the single PD controller proposed by Khalil et al. [5]. The proportional gain was set to equal 1, and the derivative gain equals $K_p = 1$, $K_i = 0$, and $K_d = 0.2$. Also, the noise levels of a control strategy with a PID controller proposed by Chikhalsouk and Bhat [15] are studied. The PID is parameterized to have the following gains: the proportional gain equals 1.9, the integral gain equals to 8.4, and the derivative gain is equal to 0.01. The measured noise levels are illustrated (Fig. 7).

8   Conclusion

Swash plate pump must be equipped with a control strategy to save on the pump power and maintain the pump in good operating condition. The kind of the controller determines the noise generated by the pump, where the current model implements a PD controller which makes the pump noisy. Using a suitable PID controller with the optimum gain reduces the noise significantly.
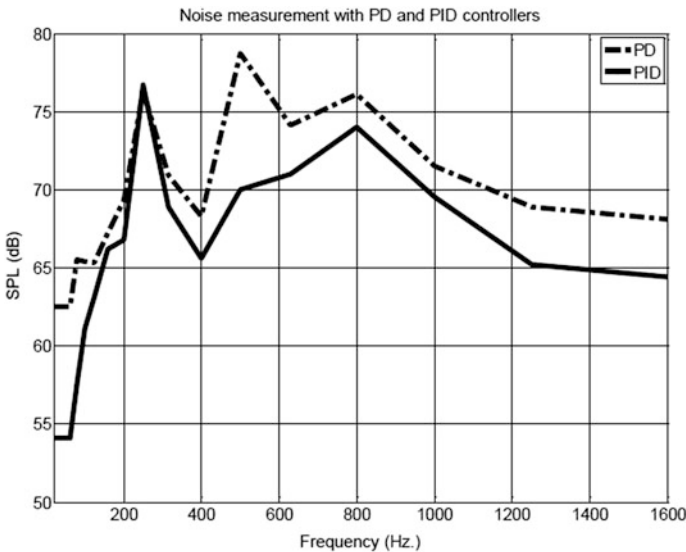
Fig. 7   Noise measurement with PD and PID controllers

References

1. Akers, S.J., Lin, S.: The control of an axial piston pump using single-stage electro-hydraulic servo valve. Proc. Am. Control Conf. **3**, 1865 (1987)
2. Kalafatis, P., Costopoulos, T.: Modeling and simulation of an axial piston variable displacement pump with pressure control. Mech. Mach. Theory **30**(4), 599–612 (1995)
3. Manring, N.D., Johnson, K.: Modeling and designing a variable-displacement open-loop pump. J. Dyn. Syst. Measure. Control **116**, 267–272 (1996)
4. Khalil M.B., Kassem, S.A.: On the Dynamics of swash plate axial piston pumps with conical cylinder blocks. In: Sixth Triennial International Symposium on Fluid Control and Visualization, pp. 13–17, Sherbrooke University, Sherbrooke (2002)
5. Khalil, M., Yurkevich, V., Svoboda, J., Bhat, R.B.: Implementation of single feedback control loop for constant power regulated swash plate axial piston pumps. Int. J. Fluid Power **3**(3), 27–36 (2002)
6. Chikhalsouk, M.H., Bhat, R.B.: Reduction of noise levels in hydraulic system driven by swash plate pumps by improving design of port plate. In: Proceedings of the Canadian Acoustics Week in Canada 2007, vol. 35, No. 3, pp. 186–187, Montreal, Canada (2007)
7. Backe, W., Kogl, C.: Secondary controlled motors in speed and torque control. In: Proceedings of the Second JHPS International Symposium on Fluid Power, 6–9 Sept, Tokyo, Japan, pp. 241–248 (1993)
8. Backe, W.: Recent research projects in hydraulics. In: Proceedings of the Second JHPS International Symposium on Fluid Power, 6–9 Sept, Tokyo, Japan, pp. 3–27 (1991)
9. Ogata, K.: Modern Control Engineering, 4th edn. Prentice Hall, India (2006)
10. Cundiff, J.S.: Fluid Power Circuits and Controls: Fundamentals and Applications. CRC Press, Roca Raton (2002)
11. Mansouri, G., Misovec, K., Johnson, B., Babbitt, G., Sturman, O.: Variable flow supply using switched-mode control of a fixed-displacement pump. In: Proceedings of the Seventh Scandinavian International Conference on Fluid Power, 30 May–June, Linkoping, Sweden, pp. 361–376 (2001)
12. Martin, M.: Load simulator using hydraulics. Master's Thesis, Department of Mechanical Engineering, University of Saskatchewan, University of Saskatchewan (1992)
13. Lantto, B., Krus, P., Palmberg, J.: Interaction between loads in load-sensing systems. In: Proceedings of the 2nd Tampere International Conference on Fluid Power, 19–21 Mar, Tampere, Finland (1991)
14. Khalil, M. Performance investigation of the swash plate axial piston pump with conical cylinder blocks. Ph.D. thesis, Concordia University, Montreal, Canada (2003)
15. Chikhalsouk, M., Bhat, R.B.: Design and Control of Hydraulic Systems Using Vibration-Based Diagnosis. ISBN 3639091418, VDM, Germany, pp. 132–154 (2008)
16. M. K. B., Khalil, Yurkevich, V., Svoboda, J., and Bhat, R. B., (2002)." Implementation of Single Feedback Control Loop for Constant Power Regulated Swash Plate Axial Piston Pumps". International Journal of Fluid Power, Vol. 3, No. 3, pp. 27–36

Discussion of Past, Present and Future Perspectives of Refrigerants and Its Future Scope

I. Vinoth Kanna and A. Devaraj

1 Introduction

There are essentially two categories of thermal plants. These are (i) thermal power plants or work producing plants and (ii) refrigeration/heat pump plants or work consuming plants [1, 2]. The work producing plants or heat engine leads to the conversion of heat to work. The work consuming plants, viz. refrigerators/heat pumps, are not those, which are in any way related to the conversion of work into heat [3–5]. No ingenuity at all is required for the conversion of work into heat. In fact, all work (mechanical/electrical energy) that is consumed in machinery is ultimately dissipated as heat to the environment. The objective of work consuming plants, actually, is to lead to the flow of heat from a low-temperature body to a high-temperature body [6]. The work is consumed to achieve this.

Refrigeration equipment, in general, is relatively smaller in size as compared to work producing plants. The capacity of power plant is in MW, whereas the capacity of refrigeration system is in kW or even less [7, 8]. A very large super cold storage or a central air conditioning plant for a multi-storey building may consume power in the range of 2000–5000 kW. A window-type air conditioner may consume only 2.5 kW of power, domestic refrigerator just 100–250 W only [9].

A refrigerating machine is a device, which will either cool or maintain a body at a temperature below that of the surroundings. Hence, heat must be made to flow from a body at low temperature to the surroundings at high temperature [10]. However, that is not possible on its own. We see the nature that heat spontaneously flows from a high-temperature body to a low-temperature body. Most refrigeration

I. Vinoth Kanna (✉) · A. Devaraj
Department of Mechanical Engineering, Vel Tech Rangarajan
Dr. Sagunthala R & D Institute of Science and Technology, Chennai, India
e-mail: vinothkanna.research@gmail.com

461

devices/plants, including air conditioners and refrigerators, are working the same, which we mention the above process by the principle of second law of thermodynamics [11].

By attaining this, we have to choose the refrigerant as a major part of the refrigeration process. Because refrigerant is main substance used in a heat pump and refrigeration cycle, actually it is a substance or mixture, usually a fluid. Plank has given individual treatment to some 50 inorganic and organic refrigerants, and many more have been discussed in this paper.

2   Refrigerant

Any substance that absorbs heat through expansion or vaporization may be called a refrigerant [1]. Refrigerant is a substance used for refrigeration, causing cooling or refrigeration. Most refrigerants commonly used today are classified into four areas:

- Chlorofluorocarbons (CFCs)
- Hydrochlorofluorocarbons (HCFCS)
- Hydrofluorocarbons (HFCs)
- Natural refrigerants
- Refrigerant blends (azeotropic and zeotropic)

2.1   Refrigerants Identification by Number and Colour Code

Number identifies refrigerants. The number follows the letter which means refrigerant. The American Society of Heating, Refrigerating and Air-conditioning (ASHRE) has standardized this identifying system [1]. Refrigerant cylinders are often colour coded to permit easy identification of the refrigerant they contain [12, 13]. This helps to prevent accidental mixing of the refrigerants within a system. Popular refrigerants, with their R-numbers and cylinder colour codes, are shown in Fig. 1. Cylinder for re-covered refrigerants is grey with yellow ends.

2.2   Chlorofluorocarbon (CFC) Refrigerant

These are the refrigerants, which contain chlorine, fluorine and carbon. R11, R12, R115, etc. are included in CFC refrigerants [14, 15]. This type of coolant can be used for commercial as well as daily purposes [14]. It was developed in the past—in the 30s—and at that time it was non-toxic, non-flammable and non-reactive [15, 16].

But in the early 70s, it was proved that it is hazardous for the layer of ozone and unfriendly for the environment [16, 17]. The chlorine atom splits the extra oxygen

Cylinder Color		Number	Refrigerant Name	Chemical Composition	General Application
Orange		R-11	Trichlorofluoromethane	CFC	Used in centrifugal chillers for large applications
White		R-12	Dichlorodifluoromethane	CFC	Versatile, widely used in reciprocating and rotary-type equipment; household and industrial applications.
Light blue		R-13	Chlorotrifluoromethane	CFC	Low-temperature refrigerant used in low stage of cascade systems.
Coral		R-13B1	Bromotrifluoromethane	CFC	Medium- to low-temperature applications with one or two stages of compression.
Light green		R-22	Chlorodifluoromethane	HCFC	Residential, commercial, and industrial applications.
Light gray		R-23	Trifluoromethane	HFC	Low-temperature refrigerant to be used as replacement in low stage of cascade system.
Purple		R-113	Trichlorotrifluoroethane	CFC	Low capacity centrifugal chillers.
Dark blue		R-114	Dichlorotetrafluoroethane	CFC	Principally used with chillers for higher capacities.
Light gray		R-123	Dichlorotrifluoroethane	HCFC	Serves as a replacement for R-11 in centrifugal chillers.
Deep green		R-124	Chlorotetrafluoroethane	HCFC	Medium-pressure refrigerant for chiller applications. Used in marine applications.
Medium brown or Tan		R-125	Pentafluoroethane	HFC	Substitute for use in low-temperature refrigeration applications.
Light (sky) blue		R-134a	Tetrafluoroethane	HFC	Medium-temperature refrigerant used in the automobile industry and refrigeration systems in residential, commercial, and industrial applications.
Coral red		R-401A	R-22 + R-152a + R-124	Zeotropic (HCFC)	Substitute for use in most medium-temperature systems.
Mustard yellow		R-401B	R-22 + R-152a + R-124	Zeotropic (HCFC)	Used in transport refrigeration equipment and domestic and commercial refrigerators.
Blue-green (Aqua)		R-401C	R-22 + R-152a + R-124	Zeotropic (HCFC)	Replacement refrigerant in mobile air conditioning.
Pale brown		R-402A	R-22 + R-125 + R-290	Zeotropic (HCFC)	Ice machines, food service, vending, supermarket.
Green-brown		R-402B	R-22 + R-125 + R-290	Zeotropic (HCFC)	Supermarket, transport, food service.
Orange		R-404A	R-125 + R-143a + R-134a	Zeotropic (HCFC)	Medium and low temperature applications.
Light gray-green		R-406A	R-22 + R-142b + R-600a	Zeotropic (HCFC)	Used for R-12 retrofit.
Bright green		R-407A	R-32 + R-125 + R-134a	Zeotropic (HFC)	Used for R-502 retrofit.
Peach		R-407B	R-32 + R-125 + R-134a	Zeotropic (HFC)	Used for R-502 retrofit.
Chocolate brown		R-407C	R-32 + R-125 + R-134a	Zeotropic (HFC)	R-22 replacement
Rose		R-410A	R-32 + R-125	Zeotropic (HFC)	Replacement refrigerant in residential air conditioning applications.
Yellow		R-500	Refrigerants 152a/12	Azeotropic (CFC)	Used with reciprocating compressors in industrial and commercial applications.
Light purple		R-502	Refrigerants 22/115	Azeotropic (CFC)	Supermarket freezers and refrigerated cases.
Aquamarine		R-503	Refrigerants 23/13	Azeotropic (CFC)	Used in low stage of cascade-type systems.
Teal		R-507A	Refrigerants 125/143a	Azeotropic (HFC)	Replacement refrigerant for low-temperature commercial refrigeration applications.
Silver		R-717	Ammonia	Inorganic Compound	Used in large reciprocating compressors and absorption-type systems.

Chlorofluorocarbons = CFC   Hydrofluorocarbons = HFCs   Hydrochlorofluorocarbons = HCFCs

Fig. 1 Colour codes of commonly used refrigerants and their typical applications

atoms in the composition of ozone, and so it is liable for ozone depletion [18]. So, CFCs were banned in the late 80s because of adverse environmental effects [19]. Nowadays, it is estimated that half of the total CFCs have been improved.

R11, R12, R13, R113, R114, R500, R502 and R503 are the top refrigerants covered under the group of CFCs [20]. Some of them are also known for the greenhouse gas effects. These refrigerants are banned (Fig. 3) because of it so high ozone concentration is represent in Fig. 2 to pollutethe environment.

2.3 Hydrochlorofluorocarbon (HCFC) Refrigerant

HCFCs were referred to as the substitute for CFCs. It contains hydrogen, chlorine, fluorine and carbon. Of course, it is not like this group's refrigerants that are not at all affecting the layer of ozone [15, 21, 22], but they affect only around 10%, which is extremely less than the CFCs [14, 22, 23].
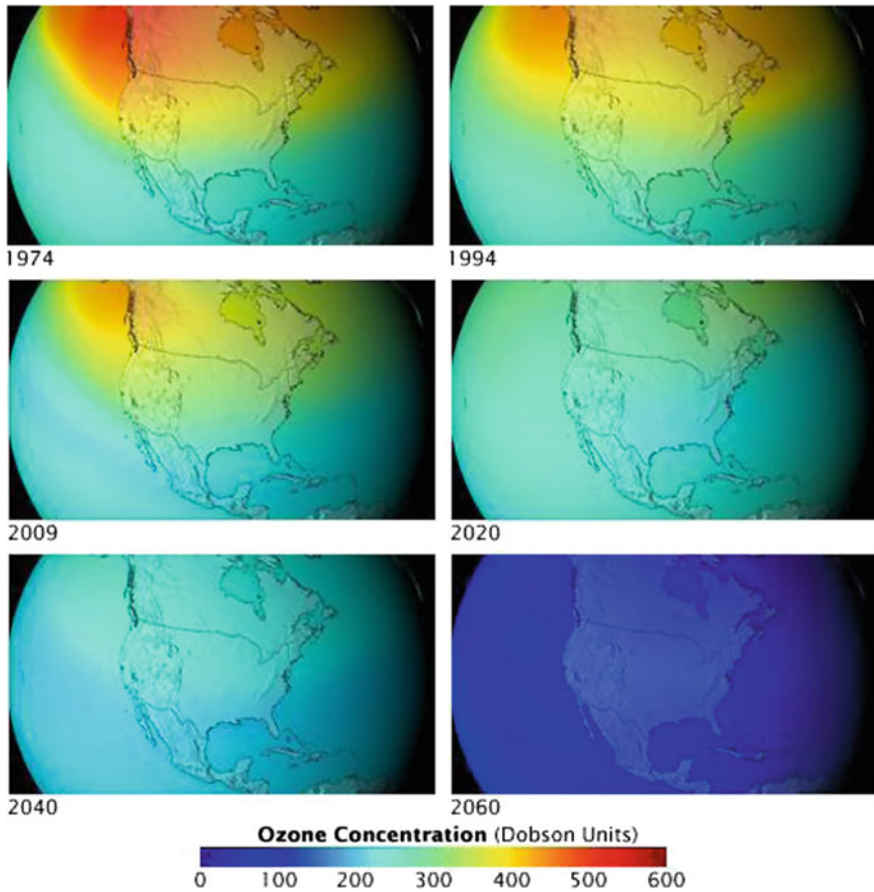
Fig. 2 NASA projection of stratospheric ozone, in Dobson units

HCFCs are non-toxic, cheap and competent [21, 22]. But yes, even if they do not harm the environment much, they are known as greenhouse gases [22, 23]! They can also deplete the ozone slowly, but continuously [18].

R22, R123, R124, R401A, R401B, R402A, R403B, R408A, R409A, R414B and R416A are the refrigerants which are covered under the group of HCFCs (Fig. 4).

2.4 Hydrofluorocarbon (HFC) Refrigerant

These refrigerants do not include any particles of chlorine. So, they are not at all harmful to the environment and do not deplete the ozone layer. But just like any
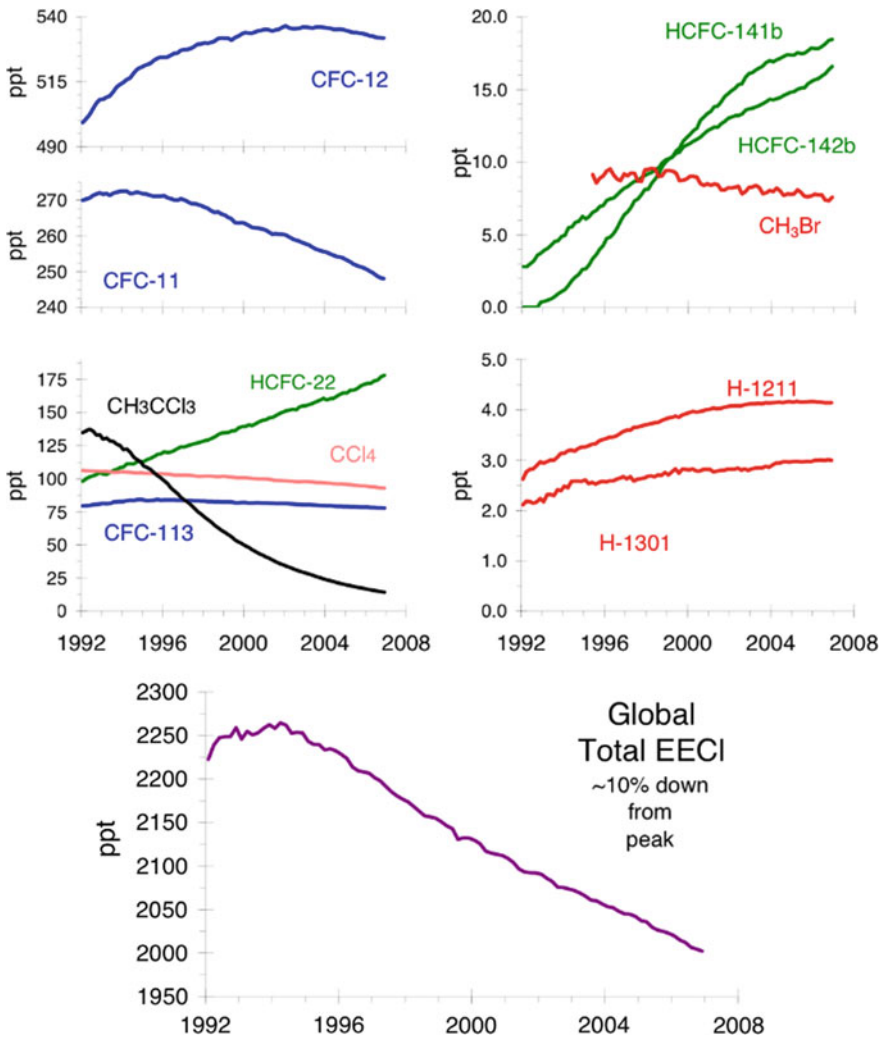
Fig. 3 Ozone-depleting gas trends

other refrigerant, they have some powerful impact on global warming as compared to natural refrigerants [24, 25].

When there was the ban of HCFCs, this group comes in. It includes hydrogen, fluorine and carbon. So, when compared to other refrigerants, it has the lower potential of global warming.

R23, R134a, R404A, R407C, R410A, R417A, R422A, R422B, R422D, R507 and R508B are included in the HFC group. This group of refrigerants is always in demand by refrigerant manufacturers because of its environment suitability [26].

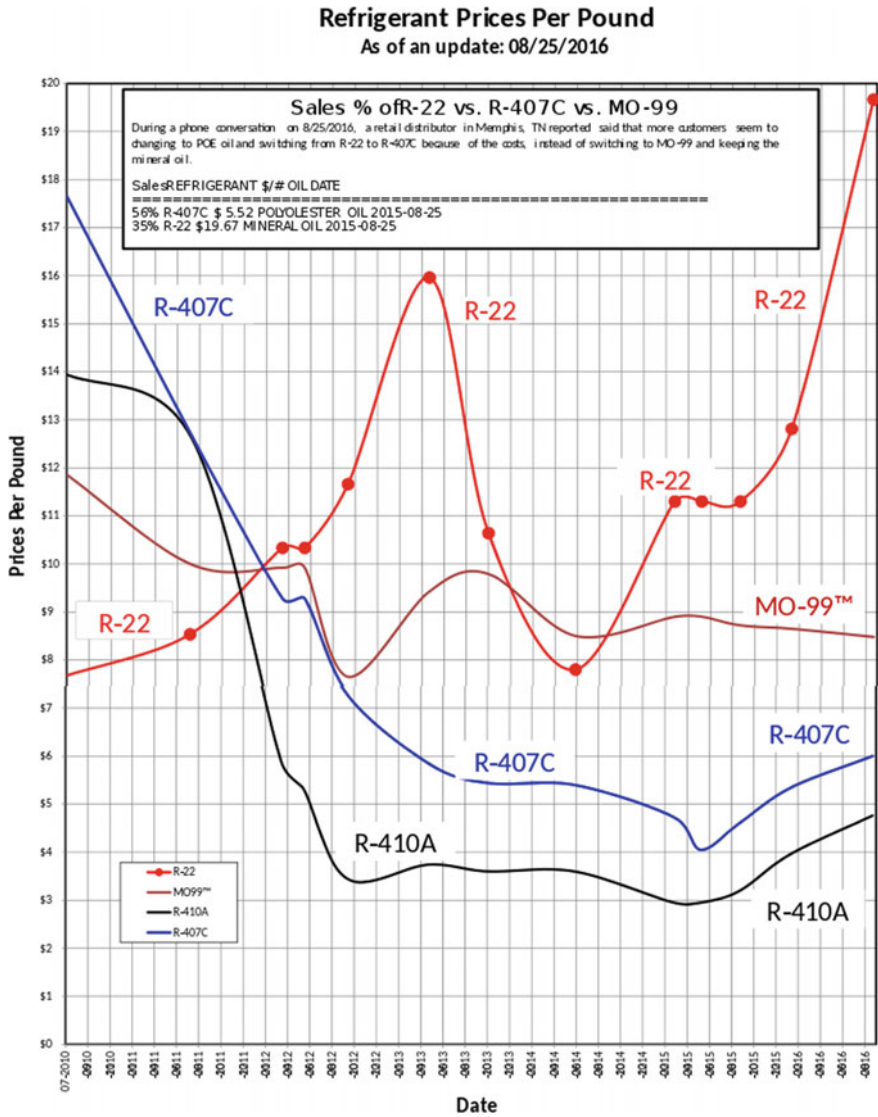**Fig. 4** HCFC price history

2.5 Natural Refrigerants

As the name suggests, natural refrigerants are completely natural. Any men like the other ones do not create them. They do not harm the nature, environment or the ozone layer [15, 16, 22].

Moreover, they are quite inexpensive as compared to other refrigerants. Air, HC, ammonia, CO_2, H_2O, etc. are the examples of natural refrigerants [27]. They have zero ozone depletion potential and negligible effects on global warming.

2.6 Refrigerant Blends (Azeotropic–Zeotropic)

The most recent days' research is being carried over by refrigerant blends, commonly referred as "azeotropic" and "zeotropic" [5]. The use of refrigerant blends is increasing due to its change in temperature and composition in order to attain better cooling effect [22]. The temperature composition and bubble and dew curves of zeotropic refrigerant are given by Figs. 5 and 6, respectively.

3   Future Refrigerant

It is observed that since 1990, there has been the modification in the air conditioning industry. R410a is a superior refrigerant that has discontinued the production of R22 refrigerant [4, 24, 25]. In this post, you will come to know the real difference between R22 and R410a refrigerant [22]. The other name of R22 refrigerant is Freon while Puron is the name given to R410a. Let's discuss the characteristics of R22 and R410a which are different types of refrigerant units so that you can easily make out the comparison between the two units [4, 5].

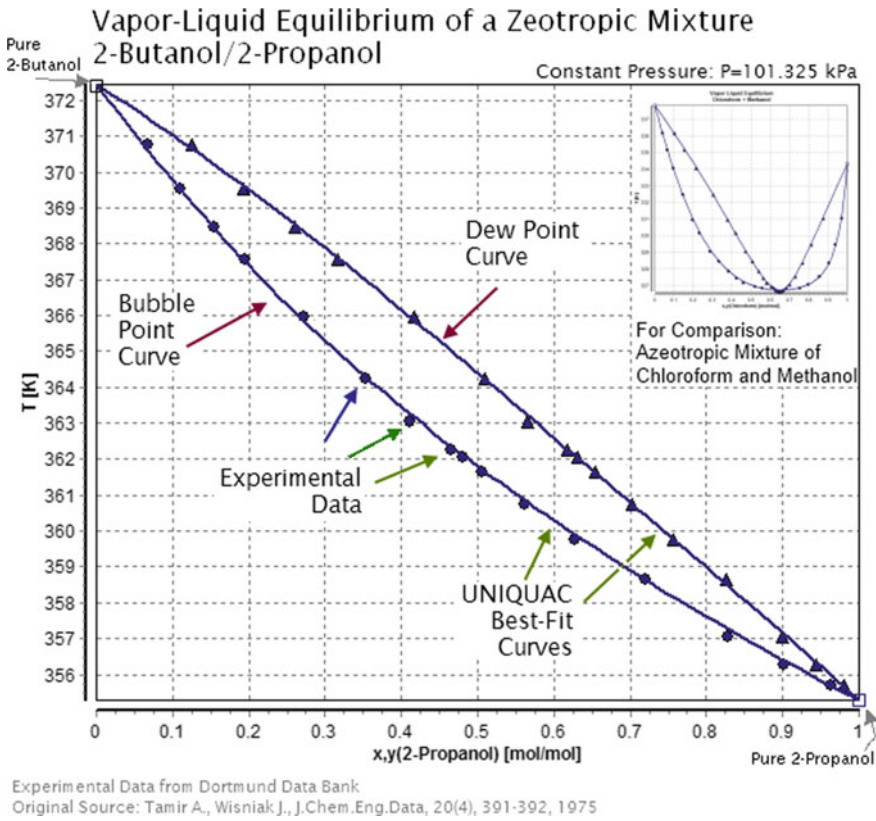**Fig. 5** Temperature composition diagram of a zeotropic mixture
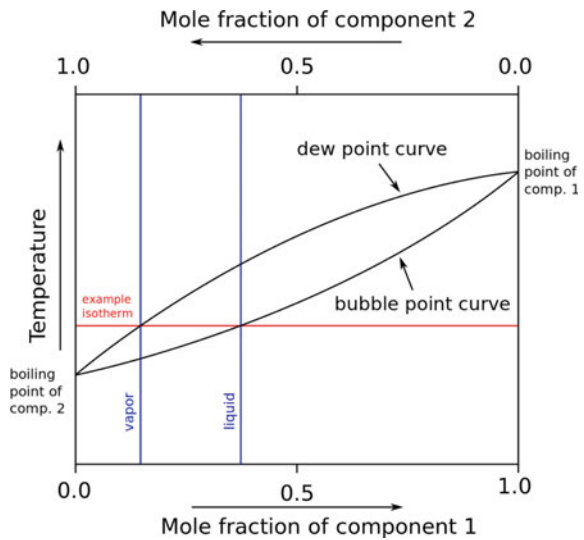
Fig. 6 Bubble and dew curves for zeotropic mixtures

3.1 Comparison Between R22 and R410a

From Table 1, you can make out the real differences of R22 versus R410a efficiency. In comparison with the R22 refrigerant, you will find R410a enjoys significant benefits. Do you know the main reason for the shift from R22 to R410a refrigerant? It is due to the environmental grounds [24–26]. If there is the leakage in the A/C compressors of R22, then it will be proved unsafe to the environment, as it will release HFCF into the air, which will cause greenhouse warming and weakening of ozone layer. For home cooling R410a A/C, compressors are suitable. By going through the R22 versus R410a, the homeowners can make out how R410a unit is resourceful for the usage [28].

In case you possess an R-22 air conditioner, then it would be better you replace it with R410a unit. In this way, you will not only save your environment but can also enjoy efficiency along with safety. You cannot interchange R410 units with R22 units. You will observe declining parts and growing demands of R22 refrigerant

Table 1 R22 versus R410a

R22	R410a
The old type of refrigerant by the brand named Freon	A new type of refrigerant by the brand named Puron
Less energy efficient as it can absorb and release heat in lesser amount	More competent as it can absorb and release heat in efficient manner
Less ecologically friendly	More environmentally friendly
Not used in newly manufactured air conditioners	Suitable for all newly manufactured air conditioners
Contributes to the reduction of ozone layer	No contribution towards the depletion of ozone layer
Its use is phased out, so you will find it more expensive	Avoid the risk of overheating and breaking down due to tougher and durable air conditioner parts

units, so the cost of this appliance is much higher than R410a [29]. The information regarding comparison between these two units will guide you in drawing the clear picture of the two units, which in turn help you in selecting the best suitable unit for efficient and outstanding results [5, 8, 18, 20].

In 2010, there was a ban on the use of R22 in the new air conditioning systems. In 2015, the R410a became the new standard for US residential air conditioning system [4, 12, 14, 20]. The US government intends to have refrigerant that enjoys ozone depletion level of 0, so they recommend R410a unit. It will become illegal to produce R22, and in 2030, there will be complete phase-out of R22 [18, 19].

3.2 R410a Refrigerant

Install the resourceful and cost-effective R410a refrigerant to enjoy productivity, performance and environmental benefits. If the operating life of your refrigerator were coming to an end, then it would be better to get it changed with the R410a refrigerant, which will help you in saving the repairing cost of an R22 refrigerant leak [11]. The long-lasting refrigerator parts are used in R410a unit, which will protect your system from overheating and breaking down. It would be safer to get your refrigerator checked by the HVAC professional who can make use of recovery machine so that you can know the right way to get your system in an appropriate and proper condition.

In the market, you will find that due to the ban on R-22, many retailers promote to "top up" the R22 refrigerant, which will cause damage [10]. Keep yourself alert and careful of false claims for repair and operation retrofitting.

4 Conclusion

Now you can make out how R410a unit is efficient and cools down better than R22. By going through this article, you will gain understanding and knowledge about R22 and R410a refrigerant units [26]. Install R410a unit, which will provide you comfortable and well-organized cooling system. Enjoy the ecologically friendly cooling network with peace of mind.

References

1. Vinoth Kanna, I.: Optimisation of the evaporator of a refrigerator employing hydrocarbon as a refrigerant. Int. J. Ambient Energy 1–8 (2018)
2. Vinoth Kanna, I., Devaraj, A., Subramani, K.: Bio diesel production by using Jatropha: the fuel for future. Int. J. Ambient Energy 1–7 (2018)
3. Wang, X., Jia, L.: Experimental study on heat transfer performance of pulsating heat pipe with refrigerants. J. Therm. Sci. **25**(5), 449–453 (2016)
4. Yoon, J.-I., Choi, K.-H., Lee, H.-S., Kim, H.-J., Son, C.-H.: Assessment of the performance of a natural gas liquefaction cycle using natural refrigerants. Heat Mass Transf. **51**(1), 95–105 (2015)
5. Amooey, A.A.: A new equation for the thermal conductivity of liquid refrigerants over wide temperature and pressure ranges. J. Eng. Phys. Thermophys. **90**(2), 392–396 (2017)
6. Lumpkin, R.: Two-phase injected and vapor-injected compression: experimental results and mapping correlation for a R-407C scroll compressor. Int. J. Refrig. **86**, 449–462 (2018)
7. Nagappan, M., Vinoth Kanna, I.: A novel technique and detailed analysis of cars in Indian roads to adopt low ground clearance. Int. J. Ambient Energy 1–7 (2018)
8. Vinoth Kanna, I., Paturu, P.: A study of hydrogen as an alternative fuel. Int. J. Ambient Energy 1–4 (2018)
9. Khan, M.H.: Conventional refrigeration systems using phase change material: a review. Int. J. Air-Cond. Refrig **24**, 1630007 (2016)
10. Vinoth Kanna, I., Vasudevan, A., Subramani, K.: Internal combustion engine efficiency enhancer by using hydrogen. Int. J. Ambient Energy 1–4 (2018)
11. Choi, J.W., Kim, S., Kang, Y.T.: CO_2 hydrate cooling system and LCC analysis for energy transportation application. Appl. Thermal Eng. **91**, 11–18. Online publication date: 1 Dec 2015 (2015)
12. Vinoth kanna, I., Pinky, D.: Automatic seat level control using MEMS programmed with Lab VIEW. Int. J. Ambient Energy 1–4 (2018)
13. Vinoth Kanna, I.: Modelling and thermal analysis of air-cooling system with fin pitch in IC engines. Int. J. Ambient Energy 1–9 (2018)
14. Bolaji, B.O., Adeleke, A.E., Adu, M.R., Olanipekun, M.U., Akinnibosun, E.: Theoretical investigation of energy-saving potential of eco-friendly R430A, R440A and R450A refrigerants in a domestic refrigerator. Iranian Journal of Science and Technology, Transactions of Mechanical Engineering
15. Blindenbach, W.L., Economou, I.G., Smits, P.J., Peters, C.J., de Swaan Arons, J.: Modeling the thermodynamic properties of CFC and HCFC compounds, and the vapor-liquid equilibria of CFC and HCFC mixtures and CFC/HCFC-hydrocarbon mixtures, with the perturbed anisotropic chain theory (PACT). Fluid Phase Equilib. **97**, 13–28 (1994)
16. Storms, W.: Double-blind, placebo-controlled study of single doses of chlorofluorocarbon (CFC) and CFC-Free cromolyn sodium for exercise-induced bronchoconstriction. Curr. Ther. Res. **60**(12), 629–637 (1999)

17. Chang, W.-K., Criddle, C.S.: Biotransformation of HCFC-22, HCFC-142b, HCFC-123, and HFC-134a by methanotrophic mixed culture MM1. Biodegradation **6**(1), 1–9 (1995)
18. Lee, J.H., Jung, C.W., Chang, Y.S., Chung, J.T., Kang, YT.: Nu and Sh correlations for LiCl solution and moist air in plate type dehumidifier. Int. J. Heat Mass Transf. **100**, 433–444. Online publication date: 1 Sept 2016 (2016)
19. Paturu, P., Vinoth kanna, I.: Experimental investigation of performance and emissions characteristics on single-cylinder direct-injection diesel engine with PSZ coating using radish biodiesel. Int. J. Ambient Energy 1–10 (2018)
20. Boumedienne, B.M., Ouadha, A., Addad, Y.: Thermodynamic analysis of hydrocarbon refrigerants-based ethylene BOG re-liquefaction system. J. Mar. Sci. Appl. **15**(3), 321–330 (2016)
21. Okada, M., Higashi, Y.: Experimental surface tensions for HFC-32, HCFC-124, HFC-125, HCFC-141b, HCFC-142b, and HFC-152a. Int. J. Thermophys. **16**(3), 791–800 (1995)
22. Li, P., Mühle, J., Montzka, S.A., Oram, D.E., Miller, B.R., Tanhua, T.: Global annual mean atmospheric histories, growth rates and seawater solubility estimations of the halogenated compounds HCFC-22, HCFC-141b, HCFC-142b, HFC-134a, HFC-125, HFC-23, PFC-14 and PFC-116. Ocean Sci. Discuss. 1–51
23. Kutsuna, S.: Determination of rate constants for aqueous reactions of HCFC-123 and HCFC-225ca with OH along with Henry's Law Constants of Several HCFCs . Int. J. Chem. Kinet. **45**(7), 440–451 (2013)
24. Beshr, M., Aute, V., Abdelaziz, O., Fricke, B., Radermacher, R.: Potential emission savings from refrigeration and air conditioning systems by using low GWP refrigerants. Int. J. Life Cycle Assess. **22**(5), 675–682 (2017)
25. Li, W., Bi, S., Zhao, G., Wu, J.: An improved prediction equation of refrigerants surface tension based on the principle of corresponding states. Chem. Res. Chin. Univ. **30**(4), 681–684 (2014)
26. Wang, F., Shen, S.Q., Li, D.Y.: Evaluation on environment-friendly refrigerants with similar normal boiling points in ejector refrigeration system. Heat and Mass Transf. **51**(7), 965–972 (2015)
27. McLinden, M.O., Steven Brown, J., Brignoli, R., Kazakov, A.F., Domanski, P.A.: Limited options for low-global-warming-potential refrigerants. Nat. Commun. **8**, 14476 (2017)
28. Chopra, K., Sahni, V., Mishra, R.S.: Thermodynamic analyses of multiple evaporators vapor compression refrigeration systems with R410A, R290, R1234YF, R502, R404A, R152A AND R134A. Int. J. Air-Cond. Refrig. **22**, 1450003 (2014)
29. Brown, J.S., Zilio, C., Cavallini, A.: The fluorinated olefin R-1234ze (Z) as a high-temperature heat pumping refrigerant. Int. J. Refrig. **32**(6), 1412–1422 (2009)

Analysis of Dynamic Probing Errors in Measuring Machines

Aitha Sudheer Kumar and C. Chandrasekaran

1 Introduction

CMM scanning probes have become a standard in coordinate metrology. It is because of the high quantity of data rapidly gathered while probing and also due to scanning technology, inspection time decreases significantly. Especially in highly competitive economic conditions, there is always a need for more efficient measuring machine and processes, because the inspection time often becomes the limiting factor in the whole manufacturing cycle. More efficiency in coordinate metrology leads to faster cycles of measurement with acceptable accuracy.

In any industry, the dimensional accuracy has major importance, as the components that are manufactured should be within the specified tolerance limits. Especially in the automotive and aerospace industries, it enables easy in measuring complex shapes and the geometrical points of the components to be in tight tolerance limits. Coordinate measuring machine has become essential for inspection of parts in many industries.

It is always difficult to inspect the complex geometrical component with conventional standard measuring equipment, to make sure the products exactly meet the specified tolerances; CMM machines are widely used in manufacturing plants. The probing system is one of the most important elements of the CMM, through which the machine contacts the specimen or workpiece (Fig. 1).

Evaluation of measurement uncertainties in CMM remains difficult; it is mainly due to the complexities of the machine with many error sources that are affecting the accuracy.

Many factors have been identified as the sources of measurement errors and uncertainties; one of the most important sources is probe system which has high influence on the measurement. Probe pre-travel variation is a significant error which

A. S. Kumar (✉) · C. Chandrasekaran
IIITD&M Kancheepuram, Chennai, India
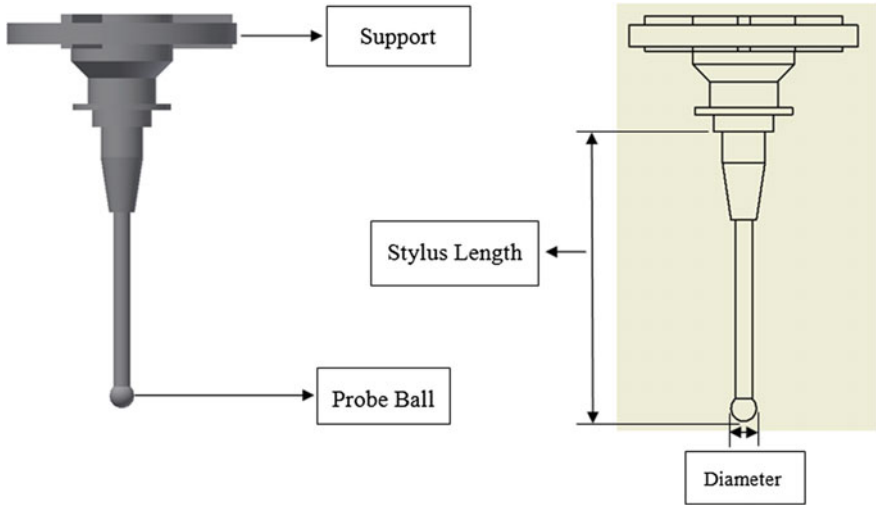e-mail: mds15m001.ccs@iiitdm.ac.in

473

Fig. 1 CAD model of the probe system

has been widely discussed in the literature, and various methods have been proposed to reduce the probing errors.

Probing errors are prone to dynamic errors during measurement on the measuring machines, and hence, it is necessary to analyse these errors. The major parameters that are affecting the metrological accuracy are mentioned below:

1. Length of the stylus and probe diameter.
2. Geometrical and material characteristics of the probe system.
3. Measuring speed and direction.

2 Model Construction

Finite element analysis software (ANSYS) has been used for analysing the errors which are occurring due to length of the stylus, probe diameter, measuring direction, measuring speed, geometrical and material characteristics.

The design of the probe system has been created using the Autodesk Inventor software, and material properties were defined individually for the probe ball, stylus and support which are mentioned in Table 1.

Then the minimum force required for generating the signal between the tripods and probe holder is applied on the ruby/silicon nitride/zirconia ball at the equator position (Fig. 2).

Table 1 Details of the material properties for the stem, probe ball and other modules

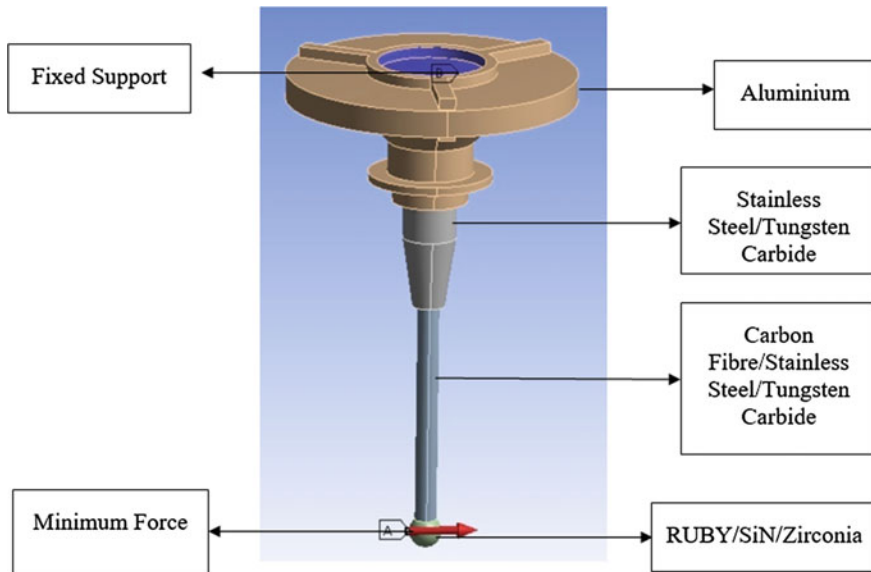| Material	Density (kg/m^3)	Young's modulus (GPa)	Poisson ratio
Ruby (ball)	3860	367	0.25
Silicon nitride (ball)	3150	288	0.26
Carbon fibre (stem)	1800	225	0.2
Aluminium (extension)	2670	69	0.32
Stainless steel (stem)	7850	203	0.275
Zirconia (ball)	6030	141	0.28
Tungsten carbide (stem)	1530	600	0.2

Fig. 2 Boundary conditions and material properties defined in the FEA software

3 Results and Discussions

The stem lengths and probe diameters considered for the analyses are mentioned in Table 2.

3.1 Analysis with Different Probe Ball Materials

The analysis was carried out initially by changing the materials of the probe ball like ruby, silicon nitride and zirconia by keeping the stem and other modules as

Table 2 Details of various probe lengths with probe ball diameter—3 and 5 mm

Probe length (mm)	Probe ball diameter (mm)	Stem diameter (mm)	Probe length (mm)	Probe ball diameter (mm)	Stem diameter (mm)
20	3	2	33	5	4
30	3	2	50	5	4
33	3	2	75	5	4
40	3	2	100	5	4
50	3	2	150	5	4

same material for different probe lengths. It is observed from Figs. 3 and 4 that probe ball diameter has negligible effect in the deflection of the probe.

3.2 Analysis with Different Stem Materials

The analysis is carried out by changing the stem materials like stainless steel, carbon fibre, tungsten carbide for different probe lengths. It is observed from Figs. 5 and 6 that stem materials and stem length have major effect on the probe system.
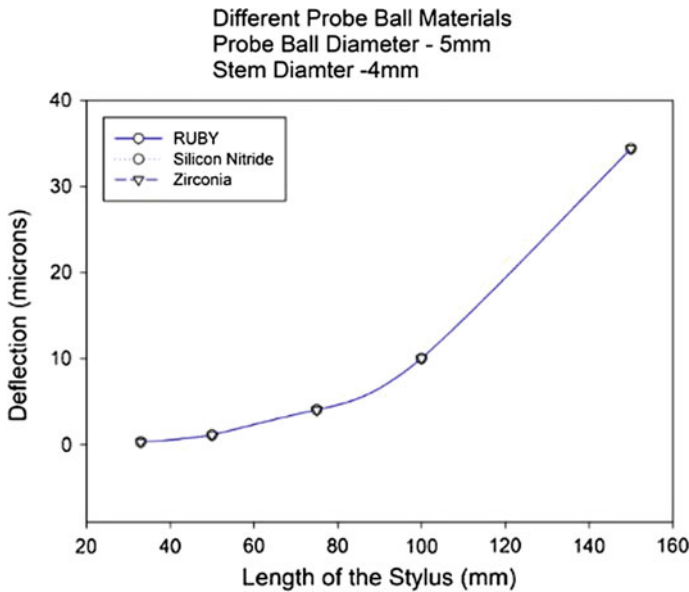

Fig. 3 Deflections of the probe due to change in probe ball material (33–150 mm)
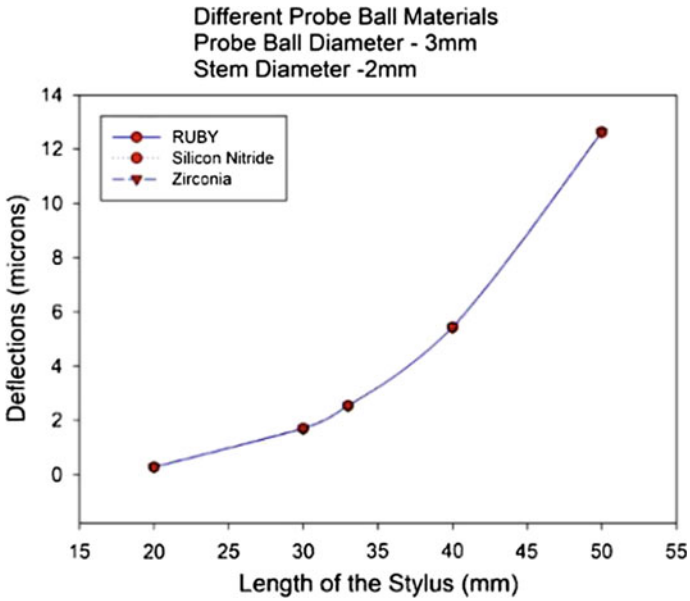
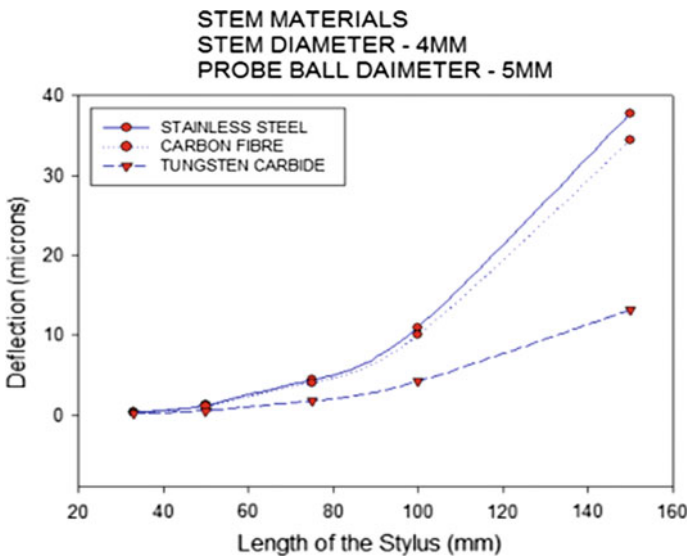**Fig. 4** Deflections of the probe due to change in probe ball material (20–50 mm)

Fig. 5 Deflections of the probe due to different stem materials (33–150 mm)
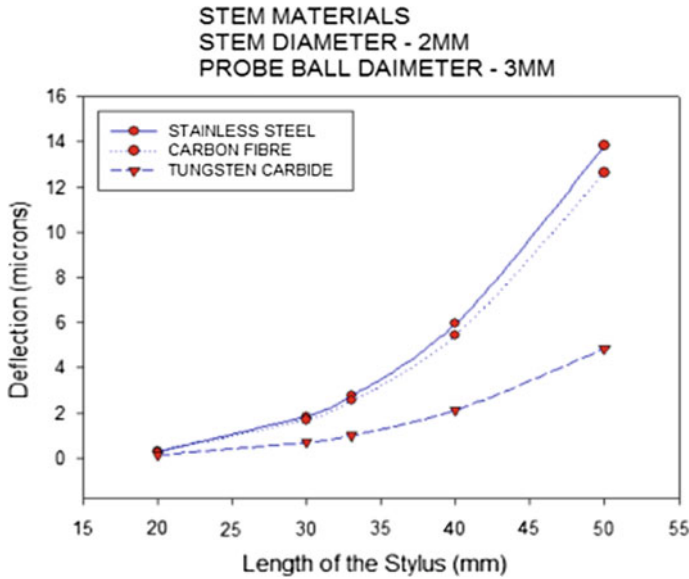
Fig. 6 Deflections of the probe due to different stem materials (20–50 mm)

3.3 Mathematical Expression for Different Stem Materials

From Figs. 5 and 6, the deflection of the probe increases proportional to the increase in stem length. The deflections observed in the probes follow a cubic spline for both stem diameter and different stem material. To obtain a best fit curve, the analysis was made on different stem lengths between 20–50 mm and 33–150 mm, with an increment of 5 mm stem length. It has been observed from Figs. 7, 8, 9, 10, 11 and 12 that curves follow cubic spline which can be represented as a third-degree polynomial equation.

The cubic spline is a third-degree polynomial having the following equation:

$$y = y_o + ax + bx^2 + cx^3$$

where y_o, a, b, c will depend on the stem diameter and stem material.

Fig. 7 Deflections of the probe with carbon fibre stem material follow a cubic spline curve (33–150 mm)
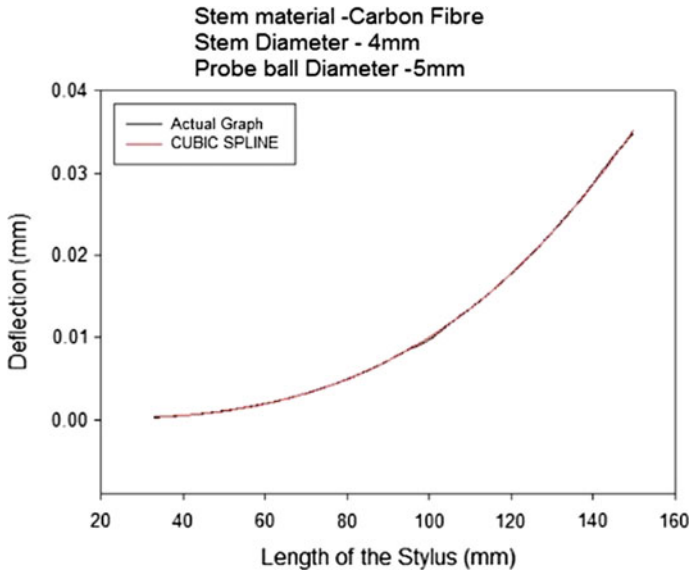

Fig. 8 Deflections of the probe with carbon fibre stem material follow a cubic spline curve (20–50 mm)

Fig. 9 Deflections of the probe with stainless steel stem material follow a cubic spline curve (33–150 mm)
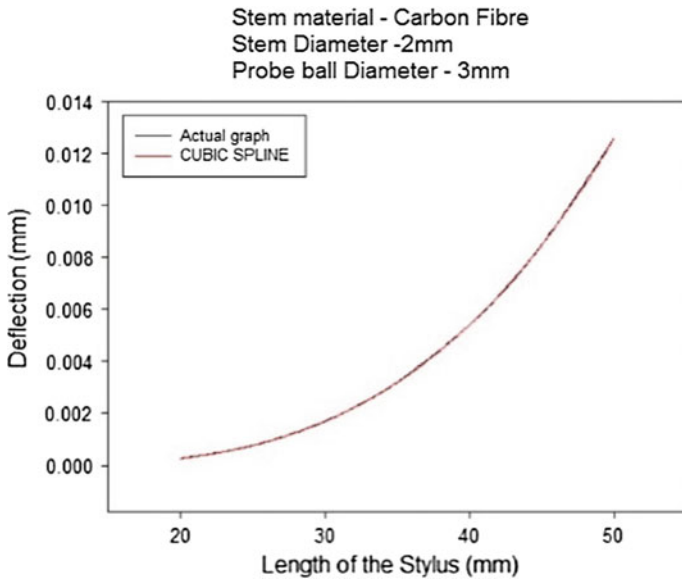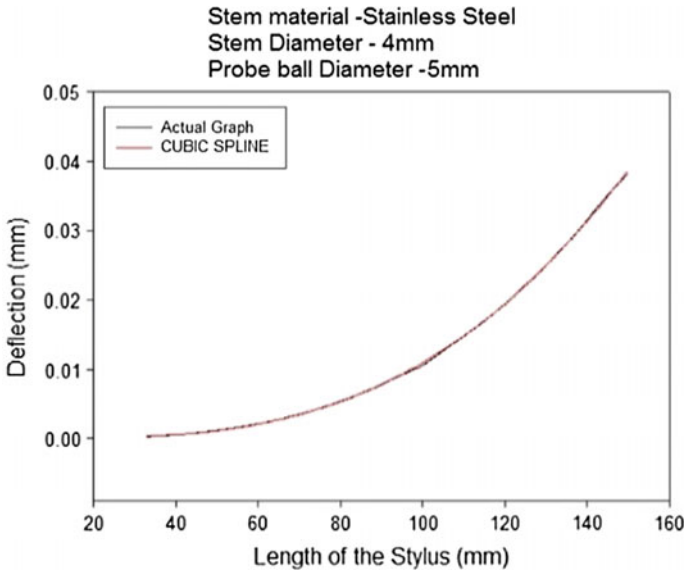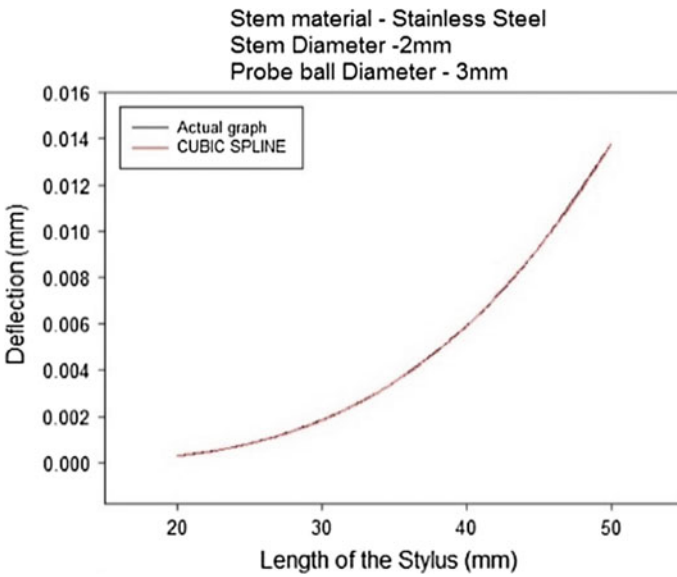

Fig. 10 Deflections of the probe with stainless steel stem material follow a cubic spline curve (20–50 mm)
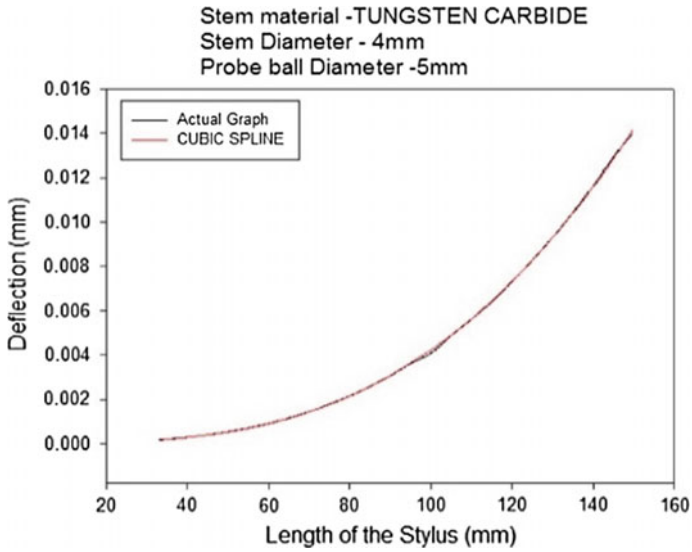
Fig. 11 Deflections of the probe with tungsten carbide stem material follow a cubic spline curve (33–150 mm)
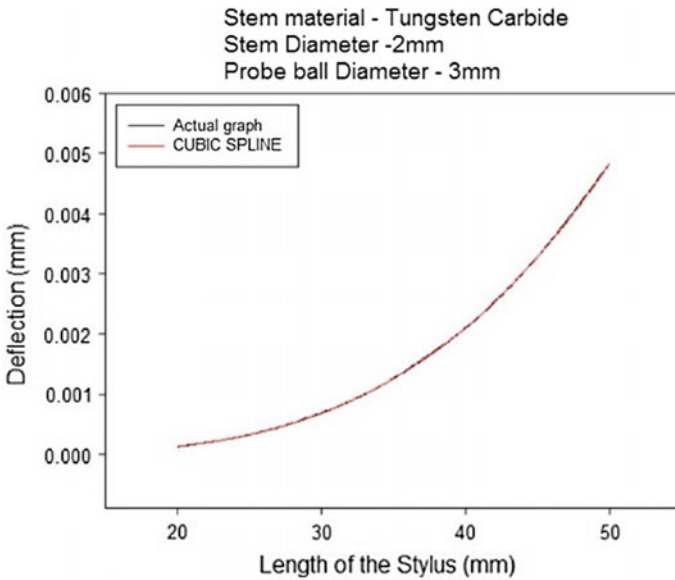
Fig. 12 Deflections of the probe with tungsten carbide stem material follow a cubic spline curve (20–50 mm)

4   Conclusions

In Sect. 3.2, it is clearly observed that the length of the stylus and the stem material have major impact on the probe behaviour.

It is observed from Sect. 3.3, deflections of the probes follow the cubic spline curve for both stem diameter and three stem materials.

From the above results it is observed as probe ball diameter and the probe ball material have no major effect on the probe system.

References

1. Zhao, B., Feng, G., Yan, L., Lijun, F.: Study on pre-travel anisotropic characteristic of touch trigger probe and its calibration method. In: 2015 IEEE 12th International Conference on Electronic Measurement & Instruments
2. da Silva, V.N.: Simulation and analysis of touch trigger stylus performance. In: ABCM Symposium Series in Mechatronics, vol. 5, ABCM (2012)
3. Krajewski, G., Woźniak, A.: Simple master artefact for CMM dynamic error identification. Precis. Eng. (2013)
4. Morse, E.P., Farooqui, S.A.: Alternative artefacts for evaluating scanning CMM performance. In: Proceedings of the ASPE 2003 Annual Meeting

Thrust Prediction Model for Varying Chamber Pressure for a Hypergolic Bipropellant Liquid Rocket Engine

P. Arun Kumar, C. Rajeev Senan, B. Ajith and Aishwarya Shankhdhar

1 Introduction

The thrust prediction for an engine becomes more vital when engine has been designed to be used for throttling purpose. The exact quantification of thrust of the engine becomes an absolute necessity. The demonstration of throttling and that too with multiple engines requires more accurate thrust prediction for all engines for smooth conduct of operations. This calls for the need of extensive simulations and hot tests in order to build confidence and reliability. This imparts the impetus for the development of a comprehensive model for the prediction of thrust. Toward this, a simplified model is developed. The model can be used to calculate the thrust for determining the profile in the ground simulation tests. This model eliminates the requirement for exhaustive hot tests of each engine to predict the thrust.

2 Methodology

The variation in thrust of an engine is achieved by altering the injection feed pressure. This causes change in the chamber pressure. The model calculates the thrust for different chamber pressures obtained by tweaking the injection pressures upstream keeping the ambient conditions same. The thrust calculated by the model is validated by the thrust measured with the help of load cells incorporated in test facility.

P. Arun Kumar (✉) · C. Rajeev Senan · B. Ajith · A. Shankhdhar
Spacecraft Propulsion Engines Group, Liquid Propulsion Systems Centre,
Valiamala, Trivandrum 695547, India
e-mail: arun_uthradom@yahoo.co.in

2.1 Test Setup

The test setup schematic for the fuel side feed is detailed in Fig. 1. Similar arrangement is employed for the oxidizer side as well. The test setup with thrust measurement fixture is shown in Fig. 2. The test was carried out on sea level version engine.

The test setup consists of a propellant tank pressurized externally by nitrogen gas at the required pressure. The metered quantity of propellants is fed into the engine through a filter. The amount of propellant flow is measured using a mass flow meter. The chamber pressure developed in the engine chamber is measured using pressure transducer, while the injection pressures are measured using transmitters. The thrust is measured using a tensile-type load cell. The accuracy and range of the sensors are as listed in Table 1.

2.2 Model Formulation

The details of model developed for predicting the thrust are dealt in this section. The thrust values are predicted at different thrust levels from 100 to 50%.

The thrust is computed from the first principles using steady flow energy equation for gas flows in nozzles with assumptions [1]. The separation point for the flow detachment from the nozzle wall is calculated. The different thrust levels have different point of separation which is quantified by Summerfield criteria [2],

$$P_s = 0.4 \, P_a \tag{1}$$

With the relation between area ratio and pressure ratio, P_e/P_c
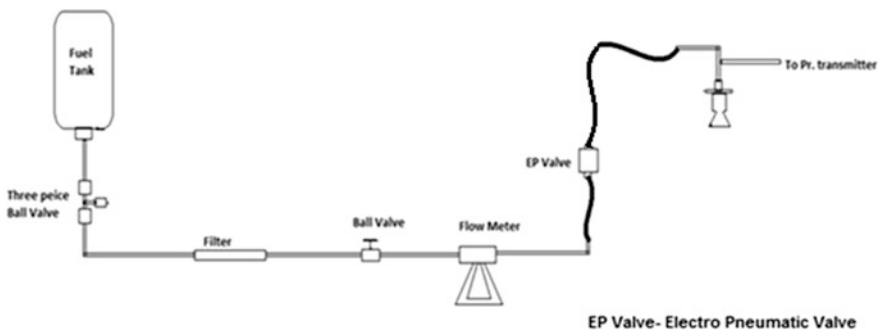
Fig. 1 Test setup schematic for fuel side alone (similar for the oxidizer side)
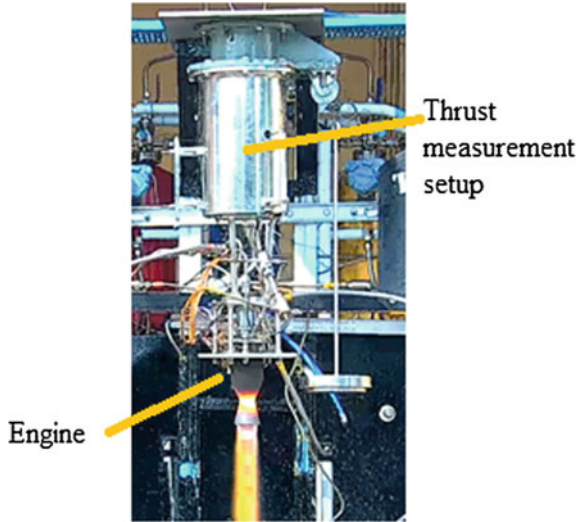
Fig. 2 Test setup with thrust measurement system

Table 1 Accuracy and range of sensors employed

Sl. no.	Parameter	Range	Nominal value	Accuracy (including the chain) (%)
1.	Combustion chamber pressure (bar)	0–10	8.6	±0.7 of full scale
2.	Propellant injection pressure. Valve inlet (bar)	0–30	18	±0.5 of full scale
3.	Flow rates (g/s)	0–200	120–190	±0.5 of full scale
4.	Thrust (kgf)	0–110	60	±0.4 of full scale

$$\frac{A_e}{A_t} = \frac{\left(\frac{2}{\gamma+1}\right)^{\frac{1}{\gamma-1}} * \left(\frac{\gamma-1}{\gamma+1}\right)^{0.5}}{\left(\frac{P_e}{P_c}\right)^{\frac{1}{\gamma}} * \left[1 - \left(\frac{P_e}{P_c}\right)^{\frac{\gamma-1}{\gamma}}\right]^{0.5}} \tag{2}$$

Taking $P_e \sim P_s$ and γ value from NASA CEA program [3], the above relation gives area ratio at the separation point for different thrust regimes. The area ratio derived through above relation for different thrust levels is tabulated in Table 2.

Table 2 Separation point at different thrust levels

% Thrust	Area ratio of separation	Separation point distance from tip (mm)
100	3.65	5.21
90	3.39	8.50
80	3.13	12.13
70	2.85	16.29
60	2.58	20.53
50	2.29	25.41

Using the area ratio, the exit area at different thrust levels can be deduced for the known throat diameter.

The thrust is obtained by the typical rocket equation [4]

$$
\begin{aligned}
F &= \dot{m}V_e + (P_e - P_a)A_e \\
&= C_f P_c A_t
\end{aligned}
\tag{3}
$$

This equation has well covered the thrust amplification factor and chamber pressure. As we know, with the variation in chamber pressure P_c the thrust amplification factor C_f also changes; hence, for calculating the thrust, using the above equation requires following inputs,

$\dot{m}$, can be deduced for different thrust regimes from the choked flow condition;
V_e, can be calculated from isentropic relations;
P_e, is taken from the Summerfield criterion.

3 Results and Discussion

The model is used to predict the thrust at different chamber pressures from the first principles which is further based on hot tests with thrust measurement. The results are detailed below.

3.1 Generation of Thrust Equation

The aim of the model is to compute the thrust with sole dependence on chamber pressure. As discussed earlier thrust depends on both C_f and P_c, the model gives thrust values with P_c as the only input. The thrust equation generated by the model incorporates the effect of thrust amplification factor C_f. A second-degree polynomial curve fit is arrived at between thrust and P_c as shown in Fig. 3.
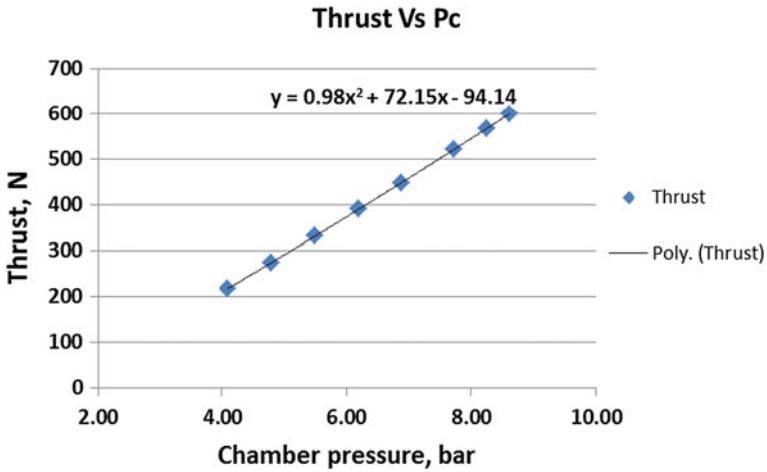
Fig. 3 Thrust versus chamber pressure

3.2 Thrust Measurement for Validation of Model

The primary objective of tests conducted is to measure the thrust values at different range of chamber pressures (P_c) and vet the same with the predicted thrust values. A series of 10 s tests at a mixture ratio of 1.55 were conducted on a sea level engine to measure the thrust at different P_c values.

For each test, thrust is measured using load cell, and the same has been compared with the computed thrust values from the model. The prediction and measured thrust values have shown a good match, and maximum deviation was found to be approximately 3% at full percentage thrust. This may be due to the difference in point of separation predicted and actual as it has minor dependence on nozzle surface finish which is not taken into account. The results are shown in Table 3.

Table 3 Prediction versus experiment results

Sl. no.	Percentage thrust	Predicted thrust (N)	Measured thrust (N)	Deviation (%)
1.	100.00	600.61	619.82	3.10
2.	96	566.91	584.5	3.01
3.	90	522.14	537.29	2.82
4.	80	448.64	460.29	2.53
5.	72	390.86	398.89	2.01
6.	64	332.33	337.30	1.47
7.	56	274.76	277.34	0.93
8.	50	218.15	218.98	0.38

4 Conclusion

A simplified model is developed to predict the thrust of the engine in sea level conditions. Modularization of the model makes it versatile irrespective of the facility where the engine is being tested.

The model can be used to generate the inputs for all throttling tests wherein the thrust prediction is indispensable. The model was validated using hot test results. The results are found to be in close agreement with the predicted performance, and maximum error is found to be 3%.

Nomenclature

C_f Thrust amplification factor (–)
A_e Area at the nozzle exit (m^2)
A_t Area of throat (m^2)
$\dot{m}$ Total mass flow rate (kg/s)
P_a Ambient pressure (bar)
P_e Pressure at the exit of nozzle (bar)
P_c Chamber pressure (bar)
P_s Pressure at the point of separation (bar)
V_e Velocity at the exit (m/s)
γ Specific heat ratio (–)

References

1. Sutton, G.P., Biblarz, O.: Rocket Propulsion Elements. John Wiley & Sons Inc, New York (2001)
2. Summerfield, M., Foster, C., Swan, W.: Flow separation in over-expanded supersonic exhaust nozzles. Jet Propulsion **24**(9), 319–321 (1954)
3. Gordon, S., Mcbride, B.J.: Computer Program for Calculation of Complex Chemical Equilibrium Composition, Rocket Performance, Incident and Reflected Shocks and Chapman-Jouguet Detonation, NASA SP 273
4. Huzel, D.K., Huang, D.: Design of Liquid Propellant Rocket Engine NASA SP 125

Experimental Studies on Different Proportions of CB-Filled Natural Rubber Composites with Precipitated Silica and Silica Gel

V. Chandran, N. Lenin, T. Maridurai, P. Jawahar, G. Vignesh and K. Sunil

1 Introduction

Natural rubber (NR) is used extensively in many applications as predominant products. It is normally very stretchy and flexible and extremely waterproof. Rubber's ability to have excellent tensile properties makes ideal for many rubber applications [1]. Generally, conventional fillers like silica or carbon black are added into the rubber approximately 13–17% of the filler to achieve the desired reinforcing strength/effect [2]. The carbon black (CB) is one of the most important classical reinforcing fillers, especially for the rubber technology for cheaper NR gum and new materials are also considered as fillers for rubber characteristics needed in the industry and one of the important parameters for the performance of a composite materials is the degree of adhesion of the matrix filler interface [3, 9]. The physical properties of the carbon nanotube (CNT)-reinforced NR showed that a considerable improvement when compared with NR/CB compounds and NR gum and also shows better rebound resilience and dynamic compression properties [4–6]. The addition of reinforcing fillers increases tear strength, modulus, tensile strength, and abrasion resistance of NR composite, and the dispersion state of filler determines the final properties of the rubber composites [7]. In addition, silica (Si) leads to long processing time, high energy consumption, and environment pollution during processing. Therefore, it is quite an urgent issue for researchers to find some new filler material/hybrid fillers which can overcome the aforesaid

V. Chandran (✉) · G. Vignesh · K. Sunil
Department of Automobile Engineering, Velammal Engineering College, Chennai, India
e-mail: chandran1979mt@gmail.com

N. Lenin
Vel Tech Rangarajan Dr. Sagunthala R&D Institute of Science and Technology,
Chennai 600062, India

T. Maridurai · P. Jawahar
Department of Production Engineering, Velammal Engineering College, Chennai, India

489

shortcoming and partially replace silica applications in rubber [8]. The SiC particles/natural rubber shows good physical properties compared to SWNT/natural rubber, which confirms the importance of silica addition [9]. Precipitated silica with particle size equivalent to that of carbon black and is used to make high-quality rubber composites [10]. The earlier investigators have not considered silica gel as a filler material into the NR compounds for their studies. The main purpose of this study is to investigate and compare the performance of natural rubber composites through physical properties on CB–silica and CB–silica gel.

2 Experimental Procedure

2.1 Materials and Compound Preparation

In this work, the following materials were used to make rubber compounds. Natural rubber, grade RMA 1X was used. Precipitated Silica, Silica gel and HAF Carbon black (N330) were used as filler materials. Silica gel crushed into fine particles (400–600 μm) by using physical stirrer. Curing accelerators such as sulphur, tetra methyl thiuram disulphide (TMTD), zinc acid, aromatic oil, stearic acid are used for processing in the rubber industry. Rubber compounds were prepared in an open two-roll mill at room temperature (28 °C). Initially, natural rubber was placed to the two-roll-mill machine which pressed and then transformed into a thin and smooth rubber sheet round one of the rolls. The operating parameters followed as two roll mills rotation 40 rpm, processing duration 4-5 min, nip gap 1.5 mm. The sequence of ingredients was provided the same for all the compounds. The natural rubber compound ratio and ingredients were followed based on the data given in Table 1. Natural rubber composite (NRC) samples were made for six proportions in terms of CB/silica and CB/silica gel loading ranges 0, 10, 20, 30, 40, 50 in phr. After processing two-roll-mill techniques, the rubber compounds were put into the button and flat rubber sheet die kit. The rubber compounds' die kit is subjected to the hydraulic press with the cup at the centre of the bottom platen. The rubber compounds were subjected to the following conditions for curing: temperature 160 °C and pressure 12.95 MPa in an electrically heated hydraulic press for a duration of 3 min.

2.2 Testing of Physical Properties

Tensile properties' tests and tear test were performed at room temperature on a universal testing machine (INSTRON 3382) at the cross-head speeds of 550 mm/min. The dumb-bell and crescent-shaped specimens were prepared according to ASTM D-412 and ASTM D-624, respectively. Button-shaped specimens were tested for hardness by Durometer (DURO TECH, model M202) shore hardness tester according to ASTM D-2240.

Table 1 Natural rubber composite formulation

Name of sample	Ingredients (phr)											Name of rubber composite
	NR	P. Si	Silica gel	CB	ZnO	Aromatic oil	Stearic acid	CZ Acc.	TMTD	Sulphur	B rods anti-oxidants	
O	100	–	–	–	5	3	2	0.9	0.3	2.5	1	NR gum
O1	100	20	–	–	5	3	2	0.9	0.3	2.5	1	Composite material-1
P1	100	20	–	10	5	3	2	0.9	0.3	2.5	1	
P2	100	20	–	20	5	3	2	0.9	0.3	2.5	1	
P3	100	20	–	30	5	3	2	0.9	0.3	2.5	1	
P4	100	20	–	40	5	3	2	0.9	0.3	2.5	1	
P5	100	20	–	50	5	3	2	0.9	0.3	2.5	1	
O2	100	–	20	–	5	3	2	0.9	0.3	2.5	1	Composite material-2
Q1	100	–	20	10	5	3	2	0.9	0.3	2.5	1	
Q2	100	–	20	20	5	3	2	0.9	0.3	2.5	1	
Q3	100	–	20	30	5	3	2	0.9	0.3	2.5	1	
Q4	100	–	20	40	5	3	2	0.9	0.3	2.5	1	
Q5	100	–	20	50	5	3	2	0.9	0.3	2.5	1	

2.3 Morphological Study

Scanning electron microscope (SEM)—model Zeiss SUPRA 35VP FESEM was used to study the fracture surface of natural rubber composites 1 and 2. All the samples were applied sputter coating with gold before being scanned to avoid poor resolution of images.

3 Results and Discussion

3.1 Physical Properties

Normally, five samples (S_1, S_2, S_3, S_4, S_5) were undergone for testing and average value was recorded for each proportion of sample and these are represented in Table 2. These average physical properties values are used to plot the following graphs. Figure 1 showed that the tensile strength gradually increased up to 40 phr of CB, and later on decreased for composite material-1. It was due to the incorporation of CB into rubber matrix and filling the pores on CB surface to create strong adhesion with Si–rubber matrix and thus eventually increasing value of tensile strength. Further increase of the CB resulted in the diminution of the interfacial adhesion between Si and CB. The same phenomena observed in composite material-2, but comparatively low values. It was due to coarse form of silica gel not bonding with the natural rubber compounds. Generally, conventional fillers

Table 2 Physical properties of NR–CB with Si/Si gel compounds

Name of samples	Tensile strength (MPa)	Elongation @ break (%)	Stress @ 100% elongation	Tear strength	Hardness
O	20.03	716	0.49	4.51	50
O1	27.77	719	0.96	5.42	51
O2	21.2	719	0.76	4.13	56
P1	29.5	651	1.00	5.54	57
P2	31.0	632	1.30	5.83	60
P3	32.2	596	1.58	5.12	62
P4	32.9	571	1.75	4.81	60
P5	26.3	572	1.80	4.35	56
Q1	23.6	734	1.17	3.91	58
Q2	26.1	732	1.66	3.40	59
Q3	24.9	696	2.13	3.13	61
Q4	22.3	671	2.25	2.90	63
Q5	19.7	622	2.35	2.63	65

Fig. 1 Tensile strength variation with CB–Si/CB–Si gel loading in NR matrix
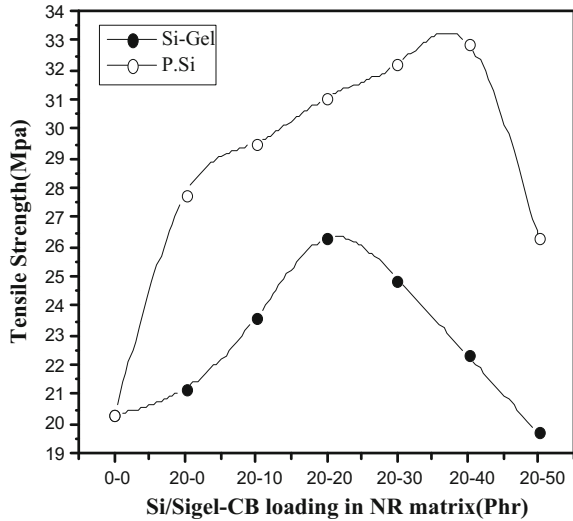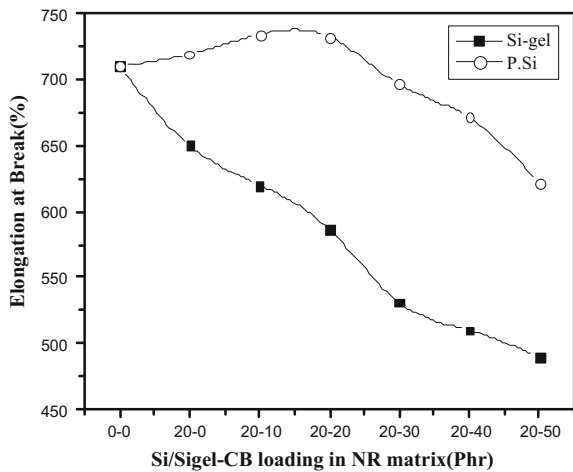

Fig. 2 Elongation at break variation with CB–Si/CB–Si gel loading in NR matrix

like silica or carbon black partial filled in NR matrix to achieve the desired reinforcing strength/effect, which was recorded by Hrachovi et al. [2].

Figure 2 showed that elongation at break (%) slightly increased and then decreased with the increasing of the CB loading. It was due to its reinforcement effect of CB porous surface. Therefore when the rubber–Si matrix filled the pores on CB surface, it probably hindered the elongation of the rubber compounds for composite material-1. A similar observation had been reported by Ismail et al. [5].

The same phenomena observed in composite material-2, but comparatively less. It was due to silica gel not having proper dispersed with rubber matrix and hence

Fig. 3 Tensile modulus
variation with CB–Si/CB–Si
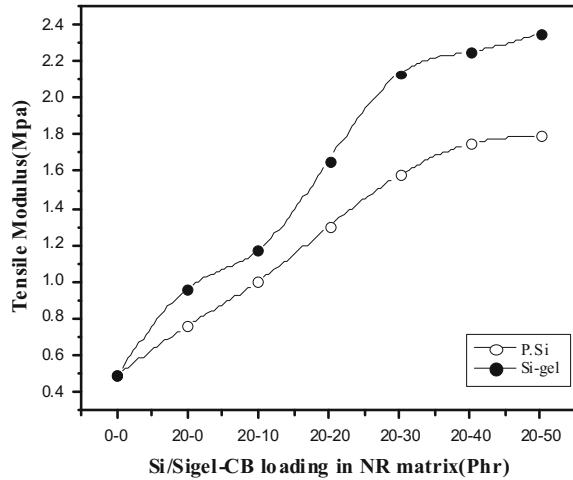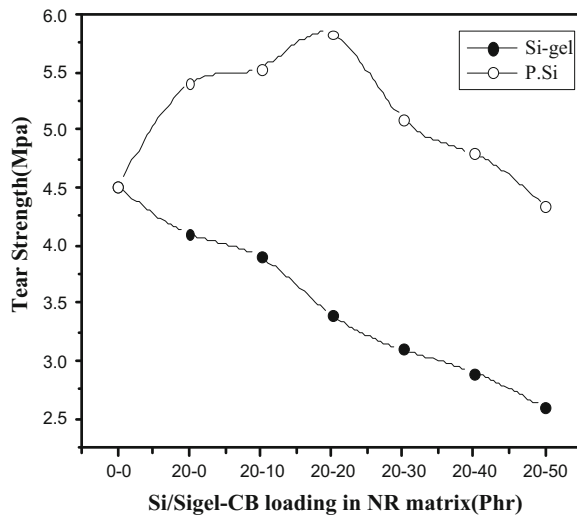gel loading in NR matrix

Fig. 4 Tear strength
variation with CB–Si/CB–Si
gel loading in NR matrix

not capable to filled the pores on CB surface. Figure 3 showed that adding the CB content in composite material-1 results in modulus gradually increases. It was due to CB not having good adhesion with the silica–rubber compounds, and thus, it behaves like rigid fillers which results in steady development of stiffness of the compounds. For composite material-2, comparatively higher tensile modulus observed which was due silica gel behaves like a coarse particulate filler with the rubber matrix leads to loosening the adhesion bonding between Si gel–CB.

Figure 4 shows that incorporation of CB into rubber–Si compound causes the tear strength to increase gradually up to 20 phr for composite material-1. It was due to retarding the aggregates and the resulting less cross-link density. The same

Fig. 5 Hardness variation
with CB–Si/CB–Si gel
loading in NR matrix
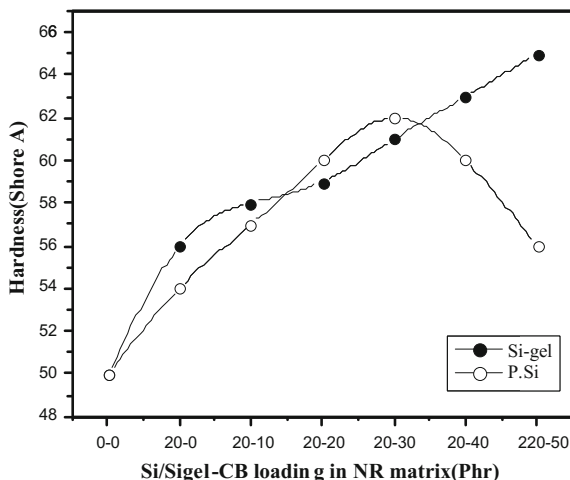
phenomena were not observed in composite material-2. In this, tear strength decreasing trend. It was due to silica gel is granular filler, which is not good bonds with NR compounds. Hardness properties were studied for various proportions and graph is plotted in Fig. 5. The hardness for composite material-1 significantly increases up to 30 phr of CB. After that, it is in decreasing trend. In composite material-2, hardness value showed increasing trend as increase of CB content with silica gel. This may be caused, silica gel has coarse filler material which led improper agglomerates with NR-CB compounds, and hence less cross link density [11].

3.2 Morphological Analysis

Figure 6 shows that SEM micrograph of tensile-fractured surface of silica-filled NR compounds at 10 phr of CB (sample P1). It showed uniform dispersion and interfacial adhesion between the Si and CB in NR matrix. The same phenomenon continues up to 30 phr of CB and there was no weakening cross-linking chains observed. Hence, these samples obtained good physical properties. Figure 7 shows that tensile-fractured surface of silica-filled NR compounds at 50 phr of CB (sample P5). It showed silica content has dispersed throughout the rubber matrix with more CB, which is not facilitating proper interfacial adhesion between the silica and rubber matrix [12]. Hence, it loosens the physical properties. In order to obtain natural rubber compounds with satisfactory physical properties, good dispersion and strong interfacial adhesion are required [7]. Similarly Fig. 8 showed that comparatively not much interfacial adhesion and uniform dispersion, because of granular structure of silica gel with rubber matrix. Hence, less physical properties are compared with NR–silica compounds. Moreover, Fig. 9 showed that more

Fig. 6 SEM micrograph of NR–silica with 10 phr of CB
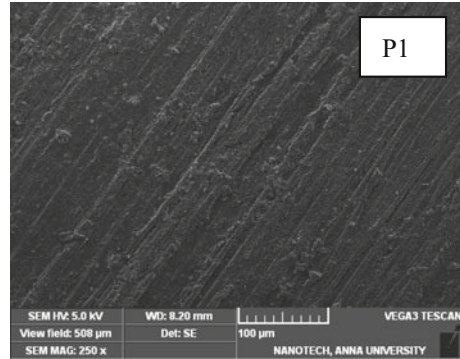
Fig. 7 SEM micrograph of NR–silica with 50 phr of CB

Fig. 8 SEM micrograph of NR–silica gel with 10 phr of CB

weaken bonds appeared in the matrix which is due to the granular structure silica gel not interfacing with CB. In this study, CB and silica fillers resulted in uniform dispersion throughout the rubber compounds, exhibiting better tensile strength, tear strength, hardness, modulus, and elongation at break compared with rubber compounds obtained from silica gel.
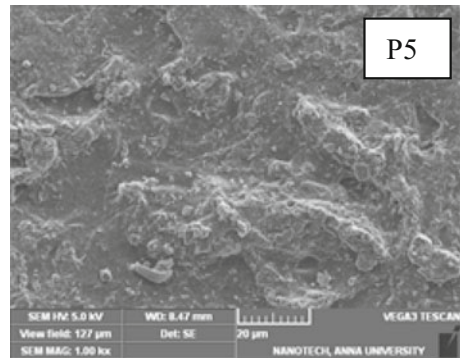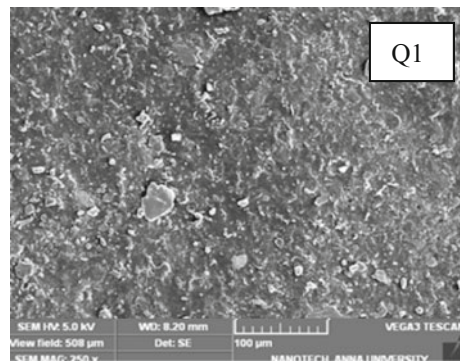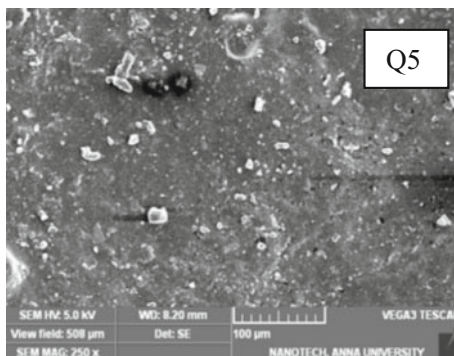
Fig. 9 SEM micrograph of NR–silica gel with 50 phr of CB

4 Conclusion

Earlier investigators not considered silica gel as a filler material for their studies. Effect of silica gel with NR compounds has been arrived and results are compared with silica. The physical properties of NR–CB compounds with Si/Si gel were investigated through tensile and tear properties. The composites obtained from silica provide better physical properties than silica gel. Hence, hybrid carbon black and silica with NR compounds found to be a superior performance over carbon black and silica gel at the same filler loading. Morphology results revealed that silica adding up composites had strong interfacial adhesion and uniform dispersion into the rubber matrix, whereas silica gel had weak adhesion and improper dispersion. Based on results, silica could be a suitable filler material than the silica gel for improving natural rubber composites performance in the basis of reliability and durability.

References

1. Liu, Y., Li, L., Wang, Q., Zhang, X.: Fracture properties of natural rubber filled with carbon black and nanoclay. J. Polym. Res. **18**(9), 859–867 (2011)
2. Hrachovi, J., Chodak, I., Komadel, P.: Modification and characterization of montmorillonite fillers used in composites with vulcanized natural rubber. Chem. Pap. **63**(2), 55–61 (2003)
3. Findik, F., Yilmaz, R., Koksal, T.: Investigation of physical and physical properties of several industrial rubbers. Mater. Des. **25**(1), 269–274 (2004)
4. Rattanasom, N., Prasertsri, S., Ruangritnumchai, T.: Comparison of the physical properties at similar hardness level of natural rubber filled with various reinforcing-fillers. Polym. Test. **28**(1), 8–12 (2009)
5. Ismail, H., Nordin, R., Noor, A.M.: Cure characteristics, tensile properties and swelling behavior of recycled rubber powder-filled natural rubber compounds. Polym. Test. **21**(2), 565–569 (2002)
6. Rajasekar, R., Pal, K., Heinrich, G.: Development of nitrile butadiene rubber–nanoclay composites with ENR as compatibilizer. Mater. Des. **30**(1), 3839–3845 (2009)

7. Mehmet, D., Oral, D.D..: Physical properties and cure characteristics of NR/nanoclay composites with two different compatibilizers. J. Appl. Polym. Sci. **121**(3), 1530–1535 (2014)

8. Kueseng, K., Jacob, K.I.: Natural rubber nanocomposites with SiC nanoparticles and carbon nanotubes. Eur. Polym. J. **42**(1), 220–227 (2006)

9. Sui, G., Zhong, W.H.: Preparation and properties of natural rubber composites reinforced with preheated carbon nanotubes. J. Polym. Adv. Technol. **19**(1), 1543–1549 (2008)

10. Chandran, V., Manvel Raj, T., Lakshmanan, T.: Evaluation of performance of natural rubber composites with different sizes of waste tyre rubber (WTR) and precipi tated silica on C-M–M. Arab. J. Sci. Eng. **40**(1), 1187–1196 (2015)

11. Karger, K, J., Meszaros, J., Barany, T.: Ground tyre rubber (GTR) in thermoplastics, thermosets and rubbers. J. Mater. Sci. **48**(2), 1–38 (2013)

12. Chandran, V., Manvel Raj, T., Lakshmanan, T.: Effect of recycled rubber particles and silica on tensile and tear properties of natural rubber composites. Mater. Sci. (MEDŽIAGOTYRA) **22**, 256–261 (2016)

Fuzzy Logic Simulation for Automatic Speed Control System

Pajarla Saiteja

1 Introduction

Electromagnetic braking means applying brakes using electronic and magnetic power. Electromagnetic brakes are frictionless brakes, and these are working under the principle of electromagnetism [1]. This frictionless braking system leads to the increase in life span and reliability of brakes. Wearing and maintenances are very less. The electromagnetic braking system is one of the advanced technologies which can replace traditional mechanical braking systems.

The working principle behind the electromagnetic braking system is when we apply the pressure on brake pedal, a magnetic flux is passed perpendicular to the rotating wheel; we can observe that the eddy current is flowing in opposite direction to the rotating wheel [1]. This magnetic flux will create an opposing force which is in opposite direction to the rotating wheel and which leads to slow down the wheel rpm. This is the concept which we are using in electromagnetic brakes. It gives better results than traditional brakes, and we can expect electromagnetic brakes in future automobiles.

Fuzzy logic techniques are introduced by Zadesh in 1965. Fuzzy logic is a form of information that represents notions that cannot be defined precisely, but it depends upon their perspectives. Fuzzy logic techniques are majorly used in machine control techniques. And it refers to the statistics that cannot be expressed as "true" or "false" but may be as "partially true." Genetic algorithms and neural networks perform similar to fuzzy, and these are alternative techniques of fuzzy logic. Fuzzy logic control system is used to overcome human errors while sorting out the solution. This makes easier to mechanize tasks that are performed by humans.

P. Saiteja (✉)
St Marys Group of Institutions, Hyderabad, India
e-mail: Pajarla.saiteja@gmail.com

2   Mathematical Calculations

2.1   Mathematical Calculation for Mechanical Braking Torque

$$\text{Torque } \tau = F \times \mu \times R$$

F Force acting on wheel
μ Coefficient of friction
R Radius of the wheel

Reaction forces at front and rear axle wheels (Fig. 1).

This is the most common way of braking the vehicle, in which braking force acts on both rear and front wheels [1].

Let F_A = Braking force provided by the front wheels = $\mu \times R_A$.

F_B = Braking force provided by the rear wheels = $\mu \times R_B$.

$$R_A = \text{m.gcos}\alpha\left(\frac{\mu h + x}{L}\right) \quad R_B = \text{m.gcos}\alpha\left(\frac{L - \mu h - x}{L}\right)$$

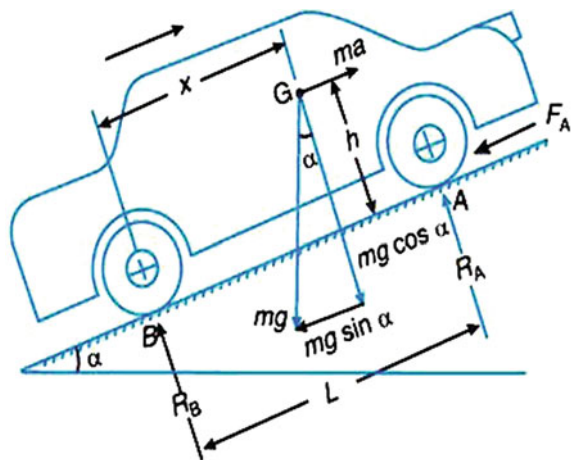R_A Reaction force at front wheels
R_B Reaction force at rear wheels

If the vehicle moves on plain surface ($\alpha = 0$):

$$R_A = \text{m.g}\left(\frac{\mu h + x}{L}\right) \quad R_B = \text{m.g}\left(\frac{L - \mu h - x}{L}\right)$$

Fig. 1 Reaction force diagram

2.2 Let Us Apply Same Concept and Formulas to Suzuki Ciaz Vehicle

<div align="center">

Overall Length   OL = 4490 mm

Wheel Base   WB = 2650 mm

Ground Clearance GC = 170 mm

Kerb Weight   KW = 1115 kg

Gross Weight   GS = 1595 kg

</div>

Braking torque calculation for Suzuki Ciaz:
At maximum load condition:

<div align="center">

Weight of the vehicle = 1600 kg

$R_A = 960$ N $R_B = 640$ N

Braking Torque at front wheel $(\tau_A) = 169$ N M

Braking Torque at rear wheel $(\tau_B) = 44$ N M

</div>

The braking torque (τ) for different loads is shown in (Table 1).

2.3 Apply This Mechanical Braking Torque Values in Electromagnetic Braking Torque Formula

Electromagnetic braking torque (τ_b):

$$\tau_b = \sigma d_s^2 A_p t_d \omega \left(\frac{\mu n}{g}\right)^2 i^2$$

Table 1 Torque (τ) at different weights

Load	Front Bτ	Rear Bτ
1100	116	30
1150	122	31
1200	127	33
1250	132	34
1300	137	35
1350	143	37
1400	148	38
1450	153	39
1500	159	41
1550	164	43
1600	169	44

σ Electrical conductivity
d_s Distance between center of disk and center of gravity, m
A_p Pole area, m^2
T_d Disk thickness, m
ω Angular velocity, rad/s
μ Permeability of air
n No. of turns
g Air gap, m
i Applied current, KA.

For this calculations, we considered $\sigma = 9.579 \times 10^7 \ \Omega \ \text{m}^{-1}$, $d_s = 25$ mm, $g = 5$ mm, $\mu = 12.568 \times 10^{-7} \ \text{NA}^{-2}$, $n = 23{,}000$, and disk is rotating with 2300 rpm as constants.

When we substitute braking torque, disk thickness, electrical conductivity, angular velocity, number of turn values into the Eq. (1), we will get variable current values. Finally we calculated required alternating power for different braking torque conditions (Table 2).

Here, we concentrated on speed controlling of a vehicle during sudden approaching of obstacles. For that, we considered that the maximum distance between vehicle and obstacle is 20 m and minimum distance is 10 m. If any obstacle comes in this range, control system will activate. And another consideration is this control system will activate only during fourth and fifth gears. And this system does not work during first, second, and third gears. And opposite hydraulic pressures will act on clutch and accelerator for getting smooth braking action. Maximum pressure on accelerator and clutch is 4 bar, minimum pressure is 2 bar, and it is explained in Table 3.

Table 3 explains the precalculated and predetermined current (amp) values for getting electromagnetic brakes at different load conditions. At 1100 N load, if an obstacle comes at 10 m distance for vehicle stopping, we require 1600 A current for front axle electromagnetic braking system and 818 A current for rear axle

Load	Front Bτ	Rear Bτ
1100	1600	818
1150	1650	832
1200	1684	858
1250	1717	857
1300	1749	884
1350	1787	909
1400	1818	921
1450	1848	933
1500	1884	957
1550	1914	980
1600	1944	991

Table 2 Required EMB current at different loads

Table 3 Precalculated fuzzy values

Load	Ab distance	Front EMBτ	Rear EMBτ	Clutch Pr	Accelerator Pr
1100	20	800	409	2	2
	10	1600	818	4	4
1150	20	825	416	2	2
	10	1650	832	4	4
1200	20	842	429	2	2
	10	1684	858	4	4
1250	20	859	429	2	2
	10	1717	857	4	4
1300	20	875	442	2	2
	10	1749	884	4	4
1350	20	894	455	2	2
	10	1787	909	4	4
1400	20	909	461	2	2
	10	1818	921	4	4
1450	20	924	467	2	2
	10	1848	933	4	4
1500	20	942	479	2	2
	10	1884	957	4	4
1550	20	957	490	2	2
	10	1914	980	4	4
1600	20	972	496	2	2
	10	1944	991	4	4

electromagnetic braking system. And during that time, 4 bar pressure will act at clutch and accelerator hydraulic systems for increasing engine and gear box life and for driver flexibility.

3 Appling Fuzzy Logic

3.1 Grouping of Fuzzy Values into Triangular Membership Function

See Table 4.

Table 4 Triangular membership function values

	Front EMBτ	Rear EMBτ	Clutch Pr	Accle Pr	Load	Ob distance
Minimum	800	409	2	2	1100	10
Maximum	1944	991	4	4	1600	20
Difference	1144	582	2	2	500	10
Difference/2	572	291	1	1	250	5
Max-(difference/2)	1372	700	3	3	1350	15
Low	800.800.1372	409.409.700	2.2.3	2.2.3	1100.1100.1350	10.10.15
Medium	800.1372.1944	409.700.991	2.3.4	2.3.4	1100.1350.1600	10.15.20
High	1372.1944.1944	700.991.991	3.4.4	3.4.4	1350.1600.1600	15.20.20

3.2 Forming into Sub-iterations

See Tables 5, 6 and 7.

3.3 Forming into Fuzzy Sets

See Fig. 2.

4 Forming of Fuzzy Rules in LabVIEW Software

See Fig. 3.

Table 5 Sub-iterated fuzzy values for low low

Load	Ab distance	Front EMBτ	Rear EMBτ	Clutch Pr	Accelerator Pr
1100	20	800	409	2	2
1150	20	825	416	2	2
1200	20	842	429	2	2
1250	20	859	429	2	2
1300	20	875	442	2	2
1350	20	894	455	2	2

Table 6 Sub-iterated fuzzy values for low medium

Load	Ab distance	Front EMBτ	Rear EMBτ	Clutch Pr	Accelerator Pr
1100	20	800	409	2	2
	10	1600	818	4	4
1150	20	825	416	2	2
	10	1650	832	4	4
1200	20	842	429	2	2
	10	1684	858	4	4
1250	20	859	429	2	2
	10	1717	857	4	4
1300	20	875	442	2	2
	10	1749	884	4	4
1350	20	894	455	2	2
	10	1787	909	4	4

Table 7 Sub-iterated fuzzy values for medium low

Load	Ab distance	Front EMBτ	Rear EMBτ	Clutch Pr	Accelerator Pr
1100	20	800	409	2	2
1150	20	825	416	2	2
1200	20	842	429	2	2
1250	20	859	429	2	2
1300	20	875	442	2	2
1350	20	894	455	2	2
1400	20	909	461	2	2
1450	20	924	467	2	2
1500	20	942	479	2	2
1550	20	957	490	2	2
1600	20	972	496	2	2

5 Input/output Values for Triangular Membership Function in LabVIEW Software

See Fig. 4.

6 Output Verification

See Fig. 5.

Low.Low			
F EMBτ	low	medium	high
R EMBτ	low	medium	high
Cl Pr	low	medium	high
A Pr	low	medium	high

Med.Low			
F EMBτ	low	high	medium
R EMBτ	low	high	medium
Cl Pr	low	high	medium
A Pr	low	high	medium

High.low			
F EMBτ	low	medium	high
R EMBτ	low	medium	high
Cl Pr	low	medium	high
A Pr	low	medium	high

Low.Med			
F EMBτ	medium	low	high
R EMBτ	medium	low	high
Cl Pr	medium	low	high
A Pr	medium	low	high

Med.Med			
F EMBτ	high	low	medium
R EMBτ	high	low	medium
Cl Pr	high	low	medium
A Pr	high	low	medium

High.Med			
F EMBτ	medium	low	high
R EMBτ	medium	low	high
Cl Pr	medium	low	high
A Pr	medium	low	high

Low.High			
F EMBτ	medium	high	low
R EMBτ	medium	high	low
Cl Pr	medium	high	low
A Pr	medium	high	low

Med.High			
F EMBτ	high	medium	low
R EMBτ	high	medium	low
Cl Pr	high	medium	low
A Pr	high	medium	low

High.High			
F EMBτ	medium	high	low
R EMBτ	medium	high	low
Cl Pr	medium	high	low
A Pr	medium	high	low

Fig. 2 Tabulation of fuzzy sets
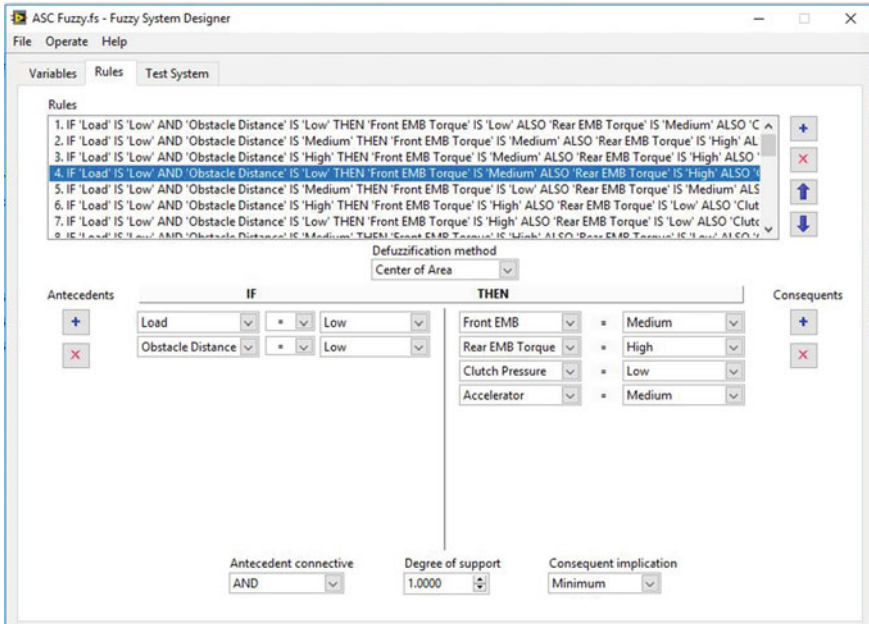
Fig. 3 Fuzzy rules in LabVIEW software
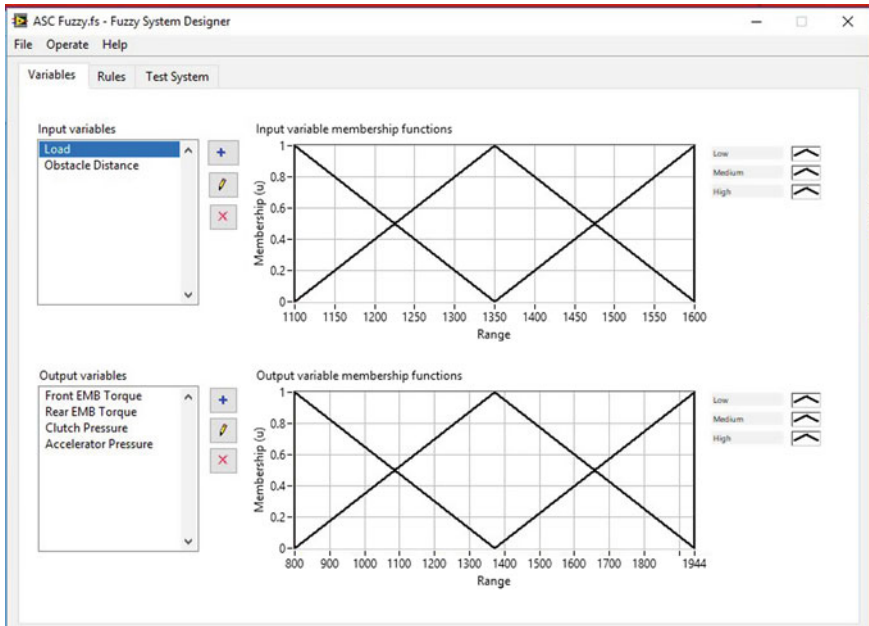
Fig. 4 Loading of input/output values in LabVIEW software
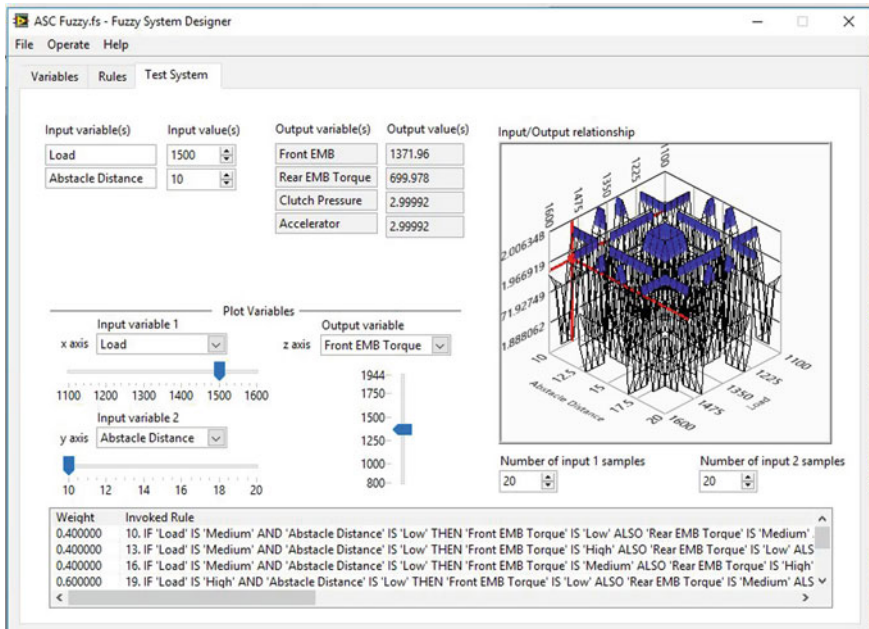
Fig. 5 Output verification at load 1500 and obstacle distance 10 m

6.1 Verification of Manually Calculated Values to LabVIEW Fuzzy Logic Controller Output

Manually calculated values at load 1500 N and obstacle distance 10 m are as follows:

The current required at front axle EMB is 1884 AV, the current required at rear axle EMB is 957 AV, the pressure required for clutch hydraulic system is 4 bar, and the pressure required for accelerator hydraulic system is 4 bar.

Fuzzy logic controller output values at 1500 N load and 10 M distance are as follows:

The current required for front axle EMB is 1372 AV, the current required for rear axle EMB is 700 AV, the pressure required for clutch hydraulic system is 3 bar, and the pressure required for accelerator hydraulic system is 3 bar.

Here, fuzzy output values are closer to the manually calculated values. By these results, we can conclude that fuzzy logic controlling technology will give good results in automatic speed controlling system.

7 Conclusion

Fuzzy is a form of knowledge representation suitable for notions that cannot be defined precisely, but which depend upon their contexts. And it used to find out the optimum solution. Genetic algorithms and neural networks perform similar to fuzzy, and these are alternative techniques of fuzzy logic. Fuzzy logic control system is used to overcome human errors while sorting out the solution. This makes it easier to mechanize tasks that are already successfully performed by humans.

This paper explains about automatic speed control of a vehicle while facing sudden obstacles (humans or other vehicles, etc.). This fuzzy control system has two input parameters: vehicle load and distance from the obstacle; vehicle load is calculated by strain gauge load cell, and obstacle distance is calculated by ultrasonic sensor. And output parameters are front axle electromagnetic braking torque, rear axle electromagnetic braking torque, pressure regulator of clutch, and pressure regulator of the accelerator. These input and output parameters are interlinked with the fuzzy logic control system. When any obstacle comes in our range of distance, this control system will activate and take input load value and distance from the obstacle and give to the fuzzy logic control system, and it will go for fuzzification and give required output values.

References

1. Sai Teja, P., Jeyanthi, S. Dr.: Fuzzy Logic Simulation for Brake by Wire Control System in Lecture Notes in Mechanical Engineering (2016). ISBN 978–981-10-1770-4
2. Schwar, R., Iserman, R., Bohm, J., Nell, J., Rieth, P.: Modeling and Control of an Electromechanical Disk Brake. SAE Paper 980600 (1998)
3. Lee, Y., Lee, W.-S.: Hardware-in-the-loop Simulation for electro-mechanical brake. In: SICE-ICASE International Joint Conference (2006)
4. Tanner, J.A., Stubbs, S.M.: Behavior of Aircraft Antiskid Braking Systems on Dry and Wet Runway surfaces: A Slip-Ratio-Controlled Systems with Ground Speed Reference from Unbraked Nose Wheel. NASA Langley Research Center, Virginia, NASA TND-8455, (1977)
5. Tanner, J. A.: Review of NASA Anti-skid Braking Research. NASA Langley Research Center, Virginia, SAE 821393, (1982)
6. Jeon, J.-W., Woo, G.-A., Lee, K.-C., Hwang, D.-H., Kim, Y.-J.: Real-Time Test of Aircraft Brake-By-Wire System with HILS & Dynamometer System
7. Isermann, R.: Fault-Diagnosis Systems: An Introduction from Fault Detection to Fault Tolerance. Springer, Berlin Heidelberg (2006)
8. Dumont, P., Aitouche, A., Bayart, M.: Fault detection of actuator faults for electric vehicle. In: IEEE International Conference on Control Applications, 2007, CCA 2007, pp. 1067–1072 (2007)
9. Gadda, C.D., Laws, S.M., Gerdes, I.C.: Generating diagnostic residuals for steer-by-wire vehicles. IEEE Tran. Control Syst. Technol. **15**, 529–540 (2007)
10. Jayabalan, R., Fahimi, B., Monitoring and fault diagnosis of multiconverter systems in hybrid electric vehicles. IEEE Trans. Veh. Technol. **55**, 1475–1484 (2006)
11. Murphey, Y.L., Masrur, M.A., Chen, Z.H., Baifang, Z.: Model-based fault diagnosis in electric drives using machine learning. IEEE IASME Trans. Mechatron. **11**, 290–303 (2006)

A Review of Contemporary Research on Root Canal Obturation and Related Quality Assessment Techniques

Pravin R. Lokhande, Deenadayalan,
Ratnakar R. Ghorpade and S. R. Srinidhi

1 Introduction

The root canal is done to save the infected teeth. Before obturating the root canal, removal of all substrate from the canal is done, which is immediately followed by cleaning and shaping to develop the logical cavity so that every practitioner can fill effectively [1]. Gutta-percha (GP) is a biocompatible material used to fill the cavity. The method of filling and sealing the root canal cavity using GP to avoid the further infection and propagation of the infection is called as root canal obturation. Obturation is done for the development of fluid-tight seal at apical foramen and total obliteration of the pulp space to prevent the percolation of fluid into root canal system [2]. Additionally, it creates a favorable biological environment for the process of peri-apical tissue healing. Obturation is the most important step in the triad of endodontic. Carefully and properly achieved obturation will lead to the formation of "fluid-tight seal" which is essential for the success of the endodontic treatment.

Mirco-leakage is defined as percolation of debris, oral fluids, microorganisms, or ions through the interface gap between restorative (filling material) and the wall of the tooth [3]. Clinical studies pointed that apical leakage of root canal obturating materials is the vital cause of endodontic treatment failures, and estimated the sealing capacity of a filling material or a filling method, generally by measuring the extent and path of penetration of a tracing agent into the filled canal. The most

P. R. Lokhande (✉) · Deenadayalan
Vel Tech University, Chennai 600062, India
e-mail: pravinrlokhande@gmail.com

R. R. Ghorpade
MIT World Peace University, Pune 411038, India

S. R. Srinidhi
Sinhgad Dental College and Hospital, Pune 411041, India

511

frequent tracers that have been used are dyes, radioactive isotopes, and bacteria and its products [4].

The sole aim of endodontic techniques is the three-dimensional filling of the canal to be obturated [5]. Various techniques are developed to achieve void-less, continuum obturated canal. The properties of ideal obturated canal always remained criteria for comparison of obturation technique. Till date, no technique is satisfying all the requirements to be called as ideal. In this article, we compared various sealing and micro-leakage assessment techniques, obturation techniques, and researches highlighting scope to be worked upon.

2 Contemporary Review and Comparison of Root Canal Obturation Techniques

In many paralleling techniques, materials were developed to improvise the obturation of the root canal. They include heat, injection, vibration, compaction, and carrier-based system. In this section, only the classification of technique and comparison is given since many researchers have already explained the techniques in detail.

2.1 Classification of Root Canal Obturation Techniques [2]

According to the mode of practical use, the obturation techniques are classified as

(1) Single-cone technique

- Custom-made roll cone technique/tailor-made gutta-percha
- Prefabricated stainless steel file method.

(2) Multiple-cone technique

- Cold and warm lateral condensation
- Warm vertical condensation
- Continuous wave of condensation
- Thermo-mechanical compaction.

(3) Chemo-plasticized gutta-percha

- Chloropercha
- Eucapercha.

(4) Thermo-plasticized injectable gutta-percha obturation

- Obtura II
- Ultrafil 3D

- Thermafil
- Solid core carrier-based systems.

(5) Paste-only root fillings

- Zinc oxide eugenol paste
- Calcium hydroxide paste
- Iodoform paste
- Paraformaldehyde containing paste.

(6) SPAD/resorcinol formaldehyde

- Diaket
- AH-26
- Lee-EndoFill
- Hydron.

2.2 Comparison of Root Canal Obturation Techniques

Tooth's structural integrity is better in case of single-cone obturation than lateral condensation. One can rationalize the use of both the continuous wave of condensation and carrier-based obturation techniques in their practice as they are both centered condensation methods. In other words, both obturation methods fill lateral canal aberrations with sealer and gutta-percha, similarly, by displacing surplus sealer and thermo-softened gutta-percha coronally as a heated plugger or carrier is driven through the canal during obturation. The displacement force and streaming effect produced pushes the filling materials laterally. Majority of the dentists use continuous wave of condensation technique.

Cold lateral condensation is known as the benchmark technique against which all obturation techniques are evaluated. It is the most commonly used technique by the dentists. The method is generic, encompassing a range of approaches in terms of master cone design and adaptation, spreader and accessory cone selection, choice of sealer and spreader application. There is little clear evidence on how it is 'best' done. Cold lateral condensation technique has good control over canal obturation length with any type of sealer. This technique fails to fill the irregularities as compared to warm vertical compaction technique.

Carrier-based obturation is fairly simple but highly technique sensitive. There are just a few procedural steps, and each step is critical and must be done correctly; otherwise, poor results can occur. Carrier systems represent another convenient means of delivering thermally softened gutta-percha to canal systems with some degree of control. This approach is typified by Thermafil which has been developed from a method involving the coverage of a conventional file with regular gutta-percha to contemporary plastic carriers coated with flowable, reduced molecular weight gutta-percha. Carrier methods do not have the overheating issues

and considered as low working temperature techniques. Warm vertical condensation of gutta-percha is the benchmark to evaluate the performance of many techniques such as warm gutta-percha, master cone, and thermo-plasticized techniques.

The Obtura II system is a handheld portable device. Ultrafil 3D system is a low working temperature device which supports three different types of disposable gutta-percha canals having needles which can be pre-curved according to canal shape. It has a portable heat unit and sets irrespective of moisture or temperature. Paste-only root fillings have a poor reputation in clinical endodontic.

Thermo-mechanical compaction techniques have simplicity and capability to fill the canal irregularities and speed. It has various disadvantages like projected parts of filling material beyond apex, instrument fracture, inability to fill the curved canal, and uncontrolled heat generation.

3 Consultation with Expert of Endodontic and Design Engineering

We had hours of discussion with ample of experts who are working in the endodontic field more than decade. Majority of them have extended the positive response to the warm vertical condensation-based techniques. Some of them said that they are dealing with device which is based on warm vertical condensation techniques. So far, we can say that dentist opinion is relying on the obturation device and its features, and doesn't matter which obturation technique the device is using.

However, according to views of experts, any obturation device is best if other devices in competition with it don't add any advancement into originality. Moreover, it is clearly revealed that for dentist best device is one being modified continuously irrespective of the performance of the design. Author's role is not to blame dentist but rather to propose system which can provide various features, viz. portability, heat, and vibration source at single tip, compatibility, cordless design, lightweight design, comfort, mobility, simple intuitive control, better ergonomics, easy to adapt updated technology, and multitasking ability.

Another psychology of the dentist is because they have been adapted to device that they are using for filling root canal cavity so it is the best system. But in response to above questions in Table 1, with respect to some features, they answered 'No' for every question. Our questions to them were set according to design features and requirements to improve device performance. However, the warm vertical condensation technique suggested by them provides the strong input in continuation with objective to achieve benefits.

Table 1 Consultation with dentist of endodontics report summary

Questions asked to dentist	Response	Author's remark
Is your obturation device portable?	No	Portability will provide ultimate convenience and ergonomics
Does the obturation device currently in your practice have the heat and vibration source at single tip?	No	Heat and vibration source at single tip will compensate problem of shrinkage of gutta-percha by ensuring three-dimensional filling of root canal cavity
Is your device compatible with more than one obturating material?	No	Increase in the compatibility of device will provide ease to select any obturating material
Is your obturation device used for treatment cordless?	No	Cordless design will provide ultimate convenience and ergonomics
Is obturation device used for treatment lightweight and handy?	No	Lightweight and handy device will provide maximum comfort and mobility
Is obturation device used for treatment have simple intuitive control?	No	Simple and intuitive control will be helpful for easy to adapt to technology
Is obturation device used for treatment capable of positioning in different angle?	No	Different tip angulations will be helpful to reach each and every point of canal and thus improve accessibility of tip

4 Contemporary Review of Micro-leakage Studies and Mechanical Sealing

Micro-leakage is defined as seepage of fluids, debris, microorganisms, or ions along with the interface between a restorative or a filling material and the wall of the tooth. Mechanical sealing provides the quantification of leakage in terms of mechanical sealing. The researchers of last five decade used various terms describing mechanical sealing ability of obturating materials, viz. sealability, effectiveness of obturating material, sealing capacity, sealing ability, quality of obturation, and density-based measurements. In the end, all the terms must be considered in an equivalent sense as mechanical sealing.

Timpawat et al. [6] compared the effect of a curved canal using silver cones, stainless steel cones, and gutta-percha cones. The study was in vitro type, and by comparing the apical seal quality, results were obtained. The canals with higher curvature value considered. Irrespective of the curvature value, gutta-percha or stainless steel noted the higher leakage at apical than silver cones.

Bradshaw et al. [7] compared sealability of thermo-plasticized gutta-percha using sealer and lateral condensation with non-thermo-plasticized GP without using sealer. They used thermo-plasticized gutta-percha which was injection-molded. Radiographic testing was done to ensure the filling of the canal and leakage was assessed using dye penetration test. It was found that GP with lateral condensation recorded the lowest value. Use of sealer promoted the sealability.

Saunders et al. [8] studied the quality of apical seal by changing the thermo-mechanical compaction technique. The design parameter considered was compactor design and variable rotor speed. He considered compactor design and two rotational speed (8000 and 16,000 rpm) forming two groups. He compared two groups and found no significant difference on apical seal quality. He also considered a hybrid of techniques.

Hata et al. [9] compared apical leakage of obturated tooth using Obtura II, Thermafil, Ultrafil regular, and firm set techniques. The result recorded shows that there is no remarkable difference in mean leakage value for different obturation materials. However, with the use of sealer, there is a significant reduction in the mean leakage value.

Sutrave et al. [10] compared the apical sealing ability of gutta-percha for three techniques: chloroform dip, eucalyptol dip, and lateral condensation for single root maxillary teeth. The study was conducted after the 21 days of root canal treatment. The leakage noted was time dependent and increasing with time. The eucalyptol dip techniques highlighted the greater leakage which is considered as severe as other techniques.

Gihotra et al. [11] carried scanning electron microscopic (SEM) study to evaluate the sealing ability of obturated canal using cold lateral, warm lateral, and warm vertical obturation techniques. In the apical one-third region of root, he found no passage using warm lateral condensation. However, there is a minimum passage present in coronal one-third region of tooth.

Al dewani et al. [12] carried research to compare the radiographic quality and sealing ability of obturated canals using lateral condensation technique. The grouping of flared and parallel canal was done and was obturated using cold lateral condensation and low-temperature thermo-plasticized gutta-percha techniques. The dye penetration test was used to assess the micro-leakage. Samples obturated with the thermoplastic method showed less leakage than the cold condensation method.

Deitch et al. [13] worked on the quantification of the density of the canal filled with the gutta-percha. He used the ultrasonically energized spreader (UES) along with the warm lateral condensation technique. He used the artificially prepared root canals using acrylic made blocks. Cold lateral condensation was used to obturate the artificial canals. The acrylic blocks manufactured undergone obturation process using UES method and the weighed after each UES process. The recorded reading indicates that the warm lateral condensation using UES resulted into denser fillings than cold lateral condensation.

5 Micro-leakage Evaluation, Quality Assessment Techniques, and Comparison

5.1 Micro-leakage Evaluation and Quality Assessment Techniques

(1) **Micro-Computed Tomography (µ-CT)**. Micro-computed tomography is a nondestructive technique based on X-ray 3D imaging used in hospitals for evaluation of obturation [14]. X-ray 3D image of first mandibular premolars is shown in Fig. 1. The pink color highlights the canal.

(2) **Radiography**. Radiography is an X-ray imaging technique used to view the internal structure of the object. X-ray generator is used to create electromagnetic radiation which is projected on the object [15]. The radiograph image is shown in Fig. 2.

(3) **CT Scans**. CT scan uses the number of X-rays processed by the computer to take the measurements at different angles. These measurements build up the cross-sectional areas which is called tomography image. This image is used to assess the quality of the obturated canal.

(4) **Cone-Beam Computed Tomography (CBCT)**. CBCT is a medical imaging technique consisting of X-ray computed tomography where divergent X-ray forms conic path to be passed on object [16]. The CBCT scan is shown in Fig. 3.

(5) **Scanning Electron Microscope (SEM)**. It is an electron microscope used to scan the surface of the object with focused beam electron which interacts with the electron in the object. After interaction, the output signal is received which gives the information about object's tomography and composition [17]. The SEM image is shown in Fig. 4.

Fig. 1 µ-CT scan of three-rooted mandibular first molar [14]

Fig. 2 Radiographic evaluation of root canal obturation quality [15]
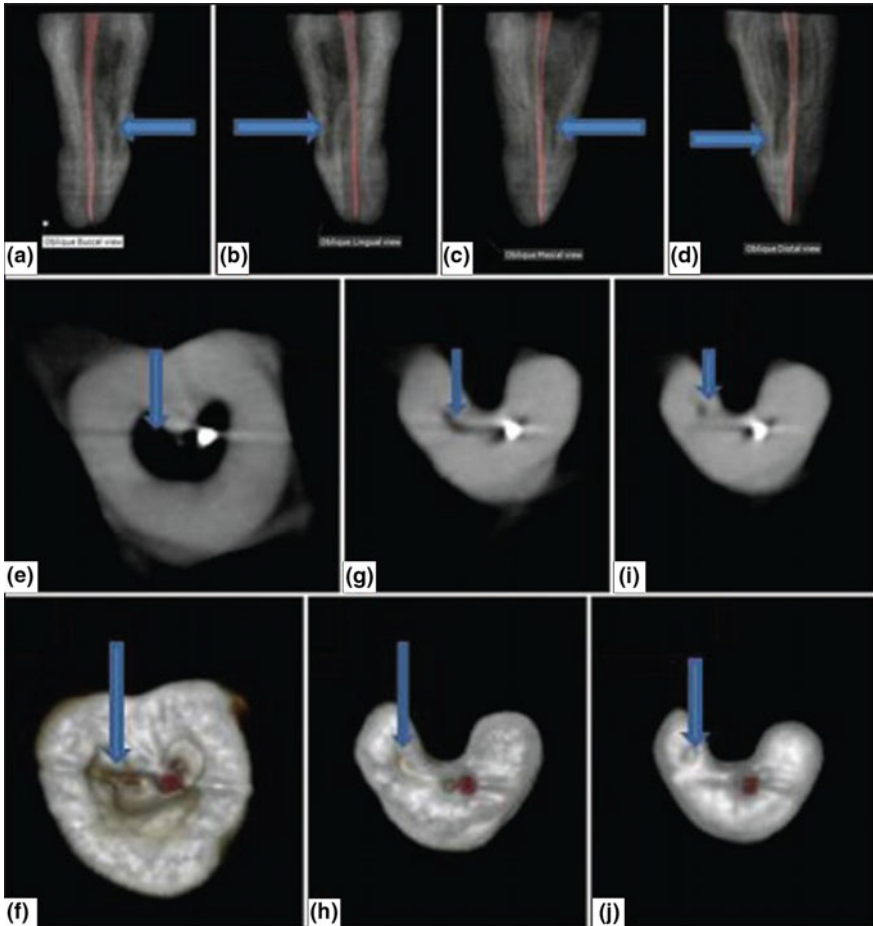
Fig. 3 CBCT image of C-shaped canal [16]
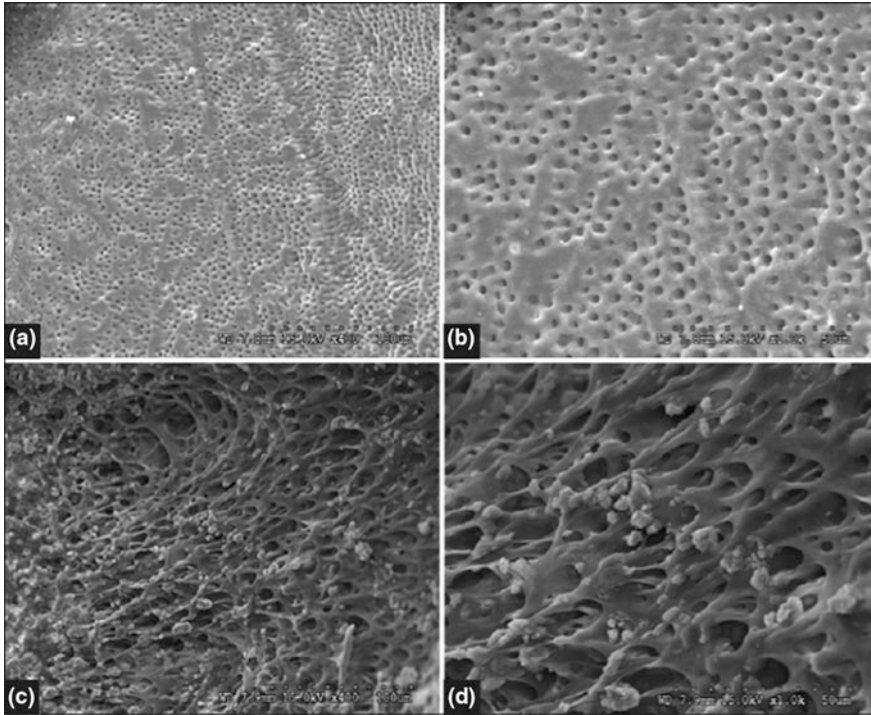
Fig. 4 Scanning electron microscope of obturated root canal [17]

(6) **Fluid Filtration Method**. Fluid filtration method is used quantitatively to evaluate the micro-leakage in the obturated canals. It measures the amount of micro-leakage in microliters per minute. The method is developed by Derkson and modified by Shaikh [18]. We have fabricated the fluid filtration system which is shown in Fig. 5.

(7) **Dye Penetration Test**. Dye penetration test is used for porosity in internal structure and surface defects of obturated canals. It works on the capillary action. There are various inspection steps like pre-cleaning, application of penetrant, excess penetrant removal, application of developer, and inspection. The conceptual image of the dye penetration test sample is shown in Fig. 6.

(8) **Bacterial Leakage Technique**. In bacterial micro-leakage technique, bacteria are used as markers. The method is firstly used by Fraser. Torabinejad firstly introduced this method as dual chamber technique. The schematic of bacterial leakage technique is shown in Fig. 7 [4].
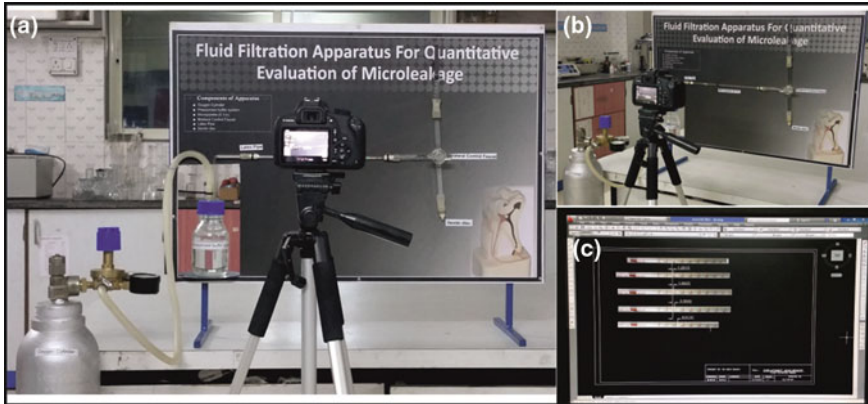
Fig. 5 Fabricated fluid filtration setup @ M.A. Rangoonwala Dental College, Pune

Fig. 6 Dye penetration samples
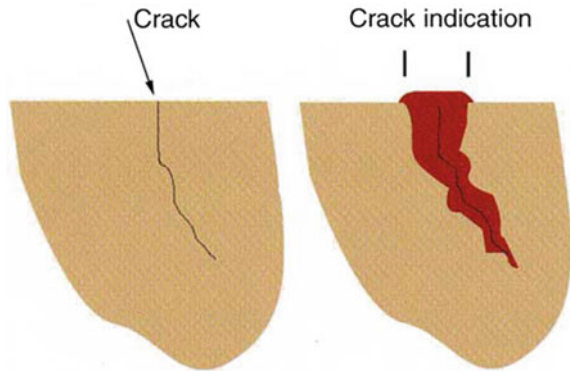
5.2 Comparison of Micro-leakage Evaluation and Quality Assessment Techniques

Based on one of the studies to compare, there is no significant difference between bacterial leakage and fluid filtration techniques. But bacterial leakage technique should be replaced with fluid filtration technique; since bacterial leakage technique requires more time, procedure is more complex and requires skilled microbiologist [4].

Comparatively, dye penetration test is simple and easy to use and less in cost but carries the disadvantages. The major drawbacks of this technique are small dye size and false-positive results which lead to overestimated leakage. Moreover, the reliability and reproducibility of result using dye penetration are challengeable.

The fluid filtration methods have a number of advantages over the chemical, radioactive tracers, bacterial, dye penetration, micro-computed tomography, and
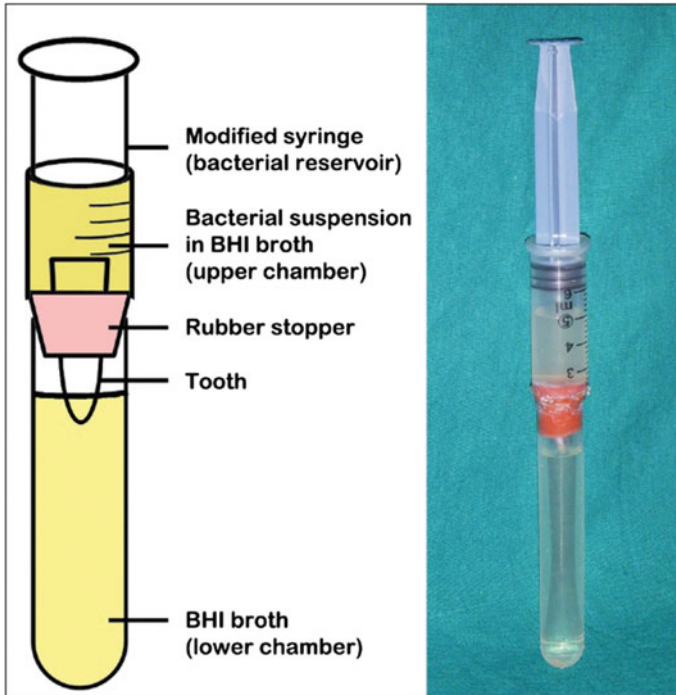
Fig. 7 Bacterial leakage technique setup

electrochemical evaluation [18]. It is nondestructive technique which evaluates the micro-leakage and provides better accuracy for small volume leakage.

Scanning electron microscope technique is a qualitative and nondestructive technique which gives the information of the surface composition and tomography. It needs the sample preparation and limited to surface of samples. Micro-computed tomography scan is also the nondestructive technique which creates 3D virtual model to evaluate the canal obturation qualitatively.

Cone-beam computed tomography, micro-computed tomography, CT scans, and scanning electron microscope are nondestructive qualitative techniques. On the other hand, fluid filtration, dye penetration, bacterial micro leakage are the experimental methods that give quantitative output. Radiography is having limitation that white lines give limited information [15]. All are used for quality assessment of the root canal obturation.

6 Most Recent Endodontic Researches

Landolo et al. [19] conducted research to evaluate the actual temperature of sodium hypochlorite when heated inside the root canal using extraoral heating and intraoral heating techniques: thermocouples placement, thermo-controlled heater, and system B. Chi et al. [20] evaluated the fatigue lives of two batches of nickel–titanium (Ni–Ti) rotary files operating in clinically simulated root canal. The cyclic fatigue is affected by strains in files and geometry of files. Cyclic fatigue analysis performed in one step indicated that cyclic fatigue life of files decreases with decreasing cylinder radius of file and increases in insertion angle.

Mothanna et al. [21] in his doctoral thesis evaluated the technical quality of root canal treatment (RCT) performed by preclinical undergraduate dental students at dental college of Taibah University, KSA, in which around 259 extracted teeth were considered for study. The evaluation criteria parameters were length, density, and taper of obturated canal. The result showed varied levels of technical quality. The same kind of research should be implemented repeatedly to improve the quality of root canal treatment in Taibah University, KSA.

Eken et al. [22] performed finite element analysis study to evaluate the effect of rotary systems on stresses. They simulated 3D-printed resin root with an oval-shaped canal. The result of their study concluded that oval-shaped canals prepared by HFs and WO were less likely to result in fracture. Wei [23] had done research with objective to compare filling quality of obturation technique in apical 5 mm of mandibular first molar mesial root canals. In conclusion, no significant difference between the compared techniques is found. Ruyan [24] studied the effect of warm vertical compaction technique on physical properties of the sealer. Warm vertical compaction influenced some properties of sealer which includes setting time, flow, and porosity.

Viapiana [25] studied the effect of needle position on irrigant flow in C-shaped root canal using CFD analysis. Authors evaluated the real-time replacement of the irrigant in the root canal over time. Orientation of the opening of the side-vented needle influences the flow pattern, velocity, apical wall pressure, and penetration into lateral canal. Ghorpade [26] studied the effect of sealer use on the heat generated at external root surface during root canal obturation using warm vertical condensation technique with system B heat source. During warm vertical compaction of gutta-percha root canal, sealers with different chemical composition absorb heat generated inside the root canal. For the purpose, authors assessed the physiochemical modifications of sealers subjected to the system B heat source.

Ghorpade [27] conducted the FEA-based modal analysis of plugger which he validated with the experimentation. In his further study, Ratnakar [28] conducted thermal and stress analysis of gutta-percha in simulated root canal using finite element analysis. In another study [29], he assessed the depth in gutta-percha (GP) to which cutter tip can be plunged, the temperature profile, thermal flux, and thermal gradient using FEA. Viapiana [25] performed finite element analysis-based study to know the fluid–structure interaction during root canal obturation.

Angereme [30] assessed the quality of fillings in canal shaped with reciprocal considering the effects of filling technique and post-insertion. They used micro-computed tomography technique to assess the quality of canal fillings.

7 Discussion

The contemporary review is useful and informative to experts, students or novice researchers, and decision makers in the fields of endodontic. It compares the various obturation techniques, sealing and micro-leakage assessment techniques, experts' opinion, and authors' view. It also provides sound basis for future work.

There is a need for the development of the obturation device having portability, heat, and vibration source at single tip, compatibility, cordless design, lightweight design, comfort, mobility, simple intuitive control, better ergonomics, easy to adapt updated technology, and multitasking ability so that every practitioner can effectively fill any type of canal where previously done researches lack of.

To automate the obturation process, there is a need of obturation device which combines both the heat and vibration source at single tip which can reduce the changeover time when sources are different.

Warm vertical condensation technique is best obturation technique mentioned in last decade, but it has shrinkage defect of softened gutta-percha during solidification. There is scope to study on heat distribution inside the plugger tip to avoid the shrinkage defect.

There is vast lack of the analytical and experimental studies which could quantify the root canal obturation or measure the micro-leakage. The fluid filtration is quantitative-based method but not used by dentist in practices. The evaluation of obturation is still based on qualitative analysis, and micro-leakage evaluation is skipped.

Among the various micro-leakage evaluation techniques, the fluid filtration technique is best in experimental category over the others in terms of accuracy, repeatability of result, ease to operate, compatibility of obturating materials, etc. Dye penetration test is the most cost-effective method but has inherent drawbacks. Bacterial micro-leakage testing requires skilled microbiologist to conduct the test. In qualitative technique category, the micro-computed tomography is the best technique as it gives 3D structure of obturated canal.

All the researchers have considered the design standard and root canal treatment protocol of their residing countries to perform research work. There is a need to develop common and uniform procedural standards for the design and root canal treatment protocols which will help to promote the technology advancement sharing.

The latest studies of last five years include cyclic fatigue evaluation of rotary files, finite element analysis-based stress and modal analysis, heat transfer with and without use of sealer, demonstration of artificial canal, etc.

References

1. Ghorpade, R.R.: Deformation studies of endodontic obturator tip using FEM approach. Int. J. Eng. Inven. **1**(4), 19–26 (2012)
2. Jain, S., Du Toit, J., Montalli, V.: Contemporary Book on Root Canal Obturation, 1st edn. India (2014)
3. Cifticia, A.: Coronal micro leakage of four endodontic temporary restorative materials: an in vitro study. Oral Surg. Oral Med. Oral Pathol. Oral Radiol. Endo. **108**, 067–070 (2009)
4. Moradi, S.: Comparison of fluid filtration and bacterial leakage techniques for evaluation of micro-leakage techniques in endodontics. Dent. Res. J. **12**(2), 109–114 (2013)
5. Schilder, H.: Filling of root canals in three dimensions. J. Endod. **32**(4), 281–290 (2006)
6. Timpawat, S.: An in vitro study of the comparative effectiveness of obturating curved root canals with gutta-percha cones, silver cones and stainless steel files. Oral Surg. Oral Med. Oral Pathol. **55**(2), 180–185 (1983)
7. Bradshaw, G.B.: The sealing ability of injection-molded thermo-plasticized gutta-percha. Int. Endod. J. **22**(1), 17–20 (1989)
8. Saunders, E.M.: The effect of variation in thermo-mechanical compaction techniques upon the quality of apical seal. Int. Endod. J. **22**(4), 163–168 (1989)
9. Hata, G.: Sealing ability of thermo-plasticized gutta-percha fill techniques as assessed by a new method of determining apical leakage. Int. Endod. J. **21**(4), 167–172 (1995)
10. Sutrave, S. Dr.: Apical sealing ability of gutta-percha by lateral condensation, chloroform dip and eucalyptol dip obturation technique: an in vitro study. Endodontology **7**, 1–7 (1995)
11. Girhotra, R.: Scanning electron microscopic evaluation of sealing ability of root canals with various obturation techniques. Endodontology **11**, 15–20 (1999)
12. Al-dewani, N.: Comparison of laterally condensed and low temperature thermo-plasticized gutta-percha root canal fillings. Int. J. Endod. **26**(12), 733–738 (2000)
13. Deitch, A.K.: A comparison of fill density obtained by supplenting cold lateral condensation with ultrasonic condensation. J. Endod. **28**(9), 665–667 (2002)
14. Nevares, J.: Efficacy of pro-taper next compared with reciproc in removing obturation material from severely curved root canals a micro-computed tomography study. Basic Res. Technol. **42**, 803–808 (2016)
15. Whitworth, J.: Methods of filling root canals: principles and practices. Endodontics **12**, 2–24 (2005)
16. Aslan, H.: Evaluating root canal configuration of mandibular incisor with cone beam computed tomography in a Turkish population. J. Dent. Sci. **10**, 359–364 (2014)
17. Angerame, D.: Resistance of endodontically treated roots restored with different fiber post systems with or without post space preparation in vitro analysis and SEM investigation. Endodonzia **30**, 111–119 (2016)

18. Shaikh, A.: A novel approach to construction and working of fluid filtration model: an experimental study. J. Sci. Innov. Res. **6**(2), 55–58 (2017)
19. Landolo, A.: 3D cleaning, a perfected technique: thermal profile assessment of heated NaOCl. Endodonzia **118**, 1–4 (2017)
20. Chi, C.W.: Cyclic fatigue behavior of nickel-titanium dental rotary files in clinical simulated root canals. J. Fromason Med. Assoc. **116**, 306–312 (2016)
21. Mothanna, K.: Technical quality assessment of root canal treatment performed by pre-clinical dental students at Taibah university. Mater. Sci. **41**, 27–32 (2016)
22. Eken, R.: Evaluation of the effect of rotary systems on stress in new testing model using a 3-dimensional printed simulated resin root with an oval shaped canal a finite element analysis study. J. Endod. **42**(8), 1273–1278 (2016)
23. Wei, Qu: Influence of warm vertical compaction techniques on physical properties of root canal sealers. J. Endod. **42**(12), 1829–1833 (2016)
24. Ruyan, W.: Evaluation of effect of needle position on irrigant flow in the c-shaped root canal using computational fluid dynamics model. J. Endod. **41**(6), 931–936 (2015)
25. Viapiana, R.: Investigation of effect of sealer use on the heat generated at external root surface during root canal obturation using warm vertical compaction technique with system B heat sources. J. Endod. **40**(4), 555–561 (2014)
26. Ghorpade, R.R.: Experimental and FEA based modal analysis of scaled up dental pin/plugger-case study in Endodontics. Int. J. Res. Advent Technol. **1**(5), 15–22 (2013)
27. Ghorpade, R.R.: Thermal and stress analysis of gutta-percha in simulated root canal using finite element analysis. Int. J. Mech. Prod. Eng. Res. Dev. **2**(4), 19–30 (2012)
28. Ratnakar, R.: Ghorpade.: Penetration depth of heated plugger on softened gutta-percha. E. J. Dent. **2**(4), 251–259 (2012)
29. Ghorpade, R.R.: Fluid structure interaction during root canal obturation FEA based case study in Endodontics. In: Technical Journal of the Institution of Engineers, pp. 230–235. Pune Local Centre, India (2014)
30. Angerame, D.: Quality of canal obturation assessed by micro-computed tomography influence of filling technique and post placement in canal shape with reciproc. Endodonzia **41**, 82–85 (2013)

Adaptive Fault Tolerance Flight Controller for Aircraft Actuator Failure

M. Silambarasan, E. Balasubramanian and G. Surendar

1 Introduction

Fault tolerance controller is widely used in many safety-critical systems such as nuclear power plants, medical equipment, space crafts, aircraft. Fault tolerance controller is classified into two categories such as passive and active. In passive controllers, the stability is achieved within the fault tolerable capacity of the robust feedback controller. Active controller achieves the stability based on reconfigurable flight controller with fault detection and identification module. The passive controllers are providing better tracking performance without any external module. Many researches are going on in the design and development of fault tolerance flight control systems. In Propulsion control aircraft system, which controls the aircraft attitude by using only differential engine thrust as an emergency backup flight control system in [1]. Some flight controllers are designed using reconfigurable control systems for failures compensations are given in [2–5]. In [6] active type controllers are used for the compensation of control surface failures. Robust control systems are used in some system by treating failure as an uncertainty in [7–10]. In this paper, we are discussing the passive type fault tolerance flight controller based on the adaptive control system to compensate the actuator failures and provide desired performance with the help of remaining active systems. The dynamic aircraft model is modified for the development of FTFCS with two separate throttle controls and independent aileron control for left and right. This model

M. Silambarasan (✉) · E. Balasubramanian · G. Surendar
Center for Autonomous System Research, Vel Tech Rangarajan
Dr. Sagunthala R&D Institute of Science and Technology, Avadi, Chennai, India
e-mail: silambu.friends@gmail.com

E. Balasubramanian
e-mail: esak.bala@gmail.com

G. Surendar
e-mail: suren.ganesh.2007@gmail.com

scheme is applied to the linearized model of transport aircraft, and a different flight controller is studied for the same system with different real-time scenarios of an unknown actuator failure of rudder struck, aileron, and engine malfunction [11].

2 Aircraft Model

To investigate the actuator failure, the general aircraft equation of motion with independent throttle and aileron is described from [11]. The nonlinear aircraft dynamic with separate left throttle (T_L) and right throttle (T_R) is described by force and moment Eq. (1)

$$
\begin{aligned}
&m(\dot{u} + qw - rv) = X - mg\,\sin\theta + (T_L - T_R)\cos\epsilon, \\
&m(\dot{v} + ru - pw) = Y + mg\,\cos\theta\,\sin\emptyset, \\
&m(\dot{w} + pv - qu) = Z + mg\,\cos\theta\,\cos\emptyset - (T_L + T_R)\sin\epsilon, \\
&I_x\dot{p} + I_{xz}\dot{r} + (I_z - I_y)qr + I_{xz}qp = L + l(T_L - T_R)\sin\epsilon; \\
&I_y\dot{q} + (I_x - I_z)pr + I_{xz}(r^2 - p^2) = M; \\
&I_z\dot{r} + I_{xz}\dot{p} + (I_y - I_x)qp - I_{xz}qr = N + l(T_L - T_R)\cos\epsilon;
\end{aligned}
\tag{1}
$$

where m is mass of the aircraft, $[u, v, w]$ are velocities along body axis, $[\dot{u}, \dot{v}, \dot{w}]$ are accelerations along body axis, $[\theta, \emptyset, \Psi]$ are pitch roll and yaw angle of the aircraft, $[p, q, r]$ are the angular velocities, $[X, Y, Z]$ are the aerodynamic forces along body axis, and $[L, M, N]$ are the aerodynamic torque, ϵ angle between thrusts, and body x-axis. Ii is moment of inertia in body axis, g is gravity force, and l is distance between the engines in x-z plane.

The linearization is done by choosing the state vector $X = [u, v, w, \emptyset, \theta, \Psi, p, q, r]^T$ and control vectors as $U = [\delta_e, \delta_{t_l}, \delta_{t_r}, \delta_{a_l} \delta_{a_r} \delta_r]^T$. The equilibrium points and linearization procedure are followed from the literature [12]. The simplified linear aircraft dynamic model is given below.

$$
\dot{X} = \begin{bmatrix} A_{4\times4}^{(1)} & A_{4\times5}^{(2)} \\ A_{5\times4}^{(3)} & A_{5\times5}^{(4)} \end{bmatrix} X + \begin{bmatrix} B_{4\times3}^{(1)} & B_{4\times3}^{(2)} \\ B_{5\times3}^{(3)} & B_{5\times3}^{(4)} \end{bmatrix} U
\tag{2}
$$

where $A^{(2)}$ and $B^{(2)}$ are zero matrices.

$$A^{(1)} = \begin{bmatrix} \bar{X}_u & \bar{X}_w & \bar{X}_q & -g\cos\theta \\ \bar{Z}_u & \bar{Z}_w & \bar{Z}_q & -g\sin\theta \\ \bar{M}_u & \bar{M}_w & \bar{M}_q & 0 \\ 0 & 0 & 1 & 0 \end{bmatrix} A^{(3)} = \begin{bmatrix} 0 & 0 & 0 & 0 \\ \bar{T}_u & \bar{T}_w & 0 & 0 \\ \bar{T}'_u & \bar{T}'_w & 0 & 0 \\ 0 & 0 & 0 & 0 \\ 0 & 0 & 0 & 0 \end{bmatrix}$$

$$A^{(4)} = \begin{bmatrix} Y_v & \bar{Y}_r & \bar{Y}_p & g\cos\theta & 0 \\ \bar{N}_v & \bar{N}_r & \bar{N}_p & 0 & 0 \\ \bar{L}_v & \bar{L}_r & \bar{L}_p & 0 & 0 \\ 0 & \tan\theta & 1 & 0 & 0 \\ 0 & \frac{1}{\cos\theta} & 0 & 0 & 0 \end{bmatrix} \tag{3}$$

$$B^{(1)} = \begin{bmatrix} X_{\delta_e} & \bar{T}_{\delta_{tl}} & \bar{T}_{\delta_{tr}} \\ Z_{\delta_e} & -\bar{T}'_{\delta_{tl}} & -\bar{T}'_{\delta_{tr}} \\ \bar{M}_{\delta_e} & 0 & 0 \\ 0 & 0 & 0 \end{bmatrix} B^{(3)} = \begin{bmatrix} 0 & 0 & 0 \\ 0 & \bar{T}''_{\delta_{tl}} & \bar{T}''_{\delta_{tr}} \\ 0 & \bar{T}'''_{\delta_{tl}} & \bar{T}'''_{\delta_{tr}} \\ 0 & 0 & 0 \\ 0 & 0 & 0 \end{bmatrix} B^{(4)} = \begin{bmatrix} Y_{\delta_{al}} & Y_{\delta_{ar}} & Y_{\delta_r} \\ \bar{N}_{\delta_{al}} & \bar{N}_{\delta_{ar}} & \bar{N}_{\delta_r} \\ \bar{L}_{\delta_{al}} & \bar{L}_{\delta_{ar}} & \bar{L}_{\delta_r} \\ 0 & 0 & 0 \\ 0 & 0 & 0 \end{bmatrix} \tag{4}$$

The parameters Xi, Zi, Mi, Yi, Ni, Li stability and control derivatives of aircraft [13] Where $i = u, v, w, p, q, r, \delta_e, \delta_{tl}, \delta_{tr}, \delta_{al}, \delta_{ar}, \delta_r$. The aircraft dynamics is framed in state space model with chosen state vector and control vector for the simulation and design.

3 Flight Controller Design

The contribution of the linear time-invariant system is $\dot{X} = AX(t) + BU(t)$; $X(t) \in R^n$, $U(t) \in R^m$. The actuators $U(t)$ may fail any time during operation. $U_i(t) = U_i, t \geq t_i, \epsilon\{1, 2, 3, …, m\}$ where t_i is an unknown failure time and U_i is an unknown failure constant [13], where actuator may strike at an unknown position at any unknown time. To achieve the control objective, the error between the desired state $X_d(t)$ and plant state $X(t)$ should be zero at any instant of time. $X(t) - X_d(t) = 0$. The conventional controllers are providing good tracking performance during normal condition without any failures.

The conventional linear quadratic regulator (LQR) provides desired state trajectory by choosing optimal feedback gain based on parameter optimization.

$$U(t) = Kx(t); \tag{5}$$

where $K = -R^{-1}B^T P$, where K is a feedback gain matrix, P satisfies the Riccati equation

$$A^T P + PA - PBR^{-1}B^T P + Q = 0, \tag{6}$$

and $Q = Q^T > 0$, and $R = R^T > 0$ are the weighting matrices.

The proposed fault tolerance controller with model reference adaptive scheme is [11]

$$U(t) = \hat{K}X(t) + \hat{k}r_d(t) + \hat{\theta} \tag{7}$$

where $\hat{K} = \left[\hat{K}_1, \hat{K}_2, \hat{K}_3, \ldots \hat{K}_m\right]^T \in R^{m \times n}, \hat{k} = \left[\hat{k}_1, \hat{k}_2, \hat{k}_3, \ldots \hat{k}_m\right]^T \in R^{m \times m}, \hat{\theta} = \left[\hat{\theta}_1, \hat{\theta}_2, \hat{\theta}_3, \ldots \hat{\theta}_m\right]^T \in R^{m \times 1}$, these parameters are updated from the below control laws.

$$\begin{aligned}
\hat{K}_i &= -\alpha_i x e^T P b_i, \quad i = 1, 2, 3, \ldots, m \\
\hat{k}_i &= -\gamma_i r_d e^T P b_i, \quad i = 1, 2, 3, \ldots, m \\
\hat{\theta}_i &= -\beta_i e^T P b_i, \quad i = 1, 2, 3, \ldots, m
\end{aligned} \tag{8}$$

where $\alpha_i = \alpha_i^T > 0$, $\gamma_i = \gamma_i^T > 0$, $\beta_i = \beta_i^T > 0$, $i = 1, 2, \ldots, m$, b_i is ith column of B, and $P = P^T$ matrix satisfying Riccati Eq. (6), error is $e = x(t) - x_d(t)$, and x is the state obtained from the reference model.

4   Simulation

The conventional and proposed controllers are applied to the transport aircraft with the rudder actuator failure scenario, and the performance is compared with the LQR and MRAC techniques.

For simulation, consider the large transport aircraft similar to B747 which is cruising at an altitude of 40,000 ft with a forward velocity of 774 ft/s (or) 527.72 mph. [11]. The linearized dynamic equation is taken from Eq. (1) and applies the derivatives of the aircraft.

$$\dot{x}(t) = \begin{bmatrix} A_{4 \times 4}^{(1)} & A_{4 \times 5}^{(2)} \\ A_{5 \times 4}^{(3)} & A_{5 \times 5}^{(4)} \end{bmatrix} x(t) + \begin{bmatrix} B_{4 \times 3}^{(1)} & B_{4 \times 3}^{(2)} \\ B_{5 \times 3}^{(3)} & B_{5 \times 3}^{(4)} \end{bmatrix} u(t) \tag{9}$$

$x = [u, v, w, \emptyset, \theta, \Psi, p, q, r]^T$, $u = [\delta_e, \delta_{t_l}, \delta_{t_r}, \delta_{a_l} \delta_{a_r} \delta_r]^T$ are state vectors of the aircraft model

$$A^{(1)} = \begin{bmatrix} -0.003 & 0.039 & 0 & -0.322 \\ -0.065 & -0.319 & 7.74 & 0 \\ 0.020 & -0.101 & -0.429 & 0 \\ 0 & 0 & 1 & 0 \end{bmatrix}; \quad A^{(3)} = \begin{bmatrix} 0 & 0 & 0 & 0 \\ 0.001 & 0.001 & 0 & 0 \\ -0.001 & -0.001 & 0 & 0 \\ 0 & 0 & 0 & 0 \\ 0 & 0 & 0 & 0 \end{bmatrix};$$

$$A^{(4)} = \begin{bmatrix} -0.0558 & -7.74 & 0 & 0.322 & 0 \\ 0.0773 & -0.115 & -0.0318 & 0 & 0 \\ -0.394 & 0.338 & -0.465 & 0 & 0 \\ 0 & 0 & 1 & 0 & 0 \\ 0 & 1 & 0 & 0 & 0 \end{bmatrix};$$

$$(10)$$

$$B^{(1)} = \begin{bmatrix} 0.01 & 1 & 1 \\ -0.065 & -0.04 & -0.04 \\ -1.16 & 0.598 & 0.598 \\ 0 & 0 & 0 \end{bmatrix}; \quad B^{(3)} = \begin{bmatrix} 0 & 0.039 & 0 \\ 0 & 0.8 & -0.7 \\ 0 & -0.5 & 0.6 \\ 0 & 0 & 0 \\ 0 & 0 & 0 \end{bmatrix};$$

$$B^{(4)} = \begin{bmatrix} 0.03 & -0.03 & 0.0564 \\ 0.0036 & 0.0036 & -0.4750 \\ 0.0715 & 0.0715 & 0.153 \\ 0 & 0 & 0 \\ 0 & 0 & 0 \end{bmatrix};$$

$$(11)$$

where $A^{(2)}$ and $B^{(2)}$ are zero matrices.

The simulation is carried out for the aircraft model with LQR, and MRAC controllers by choosing the constants satisfy the conditions given in flight control design. In these studies, the rudder actuator failure is considered, where the rudder is struck in a position at the angle of 15°. This may cause due to mechanical jamming or hydraulic system failures in aircraft.

The adaptive compensation performance of longitudinal and lateral dynamics of transport aircraft moving in constant motion with rudder struck at 15° angle is shown in Figs. 1 and 2. Figure 3 shows the control command to compensate the failure in MRAC. In this, the engine differential and independent aileron control act as redundant and also compensate the force created by the fault rudder.

Fig. 1 State response of longitudinal dynamic with rudder struck at 15° angle
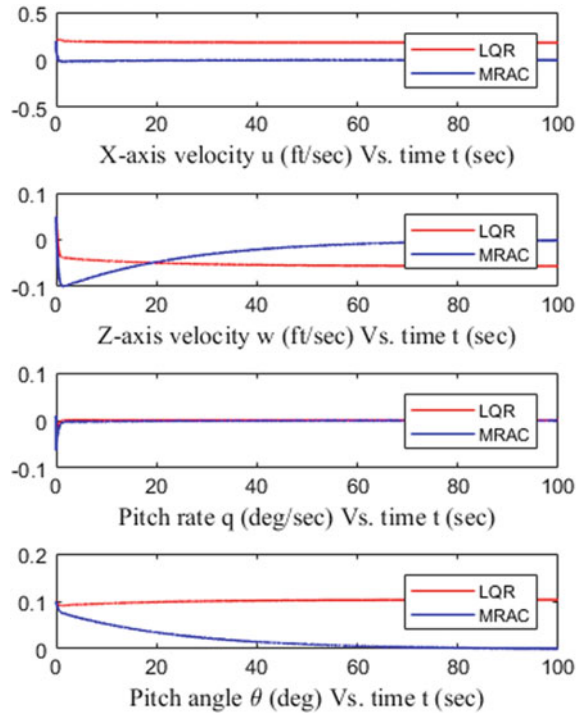
5 Conclusion

In this work, the failure of rudder actuator for a typical aircraft structure is compensated using MRAC. The control of the vehicle is attained through the compensation of remaining control surfaces using a linearized model. Comparative performance evaluation of MRAC and LQR controllers suggested that MRAC achieved better control ability during unknown failure conditions. The simulation results of longitudinal and lateral response of commercial aircraft demonstrated the effectiveness of the controller.

Fig. 2 State response of lateral dynamic with rudder struck at 15° angle

Y-axis velocity v (ft/sec) Vs. time t(sec)

Roll rate p (deg/sec) Vs. time t (sec)

Yaw rate r (deg/sec) Vs. time t (sec)

Roll angle ϕ (deg) Vs. time t (sec)

Yaw angle ψ (deg) Vs. time t(sec)
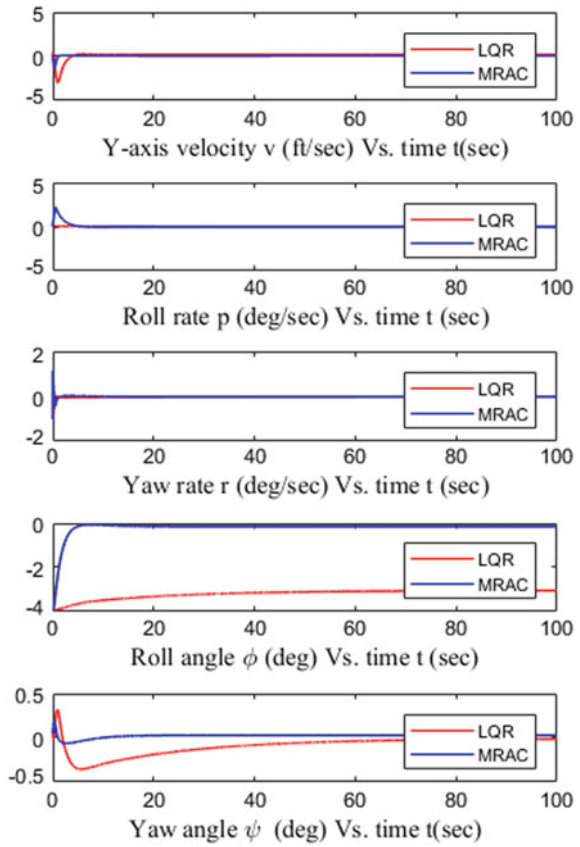
Fig. 3 Control signal for MRAC with rudder struck at 15° angle
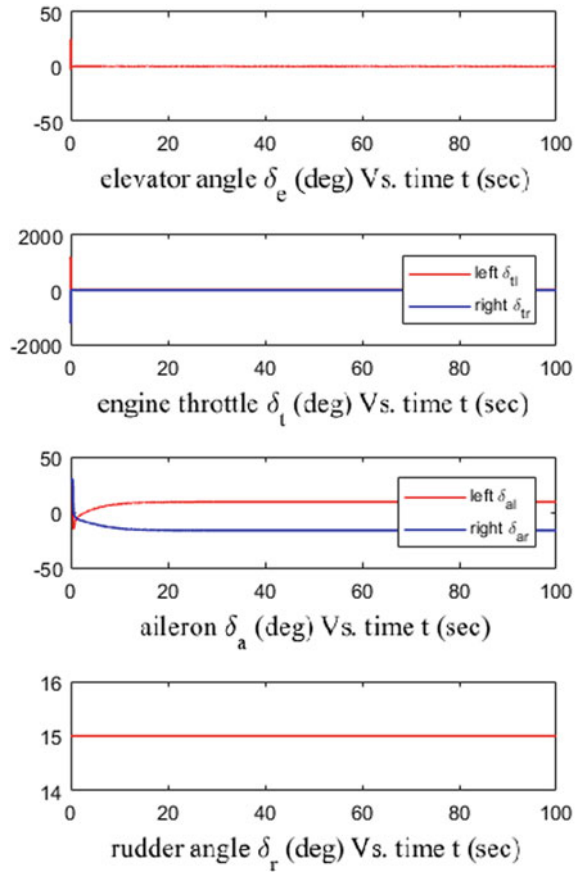
References

1. Burken, J.J., Burcham, F.W.: Flight-test results of propulsion-only emergency control system on MD-11 airplane. J. Guid. Control Dyn. 980–987 (1997)
2. Boskovic, J.D., Mehra, R.K.: A multiple model-based reconfigurable flight control system design. In: Proceedings of the 37th IEEE Conference on Decision and Control, vol. 4, IEEE (1998)
3. Boskovic, J.D., Mehra, R.K.: A multiple model-based reconfigurable flight control system design. In: Proceedings of the 37th IEEE Conference on Decision and Control, pp. 4503–4508 (1998)
4. Boskovic, J.D., Yu, S.H., Mehra, R.K.: Stable adaptive fault-tolerant control of over actuated aircraft using multiple models switching and tuning. In: Proceedings of AIAA Guidance, Navigation, and Control Conference and Exhibit, vol. 1, pp. 739–749 (1998)
5. Boskovic, J.D., Mehra, R.K.: Stable multiple model adaptive flight control for accommodation of a large class of control effector failures. In: Proceedings of the American Control Conference, pp. 1920–1924 (1999)
6. Zhang, Y.M., Jiang, J.: Integrated active fault-tolerant control using IMM approach. IEEE Trans. Aerosp. Electron. Syst. **37**(4), 1221–1235 (2001)
7. Boskovic, J.D., Mehra, R.K.: An adaptive scheme for compensation of loss of effectiveness of flight control effectors. In: Proceedings of the 40th IEEE Conference on Decision and Control, pp. 2448–2453 (2001)
8. Veillette, R.J., Medanic, J.V., Perkins, W.R.: Designs of reliable control systems. IEEE Trans. Autom. Control **37**(3), 290–304 (1992)
9. Liang, Y.W., Liaw, D.C., Lee, T.C.: Reliable control of nonlinear systems. IEEE Trans. Autom. Control **45**(4), 706–710 (2000)
10. Liao, F., Wang, J.L., Yang, G.H.: Reliable robust flight tracking control. An LMI approach. IEEE Trans. Control Syst. Technol. **10**(1), 76–89 (2002)
11. Zhao, Q., Jiang, J.: Reliable state-feedback control systems design against actuator failures. Automatica **30**(10), 1267–1272 (1998)
12. Liu, Y., et al.: Adaptive compensation of aircraft actuation failures using an engine differential model. IEEE Trans. Control Syst. Technol. **16**(5), 971–982 (2008)
13. Bryson, Jr., A.E.: Control of Spacecraft and Aircraft. Princeton University Press (2015)

Author Index